The Infrared & Electro-Optical Systems Handbook

VOLUME 7

Countermeasure Systems

David H. Pollock, *Editor*

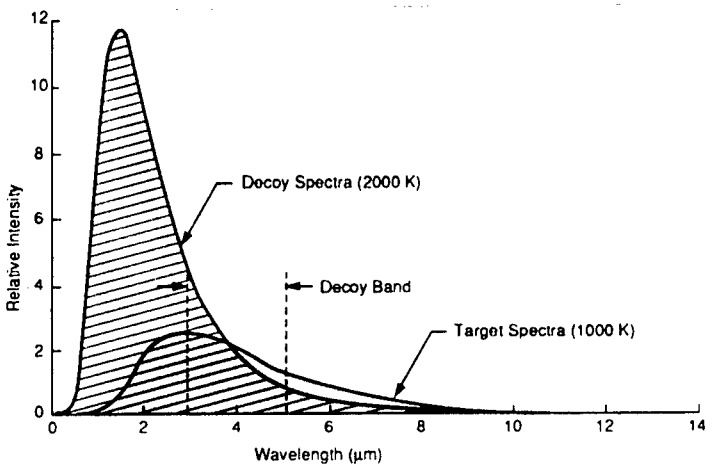

Countermeasure Systems

VOLUME 7

The Infrared and Electro-Optical Systems Handbook

The Infrared and Electro-Optical Systems Handbook

Joseph S. Accetta, David L. Shumaker, *Executive Editors*

Chapter 3. Optomechanical System Design, Daniel Vukobratovich
Chapter 4. Infrared Imaging System Testing, Gerald C. Holst
Chapter 5. Tracking and Control Systems, Robert E. Nasburg
Chapter 6. Signature Prediction and Modeling, John A. Conant, Malcolm A. LeCompte

■ **VOLUME 5.** **Passive Electro-Optical Systems,**
Stephen B. Campana, *Editor*

Chapter 1. Infrared Line Scanning Systems, William L. McCracken
Chapter 2. Forward-Looking Infrared Systems, George S. Hopper
Chapter 3. Staring-Sensor Systems, Michael J. Cantella
Chapter 4. Infrared Search and Track Systems, Joseph S. Accetta

■ **VOLUME 6.** **Active Electro-Optical Systems,** Clifton S. Fox, *Editor*

Chapter 1. Laser Radar, Gary W. Kamerman
Chapter 2. Laser Rangefinders, Robert W. Byren
Chapter 3. Millimeter-Wave Radar, Elmer L. Johansen
Chapter 4. Fiber Optic Systems, Norris E. Lewis, Michael B. Miller

■ **VOLUME 7.** **Countermeasure Systems,** David Pollock, *Editor*

Chapter 1. Warning Systems, Donald W. Wilmot, William R. Owens, Robert J. Shelton
Chapter 2. Camouflage, Suppression, and Screening Systems, David E. Schmieder, Grayson W. Walker
Chapter 3. Active Infrared Countermeasures, Charles J. Tranchita, Kazimieras Jakstas, Robert G. Palazzo, Joseph C. O'Connell
Chapter 4. Expendable Decoys, Neal Brune
Chapter 5. Optical and Sensor Protection, Michael C. Dudzik
Chapter 6. Obscuration Countermeasures, Donald W. Hoock, Jr., Robert A. Sutherland

■ **VOLUME 8.** **Emerging Systems and Technologies,**
Stanley R. Robinson, Editor

Chapter 1. Unconventional Imaging Systems, Carl C. Aleksoff, J. Christopher Dainty, James R. Fienup, Robert Q. Fugate, Jean-Marie Mariotti, Peter Nisenson, Francois Roddier
Chapter 2. Adaptive Optics, Robert K. Tyson, Peter B. Ulrich
Chapter 3. Sensor and Data Fusion, Alan N. Steinberg
Chapter 4. Automatic Target Recognition Systems, James W. Sherman, David N. Spector, C. W. "Ron" Swonger, Lloyd G. Clark, Edmund G. Zelnio, Terry L. Jones, Martin J. Lahart
Chapter 5. Directed Energy Systems, Gary Golnik
Chapter 6. Holography, Emmett N. Leith
Chapter 7. System Design Considerations for a Visually-Coupled System, Brian H. Tsou

Copublished by

Infrared Information Analysis Center
Environmental Research Institute of Michigan
Ann Arbor, Michigan USA

and

SPIE OPTICAL ENGINEERING PRESS
Bellingham, Washington USA

Sponsored by

Defense Technical Information Center, DTIC-DF
Cameron Station, Alexandria, Virginia 22304-6145

Countermeasure Systems

David H. Pollock, *Editor*
David H. Pollock Consultants, Inc.

VOLUME 7

The Infrared and Electro-Optical Systems Handbook

Joseph S. Accetta, David L. Shumaker, *Executive Editors*
Environmental Research Institute of Michigan

Library of Congress Cataloging-in-Publication Data

The Infrared and electro-optical systems handbook / Joseph S. Accetta, David L. Shumaker, executive editors.
p. cm.
Spine title: IR/EO systems handbook.
Cover title: The Infrared & electro-optical systems handbook.
Completely rev. ed. of: Infrared handbook. 1978
Includes bibliographical references and indexes.
Contents: v. 1. Sources of radiation / George J. Zissis, editor — v. 2. Atmospheric propagation of radiation / Fred G. Smith, editor — v. 3. Electro-optical components / William D. Rogatto, editor — v. 4. Electro-optical systems design, analysis, and testing / Michael C. Dudzik, editor — v. 5. Passive electro-optical systems / Stephen B. Campana, editor — v. 6. Active electro-optical systems / Clifton S. Fox, editor — v. 7. Countermeasure systems / David Pollock, editor — v. 8. Emerging systems and technologies / Stanley R. Robinson, editor.
ISBN 0-8194-1072-1
1. Infrared technology—Handbooks, manuals, etc. 2. Electrooptical devices—Handbooks, manuals, etc. I. Accetta, J. S. II. Shumaker, David L. III. Infrared handbook. IV. Title: IR/EO systems handbook. V. Title: Infrared & electro-optical systems handbook.
TA1570.I5 1993
621.36'2—dc20 92-38055
CIP

Copublished by

Infrared Information Analysis Center
Environmental Research Institute of Michigan
P.O. Box 134001
Ann Arbor, Michigan 48113-4001

and

SPIE Optical Engineering Press
P.O. Box 10
Bellingham, Washington 98227-0010

PRINTED IN THE UNITED STATES OF AMERICA

Preface

The Infrared and Electro-Optical Systems Handbook is a joint product of the Infrared Information Analysis Center (IRIA) and the International Society for Optical Engineering (SPIE). Sponsored by the Defense Technical Information Center (DTIC), this work is an outgrowth of its predecessor, *The Infrared Handbook,* published in 1978. The circulation of nearly 20,000 copies is adequate testimony to its wide acceptance in the electro-optics and infrared communities. *The Infrared Handbook* was itself preceded by *The Handbook of Military Infrared Technology.* Since its original inception, new topics and technologies have emerged for which little or no reference material exists. This work is intended to update and complement the current *Infrared Handbook* by revision, addition of new materials, and reformatting to increase its utility. Of necessity, some material from the current book was reproduced as is, having been adjudged as being current and adequate. The 45 chapters represent most subject areas of current activity in the military, aerospace, and civilian communities and contain material that has rarely appeared so extensively in the open literature.

Because the contents are in part derivatives of advanced military technology, it seemed reasonable to categorize those chapters dealing with systems in analogy to the specialty groups comprising the annual Infrared Information Symposia (IRIS), a Department of Defense (DoD) sponsored forum administered by the Infrared Information Analysis Center of the Environmental Research Institute of Michigan (ERIM); thus, the presence of chapters on active, passive, and countermeasure systems.

There appears to be no general agreement on what format constitutes a "handbook." The term has been applied to a number of reference works with markedly different presentation styles ranging from data compendiums to tutorials. In the process of organizing this book, we were obliged to embrace a style of our choosing that best seemed to satisfy the objectives of the book: to provide derivational material data, descriptions, equations, procedures, and examples that will enable an investigator with a basic engineering and science education, but not necessarily an extensive background in the specific technology, to solve the types of problems he or she will encounter in design and analysis of electro-optical systems. Usability was the prime consideration. In addition, we wanted each chapter to be largely self-contained to avoid time-consuming and tedious referrals to other chapters. Although best addressed by example, the essence of our handbook style embodies four essential ingredients: a brief but well-referenced tutorial, a practical formulary, pertinent data, and, finally, example problems illustrating the use of the formulary and data.

The final product represents varying degrees of success in achieving this structure, with some chapters being quite successful in meeting our objectives and others following a somewhat different organization. Suffice it to say that the practical exigencies of organizing and producing a compendium of this magnitude necessitated some compromises and latitude. Its ultimate success will be judged by the community that it serves. Although largely oriented toward system applications, a good measure of this book concentrates on topics endemic and fundamental to systems performance. It is organized into eight volumes:

Volume 1, edited by George Zissis of ERIM, treats sources of radiation, including both artificial and natural sources, the latter of which in most military applications is generally regarded as background radiation.

Volume 2, edited by Fred Smith of OptiMetrics, Inc., treats the propagation of radiation. It features significant amounts of new material and data on absorption, scattering, and turbulence, including nonlinear propagation relevant to high-energy laser systems and propagation through aerodynamically induced flow relevant to systems mounted on high-performance aircraft.

Volume 3, edited by William Rogatto of Santa Barbara Research Center, treats traditional system components and devices and includes recent material on focal plane array read-out electronics.

Volume 4, edited by Michael Dudzik of ERIM, treats system design, analysis, and testing, including adjunct technology and methods such as trackers, mechanical design considerations, and signature modeling.

Volume 5, edited by Stephen Campana of the Naval Air Warfare Center, treats contemporary infrared passive systems such as FLIRs, IRSTs, IR line scanners, and staring array configurations.

Volume 6, edited by Clifton Fox of the Night Vision and Electronic Sensors Directorate, treats active systems and includes mostly new material on laser radar, laser rangefinders, millimeter-wave systems, and fiber optic systems.

Volume 7, edited by David Pollock, consultant, treats a number of countermeasure topics rarely appearing in the open literature.

Volume 8, edited by Stanley Robinson of ERIM, treats emerging technologies such as unconventional imaging, synthetic arrays, sensor and data fusion, adaptive optics, and automatic target recognition.

Acknowledgments

It is extremely difficult to give credit to all the people and organizations that contributed to this project in diverse ways. A significant amount of material in this book was generated by the sheer dedication and professionalism of many esteemed members of the IR and EO community who unselfishly contributed extensive amounts of precious personal time to this effort and to whom the modest honorarium extended was scarcely an inducement. Their contributions speak elegantly of their skills.

Directly involved were some 85 authors and editors from numerous organizations, as well as scores of technical reviewers, copyeditors, graphic artists, and photographers whose skill contributed immeasurably to the final product.

We acknowledge the extensive material and moral support given to this project by various members of the managements of all the sponsoring and supporting organizations. In many cases, organizations donated staff time and internal resources to the preparation of this book. Specifically, we would like to acknowledge J. MacCallum of DoD, W. Brown and J. Walker of ERIM, and J. Yaver of SPIE, who had the foresight and confidence to invest significant resources in the preparation of this book. We also extend our appreciation to P. Klinefelter, B. McCabe, and F. Frank of DTIC for their administrative support during the course of this program.

Supporting ERIM staff included Ivan Clemons, Jenni Cook, Tim Kellman, Lisa Lyons, Judy Steeh, Barbara Wood, and the members of their respective organizations that contributed to this project.

We acknowledge Lorretta Palagi and the publications staff at SPIE for a professional approach to the truly monumental task of transforming the manuscripts into presentable copy and the patience required to interact effectively with the authors.

We would like to pay special tribute to Nancy Hall of the IRIA Center at ERIM who administrated this at times chaotic project with considerable interpersonal skill, marshaling the numerous manuscripts and coordinating the myriad details characteristic of a work of this magnitude.

We properly dedicate this book to the people who created it and trust it will stand as a monument to their skills, experience, and dedication. It is, in the final analysis, a product of the community it is intended to serve.

Joseph S. Accetta
David L. Shumaker
Ann Arbor, Michigan

January 1993

Notices and Disclaimer

This handbook was prepared by the Infrared Information Analysis Center (IRIA) in cooperation with the International Society for Optical Engineering (SPIE). The IRIA Center, Environmental Research Institute of Michigan, is a Defense Technical Information Center-sponsored activity under contract DLA-800-C-393 and administrated by the Defense Electronics Supply Center, Defense Logistics Agency.

This work relates to the aforementioned ERIM contract and is in part sponsored by the Department of Defense; however, the contents do not necessarily reflect the position or the policy of the Department of Defense or the United States government and no official endorsement should be inferred.

The use of product names does not in any way constitute an endorsement of the product by the authors, editors, Department of Defense or any of its agencies, the Environmental Research Institute of Michigan, or the International Society for Optical Engineering.

The information in this handbook is judged to be from the best available sources; however, the authors, editors, Department of Defense or any of its agencies, the Environmental Research Institute of Michigan, or the International Society for Optical Engineering do not assume any liability for the validity of the information contained herein or for any consequence of its use.

Contents

Introduction

This volume is devoted to the technologies that deny an adversary the use of the optical and infrared portions of the electromagnetic spectrum. Conversely, the material contained in the following chapters describes the exploitation of this same spectrum for achieving a tactical advantage.

Military forces all over the world are placed in jeopardy by sophisticated weaponry, which is now available to more governments and peoples than ever before. The proliferation of hand-held infrared guided surface-to-air missiles makes any aircraft in the world a potential target. A single aircraft today represents a fly-away cost comparable to a significant fraction of the total aircraft costs the United States incurred during World War II.

Combine the threat aspect with the cost of platforms and the result should be motivation to protect platforms from infrared threats. As a consequence, equipment is needed that can increase the survivability of platforms in a militarily hostile environment. This volume is dedicated to providing a primer for those interested in designing and developing these types of survivability equipment.

The volume is made up of six chapters. Chapter 1 is a description of warning systems. This includes missile warning, laser warning, and threat platform detection. A great deal of the material is associated with clutter suppression, the detection of targets in a background (and foreground) of competing signals. The interest and practicability of modern warning systems is derived from the application of microprocessors to the problem of clutter suppression and false alarm reduction. In the early 1960s there was a flurry of activity to include infrared warning systems on the F-111, B-52, and other contemporary platforms. It soon became apparent that the system operator, sometimes the pilot, could not distinguish the target signal from the background-generated signals. As a consequence, infrared warning systems fell into a period of very limited use. It was not until the 1980s and the advent of heavy emphasis on signal processing by microprocessors that infrared and electro-optical warning systems were again funded for development. Today there are several systems in production or already deployed. These include the AN/AVR-2 laser detection set and the AN/AAR-44 and AN/AAR-47 missile warning systems. Also, many systems are in development for the F-22 and B-2.

Warning systems are the beginning of the countermeasure process. This element of the self-protection suite determines threat presence, threat bearing, and, under certain conditions, degree of lethality. With this information the operator and/or pilot can take effective evasive action and activate countermeasures. Some systems automate this process. The effectiveness of warning has been well documented. Statistical data from Vietnam and the various Israeli wars have shown that in only 20% of the aircraft losses from surface-to-air

missiles were the pilots aware of the missile. The implication is that a warning could significantly reduce aircraft losses.

Chapter 1, prepared by Donald W. Wilmot, William R. Owens, and Robert J. Shelton of Georgia Tech, was enhanced by the review and contributions of many people within the warning systems community. Louis A. Williams, Jr., of Louis A. Williams and Associates; Jack H. Parker, Jr., of the Air Force Wright Laboratories; Joseph J. Bastian and associates of Ball Systems Engineering Division; and C. E. Newsom and associates of SciTec, Inc., contributed material in several critical areas. In addition, several individuals, including David E. Schmieder and Edward M. Patterson of Georgia Tech, consulted with the authors on various key issues. Finally, a number of senior researchers contributed to the final product by reviewing the various drafts and offering a variety of suggestions that have improved the chapter. These included Richard J. Manning, Neal Butler, and their colleagues at Loral Infrared and Imaging Systems; Wayne Paige, Robert Basta, and David Cunningham from Hughes Danbury Optical Systems; Wayne DeVilbiss from U.S. Army CECOM; Richard B. Cunningham and Richard B. Sanderson of the U.S. Air Force Wright Laboratories; and many others.

Chapter 2, Camouflage, Suppression, and Screening Systems, provides an understanding of the techniques needed to mask a platform by blending into its background, thus reducing or eliminating the threat's ability to acquire the platform as a target. This can be achieved through contrast reduction or paint schemes to obscure shape. During World War II paint schemes were used very effectively to reduce the ability to sight ships at sea visually. Also during World War II a technique was developed to allow antisubmarine aircraft to avoid detection by surfaced submarines. This technique was called *Yehudi.* Lights were added to the leading edge of the wings of antisubmarine bombers. The lights replaced the background illumination that the aircraft were blocking, reducing the aircraft-to-background contrast. The reduced contrast delayed visual detection of the aircraft until the submarines had insufficient time to submerge.

Chapter 2 describes methods for reducing platform detection in the visible and infrared bands of the spectrum. Many modern weapons systems depend on visual sighting for either their primary or secondary means of target acquisition. This chapter provides the technical foundation for the use of emissivity and reflectivity control for degrading the contrast, which provides the basis for the detection and acquisition by these systems.

The authors of Chapter 2 are David E. Schmieder of Georgia Tech Research Institute and Grayson W. Walker of the U.S. Army Belvoir Research, Development and Engineering Center.

Chapter 3, Active Infrared Countermeasures, explains the technology for protecting platforms from heat-seeking missiles, which obtain their guidance inputs from the infrared signature of the target platform. Active infrared countermeasures, in contrast to off-board expendable decoys, are on-board systems that utilize an active radiator to augment the signal that the missile receives from the platform engines and other radiating body parts. The active radiator can be derived from numerous sources: lasers, arc lamps, incandescent lamps, or cavities heated by burning fuel.

These types of systems evolved during the mid-1960s to respond to the terrible toll infrared missiles were imposing on U.S. fixed-wing and rotary-winged

aircraft in South Vietnam. The development of these systems by Sanders Associates (now Lockheed-Sanders), Northrop (then Hallicrafters), and Xerox Electro-Optical Systems (now Loral EOS) was one of the true technology successes to come out of the Vietnam war. These efforts were the direct antecedents of the systems now in inventory, the AN/AAQ-4, AN/ALQ-123, AN/AAQ-8, AN/ALQ-132, AN/ALQ-144, AN/ALQ-147, and AN/ALQ-157. The primary applications for these systems today are to protect the aircraft most susceptible to surface-to-air shoulder-fired missiles, the slow fixed-wing transport aircraft and low-flying helicopters. Every U.S. Army and Marine Corps helicopter is equipped with either the AN/ALQ-144 or AN/ALQ-157.

The authors of Chapter 3 are Charles J. Tranchita, Kazimieras Jakstas, and Robert Palazzo of Northrop Defense Systems and Joseph O'Connell of U.S. Army CECOM.

Chapter 4, Expendable Decoys, addresses flare technology to defeat infrared guided missiles. The active infrared countermeasure systems discussed in Chapter 3 required modulation schemes to be applied to the output of the active radiating source to provide a time-varying signal at the missile seeker. This signal would then interact with the seeker reticle modulated signal. The result generates false guidance commands to the missile aerodynamic control surfaces. Expendable decoys, in contrast, generate a very high intensity radiation source resulting from a chemical or pyrotechnic reaction. The reaction usually involves the burning of magnesium powder in the presence of other constituents, which creates magnesium fluoride and magnesium oxide, providing very high signals in the CO_2 and H_2O bands in the mid-infrared spectrum. The high signals received by the seeker mask the defended platform's much lower radiated signals and the missile is successfully decoyed away from the aircraft.

The decoy is ejected away from the defended platform by an explosive charge drawing the threat away. Much of the chapter discussion is devoted to the science of generating the appropriate spectral and temporal characteristics to cause the missile seeker to accept the decoy signals over those from the defended platform. Flare decoys are the primary defense against heat-seeking missiles for many high-performance fighter aircraft in addition to helicopters and slower flying transport aircraft.

Chapter 4, prepared by Neal Brune of Tracor Aerospace, Inc., incorporates contributions on flare chemistry from Carl Dinerman, Tracor Aerospace, Inc. Also, thanks are owed to Bernard Douda, NWSC Crane, and Joseph Koesters, Wright Laboratories, for reviewing the chapter and making very useful comments and suggestions.

The fifth chapter is on optical and sensor protection. With the advent of laser systems for military applications there is a very real possibility of intentional and unintentional illumination of optical sensors by lasers. Due to the focusing properties of optics, this laser energy can be intensified such that lens elements and/or detectors (even the eye) in the focal plane can be damaged or destroyed. This chapter discusses, in a generic fashion, what steps can be taken in the sensor design process to incorporate protection.

The author of Chapter 5 is Michael Dudzik of the Environmental Research Institute of Michigan.

The sixth chapter of this volume is on obscuration countermeasures. This chapter presents the fundamentals of the absorbing and scattering of radiation

through obscuring media. This concept of countermeasures is to lay down a screen between you and your adversary. The obscuring medium can be tailored to be spectrally selective such that some sensors will be affected and others will not. In addition to intentional obscuring screen media, there is the impact of smoke and dust due to battle. During World War II smoke screens were used extensively at sea by ships as well as by tanks during armored forces engagements.

Chapter 6 was prepared by Donald W. Hoock, Jr., and Robert A. Sutherland of the U.S. Army Research Laboratory, Battlefield Environment Directorate.

This infrared countermeasures volume is intended to provide an introduction to the topic. Obviously not all the aspects of each subject could be presented due to security classification, but sufficient material has been made available to provide any interested reader the means to seek additional information elsewhere. In other words, this volume is an excellent beginning for anyone learning about infrared countermeasures. If used in that context the authors will have achieved their objective.

David H. Pollock
Westwood, New Jersey

January 1993

CHAPTER 1

Warning Systems

Donald W. Wilmot
William R. Owens
Robert J. Shelton
Georgia Tech Research Institute
Atlanta, Georgia

CONTENTS

1.1 INTRODUCTION

The function of a *warning* system is to detect *threats* approaching the system and to alert the protected entity (nation, aircraft, ship, ground vehicle, soldier) about a near-term danger. Thus, it differs in philosophy, and in the applied technologies, from reconnaissance and surveillance, which involve the longer term observation and characterization of a potential adversary, and from tracking and/or fire control, which involve detailed concentration on a detected threat.

Typical warning scenarios involve (1) a platform, or area, to be protected; (2) an immediate danger; and (3) an environment containing a variety of benign objects/events that must be distinguished from the potential threat. Usually a warning device is continuously operative, has a wide field of regard, and covers a broad range of threat parameters.

The warning function involves continuous observation of the activities within its environment, detection/recognition of threats, detailed characterization of the threat, and alerting of its *platform*. Threat characterization must be of high reliability to avoid disturbing the platform with spurious alarms; also, it must be sufficient to enable the platform to initiate appropriate responsive actions. Once the warning system has alerted its platform to the impending threat, characterized it, and located it, the subsequent defensive action passes to other elements in the platform defensive/offensive suite.

1.1.1 Types of Warning Receivers

There are many types of warning equipments and scenarios. In principle, these include such devices as fire alarms, nuclear reactor safety alarms, and laser radars. However, the scope of the present treatment is restricted to passive systems that warn a platform about an attack in process from an adversary platform. In the cases treated herein, the attack is characterized, at least in part, by the emission of visual, infrared, or laser radiation by the attacker. Thus, all systems addressed herein can be referred to as warning *receivers*.

Warning receivers can be characterized based on their general application as *tactical* and *strategic*, and they can be further differentiated by whether the threat emissions on which they operate are intentional or inadvertent. An aircraft-mounted missile warning receiver watching for approaching surface-to-air missiles (SAMs) is a common tactical system. Such systems typically protect individual vehicles, whereas strategic warning receivers are those that protect a large area, or nation. A satellite-borne IR warning receiver, designed to detect intercontinental ballistic missiles (ICBMs), is an obvious strategic example. Traditional IR warning receivers were designed to operate on the inadvertent emissions from threat missiles. However, as laser fire control systems and laser weapons have entered the military inventory, laser warning receivers, analogous to microwave radar warning receivers (RWRs), have evolved as well.

This chapter addresses strategic and tactical warning receivers operating on the inadvertent emissions of strategic and tactical aircraft and missiles throughout the optical spectrum from the ultraviolet to the far infrared and introduces related systems operating within the millimeter and microwave

regions. It also addresses laser warning receivers (LWRs) operating within this same spectrum.

Typical warning receivers addressed in detail herein include (1) tactical missile warning receivers (MWRs) operating over the entire optical spectrum on the plume and body emissions of tactical missiles, (2) satellite-borne systems that detect ICBM launches and strategic aircraft against the earth background, and (3) laser warning receivers for aircraft, ground vehicle, sea-based, and space-based platforms.

1.1.2 Distinctions among MWRs, FLIRs, and IRSTSs

Although warning receivers often perform sophisticated spatial analyses on the candidate threat and its surrounding environment, and although most such systems provide target position data, they are not usually imaging systems in the classical sense of providing a pictorial display to the system operator. Rather they process the scene data, test candidate threats against preprogrammed criteria, and then alert the operator to the nature and direction of an impending attack. If the operator response requires the use of imagery, it is provided by some other element of the defensive/offensive suite, such as the forward looking infrared systems (FLIRs) and the infrared search and track sets (IRSTSs). FLIRs are usually regarded as *IR televisions* in that their function is to provide a detailed target scene (of limited field of view) to the operator, whereas IRSTSs are often regarded as *passive radars* because their function is to provide a wide field of coverage at rapid scan rates and relatively low resolution. As the angular resolution of IR warning receivers improves, there will be less distinction between the IR warning receivers and the IRSTSs. The MWR also differs from the typical IRSTS on the basis of its military mission—the MWR is always a component of the platform defensive system, whereas the IRSTS may be an element of the offensive fire control suite.

1.1.3 Plan of the Chapter

Section 1.2 of this chapter outlines the scope of the warning receiver treatment herein and establishes the illustrative examples and measures of effectiveness for the various types of receivers addressed.

Section 1.3 presents the phenomenology of the target and background observables. It addresses the specific issues needed for subsequent warning receiver performance calculations, while relying heavily on signature, atmospheric, and background data developed in preceding chapters.

Section 1.4 presents the analytical framework for warning receiver detection calculations. An overview of the general theory of signal detection in the presence of noise is presented. Specific statistical models commonly encountered in the analysis of warning receivers are described, and sample SNR and detection calculations are included. A variety of signal detection concepts are introduced, and some of the practical problems associated with real detection systems are also discussed.

Section 1.5 presents the detailed analysis of tactical missile warning receivers by means of various example calculations and then outlines the practical equipment trade-offs and constraints for key applications.

Section 1.6 presents an overview of space-based strategic warning systems. Aspects of strategic warning systems that distinguish them from tactical systems are emphasized in this section. Some of the key issues associated with satellite platforms, strategic targets, earth backgrounds, and sensor testing are discussed. A sample system design analysis of a strategic missile warning system sensor is also presented in this section.

Section 1.7 presents the detailed analysis of laser warning receivers by means of various example calculations and then outlines the equipment tradeoffs and constraints involved in such applications.

Table 1.1 lists the symbols used in the chapter and provides the nomenclature and units that apply to each symbol.

Table 1.1 Symbols, Nomenclature, and Units

Symbol	Nomenclature	Units
a	Length of semimajor axis of satellite orbit	k
a	Solar absorptivity coefficient	dimensionless
A	Area	m^2
A_c	Effective collecting area of optical system	m^2
A_d	Detector area	m^2
A_T	Projected physical area of target	m^2
AGL	Above ground level	m
B_{IF}	IF amplifier bandwidth	Hz
B_N	Amplifier bandwidth	Hz
c	Heat capacity	J/g
c	Speed of light in vacuum	m/s
C	Contrast	various
C_{ij}	Cost of choosing hypothesis H_i when H_j is true	dimensionless
C_n^2	Atmospheric factor related to refractive index	$m^{-2/3}$
d	Diameter	m
D	Antenna diameter	m
D^*	Detector specific detectivity	cm $Hz^{1/2}$ W^{-1}
d_g	Grating spacing	m
$D_k(x)$	Difference image intensity, frame k	dimensionless
e	Charge of an electron	C
E	Irradiance	W/m^2
$E(R)$	In-band target irradiance at entrance aperture of sensor when the target is at a slant range of R	W/m^2
f	Frequency	Hz
f	Spatial frequency	cycles/rad
f	Effective focal length	m
f	Solar radiative flux	W/m^2
F	Radiometer noise figure	dimensionless
$F\#$	Ratio of focal length to diameter	dimensionless
FAR	False alarm rate	s^{-1}
f_0	Bandwidth of an ideal low pass filter	Hz

(continued)

Table 1.1 *(continued)*

Symbol	Nomenclature	Units
G	Optical gain	dimensionless
h	Altitude above the surface of the earth	k
$H(f)$	Filter transfer function	dimensionless
H_1	Target present hypothesis	dimensionless
H_0	Target not present hypothesis	dimensionless
$H_p(\mathbf{f})$	Fourier transform of $h_p(\mathbf{x})$ evaluated at spatial frequency $\mathbf{f}$	dimensionless
$h_p(\mathbf{x})$	Linear weighting function	dimensionless
I	Current	A
I_B	Average (dc) background current	A
$I_k(x)$	Intensity in frame k at position x	dimensionless
I_{rms}	Root-mean-square value of ac portion of noise	A
I_s	Signal current	A
I_T	Threshold current	A
I	Radiant intensity	W/sr
I_{app}	Apparent in-band radiant intensity	W/sr
I_0	Source intensity	W/sr
k	Radiant intensity/thrust ratio	$\text{W sr}^{-1}\text{ N}^{-1}$
k	Wave number ($1/\lambda$)	m^{-1}
k	Thermal conductivity	$\text{W m}^{-1}\text{ K}^{-1}$
k	Boltzmann's constant	J/K
K_R	Radiometer constant (1 to $3\sqrt{2}$, depends on scan)	dimensionless
L_{fp}	Length of a detector footprint	m
LUX	Illuminance	lumens/m^2
M_n	Joint probability density function normalization factor	dimensionless
n	Index of refraction	dimensionless
N	Thrust of missile engine	N
N	Number of target-sized cells in image	dimensionless
N_B	Apparent radiance of the background	$\text{W m}^{-2}\text{ sr}^{-1}$
N_d	Number of detectors	dimensionless
NEI	Noise equivalent irradiance; input irradiance	W/m^2
NEP	Noise equivalent power	W
N_{eq}	Number of noise equivalent charge carriers	dimensionless
NET	Noise equivalent target	W/sr
N_T	Average radiance of a target	$\text{W m}^{-2}\text{ sr}^{-1}$
$N(\mathbf{x})$	Scene radiance at position $\mathbf{x}$ in the image plane	$\text{W m}^{-2}\text{ sr}^{-1}$
P	Power	W
$P(n)$	Probability of n photons arriving in a measurement	dimensionless
$p(x_1, x_2, \ldots, x_n)$	Joint probability density function observed values $\{x_1, x_2, \ldots, x_n\}$	dimensionless
P_D	Probability of detection	dimensionless
P_{FA}	Probability of false alarm	dimensionless
$p_N(I)\,dI$	Probability that the noise waveform results in a current between I and $I + dI$	dimensionless
P_0	Probability of a threshold exceedance when a target is not present	dimensionless
$p_s(I)$	Probability density function for signal plus noise	dimensionless

Table 1.1 *(continued)*

Symbol	Nomenclature	Units
Q_1	Probability of choosing H_0 when H_1 is true	dimensionless
Q_e	Energy	J
Q_0	Probability of choosing H_1 when H_0 is true	dimensionless
r	Distance variable	m
R	Slant range from the sensor to the target	m
R_1	Region of decision space corresponding to hypothesis H_1	m
R_d	Detector resistance	Ω
R	Detector responsivity	A/W
R_λ	Detector responsivity at wavelength λ	A/W
R_e	Radius of the earth	km
R_0	Region of decision space corresponding to hypothesis H_0	m
R_0	Radius of a circular orbit	km
r_t	Surface temperature correlation length	m
R_v	Visibility range	km
SCR	Signal-to-clutter ratio	dimensionless
SNR	Peak signal-to-rms-noise ratio	dimensionless
t	Time	s
T	Temperature	°C or K
T_a	Antenna temperature	K
t_c	Coherence time	s
t_d	Detector dwell time	s
T_f	Available surveillance volume scan time	s
t_i	Integration time	s
T_m	Mean time between successive maxima of a noise waveform	dimensionless
TNR	Threshold-to-rms-noise ratio	dimensionless
T_0	Standard temperature (290 K)	K
T_p	Orbital period	s
TTI, TTG	Time to intercept, time to go	s
v	Orbital velocity	m/s
V	Visibility	km
V_p	Peak pulse signal amplitude	V
$v(t)$	Signal waveform in a scanning sensor	V
v_g	Speed of a satellite subpoint over the surface of the earth	m/s
V_{mc}	Missile closing velocity	m/s
w	Wind velocity	m/s
$W(\mathbf{f})$	Wiener spectrum at spatial frequency $\mathbf{f}$	dimensionless
$\mathbf{x},\mathbf{y}$	Position vectors in the image plane of a sensor	m
x	Dimension variable	m
x_c	Coherence length	m
y	Dimension variable	m
z	Dimension variable	m
Greek:		
$\langle x_j \rangle$	Ensemble average of x_j	dimensionless

(continued)

Table 1.1 *(continued)*

Symbol	Nomenclature	Units
α	Attenuation coefficient or extinction coefficient	km^{-1}
δ	Absolute humidity	g/m^3
$\Delta\lambda$	Optical bandwidth or spectral linewidth	μm, Å
Δf	Electronic bandwidth or noise equivalent bandwidth	Hz
Δl_c	Effective coherence length	m
Δt_c	Effective coherence time	s
ΔT_T	Target radiometric contrast	K
ε	Emissivity	dimensionless
ζ	Output of a signal processor	dimensionless
η	Radiation efficiency	dimensionless
η	Noise spectral density	A^2/Hz
η_A	Aperture efficiency	dimensionless
η_s	Scan efficiency factor	dimensionless
θ	Zenith angle	deg
θ	Linear angle	rad
κ	Threshold setting	dimensionless
λ	Wavelength	μm
$t\Lambda(x_1, x_2, \ldots, x_n)$	Likelihood ratio	dimensionless
μ	Gravitational parameter	dimensionless
μ	Magnetic permeability	$Wb\ A^{-1}\ m^{-1}$
$\boldsymbol{\mu}$	Inverse of the covariance matrix $\boldsymbol{\Phi}$	dimensionless
μ_1	Average number of photons arriving, target present	dimensionless
μ_{jk}	Elements of the matrix $\boldsymbol{\mu}$	dimensionless
μ_0	Average number of photons arriving, no target	dimensionless
μ_p	Average photon arrival rate	dimensionless
ν	Frequency	Hz
ρ	Reflectivity (diffuse hemispheric)	dimensionless
ρ_0	Lateral coherence diameter	cm
σ	Standard deviation	dimensionless
σ	Water surface slope standard deviation	dimensionless
σ	Stephan-Boltzmann constant	$W\ m^{-2}\ K^{-4}$
σ	Electrical conductivity	$\Omega^{-1}\ m^{-1}$
σ^2	Variance	dimensionless
σ_i	Standard deviation of counts in cell i	dimensionless
τ	Transmission loss	dimensionless
τ	Detector dwell time (also t)	s
$\tau_a(R)$	Atmospheric transmission at a slant range R	dimensionless
τ_o	Effective transmission of an optical system	dimensionless
υ	Pulse visibility factor	dimensionless
ϕ	Plane angle	rad
Φ	Latitude	deg
$\boldsymbol{\Phi}$	Covariance matrix	dimensionless
$\lvert\det \boldsymbol{\Phi}\rvert$	Determinant of the matrix $\boldsymbol{\Phi}$	dimensionless
$X(r,t)$	Characteristic scintillation	dimensionless
Ω	Solid angle subtended by sensor FOV or radiation solid angle	sr

1.2 SCOPE

1.2.1 Spectral Ranges Covered

1.2.1.1 Target Passive Signatures. Although the emphasis in this handbook is on infrared radiation and technology, this section includes a consideration of the broader optical portion of the electromagnetic spectrum, ranging from ultraviolet through visible and infrared and into the near-millimeter-wave region. The latter is limited to passive radiometric considerations and does not address millimeter-wave radars. The breadth of spectral consideration is determined by the fact that passive information is available in all of these regions to distinguish potential man-made threats from natural backgrounds.

At the core of our discussions are the mid- and long-wavelength infrared emissions from heated missile parts and exhaust products. These represent the most consistently available and detectable signature information. Other significant signature features include reflected visible and near-infrared solar radiation, exhaust plume emissions in the ultraviolet and visible regions, cold sky reflections in the millimeter-wave regions, and negative contrast ultraviolet and visible signatures against a bright daylight sky.

The spectral nomenclature used in this section is indicated in Table 1.2. The regions named are consistent with current common usage.

1.2.1.2 Laser Threats. Laser warning receivers must operate over the entire spectrum of military fire control and weapon lasers. In general, this encompasses the spectral range from the UV to the far IR. However, specific application requirements and historical laser evolution result in various specific lasers being dominant in individual scenarios.[1]

During the 1960s and the 1970s military lasers consisted of solid state ruby, neodymium-doped glass (Nd:glass) and yttrium aluminum garnet (Nd:YAG), and gallium arsenide (GaAs) materials. The ruby and Nd:glass were used for rangefinders, whereas the Nd:YAG became the standard for laser designators (which often also resulted in its use for ranging as well). The semiconductor GaAs laser found applications in communications and shorter range rangefinding situations. By the 1980s, carbon dioxide (CO_2) lasers were in use as rangefinders, and by the end of the 1980s both GaAs and CO_2 lasers were being applied in laser beam-rider systems.

At the beginning of the 1990s there are a rich variety of lasers under development for a variety of military applications.[2] These include eyesafe lasers in the 1- to 3-μm band to replace the visually dangerous ruby and neodymium systems; tunable visual and near-IR lasers to reduce the countermeasure vulnerability of the fixed frequency ruby and neodymium lasers; 3- to 5-μm lasers for heat-seeking missile and IRSTS countermeasures, 8- to 12-μm lasers for FLIR countermeasures; CO_2 and other high-coherence laser systems for laser radar and communications applications; and high-power CO_2, chemical, excimer, and free-electron lasers for weapons applications. Figure 1.1 indicates the spectral range covered by various types of lasers.

Table 1.2 Spectral Nomenclature

Band Name	Wavelengths (micrometers)
Vacuum ultraviolet	0.05 - 0.20
Short ultraviolet (UV-C)	0.20 - 0.29
Solar blind ultraviolet	0.25 - 0.28
Middle wave ultraviolet (UV-B)	0.29 - 0.32
Long wave ultraviolet (UV-A)	0.32 - 0.40
Visible	0.40 - 0.70
Near infrared (NIR)	0.70 - 2.0
Short wave infrared	2.0 - 3.0
Middle wave infrared (nominal 3-5 μm)	3.0 - 6.0
Plume band	4.0 - 5.0
Blue spike band	4.1 - 4.3
Red spike band	4.3 - 4.6
Long wave (far) infrared (nominal 8-12 μm)	6.0 - 15.0
Extreme infrared	15.0 - 100
Near millimeter wave	100 - 1000
Millimeter wave	1000 - 10 000

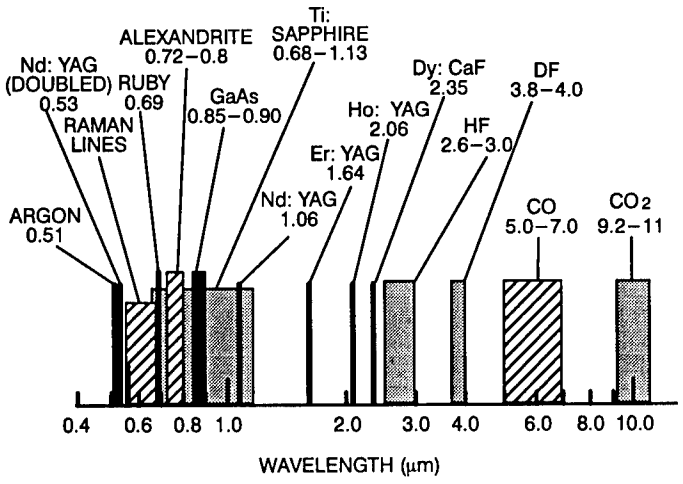

Fig. 1.1 Laser spectral range.

1.2.2 Illustrative Examples

Throughout the remainder of this chapter a few specific situations are used to illustrate the calculational procedures and typical values encountered. The examples have been chosen to be representative of three types of problems. The first example deals with a tactical situation involving short ranges and limited processing times. The second example is a strategic situation, with longer ranges and longer data collection and processing times. The third example is specific to laser warning receivers. The details of each situation are set forth in the following. Deviations from these baseline situations are explored to illustrate dependencies, but unless stated otherwise explicitly, the baseline conditions apply.

1.2.2.1 Tactical Situation. Tactical missile warning receivers can be used to warn against air-to-ground, surface-to-air, air-to-air, and air- (or surface-) to-surface missiles. Each presents a unique set of background clutter situations as well as threat approach angles and speeds. The case of airborne platforms defending against air-to-air or surface-to-air missiles presents one of the more challenging problems in terms of signatures, backgrounds, and reaction times.

The platform supporting the missile warning receiver in the example is a helicopter moving at 100 km/h at an altitude of 200 m. [This is approximately a speed of 65 knots at an altitude of 600 ft above ground level (AGL). We use SI units consistently in this chapter, although knots and feet are still in common use for speed and altitude.]

The missile is a surface-to-air missile with passive infrared guidance. It is launched at a range of 5 km from the helicopter and travels in the same direction as the helicopter. The missile is assumed to end its powered phase approximately midway along the trajectory to the target. During the powered phase of its flight, it has a signature of 1000 W/sr in the 3- to 5-μm spectral band.

The background seen by the warning receiver is a mixture of trees, grass, and bare earth below the horizon and clear sky above the horizon. It is near noon on a clear summer day at middle latitudes. Significant clutter can be expected below the horizon. Atmospheric conditions are those of the mid-latitude summer model used in LOWTRAN.[3] Table 1.3 lists atmospheric transmittance over several tactical ranges for some wavelength bands of interest. Two other helicopters are traveling in the same direction within a 2-km radius of the platform vehicle, and present possible false targets. Their signatures are 1000 W/sr each in the 3- to 5-μm band. Another missile has been launched independently against the more distant of the other two helicopters. The receiver must reject this missile as a nonthreat.

The instantaneous field of view of the warning receiver is such that the target is spatially unresolved at the time of detection and declaration. It is also assumed that the signature of the target is low enough to be comparable to the clutter level (i.e., the signal-to-clutter level is less than 10) in the band of interest after burnout. The platform of the MWR is unstable and moving, and the missile is moving against the background.

A hypothetical nodding spinball warning receiver with three lenses, similar to the one described in Sec. 1.5, is assumed for the tactical platform. The optical design parameters of the tactical warning receiver are assumed to be aperture

Table 1.3 Atmospheric Transmittances for Tactical Example

Range (km)	Wavelength Band			
	0.25 - 0.28 μm	2.0 - 3.5 μm	3.5 - 5.0 μm	8.0 - 12.0 μm
0.5	0.366	0.608	0.725	0.921
1.0	0.139	0.546	0.667	0.877
2.0	0.022	0.477	0.593	0.808
5.0	0.001	0.379	0.467	0.657
10	...	...	0.354	0.482
20	...	...	0.233	0.288

diameter 45 mm, $F\#$ 1.78, focal length 80 mm, and 70% optical transmission. A closed cycle Joule-Thompson cooled linear array of 10 PbSe detector elements, each 0.115 × 0.115 mm, with an array elemental center-to-center angular subtense of 1.75 mrad and an instantaneous field of view (IFOV) of 1.44 × 1.44 mrad provide an array elevation field of view of 1.0 deg. The D^* of the detector in the 3.0 to 5.0 band is 1×10^{10} W^{-1} cm $Hz^{1/2}$. The spinball scans a 15 × 6 deg (azimuth × elevation) field at a velocity of 4000 deg/s. This is a frame rate of 1.85/s or 48,500 pixels/s. Scan efficiency is 42%.

1.2.2.2 Strategic Situation. Electro-optical/infrared (EO/IR) strategic warning receivers might be used to provide warning against threats that range in size from large intercontinental ballistic missiles to small cruise missiles. Strategic aircraft (e.g., long-range bombers) are also potential targets for EO/IR strategic warning systems. Beyond providing warning against missile and aircraft attacks, strategic EO/IR sensors can also play a role in strategic surveillance, including ocean surveillance and surveillance of strategic relocatable targets (SRTs). Applications considered in this handbook are limited to strategic sensors designed to detect strategic missiles and aircraft.

To provide the wide-area coverage of distant threat volumes, strategic warning sensors are typically based on satellite platforms. The altitude of such platforms can be anywhere from approximately 100 km to tens of thousands of kilometers, depending on the application and design concept.

The spectral wavelength band in which an EO/IR strategic warning system might operate also depends on the specific application. Because the exhaust plumes of ICBMs and other large strategic missiles are intense infrared sources that radiate most strongly in the near- and mid-IR parts of the spectrum, near-

and mid-IR sensor concepts are usually considered for ICBM warning applications. There are, however, concepts that call for ICBM warning sensors to operate in the UV part of the spectrum. At the other end of the spectrum, long-wave infrared (LWIR) sensors may be the most appropriate for the detection of cruise missiles and strategic aircraft. For these types of targets, the IR radiation from engine exhaust plumes is often a relatively minor contributor to the overall IR signature. Thermal emission, peaking in the LWIR part of the spectrum, from relatively cool surfaces on the air vehicle, often dominate the IR signature of these targets.

Background signatures play an important role in the design of a strategic warning system. Even for the most intense strategic targets, background clutter might limit the performance of the system. Typically, the spatial extent of a strategic target is small compared to the size of the background area that contributes to the output of a detector. This area is called the detector footprint. Large detector footprints lead to large background signals that are a source of noise and clutter. For near-IR sensors, background solar clutter can mask the signals radiated by an ICBM. For LWIR sensors operating in the atmospheric windows, terrain clutter and cloud clutter can make the task of detecting strategic aircraft and cruise missiles very difficult. Consequently, the selection of a detector footprint size is a critical element in the design of a strategic sensor. The selection involves trade-offs among sensor altitude, optics size, number of detectors, spectral band, and clutter processing concepts. Typically, the footprint size (at the surface of the earth) that results from these trade-offs is of the order of 100 m to a kilometer or so, projected onto the earth's surface.

The EO/IR technology required to develop a strategic sensor is usually quite different from the technology associated with tactical sensor development. Because strategic sensors must detect targets at very long ranges and over large search fields, large optics (of the order of 1 m in diameter) and large focal plane arrays (hundreds of thousands of detectors) are usually required. Because they operate in space, there are unique power, cooling, communications, and support requirements. Operation in the radiation environment of space and testing, prior to deployment in space, are other important considerations in the development of strategic sensors.

1.2.2.3 Laser Warning System Scenario(s). Laser warning receivers are applicable to fixed-wing aircraft, helicopters, ground vehicles, ships, and satellites.[4] Functionally, they alert the platform to impending attack involving fire control, or weapon, lasers; they also may directly activate appropriate countermeasures.[5] There are two related, but inherently different, scenarios involving laser receivers: (1) self-protection (i.e., warning) and (2) general monitoring of the adjacent field of battle, termed electronic support measures (ESM) in the electronic warfare (EW) community. These two scenarios are illustrated in Figs. 1.2 and 1.3, respectively.

The laser warning receiver self-protection example of Fig. 1.2 consists of a heliborne laser designator (or rangefinder) illuminating a tank from a range of 2 km. The laser is assumed to be a 1.06-μm Nd:YAG system with an output energy of 150 mJ, a pulse duration of 30 ns, and a beam divergence (full angle)

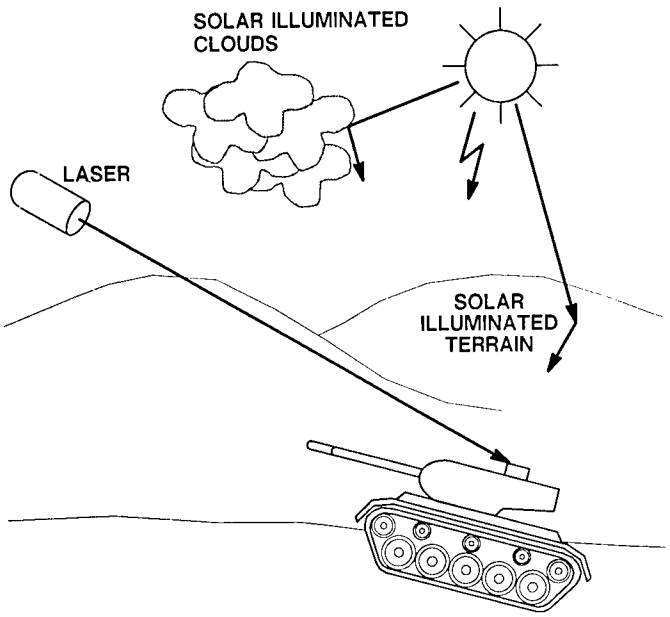

Fig. 1.2 Laser warning receiver scenario—self-protection.

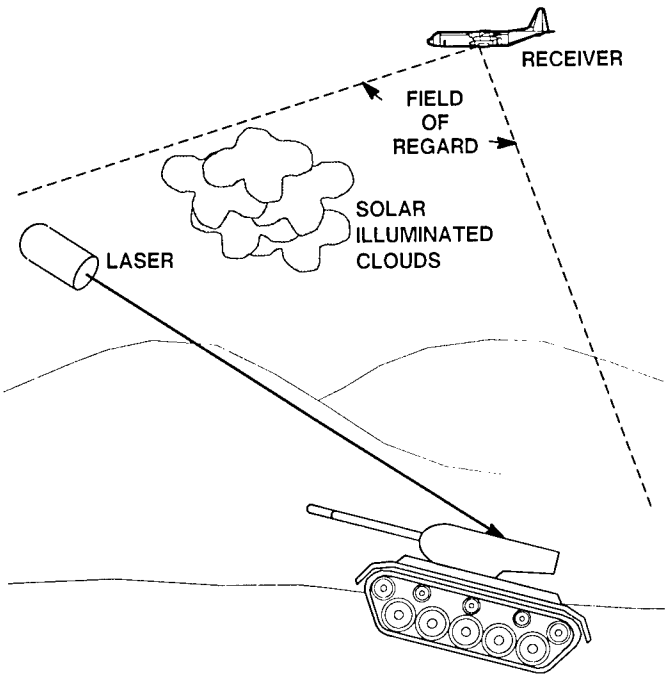

Fig. 1.3 Laser warning receiver scenario—ESM.

of 0.25 mrad. The laser is 100 m above ground level and there are no smoke or clouds intervening between the laser and its target. The local weather conditions correspond to a "clear, standard day" with a visibility of 23 km. Note, that the assumed laser beamwidth, 0.25 mrad, subtends only 0.5 m at the tank, and it is not at all certain that the beam will strike the tank at the point where the laser warning receiver is located.

The ESM scenario of Fig. 1.3 involves three participants; the laser designator and its tank target, as previously illustrated in Fig. 1.2, and an airborne laser ESM system located many kilometers away from the designator/tank engagement. Environmental conditions are the same for both scenarios. The objective of the standoff ESM system is to determine the level of laser activity on the battlefield, measure the laser parameters, and locate the threat lasers. In this case, the threat lasers are not targeted toward the laser receiver platform. Although this scenario is not addressed in detail in this chapter, understanding of its similarity to, and difference from, the more classic warning scenario is important to avoid confusion between these two scenarios. The equipment requirements for these two situations are often drastically different.

1.2.3 Measures of Effectiveness

Many system-level performance parameters can be used to describe the effectiveness of a warning receiver. These range from general factors such as probability of detection and false alarm rate to more specific characteristics such as direction-finding resolution.

1.2.3.1 Missile Warning Receivers. Table 1.4 lists[6] some measures of effectiveness (MOEs) associated with missile warning receivers. The table also contains a definition of the MOEs and typical or desirable values of the MOE that might be required in tactical and strategic situations.

An important distinction in the table of MOEs is that between detection range and declaration range. The first is always greater than the second, because time is needed to process information and decide if the detected object is a threat or not. (If the range were increasing with time, it is unlikely that the object would be declared a threat.) The interval between the two events is often called *latency time.*

The individual measures of effectiveness are not independent. For instance, it is always possible to increase the probability of detection or declaration by relaxing thresholds and other decision criteria; these same actions increase the false alarm rate. False alarm rates can likewise be lowered at the expense of missed detections or declarations. At the extreme, a nonoperating sensor yields an ideal false alarm rate of zero, which is accompanied by obviously unacceptable rates of detection and declaration.

Time to go (TTG) or time to impact (TTI) are parameters determined from system estimates of range at declaration and the closing speed of the missile.

SNR and signal-to-clutter ratio (SCR), which are intermediate parameters that determine the values of various measures of effectiveness, are not listed in this table. They are discussed with more detail in the sections on target signatures, backgrounds, and clutter.

Table 1.4 MWR Measures of Effectiveness and Typical or Desirable Values

MOE	Definition	Tactical	Strategic
P_D	Detection probability	0.95-0.99+	0.98+
FAR	False Alarm Rate	1.0 - 0.1/hr	10^{-3} /day
FAR_n	Noise induced FAR	10^{-3}-10^{-4} /hr	10^{-8} /day
FAR_c	Clutter induced FAR	10^{-1} /hr	10^{-4} /day
R_d	Detection range	1-10 km	10^2-10^4 km
R_{dec}	Declaration range	1-10 km	10^2-10^4 km
FOR	Field of regard	0-360° az ± 45° el	0.1-1 ster
DOA	Direction of arrival resolution	± 45° az	NA
TTG(TTI)	Time to go (impact)	1-30 s	1-30 min
TTI_{max}	Warning time (maximum TTI)	2-30 s	1-30 min
V_{mc}	Missile closing velocity resolution	± 10 m/s	NA
N_m	Number of missiles handled	< 10	< 100
Prioritization	Ability to prioritize among multiple threats	Yes	Yes
Latency	Processing time - detection to declaration	0.5 s	10 s
Blanking	Blank after detect or CM activation	Yes	No
NEI	Noise equivalent irradiance (sensitivity)	Band dependent	Band dependent
Altitude	Min. & max. operating alts.	0-10 km	10^2-10^4 km
Outputs	Signals to human or CPU		

1.2.3.2 Laser Warning Receivers. Laser warning measures of effectiveness for the self-protect scenario relate to the efficiency with which the laser intercept enables the threatened platform to take protective action. Functionally, this involves detection of the signal, discrimination of real signals from false signals, characterization of the laser, and localization of the source. Table 1.5 presents common self-protection LWR measures of effectiveness and typical ranges for them.

Signal detection is related to system sensitivity and is usually limited by solar-shot noise and Johnson noise in the visible and near-IR regime and by detector/thermal noise in the mid and far infrared. For laser warning receivers, the source energy may strike the receiver directly, or it may be directed toward the receiver from an intermediate scattering object. As a result, the incident signal level from the same nominal scenario can range over many orders of magnitude, depending on exactly how the laser energy reaches the receiver. Thus, because typical scenarios can readily expose such a system to a signal range of 4 to 10 orders of magnitude, receiver dynamic range is as important

Table 1.5 LWR Measures of Effectiveness

Measure of Effectiveness	Common Value
Sensitivity	10^{-6} to 10^{-3} W/cm^2
Peak Signal for Correct Analysis	1 to 10^{+3} W/cm^2
Dynamic Range (Analytic)	10^{+4} to 10^{+8} irradiance ratio
Dynamic Range (Destruction)	10^{+8} to 10^{+12} irradiance ratio
False Alarm Rate	1 per hour or per day or per mission
Probability of Detection	0.9 to 0.99
Spectral Resolution	Band to 0.01 μm
Temporal Resolution (Duration)	<100 ns
Temporal Resolution (PRF)	1 to 10^{-3} s
Temporal Resolution (Interval)	10^{-1} to 10^{-7} s
Direction of Arrival	1° to 45°

as receiver sensitivity. In particular, it is important that the directly incident laser signal not destroy the receiver nor cause saturation effects that result in incorrect signal characterization. The system sensitivity along with the largest signal that is correctly analyzed are the primary intensity-related measures of merit. These combine to define the dynamic range over which the system carries out a proper analysis, whereas the signal level at system destruction limits the survivable dynamic range.

Effective false target rejection is a major LWR requirement. Sun glint, lightning, gun flashes, explosions, various optical beacons, and virtually any transient light source are potential false targets. These are rejected by LWRs that employ coherent detection techniques. Steady optical sources, such as battlefield fires, which can be difficult problems for a missile warning receiver, are readily rejected by the transient-oriented circuitry of typical laser warning receivers. Typically, complete immunity to all false sources is usually desired, whereas white-noise-generated false alarms are typically specified in terms of a maximum number of false alarms per unit time (related to a typical mission duration). In addition, most LWR specifications include an appropriate electromagnetic interference (EMI) requirement.

It is common to specify LWR performance in terms of a simple radiometric probability of detection for a specific minimum laser intensity.

Threat parametric characterization can be carried out at two different levels. For LWRs that serve only to alert the platform and define the threat, it may be adequate to make coarse measurements of laser wavelength, intensity, duration, and pulse repetition frequency to distinguish among weapon, rangefinding, designating, communication, or countermeasure lasers. Typically, weapon lasers are at specific wavelengths and usually have long-duration pulses, rangefinders are of short duration and low repetition rates; designators are similar to rangefinders but at higher repetition rates; countermeasure lasers are also similar to rangefinders but of substantially higher intensity,

and communication lasers are modulated continuous wave (cw) sources, or very high repetition rate pulsed ones. Consequently, the LWR community often speaks in terms of *binning* the laser parameters for threat recognition.

For LWRs that are directly linked to laser countermeasure transmitters, it may be necessary to derive a detailed characterization of the laser waveform from the intercept. Typically, this involves accurate measurement of the pulse repetition rate and/or pulse interval. The accuracy required for such applications can require measurement precision that is a small fraction of the basic signal parameter involved.

The threat localization issue for laser warning receivers is quite different than it is for the missile warning receivers because of the potential ambiguity in the actual source of the photons incident on the receiver. For a directly incident beam, threat localization can be relatively straightforward. However, should the intercept involve target or atmospherically scattered photons, it is much more difficult to derive threat directional data. In particular, these secondary scatter/reflection intercepts can cause some types of systems to provide misleading directional data. In such cases the location figure of merit should be a two-element criteria: first, indicating whether the intercept is direct, or not, and then, if direct, indicating the threat direction to some degree of precision. Angular accuracy requirements vary with platform and scenario. In most situations a minimum of quadrant localization is desired. For airborne laser receivers a specification analogous to that required for conventional radar warning receivers (RWRs), a few degrees may be adequate, whereas precise counterattack may require directional accuracy to better than a milliradian.

For laser ESM scenarios, as defined in Fig. 1.3, receiver sensitivity is the dominant measure of effectiveness. Three-dimensional source localization (not just instantaneous direction) is usually desired; as is detailed, wideband characterization of the laser waveform; i.e., duration and pulse repetition rate (or interval).

1.3 OBSERVABLES

1.3.1 At the Source

1.3.1.1 Tactical Missile Observables. Missiles generate characteristic emissions in the optical bands that are inadvertent to their propulsion and vital to the detection and warning process. The most prominent of these are associated with the combustion of fuel during boost and sustain phases.[7] Discrete frequency emissions from rotational and vibrational transitions of water vapor and carbon dioxide molecules account for much of the exhaust emission. In addition to the well-known 4.3- and 2.7-μm bands from CO_2 and H_2O, there are a wealth of transitions in the visible and ultraviolet spectral bands, some of which originate from trace constituents in the fuel. Table 1.6 lists a few of the more common line emissions found in missile plumes. The practical use of any of these optical emissions for warning purposes is determined by atmospheric transmission properties, detector and optics technology, and background and clutter levels. It is likely that efforts in missile propulsion technology will be directed toward reducing many of these unintentional

Table 1.6 Common Plume Spectral Lines

Wavelength (μm)	Origin	Comments
15	CO_2	
6.3	H_2O	Intense, heavy attenuation
4.9	CO_2	
4.3	CO_2	Intense, moderate transmission
2.7	H_2O	Intense, heavy attenuation
2.7	CO_2	
2.0	CO_2	
1.87	H_2O	
1.38	H_2O	
1.14	H_2O	

characteristic emissions, so their presence in future-generation missiles cannot always be assumed.

The intensity of plume emissions varies with many factors such as angle of the missile relative to the receiver, altitude and velocity of the missile, and so on. Figure 1.4 shows[6] some qualitative variations in plume intensities. The viewing angle of the missile determines how much of the plume is obscured by the missile body. Variations of MWR look angle along the trajectory of the missile depend on the type of guidance in use by the missile. As examples, consider proportional navigation guidance and command line-of-sight guidance. With proportional navigation the missile is always seen at a constant look angle from the target. On the other hand, command line-of-sight schemes, such as beam-rider missiles, appear at a varying look angle to the aircraft, but always line up with the same point on the ground. The latter are more difficult to detect because they remain fixed with respect to the background clutter features. The variations in signature resulting from changing look angle may deceive warning receiver signal processors that depend on intensity variations to deduce range and velocity.

In addition to the discrete, combustion-related lines discussed, the skin of the missile also provides detectable radiation. Slight temperature or emissivity differences between the missile skin and adjacent background areas or reflections from the skin may prove more robust indicators than plume emissions. The high speeds of most missiles contribute to the temperature difference because of aerodynamic heating effects, which remain difficult to counter or avoid. The ratio of plume to skin radiation in the missile signature varies with the view angle, which, as noted, may vary along the trajectory.

In addition to the discussed gaseous constituents, the exhaust plume may also contain carbon particles that behave as graybody emitters at a temperature approximately equal to the exhaust gas temperature. Exhaust gas temperatures vary with fuel and motor design. An approximate temperature for a kerosene and liquid oxygen missile exhaust is 2000 K, and the radiant in-

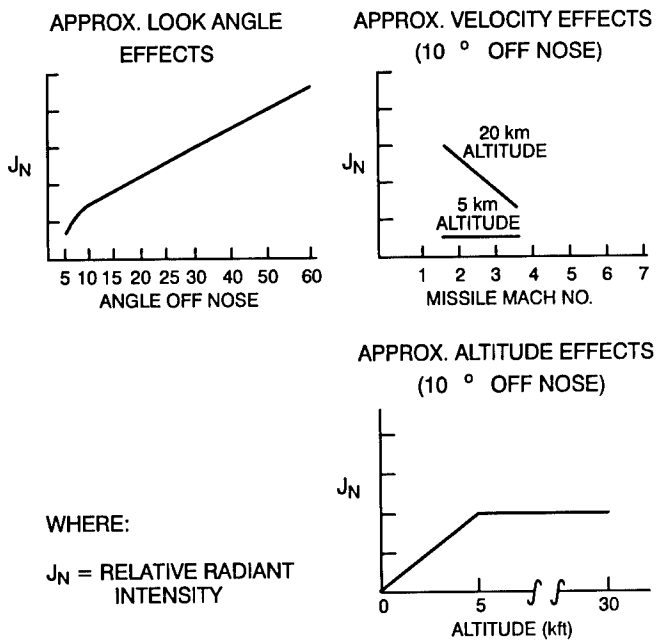

Fig. 1.4 Radiant intensity variations that affect IR amplitude discrimination.

tensity in the CO_2 plume band for a vehicle of this type is typically 10^6 W/sr, plus or minus an order of magnitude.[8] Small tactical missiles with solid fuels would exhibit signatures in the range of 10^3 to 10^4 W/sr in the same band. Scaling to other spectral bands depends on the relative contribution of line emissions, exhaust gas continuum, and skin and tailpipe thermal emissions in a given situation.

The intensity of the missile signature depends strongly on the type and size of motor. As a first approximation, it can be assumed that the signature intensity in any of the optical bands is proportional to the rate of fuel combustion, which is approximately proportional to the thrust of the motor. A rule of thumb for scaling missile signatures is thus

$$I = kN \ , \tag{1.1}$$

where k depends on the spectral band. A more realistic scaling approach sets intensity proportional to a power of thrust:

$$I = kN^{\alpha} \ , \tag{1.2}$$

where I is in watts per steradian, N is in newtons, and both k and α are band dependent.

Real missile motors do not maintain constant thrust with time. In addition to the major thrust phases of the missile (launch, boost, sustain, and burnout), there are variations within each phase. Figure 1.5 shows thrust versus time

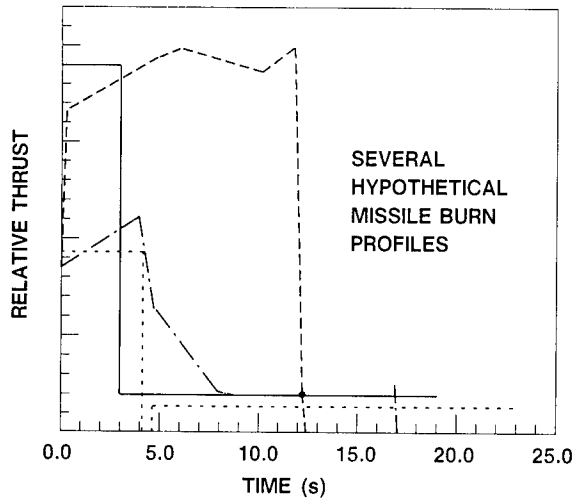

Fig. 1.5 Thrust versus time for several missiles.

for several missile types. A scaling law for the effect of viewing angle variations in observed signature is

$$I_\theta = I_{90} \sin(\theta + \phi) \ , \tag{1.3}$$

where I_{90} is the intensity at beam viewing angle ($\theta = 90$ deg) and θ is the azimuth angle of the observed missile. The offset angle ϕ is a small correction whose value depends on the geometry of the missile and plume.

Ultraviolet emissions from exhaust plumes are another source of missile observable. Figure 1.6 shows[9] spectral radiometric data from the combustion of JP4 fuel in an F404 turbojet aircraft engine in afterburner mode. Very high speed missiles also generate ultraviolet radiation in the bow shock wave. Gas temperatures in the bow shock wave of a 7800 mile/h post burnout missile at a 25 mile altitude have been measured at over 6000 K. This source of radiation, however, is more significant for strategic missiles than for tactical missiles.

Visible waveband detection of threat missiles may be based either on the emitted light from the rocket plume or from scattered ambient light from the missile body. The former case is similar to the infrared band, with plume intensity proportional to some power of the rocket motor thrust. The second case depends on the contrast between reflected ambient illumination from the missile body and that reflected from adjacent background areas. Ambient illumination levels are discussed in Sec. 1.3.3, along with background material reflectances in the visible waveband. Target reflectances depend on the outer surface of the missile skin, which may be paint or other protective coatings rather than polished bare metal. Reflectances of some bare metals at wavelengths from the ultraviolet and visible through the infrared are shown[10] in Table 1.7. Reflectivities for other metals and other wavelengths can be estimated by the Hagen-Rubens relation.[10]

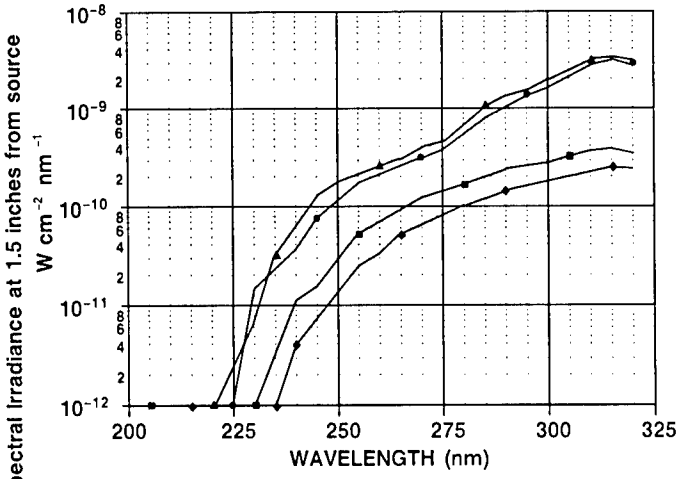

Fig. 1.6 UV spectral data from F404 engine.

Table 1.7 Reflectivity of Metals (%) (Normal Incidence)

Wavelength (μm)	Copper	Gold	Nickel	Steel
0.25	25.9	38.8	37.8	32.9
0.36	27.3	27.9	48.8	45.0
0.45	37.0	33.1	59.4	54.4
0.50	43.7	47.0	60.8	54.8
0.60	71.8	84.4	64.9	55.4
0.70	83.1	92.3	68.8	57.6
0.80	88.6	94.9	69.6	58.0
1.00	90.1		72.0	63.1
2.00	95.5	96.8	83.5	76.7
3.00	97.1		88.7	83.0
4.00	97.3	96.9	91.1	87.8
9.00	98.4	98.0	95.6	92.9

$$\rho \approx 1 - \frac{2}{n} = 1 - \frac{2}{c}\left(\frac{4\pi\nu}{\mu\sigma}\right)^{1/2}, \tag{1.4}$$

where ρ is reflectivity, n is index of refraction, c is speed of light in vacuum, ν is frequency of the radiation, μ is absolute magnetic permeability, and σ is electrical conductivity. Because σ is very large for most metals, their reflectivities are high.

U.S. military paints are described by a five-digit classification system known as Federal Standard 595a. The third and fourth digit of this number are the visible band reflectance in percent. The first digit describes the approximate directional reflection properties of the coating according to gloss or highly specular = 1, semigloss = 2, and lusterless or diffuse = 3. Differences in reflectances between target and background are much better than hue or color differences for target detection. In the case of glossy surfaces, glint or glare from sunlight or moonlight may also supply a transient indication of target presence, but water, snow, and ice backgrounds can produce similar specular reflections. Figure 1.7 shows[11] spectral variations of diffuse spectral reflectances for a number of typical real target materials from the near ultraviolet through the visible spectral region.

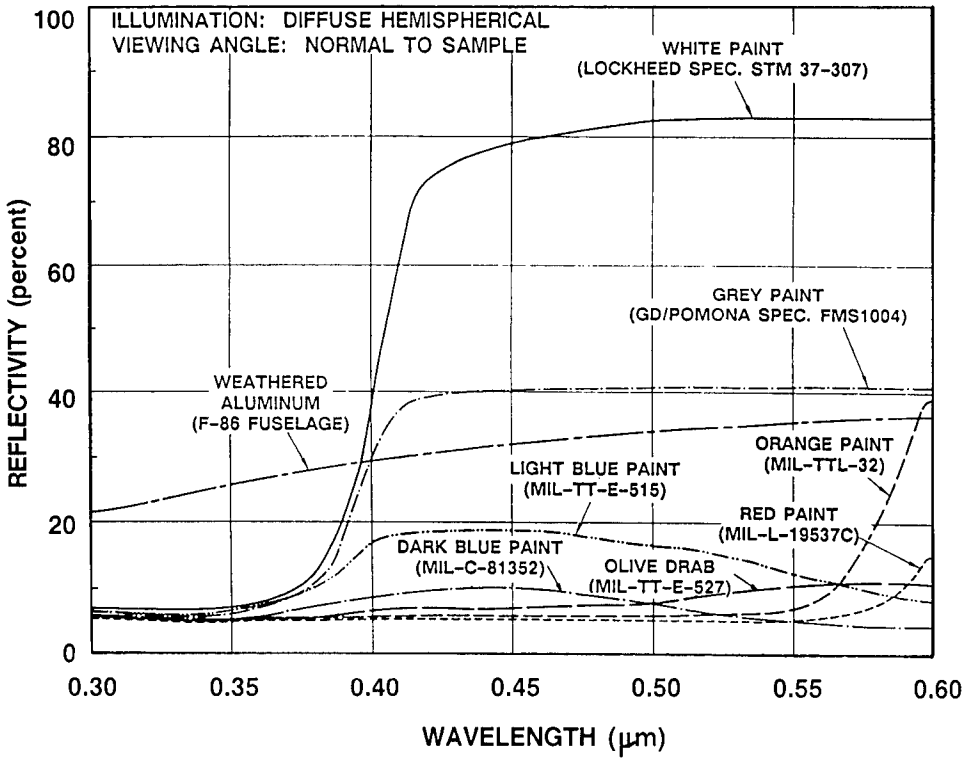

Fig. 1.7 Diffuse reflectances of target materials in ultraviolet and visible spectral regions.

The millimeter wave and near millimeter wave regions can also be used for target detection by exploiting reflectance differences. Most metallic objects are highly reflective at 35 GHz, whereas natural terrain backgrounds are more emissive (see Sec. 1.3.3). For a downward looking situation, the reflected cold sky can provide sufficient contrast against the warmer earth backgrounds to permit target detection. Water and snow/ice again provide problematic background situations.

1.3.1.2 Strategic Target Observables. The EO/IR observables associated with strategic targets depend strongly on the specific targets that are to be observed. Large ICBMs emit strongly in the infrared part of the spectrum as a result of the intense IR radiation from their rocket exhaust plumes. By comparison, strategic cruise missiles and strategic aircraft effectively radiate very little infrared energy.

ICBMs and submarine-launched ballistic missiles (SLBMs) have significantly more thrust than tactical missiles, resulting in significantly larger EO/IR signatures. To generate this thrust, large quantities of fuel must be burned, resulting in a tremendous amount of heat energy being released in the rocket exhaust. This heat energy results in intense electromagnetic energy being radiated in the EO/IR part of the spectrum. In a spectral band 1 μm wide centered near a wavelength of 2.7 μm, the exhaust of the first stage of an ICBM might effectively radiate as much as 1 MW/sr or more.

As is the case for tactical missiles, ICBMs and SLBMs usually contain water vapor, carbon dioxide gas, and sometimes solid particulates in their exhaust plumes at temperatures near 2000 K. Consequently, the 2.7- and 4.3-μm *missile bands* are the spectral bands most often (but not exclusively) considered for ICBM/SLBM missile warning.

For cruise missiles and strategic aircraft, the emissions from hot exhaust gases are much smaller than for ICBMs and SLBMs. The reason for this is primarily that the motors on these vehicles generate much less thrust than the motors on an ICBM or SLBM. In addition, these vehicles must be detected at lower altitudes than strategic ballistic missiles. This results in long atmospheric slant paths from the target to the sensor, and atmospheric transmission over these long paths greatly reduces the apparent target intensity in the *missile plume bands*.

Because of the difficulty with detecting cruise missiles and strategic aircraft in the missile bands, sensor concepts involving operation in the atmospheric window bands (e.g., the 8- to 12-μm LWIR band) are often considered for cruise missile and strategic missile detection. In these bands, the EO/IR observables result from the air vehicle itself, rather than its exhaust plumes. The phenomenology leading to these signatures is basically the same as for tactical aircraft.

1.3.1.3 Laser Warning Observables

Basic Source Parameters. The basic laser parameters are determined by the laser material, the laser cavity (or resonator), and the laser pumping mechanism. Individual laser configurations are application specific and selected to provide the appropriate parameters required. The choices are dictated by the available technology.

Laser wavelength is primarily determined by the laser material with a variety of individual laser "lines" possible from any individual material. The specific laser line emitted is selected by the resonant cavity employed. Laser polarization is also cavity configuration dependent; whereas typical gas lasers are linearly polarized, many high energy, solid-state, military lasers radiate an unpolarized beam.

Polarization, purity of wavelength, and beamwidth are related to the modal properties of the laser. A laser operating in a single longitudinal mode and a single transverse mode will have a well-defined polarization, a narrow spectral width, and can be collimated into a narrow diffraction-limited beam. Conversely, a laser operating in a highly multimode manner is often unpolarized, has a broad spectral width, and radiates as an area source of wide beamwidth. The laser designer strives to achieve high-efficiency, low-mode operation for most applications as this results in higher power density on target. As laser output power is increased, various optical and thermal imperfections and nonlinearities limit the single-mode power output. Consequently, tactical military lasers are often highly multimode devices. Further elaboration of the basic laser properties requires specific discussion of laser type (gas, solid state, chemical, semiconductor, and so on), lasing element (neodymium, CO_2, gallium arsenide, and so on), host material (yttrium aluminum garnet, glass, ruby, and so on), pump mechanism (flash tube, electronic, diode laser, and so on), and cavity type (confocal, planar, unstable, Q-switched, and so on) all of which are beyond the scope of this section.

The temporal structure of a laser beam is also a function of the various parameters outlined here. Some of the relations that are important to laser discrimination and recognition processing are now discussed briefly.

In general terms, current military lasers can be temporally characterized as continuous wave, long-pulse, or short-pulse lasers. These distinctions are a function both of the inherent laser mechanisms involved and of the military application.

The cw lasers, of which gallium arsenide semiconductor lasers and CO_2 gas lasers are examples, are usually modulated at high rates, from kilohertz to gigahertz, and are used in applications such as communications or missile guidance, in which they can carry large amounts of information; in laser radars wherein heterodyne detection is used; or, in the case of the semiconductor lasers, in missile proximity fuze applications where small size is important.

In applications where high energy is important and short durations are not required, lasers, such as ruby or neodymium:glass, can be pumped with a burst of energy (flash tube) and then be allowed to lase during the normal relaxation time of the laser medium. Although this varies considerably among materials, it is often in the 0.10- to 0.5-ms regime. Laser illumination and weapon systems often fall into this category.

When short pulse duration is important, or high peak powers are desired, Q-switched lasers may be used. The resonant cavity of such lasers is disabled, sometimes by misaligning one mirror, until the laser pumping is completed, and then the cavity is realigned quickly and the laser pulse grows very rapidly, depleting the "inversion," at which time lasing ceases. This is the common mode of operation for the Nd:YAG lasers used in rangefinders and designators. Typically, the pulse duration of such lasers is in the 15- to 30-ns range and the pulse repetition rate may vary from 1 Hz to tens of kilohertz.

Coherence. Propagation of electromagnetic waves is a four-dimensional process. For the situations of interest in this chapter, a laser beam can be envisioned as propagating during a time t in a direction z and expanding orthogonally in x and y. When such a beam originates at a source that radiates at precisely the same frequency (wavelength) at all times, the wave travels regularly with the instantaneous intensity at each point along the direction of propagation and is totally described in terms of the intensity at the source at that instant and the number of wavelengths, or partial wavelengths, between the source and the observation point as illustrated in Fig. 1.8(a). If, however, the source were to change wavelength slightly, on a random basis, the regularity of the propagating wave is affected as well. The instantaneous amplitude is described by a simple, deterministic, sinusoid over an interval that corresponds to the time during which the source radiated a specific frequency as shown in Fig. 1.8(b). The property of an electromagnetic field whereby the field at one specific point and time correlates with the field as observed at another point and time is termed *coherence.*

Real sources, even lasers, are imperfect, and their output can be regarded as constantly varying over some range of frequencies.[12] The wavelength variation corresponding to this frequency fluctuation (or spread) is termed the *linewidth* of the laser. The time during which the laser emission effectively consists of a pure single-frequency wave is referred to as the *coherence time* of the laser, and the longitudinal distance along which the wave propagates during this coherence time is called the *coherence length.* The relationships among the wavelength, linewidth, coherence length, and coherence time are defined in Fig. 1.8(b). Equation (1.5) is the basic relation between the frequency, velocity, and wavelength. In Eq. (1.6), coherence length and coherence time are related quantitatively, as illustrated in Fig. 1.8(b); and in Eq. (1.7), coherence length is expressed in terms of the spectral linewidth.[13] There is a large body of literature on the nuances of optical coherence theory including Marathay,[14] Mandel and Wolf,[15] and Baron and Parrent.[16] For the purposes of laser warning receiver analysis, the following relations are particularly germane because coherence discrimination is usually implemented in terms of a coherence length measurement:

$$\lambda = \frac{c}{\nu} , \tag{1.5}$$

$$\Delta l_c = c\Delta t_c , \tag{1.6}$$

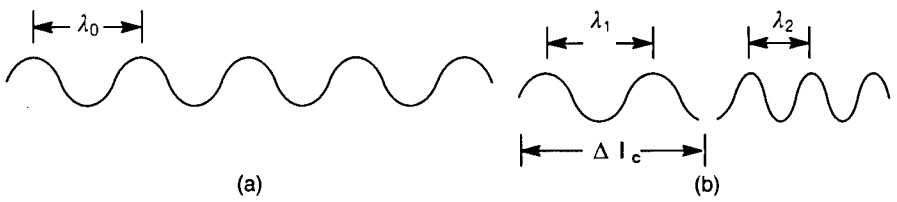

Fig. 1.8 Laser coherence length concept: (a) coherent wave and (b) partially coherent wave.

$$\Delta l_c = \frac{\lambda^2}{\Delta\lambda} , \tag{1.7}$$

where λ is the wavelength in meters, c is the speed of light in meters per second, ν is the frequency of the wave in hertz, Δl_c and Δt_c are the coherence length and coherence time, respectively. The net result of Eq. (1.7) is to define the laser coherence length in terms of the spectral linewidth $\Delta\lambda$, which is the laser parameter typically measured or specified.

As a consequence of the temporal element in this description, coherence is often termed *temporal coherence.* From the perspective of the coherence degradation along the direction of propagation, it is also termed *longitudinal coherence.*

For a few lasers, such as the CO_2 lasers used in superheterodyne laser radars, temporal coherence is a primary parameter that is carefully selected, monitored, and controlled because it is directly related to system performance. For most other military applications, coherence is a secondary parameter. Although much more coherent than the sun or other natural sources, such lasers are only partially coherent, and coherence *per se* is ignored, whereas the focus is on beamwidth, bandwidth, and resultant power density. Table 1.8 lists the coherence length of lasers and other sources as calculated from typical laser specification sheets.[17]

If the beam, even one from a "coherent" laser, is traveling through a propagation medium that itself is changing with time in a random fashion, then we also expect to find a reduction in the longitudinal coherence length. In addition, if the propagation medium exhibits variations laterally across the beam (i.e., at right angles to the direction of propagation) it may be said that the *lateral* coherence of the beam is affected. Because the atmosphere is in a constant state of turbulence and its turbulence is reflected in its optical properties, such effects must be considered in the design of laser warning receivers that measure coherence, or use it to distinguish among sources. The somewhat artificial distinction between longitudinal and lateral coherence is useful for

Table 1.8 Coherence Length of Lasers and Other Sources

Source	Approximate Coherence Length (meters)
Incandescent (Unfiltered)	10^{-7}
Sun (Silicon Band)	10^{-6}
Light Emitting Diode (LED)	10^{-4}
He Ne Laser	10^{-1}
Diode Lasers	10^{-4} to 1
Dye Lasers	10^{-4} to 1
CO_2 Lasers	10^{-4} to 10^{+4}

LWR considerations because of the different origins of the *incoherence*—the laser source linewidth is the dominant contributor to temporal (or longitudinal) coherence degradation, whereas the atmospheric effects are the dominant contributor to lateral coherence degradation. Section 1.7 illustrates the ways in which the coherence in these two dimensions affects the design of laser warning receivers.

Radiation Patterns. Optical sources can be characterized as either area sources or point sources. Conventional optical sources generally behave as area sources. For illumination systems consisting of an area source and an optical system focused at infinity, the output beamwidth is well modeled by a cone of rays (not necessarily circularly symmetrical) originating from the final collimating optic with a beamwidth given by the throughput relationship

$$A_s \times \Omega_s = A_o \times \Omega_o \ , \tag{1.8}$$

where the first product refers to the radiation source area and its angular radiation pattern, whereas the second product refers to the output optic area and its angular radiation pattern. The conical beam with a linearly expanding beam diameter is an accurate presentation of the behavior of such beams at distances that are long with respect to the diameter of the final optic. Some, if not most, military laser systems are very highly multimode devices, and they are well represented by this model with the intensity internal to the beam having a Gaussian distribution.

Coherent, single-mode lasers, even when they emanate from a large diameter laser cavity, are better characterized as point sources, are capable of diffraction-limited performance, and are typically used in diffraction-limited optical configurations. Figure 1.9 illustrates the spatial evolution of a diffraction-limited beam intensity, which appears initially to be cylindrical evolving into the expected conical form as it reaches a distance of $d^2/2.44\lambda$ from the aperture, where d is the diameter of the aperture. By $2d^2/\lambda$ it has settled into a steady conical expansion corresponding to an intensity reduction with range of $1/R^2$; at shorter ranges the intensity of the beam is quite complex.[13,18,19]

At optical wavelengths where λ is a small number, this well behaved $1/R^2$ region may not be established until the laser beam is many kilometers from the laser. The region in which the beam exhibits the $1/R^2$ dependence is termed the *far field*, and the close-in region is the *near field*.

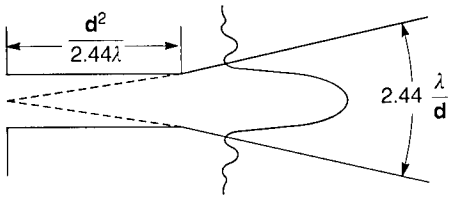

Fig. 1.9 Spatial evolution of the beam from a uniformly illuminated aperture.

Within the far-field region, the irradiance $E(\theta,\phi)$ of the laser beam directly incident on a laser warning receiver is given by

$$E(\theta,\phi) = \frac{I(\theta,\phi)\tau}{R^2} , \tag{1.9}$$

where $I(\theta,\phi)$ is the source radiant intensity in watts per steradian, τ represents the transmission of the intervening atmosphere, and (θ,ϕ) are the angular coordinates of the receiver with respect to the center of the beam. To determine the total received power it is only necessary to integrate the beam irradiance over the aperture.

For distances within the near-field range, the situation is much more complex and requires solution of the Fresnel integrals.[13]

Uniformly illuminated circular apertures produce the [Bessel(x)]/x pattern illustrated in Fig. 1.9; Bessel(x) refers to the Bessel function tabulated in various mathematical handbooks and tables.[20] The resultant optical beam shapes, including the sidelobes, are identical, in principle, with those found in microwave-radar beams. However, because typical lasers seldom uniformly illuminate their output optics and, typically, the output amplitude distribution is Gaussian shaped, the off-axis direct-beam intensity is usually relatively low.[21] Thus, typical laser warning receiver scenarios seldom involve intercept of distinct sidelobes, as do the analogous radar warning receivers. However, the materials of the laser optics, as well as the internal structures, mounting elements, etc., do cause off-axis scattering and reflection, which is somewhat analogous to the sidelobes of the microwave regime. Most of this spurious scatter arises as the laser beam exits the laser and is referred to as *port scatter*.[22] It typically has three specific sources: (1) scatter from the optical material of the collimating lens, which is relatively omnidirectional and 3 to 6 orders of magnitude lower than the main beam; (2) multiple reflections among the various lens and laser surfaces, the intensity of which is a strong function of the specific configuration; and (3) strong spurious, specular, reflections from specific internal structures. The latter may be highly directive and collimated and only a few orders of magnitude less intense than the main beam.

1.3.2 Propagation through the Atmosphere

1.3.2.1 Missile Signature Propagation Overview. The utility of a particular emission line or band for warning purposes depends on its transmission through the atmosphere, among other factors. Some more obvious candidates, such as the molecular transition band of CO_2 at 4.3 μm, are made less appealing by their attenuation over moderate pathlengths. In this case, the outer edges of a temperature-broadened emission line can propagate for some distance through cooler atmospheric CO_2. Figure 1.10 shows[11] the effect of atmospheric attenuation on the spectral distribution of plume emissions. Ultraviolet radiation, which appears attractive for warning purposes because of the low natural background and clutter levels at low altitudes, suffers significant atmospheric scattering as well as absorption over modest pathlengths.

The topic of atmospheric transmission is treated extensively elsewhere in this handbook. This section explores only the impact of atmospheric effects on typical missile observables and provides estimation rules for design purposes.

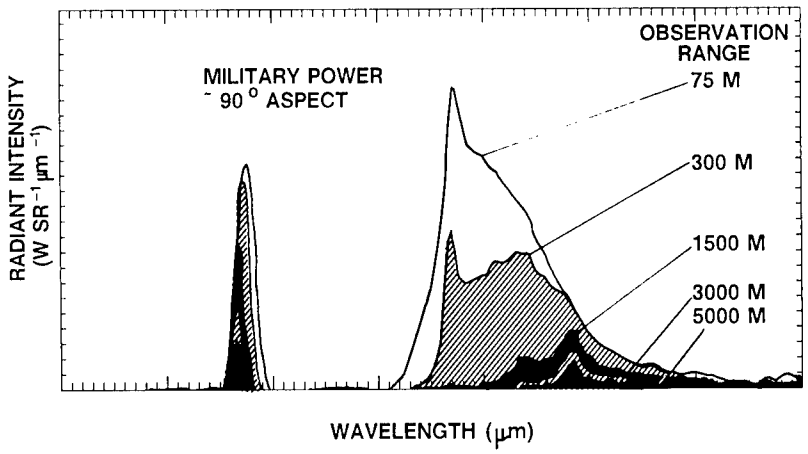

Fig. 1.10 Modification of spectral distribution of plume emission by atmospheric attenuation.

1.3.2.2 Tactical Missile Signature Propagation. In a tactical situation, where path lengths are moderate and homogeneity of the atmosphere can be assumed, it is possible to use a Beer's law estimate to approximate atmospheric effects, although a detailed spectral calculation like FASCODE[23] or HITRAN[24] would be more accurate. Intermediate resolution models like LOWTRAN[25] or UVTRAN[26] are useful if plume radiation is not dominant. The extinction coefficient depends on the detection band and spectral distribution of the source.

Degraded atmospheric conditions can change these extinction coefficients dramatically. Table 1.9 shows[27] some coefficients for the 8- to 12-μm band under less than ideal weather conditions.

Table 1.9 Extinction Coefficients in 8- to 12-μm Band

Weather Condition	Extinction Coefficient (km^{-1})
Haze	0.105
Light fog	1.9
Moderate fog	3.5
Heavy fog	9.2
Light rain	0.36
Moderate rain	0.69
Heavy rain	1.39
Light snow	0.51
Moderate snow	2.8
Heavy snow	9.2
Very clear and dry	0.05
Clear	0.08

An empirical expression[10] for atmospheric attenuation as a function of wavelength and visible band visibility (a figure normally available from meteorological reports) is given by

$$\tau_A = \exp\left[\frac{-3.91}{V}\left(\frac{\lambda}{0.55}\right)^{-q} R\right], \tag{1.10}$$

where V is the visibility and R the range, both in kilometers, and λ is the wavelength in micrometers. The exponent q depends on the size distribution of scattering particles; typical values are 1.6 for high visibility, 1.3 for average conditions, and 0.585 $V^{1/3}$ for low visibilities (<6 km).

The choice of spectral band should not be made on atmospheric transmission alone. Other factors such as target size and contrast with background enter into the considerations. Figures 1.11 and 1.12 compare[28] the SNR for two different bands for different situations. The first is based on a man-sized target with no aerosol in the atmosphere and short ranges. The man is approximately the size of tactical missile targets. Note that the 8- to 12-μm band is better for short ranges, but a BLIP (background-limited performance) detector in the 3- to 5-μm band could outperform the 8- to 12-μm system at ranges beyond 5 km. The second figure is for a small, high-temperature target at high altitude and longer ranges. It is important to note that no plume emissions are considered here, only hot blackbody radiation from a tailpipe, for example, and that the higher clutter levels in the 8- to 12-μm band are not considered. The 3- to 5-μm band is better under these conditions. However, with current detector technology, the 8- to 12-μm band is still superior in a *tropical environment* for all but very hot targets. At long ranges and with hot targets the 3- to 5-μm band could potentially emerge as superior with detector technology improvements.

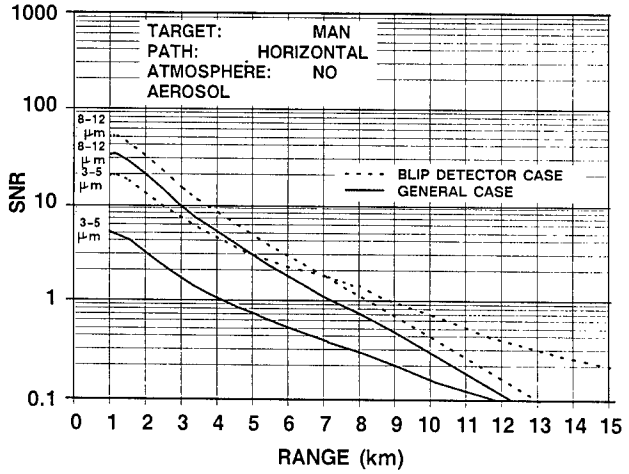

Fig. 1.11 SNR for man-sized target.[28]

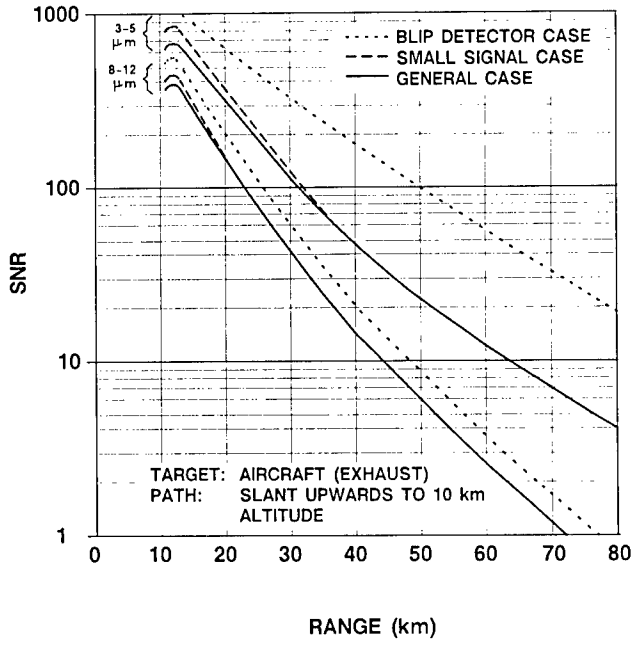

Fig. 1.12 SNR for small, hot targets.[28]

The effect of atmosphere on target to background contrast is generally the primary concern, so a more careful definition of contrast is in order. Absolute contrast at zero range, defined as the difference between target and background radiances (or temperatures) at the target can be written

$$C_A = N_T - N_B \ , \tag{1.11}$$

where the subscripts T and B refer to target and background radiances respectively. In the case of airborne targets, the background radiance is understood to be that coming from the atmosphere behind the plane of the target for the following discussions. The units of this contrast parameter are units of radiance (or temperature). More frequently encountered is the relative contrast

$$C_R = \frac{N_T - N_B}{(1/2)(N_T + N_B)} \approx \frac{N_T - N_B}{N_B} \ , \tag{1.12}$$

which is unitless.

The effects of atmospheric attenuation and path emission on contrast depend on which definition of contrast is involved. For relatively flat target and background spectral radiance distributions, the band-averaged atmospheric path transmittance τ can be applied to the in band radiances. In the case of absolute contrast, the emission factors cancel and the contrast is reduced by the band averaged atmospheric path transmittance factor. In the case of relative contrast, the emission term cannot be neglected in general. If the transmitted radiances are represented by lowercase symbols and defined as

$$n_T = N_T\tau + N_{ae} \qquad n_B = N_B\tau + N_{ae} \ , \tag{1.13}$$

where τ is the band averaged atmospheric transmittance and N_{ae} is the atmospheric path emission in the same spectral band, then the two transmitted contrasts can be written as

$$c_A = n_T - n_B = \tau(N_T - N_B) = \tau C_A \ , \tag{1.14}$$

and

$$c_R = \frac{n_T - n_B}{(1/2)(n_T + n_B)} = \frac{\tau(N_T - N_B) + N_{ae} - N_{ae}}{(1/2)\tau(N_T + N_B) + N_{ae}} \tag{1.15}$$

$$= \frac{N_T - N_B}{N_{ae}/\tau + (N_T + N_B)/2} = C_R\left(\frac{N_T + N_B}{N_T + N_B + 2N_{ae}/\tau}\right)$$

$$\approx \tau C_R\left(\frac{N_B}{\tau N_B + N_{ae}}\right) \ . \tag{1.16}$$

In some cases, such as short horizontal paths, $N_B\tau + N_{ae} \approx N_B$ and we are left with $c_R \approx \tau C_R$. In these expressions lowercase symbols refer to transmitted radiances or contrasts, whereas uppercase symbols are zero range values. For a further discussion of contrast in relation to electro-optical systems analysis methods, see Pinson.[29]

1.3.2.3 Strategic Target Signature Propagation. For strategic warning sensors designed to detect ICBMs and SLBMs by their emissions in the missile plume bands, atmospheric transmission plays a key role in determining the apparent intensity of the missile as it rises through the atmosphere. While the missile is low in the atmosphere, much of the IR radiation of the exhaust plume is absorbed by the water vapor and carbon dioxide gas in the atmosphere. However, as the missile rises in altitude, the concentration of water and carbon dioxide in the atmosphere rapidly decreases, and the atmospheric transmission from the target to the sensor greatly improves, resulting in orders of magnitude increases in the apparent intensity of the missile.

Signature propagation considerations for cruise missiles and strategic aircraft are much the same as for tactical aircraft, although the slant paths are typically longer and extend from the target to a sensor in space. Nonetheless, the treatment of contrast propagation presented in Sec. 1.3.2.2 also applies here.

1.3.2.4 Laser Signature Propagation

Atmospheric Attenuation. Lambert's law (i.e., the exponential attenuation of power with distance) is an adequate representation of the average reduction of laser intensity as it propagates from the source to the laser warning receiver:

$$\tau = \exp(-\alpha R) \ , \tag{1.17}$$

where τ is the transmission factor, α is the attenuation coefficient in inverse

kilometers, and R is the range in kilometers. Laser attenuation and scattering coefficients are tabulated in the literature; see, for instance, Kneizys.[30]

For slant paths through a nonhomogeneous atmosphere, Eq. (1.17) must be expanded to take into account the variation of α along the path. Equation (1.10) of Sec. 1.3.2.2 can be used to estimate laser attenuation as a function of visibility range.

Attenuation, although important to LWR system performance, is not the only significant atmospheric issue. Atmospheric scatter and atmospheric *scintillation*, which are discussed in the sections that follow, are items of major concern.

Atmospheric Scatter. Figure 1.13 shows the components of the atmospheric attenuation discussed in the prior section. (Absorbers other than O_3 have been omitted in the development of this figure.) Throughout the visual and into the mid-IR spectral region, the dominant source of near-earth and low-altitude

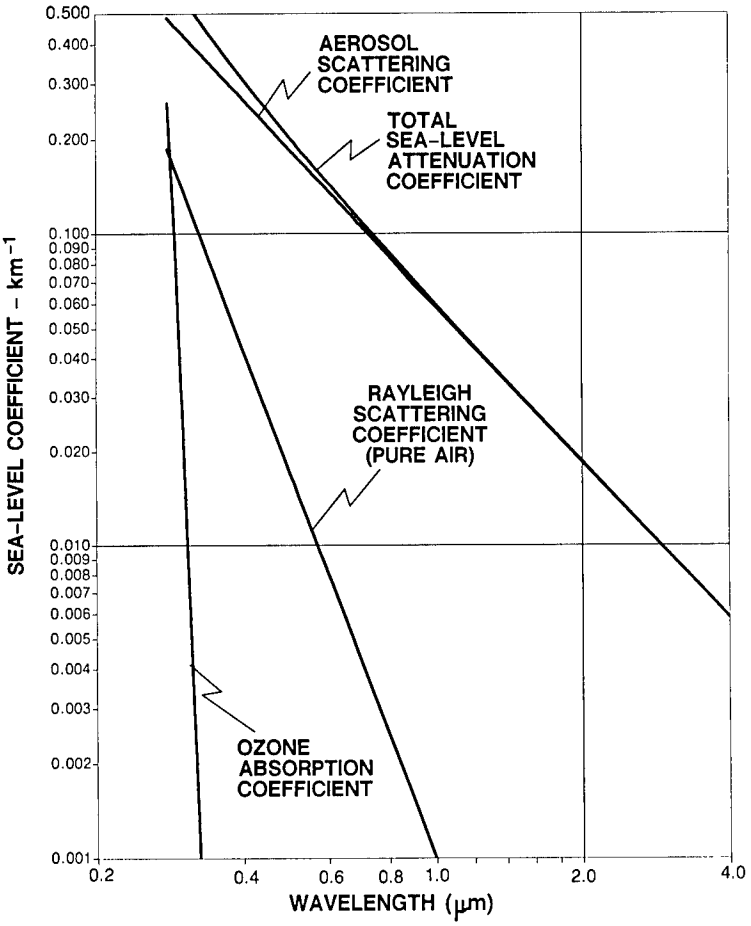

Fig. 1.13 Components of atmospheric attenuation.

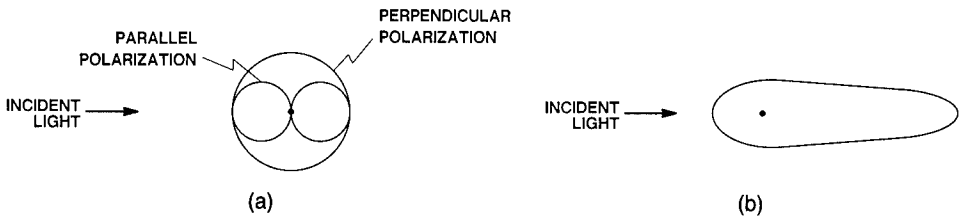

Fig. 1.14 Angular scatter patterns: (a) atoms (Rayleigh) and (b) aerosols (Mie)—not to scale; front to back ratio can be of the order of 100 to 1.

attenuation is the aerosol scattering component. Thus, in this region, the light that is attenuated is not absorbed, just redirected. (This figure is based on that originally presented by the *RCA Electro-Optics Handbook*[31] replotted by Patterson[32] with data from Patterson and Gillespie[26] and corresponds approximately to a 23-km visibility.)

In Sec. 1.2.2.3, on typical scenarios, reference was made to the fact that typical laser beamwidths, when incident on their targets, may be smaller in extent than the target itself. As a result, the laser beam may not directly strike the laser warning receiver. However, when it is not directly incident, it usually passes nearby. Thus, detection of light scattered from the adjacent air is a major aspect of LWR design. Figure 1.14 shows the angular scattering functions for the two major scattering components, atoms and aerosols. Atomic scatterers, dominant in the UV spectrum and in the upper atmosphere, are relatively isotropic (Rayleigh scattering), whereas the larger aerosols, dominant at the lower altitudes, scatter preferentially in the forward direction (Mie scattering). Fortunately, this results in a relatively large available signal for the tactical laser warning receiver, even in a "near-miss" situation. The specific angular scattering function that applies to a system calculation is a function of the atmospheric constituents, and their size distribution, as well as the specifics of Mie scattering theory that treats the scattering pattern of the individual aerosol particle. This, in turn, requires that we define the atmospheric conditions before we can quantify these effects. Ishimaru[33] provides an overview to this area; Zardecki and Deepak[34] and Bissonnette[35] address the specific case of narrow-band, near-axis laser scatter for very low visibility conditions, and Kabanov et al.[36] provides a statistical model of angular intensity of the scattered light for *coastal haze* conditions applicable to the off-axis scenario (see Sec. 1.2.2.3).

Target Scatter/"Splash." For the self-protection scenario, the laser warning receiver is located on the laser target platform. As discussed previously, the laser is not always directly incident on the receiver, and the laser photons must reach the receiver via a secondary scatter, or reflection, process. One scatter source, the adjacent atmosphere, is discussed in the prior section. The other scatter source is the target vehicle itself. Laser warning receivers may be positioned so that they view the scatter from a portion of their own platform. To avoid confusion with the atmospheric scatter case we will, occasionally, refer to this latter situation as *target splash.*

Signal intensity from target splash intercepts is a function of the vehicle bidirectional reflectance distribution function (BRDF), which describes the

intensity of light scattered in a particular direction as a function of light incident in some other direction.[37] The scatter from most vehicle surfaces is more or less proportional to the cosine of the angle off the normal to the surface (i.e., Lambertian) with some specular components. The intensity of the splash is a function of surface material, surface texture, incident angle, and viewing angle. For land vehicles this signature is dominated by the environmental conditions at the time (i.e., mud, dirt, dust, and so on).

For the standoff ESM scenario, target splash from a distant target can be the primary signal source.

Atmospheric Scintillation. Atmospheric turbulence potentially affects laser warning receiver analysis and design in several ways: it causes random angular deflection of the beam; it reduces the long-term temporal coherence of the beam; and it causes the initially smooth wavefront to degenerate into a series of overlapping sectors that randomly interfere with each other, resulting in a mottled beam.[38] The first two effects are minor with respect to terrestrial laser warning receivers that are targeting typical tactical lasers: the beam wander is of the order of tens of microradians, whereas the laser beams are often 10 to 100 times wider; similarly, the temporal fluctuations occur at millisecond rates, and the coherence times of the lasers of interest are seldom that long. However, the mottling of the beam, illustrated[39] conceptually in Fig. 1.15, becomes a practical issue in two ways: (1) lateral motion of either the laser or the receiver and the natural turbulent motion of the atmosphere produces temporal amplitude fluctuations of the signal directly incident on the LWR and (2) the random instantaneous transverse irradiance pattern can severely impact the performance of specific LWR configurations.

Scintillation effects are addressed in depth elsewhere in this Handbook; the LWR relevant issues are reviewed briefly herein.

The irradiance fluctuations can be readily visualized by envisioning a point detector positioned within the pattern of Fig. 1.16 as the black and white pattern therein moves randomly.[40] It also can be visually appreciated that the larger the receiver gets, the more cells it covers, and the less fluctuation there

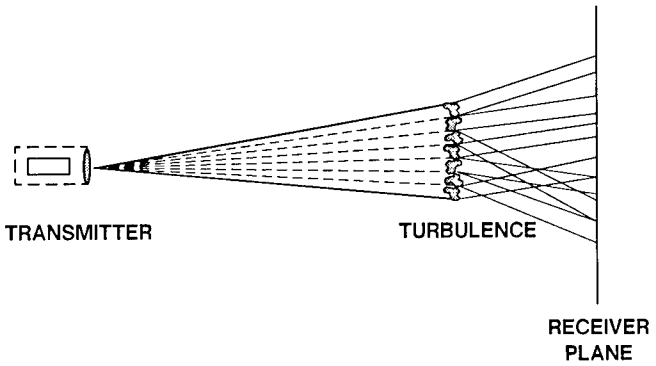

Fig. 1.15 Illustration of the origin of scintillation effects (conceptual). (From Ref. 40; reprinted by permission of John Wiley & Sons, Inc.)

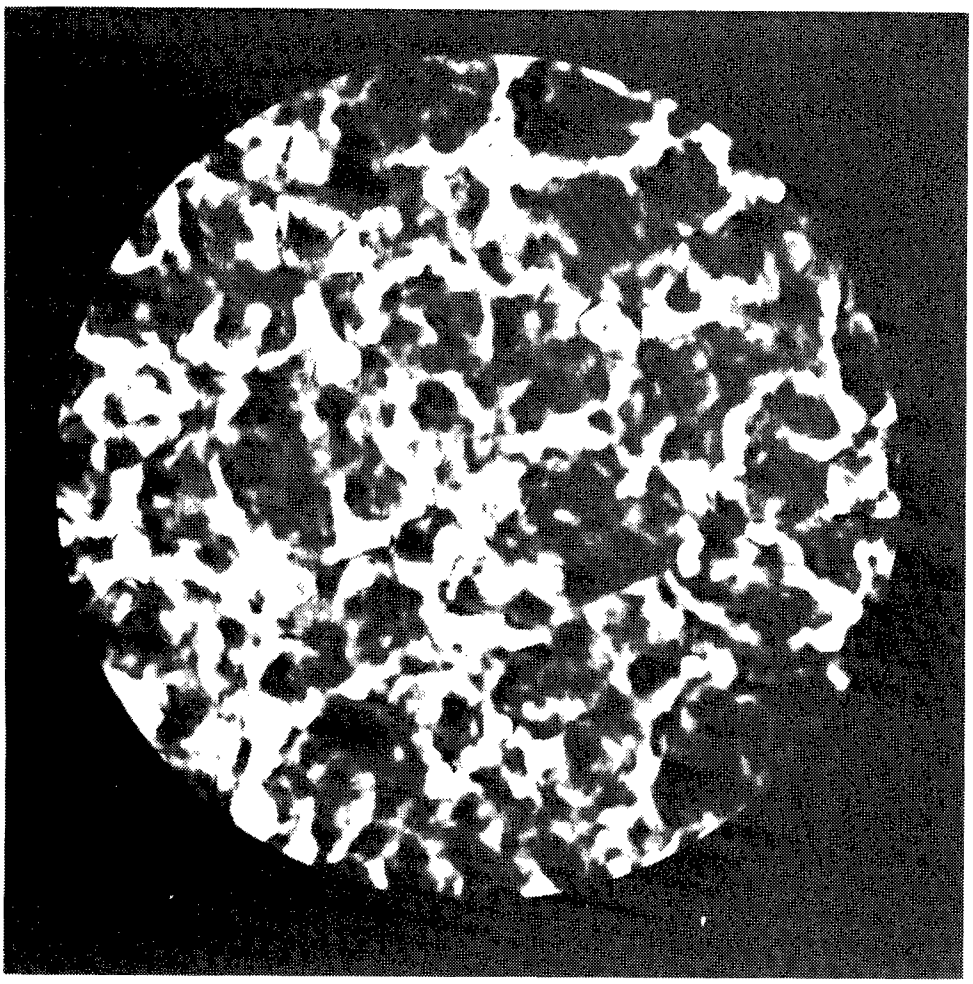

Fig. 1.16 Atmospheric scintillation appearance.[40]

will be in the detected signal. Typically, laser warning receivers are small aperture devices; therefore, the scintillation-induced signal level fluctuations must be incorporated in system design/analysis. The usual approach is to estimate the variation expected and to allow an additional system *gain margin* (i.e., more sensitivity than would be required in the absence of scintillation, to obtain the requisite probability of detection).[41]

The transverse variation in wavefront amplitude also impacts the optical configurations involved in the parametric characterization of the intercepted laser. This is discussed in depth in Sec. 1.7. The issue in this regard has to do with the wavefront-sampling process by which separate, adjacent apertures or detectors extract energy from the beam. Subsequently, their outputs are compared to deduce beam coherence, direction, or wavelength. Obviously, the result of comparing the intensities of adjacent detectors will be perturbed by a pattern like that of Fig. 1.16. As a result, many equipment configurations that operate well in the laboratory are defeated by scintillation in the field.

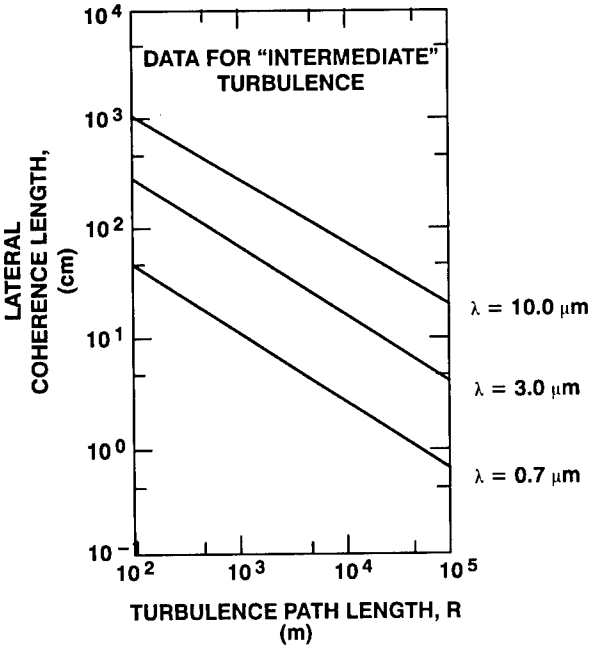

Fig. 1.17 Lateral coherence length versus turbulence path length.[42]

From the perspective of propagation observables, the transverse characterization of a propagating beam involves the measurement of the transverse coherence diameter. Note that although the transverse irradiance distribution and the transverse coherence dimensions are related, they are two different parameters. Transverse coherence measurement has been carried out by several investigators. Figure 1.17 presents[39,42] the transverse coherence diameter for some typical conditions.

Note, that for a typical example, say a 0.6943-μm ruby laser beam on a horizontal path several kilometers long, the transverse coherence distance is of the order of several centimeters. Many, if not most, laser warning receivers are smaller than this; thus, adjacent apertures close together could be expected to characterize the source properly. However, coherence diameter, which is the most commonly measured transverse scintillation parameter, is only a partial characterization of the beam. Because the sharp peaks and valleys of the transverse amplitude distribution arise from the destructive interference of adjacent beam segments and the beam is not coherent beyond its coherence diameter, it follows that the detailed structure of the peaks and valleys occur over an even smaller lateral distance. If searching for a small, relatively constant amplitude segment of the beam, one must use a sector that may be a $\frac{1}{10}$ to a $\frac{1}{100}$ of the transverse coherence diameter.

1.3.3 Backgrounds and Clutter

In many cases, the performance of warning systems is clutter limited rather than noise limited. The key to probability of detection and false alarm rate is

the signal-to-clutter ratio rather than the SNR. Signal is usually defined as the difference between the irradiance from a target containing resolution element and that from an adjacent resolution element. The signal-to-clutter ratio thus involves the local background mean as well as variations in the background and the target intensity. This section includes a brief survey of the background and clutter properties likely to be encountered in passive warning situations. Terrain clutter is discussed separately from cloud and sky clutter. Various clutter metrics useful in evaluating system performance are defined and typical values presented. A short discussion of background levels at typical threat laser wavelengths concludes the subsection.

1.3.3.1 Terrain Backgrounds. In the spectral region below 4 μm, reflected and scattered solar radiation is one of the major contributors to background radiation levels. It is unlikely that specular reflections will be significant from missile bodies, because missile designers will probably attempt to avoid glint and glare signatures. A comparison of diffuse reflectances of various backgrounds and target materials may be of some use. Table 1.10 lists[43,44] short-wavelength reflectances for a number of background materials. These values are for high elevation angles. Caution should be used in applying them at angles below 30 deg, where most surfaces become more specular in their behavior.

Table 1.10 emphasizes vegetation backgrounds and short-wavelength IR. For visible wavelengths, a summary of general terrain background reflectances is contained in Table 1.11, which is taken from Ref. 45.

Spectral variations in reflectance are much more pronounced below 4 μm than above, so the values quoted in these tables should not be extended beyond the spectral ranges indicated therein. Figure 1.18 shows spectral variations from the UV out to 4 μm for several backgrounds likely to be encountered in down-looking situations. The effect of chlorophyll on the reflectivity of vegetation at 0.72 to 1.3 μm should be noted. Few man-made surfaces exhibit such pronounced changes over limited wavelength differences.

Table 1.10 Short-Wavelength IR Background Reflectances

Material or Background Type	Hemispheric Reflectance (%)
Grass	24%
Wheat	26
Maize	22
Pineapple	15
Sugar cane	15
Deciduous woodland	18
Coniferous woodland	16
Swamp forest	12
Open water	05
Dry soil (light color)	32

Table 1.11 Luminous (i.e., Visible Band) Reflectances for Backgrounds (from Ref. 45)

Background Feature		Approximate Reflectance (%)
Water Surfaces	Bay	3-4
	Bay and river	6-10
	Inland waters	5-10
	Ocean	3-7
	Ocean, deep	3-5
Vegetation	Forest (jungle)	3-6
	Forest (open)	4-10
	Fields, dry plowed	20-25
	Fields, green	3-6
	Fields, wheat	7-10
	Grass, dry	15-25
Soils/Snow	Ground, bare	10-20
	Ground, very white	11-15
	Ground, some trees	7-10
	Sand, dry	24-31
	Sand, wet	18
	Rock	12-30
	Snow, white field	70-86
Man Made	Concrete	15-35
	Blacktop	8-9
Clouds	Clouds, dense, opaque	55-78
	Clouds, nearly opaque	44-55
	Clouds, thin	36-40
General Terrain Types	Average terrain, except barren land	5-6
	Barren land	13
	Sand, snow, and salt flats	20-40
	Mature or old growth	4-10
	New growth	7-15
	Dormant or dry growth	15-25
	Inland water	7

The intensity and spectral distribution of natural illumination sources are just as significant as the reflectances of the target and background materials. Figure 1.19 indicates[45] the variation in intensity of visible band illumination under various situations. Systems that depend solely on reflected ambient illumination to detect targets must have a high sensitivity if they are to provide night capabilities. Conversely, short-wavelength emissions from the missile plume are more easily detected against the lower background and clutter levels that exist during night or low-illumination periods. Ultraviolet radiation is strongly absorbed or scattered in the atmosphere. In the *solar blind* region of the UV spectrum from 250 to 280 nm, very little natural solar illumination reaches the earth.

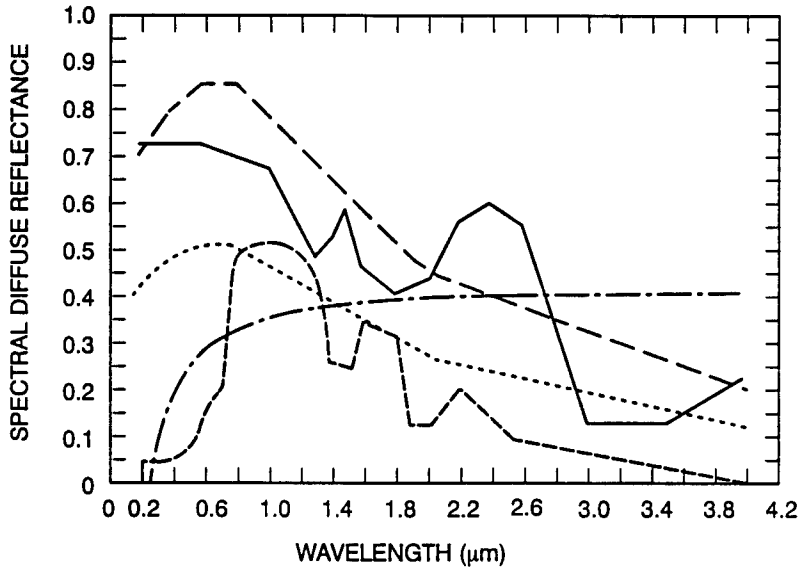

——— CLOUDS. DIRECTIONAL REFLECTANCE OF A MIDDLE LAYER CLOUD.
— — - WINTER SNOW AND ICE. DIRECTIONAL REFLECTANCE OF DRY SNOW.
····· SUMMER ICE. DIRECTIONAL REFLECTANCE OF SUMMER ARCTIC ICE.
—·— SOIL AND ROCKS. DATA REPRESENT THE AVERAGE VALUES OF THE BIDIRECTIONAL REFLECTANCE, ϱ_λ (45°, 0, 0, 0), OF GRAVEL, WET CLAY, DRY CLAY, TUFF BEDROCK AND SANDY LOAM.
– – – – VEGETATION. DATA REPRESENT THE AVERAGE VALUES OF DIRECTIONAL REFLECTANCE OF MANY TYPES OF VEGETATION (FROM THE ERIM DATA FILE[44]).

Fig. 1.18 Spectral variation for several downlooking backgrounds.

At wavelengths above 4 μm, emitted radiation dominates reflected radiation in most tactical situations. Background and clutter levels are determined by the physical temperature of the terrain surface and the emissivity of the materials. Environmental effects induce variations in material temperatures throughout diurnal and seasonal cycles. Figure 1.20 shows[46] typical summer diurnal variations in temperature over several days for eight common terrain background materials. Most background scenes are a mixture of several of these materials. The cyclic variations are also evident in clutter levels that result from transitions from one material type to another. Seasonal cycles change not only the temperatures but also the physical characteristics of many background materials, most notably deciduous vegetation and snow and ice covers. Less readily sensed environmental factors, such as the water concentration at root level, determine equilibrium temperatures and surface optical properties. Figure 1.21 illustrates[47] how the root level water concentration affects midday air to leaf temperatures under strong sunlight conditions. Differences in plant species sensitivities to root level moisture may enhance clutter levels in a multiple crop area. Soil temperatures are also dependent upon the water content of the soil. Table 1.12 shows some measured soil to ambient

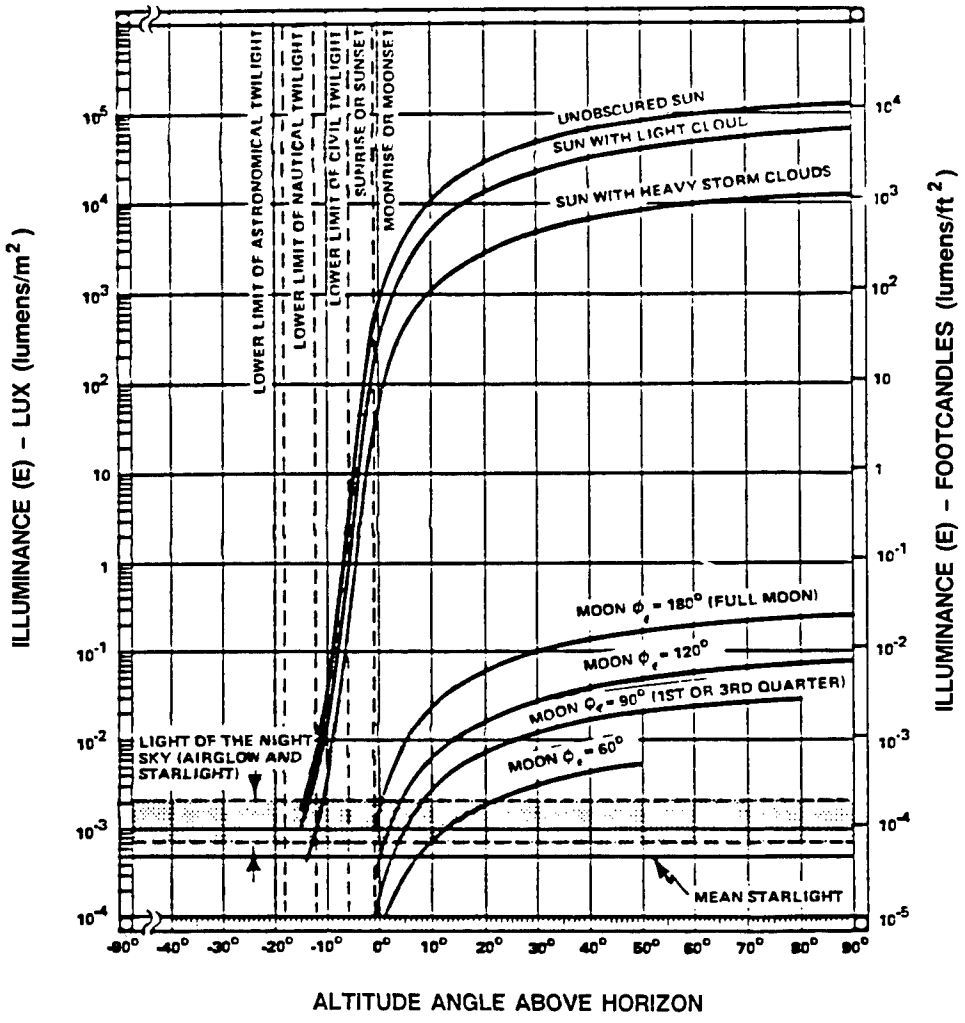

Fig. 1.19 Ambient light levels under different conditions.

air temperature differences at midday as a function of the volumetric water content.

The effect of rain on terrain backgrounds is to reduce signal contrast as well as background clutter. Surfaces are driven to temperatures near to that of the falling rain, and surface optical property differences are minimized by the wetting effects. The temperature of a falling raindrop approaches the wet bulb temperature of the surrounding air within a few seconds,[48] so the ambient wet bulb temperature is a good approximation for terrain background temperatures after a short period of rain.

It is often assumed that terrain background materials will exhibit a Lambertian type emissivity variation with viewing angle. Although this may be a reasonable assumption if no other data are available, most natural surfaces are not Lambertian. Figure 1.22 shows[46] the mean effective temperature of a

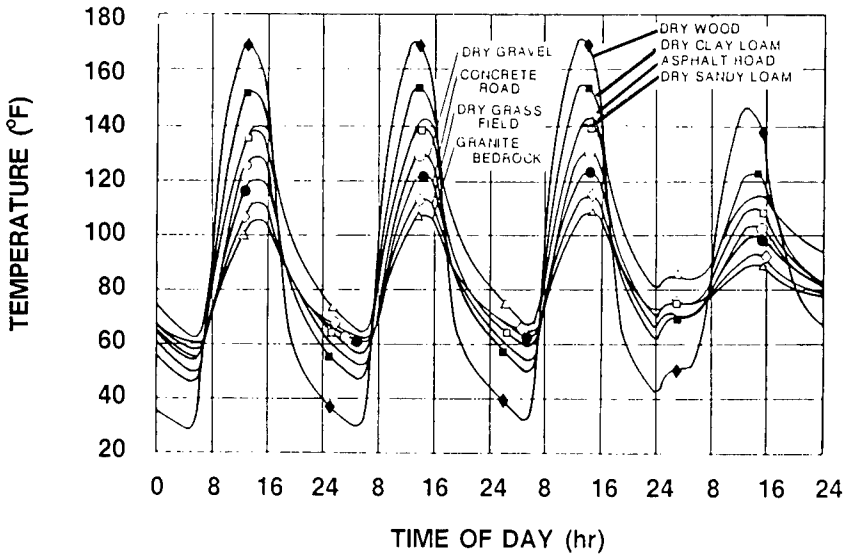

Fig. 1.20 Diurnal variations of terrestrial backgrounds.

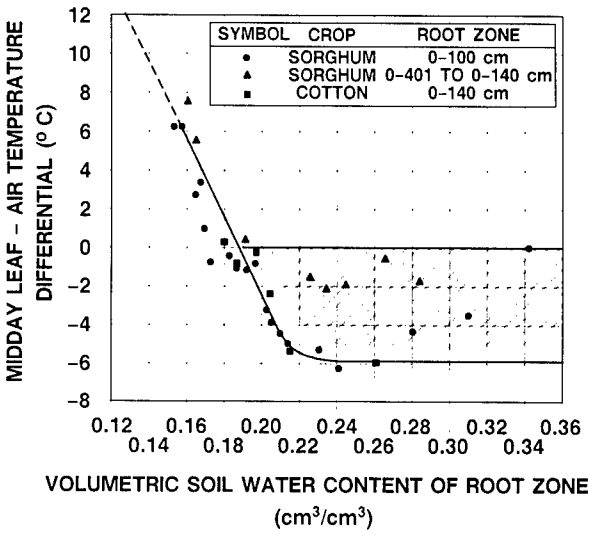

Fig. 1.21 Soil moisture effects on vegetation backgrounds.[47]

Table 1.12 Soil-to-Air Temperature Differences as a Function of Soil Water Content

Soil Water Volumetric Concentration (cm^3/cm^3)	Midday Soil-Air Temperature Difference (°C)
0.00	27
0.08	19
0.16	11
0.27	0

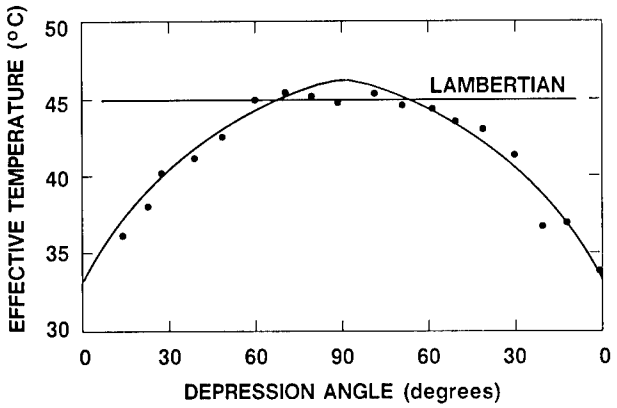

Fig. 1.22 Apparent effective temperature as a function of depression angle.

small sample area of grass viewed from various depression angles. Some of this variation may result from partial obscuration of the dirt beneath the grass in the case of short cropped grass. Similar studies of dirt, asphalt, and other materials show similar but less pronounced variations with depression angle. Other statistical parameters of the clutter such as standard deviation, correlation length, and other spatial parameters, also vary with viewing angle.

Special Cases—Water and Snow Backgrounds. The optical properties of water surfaces are very dependent on viewing angle. For a flat water surface, the reflectivity and emissivity can be calculated directly from the index of refraction at a given wavelength. However, water backgrounds are rarely encountered in a flat condition. Wind is the primary driver of surface irregularities on large bodies of water. Cox and Munk[49] have developed an algorithm for relating water surface angles with prevailing wind conditions. The sea surface is treated as many facets whose slope components exhibit a Gaussian distribution. The anisotropy in facet orientations depends on wind direction anisotropy. Equation (1.18) relates the mean square slope σ^2 to the masthead wind velocity, w in meters/second (our primary concern with water waves is the potential for false alarms due to sun glint or other reflections):

$$\sigma^2 = 0.003 + 0.00512w \pm 0.004 \ . \tag{1.18}$$

Models for estimating the equilibrium temperature of water surfaces are of limited value because of the strong local variations in water temperatures. In the case of small isolated bodies of water, the physical temperature can be estimated using an empirical relation[50] given by

$$T_w = 56.182 - 0.95454\Phi + 0.0021307\Phi^2 + \Delta T_{\text{month}} \ , \tag{1.19}$$

where T_w is the water temperature in Celsius, Φ is the latitude in degrees, and ΔT_{month} is a correction term for monthly variations given in Table 1.13. The numerical values were determined by Cloud[50] using data from the U.S. Geological Survey Station, Reston, Virginia.

Table 1.13 Water Temperature Monthly Corrections (°C) (from Ref. 49)

Month	Temperature	Month	Temperature
Jan	-12.5	Jul	+2.8
Feb	-11.1	Aug	+1.45
Mar	-10.1	Sep	0.00
Apr	-6.2	Oct	-4.22
May	-2.2	Nov	-8.45
Jun	+0.3	Dec	-10.50

The emissivity of water surfaces in the infrared varies with both wavelength and viewing angle. Figure 1.23 shows[51] the emissivity of flat water surfaces as a function of depression angle for the spectral range between 1 and 15 μm. Note the nonlinear vertical scale selected to emphasize small variations near 1.0.

The angle at which water is viewed has a strong effect on infrared emissivity. Figure 1.24 shows[52] this in the form of an apparent temperature difference between the surface and the corresponding blackbody temperature at three different wavelengths. Zenith angle is the primary variable. Wind speeds of 0, 1, 5, and 15 m/s are illustrated. The effect of surface roughness on apparent temperature is illustrated[52] in Fig. 1.25. In the case of sea water, the salinity has some effect on the surface optical properties. However, the effective temperature difference between pure water and sea water is much less than the other illustrated effects. It ranges from 0.02°C near zenith to 0.05°C at about 85 deg from zenith. The sign is always negative (sea water appears colder than pure water by 1/20 of a degree or less). Figure 1.26 shows[52] the ratio of relative reflectances for pure and sea waters in the region from 4 to 16 μm.

Snow backgrounds introduce another factor—the age of the snow surface. Fresh fallen snow is nearly black in the infrared bands, but the emissivity

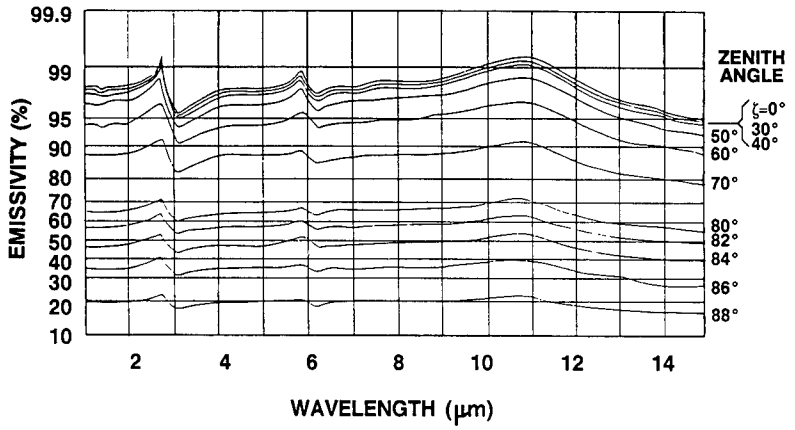

Fig. 1.23 Spectral emissivity of water in the infrared region for several angles of view.[51]

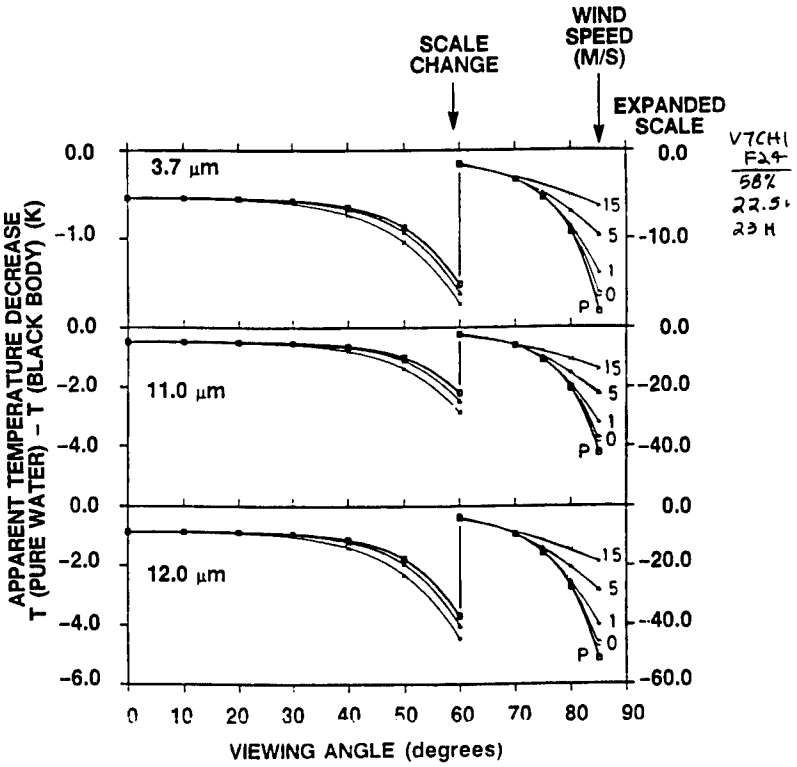

Fig. 1.24 Effect of viewing angle on apparent temperature of water (as a function of wind speed and wavelength).[52]

decreases with time. Sublimation and thawing, along with refreezing cycles, alter the surface properties. Figure 1.27 shows[53] the spectral reflectance of snow with natural aging.

Table 1.14 shows[54] some measured reflectance data on various snow types for the 3- to 5- and 8- to 12-μm bands. Note the nominal factor of three variation in both bands.

Other spectral regions, besides the visible and infrared are effected by aging and cycle effects in snow. Passive millimeter-wave radiometers can detect strong variations in surface reflectivity when snow has been thawed and refrozen. This phenomenon, known as metamorphic (or refrozen) snow, can generate contrasting patches of the order of meters in diameter across the snow surface.

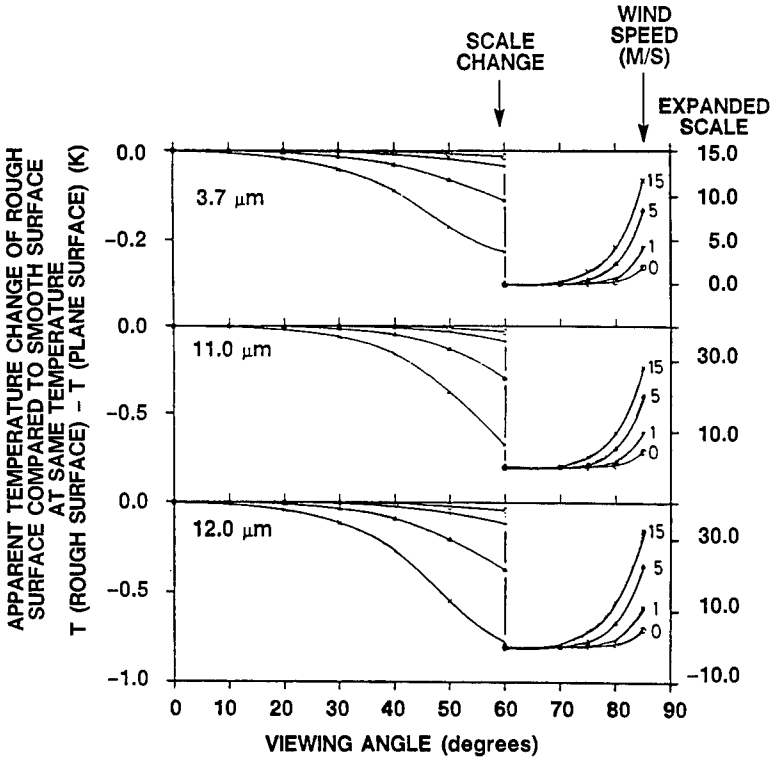

Fig. 1.25 Effect of surface roughness on apparent temperature (as a function of wind velocity and wavelength).

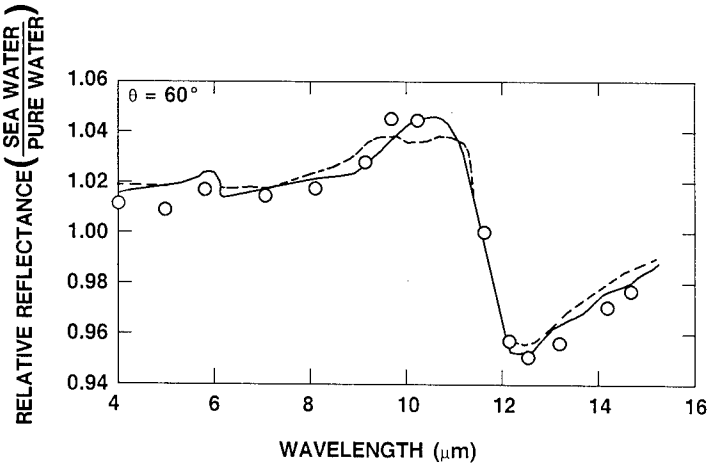

Fig. 1.26 Relative reflectance of artificial ocean water as a function of wavelength at a 60-deg angle of incidence to a plane surface. Measured data and salinity corrections to two sets of pure water refractive index data are shown.[52]

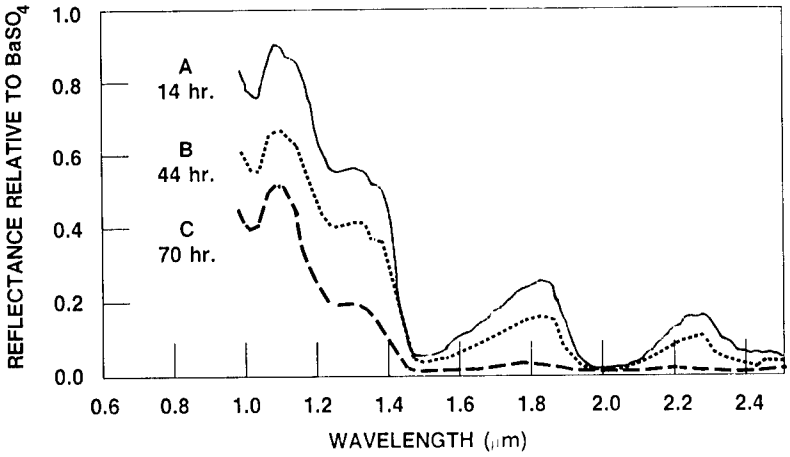

		A	B	C
SNOW CONDITION:	NATURAL AGING	14 hr	44 hr	70 hr
SNOW DENSITY:	g cm^{-3}	0.97	0.104	0.347
SNOW HARDNESS:	g cm^{-2}	≈4.5	≈4	50+

$BaSO_4$ IS A COMMON REFLECTANCE STANDARD WITH A NOMINAL REFLECTANCE OF ONE IN THIS RANGE.

Fig. 1.27 Snow reflectance changes with aging.

Table 1.14 Reflectance of Various Snow Types

Snow Characteristics		Reflectance (%)	
Density (kg/m^3)	Description	3-5 μm Band	8-12 μm Band
160	Metamorphosed grains 0.1-1 mm, some clustering, pock marked surface, 1 mm peak to trough	1.27	0.51
220	Broken crystals, 0.1-1 mm, drifting snow, very flat	0.94	0.44
320	Melt-freeze ice crust, pocked surface, 3 mm peak to trough	2.86	1.46

1.3.3.2 Cloud and Sky Backgrounds. Clear sky background levels in the infrared are determined by the emission and scattering of the atmosphere components along the line of sight at each wavelength. A code such as LOWTRAN[3] is useful for calculation of path emissions. In window regions such as the 8- to 12-μm band, the elevation angle determines the path length to space (effective temperature of 3 K), hence colder backgrounds can be ex-

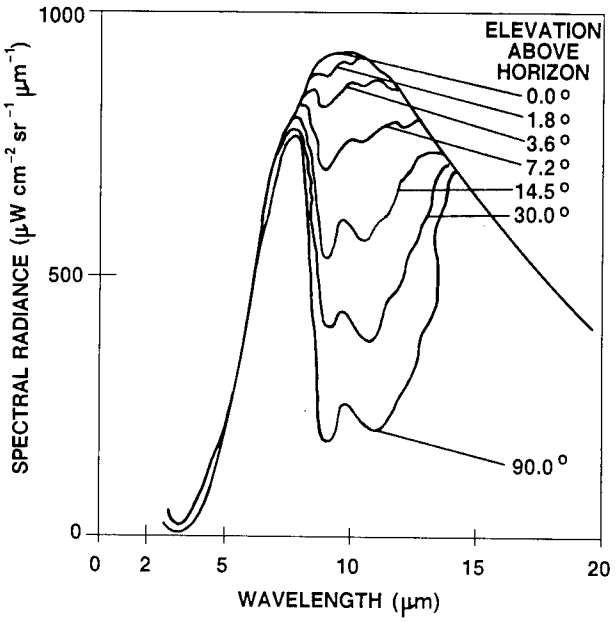

Fig. 1.28 Clear sky spectral background.[55]

pected near the zenith. Figure 1.28 shows[55] the clear sky spectral background as a function of elevation angle.

An empirical equation for estimating the clear sky zenith radiometric temperature as a function of ground level air temperature and humidity has been derived by Idso.[56] It treats the atmosphere as a graybody at ground level air temperature with an emissivity ε, which is dependent on temperature and humidity. The equation can be used for broadband radiance or for narrower 8- to 12-μm or 11 to 12-μm bands with different sets of numerical coefficients. The equation is

$$T_{\text{sky}} = \varepsilon^{1/4} T_{\text{air}} = [a + b\delta^2 \exp(c/T_{\text{air}})]^{1/4} T_{\text{air}} , \tag{1.20}$$

where δ is the water vapor pressure in mbars and the coefficients a, b, and c are band dependent. For the broad 8- to 14-μm band, $a = 0.24$, $b = 2.98 \times 10^{-8}$, and $c = 3000$. For the narrower 10.5- to 12.5-μm band, which is useful for calculating cold sky reflectances, $a = 0.10$, $b = 3.53 \times 10^{-8}$, and $c = 3000$. For the full thermal spectrum, the expression takes the form

$$T_{\text{sky}} = [0.70 + 5.95 \times 10^{-5}\delta \exp(1500/T_{\text{air}})]^{1/4} T_{\text{air}} . \tag{1.21}$$

The Idso approach is convenient for zenith sky temperatures in the broad bands indicated. A more general empirical approach due to Martin and Berdahl[57]

predicts clear sky emissivity as a function of wavelength λ and zenith angle θ. Sky emissivity is given by

$$\varepsilon_s(\lambda,\theta) = 1 - (1 - \varepsilon_s')\left[\frac{t(\lambda)}{t_{\text{av}}}\right] \exp[b(1.7 - 1/\cos\theta)] \ , \tag{1.22}$$

where ε_s', the total sky emissivity, can be estimated from the dew point temperature T_{dp} in kelvins by

$$\varepsilon_s' = 0.711 + 0.56\left(\frac{T_{\text{dp}}}{100}\right) + 0.73\left(\frac{T_{\text{dp}}}{100}\right)^2 \ , \tag{1.23}$$

and the factors b and $[t(\lambda)/t_{\text{av}}]$ are determined from Table 1.15.

In the visible and ultraviolet spectral regions, sky backgrounds are primarily the result of scattered solar radiation. During daylight hours this scattered background radiation is so intense that postburnout missiles or other passive targets are potentially detectable due to their negative contrast against the "bright" sky. The intensity of the scattered sky radiation decreases with altitude.

Cloud-filled skies represent a different background and clutter case for tactical situations. In the infrared, clouds behave as graybodies with an emissivity near one. The equilibrium temperature of the under side of a cloud layer is usually close to the ambient air temperature at the altitude of the cloud base. This can be estimated from the ground level air temperature and the typical air temperature lapse rate by

$$T_{\text{air}}(h) = T_{\text{air}}(0) - 6h \ , \tag{1.24}$$

where $T_{\text{air}}(0)$ is the ground level ambient air temperature in degrees Celsius and h is the height of the cloud base in kilometers.

Table 1.15 Best-Fit Parameters for Determining Sky Emissivity (from Ref. 57)

Wavelength (μm)	$b = A\ \epsilon_s' + B$		$t(\lambda)/t_{av} = C\ \epsilon_s' + D$	
	A	*B*	*C*	*D*
3-33 (Broad band)	1.493	-0.867	1.124	0.600
8-14	1.792	-1.113	1.807	1.034
8.8	1.281	-0.771	5.119	-1.192
9.6	1.305	-0.715	5.321	-1.609
11	1.778	-1.159	3.174	0.452
15	-5.778	5.258	0.041	-0.007
17-22	-0.691	1.653	-1.549	1.298

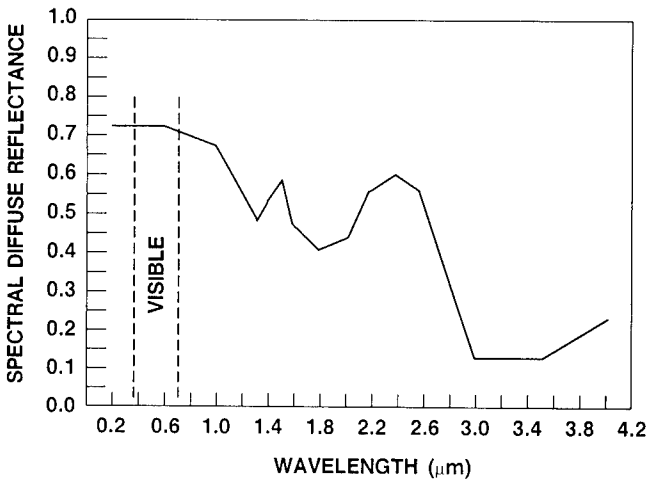

Fig. 1.29 Measured spectral cloud reflectance.

Clouds are frequently broken and irregular instead of uniform overcast, in which case clutter statistics become significant. In the case of down-looking sensors, cloud tops often provide a source of reflected solar radiation, also generating high clutter levels. Figure 1.29 shows[58] the spectral variation in cloud reflectance from the ultraviolet into the mid infrared.

1.3.3.3 Clutter. Backgrounds are rarely uniform and stationary, so the spatial and temporal variation in backgrounds must be considered in missile detection problems. With the exception of sun glint from choppy water surfaces and cloud edges (see Fig. 1.42 in Sec. 1.5.1.1 for an example) and platform-motion-induced effects, naturally occurring temporal variations are generally insignificant in tactical situations and easily compensated for in strategic situations. Spatial variations in background radiance, on the other hand, place severe demands on detection algorithms.

The definition of appropriate clutter metrics depends on the sensor system and target size and location. A two-dimensional Fourier transform or autocorrelation function of the received image provide most of the detail needed to characterize the clutter, but are difficult to implement in real time. Simpler metrics, such as standard deviation of the radiance, may be misleading because of undefined spatial frequencies. A clutter metric suggested by Schmieder and Weathersby[59] uses standard deviations within target-sized areas and has been shown to correlate well with the ability of human observers to detect targets in clutter. It is

$$\text{clutter metric} = \left(\sum_{i=1}^{N} \frac{\sigma_i^2}{N} \right)^{1/2}, \tag{1.25}$$

where the image space has been divided into N approximately target-sized cells and σ_i is the standard deviation in each cell. This definition is of limited

utility when the target is smaller than the instantaneous field of view of the sensor, which is the case with many present day sensor systems, but may be useful with future high resolution missile warning systems. The signal-to-clutter ratio (SCR) can be related to system performance. Techniques to isolate targets from clutter are discussed in Sec. 1.4.2.6.

The one-dimensional power spectral density (PSD) is frequently used to describe background clutter. The frequency dependence of natural background PSDs is often well behaved, following a $\text{PSD}(f) = Cf^{-n}$ form, where f is the spatial frequency (in cycles per angular or linear unit) and n is either 1 or 2. Figure 1.30 shows[60] a representative one-dimensional clutter PSD from the red spike region (4.39 to 4.57 μm). Note the shift in behavior from $1/f^2$ at lower frequencies (typical of cloud structures) to $1/f$ at higher frequencies (typical of structured ground patterns). The units of this PSD are $(\mu\text{W sr}^{-1}\ \text{cm}^{-2}\ \mu\text{m}^{-1})^2/(\text{cycles/km})$. The constant C relating PSD to frequency, which depends on spectral band and clutter levels, can range from 10^{-1} to 10^3. Nominal values of 1 for the exponent and proportionality constant can be used as a first approximation for estimating clutter levels.

One-dimensional PSDs are a convenient metric for clutter considerations, but real-world backgrounds are isotropic only for direct downward or upward viewed scenes, and not always then. Nonvertical viewing angles introduce an anisotropy to the background image that can be corrected with the cosine of the depression angle, if known.

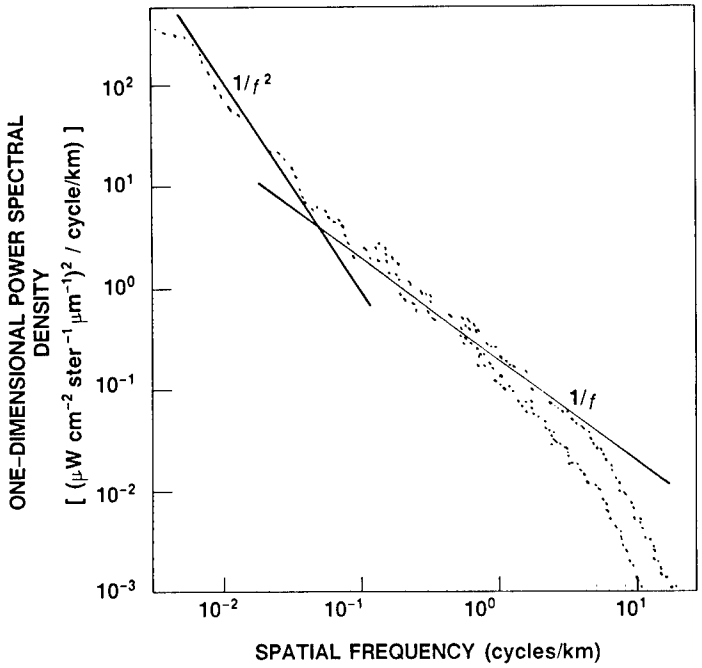

Fig. 1.30 PSD curve showing $1/f$ variations.[60]

Atmospheric attenuation of clutter contrast must also be considered. Ranges from observer to target and observer to background plane are generally not equal, and contrast attenuation is greater for the clutter than for the target signal level. For nonvertical viewing angles, the foreground clutter is attenuated less than the distant background clutter.

Clutter levels are subject to environmental factors and exhibit diurnal and seasonal variations. Hetzler[61] has studied diurnal and seasonal variations of distant hilly and mountainous terrains in the western United States and noted dependencies on solar load and sun angle. Balick and Doak[62] have documented the relation between observer and sun angles on forested backgrounds. Clutter autocorrelation functions can provide an indication of the severity of the clutter for typical target-sized objects. The distribution of spatial frequencies in terrain clutter varies over the diurnal cycle.

Ben-Yosef[63] suggested an empirical model for estimating the clutter autocorrelation function once physical parameters of the terrain have been estimated from measurement data. The physical parameters are the heat capacity, the heat conductivity, and the solar absorption coefficient of a surface element. If $T(x,y)$ is the temperature of a surface element at position (x,y), the autocorrelation function is defined as

$$R_T(\Delta x,\Delta y) = \langle [T(x + \Delta x, y + \Delta y) - \langle T \rangle] * [T(x,y) - \langle T \rangle] \rangle \ , \tag{1.26}$$

where the averages $\langle\ \rangle$ are taken over the entire scene. The fixed terrain parameters are heat capacity $c(x,y)$, heat conductivity $k(x,y)$, and the solar absorption coefficient $a(x,y)$. They have correlation lengths of r_c, r_k, and r_a, respectively. The autocorrelation function of the terrain area can be expressed as

$$R_T(r) = (A_1 + A_2) \exp(-r/r_T) \ , \tag{1.27}$$

where r_T is the surface temperature correlation length, a function of time, and can be expressed as

$$r_T(t) = \frac{A_1 + A_2}{A_1 + \beta A_2} \ . \tag{1.28}$$

The factor β is the ratio of the conductivity and absorption correlation lengths, $\beta = r_k/r_a$, and the time dependent quantities A_1 and A_2 are given by

$$A_1(t) = [Kf(t) - C]^2 \quad A_2(t) = [Kf(t)]^2 \ . \tag{1.29}$$

The main time dependent variable is the radiative flux $f(t)$, usually the solar load, and the factors K and C are coefficients to the stationary state solution for the ground temperature distribution

$$T(x,y,t) = Kf(t)\frac{a(x,y)}{k(x,y)} - C\frac{1}{k(x,y)} \ . \tag{1.30}$$

If the three autocorrelation lengths of the physical parameters can be obtained from knowledge of the terrain composition or analysis of several thermal im-

ages of the area, the temperature autocorrelation function (and consequently PSD) can be calculated for any given radiative flux input $f(t)$.

A subset of the clutter problem is that of discontinuities in the background components. Interfaces between land and water, or vegetation and bare soil, can exhibit discrete changes in radiance even greater than that of the clutter on either side. Spatial filtering can usually discriminate against these discontinuities, but the importance of adaptive local thresholding to accommodate these rapid shifts in background level should not be ignored.

1.3.3.4 Earth Background for Strategic Targets. When viewed from space, the earth and its atmosphere represent sources of intense EO/IR background signals. This background results in noise and clutter that can compete with actual targets in the detection process. For sensors operating in atmospheric window bands, the hard earth, with all the variability of its terrain and sky features, represents a major source of clutter. This clutter makes the detection of cruise missiles and strategic aircraft very difficult. Even for sensors operating in missile plume bands, the view from space can be quite cluttered. Although the atmosphere might be semiopaque in these bands, solar reflections off high clouds can effectively blind sensors operating in the near-IR portion of the spectrum.

In addition to being a source of noise and clutter, earth backgrounds can have a profound effect on the apparent signature of the less intense strategic targets (namely, cruise missiles and strategic aircraft). For example, because strategic targets may be viewed against a warm-earth background, the apparent radiance of the target may be less than the brightness of the background, resulting in negative contrast signatures. As a result, strategic warning sensors might have to deal with positive contrast targets, negative contrast targets, and in some cases, targets that have zero contrast in a particular spectral band.

1.3.3.5 Background Levels for Laser Warning. LWR background sources give rise to a steady level of background noise and spurious signal-like events. Potential false signals within laser warning receivers are contributed by several sources including

- scene clutter resulting from steady-state solar reflectance and thermal self-emission
- sun glint
- battlefield sources, such as gunflashes and fires
- lightning
- electromagnetic interference (EMI)
- cosmic rays.

Typical, static scene clutter, either solar or thermal, is not usually a significant issue within laser warning receivers because LWRs are usually staring systems, sometimes even nonimaging, often with low angular resolution. In addition, they typically are electronically designed to optimize the SNR of short pulses in the micro- and nanosecond regimes and, thus, usually incorporate high-pass filters that tend to block any residual scene image structure.

The constant noise background that arises from the quantum statistical variations (*shot noise*) in the detected background photons is the dominant

source of noise in many laser warning receivers. For LWRs at wavelengths shorter than 2.5 to 3.0 μm, the solar background is the primary noise source; for longer wavelength systems the dominant shot noise source tends to be the thermal background.

Sun glint from various reflective, or refractive, surfaces that have some relative angular motion with respect to the laser warning receiver can cause very large signals with surprisingly rapid rise times. Typical sun glint sources include reflection from vehicular windshields, from water surfaces (when the LWR is aircraft mounted), and even from water droplets in sea-going scenarios.

Battlefield sources, such as gun flashes and the transient pulses associated with explosives, are potential false alarm sources, particularly when the optical rise time is rapid. Note that some such sources, many large caliber gunflashes for instance, also have a multipulse transient that can spoof laser warning receiver circuits that use multipulse logic to reject false targets. On the other hand, battlefield fires that are a prime source of concern to airborne missile warning receivers are of little significance to laser warning receivers since they are relatively static and are rejected by the high-pass circuits involved.

Lightning is a serious problem with laser warning receivers; it is intense, has a rapid rise time, and exhibits multipulse structure. Moreover, the lightning photons are accompanied by a strong electromagnetic pulse in the rf range. Lightning has been characterized,[64] and its parameters with respect to laser warning receiver design have been studied.

Electromagnetic interference, primarily from weapon system associated radars, has been a common source of laser warning receiver false alarms. This has occurred because many military lasers, specifically rangefinders, are collocated with, and operated in conjunction with, high-power fire control radars. Typically, this has not been an issue with the radar warning receiver community because these signals are, in fact, their target source.

Cosmic rays are energetic, charged particles that constantly bombard the earth, originating mostly from solar sources. Typical particle counts are of the order of several particles per minute per meter squared and vary with a variety of astronomical, geographical, and local conditions.[65] When a laser warning receiver is designed to respond to, and alert upon, a single-pulse laser rangefinder, it becomes susceptible to cosmic rays as a false signal source. A portion of these rays, as they bombard the receiver, pass through the detector junction/surface and release electrons that are indistinguishable (in conventional detectors) from laser-generated photoelectrons.

1.4 SIGNAL DETECTION THEORY

1.4.1 Introduction

Before a warning receiver can provide warning of an impending threat, it must first detect the threat. To accomplish this function in a timely fashion, the threat usually must be detected at long range. At such a range, the signal produced by the threat and received by the warning receiver may be weak and difficult to detect. Noise, generated by several sources, competes with the threat signal for detection. On occasion, the threat signal may be so weak that the noise effectively masks it, and the warning receiver is unable to detect the

threat. Sometimes, noise may cause the warning receiver to indicate the presence of a threat when there is no threat present. Because noise causes these missed detections and false alarms to occur on a random basis, the process of signal detection must be described in statistical terms. Specifically, we must describe the process in terms of probabilities; viz., the probability of detection and the probability of false alarm.

If a warning receiver were to make many independent observations of a target under identical conditions, the target would be detected only some fraction of the time. This fraction is the conditional probability of detection P_D. It is the probability that a target is detected given the condition that a target is present. Likewise, if the receiver were to make many independent observations with no target present, it would declare a target to be present some fraction of the time. This fraction is the conditional probability of false alarm P_{FA}, and those false target declarations are false alarms. Since warning receivers continually monitor the environment, false alarms will be generated in a random fashion over time. The average number of false alarms per unit time is the false alarm rate (FAR).

The key figures of merit describing the detection performance of a warning receiver are P_D, P_{FA}, and FAR. They are, of course, functions of the design parameters of the warning receiver, target parameters, and environmental parameters. Determining the value of these functions for a particular warning receiver design and specific threat conditions requires that the signal and noise at the receiver detection decision circuit be described in statistical terms. Specifically, the probability functions describing the signals in the detection circuits for the case when a target is present and the case when a target is not present must be determined.

The required probability function depends on the target signal characteristics and the nature of the dominant noise sources present in the particular sensor application. In some cases, the dominant source of noise may be noise originating in the sensor electronics. Examples of this kind of noise are preamplifier noise and electronic readout noise. Another important source of noise originates in the quantum nature of the detection process. In the process of converting incoming IR energy into an electrical current, discrete packets of light energy (photons) generate photoelectrons in a random fashion. As a result, the number of photoelectrons collected in a measurement interval is a random quantity. In many EO sensor applications, the fluctuations in this quantity can represent a major source of noise. For example, if a weak IR target is being viewed against a bright, uniform IR background, the quantum fluctuations in the observed background level may limit the detectability of the target. A sensor operating under these conditions is said to be a *background limited performance* (BLIP) sensor.

Yet another factor that can limit the detectability of a target is background clutter. As EO/IR technology has advanced, it has become possible to develop warning systems with the sensitivity required to respond to low-signature threats. For these sensors, the detection performance is often limited by structure in the signals produced by the backgrounds against which the targets must be detected. This type of background structure is called *clutter*. Clutter signals usually exhibit noiselike qualities and are often described in statistical terms. The analysis of problems involving target detection in clutter often

involves the same techniques as used in the analysis of problems involving signal detection in random noise.

This section introduces some of the basic concepts in the theory of signal detection in the presence of noise and clutter. Some of the more common statistical functions encountered in the analysis of EO/IR signal detection problems are described. Examples of detection performance calculations are also presented, and advanced signal detection concepts are introduced.

1.4.2 General Theory

1.4.2.1 Gaussian Probability Density Function (Single Event in White Noise). In the simplest form of target detection in an IR warning receiver, the output of a detector channel is filtered by a linear time-invariant filter to reduce the effect of noise and is then compared to a fixed threshold level. Anytime the filter output exceeds the threshold level, a target is declared to be present.

For a passive IR receiver designed to detect a target that is intense enough so that quantum fluctuations of the signal can be neglected, the threat signal can be modeled as a deterministic signal. For example, when the target is at a long range from the receiver, it can be modeled as a point source with a constant radiant intensity. The irradiance at the entrance aperture produced by this target can be calculated by including the effects of range and the propagation path transmission. This irradiance is focused by the optics onto a detector where the IR radiation is converted into an electrical current. Because the target point image, in general, moves across the detector as a consequence of real target motion or optical scanning by the warning receiver, the detector current varies with time. With a knowledge of the optical blur function, the detector geometry and responsivity, and the image motion, this time-varying current can be calculated. The output of the filter can finally be determined using the known input current waveform and linear filter theory.

The signal appearing at the threshold detector is also corrupted by noise. There are many important instances when signal and noise may be described independently of one another. One such case is the background limited performance case. When a sensor is operating under BLIP conditions, the dominant source of noise is the fluctuation in the background current level that results from the quantum nature of light. The characteristics of these fluctuations are essentially unchanged by the addition of a signal that is small compared to the average intensity of the background. For such a case, the signal and noise may be considered to be additive. That is, the waveform at the input to the threshold circuit may be considered to consist of the signal current described previously plus a noise waveform. This noise waveform is independent of the signal waveform and has the same characteristics whether or not a signal is present.

With the additive signal and noise model, a noise waveform is introduced to the detector channel prior to the filter. It is usually the case that the noise waveform varies rapidly in time compared to the response time of the filter. That is, the bandwidth of the noise is large compared to the bandwidth of the filter, and the noise current at the input to the filter can be modeled as *white noise* with a spectral density of η in square amperes per hertz. Under these

conditions, the noise waveform at the output of the filter is characterized by a Gaussian probability density function. Specifically, the probability that the noise waveform results in a current between I and $(I + dI)$ is $p_N(I)\,dI$ with $p_N(I)$ given by the following expression:

$$p_N(I) = \frac{1}{\sqrt{2\pi}\,I_{\text{rms}}} \exp\left[- \frac{(I - I_B)^2}{2I_{\text{rms}}^2} \right] , \tag{1.31}$$

where I_B is the average (or dc) current and I_{rms} is the root-mean-square value of the ac portion of the noise waveform. In terms of the noise spectral density at the input to the filter, the I_{rms} current is given by the following expression:

$$I_{\text{rms}} = (\eta \Delta f)^{1/2} . \tag{1.32}$$

In this expression, Δf is the noise equivalent bandwidth of the filter and is obtained from the filter transfer function $H(f)$ by the following expression:

$$\Delta f = \int_0^\infty |H(f)|^2 \, df . \tag{1.33}$$

When a deterministic signal is added to the noise waveform, the probability density function that describes the filtered output current is still a Gaussian density function. The probability that the output current is between I and $(I + dI)$ at a time corresponding to a particular point in the deterministic signal (say at the peak of the signal) is $p_S(I)\,dI$, where $p_S(I)$ is given by the following expression:

$$p_S(I) = \frac{1}{\sqrt{2\pi}\,I_{\text{rms}}} \exp\left[- \frac{(I - I_B - I_S)^2}{2I_{\text{rms}}^2} \right] . \tag{1.34}$$

The variance associated with this probability density function is the same as before, but now the mean value has been shifted by an amount equal to I_s, the value of the deterministic signal at the selected point in time.

With the probability density function for the signal plus noise known, it is possible to determine the probability of detection. A very good approximation is that the probability of detection is equal to the probability that the value of the signal plus noise current exceeds the threshold current I_T at the instant the deterministic signal reaches its peak value. That is, the probability of detection P_D is given by the following expression:

$$P_D = \int_{I_T}^\infty p_S(I)\, dI . \tag{1.35}$$

Defining the peak signal-to-rms-noise ratio (SNR) as I_s/I_{rms}, and the threshold-to-noise ratio (TNR) as $(I_T - I_B)/I_{\text{rms}}$, the expression for P_D can be rewritten in the following form:

$$P_D = \frac{1}{\sqrt{2\pi}} \int_{(\mathrm{TNR}-\mathrm{SNR})}^{\infty} \exp(-u^2/2)\, du \ , \tag{1.36}$$

where the integration variable u is the normalized current, $(I - I_B - I_S)/I_{\mathrm{rms}}$.

Figure 1.31 presents a plot of the above expression for P_D versus TNR minus SNR. The figure shows that when the noise and signal-plus-noise cases can be characterized by Gaussian probability density functions with equal variances, a value of SNR minus TNR equal to 1.28 is required to achieve a P_D of 0.90.

As might be expected, P_D increases toward unity as the threshold current is set to lower values. However, doing so also increases the probability of false alarm. This is illustrated by Fig. 1.32. This figure shows two Gaussian probability density functions, both with the same variance. One density corresponds

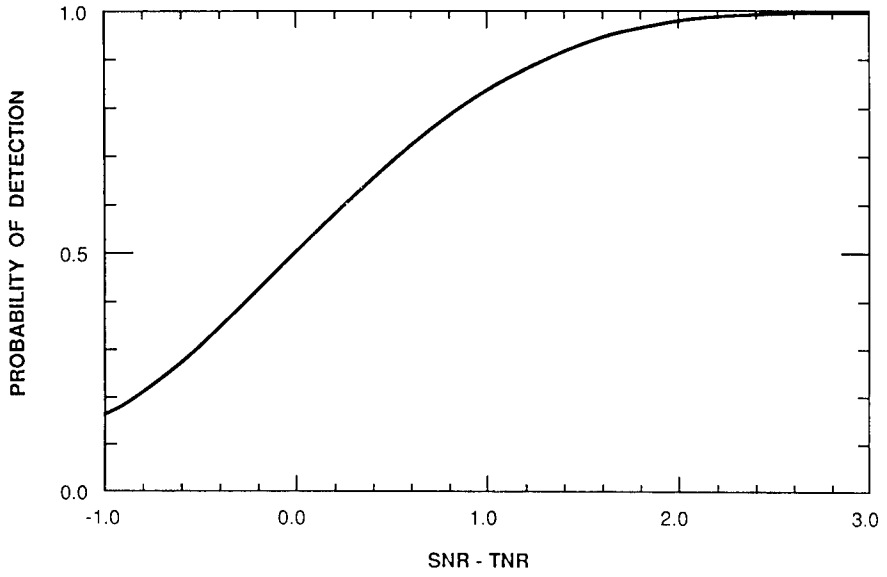

Fig. 1.31 Probability of detection as a function of SNR and threshold setting.

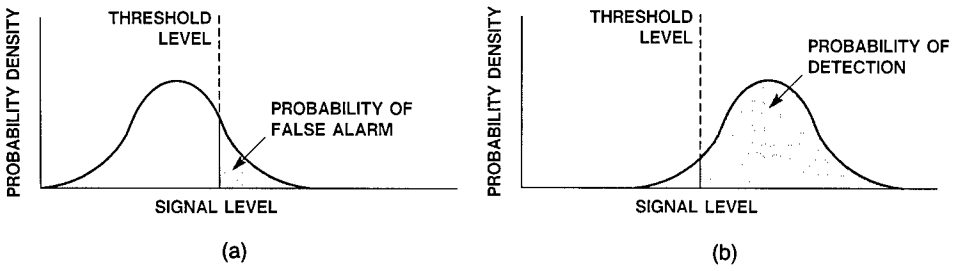

Fig. 1.32 Probability of detection and false alarm for (a) no target present, where shaded area represents the false alarm probability, and (b) target present, where shaded area represents the probability of detection.

to the noise-only waveform and is centered at a mean value of I_B. The other density function corresponds to the signal-plus-noise case and is centered at a mean value of $I_B + I_s$. For a detection threshold set at I_T as shown in the figure, the area under the portion of the signal-plus-noise density curve corresponding to current values above the threshold current I_T is the probability of detection. This is indicated by the shaded area in the figure. As the threshold setting is lowered, this area, corresponding to the probability of detection, increases toward unity, but so does the area under the noise-only curve, corresponding to the probability of false alarm.

The probability of false alarm during an observation interval will, of course, lead to a false alarm rate in a system that continually searches for targets. Rice[66] solved a problem that allows us to relate the FAR to the TNR. He analyzed the statistical properties of white noise filtered by an ideal low-pass filter of bandwidth f_0 and determined the mean time between successive maxima in the filtered noise. Assuming the filter in the threshold detection circuit is a low-pass filter, then to a good approximation, this time is also the mean time between false alarms in the threshold detection circuit. Using Rice's expression for mean time between successive maxima, T_m, the FAR is given by the following:

$$T_m = \frac{\sqrt{3}}{f_0} \exp(\mathrm{TNR}^2/2) \ , \tag{1.37}$$

$$\mathrm{FAR} = \frac{1}{T_m} \ . \tag{1.38}$$

This expression is plotted in Fig. 1.33 with FAR/f_0 as a function of TNR.

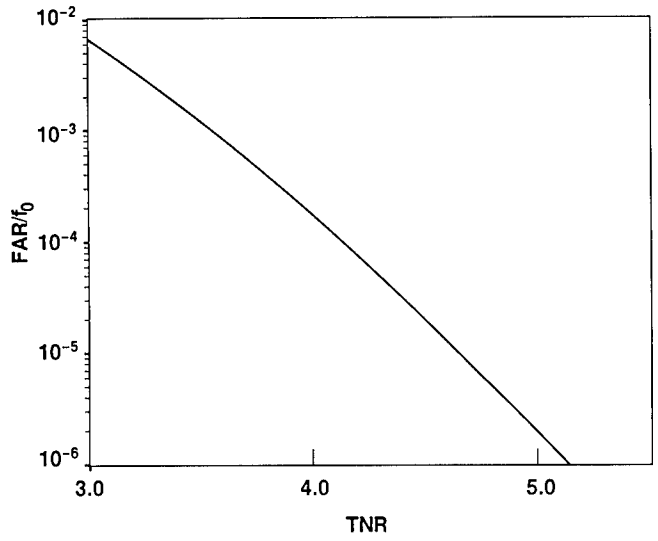

Fig. 1.33 Probability of false alarm as a function of threshold setting.

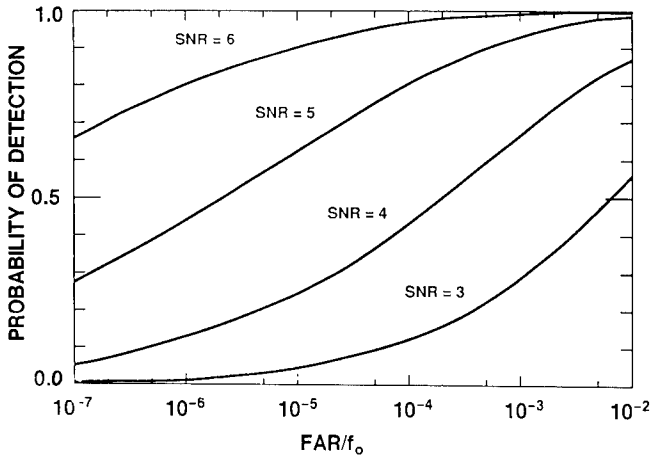

Fig. 1.34 Receiver operating characteristic curves. Plots of probability of detection versus false alarm rate with SNR as a parameter.

The probability of detection data presented in Fig. 1.31 and the FAR data presented in Fig. 1.33 can be combined to show the probability of detection as a function of the FAR with SNR as a parameter. The result of doing this for the previously presented detector example is shown in Fig. 1.34. The curves in this figure are the receiver operating characteristic for pulse detection in the presence of additive filtered white noise.

If we assume that a real filter can be approximated by an ideal low-pass filter with a bandwidth f_0, we can use Fig. 1.34 to determine the detection range of a point target in the presence of white Gaussian noise. To do this, we must determine the SNR. Obtaining the SNR for a sensor viewing a point target is straightforward if the sensor sensitivity can be expressed in terms of a noise equivalent irradiance (NEI). By definition, the SNR in terms of the NEI is given by the following expression:

$$\text{SNR} = \frac{E(R)}{\text{NEI}} , \tag{1.39}$$

where $E(R)$ is the in-band target irradiance at the entrance aperture of the sensor when the target is at a slant range of R from the sensor. In this example,

source intensity I_0	= 100 W/sr
slant range R	= 5 km
atmospheric transmission $\tau_a(R)$	= 0.3
NEI	= 2×10^{-11} W/cm^2
filter bandwidth	= 10,000 Hz

$$E(R) = \frac{I_0}{R^2}\tau_a(R) = 12 \times 10^{-11} \text{ W/cm}^2 , \tag{1.40}$$

$$\text{SNR} = \frac{E(R)}{\text{NEI}} = 6 \ . \tag{1.41}$$

From Fig. 1.34, we see that we can achieve a probability of detection of 0.9 and a FAR of 0.08 per second. The value of SNR minus TNR at this operating point, as obtained from Fig. 1.31, is 1.28. Consequently, the TNR must be set at 4.72 for the receiver to perform at this operating point.

1.4.2.2 Matched Filter Detection. In the example just presented, the specification of the sensor NEI allowed the detection statistics to be determined. The determination of the sensor NEI requires a detailed signal-to-noise calculation. In general, this calculation must consider the ability of the sensor optics to collect energy radiated by the target and transfer that energy to a detector; the noise and response characteristics of the detector; and the effect of signal processing on the SNR. An example of a scanning sensor designed to detect point targets is used to illustrate this type of calculation.

The input to the sensor is the irradiance E resulting from a point source at a slant range R. That is,

$$E(R) = \frac{I_0}{R^2}\tau_a(R) \ , \tag{1.42}$$

where I_0 is the source intensity in watts per steradian and τ_a is the path transmission. In general, the source intensity and path transmission are functions of wavelength over the spectral range of the sensor, and I and τ_a must be defined in terms of appropriate spectral averages. In this example, we consider all quantities to be appropriate spectral averages.

The energy gathering ability of the sensor optics is characterized by the area of its collecting aperture A_0 and the overall transmission of the optics τ_o. The IR radiation collected by the optics is focused onto a detector where it is converted to an electrical signal. In general, this electrical signal is a function of time because the focused energy moves across the detector as a result of target motion or, in the case of a scanning sensor, because of optical scanning. In the ideal case of uniform detector response across the detector surface, fast electrical response of the detector, and perfect focusing of the collected energy, the electrical signal $v(t)$ is a rectangular pulse of duration t_d. The time t_d is the time it takes for the focused energy to traverse the detector and is called the detector dwell time.

The noise associated with the detector, particularly in the case of scanning systems, is often characterized in terms of the detector's specific detectivity D^*. This parameter is defined as follows:

$$D^* = \frac{(A_d \Delta f)^{1/2}}{\text{NEP}} \ , \tag{1.43}$$

where NEP is the detector noise equivalent power, A_d is the area of the detector, and Δf is the noise equivalent bandwidth of the electrical filter used to filter the signal.

In a scanning system, the target produces a signal pulse as it traverses the detector. The filter must be selected to maximize the SNR. Decreasing the bandwidth decreases the noise at the output but also decreases the signal. A point is reached where a reduction in the bandwidth results in a reduced SNR. Increasing the bandwidth too much causes the noise to increase and an overall reduction in SNR. The optimum bandwidth is achieved with a "matched filter." For the ideal case of a rectangular pulse of duration, t_d, the noise equivalent bandwidth is equal to $1/(2t_d)$.

Since the NEP is by definition the power incident on the detector that produces an SNR of unity, the SNR produced by a point target is as follows:

$$\text{SNR} = \left(\frac{I_0\tau_a}{R^2}\right)(A_0\tau_o)\left(\frac{1}{\text{NEP}}\right) . \tag{1.44}$$

In this expression for SNR, the first term in parentheses is the signal irradiance at the entrance aperture of the sensor, the second term accounts for the light gathering power of the optics, and the last term represents the sensitivity of the detector. Using the definition of D^* and the noise equivalent bandwidth for a filter matched to a rectangular pulse, the expression for the SNR is

$$\text{SNR} = \frac{I_0\tau_a A_0\tau_o D^*(2t_d)^{1/2}}{R^2\sqrt{A_d}} . \tag{1.45}$$

This expression is valid for the ideal case of perfect matched filter processing and perfect focusing of the collected light onto the detector. In practice, it may not be possible to achieve perfect matched filter processing, and all of the light collected by the optical system might not be completely focused onto the detector. As a result, the SNR achieved in a practical system may be somewhat lower than predicted by Eq. (1.45). Following Hudson,[18] these processing and optical inefficiencies can be accounted for by introducing the pulse visibility factor υ, defined as follows:

$$\upsilon = \left(\frac{V_p}{V_{ss}}\right)^2 \frac{1}{t_d\Delta f} , \tag{1.46}$$

where V_p is the peak pulse amplitude of the signal pulse at the output of the signal processor and V_{ss} is the peak amplitude that would be observed if there were none of the losses described above. Using this definition of υ, the expression for SNR for the nonideal case can be written as follows:

$$\text{SNR} = \frac{I_0\tau_a A_0\tau_o D^*(\upsilon t_d)^{1/2}}{R^2\sqrt{A_d}} . \tag{1.47}$$

The maximum value that υ can assume is 2; its actual value can be determined by an analysis of the current waveform generated at the detector and the transfer function of the processing electronics.

1.4.2.3 Integrate-and-Dump Detection. In the matched filter detection example, the detector output is a continuous analog signal that is filtered by an electrical filter before being applied to a threshold detection circuit. This is the usual type of detection processing applied to simple scanning systems as well as typical laser warning receivers. However, for staring sensor systems, a different kind of detection processing is often utilized. In staring systems, the signal current is often applied to an integrate-and-dump circuit. In this circuit, the signal current is integrated for a time t_i, the integration time. At the end of the integration period, the output of the integrator is sampled and the integrator is reset, or "dumped," before integrating to obtain the next sample. The sampled signal at the output of the integrator represents the total number of charge carriers that were generated by the detector during the integration time and is compared to a threshold level to determine if a target is present.

Instead of using D^* to characterize the sensitivity of a detector and integrate-and-dump circuit, its sensitivity can be specified in terms of the detector responsivity R_λ and the number of noise equivalent charge carriers N_{eq}. The responsivity is the number of amperes of electrical current produced by the detector per watt of incident optical power, and N_{eq} is the number of signal charge carriers that must be produced at the detector in an integration time to produce an SNR of unity at the output of the integrate-and-dump circuit. Using these definitions, the SNR for an ideal integrate-and-dump detection system is

$$\text{SNR} = \frac{I_0 T_a A_0 T_0 R_\lambda}{R^2 e N_{eq}} , \tag{1.48}$$

where e is the electronic charge, 1.6×10^{-19} C.

1.4.2.4 Binomial Probability Function (Multiple Observations). The detection performance of a warning receiver is sometimes improved by using M-out-of-N detection logic. For this case, N independent observations are made and a target detection is declared if the detection threshold is exceeded M times. If the probability of a threshold crossing caused by the presence of a target is P_1, the probability of detection P_d for an M-out-of-N detector is

$$P_d = \sum_{J=M}^{N} \frac{N!}{J!(N-J)!} P_1^J (1 - P_1)^{N-J} . \tag{1.49}$$

This probability function is the binomial probability function.

If P_0 is the probability that an observation results in a threshold exceedance when a target is not present, the probability of false alarm P_{FA} for an M-out-of-N detector is

$$P_{FA} = \sum_{J=M}^{N} \frac{N!}{J!(N-J)!} P_0^J (1 - P_0)^{N-J} . \tag{1.50}$$

The design procedure for an M-out-of-N detector usually begins with a specified probability of false alarm requirement. For a fixed number of observations N, the designer can solve the P_{FA} equation to determine the combinations of M and P_0 that result in the specified false alarm probability. Given the probability functions that describe the signals for the case when the target is present and the case when the target is not present, the designer can determine the single-look probability of detection P_1, corresponding to each (M,P_0) combination. Then, for each (M,P_0,P_1), the P_d equation can be evaluated to give the probability of detection as a function of M. The value of M that gives the largest probability of detection can then be determined by the designer. This procedure is repeated for different values of N to determine the sensitivity of the probability of detection (for a fixed probability of false alarm) to the number of observations.

1.4.2.5 Poisson Probability (Low Intensity/Quantum Effects). In situations where only a small number of photons are available for detection in a measurement interval, the Poisson distribution gives the probability of detecting a specified number of photons in terms of the average arrival rate of the photons. For an average arrival rate of μ_p photons per measurement interval, the probability of n photons arriving in any specific measurement interval is $P(n)$, given by the following expression:

$$P(n) = \frac{\exp(-\mu_p)\mu_p^n}{n!} \quad . \tag{1.51}$$

In terms of μ_0, the average number of photons arriving when no target is present, the probability of false alarm, P_{FA} is

$$P_{FA} = \sum_{n=\kappa}^{\infty} \frac{\exp(-\mu_0)\mu_0^n}{n!} \quad , \tag{1.52}$$

where κ is the threshold setting for the detector. For a specified false alarm probability, this expression can be solved to establish the proper threshold setting.

The probability of detection P_D is given by the following expression:

$$P_D = \sum_{n=\kappa}^{\infty} \exp(-\mu_1)\frac{\mu_1^n}{n!} \quad , \tag{1.53}$$

where μ_1 is the average number of photons arriving when the target is present and κ is the threshold setting. By using the value of κ obtained by solving the false alarm expression, the probability of detection that can be achieved for a specified false alarm rate can be determined as a function of the photon arrival rates μ_0 and μ_1.

1.4.2.6 Signal Detection in Clutter. The treatment of the detection process presented in Sec. 1.4.2.1 dealt with the detection of a signal pulse in the presence of white Gaussian noise in a single receiver channel. This example is particularly relevant when the dominant source of noise in a warning re-

ceiver is internally generated or results from quantum fluctuations in the detected IR flux. Usually, however, targets must be detected against a spatially and temporally structured background. Often, this background clutter represents the noise source that limits the detectability of the target. To minimize the effect of clutter, detection concepts that go beyond simple thresholding concepts must be utilized. In such cases, the simple statistical models previously presented can be used to establish first-order system design parameters or the upper limit on sensor performance, but they are not adequate for completely describing the performance of sensors that utilize sophisticated clutter rejection techniques.

In some cases, adequate detection performance can be achieved using a single detector channel and appropriate signal processing. A classic approach to the detection of an IR point source threat is a combination of spatial and temporal discrimination.[67] One hardware implementation consists of a spatially scanned IR detector, a postdetection threshold circuit, a pulse-width-measuring circuit, and a tracking circuit that associates threshold crossing data (e.g., position and intensity) obtained in multiple observation frames. Because in a scanning system, there is a direct correspondence between the pulse width of a signal and its spatial extent, spatial discrimination is provided by the combination of a scanning detector and postdetection filtering. Because clutter sources are often larger in spatial extent than the targets that are to be detected, long-pulse-width waveforms are rejected as clutter. Temporal discrimination is provided by the tracking circuit. Using the tracker, candidate signals that exceed threshold must also form tracks that satisfy certain track criteria (e.g., rate of intensity growth and track velocity) before they are declared to result from the presence of a target. Sophistication can be added by means of postdetection filtering, automatic gain controls, threshold or pulse width adaptation, and higher order, multiple trackers.

The use of a track processor to improve detection performance is one example of the use of multiple observations to enhance the detection process. For this example, multiple frames of data are used to determine the presence or absence of a target. Other examples of multiple observation detection schemes utilized by warning receivers include multispectral observations, polarization measurements, and two-dimensional spatial sampling. For such systems, probability functions that give the probabilities of occurrence for various combinations of observational outcomes are required. These probability functions are called joint probability density functions. For the case of n observations, $p(x_1, x_2, \ldots, x_n)$ is the joint probability density function for the set of observations $\{O_1, O_2, \ldots, O_n\}$. The probability that O_1 is between x_1 and $x_1 + dx_1$, O_2 is between x_2 and $x_2 + dx_2, \ldots, O_n$ is between x_n and $x_n + dx_n$ is $p(x_1, x_2, \ldots, x_n)\, dx_1\, dx_2 \ldots dx_n$.

A commonly used and often useful example of a joint probability density function is the density function for a Gaussian process consisting of n observations. This density function is the generalization of the probability density function for the one-dimensional Gaussian process described previously. It is given by the following expression:

$$p(x_1,x_2, \ldots, x_n) = M_n \exp\left[-\frac{1}{2} \sum_{j=1}^{n} \sum_{k=1}^{n} \mu_{jk}(x_j - \langle x_j \rangle)(x_k - \langle x_k \rangle) \right] \quad (1.54)$$

where $\{x_1, x_2, \ldots, x_n\}$ are the observed values, M_n is a normalization factor, $\langle x_j \rangle$ is the ensemble average of the observed values, and μ_{jk} are the elements of the matrix $\boldsymbol{\mu}$. The matrix $\boldsymbol{\mu}$ is the inverse of the covariance matrix $\boldsymbol{\Phi}$, where elements of $\boldsymbol{\Phi}$ are defined as follows:

$$\Phi_{ij} = \langle x_i x_j \rangle - \langle x_i \rangle \langle x_j \rangle \ , \tag{1.55}$$

where the brackets $\langle\ \rangle$ denote an ensemble average. Also, the normalization constant M_n is related to $\boldsymbol{\Phi}$ by the following expression:

$$M_n = (2\pi)^{-1/2} |\det \boldsymbol{\Phi}|^{-1/2} \ , \tag{1.56}$$

where $|\det \boldsymbol{\Phi}|$ refers to the determinant of the matrix. In Eq. (1.54) M_n is the normalization constant required so that the joint probability density functions integrated over all possible outcomes is unity. The ensemble averages $\langle x_i \rangle$ characterize the values about which the observations are clustered, just as the mean value does in the case of the one-dimensional Gaussian density function. Whereas a single parameter describes the variance of the observed values in the case of the one-dimensional Gaussian process, an array of parameters is required to specify the variance of the observed values for the case of n observations. These parameters are the elements $\boldsymbol{\Phi}_{ij}$ of the covariance matrix.

For the simple case of n statistically independent observations, each with a Gaussian distribution characterized by a variance σ^2, the covariance matrix is an $n \times n$ diagonal matrix with each element equal to σ^2. The probability density function for this case is

$$p(x_1, x_2, \ldots, x_n) = (2\pi\sigma^2)^{-n/2} \exp\left[- \sum_{i=1}^{n} (x_i - \langle x_i \rangle)^2 / 2\sigma^2 \right] . \tag{1.57}$$

For the general Gaussian density function previously defined, the probability density is given as a function of the observation variables $\{x_1, x_2, \ldots, x_n\}$. If we consider these variables to be the coordinates of an n-dimensional Cartesian coordinate system, then from the definition of the Gaussian density function, the surfaces of constant probability density in this coordinate space are generalized ellipsoids defined by the following relationship:

$$\sum_{j=1}^{n} \sum_{k=1}^{n} \mu_{jk} (x_j - \langle x_j \rangle)(x_k - \langle x_k \rangle) = \text{constant} \ . \tag{1.58}$$

The two-dimensional case is easiest to visualize. For that case we have a two-dimensional coordinate space, and the contour of constant probability density is an ellipse.

When observations are made that include different classes of objects, such as target objects and clutter objects, different joint probability density functions characterize each object class. For reliable detection (i.e., distinction between target and clutter) to be achieved, these density functions must be well separated in the described observation coordinate space. Quantitative measures

of the degree of separation, such as the Mahalanobis distance,[68] can be defined and used to assign particular observations to the appropriate object class.

Figure 1.35 from Pollock[69] shows an example of some actual multiple observation IR data. The data were obtained by making observations of an infrared target and a clutter background in two spectral bands. Each observation consists of a measurement of the intensity I_1 in one spectral band and the intensity I_2 in the other spectral band. The results of the observations are shown plotted in Fig. 1.35 as a scatter diagram, with the density of points in the I_1-I_2 plane being representative of the probability density functions of the target and background. Also shown in the figure are ellipses centered on the centroids of the target and background data points. The sizes of the ellipses are chosen so that 95% of the target data points falls within the boundary of one of the ellipses and 95% of the background clutter data points falls within the boundary of the other ellipse. These ellipses overlap significantly, indicating that this particular two-color observation scheme does not result in good target/clutter discrimination.

The distribution of data points within the ellipses shown in Fig. 1.35 also indicate that the density function describing the target and clutter for this particular case are not approximated very well by Gaussian density functions. This is often the case for actual infrared measurement data. For the case of multicolor observations, the contours of equal probability density usually assume irregular shapes, such as shown[69] in Fig. 1.36 for the case of three-color IR observations.

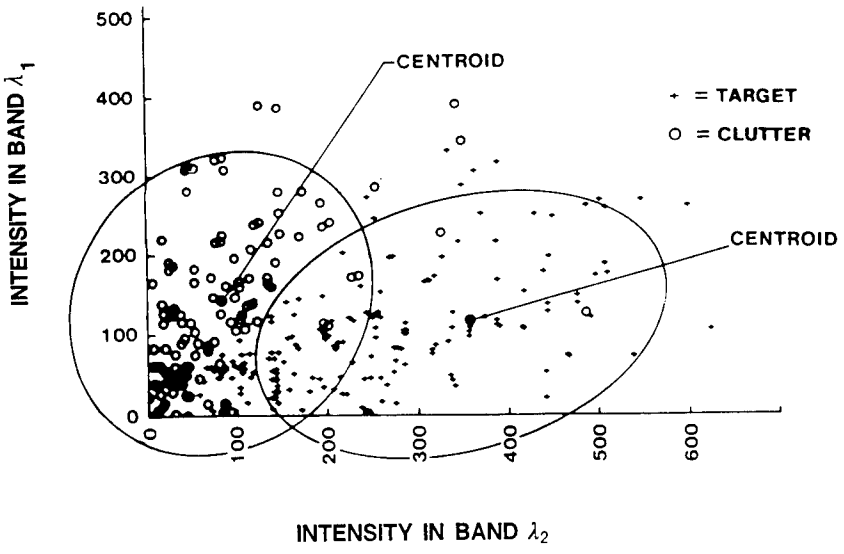

Fig. 1.35 Two-color IR target and clutter data.[69]

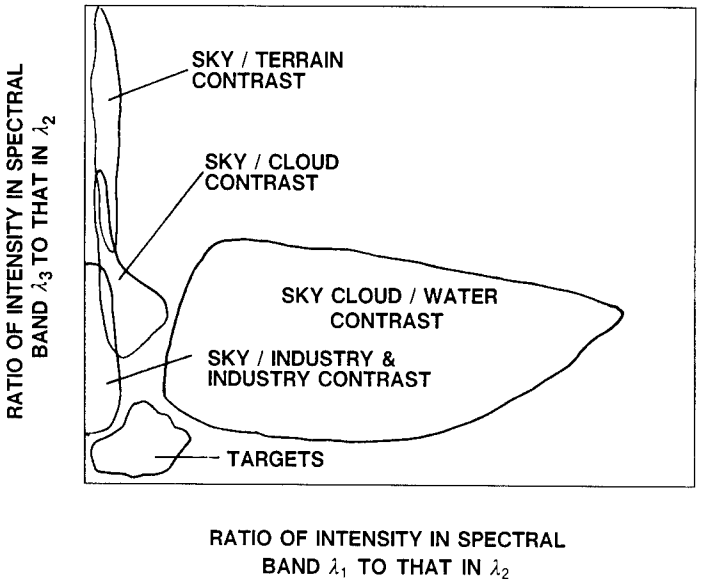

Fig. 1.36 Three-color IR data for targets and different classes of clutter.[69]

1.4.2.7 Decision Theory. Whether a warning receiver is to declare a target present or not present based on a single observation or on multiple observations, some strategy for deciding whether or not a threat is present must be implemented. The selection of an appropriate decision strategy is important because each time a warning receiver makes a wrong decision, a cost is incurred. For example, if a threat was declared to be present when there was no threat, a flare might be released, and the supply of flares available to counter actual threats would be unnecessarily reduced. If the warning receiver fails to declare a threat when there is in fact a threat present, the platform that was to be alerted by the warning receiver might be destroyed by the threat.

A variety of decision strategies are possible. One strategy is the Bayes decision strategy in which the average risk per decision is minimized. Mathematically, risk is defined as the cost associated with a particular decision times the probability of that decision occurring. In the case of a detector that must choose between hypothesis H_1 (target present) and hypothesis H_0 (target not present), the average risk $\bar{r}$ is

$$\bar{r} = C_{00}(1 - Q_0) + C_{10}Q_0 + C_{01}Q_1 + C_{11}(1 - Q_1) \ , \tag{1.59}$$

where C_{ij} is the cost of choosing hypothesis H_i when H_j is true $(i,j = 0,1)$, Q_0 is the probability of choosing hypothesis H_1 when H_0 is true (error of the first kind), and Q_1 is the probability of choosing hypothesis H_0 when H_1 is true (error of the second kind). In a receiver based on the Bayes decision strategy, the decision process is one that minimizes this expression.

The minimization of the average risk involves the selection of an appropriate decision surface. For the case of a decision based on an observation consisting of n measurements $(x_1, x_2, \ldots, x_n)$, the outcome of an observation can be presented as a point in an n-dimensional Cartesian space with coordinates $(x_1, x_2, \ldots, x_n)$. This Cartesian space can be divided into two regions, R_1 and R_0, such that if the point representing an observation falls in R_1, hypothesis H_1 is selected, and if the point falls in R_0, hypothesis H_0 is selected. The surface that separates these two regions is the decision surface.

The choice of a decision surface influences the values of Q_0 and Q_1 appearing in the expression for the Bayes average risk. The designer of a receiver based on the Bayes decision criterion must select the decision surface so the resulting values of Q_0 and Q_1 minimize the average risk. Techniques for doing this are described by Helstrom.[70]

Often it is not possible to implement a detection algorithm based on the Bayes criterion because of the difficulty with assigning a value to the cost of an error or because the prior probability of a target being present is not known.

For the case of a warning receiver, a common alternative criteria is based on the assumptions that the prior probability of a target being present is usually very low, and that a reasonable decision criterion for the receiver is one that results in a specified false alarm rate while achieving a maximum possible detection probability. This detection criterion is the Neyman-Pearson detection criterion.

As was the case for the Bayes detection criterion, the appropriate decision surface must be found to implement a receiver based on the Neyman-Pearson detection criterion. For the Neyman-Pearson case, the regions R_1 and R_0 must be found such that Q_0 is equal to a specified false alarm probability, and the probability of detection $(1 - Q_1)$ is a maximum. The corresponding decision surface can be obtained in terms of the conditional joint probability density functions $p_0(x_1, x_2, \ldots, x_n)$ and $p_1(x_1, x_2, \ldots, x_n)$, where $p_0(x_1, x_2, \ldots, x_n)$ is the joint probability density for the case of no target present (H_0), and $p_1(x_1, x_2, \ldots, x_n)$ is the joint probability density for the target present case (H_1). In terms of these density functions, the equation defining the decision surface is[70]

$$\frac{p_1(x_1, x_2, \ldots, x_n)}{p_0(x_1, x_2, \ldots, x_n)} \equiv \Lambda(x_1, x_2, \ldots, x_n) = \Lambda_0 \ , \tag{1.60}$$

where Λ_0 is a constant chosen to give the specified false alarm probability, Q_0. The function $\Lambda(x_1, x_2, \ldots, x_n)$ is called the likelihood ratio; implementation of the Neyman-Pearson criterion is accomplished by evaluating this function for the observed signal and determining whether the result is greater than or less than the constant Λ_0. If it is greater than Λ_0, the observation point is in region R_1, and a target is declared to be detected. If it is less than Λ_0, the observation point is in region R_0, and the no target present hypothesis is chosen.

The Neyman-Pearson decision strategy based on likelihood ratios described here requires that the joint probability density functions be known. In situations where the detection process is limited by background clutter, these functions are often not known *a priori*. In some cases, the density functions

can be considered to be known functions with a number of unknown parameters. As the warning receiver makes observations, these parameters can be estimated, and likelihood ratio techniques can be applied. Such receivers can be adaptive in the sense that the parameter estimates made by the receiver can change as the background and target characteristics change. By continually updating these parameters, the receiver can be designed so that some aspects of its detection performance remain unchanged as its operating environment changes. For example, a receiver might be designed to yield a constant false alarm rate as it searches for targets against different types of backgrounds. Such a receiver is called a constant false alarm rate (CFAR) receiver.

Still more general detection techniques can be applied when little is known *a priori* about the probability density functions. In distribution-free detectors, as few assumptions as possible are made about the distribution functions. This type of receiver is designed so that a constant level performance (e.g., a constant false alarm rate) is achieved without a specific knowledge of the density functions. Pattern recognition and artificial intelligence techniques are additional examples of techniques that can be utilized when the designer of a warning receiver has inadequate data about the statistics of the targets and their background.

1.4.3 Signal Detection Issues in Modern Warning Systems

The Gaussian and the Poisson probability functions described previously adequately model a number of important noise processes encountered in the analysis of the detection capability of warning systems. However, as previously discussed, the performance of modern EO/IR warning systems is often limited by the natural or man-made variations in the background scene in which targets must be detected. Consequently, characterization of the statistical properties of background variations, or background clutter, is an important element in the analysis of such warning systems.

In some cases, relatively simple statistical models can be used to describe backgrounds quite well. For example, Hunt and Cannon[71] suggested that optical image clutter can often be modeled as a Gaussian random process provided that the model allows the mean to vary rapidly in space and the covariance to vary more slowly in space.

Description of background clutter in terms of a Wiener spectrum is also common. Such a description is particularly useful for the determination of the output variance of a linear processor acting on the background. For such a processor, the output in terms of the scene radiance at the image plane of a sensor can be mathematically modeled as follows:

$$\zeta = \int h_p(\mathbf{x}) N(\mathbf{x})\, d\mathbf{x} \ , \tag{1.61}$$

where $N(\mathbf{x})$ is the scene radiance at position $\mathbf{x}$, $h_p(\mathbf{x})$ is the linear weighting function for the processor, the integral is over the complete image, and ζ is the output of the processor. If the scene radiance can be modeled as a random process, the processor output is a random variable. Typically, we are interested in variations of the background scene radiance about the average value of

background radiance level. Under such circumstances, we can take the average background radiance to be zero and model the scene radiance as a zero-mean random process. Then, the variance of the processor output is as follows:

$$\langle \zeta^2 \rangle = \iint h_p(\mathbf{x}) h_p(\mathbf{y}) \langle N(\mathbf{x}) N(\mathbf{y}) \rangle \, d\mathbf{x} \, d\mathbf{y} \ , \tag{1.62}$$

where the brackets denote a statistical ensemble average and the order of spatial integration and statistical averaging has been interchanged. The function $\langle N(\mathbf{x})N(\mathbf{y}) \rangle$ is the autocorrelation function of the background. Provided this function is stationary, in the sense that it depends only on the difference between $\mathbf{x}$ and $\mathbf{y}$, the Wiener spectrum can be defined as the Fourier transform of the autocorrelation function. Specifically,

$$W(\mathbf{f}) = \int \langle N(\mathbf{x}) N(\mathbf{x} + \boldsymbol{\delta}) \rangle \exp[-2\pi \boldsymbol{\delta} \cdot \mathbf{f}] \, d\boldsymbol{\delta} \ , \tag{1.63}$$

where $W(\mathbf{f})$ is the Wiener spectrum and $\mathbf{f}$ is the spatial frequency. With this definition, the expression for the variance of the processor output becomes

$$\langle \zeta^2 \rangle = \int |H_p(\mathbf{f})|^2 W(\mathbf{f}) \, d\mathbf{f} \ , \tag{1.64}$$

where $H_p(\mathbf{f})$ is the Fourier transform of $h_p(\mathbf{x})$.

Although statistical models such as those described here can sometimes be used to accurately describe backgrounds and are often used in the first-order design of warning systems, they frequently fail to be useful for predicting the ultimate detection performance of a clutter-limited warning receiver. For example, although a Wiener spectrum description of a background may be useful for calculating the variance of the output from a signal processor, there is no guarantee that the statistics of the output are such that a knowledge of the variance can be used to predict false alarm rates. If the statistics of the output were Gaussian, a knowledge of the variance would allow the probability of false alarm to be calculated, as shown previously. However, many clutter backgrounds are characterized by the presence of "rare" features (e.g., man-made objects, solar glints, and so on) that provide the major source of false alarms for a warning system. The probability density function for the signal processor output would be decidedly non-Gaussian in such a case, and a knowledge of the variance would not be sufficient for the calculation of the false alarm rate.

Consequently, issues relating to the validity of detection performance predictions often arise in the development of modern, clutter-limited warning systems. To deal with these issues, designers rely as much as possible on empirical background data. To support the requirement for background data, there have been numerous and varied background data collection efforts. Simulation, using empirical data, has become an important tool in warning system design. By using simulation techniques and measured background data, simple statistical models can be avoided and more accurate detection performance predictions can be made.

However, although the empirical data bases and simulation techniques have proven useful, they are not without problems and issues. With background data, there is the issue of data reduction. Simplified statistical models of backgrounds, such as those exemplified by Wiener spectrum descriptions, use parametric descriptions that are obtained by averaging appropriate quantities over a large set of background samples (i.e., statistical ensemble averaging). If such descriptions are avoided in a detection performance analysis, the massive amounts of essentially unreduced data must be used instead. Furthermore, there are often issues associated with the completeness of the background data base as well as its accuracy. Typically some form of data extrapolation is required since it is not unusual for an existing data base to contain data collected under conditions somewhat different from those that are simulated. Finally, with any simulation, validation is always an important issue.

As a result of the difficulties associated with detection performance prediction by analytic and simulation techniques, field testing usually is an extremely important step in the assessment of warning system performance. Preprototype development and testing is usually a critical element in the development of a modern clutter-limited warning system. Prior to the field testing of the prototype system, the warning system designer must face the challenge of efficiently designing a system with the sufficient robustness to compensate for the uncertainties of the performance prediction process.

1.4.4 Signal Detection Issues in Laser Warning Systems

1.4.4.1 Overview. To apply the general signal detection theory of Sec. 1.4.2 to laser warning receivers, it is necessary to address the statistical properties of the laser signal, the system noise, and the relevant clutter.

The laser signal differs from the signals involved in the missile warning receivers because of its coherence. There are two distinct consequences of laser coherence with respect to signal detection. One consequence relates to the statistics of laser light generation and amplification. The phenomenology of laser photon statistics may become an issue whenever the laser receiver is detection limited by the *noise in signal;* i.e., signal shot noise. Although this is a common situation with superheterodyne, or coherent, laser transceivers that operate in a photon-counting regime, it is seldom the limiting noise for direct-detection laser warning receivers and is not addressed herein. A more significant consequence of the source coherence is that the laser beam experiences scintillation, described in Sec. 1.3.2.4, as it propagates through the atmosphere. Consequently, the statistics of the atmospheric turbulence are imparted to the detected laser signal and become a significant factor in terrestrial laser warning receiver design and analysis.

The detector and background noise parameters applicable to the laser case are similar to those applicable to the missile detector situation, any differences are a function of the different spectral regimes and temporal bandwidths involved and are not a consequence of the laser source *per se.*

Similarly, clutter in the laser warning regime differs only from that of concern in the missile warning case because of the different spectral bands and optical configurations involved.

1.4.4.2 Laser Pulse Detection in White Noise. Laser warning receivers, operating in the visible through the near-IR, up to wavelengths as long as 3 μm, are potentially noise limited by the shot noise associated with the solar background. Longer wavelength systems are typically background limited by the thermal background, either that of the external scene, or the internal background of the receiver system. In the visual to near-IR regime, the solar background may be suppressed by spectral filtering (in some configurations), and in the mid- and far-IR the thermal background is suppressed by the use of "cold" filters and "cold" baffles, both situations resulting in a lower magnitude of noise flux striking the detector. When the relevant noise flux and, therefore, the magnitude of its statistical fluctuations is reduced, then other noise sources become dominant. For background shot noise and for the majority of the detector noises relevant to LWR applications, the noise spectrum is constant with frequency; i.e., white noise, and the equations of Sec. 1.4.2.1 apply, assuming that the laser signal is a deterministic quantity. However, in most near-earth scenarios, the latter assumption is negated by the effect of the atmosphere on the propagating beam.

1.4.4.3 Laser Signal Statistics in the Presence of Scintillation. The statistics of the laser signal incident on the detector are a complex function of the laser transmitter, the detector optics, and the atmospheric conditions over the path.[72] (The scintillation phenomena is illustrated in Sec. 1.3.2.4.) The laser signal is characterized by its probability density function (PDF); i.e., the probability that the signal irradiance is in the range between E and $E + \Delta E$. Alternatively, some authors characterize scintillation effects in terms of the cumulative probability that the laser irradiance is above some value. Figure 1.37 shows a plot of the cumulative probability of the laser intensity as incident on a small detector after traveling over an 8-km near-earth path.[73] These data

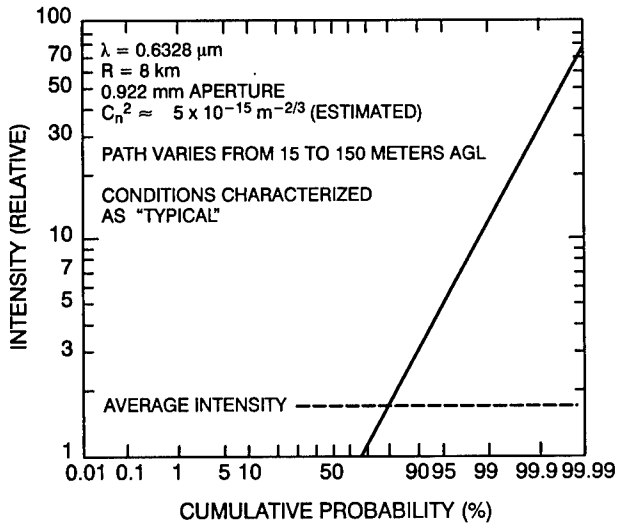

Fig. 1.37 Probability distribution for scintillation measured over an 8-km near-earth path.[73]

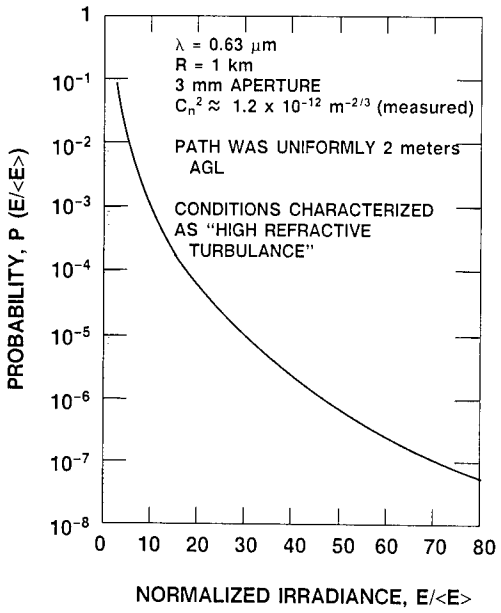

Fig. 1.38 Probability density of normalized irradiance measured for high irradiance values over a 1-km near-earth path.[74]

indicate that the laser irradiance is at, or below, its average value about 75% of the time and is at, or below, 10 times its average value about 99% of the time. Figure 1.38 shows a plot of the probability density (PDF) of the laser intensity for a 1-km near-earth path.[74] (Note that these two illustrations involve data taken at different ranges, locations, and times and are not necessarily comparable situations.) The following paragraphs outline the procedures necessary to quantify the effects of such scintillation on the LWR detection process.

The statistics of laser scintillation have been studied for many years, and a rigorous analytic solution relating the incident irradiance to the atmospheric and test parameters exists only for the cases of very weak scintillation and very strong scintillation. For the case of weak scintillation, the probability density function is *log-normal*, and for very strong scintillation it is *negative exponential*.[75] However, many, if not most, practical LWR cases involve the regime between these two extremes.

For the purposes of LWR analysis, the weak scintillation theory is appropriate for short-range, low-turbulence conditions, whereas experimental data (coupled with the assumption that the statistics of the scintillation remain approximately log-normal) can be used for first-order design at higher levels of scintillation as illustrated next.

In optical scintillation theory, the signal irradiance is traditionally expressed in terms of its randomly fluctuating field amplitude, $\chi(r,t)$, as

$$E(r,t) = \langle E(r) \rangle \exp[2\chi(r,t)] \ , \tag{1.65}$$

where $E(r,t)$ is the laser irradiance at the point r and time t and $\langle E(r)\rangle$ is the time-averaged value of the irradiance. The irradiance E in this expression is the relevant variable for LWR signal analysis. Normalizing to the average value and taking the natural logarithm (i.e., to the base e) of both sides of this equation yields

$$\ln \frac{E(r,t)}{\langle E(r)\rangle} = 2\chi(r,t) \ , \tag{1.66}$$

As a consequence of the interaction of the propagating field with the many random, refractive index variations along its path, the log-amplitude of the field, $\chi(r,t)$, tends to be a random variable with Gaussian, or "normal" statistics.[73] Hence, the logarithm of the irradiance is also a random variable with "normal" statistics and laser signal scintillation is referred to as being "log-normal." Note that the normal function is fully defined by its mean and its variance σ^2, and that the square root of its variance is the root-mean-square (rms) signal fluctuation. Thus, so long as the scintillation is properly characterized by log normal statistics, the signal statistics are fully defined by the variance of the log-irradiance.

Because analytic treatments of this subject address the electromagnetic field amplitude, rather than the irradiance, of the laser beam, the literature typically quantifies the variance of the log amplitude, rather than the variance of the irradiance. For the case of log-normal statistics, the variance of the log-irradiance is related to the variance of the log-amplitude by the simple expression

$$\sigma_E^2 = 4\sigma_\chi^2 \ , \tag{1.67}$$

where σ_E^2 is the variance of the log irradiance and σ_χ^2 is the variance of the log amplitude; i.e. the variance of the log irradiance is simply four times the variance of the log amplitude.[76]

In the weak scintillation region the variance σ_χ^2 of the log amplitude is given by the expression

$$\sigma_\chi^2 = 0.124 k^{7/6} R^{11/6} \overline{C_n^2} \ , \tag{1.68}$$

where $\overline{C_n^2}$ is the atmospheric refractive index structure constant averaged over the path length R in meters and k is the wavenumber ($2\pi/\lambda$) in inverse meters. The parameter C_n^2 is a description of the atmospheric internal turbulence, not of the optical propagation *per se*. However, estimation of this parameter is the first and most critical element in quantifying the optical signal fluctuations. The parameter C_n^2 decreases with altitude and is a strong function of time of day and the local terrain and/or terrain variations.

From Eq. (1.68), the scintillation is approximately an inverse function of wavelength. As a consequence, scintillation effects that are very important to laser warning receiver analysis in the visual and near-IR bands are minor at the longer laser wavelengths near 10 μm.

Equation (1.68) was developed specifically for the case of a spherical wave, and the literature contains other deviations carried out assuming a plane wave

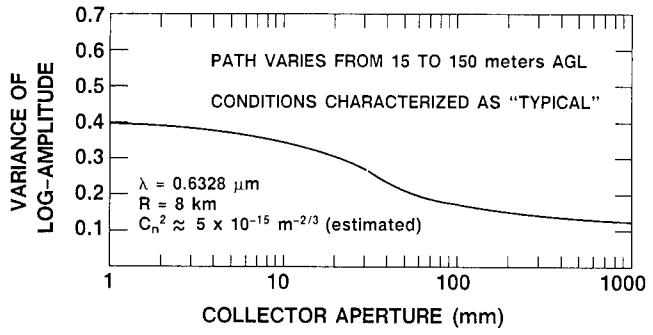

Fig. 1.39 Dependence of log-amplitude variance on collection aperture diameter over an 8-km near-earth path.[73]

situation in which the numerical term 0.124 becomes 0.31. It can be shown that Eq. (1.68) with the constant equal to 0.124 also holds for a detector located in the far field of a typical laser beam.[73]

These equations address the scintillation at a point in space, rather than over the aperture of a detector. A large optical aperture averages over the time-varying, spatially inhomogeneous laser beam, resulting in less signal variation.[77] Figure 1.39 indicates[73] that the averaging effect is small for apertures of a few millimeters or less, which is typical of many laser warning receivers. Thus, the aperture-averaging computation, which may be a critical issue in computing the performance of large-aperture laser radar or laser communication systems, can usually be neglected for laser warning receiver performance analysis.

The cumulative probability of the irradiance for log normal signal variations is given by the expression

$$P(E_n) = \frac{1}{2}\left\{1 + \operatorname{erf}\left[\frac{\ln E_n + (1/2)\sigma_E^2}{(2\sigma_E^2)^{1/2}}\right]\right\}, \tag{1.69}$$

where $P(E_n)$ is the cumulative probability that the irradiance will be equal or less than the value E_n, with E_n the normalized irradiance, $E/\langle E\rangle$, and σ_E^2 is the variance of the log-irradiance. The standard error function (erf) is tabulated in many mathematical tables.[78] [Note that the logarithm specified in this equation is the natural log (i.e., to the base e), whereas incident irradiance ratios are often specified in terms of an appropriate intensity ratio stated in terms of decibels, which are defined as 10 times the common log (i.e., to the base ten) of the irradiance.]

For situations in which the weak scintillation approximation holds, the statistics of the irradiance incident on a detector are determined by calculating the log amplitude variance from Eq. (1.68) converting it to the log irradiance variance with Eq. (1.67) and applying this variance to Eq. (1.69).

The weak scintillation situation holds for atmospheric conditions and path lengths such that

$$\sigma_\chi^2 < 0.3 \ . \tag{1.70}$$

Experimental data indicate that, although the weak scintillation approximations fail and Eq. (1.68) for the log amplitude variance becomes invalid beyond the limits of Eq. (1.70), the scintillation statistics retain their log-normal form over a larger range, which includes much of the range of interest for LWR computations. Thus, for longer distances and/or worse atmospheric conditions, it is often acceptable to utilize experimental amplitude variance data [rather than the parametric relation of Eq. (1.68)] and yet continue to rely on Eqs. (1.67) and (1.69) to estimate the probable signal statistics.

For our purposes, the scintillation magnitude can be illustrated by assuming an approximately worst case corresponding to the beginning of the scintillation saturation regime with the variance of the log amplitude at its saturating value of 0.3. Using Eqs. (1.67) and (1.69) and plotting the resultant cumulative probability that the incident irradiance is equal to or less than the value indicated on the x axis, we obtain the solid curve of Fig. 1.40 where the incident irradiance on the x axis is expressed in terms of decibels above (or below) the normalized irradiance. This data is representative of visual and near-IR laser scintillation over typical, near-earth tactical engagements with the signal fluctuations decreasing as the LWR is designed for higher altitude and longer wavelength scenarios.

The LWR design and testing implications of these incident irradiance fluctuations can be better illustrated by considering the quantity "one minus the cumulative probability," which is plotted as the dashed curve of Fig. 1.40. This quantity corresponds to the probability of detection (in the absence of solar or detector noise) that would be expected with the system threshold value set at the level indicated on the x axis. Note that the probability of detection would be about 29% with the system threshold set at the average and would not reach 98% until the threshold level was reduced 13 dB (a factor of 20) below the average value. From the perspective of an LWR field test or operational deployment, the instantaneous signal level is more than 6 dB (a factor of 4) above the average about 4% of the time, and this might result in incorrect, overly optimistic, estimates of the observed system performance, or an excessive estimation of the laser source energy. Thus, these occasional high-intensity excursions may give rise to apparently anomalous behavior during system testing and/or deployed operation.

In the presence of scintillation, the instantaneous incident signal level is often below the average (nonscintillating) value. One effect of this phenomena is that an LWR that is specified in terms of its probability of detection exhibits degraded effective sensitivity during field operations. For instance, to achieve a specified probability of detection of 94% in the presence of the scintillation represented by Fig. 1.40 an LWR with a sensitivity of 10^{-4} W/cm^2 at the specified (or even higher) probability as measured in the laboratory (no scintillation) would have to be derated by 10 dB (a factor of 10) to a sensitivity of 10^{-3} W/cm in the field. (This general approach leads to the concept of *gain margin.*[41])

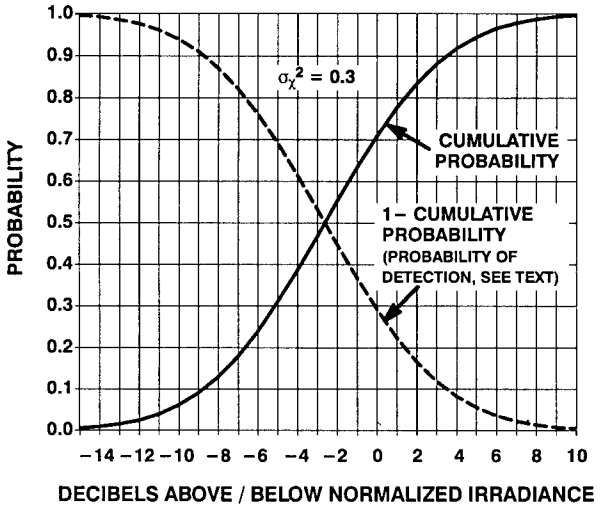

Fig. 1.40 Cumulative probability near saturation.

1.5 TACTICAL MISSILE WARNING RECEIVERS[a]

1.5.1 Signal Processing Considerations

The problem of detecting a passively guided threat missile from a tactical aircraft platform presents challenging requirements. The missile warning system must function continuously without air crew intervention, declare a threat rapidly, and be capable of activating countermeasures within the limited time before missile impact. The missiles present a variety of sizes, signatures, and trajectories, and background and clutter levels are often comparable with missile signatures. Missile signatures may change during the trajectory as the missile passes from boost to sustain or postburnout phases. The system must detect threat missiles with a very high probability, while minimizing false alarms. It must also be capable of distinguishing false targets, such as other aircraft and their weapon firings and flares, as well as missiles that are not threats (e.g., not approaching the aircraft).

Several approaches to the tactical missile warning problem have been explored by system developers. These include active radar systems, often pulsed Doppler, which provide information on the range, position, and velocity of the missile; passive infrared systems, which offer covertness at the cost of limited information on range and velocity; and various other electro-optical systems exploiting special features of one or another spectral band.

Active radar systems suffer from a limited detection range and lack of covertness. One advantage, however, is that these systems will detect threats

[a]Portions of this section were written by Louis A. Williams, Jr., of Louis A. Williams, Jr., and Associates, Cincinnati, Ohio.

regardless of burnout conditions. Thus, the active pulse Doppler MWR can function effectively as long as it has a detection range adequate for countermeasures effectiveness. This can be contrasted with warning receivers that depend on plume emissions and, hence, must detect the missile at longer ranges prior to its burnout. Another problem facing active radar missile warning receiver systems is the low cross section of threat missiles and the potential of even lower values from developments in signature reduction technology.

Passive infrared warning systems provide covertness and a reasonable detection range, but are limited in their ability to detect postburnout missiles against severe infrared clutter backgrounds. Atmospheric signal attenuation may also limit detection times.

Systems operating in low transmission spectral regions may offer covertness coupled with low background and clutter problems. However, the very factors that lead to low background levels, namely attenuation of background and clutter radiation, also limit the missile detection range of the system. As is the case with the passive infrared MWR systems, clever signal processing algorithms are required to extract enough information to declare the object a threat and to reject a wide range of potential false targets.

The optimum missile warning system might be a fusion of several of the active and passive sensors and technologies. A properly fused system would not just "OR" the outputs of two independent sensors or systems, but would constantly monitor the total environment and alter the weightings (or even operational status) of the sensors as the situation demanded. The multispectral sensor fusion approach for missile warning receivers, however, may require additional considerations. Cost and aircraft integration constraints are major factors in missile warning receiver systems, and the concept of fusing two or more already expensive systems requires careful design and planning. Active systems are not within the scope of this chapter, so the remaining discussions of multisensor systems and sensor fusion refer to two or more passive optical sensors.

1.5.1.1 Spectral Band Selection

Overview. The choice of spectral band(s) for a warning receiver is generally determined by a consideration of threat signature characteristics and anticipated clutter conditions as well as scenario aspects. Short-range missiles probably will still be in boost phase at the time of detection, and in this mode, the 3- to 5-μm plume band provides better signal-to-clutter ratios than the 8- to 12-μm band. Longer range missiles will enter sustain or coast phases long before impact, and the system must be able to continue to detect the missile from the longer wavelength skin emissions or reflected radiation.

Because of the difference in atmospheric attenuation with wavelength, the use of a carefully selected dual-band system may provide information about the range (and velocity) of the source of radiation. The determination of range depends on dual-band measurements at two distinct time intervals with sufficiently different band ratios. Figure 1.41, based on LOWTRAN calculations, shows relative band intensity ratios as a function of range for several different band pairs in the infrared. The source of radiation for these curves is a 600°C blackbody, typical of a hot missile exhaust pipe. Note that most of the curves

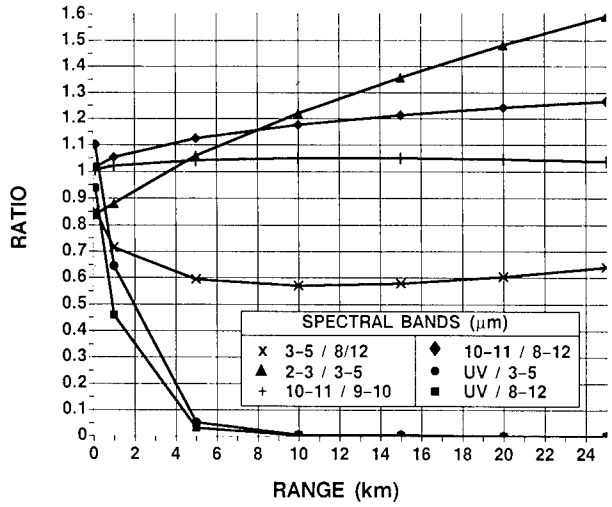

Fig. 1.41 Relative band ratios versus range.

become nearly horizontal beyond 10 km. SNRs also diminish with range, so the accuracy of intensity ratios is decreased along with the sensitivity to range variation. In tactical situations, we are rarely concerned with declaration at ranges beyond 10 km.

Typically, system performance can be classified as either noise-limited or clutter-limited. With the exception of clear blue sky backgrounds, most situations are clutter-limited. Although SNR can be optimized by proper system design, signal-to-clutter ratio is determined by the nature of the background and target. The significance of a given signal-to-clutter ratio can be modified with proper filtering and other signal processing techniques.

Spectral Band Trade-Offs in the Infrared Spectrum. A variety of clutter rejection techniques have been used in the development of infrared sensors. Spatial discrimination techniques have included spatial filtering and matched filtering. Temporal discrimination techniques have included scan-to-scan correlation and signal growth. Spectral discrimination techniques have included two or more spectral bands, spectral ratios, spectral differences, and adaptive spectral processing. Adaptive thresholds have used tapped delay lines, variable high- and low-pass filters, and two-dimensional adaptation. Postprocessing discrimination has included such factors as track density, track density variation, threshold crossing rates, azimuth and/or elevation tracking rates or accelerations, and azimuth and/or elevation location.

In the 3- to 5-μm spectral region with light clutter, a spatial filter matched to the width of the target can be quite effective in reducing the large-scale earth and cloud shapes in the field of view. Examples of spatial signatures are shown in Fig. 1.42. In the first example, the postulated target is in a benign environment, and little clutter discrimination is necessary. In the second example, the same signal is viewed against an earth background. A spatial filter matched to the width of the target signal is fairly effective against the low-

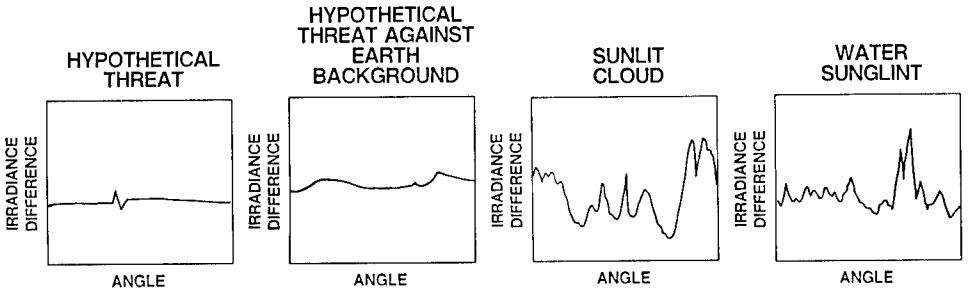

Fig. 1.42 Spatial signature characteristics.

frequency hump to the left of the target and is moderately effective against the more pronounced hump to the right of the target.

As the threshold is decreased, the variations in background clutter become more significant, because a threshold significantly above the clutter at one point in the field of view may produce excessive false alarms in another part of the field of view. Adaptation of spatial filtering and/or threshold level to the varying background has proven to be an effective way to increase system sensitivity for a given false alarm rate. The concept can be envisioned as two parallel channels—one measuring the background statistics, usually in the region around the target channel, and the other channel using the first channel's measure as the baseline for a target threshold setting. The adaptive filter frequently has a feedback loop to maintain a constant false alarm rate. An advantage of the CFAR approach is that the load on the postthreshold computational circuits remains constant. A disadvantage is that there is loss of sensitivity in uncluttered environments when compared with a simple threshold. The advantages usually far outweigh the disadvantages.

One of the major problems for spatial filtering is bright sunlit objects. Figure 1.42 shows the problems that can be caused by *sun glint.* Typical data from sunlit clouds and water sun glint are shown in the right two traces in the figure. Bright sunlit objects can have numerous pointlike characteristics resulting in many false alarms if no discrimiation techniques other than spatial are used. Even in heavy clutter, however, spatial filtering is a valuable prefilter to select only pointlike objects for further processing. The dynamic range and linearity of the spatial processor must be adequate to pass the characteristics used in the latter processing.

Tracking algorithms can be used to separate some sun glints from targets. Temporal discrimination of this fashion can produce massive computational requirements in regions of heavy clutter. Another potential problem with temporal discrimination is that the threat signal may vary. For example, an aircraft target may fly through clouds or change in aspect angle with respect to the viewer. Figure 1.43 shows some representative temporal signatures to illustrate the point. The first example in the figure shows a well-behaved target. The second example shows a target that is varying because of changes in aspect and atmospheric transmission. Both plots are for a target that is approaching the observer, and the time axis is time to intercept.

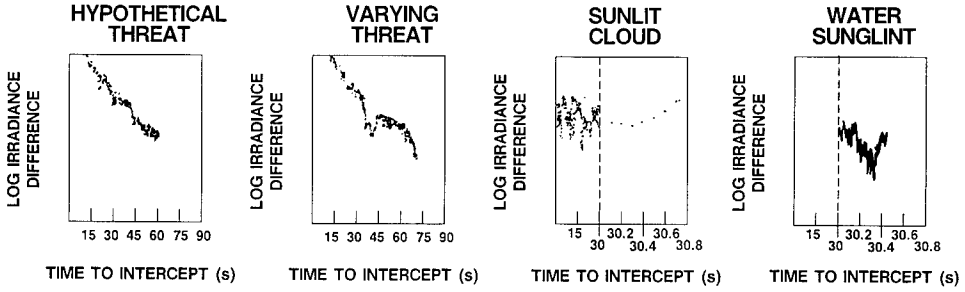

Fig. 1.43 Temporal signature characteristics.

If the tracking algorithm accepts such short-term variations for valid targets, the system will suffer from an increased false alarm rate from clutter sources. More complex tracking algorithms require more computer speed and memory capacity. Even with more complex algorithms, the threshold must be increased in heavy clutter regions to avoid increased false alarms or computer overload. Sun glint can exhibit even faster short-term variations than most targets, as shown in the right two plots in Fig. 1.43. In the right two plots, the time scale is partly expanded to show the short-term variations of sun glint. For water sun glint, the irradiance difference incident on a given pixel can change significantly in milliseconds.

An approach that has been used with some success is spectral processing. Spectral processing is based on the idea that the spectral shape of a sun glint and a target are recognizably different because of the large difference in temperature and spectral emissivity of the sources. Spectral discrimination is usually added to a system in addition to spatial and temporal discrimination. Spectral discrimination is especially effective against sun glint for low-altitude aircraft and missiles.

Sample spectral signatures are shown in Fig. 1.44. A hypothetical target similar to a small blackbody viewed at long range is shown on the top left of the figure. Various background signatures are shown in the other plots in the figure. The energy below the CO_2 notch at 4.4 μm is higher than the energy above the notch for the sunlit cloud and the water sun glint. The reverse is true for the target and the ground clutter shown. This difference forms the basis for many spectral discrimination schemes.

Spectral discrimination requires a more complex focal plane and analog circuits. One way of providing spectral discrimination is to have parallel detector arrays view the same instantaneous fields of view through different spectral filters. The signal ratios between common elements in the two arrays are related to the temperature and emissivity of the source and, thereby, provide a discriminant. Potential problem areas for spectral discrimination include the short-term variations in some types of clutter (e.g., water sun glint) when compared with the time to switch between detector arrays, selection of spectral bands that minimize variations with range and weather, and maintaining wide dynamic range and linear performance in the signal processing ahead of the spectral discrimination circuits.

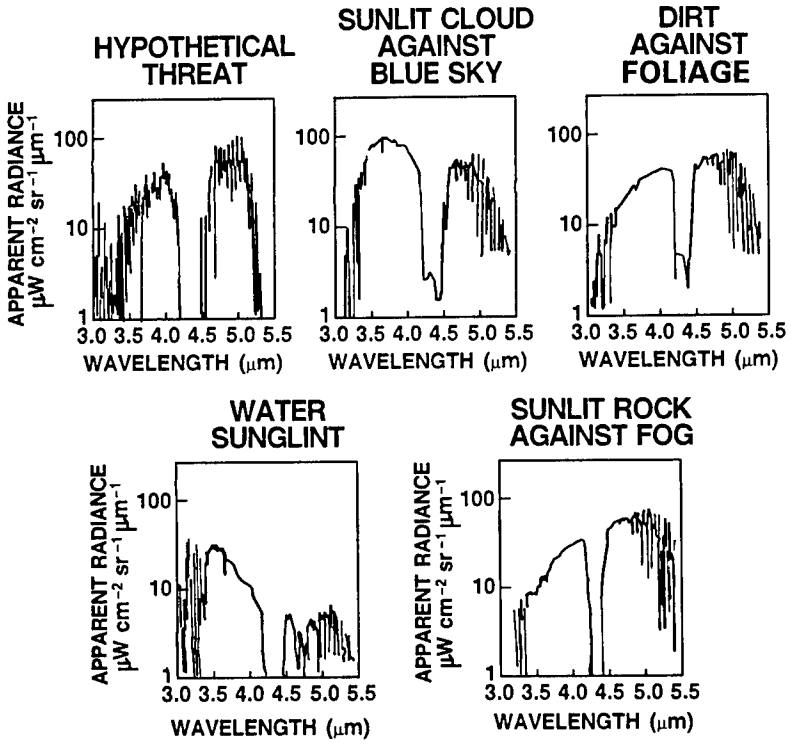

Fig. 1.44 Spectral contrast signatures.

Spectral Band Trade-Offs in the Ultraviolet and Visual Spectrum. The use of ultraviolet radiation to detect missile plumes has been explored by various workers. A photon counting detector consisting of a multi-anode microchannel array has been used to obtain UV imagery of a Polar Bear Scout rocket plume at a range of 1.2 km in the 250- to 270-nm range.[79] An SNR of nearly 150 was obtained as a result of the low natural background illumination in this particular band. However, atmospheric attenuation of the radiation from the 9-m-long by 1.8-m-diam plume, whose temperature was estimated at 2300 K for the aluminized solid fuel, reduced photon levels to the point where long integration times were necessary for detection and image generation.

Under sunlight conditions, the visible band may provide the best possible condition for detection of postburnout missiles.[80] The intense visible radiation associated with most missile exhaust plumes makes the band useful for boost and sustain phases with or without sunlight. Because plume temperatures are on the order of 1500 to 2500 K (peak radiation at 1 to 2 μm), whereas solar radiation has a distribution characteristic of a 5900-K source (peak radiation at 0.55 μm), it should be possible to reject solar glint from sea and clouds with a dual-band system.

Detecting Subpixel Targets. Tactical warning receivers must offer constant surveillance of a large field of regard, so high-resolution imagery of the potential target is generally not practical. Consequently, most detection events

involve targets whose extent is of the same order or less than the instantaneous field of view, or subpixel targets. In the tactical scenario defined in Sec. 1.2.2, the range to target is 10 km at launch and 5 km at burnout. If the missile is assumed to be 1 m in length, it subtends a maximum of 0.1 mrad if seen broadside. In the case of plume detection, the plume can be treated also as a 1-m-long target. A threat missile approaching the platform will most likely present an aspect angle of no more than 30 deg off the nose, so the projected length of missile body or plume will be less than 0.5 m, or less than 0.1 mrad at the warning receiver at burnout.

Working with subpixel targets limits some of the spatial filtering or pattern recognition techniques that might be used for detection and classification. Most of the algorithms useful in this context exploit the fact that the target moves against a cluttered but stable background. A simple frame-to-frame or scan-to-scan differencing is often inadequate because of motion of the sensor with respect to the fixed background. Double differencing and various interpolation techniques have been used to compensate for background shifting. Casasent et al.[81] have evaluated the performance of six different algorithms (single differencing, double differencing, linear interpolated differencing, parabolic interpolated differencing, spatial differencing, and spatial filtering) for detection and tracking of subpixel targets in a moving background. The assumptions of this study are close to those of our tactical situations. The targets are small in size (a few pixels at most, if not subpixel), target radiances are close to those of the background level, targets move relatively fast compared to the background, the background movement between frames or scans is usually less than a pixel, and sensor noise level is low compared to target and background signals.

If $I_k(x)$ is the intensity in frame k at position x, single differencing can be defined as

$$D_k(x) = \frac{[I_k(x) - I_{k-1}(x)]}{2} , \tag{1.71}$$

where $D_k(x)$ is the difference image intensity. In the benign case of stationary background, the only nonzero parts of this image are the pixels that differ because of target motion and, at a lower level, the increased uncorrelated noise. Double differencing is described by

$$D_k(x) = -\frac{1}{2}I_k(x) + I_{k-1}(x) - \frac{1}{2}I_{k-2}(x) , \tag{1.72}$$

and requires three frames or scans containing the target to perform detection. The linear and parabolic interpolation differencing schemes use two or three frames to estimate the background subpixel shift. The differencing operation takes the form of

$$D_k(x) = I_{k-1}(x) - \hat{I}_k(x) , \tag{1.73}$$

where the shifted frame $\hat{I}_k(x)$ is obtained from the estimated shift Δ_B by

$$\hat{I}_k(x) = (1 - \Delta_B)I_k(x) + \Delta_B I_{k-1}(x) \ , \tag{1.74}$$

in the case of linear interpolation, or

$$\hat{I}(x) = \frac{\Delta_B(\Delta_B + 1)}{2} I_{k-1}(x) + (1 - \Delta_B^2)I_k(x) + \frac{\Delta_B(\Delta_B - 1)}{2} I_{k+1}(x) \ , \tag{1.75}$$

for the case of parabolic interpolation. Both of these interpolation methods attempt to align the backgrounds before subtracting, thus compensating for sensor motion or jitter.

Spatial filtering, described more fully by Wang,[82] uses only one frame at a time, but exploits the spatial correlation of backgrounds to distinguish them from the more correlated target with a 3- × 3-pixel-square filter mask. Temporal information (the movement of the target against the background) is ignored in this approach. Spatial differencing, proposed by Patterson et al.,[83] considers 3- × 3-pixel windows centered at the same point in successive frames. The center pixel from the current frame is subtracted from the 9 pixels of the same window in the previous frame. The magnitude of the smallest of the nine differences is the quantity of interest. If a target has moved out of a window between frames, this quantity will be larger than for nontarget containing windows. The method is insensitive to targets that move less than a pixel between frames.

Figures of merit for the algorithms include a background suppression factor (BSF), which is the ratio of variances of a background-only image before and after processing, the ratio of target signal strength after processing to before processing, and the uncorrelated noise variance in the output image. Of the six algorithms considered, parabolic interpolated differencing outperforms the others by most figures of merit, but implementation in realtime situations may require parallel processing.

1.5.1.2 Millimeter-Wave Detection. In the case of passive millimeter-wave radiometers, the principal target detection mechanism is a difference in reflected ambient radiation from the target and from adjacent background surfaces. The source of the radiation is usually a cold sky for down-looking cases. Targets are more reflective than typical background materials and thus show negative contrast. Common millimeter-wave frequencies for target detection are 35 GHz (9000 μm) and 94 GHz (3500 μm), based on atmospheric transmission considerations. Typical sky temperatures at these two wavelengths are indicated[84] in Table 1.16.

The sky is effectively warmer at 94 GHz than at 35 GHz, as can be seen in the table, and becomes even more so with higher humidities. This leads to a preference for 35 GHz for passive systems. An idea of the variation in material reflectances at normal incidence can be obtained[84] from Table 1.17, which shows emissivities at normal incidence for a number of terrain-type materials as well as metal. Because of the increasing penetration with longer wave-

Table 1.16 Radiometric Sky Temperature Variations with Atmospheric Conditions

Condition	35 GHz	94 GHz
Clear	34 K	60 K
Fog (0.32 g/m^3)	58	150
Rain (2 mm/hr)	77	143
Rain (4 mm/hr)	120	255

Table 1.17 Material Emissivities at Normal Incidence at 35 GHz (from Ref. 84)

Material	Emissivity
Sand	0.90
Asphalt	0.83
Concrete	0.76
Plowed soil	0.92
Coarse gravel	0.84
Heavy vegetation	0.93
Smooth rock	0.75
Dry grass	0.91
Dry snow (deep)	0.88-0.76
Metal	0.0

lengths, surface properties are less important at millimeter wavelengths than at visible or infrared wavelengths.

The radiometric contrast of the target with respect to background is given by

$$\Delta T_T = \varepsilon_{tgt} T_{tgt} + \rho_{tgt} T_{sky} - \varepsilon_{bkd} T_{bkd} - \rho_{bkd} T_{bkd} , \tag{1.76}$$

where the emissivity ε and the reflectivity ρ are approximately complementary ($\varepsilon + \rho \approx 1$). Maximum detection range is determined by the target radiometric contrast and factors characterizing the antenna, the radiometer sensitivity, and the processing parameters. The passive radiometer range equation[84] can be written in the form

$$R = \left(\left(\frac{\eta_A \pi D^2}{4\lambda^2} \right) (A_T \Delta T_T) \left\{ \frac{(B_{IF}/2B_N)^{1/2}}{K_R[T_a + (F-1)T_0]} \right\} \left[\frac{1}{(SNR)^{1/2}} \right] \right)^{1/2} , \tag{1.77}$$

where the four major terms represent antenna, target, radiometer, and processing contributions, respectively. The parameters are

Antenna

η_A = aperture efficiency
D = antenna diameter
λ = operating wavelength
η = radiation efficiency

Target

A_T = projected physical area of target
ΔT_T = target radiometric contrast

Radiometer

B_{IF} = IF amplifier bandwidth
B_N = amplifier bandwidth
T_a = antenna temperature of background
F = radiometer noise figure
T_0 = standard temperature (290 K)
K_R = radiometer constant (1 to $3\sqrt{2}$ depending on scan)

Processing

SNR = power SNR.

A simpler form of the range equation can be written as

$$R = \left[\frac{\eta_A A_T \Delta T_T}{\Omega_A \Delta T_{\min} (\mathrm{SNR})^{1/2}}\right]^{1/2}, \tag{1.78}$$

where Ω_A is the antenna solid angle and $\Delta T_{\min}$ is the minimum detectable rms temperature difference, usually of the order of 0.1 K or better for state-of-the-art radiometers.

Note that range increases with antenna diameter and operating frequency (except for atmospheric attenuation effects), decreases with the square root of the receiver noise figure F, and is relatively insensitive to SNR. Atmospheric attenuation effects are summarized[84] in Table 1.18.

1.5.1.3 False Alarms and False Target Rejection

Overview. The most serious defect in a warning system is a missed event. The consequences of a missed detection for a warning system are much more severe than for a search and track or target detection system, so the system designer places a premium on maximizing probability of detection. The consequence may be an increase in false alarms and false target declarations. (In the following paragraphs, false alarms are considered as the result of noise or natural background clutter, whereas false targets are considered to result from man-made objects in the scene that do not pose a threat to the platform.)

False targets are rejected by virtue of their trajectory or classified by their radiometric properties. False alarms must be rejected by considerations of recent noise and/or clutter statistical properties. Sophisticated signal processing algorithms will do much to reduce the false alarm rate, as discussed in the previous section. False target rejection, however, usually demands more information about the source of the radiation.

Table 1.18 Atmospheric Attenuation in Millimeter-Wave Bands (from Ref. 84)

Parameter		One Way Loss (dB/km)	
		35 GHz	94 GHz
Clear air:		0.12	0.4
Rain:	(mm/hr)		
	0.25	0.07	0.17
	1.0	0.24	0.95
	4.0	1.0	3.0
	16.0	4.0	7.4
Cloud:	(Type)		
	Rain	5.14	35.04
	Dry	0.50	3.78
Fog:	(g/m^3)		
	0.01 (light)	0.006	0.035
	0.10 (thick)	0.06	0.35
	1.0 (dense)	0.6	3.5
Snow (0°C)		0.007	0.0028

False Targets. False targets are due to man-made objects or events that satisfy some of the criteria that the warning receiver uses to detect targets, but fail in others. Examples of false targets include fuel-fed ground fires, flares (both countermeasure and illuminating), artillery firings, napalm, aircraft, and other missiles and rockets, both friendly and hostile but threatening other platforms. Depending on the receiver spectral band, sun glint from reflective objects, arc welders, industrial fires, and bright lights can also be false targets.

Position and velocity information are among the most useful discriminants for rejecting false targets. An object that remains fixed in relation to the background or increases its range from the platform is probably not a threat. Unfortunately most tactical warning systems sacrifice direction and range accuracy for response time. A dual-band system may provide adequate range rate of change information without sacrificing response times by monitoring changes in band ratios. Motion of the point source relative to a fixed background pattern can be detected with correlation techniques, but this provides little information about the radial velocity of the target with respect to the platform. Furthermore, systems with command line-of-sight guidance may not exhibit detectable tangential motion.

Exploitation of the inverse square variation of irradiance with range is one of the more direct sources of information on range rate of change. It is also, like the band-ratio method, a technique whose accuracy and sensitivity decrease with increased range, but it may be practical at tactical ranges. It assumes a constant radiation output from the target over the interval in question. A low SNR can adversely impact range estimation accuracy in such a

system. In addition to system noise, clutter related variations in the local background level, target aspect variations, and local path attenuation can induce errors in this technique.

1.5.1.4 Direction of Arrival. The type and accuracy of direction of arrival information depends primarily on whether the system is of the scanning or staring type (see Sec. 1.5.2.1). In the case of a mechanically scanned detector (or detector array), the direction of the missile can be determined from the orientation of the scan mechanism at the time of detection. Accuracy depends on the instantaneous field of view of the detectors, the scan rate, and the signal processing techniques used for detection. Staring systems are limited by the number of detector elements and the field of view of each. Accuracy is generally no better than a single pixel, and probably several times that limit.

As previously indicated in Table 1.4, an accuracy of 90 deg is often adequate for tactical situations and most countermeasures. This level of accuracy provides adequate information to select which of several flare dispense units to use, for example. Advanced countermeasures, which may concentrate their energy into a narrow range of angles, put greater demands on angle-of-arrival accuracy. Sampling or scan rates must still remain high to maximize the response time available for countermeasure use.

Platform jitter or line-of-sight instability can also degrade angle-of-arrival accuracy. If the (platform) line-of-sight motion has spectral components of significant amplitude at frequencies higher than the detector sampling frequency, high-resolution images are blurred, having an effective point spread function larger than predicted statically. Techniques have been developed[79] to compensate for line-of-sight motion in low-photon-rate situations. Using the line of sight x,y error signal from a gyroscope or accelerometer, the instantaneous error is subtracted from each detected photon event, and the corrected position is stored in memory. This technique has been demonstrated by detection and imaging of a rocket plume in the 250- to 270-nm ultraviolet region. High temporal resolution (100 ns) permits processing of individual photon events. Typical vidicon or charge-coupled devices (CCD) have temporal resolution of about 1/30 s, and the technique becomes less useful when such detectors are used.

1.5.1.5 Range and Time to Impact Estimates. One method of estimating the missile range and velocity is an analysis of the intensity history of the received signal. The irradiance at the receiver varies with source intensity, range (via the $1/R^2$ effect), and atmospheric attenuation and can be approximated by

$$E_r = \frac{1}{r^2} I \exp(-\alpha r) + N_c \ , \tag{1.79}$$

where I is source radiant intensity, r is range, α is atmospheric extinction coefficient, N_c is noise or clutter, and E_r is the in-band irradiance at the receiver.

The time derivative of this irradiance, which can be determined from a time history of the received signal by the relation

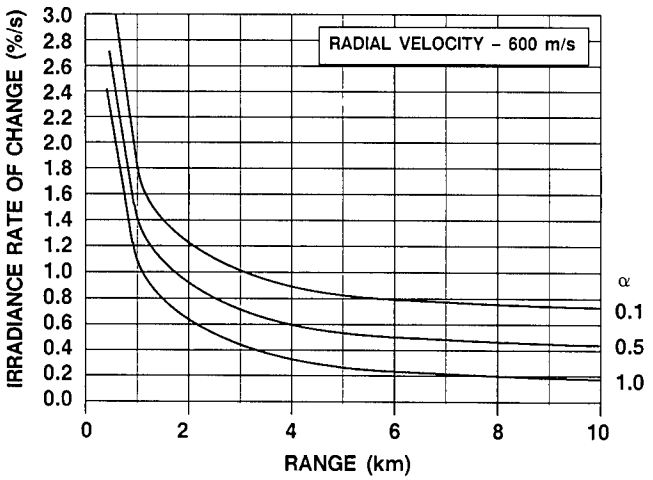

Fig. 1.45 Time variation of signature with range in the infrared for selected values of atmospheric attenuation.

$$\frac{dE_r}{dt} = -E_r\left(\frac{2}{r} + \alpha\right)\frac{dr}{dt}\,, \tag{1.80}$$

contains information about the range and its time derivative, the radial velocity, dr/dt. At long ranges, $2/r$ is small compared to α and the atmospheric attenuation predominates. The time to intercept, TTI $= -r/(dr/dt)$, can be expressed in terms of the rate of change of the irradiance at the receiver as

$$\text{TTI} = \frac{2}{[-d(\ln E_r)]/dt - \alpha(dr/dt)}\,. \tag{1.81}$$

Figure 1.45 shows the percentage variation in intensity per second as a function of range for extinction coefficients of 0.1, 0.5, and 1.0 km^{-1} and a radial velocity of 600 m/s. The small relative change in intensity at long ranges, when the signal is lower, indicates the susceptibility of this technique to system noise.

A major weakness in this approach is the assumption that the output of the missile is constant with time. Figure 1.5 gave outputs as a function of time for several typical missiles from which constant output was shown to be an exceptional situation.

1.5.1.6 Discrimination—Threat Versus Nonthreat. If the only source of missilelike radiation in the vicinity were the approaching threat missile, the function of the warning receiver would be nothing more than detection and providing range and direction information. In tactical situations, however, there are likely to be numerous other objects of a similar nature in the vicinity of the platform. The majority of these probably pose no threat to the platform, but to make that decision requires some degree of classification on the part of the warning system.

Trajectory information is the most useful data for threat classification for IR systems. During the final intercept phase, the angular velocity of a true threat is near zero. Prior to that phase, an increasing irradiance level may indicate an approaching object, but a collision trajectory is not confirmed. Decreasing intensity does not necessarily make the object a nonthreat. At burnout, the intensity from an approaching missile exhibits a decrease with time, but the magnitude and rate of this decrease make it easy to distinguish from a receding missile.

In a system with poor direction of arrival resolution, time to intercept may be the only available trajectory information. If an object shows a TTI that decreases at a rate consistent with supersonic radial velocity, it is reasonable to declare it a potential threat. If this high-speed approach continues to within a few seconds TTI, a threat is almost certain, and countermeasures should be activated.

Spectral discrimination techniques of the sort used to reject clutter and false targets can be applied to the classification problem also. A primary issue is the difference between aircraft exhaust spectra and missile or rocket exhausts. Many of the same exhaust products are present in both, so line emissions may not be an adequate distinction. Temperature differences, however, offer a possible discriminant. The exhaust temperature of missile engines is often[8] of the order of 2000 K, whereas nonafterburning turbojet exhausts fall in the range of 1000 K. The former temperature has a spectrum peaking at 1.45 μm, whereas the latter peaks at 2.90 μm.

1.5.2 Equipment Considerations

Several factors drive the physical size and weight of a warning system constrained to achieve a specified combination of operational requirements such as field of regard, sensitivity, refresh rate, and environmental tolerance.

1.5.2.1 Scanning/Staring. One of the first decisions after the choice of spectral region is the selection of a method for converting the temporal and spatial variations in each pixel of the field of view into one or more time-varying electrical signals. One method for achieving this end is two-dimensional electromechanical scanning. Scanning systems may use a single detector or a detector array. A second method for achieving this end uses a fixed field of view or *staring* detector. Staring systems may also use either a single detector or a detector array.

The choice of a scanning versus a staring sensor is driven by system as well as hardware implementation design constraints. Scanning systems are not useful for detecting short-duration features that may be critical for some types of missile declaration or false target rejection methods. Staring systems, because they cover the entire field of regard continuously, do not miss short-duration events.

A staring system, on the other hand, requires a detector array with a large number of elements to achieve the same spatial resolution a scanning system can provide with relatively few elements. High spatial resolution is important for some types of missile declaration or false target rejection methods. Scanning systems can provide high resolution with far fewer detectors than staring

systems. Cost, size, weight, reliability, and aircraft integration all become factors in the final selection of scanning versus staring.

Electromechanical scanning can be divided into object plane scanning and image plane scanning. Object plane scanning requires larger mechanically moving parts than image plane scanning, but the off-axis imaging requirements on the optics are reduced, and the defocusing problems of image plane scanners are eliminated. Staring systems with more than 1 pixel can consist either of a continuous surface detector scanned by an electron beam (e.g., a vidicon) or a mosaic of discrete detector elements scanned by analog or digital circuitry connected to, or part of, the mosaic. Like image plane scanners, large field-of-view staring systems can have challenging optical design problems.

One of the more successful object plane mechanical scanners used for tactical infrared warning is the spinball. The spinball consists of a number of lenses—typically three or four—mounted in a great circle in a ball-shaped assembly that rotates around a linear detector array (see Fig. 1.46). As the ball spins on the array axis, each lens in turn scans one bar of object space. Successive bar scans can be either coincident with the previous bars or can be offset to scan a larger field of view. In practice, the bars may be offset by optical wedges in front of each lens rather than by tilting the axis of the great circle. The advantages of the spinball include continuous rotational motion, constant velocity scan, high scan efficiency, large scan fields of view, and high frame rates. The disadvantages include limited resolution, inability to cold shield or cold filter the detectors, and multiple optics.

Most developmental activities are concentrated on two-dimensional staring detector arrays, even though most current operational systems use mechanical scanning. The mosaic offers potential advantages in reliability, production cost, and higher performance. Optical designs to accommodate staring arrays are also the subject of research and development.

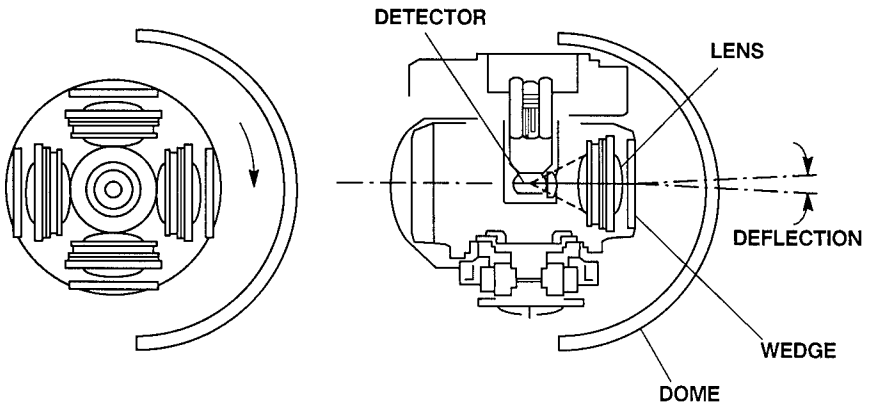

Fig. 1.46 Spinball object plane mechanical scanner.

1.5.2.2 Sensitivity. With a mechanical bar scan, the electrical bandwidth needed to provide optimum response to a point source is approximately

$$\Delta f = \frac{1}{2t_d} , \tag{1.82}$$

where t_d is the detector dwell time. The dwell time is given by

$$t_d = \frac{\alpha\beta n k_{se} T}{\Omega_\alpha \Omega_\beta} , \tag{1.83}$$

where

α = detector azimuthal subtense
β = detector elevation subtense
n = number of detectors
k_{se} = scan efficiency
T = frame time
Ω_α = azimuthal total field of view
Ω_β = elevation total field of view.

The dwell time for a staring detector is just the scan efficiency times the frame time, so the required bandwidth for a staring array can be substantially less than for a scanning array. (Of course, the required number of detectors for a given field of view and resolution will be proportionally more.) The resulting increased sensitivity tends to compensate for the poorer detectivity of current staring arrays compared with the smaller linear arrays designed for mechanical scanning systems.

The sensitivity of a warning receiver is usually given as the noise equivalent irradiance. A simplified formula for NEI is

$$\text{NEI} = \frac{2F[\Omega(\Delta f)]^{1/2}}{D_o^2 D^* \tau_o} , \tag{1.84}$$

where

F = optical focal length
Ω = $\alpha\beta$
D_o = optic diameter
D^* = specific detectivity of the detector
τ_o = optical transmission.

The optic diameter plays three important roles in warning receiver design. First, the optic diameter, and thus the optical aperture, directly influences the system sensitivity. Second, the optic diameter determines the ultimate limit on system resolution, although most warning receivers are sensitivity limited rather than resolution limited. Finally, the optic diameter, together with the field-of-regard and stabilization approach, determine the cross-sectional area of the receiver. For an airborne system, the cross-sectional area is important both from a drag point of view and in terms of radar cross section.

Spectral bandwidth is usually controlled by using a spectral filter ahead of the detector. In the infrared region, the spectral filter should be cooled for best performance by mounting it in the detector dewar. The purpose of cooling the filter is to reduce the out-of-band self-emission of the filter. In the visible region, self-emission is not the predominant photon source, and cooling is not a common practice.

A variety of noise sources influence the value of D^* that can be achieved in a particular system configuration. Significant sources of noise might include background-induced photon noise, detector load resistor noise, detector $1/f$ noise, amplifier noise, and readout noise.

Because the magnitude of the mentioned noise sources depends on the specific detector operating conditions and configuration, care must be utilized when assigning a value to D^* in the system sensitivity equation. It must be remembered that D^* for a particular detector/amplifier combination is a function of the wavelength of the incoming signal radiation, the frequency at which the signal is *chopped*, and the level of the background flux incident on the detector. Care should be taken to see that the value of D^* used in a system sensitivity calculation corresponds to the conditions under which the detector must operate in the sensor. Specifically, the D^* should be appropriate for the target wavelength, the detector dwell time, and the incident background flux.

For example, often the D^* for a detector is measured in the laboratory under conditions of high background flux levels. Under such conditions, a photon-induced background noise might be the dominant source of noise, and the detector is said to be operating as a background limited performance detector. If this same detector is used in a warning receiver design that utilizes a cold shield to reduce the background flux incident on the detector, then the D^* measured in the laboratory under conditions of high background flux would not be the appropriate value of D^* to use in the system sensitivity calculation. For a BLIP detector, D^* scales as 1 over the square root of the background flux level.

The detector load resistor noise is usually thermal noise, whereas the amplifier noise current is a function of the amplifier short circuit noise voltage, open circuit noise current, and equivalent input circuit impedance including device capacitance.

In the infrared region, the detector is usually cooled to reduce the detector thermal noise current to an insignificant value. For a spectrally wideband detector, the preamplifier noise and load resistor noise are usually small compared with the photon noise, and such systems are typically background limited.

Conversely, for a narrow-band detector, if a cold filter and cold shield are used to reduce the background photon flux, the photon noise current can be decreased to the point where the load resistor and/or amplifier noise is dominant. In other words, as the optical spectral bandwidth and the detector's warm field of view are decreased, a point is reached where the system detection capability is limited by load resistor and/or amplifier noise rather than by detector performance. In the infrared region, extremely small spectral passbands are required to reach the point where the system is amplifier noise limited.

In the visible spectrum, the primary source of unwanted background photons is solar reflection and scattering rather than thermal background emission.

At night, the solar flux is essentially zero and no improvement in NEP is provided by a narrow spectral filter; the photon noise current is already as small as can be achieved. Conversely, a wide spectral passband incurs little, if any, loss in sensitivity. With a good detector, the detector dark current is small, and the detector D^*, which is proportional to the reciprocal of the detector noise current, is quite high. With an avalanche photodiode or photomultiplier and a good amplifier, individual photons can be counted.

During the day, the solar flux is large enough that the photon noise dominates and other noise sources are not very important. Under these conditions a very narrow spectral filter (i.e., less than 1%) is required to reduce the photon noise to a level comparable to the other noise sources. Conversely, a wide spectral passband passes so much solar flux that system sensitivity may be quite poor.

1.5.2.3 System Implementation. Warning receiver display techniques usually are limited to situation awareness displays. Detection of a threat surface-to-air or air-to-air missile usually occurs only a few seconds before countermeasures must be deployed. Automatic interaction between the warning receiver and the countermeasures dispenser minimizes the time delay in initiating a response to a perceived threat.

Other factors that become significant in the final design of a warning receiver are the interactions between the warning receiver and its platform, especially if the platform is a highly maneuvering aircraft. Stabilization may be accomplished either electronically or mechanically, with electronic stabilization the more common. EMI from the platform may be a limiting factor in the sensitivity achieved by the receiver. High-powered radios or radars can induce signals in the sensitive detector circuits of a warning receiver. Finally, the physical size and weight of the warning receiver can limit its applicability. Especially for small helicopters, weight and power consumption may play the deciding role in determining whether a particular warning receiver can be used.

1.5.3 Numerical Example

As an example of potential system performance, consider the system and scenario described for tactical situations in Sec. 1.2. The 1.44-mrad IFOV corresponds to 7.2 m for a missile range of 5 km, so the missile is unresolved. The dwell time for the spinball system described is 0.172 ms [Eq. (1.83)] with a corresponding bandwidth of nearly 30 kHz [Eq. (1.82)]. The NEI is then 2.8×10^{-7} W/m^2 [Eq. (1.84)].

With a 1000 W/sr target signal at a range of 5 km and an atmospheric transmittance of 0.48, the target irradiance is 1.9×10^{-5} W/m^2, so the SNR is nearly 70. A typical background in this case would be distant vegetation and atmospheric emission from the region beyond the missile. Assuming an air temperature of 10°C and an emissivity of 0.98, the Planck equation[8] yields a background radiance of 1 W m^{-2} sr^{-1}. Hence, adjacent pixels would have an irradiance of about 10^{-6} W/m^2, yielding a signal level 20 times the background level. For a benign vegetation background, the clutter level at this resolution will be[61] equivalent to 1°C or a radiance variation of about 2%, so the SCR is nearly 1000.

From the discussion of Sec. 1.4.2.1, if the threshold level is selected for a TNR of 10, a FAR of 3×10^{-17} per second is attained and the detection probability is in excess of 0.999. This is clearly a benign situation. Even if the missile signature drops to 10 W/sr after burnout, the SCR is still 10 and a TNR of 10 is still possible.

1.5.4 Testing

Testing of an entire tactical missile warning receiver, as opposed to individual component testing, presents a number of challenges. The firing of missiles (even unarmed) against warning receivers on manned aircraft platforms presents unacceptable safety hazards, however, drone testing has been carried out with success.[85] Devices that simulate the variation in target irradiance resulting from R^2 and atmospheric transmission changes can be constructed using filter wheels or other mechanical or electronic controls on the source of illumination. Simulating realistic background clutter and receiver and missile motions require a more complex test bed. Developments in infrared scene simulators suggest the possibility of high-fidelity real-time total scene projection at some future date.

Flight line testing of installed systems to verify performance is less demanding in terms of the diversity of conditions and fidelity required. A simple filter wheel and source device can be utilized for performance confirmation testing.

1.6 STRATEGIC WARNING RECEIVERS

1.6.1 Introduction

Another important class of IR warning receiver is the strategic IR warning system. IR sensors may be used to detect intercontinental ballistic missiles (ICBMs), submarine launched ballistic missiles (SLBMs), strategic bombers, and cruise missiles. As is the case for tactical missile warning systems, a strategic warning system must provide continual surveillance of a threat volume, detect threats with a high probability of detection and low false alarm rate, and communicate warning and threat assessments to the appropriate user in a timely fashion. Here, however, it is the strategic forces of a country that are to be warned as opposed to a tactical platform, such as a single aircraft.

Although a top-level functional description of a strategic warning system might be similar to that of a tactical warning system, the nature of the strategic warning problem leads to major differences in the design of strategic and tactical sensors. These differences result primarily from the global nature of the threat. A strategic attack can be initiated from virtually any place on earth. As a result, the threat volume that must be covered by a strategic warning sensor is much larger than that of a tactical sensor, and the ranges at which threats must be detected by strategic sensors are typically orders of magnitude longer than the detection ranges required for tactical sensors.

Another key difference between strategic and tactical warning systems involves the nature of the sensor platform. In the tactical case, the warning system is usually situated on the platform that is to receive the threat warning.

In the strategic case, it is not a single platform that is to receive the warning; it is the strategic force. Furthermore, because of the far-reaching nature of the threat, strategic warning systems must often be situated at long standoff ranges from the strategic forces that require the threat warning. Consequently, strategic warning systems usually are located on dedicated surveillance platforms, with the most common such platforms being airborne and satellite surveillance platforms.

Because there are major differences between the requirements for strategic and tactical warning systems, it is natural that the designer of a strategic system must face different design challenges than the designer of a tactical warning system. Because of the requirement for high sensitivity (i.e., long detection ranges), the designer of a strategic IR warning system often considers designs with large optics, large IR focal plane arrays (FPAs), and extensive signal and data processing. Because strategic warning systems may have to be deployed in space, space power and cryogenic cooling technology are critical elements in the design of strategic systems. In addition, the issues of platform survivability and communications must be considered in the design of dedicated surveillance platforms.

This section summarizes some of the key features of strategic warning systems and highlights design issues associated with these systems. Characteristics of strategic targets are discussed, and platform options and design concepts are described.

1.6.2 Target Characteristics

1.6.2.1 Ballistic Missile Trajectories. The trajectory of an ICBM consists of four distinct phases—the boost phase, the postboost phase, the midcourse phase, and the terminal phase.

During the *boost phase*, multistage rocket engines lift the missile payload to an altitude of approximately 200 km with speeds in the neighborhood of 7 km/s. At this point, the powerful booster engines shut down, and the payload has enough kinetic energy to follow a ballistic (free-fall) trajectory thousands of miles to its target.

The energy imparted to the payload during the boost phase is derived from the chemical reaction involving the rocket engine propellants. This reaction may involve either solid or liquid propellants, but in either case, the reaction is highly exothermic and a large amount of heat is generated. Although much of this heat is converted into thrust, some invariably results in the generation of a strong IR/EO signature. It is this signature that occurs during the boost phase, which typically lasts only a few minutes, that makes an ICBM most susceptible to detection by an IR/EO strategic warning system.

Many modern ICBM missile systems are multiple, independent reentry vehicle (MIRV) systems. They carry a number of reentry vehicles (RVs) that can be aimed at different targets. A postboost vehicle (PBV) maneuvers to different trajectories and drops each RV off when it arrives at its intended target trajectory. Decoys (RV replicas, balloons, chaff, and so on) may also be deployed by the PBV during this phase. This is the postboost phase of the trajectory.

The *postboost phase* is particularly important in the design of an antiballistic missile (ABM) system, because a single ABM "shot" could destroy multiple

RVs if it destroys the PBV before it deploys all of its RVs. However, from a strategic warning point of view, this phase is less important than the boost phase. Although a PBV does use rocket motors to maneuver, these are small motors with IR/EO signatures that would be difficult to detect by an early warning surveillance system.

Likewise, the *midcourse phase* is not the phase where a strategic warning system is likely to be utilized. This phase refers to the time from RV deployment to the time when the RVs reenter the earth's atmosphere. During this time period, the RVs, along with any decoys or other penetration aids (penaids) that might have been deployed by the PBV, fall freely under the influence of gravity toward their targets. While falling in the vacuum of space, the RVs radiate very little IR energy. They have small emissivity-area products, and depending on their thermal design, may be quite cool (approximately 200 K). Consequently, they are very poor IR targets, and typically are not candidate targets for IR strategic warning systems.

The last few minutes of the ICBM trajectory is called the *terminal phase.* During these final few minutes, the RVs and their associated penaids reenter the earth's atmosphere. As they reenter, atmospheric drag strips the lighter penaids from the vicinity of the RVs and also causes heating of the RVs, making them good IR targets.

Although the terminal phase is important in the consideration of ABM system concepts that utilize terminal defense options, the strategic warning function must be accomplished much earlier in the ICBM trajectory.

1.6.2.2 Ballistic Missile IR Signatures. Boost phase signatures of a ballistic missile show great variability depending on the propellant type, size of the missile, and flight conditions. The hot exhaust plume of a solid propellant missile contains particles that lead to continuum radiation in the IR part of the spectrum. On the other hand, liquid propellant systems may contain only hot gases in their exhaust, resulting in the radiation of IR energy into discrete spectral bands. These bands are determined by the specific gases that are present in the exhaust plume. Consequently, a critical consideration in the selection of a spectral band for a strategic warning system involves an assessment of the exhaust products of the missile systems that are to be observed.

The vast majority of chemical rocket engines use as a source of energy chemical reactions that result in the exothermic formation of oxides. The most common oxides formed are water (H_2O) and carbon dioxide (CO_2). For example, the propellant combination of hydrazine (fuel) and nitrogen tetroxide (oxidizer) results in the formation of both water and carbon dioxide in the combustion process. The fuel/oxidizer combination of hydrogen (H_2) and oxygen (O_2), used in the Space Shuttle's main engines, results in the formation of water in the combustion process.

Because water vapor and carbon dioxide are commonly present in the exhaust products in ballistic missile boosters, the IR bands in which they radiate are leading candidates for strategic warning sensor bands. At temperatures typical of those found in the exhaust of a ballistic missile, water vapor radiates strongly in IR bands centered at 2.7 and 6.3 μm. Carbon dioxide radiates strongly in a band centered at 4.3 μm.

Although it may be that the vast majority of strategic rocket engines discharge large quantities of water and carbon dioxide in their exhaust plumes,

thereby making the IR emission bands of these species logical candidates for the spectral bandpass of a strategic warning sensor, the possibility exists that strategic rockets that do not radiate strongly in these bands could be developed. For example, the developers of rocket engines have considered the possibility of designing rockets that use high-energy propellants. Some of these propellants produce neither water nor carbon dioxide at the exit plane of the rocket motor.

A rough estimate of the IR energy radiated by a strategic missile can be made on the basis of the size of the visible plume and the temperature of the plume.[86] At low altitude, the visible exhaust plume of an ICBM is approximately 4 m in diameter and 50 m long; the plume temperature at the exit nozzle is approximately 1800 K; the average temperature of the visible plume is about 1400 K. A blackbody at a temperature of 1400 K has a peak spectral radiant exitance of 7×10^4 W $m^{-2}\mu m^{-1}$ at a wavelength of 2.1 μm. Considering the plume to be a blackbody with surface area of 600 m^2, we arrive at an estimate of 40 MW of radiated power in a 1-μm spectral band. The amount of this power that is collected by a strategic warning system depends on the viewing aspect. If we assume, for the sake of this rough estimate, that the plume radiates isotropically, then we conclude that an ICBM will radiate on the order of 3 MW/sr in a typical plume band.

Although this estimate of the plume signature of an ICBM serves to show that strategic missiles are very intense IR targets, the accurate determination of the IR signature of an ICBM is a complicated problem. At low altitude, atmospheric transmission is an important factor that must be considered. As is the case for tactical missile signatures, a sizeable fraction of the total IR energy radiated by a missile plume is absorbed by the atmosphere. However, as an ICBM rises above the heaviest concentrations of water and carbon dioxide in the atmosphere, the atmospheric transmission improves, and the apparent IR intensity of the missile increases. At higher altitudes, the signature changes as a consequence of the multistage nature of an ICBM. The latter stages of an ICBM have less thrust than the first stage of an ICBM and correspondingly have less intense IR signatures. Also, at high altitude, the missile is moving very fast in a rarified atmosphere, leading to a complicated interaction of plume and atmosphere. This interaction plays a major role in determining the high-altitude signature of an ICBM.

1.6.2.3 Strategic Aircraft Signatures. Whereas the strategic ballistic missiles are very intense IR targets because of the large amount of IR energy radiated by their exhaust plumes, strategic aircraft are relatively weak IR targets and pose a significantly more difficult detection problem for a strategic warning receiver. The jet engines on a strategic aircraft operating under cruise conditions have orders of magnitude less thrust than a strategic ballistic missile. Consequently the IR energy radiated by the exhaust plumes of these engines are also orders of magnitude less. Detection from an orbital platform of strategic aircraft by virtue of their engine exhaust plumes is also complicated by the fact that the spatial extent of the engine exhaust plumes are relatively small, and the line of sight to the plumes may be obscured by the aircraft fuselage and wings. Also, because strategic aircraft must be detected at lower

altitudes than strategic ballistic missiles, atmospheric transmission losses add to the difficulty of detecting strategic aircraft engine exhaust plumes.

Another source of IR energy emanating from a strategic aircraft that could be exploited by a strategic warning system is the IR radiation that is (by reflection and thermal emission) radiated by the aircraft structure. In terms of the average radiance of the aircraft structures, N_T, and the projected area of the aircraft as seen from the position of the sensor, A_T, the radiant intensity of the aircraft structure is $N_T A_T$. The apparent intensity level actually observed at a sensor is this intensity level attenuated by the transmission of the intervening atmospheric path plus the contribution from the radiance of the path.

When making sensor signal level calculations, it is typically not the apparent intensity level *per se* of the target that is important. What is important is the contrast between the target and the background. Thus, we define the apparent contrast intensity of the target to be the difference between the apparent intensity of the target and the apparent intensity of the background that is obscured by the target. Using this definition, the apparent radiant intensity I_{app} of the aircraft structure is given by the expression

$$I_{app} = (N_T - N_B)A_T\tau \ , \tag{1.85}$$

where τ is the atmospheric transmission from the aircraft to the sensor and $N_B A_T$ is the radiant intensity of the background that is obscured by the aircraft.

To make a rough estimate of this intensity level, we consider the case of a 280-K background, a 285-K target with an emissivity of unity, a target area of 100 m^2, and a transmission of 70%. For such a case, the apparent contrast intensity of the target in the 8- to 12-μm spectral band is approximately 200 W/sr.

A strategic sensor based in space to collect IR energy radiated by the hardbody of a strategic aircraft typically must operate in an atmospheric transmission window band. The sensor must be capable of detecting energy that passes through long atmospheric slant paths, particularly for aircraft and cruise missiles flying at altitudes near sea level. For these IR sensor applications, spectral bands with the highest possible transmission within the 3- to 5- and 8- to 12-μm atmospheric transmission windows are most often considered. This is in contrast to tactical and strategic ballistic missile warning systems that may be designed to operate at the edge of an atmospheric transmission window band where plume radiation from the target might be concentrated.

An important feature of the hardbody signature of an aircraft, as implied by the expression for the apparent target intensity, is that these signatures can be either positive contrast or negative contrast signatures. That is, when the average target radiance, N_T is greater than the apparent background radiance N_B, the apparent intensity of the target is positive; when the average target radiance N_T is less than the apparent background radiance, N_B, the apparent intensity of the target is negative.

Because both N_B and N_T vary with target altitude, the hardbody signature of a strategic aircraft is a function of the altitude of the aircraft. As a function of altitude, the signature may change from a positive contrast signature to a negative contrast signature. For such a case, there would be an altitude where

the apparent target intensity would be zero. Obviously, a target with zero apparent intensity cannot be detected by a strategic warning system. However, the apparent target signature also depends on the wavelength band of the sensor, and in general, when the apparent target signature is zero in one band, another band can be found where the apparent intensity is nonzero. Consequently, sensor concepts involving the use of multiple spectral observation bands might be considered for strategic systems that must rely on aircraft hardbody signatures for their detection capability.

1.6.3 Backgrounds

Background clutter presents a particularly severe problem for strategic warning sensors designed to detect aircraft and cruise missiles. Because these targets are effectively low-intensity point targets, the signals they produce at the sensor are typically a small fraction of the average background level. In order that the signal be detectable above the sensor noise, the average background level must be made as small as possible by utilizing small detector footprints. However, even when the detector footprint has been made small enough so that the target can be detected above the average background, spatial and temporal variations in the background level make it difficult to reliably detect low-intensity targets.

For the case of strategic warning systems designed to detect aircraft, IR sensors are typically required to operate in the atmospheric IR transmission windows. Operating in these bands, they must contend with sources of clutter on the surface of the earth and in the intervening atmosphere. Radiance variations associated with different terrain features and clouds are often comparable in magnitude with the radiance difference between a strategic target and its local background. When these background variations are summed over the entire detector footprint, the variations in the background signal level may exceed the signal level by orders of magnitude for low-intensity targets. Consequently, strategic warning systems designed to detect aircraft and cruise missiles must utilize sophisticated clutter rejection techniques. The spatial resolution required for a strategic warning receiver depends on the specific operational requirements imposed on the system. For example, strategic sensors might not only have to provide warning of a missile launch but also might be required to provide an estimate of certain tactical parameters, such as launch raid size, launch pad location, and missile type. Operational requirements such as these might ultimately determine the spatial resolution requirements for the strategic warning system. However, a more fundamental factor that must always be considered in the establishment of a spatial resolution design point is the influence of background signals on the detection process. The strength of the background signals that compete with signals from relatively localized target sources (e.g., missile plumes and strategic aircraft) increases as the size of the detector footprint on the earth background increases. Too large a footprint leads to an unacceptable level of false alarms caused by background clutter.

For the case of IR sensors designed to detect strategic missile boosters, background clutter caused by solar reflections typically represents the most stressing background signal. An estimate[86] can be made by starting with the

fact that the solar flux above the earth's atmosphere in a spectral band from 2 to 3 μm is approximately 50 W/m^2. Atmospheric absorption in a missile detection band near 2.7 severely attenuates the solar radiation that is reflected from the earth background to the sensor. Assuming that only 0.005 W/m^2 out of the original 50 W/m^2 is reflected by the background, a detector footprint of 10 × 10 km is exposed to a total background signal of 0.5 MW.

The fraction of this power that is radiated in the direction of the sensor depends on the viewing geometry. For points on the surface of the earth where the solar energy is reflected at a near-specular angle to the sensor, the background intensity is the greatest. Because these near-specular points comprise a relatively small fraction of the surveillance volume, it may be acceptable to "blank" this region to eliminate it as a source of false alarms. Doing this would require a second sensor to view this region at a nonspecular angle to maintain complete coverage of the surveillance volume.

A rough estimate of the intensity of the solar background at nonspecular angles of reflection can be made by assuming that the background is a diffuse reflector. With this assumption, the background intensity from a 10 × 10-km detector footprint corresponds to an intensity of 200 kW/sr. Although this background level is large, the peak IR intensity produced by a typical ICBM may be more than an order of magnitude larger than this value. Thus, strategic warning sensors with detector footprints as large as 10 × 10 km might provide adequate performance. Such a footprint size can readily be achieved from geosynchronous altitudes and higher.

The strategic missile threat includes SLBMs as well as ICBMs. In addition, warning systems might also be required to track the upper stages of the ICBMs. Because both SLBMs and ICBM upper stages produce considerably less thrust than the first stage of an ICBM, the IR radiation from their exhaust plumes is less intense than the radiation from a first stage ICBM missile plume. Consequently, detection thresholds must be set lower and smaller detector footprints must be utilized to minimize the number of false alarms generated by the background. Bloembergen et al.[86] conclude that a 2- × 2-km detector footprint would be an appropriate size for the reliable detection of a 300-kW/sr target. Such a spatial resolution can also be readily achieved from geosynchronous altitude. For example, the sensor aperture diameter required to match a diffraction-limited spot to a 2- × 2-km detector footprint at a range of 40,000 km and wavelength of 3 μm is only 6 in.

1.6.4 Sensor Concepts

1.6.4.1 Space Platform Considerations. Strategic warning systems are often required to have coverage that is both global and continual. Consequently, the platforms most often considered for strategic EO/IR warning sensors are satellite platforms in earth orbit. The selection of an appropriate earth orbit to give the required coverage involves many factors. For example, for an earth-looking system in a low earth orbit, the effective search field about the point on the surface of the earth directly beneath the satellite (the satellite *subpoint*) may be quite limited. Furthermore, because of the speed with which the satellite moves with respect to the surface of the earth, this limited field of coverage moves rapidly past areas that must be monitored by the system. Con-

sequently, a fairly sizeable constellation of satellites might be required to provide the necessary spatial and temporal coverage. On the other hand, fewer satellites in high earth orbit might provide the necessary coverage, but because of the longer slant ranges involved, larger sensors might be required to achieve the necessary sensitivity and spatial resolution.

There are numerous other factors that affect the selection of an orbit, including the space environment itself. The lifetime and performance of sensors could be seriously affected by operation in the Van Allen radiation belt. This belt of trapped high-energy charged particles consists of an inner and outer portion. The inner belt begins at an altitude of approximately 250 to 750 miles, depending on latitude, and extends to an altitude of approximately 6200 miles. The outer belt begins at an altitude of approximately 6200 miles and extends to an altitude between 37,000 and 52,000 miles, depending on solar activity.[87]

Satellite Orbits. The spatial coverage provided by space-based strategic sensors is in large part constrained by the orbital parameters of the satellite platform. In general, earth satellites follow an elliptical path as they orbit around the earth. The speed of the satellite subpoint as it passes over a particular point on the surface of the earth depends on the orbital altitude of the platform. Strategic warning sensors might be deployed at orbital altitudes ranging from a few hundred kilometers to 36,000 km or higher. The path taken by the satellite subpoint, the satellite ground track, depends on the parameters necessary to completely define the orbital ellipse and the gravitational law that describes the way in which the satellite moves along its elliptical path.

To completely describe the orbit of an earth satellite, a number of parameters, or orbital elements, must be specified.[88] First, the size and shape of the orbit must be specified. In the case of an elliptical orbit, the parameters that do this are the length of the semimajor axis and the eccentricity of the ellipse. The orientation of the ellipse in inertial space must also be specified. Three parameters are required to do this. To specify the orientation of the orbit, a reference coordinate system must be defined. A commonly used reference system is the so-called geocentric-equatorial coordinate system. The origin of this nonrotating Cartesian coordinate system is at the center of the earth with the Z axis pointing in the direction of the North Pole. The X axis points in the direction of the vernal equinox, the direction from the center of the sun to the center of the earth at the instant of the vernal equinox. In this coordinate system, the orbital inclination angle is specified as the angle between the normal to the orbital plane and the Z axis. The point where the satellite crosses the XY plane heading north is called the *ascending node*, and the angle between the X axis and the line from the origin to ascending node is called the *longitude of the ascending node*. The description of the orientation of the orbit is completed by specifying the argument of *perigee*. This is the angle between the line from the origin to the ascending node and the line from the origin to the point of closest approach to the earth (perigee), measured in the direction of the satellite's motion. The final parameter describing the orbit is the time of perigee passage. This is the time when the satellite was at perigee and specifies the phase of the orbital motion.

The period of the orbit depends only on the size of the semimajor axis of the orbital ellipse and is given by the following expression[88]:

$$T_p = \frac{2\pi}{\sqrt{\mu}} a^{3/2} , \tag{1.86}$$

where T_p is the orbital period, a is the length of the semimajor axis, and μ is the gravitational parameter equal to 3.986×10^5 km^3/s^2. For circular orbits, this expression can be rewritten in terms of the satellite altitude h as follows:

$$T_p = 1.66 \times 10^{-4}(6370 + h)^{3/2} \quad [\text{min}] , \tag{1.87}$$

where h is expressed in kilometers. Also, for circular orbits, the orbital velocity v is

$$v = \left(\frac{\mu}{R_o}\right)^{1/2} , \tag{1.88}$$

where R_o is the radius of the orbit. In terms of the satellite altitude (in kilometers), the orbital velocity is

$$v = \frac{631}{(6370 + h)^{1/2}} \quad [\text{km/s}] . \tag{1.89}$$

The expressions for orbital period and orbital velocity are plotted in Fig. 1.47. From the figure we see that orbital velocity of a low-altitude satellite at about

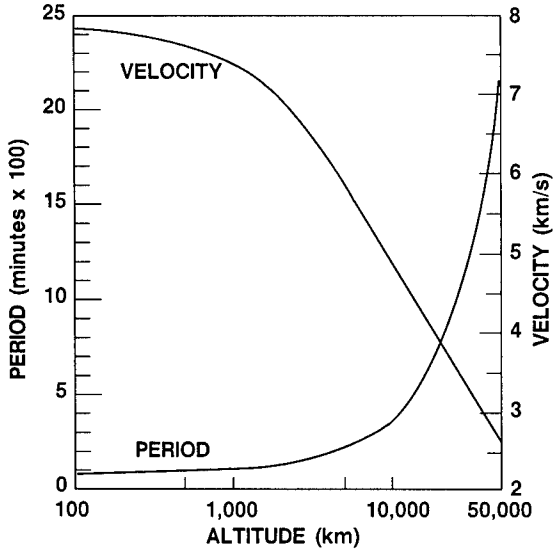

Fig. 1.47 Orbital period and velocity versus orbital altitude (circular orbits).

200 km is approximately 7.8 km/s. Neglecting the rotation of the earth, the speed v_g of the satellite subpoint over the surface of the earth is

$$v_g = \left(\frac{R_e}{R_e + h}\right)v \ , \tag{1.90}$$

where R_e is the radius of the earth. Thus, for low-altitude satellites, where the altitude is much smaller than the radius of the earth, the satellite ground track moves with a speed that is approximately equal to the orbital velocity. Consequently, a low-altitude surveillance satellite passes over the observation area quite rapidly. On the other hand, satellites at higher altitudes dwell over a target area longer. For one particular type of orbit, the *geostationary orbit*, the satellite subpoint remains stationary on the surface of the earth. This occurs when the satellite is in an equatorial orbit at an altitude of 35,800 km. This is a particularly useful orbit for a strategic surveillance sensor system.

1.6.4.2 Sensor Design Options. Early strategic surveillance sensors operating in the infrared part of the spectrum typically achieved the necessary spatial coverage by scanning discrete infrared detectors over the search field of view. Scanning was necessary because the number of resolution cells in the search field usually exceeded the number of discrete IR detectors available to the sensor. A wide variety of scanning techniques have been applied to space-based IR sensors. Often, scanning has been accomplished by relying at least in part on the motion of the platform to provide the necessary scan motion. Spinning the spacecraft to scan the instantaneous field of view of the sensor has been employed on such early systems as the Tiros and Nimbus meteorological satellites. For low-altitude sensors that fly over the surveillance area, the motion of the spacecraft along its flight path might be used to scan a linear array along a swath beneath the spacecraft. This scan mode is called pushbroom scanning.[89] A variation to this type of scanning utilizes an electro-optical scanner to obtain cross-track scanning while the spacecraft motion provides the in-track scanning. An example of a sensor design based on this scanning concept is the thematic mapper sensor.[90]

With the development of IR focal plane array technology, staring IR sensor concepts have become an option for strategic warning systems. In these concepts, the total search field of view is spatially sampled by a large array of detectors. Because the individual detectors do not have to scan the field of view, long integration times can be achieved with the resulting benefit of improved sensor sensitivity. However, the price of this improved sensitivity is a very large number of detectors. For example, as seen from a geostationary orbit, the surface of the earth subtends an angle of 17.4 deg. A detector with a 2- × 2-km footprint at nadir subtends an angle of 56 μrad. For a staring sensor to cover all of the earth's surface visible from geosynchronous orbit would require 23 million detectors.

In addition to providing improved sensitivity, staring sensors are particularly well-suited for moving target indication (MTI) detection applications. In these applications, the sensor attempts to detect a target that is moving over a cluttered but stationary background; e.g., a strategic aircraft flying over varied terrain. With the field of view of a staring sensor held fixed with respect

to the stationary background, clutter can be rejected by taking differences of successive frames of data. For detectors viewing only the background with no target present, the differencing process results in a zero output signal. For those detectors that are traversed by the moving target, the differencing process results in a detectable, nonzero signal.

This type of MTI detection can be readily implemented for earth-looking sensors in geostationary orbit. From such an orbit, a sensor can "stare" at a background that is effectively stationary, with only some residual motion resulting from sensor line-of-sight drift and jitter, and some relative motion of elements within the background (e.g., clouds moving with respect to the surface of the earth). However, implementing this kind of detection scheme for sensors in orbits other than geostationary orbits is more difficult because the ground track of the sensor moves with respect to the surface of the earth. For these situations, the step-stare technique is a candidate for achieving the MTI detection capability of a staring sensor.

In the step-stare approach, the footprint of the sensor detectors is held on a fixed observation point for the period of time required to collect the necessary number of frames of staring data. This is the staring portion of the step-stare cycle. After this data has been collected, the detector footprint is moved, or *stepped* to a new observation region. This is the step portion of the cycle. This step-stare cycle continues as the satellite moves along its orbital path and is analogous to the vertical/horizontal (V/H) compensation technique used in airborne photoreconnaissance systems for platform motion compensation.

There are a number of practical difficulties associated with the effective implementation of the step-stare concept for a space-based strategic warning system. For example, for an instantaneous field of view of a reasonable size, different points on the surface of the earth within the field of view move with different velocities with respect to the satellite, making it difficult to stare at the whole background contained in the instantaneous field of view. Furthermore, because background elements such as clouds and terrain features are at different altitudes, they move with different angular velocities as seen from the moving sensor platform. As a consequence, the platform motion induces apparent motion in the background that degrades the performance of MTI detection concepts.

1.6.5 Strategic Warning Sensor Design Example

A figure of merit that is commonly used to characterize the sensitivity of a strategic missile warning system is the noise equivalent target (NET). NET is defined as the apparent in-band target intensity that produces an SNR of unity at the output of the sensor detection circuits. In terms of slant range from the sensor to the target R, the collecting area of the sensor optics A_c, the effective transmission of the optics τ_o, and the noise equivalent power (NEP) of the detector, the NET is given by the following expression:

$$\text{NET} = \frac{R^2 \text{NEP}}{A_c \tau_o} \,. \tag{1.91}$$

This expression can be rewritten as

$$\text{NET} = \frac{R^2(A_d \Delta f)^{1/2}}{D^* A_c \tau_o} , \tag{1.92}$$

where NEP has been written in terms of the detector D^*, the detector area A_d, and the noise equivalent bandwidth of the processing filter Δf.

For a scanning sensor, the noise equivalent bandwidth can be related to the detector dwell time τ_d, the time it takes for the detector footprint to scan across a fixed point in the search volume. Assuming that the processing filter is a matched filter for a rectangular signal pulse of duration τ_d, the noise equivalent bandwidth is

$$\Delta f = \frac{1}{2\tau_d} . \tag{1.93}$$

The detector dwell time is determined by the size of the surveillance volume, the amount of time available for scanning the complete surveillance volume, the size of the detector field of view, and the number of detectors in the sensor focal plane. Specifically, the detector dwell time is given by the following expression:

$$\tau_d = \frac{\eta_s T_f N_d \Omega}{\Omega_s} , \tag{1.94}$$

where T_f is the time available to completely scan the surveillance volume, Ω_s is the solid angle subtended by the search volume, Ω is the solid angle subtended by the detector field of view, N_d is the number of detectors, and η_s is a scan efficiency factor.

The detector field of view can be written in terms of the size of the detector footprint at the range to the target. Assuming square detectors, we have

$$\Omega = (L_{\text{fp}}/R)^2 , \tag{1.95}$$

where L_{fp} is the length of the detector footprint. We also have

$$\Omega = \frac{A_d}{f^2} , \tag{1.96}$$

where f is the effective focal length of the system.

Substituting the expressions for the noise equivalent bandwidth, the detector dwell time, and the detector field of view into the expression for NET, we find

$$\text{NET} = \frac{R(F\#)^2 L_{\text{fp}}}{\tau_o D^* \pi} \left(\frac{8\Omega_s}{\eta_s T_f N_d A_d} \right)^{1/2} , \tag{1.97}$$

where the area of the collecting aperture has been taken to be circular with a diameter D and $F\#$ is the focal ratio f/D.

As a specific example, we consider a missile surveillance sensor located in a geosynchronous orbit for the purpose of detecting ICBM and SLBM launches. The nominal slant range from the sensor to the target is 40,000 km. We take the size of the detector footprint at nadir to be 2 km. The surveillance volume is 0.008 sr, the solid angle subtended by the earth as seen from synchronous altitude. A total of 5000 detectors are assumed. Each detector is 0.01×0.01 cm and has a D^* of 5×10^{11} W^{-1} cm Hz$^{1/2}$. The optical system is an $f/4$ system and has effective transmission of 0.5. This corresponds to an aperture diameter of half a meter. Fifteen seconds are allocated for scanning the search volume with a scan efficiency of 0.8. Substituting these parameter values into Eq. (1.97), the expression for NET, we find that this sensor has an NET of 1.6 kW/sr.

1.6.6 Testing

The testing of strategic warning systems poses problems that can be quite different from those encountered in the testing of tactical warning systems. These differences relate primarily to the fact that strategic sensors are usually larger and more sensitive than tactical sensors and must typically operate in a space environment.

Because of the long range at which strategic sensors must operate and because of their large search fields, strategic sensors often have large optics and many detectors. Mirrors of diameters equal to a meter, or more, and infrared detector arrays with elements numbering in the hundreds of thousands must be tested. Special facilities are usually required to test these types of components and systems.[91] At the component level, components must be tested for their ability to operate in the vacuum of space under conditions of weightlessness and exposure to high-energy radiation and solar loading. Testing of these sensors at the system level requires test facilities that include large vacuum chambers, accurately controlled infrared sources, and extensive signal and data processing support.

Unlike tactical warning systems, EO/IR strategic warning sensors are produced in limited numbers. A complete constellation of strategic warning sensors might consist of only a few satellites. Typically, each sensor is developed and placed in orbit at great expense. Often, these sensors are placed in orbits such as geosynchronous orbit where they are inaccessible for repair. For these sensors, an on-orbit failure represents a great monetary loss as well as a possibly significant and lengthy reduction in strategic warning capability. For these reasons, ground testing is an extremely important aspect of strategic warning sensor development.

1.7 LASER WARNING SYSTEMS

1.7.1 Overview of a Laser Intercept Event

Figure 1.48 illustrates a typical laser intercept event as defined in Sec. 1.2.2.3. Radiation from a variety of laser and nonlaser sources impinge on the laser warning receiver. There are four distinctly different laser intercept paths potentially associated with the threat laser. These include

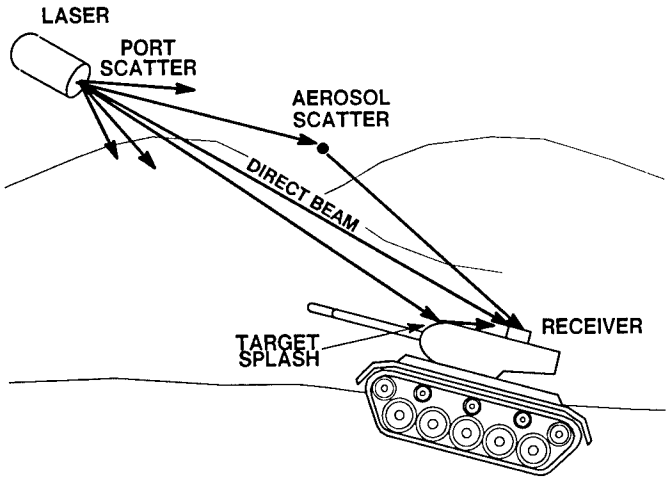

Fig. 1.48 Laser warning receiver—incident energy.

- the direct beam—the most intense source and the best temporal replica of the initial laser pulse
- the splash of the laser on an adjacent portion of the target vehicle (or adjacent objects)—sometimes the largest available intercept as the laser beam size is often smaller than the vehicle and it may not directly strike the receiver
- scatter of the laser off the adjacent atmosphere—resulting in a weak, temporally stretched version of the laser pulse
- scatter arising from internal coatings and dirt at the laser port—a weak, wide-angle beam with a few high-intensity angular spikes.

Note that only two of these four intercept paths (i.e., the direct beam and the port scatter) reach the receiver from the angular location of the target. The source of the target splash and atmosphere scatter have very little relationship to the location of the threat laser. This may have major implications for direction finding (DF) systems.

The aerosol-scatter intercept plays an important role in standoff ESM applications (see Sec. 1.2.2.3).

In addition to the laser, the receiver is exposed to high-intensity solar radiation; either directly from the sun in the field of view (FOV) (most LWRs are wide FOV and the sun may always be in the FOV) and/or from cloud, aerosol, and terrain scatter.

1.7.2 System Overview

LWR development is currently in a dynamic state.[92,93] Figure 1.49 presents a list of design decisions that must be addressed explicitly, or implicitly, in the development or selection of a LWR. This decision-tree is intended to (1) tie together the individual parameter discussions herein, (2) serve as an ordered list for the designer/purchaser of an LWR as they contemplate the smorgasbord

- SPECTRAL BAND
  - VISIBLE/SILICON BAND
  - EYE-SAFE
  - IRCM THREATS
  - CO_2/THERMAL BAND
- SCENARIO
  - RANGE
  - ANGULAR COVERAGE
  - PLATFORM DYNAMICS
  - DIRECT INCIDENCE VS. SCATTER/SPLASH
- PARAMETRIC ACCURACY / PRECISION
  - BINNING VS. CONTINUOUS
  - SOURCE LOCALIZATION ACCURACY / PRECISION
    - DIRECT INCIDENCE
      - DEGREES
      - MILLIRADIANS
      - DYNAMICS
    - SCATTER/SPLASH INCIDENCE
  - SPECTRAL ACCURACY / PRECISION
    - TARGET ID
    - FALSE ALARM REJECTION
  - AMPLITUDE ACCURACY / PRECISION
    - ABSOLUTE
    - RELATIVE
    - "GRACEFUL" DEGRADATION
  - TEMPORAL ACCURACY / PRECISION
    - SUNGLINT REJECTION
    - BINS
    - PRECISE
      - PULSE DURATION
      - PULSE INTERVAL

Fig. 1.49 Laser warning receiver design issues.

of subsystems from which an LWR is assembled, and (3) provide an outline for the system design process. Subsequent paragraphs pose the design/performance questions that must be addressed for the individual items listed in the figure.

1.7.2.1 Spectral Band and Target Lasers. Spectral band coverage tends to fall into four ranges: the visible/near-IR silicon band, which includes the bulk of currently deployed threat lasers; the extension of this band into the eyesafe 1- to 3-μm regime; the 8- to 12-μm band, primarily for the CO_2 laser near 10.6 μm; and the 3- to 5-μm band to cover potential missile and IRSTS countermeasure lasers.

Should the system address low-coherence, low-power, semiconductor lasers? Should it intercept, and analyze, nonlaser sources such as arc lamps and photoilluminators, either for inherent data on such systems, or to provide unambiguous identification, and, therefore, rejection of, these nonlasers?

1.7.2.2 Scenario. Should the system be configured for only direct intercept, or should it also receive signals scattered from adjacent portions of the platform, or from the adjacent air? If so, does it need direction of arrival (DOA) capability; what does DOA mean in these cases? Will the DOA, spectral, and/or coherence subsystems "work" with splash and scatter sources? Should the system inter-

cept splash and/or scatter when the threat laser is attacking an adjacent platform, or just when it is attacking the protected platform?

Both sensitivity and angular coverage are driven by scenario details that include platform dynamics, terrain, altitude, and range variations as well as the obvious parameter of range to the target.

1.7.2.3 Parametric Measurement. What precision and accuracy is required for the measured laser parameters? All the parametric specifications should be considered as a group rather than individually. There is no need to measure a parameter such as pulse duration or wavelength to a high accuracy, or at all, if other easier to measure parameters allow the system to identify the threat sufficiently to enable successful countermeasure/avoidance.

In all of these measurements, it may be possible that general *binning* of parameters, as opposed to high-precision parametric characterization, provides all the data necessary to deduce the threat nature and initiate the counter-response.

1.7.2.4 Source Localization Measurement. Location may be an ambiguous parameter for LWRs. Typically, laser source location, rather than the site of the scattering or reflecting object/aerosol is the desired parameter. It may be necessary to determine whether the source is a direct hit, or scatter from an adjacent tree or cloud, so that the platform does not turn away from the real threat and counterattack the tree! What accuracy is required for location data? The airborne RWR community has fielded many systems with several degrees of direction of arrival angular precision; why must the LWR be better? Conversely, a particular application may require high accuracy to initiate counter fire or some other directive countermeasure.

1.7.2.5 Spectral Measurement. Is spectral data important to target identification, or is it sufficient to know that the source is coherent and to assess its function by its temporal characteristics? Is the spectral difference between Nd:YAG and Nd:glass truly important, or are their different temporal characteristics sufficient to flag the YAG as a designator and the glass as a range-finder, or countermeasure? Possibly spectral resolution is not needed at all, just solar rejection, which can be provided by rise time or coherence measurements.

1.7.2.6 Amplitude Measurement. In the ESM application of the Fig. 1.3 system, sensitivity is a dominant requirement, whereas for the LWR self-protection application, the sensitivity is more readily obtained and a major amplitude consideration for an LWR is to avoid direct-incidence detector destruction. The next concern is to ensure that a saturating signal results in a "graceful" measurement degradation. It can be catastrophic if the pulse stretching often associated with laser saturation causes the system to classify a nearby, threatening laser as merely "sun glint." (Electronic circuits such as logarithmic amplifiers can provide a wide dynamic range for amplitude measurement.) Is absolute amplitude determination of military value? Why? What should be concluded from such data? Possibly only relative amplitude between two spectral, angle, or coherence measuring channels is required. If so, it is necessary to account for the impact of scintillation on the measurements.

1.7.2.7 Temporal Measurement. Coarse temporal measurements can often be used to bin the different categories of laser threats; i.e., rangefinder, designator, and so on. However, precise temporal measurements may be necessary to establish the pulse repetition frequency (PRF) or the pulse interval modulation (PIM) code for designator countermeasures. Precise pulse duration and pulse shape data is seldom required in laser warning situations, unless rise-time measurements are used for threat/sun glint discrimination.

One troublesome problem with pulse duration measurements is establishing the portion of the pulse on which the measurement is to be made. Should it be the 3-dB point? For single, several-nanosecond-long pulses, this is an important issue. How is the 3-dB point to be determined; sample and hold the entire pulse? (To do this accurately may require more than a 100-MHz bandwidth.) Can it be stored in an optical fiber, or digital rf memory (DRFM)-type circuit? Possibly a simple hard-limiter with threshold-crossing logic is adequate even if there is some ambiguity about the exact measurement point? Even if the single pulse constraint is relaxed and pulse duration is only required for trains of pulses, will there be a problem establishing a meaningful 3-dB point, in the presence of signal scintillation?

1.7.2.8 Noise, False Alarms, and False Signals. Probability of detection, particularly for the direct incidence case, is often easy to come by; but false alarms are a common problem. The noise bandwidth must be kept low and the detection thresholds high to avoid shot noise and electronic noise false alarms. When noise external to the detector becomes the limiting parameter, as is often the case because of Johnson noise in the load resistor, or preamplifier noise, postdetection gain within the detector can be used to override it. In the silicon band, avalanche diodes with a postdetection internal gain of 10 to 100 may be used for this purpose.

When white noise false alarms are within specifications, sun glint, EMI, and even cosmic rays may become a significant source of false "signals." Historically, it has always been one of these three that has degraded otherwise successful LWR development efforts. Sun glint can be attacked by spectral filtering as well as by coherence and temporal discrimination. In addition to the usual EMI suppression techniques, the LWR may require an optically blind, but otherwise identical, coincidence channel to reject spurious rf signals. Finally, cosmic rays (arriving at a rate on the order of a few per minute per square meter) have reportedly been to blame for the inability of such systems to achieve the requisite one per hour, per day, or per mission false alarm rates, when the system has single pulse requirements placed on it. In this case, correlation of adjacent, identical, optical channels may be required.

1.7.3 Radiometric Analysis

1.7.3.1 Peak Amplitude—Sample Problem. Figure 1.50 shows the signal irradiance E_{inc} in watts per square centimeter, for the directly incident laser beam on the LWR in the self-protection scenario outlined in Sec. 1.2.2.3. The six curves present the incident irradiance as a function of distance from the 0.150-J, 2.5×10^{-4} rad, laser source for different visibility ranges; ∞, 23, 10, 6, 3, and 2 km, respectively. The system parameters involved are discussed in

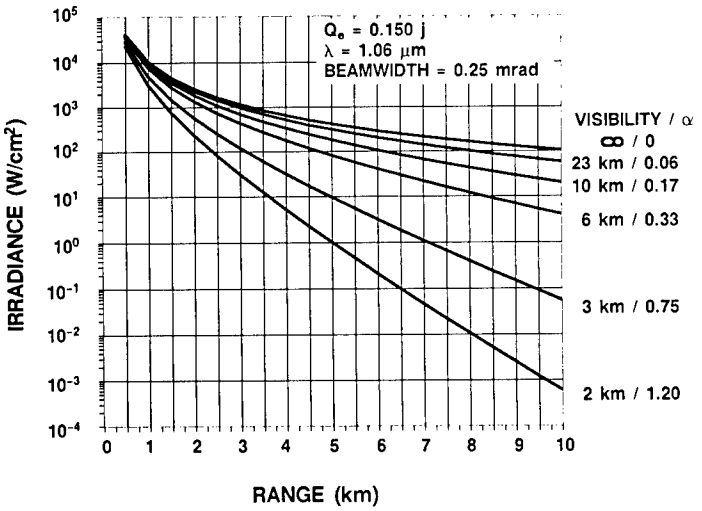

Fig. 1.50 Direct incidence signal intensity for sample scenario with visibility as a parameter.

Secs. 1.3.1.3 and 1.3.2.4. The curves of Fig. 1.50 are plotted from the following equation:

$$E_{\text{inc}} \approx 10^{-10} \frac{4}{\pi} \frac{Q_e}{\Delta t \theta^2} \frac{\exp(-\alpha R)}{R^2} \quad [\text{W/cm}^2] \ , \tag{1.98}$$

where Q_e is the initial laser energy in joules, Δt is the pulse duration in seconds, θ is the angular beamwidth in radians; R is the range in kilometers; and α is the attenuation coefficient in inverse kilometers. This expression assumes a uniform circular beam and a rectangular pulse shape.

These curves illustrate two issues: (1) for typical tactical ranges, directly incident irradiance is measured in watts per square centimeter to kilowatts per square centimeter; therefore detection is relatively easy, whereas saturation and burnout are the problems, and (2) atmospheric attenuation (i.e., weather) is the dominant factor at long ranges (as in air force and navy scenarios), whereas it makes less difference at a few kilometers (as in army scenarios).

Figure 1.51 shows the signal irradiance, in watts per square centimeters, on a receiver at distances of 0.5 and 4 m, respectively, from an illuminated spot, a situation that might occur when the incident laser beam strikes the target but is not incident directly on the LWR. The receiver is presumed to be pointed directly toward the illuminated spot, and the reflecting surface is assumed to be a Lambertian reflector (see Sec. 1.3.2.4). The three parametric curves for each offset show the signal level on the receiver for visibility conditions of 23-, 6-, and 3-km visibility ranges, respectively, with the receiver at an angle of 60 deg off the perpendicular to the surface. These curves have been computed with the following equation:

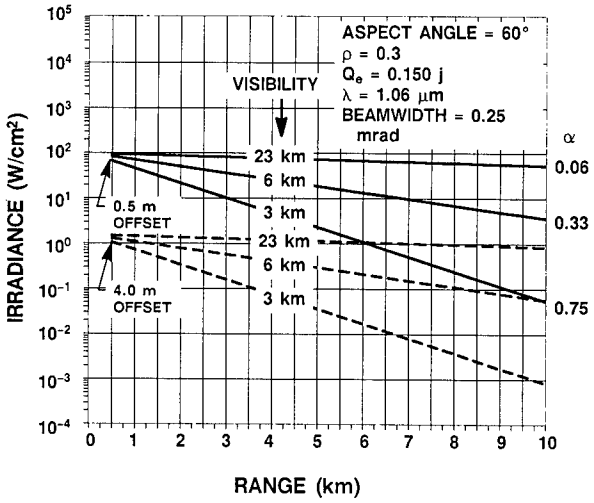

Fig. 1.51 Target splash signal level for sample scenario with visibility and receiver/spot offset as parameters.

$$E_{\text{inc}} \approx \frac{10^{-4}}{\pi} \rho \cos\beta \frac{Q_e}{\Delta t} \frac{\exp(-\alpha R)}{r^2} \quad [\text{W/cm}^2] \ , \tag{1.99}$$

where Q_e is the laser energy in joules, Δt is the pulse duration in seconds, R is the laser-to-target range in kilometers, β is the angle of the receiver relative to the perpendicular to the surface, and r is the offset of the receiver from the illuminated spot in meters. This expression assumes a rectangular laser pulse and that the laser spot on the target appears as a point source to the receiver (implying that the subtended spot is smaller than the receiver spatial resolution and all scattering centers on the target are viewed with the same detection efficiency). In addition, the Lambertian scattering assumption, while reasonably illustrative, is by no means adequate for an accurate signal prediction, and the actual bidirectional reflectance distribution function (BRDF) of the specific target of interest must be considered (Sec. 1.3.2.4).

Note that for the stated conditions the intensity of the target splash incident on the detector is of the same order as that of the direct beam. This conclusion is somewhat counterintuitive, as one might expect the target-scattered signal to be substantially weaker than that which was directly incident on the detector. This rough equivalence is a consequence of the fact that, the applicable *spreading loss* in the case of direct incidence is determined by the large target/receiver separation R, and in the splash case by the much shorter off-set range r. This tends to compensate for the wide angle of the Lambertian scattering. The parametric relation between the direct beam and the target splash irradiances is given by the expression

$$\frac{E_{\text{direct}}}{E_{\text{splash}}} \approx \frac{4 \times 10^{-6}}{\rho \cos\beta\theta^2} \frac{r^2}{R^2} \ , \tag{1.100}$$

where r is the offset in meters and R is the laser to LWR distance in kilometers. For the present 2-km range and 0.5-m offset, this ratio is equal to 26.7, and at 10 km the ratio is 1.07. Hence, the laser scatter from the LWR platform, and/or adjacent objects, is a potentially significant design parameter, which might be exploited to increase the probability of detection or, conversely, might give rise to false direction indications in some configurations.

For laser/target/receiver geometries, wherein the laser spot is outside the receiver FOV and/or the angle between the receiver and the normal to the scattering surface approaches 90 deg, the scattered signal incident on the LWR approaches zero. For that reason the system designer exploiting this phenomenon might consider a separate channel/detector pointed toward the platform itself.

Wide-field-of-view, wideband, laser warning receivers can be readily constructed with a sensitivity in the 1 mW/cm^2 range (for 10^{-5} W/cm^2 sensitivity, or better, substantial performance trade-offs are required). Thus, detection of target splash by a receiver located on the same target but outside the direct beam is quite practical in many situations of tactical interest. In particular, note that even for the 4-m offset the detection range of a 10-mW/cm^2 receiver would exceed the visibility range; thereby enabling warning against most optically targeted weapons involving lasers of this size.

The incident signal level resulting from atmospheric scattering requires a more complex treatment because total irradiance at the receiver is a function of the angular scattering function of the aerosols as well as the attenuation. The angular scattering pattern is a function of the aerosol constituents, their density, and their size distribution. Section 1.3.2.4 addresses the issues involved.

The irradiance incident on an LWR located off the axis of the laser beam results from several sources as discussed in Sec. 1.3. The relative contributions of port scatter and aerosol scatter are a function of the specific threat, its output optics, and the prevailing atmospheric conditions. Figure 1.52 indicates[94] the relative contributions for arguably "typical" laser warning threats/conditions. Note that for the typical visible/near-IR-band situation, the aerosol scatter is the dominant contributor for most near-axis intercepts.

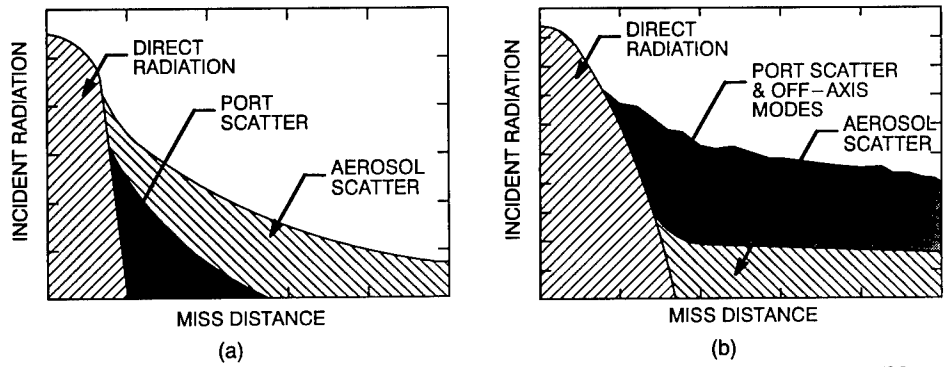

Fig. 1.52 Components of off-axis incident irradiance for typical laser threats: (a) visible/near-IR bands and (b) far-IR bands.

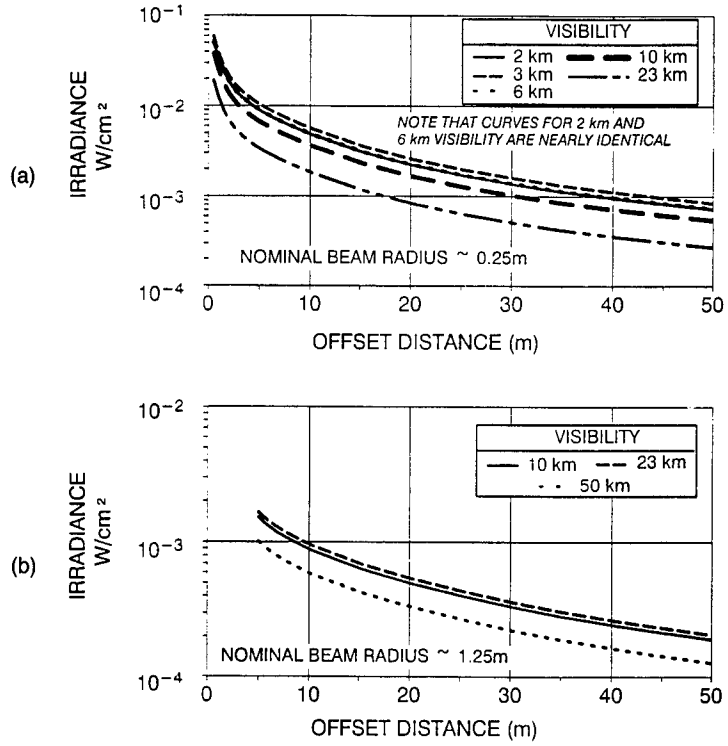

Fig. 1.53 Near-axis scatter signal levels for various visibilities and ranges: (a) 2-km range and (b) 10-km range.

For aerosol scattering, visibility alone is no longer an adequate atmospheric descriptor (as it is for the atmospheric attenuation incorporated within the prior direct incidence and target splash calculations), and the calculations are cast in terms of various standardized atmospheric conditions. Such calculations are based on the theoretical literature[95,96] and reflected in various laser propagation codes.[97–99] Unfortunately, these codes, which are available to and used throughout the electro-optics community, do not at this time incorporate the necessary off-axis scatter algorithms. Thus, each investigator/analyst has his own variant of the standard theory and codes.

Figure 1.53 presents[100] an array of accurately calculated atmospheric-scatter plots for a variety of laser intercept scenarios and environmental conditions. The atmospheric model adopted for these calculations is mid-latitude winter with an aerosol model corresponding to the Fenn-Shettle rural (75% relative humidity) conditions.[101] The cases selected correspond to the 2-km sample scenario and the longer range, 10-km variant of it and include a range of visibility conditions corresponding to those used for the direct incidence and target splash calculations illustrated. For low-visibility conditions, it may be necessary to consider multiple scatter photon paths as well as the simple, single-scatter situation discussed in Sec. 1.3. The model used to generate these plots includes the effect of multiple scatter, which was found to be negligible for the specific cases plotted.

From the calculations and data presented it can be concluded that a laser warning receiver, with a sensitivity of the order of milliwatts per square centimeter can detect lasers incident on or passing near its platform for the tactical situation represented by the sample problem. Note also that there is a stringent dynamic range specification since the direct beam is 50-dB optical (10 log, optical power) or 100-dB electrical (20 log, output current) above the scatter signal levels and it is at absolute levels approaching detector and preamplifier damage, or nonlinearity, thresholds.

1.7.3.2 Duration. Figure 1.54 shows a laser in the upper left corner transmitting over a 2-km path corresponding to the example scenario. Three detectors are represented in this figure at three different aspects with respect to the beam.

The receiver at the end of the laser beam, corresponding to the self-protection scenario, is illuminated directly by the laser. Its output pulse occurs about 6.7 μs after the laser fires, its temporal shape is that of the laser pulse, of the order of 30 ns, and its peak intensity is shown in Fig. 1.50.

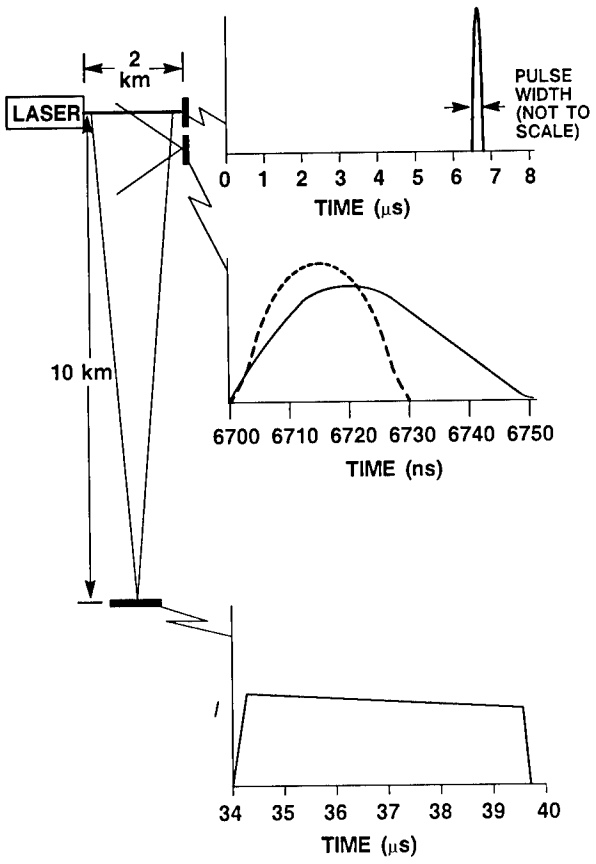

Fig. 1.54 Atmospheric scatter—received pulse duration as a function of receiver location and field of view.

Next to that receiver we have positioned another one, just outside the laser beam and pointed directly at the source. The pulse at this receiver results from atmospheric and port scatter. Only the atmospheric scatter is represented in the output waveform shown here. Air molecules and aerosols at the aperture of the laser scatter light directly to the detector. The path length for this scattered light is just the radial distance 2 km, and this scatter forms the leading edge of the received pulse. Later, molecules farther away from the laser are illuminated, and then they side-scatter light into the receiver. The path length for this scattered light is slightly longer so it arrives later. (The original laser pulse is shown dotted in the figure.) This receiver is also at a larger angle to the beam and the scattering function is less; thus, the intensity is lower. These phenomena cause the slightly stretched pulse shown in the figure.

The third receiver illustrated is orthogonal to the laser beam and corresponds to the ESM application. The laser receiver is assumed to have a 10 deg field of view and is located 10 km from the laser beam. As a result it views a 1.74-km portion of the laser path. The laser pulse takes 5.8 μs to traverse this field, side-scattering at a low intensity, as it goes across. The received pulse shape has a rise and fall time determined by the laser output rise and fall times, a duration nominally equal to the transit time, and an intrapulse temporal drop-off because of the attenuation experienced by the pulse as it transits the field.

This variation of pulse shape as a function of receiver FOV and beam aspect is an important factor in system design when it is necessary for the system to detect atmospheric scatter. Note that the matched filter for the wide, low-intensity side-scatter would have a narrower electronic bandwidth than one designed for the shorter direct beam by approximately the ratio of their durations, or about 5.2×10^{-3}, and that this would correspond to a sensitivity improvement proportional to the inverse of its square root, or about 13.9. This potential for reducing the white noise associated with the stretched pulse partially compensates for the intensity reduction resulting from the angular scattering pattern in this direction.

1.7.3.3 Signal Scintillation. The signal level incident on the laser warning receiver is a function of atmospheric scintillation effects and varies in time in a random fashion. The magnitude of the variation is a function of the atmospheric conditions and of the aperture area of the receiver as discussed in Secs. 1.3.2.4 and 1.4.4.3. Because the typical laser warning receiver has a small effective aperture, little aperture averaging takes place, and the signal scintillation is often that of a point detector. As a result, the incident signal level must be treated statistically, and the postdetection processing must allow for the signal fluctuations involved. From the example computed in Sec. 1.4.4.3 (using the saturating level of the signal variance), it was determined that the receiver would need more sensitivity (i.e., a scintillation gain margin) by about 10 dB (optical) to detect reliably a scintillating pulse than it would need to detect the same pulse in the absence of scintillation.

It turns out that this signal scintillation is less of a concern in LWR design, at least with respect to the system sensitivity requirements, than it is in many other laser applications. This can be better appreciated by considering the

typical short-range/near-ground scenarios and long-range/air-ground scenarios separately.

Note from Fig. 1.50 that direct incidence detection at the shorter ranges requires a sensitivity only of the order of 1 W/cm^2 and that the more stringent sensitivity requirement, say 10^{-3} W/cm^2, is driven by the necessity to achieve effective near-axis scatter intercepts. Moreover, if the origin of the atmospherically scattered (and target splash) illumination is considered, one finds that the incident signal consists of contributions from many independent scattering centers (aerosols) distributed over many turbulent atmospheric *cells*. As a result, it can be shown that there is very little scintillation associated with the scattered signal. Hence, in a receiver configured for such a scenario, the design sensitivity is driven by the lower level off-axis scatter requirement. This off-axis signal does not have any appreciable scintillation variation and it is at least a few orders of magnitude lower than the scintillating, directly incident signal. Hence, there is virtually always an inherent gain margin sufficient to ensure reliable detection of the directly incident scintillating signal. (Scintillation-related saturation may be a design problem.)

In the longer range ground-to-air situation, as the range increases, the physical dimensions of the laser beam on the target also increase, whereas the aerosol scatter decreases; hence, the probability that the detection is a result of direct incidence increases. In that case, the scintillation margin becomes more important, but much of the path is in higher altitude less-turbulent air and the magnitude of the direct beam scintillation is substantially less.

Although the signal amplitude variations (scintillation) caused by atmospheric turbulence have less impact on the LWR sensitivity requirements than might be expected, the mottled spatial pattern imparted to the beam by the turbulent atmosphere has significant practical implications for the optical configurations used for coherence, spectral, and directional measurements as discussed in Sec. 1.7.4.1.

1.7.3.4 Noise Levels

Solar Shot Noise in Visible-Band Systems. A common "worst case" for solar irradiation on a laser warning receiver is for the sun to be in the field of view. The average current from this solar energy is given by the expression

$$I_{\text{solar}} = R_\lambda E_\lambda \Delta\lambda A_r \tau \ , \tag{1.101}$$

where R_λ is the detector responsivity in amperes per watt at the wavelength of interest, E_λ is the solar spectral irradiance in watts per square meter per micrometer at the wavelength of interest, $\Delta\lambda$ is the spectral bandwidth in micrometers, A_r is the effective collection area of the receiver in square meters, and τ is transmittance of the optics. The statistical variation of this average current gives rise to the solar shot noise according to the relation

$$I_{\text{shot}} = (2eI_{\text{solar}}\Delta f)^{1/2} \ , \tag{1.102}$$

where e is the charge of an electron, 1.6×10^{-19} C, and Δf is the electronic noise bandwidth.

It is convenient at this point to introduce the concept of system optical gain G, which is the ratio of the irradiance incident on the collection aperture to the irradiance within the focal spot at the detector. For many systems, this is equal to the ratio of receiver to detector areas, A_R/A_d. For most optical systems, G has a large value; 10^6 is not uncommon. However, for typical wide-FOV laser warning receivers, G is often of the order of unity as a consequence of the throughput constraints, and the receiver effective collection area is often nominally equal to the detector area.

Combining these expressions, we can express the solar shot noise current by the following equation:

$$I_{\text{solar shot}} = (2e\tau GR_\lambda)^{1/2}(E_\lambda \Delta\lambda)^{1/2}(A_d \Delta f)^{1/2} \ . \tag{1.103}$$

For the situation where the responsivity is 0.65 A/W (typical for silicon detectors at near-IR wavelengths), the optical gain-transmittance product is 1; the electronic system is designed as a matched filter for the laser pulse with $\Delta f = 1/(2\Delta t)$, and A_d is expressed in square centimeters, Eq. (1.103) reduces to

$$I_{\text{solar shot}} = 3.23 \times 10^{-12}(E_\lambda \Delta\lambda)^{1/2}\left(\frac{A_d}{\Delta t}\right)^{1/2} \quad [\text{A}] \ . \tag{1.104}$$

Assuming a pulse duration of 30 ns and a detector area of 2.5×10^{-3} cm^2 (i.e., 0.5 mm linear dimension), for the sample scenario and noting that 1200 W m^{-2} μm^{-1} is a reasonable average value for E_λ over the visible band and that 400 W m^{-2} μm^{-1} is reasonable in the vicinity of 0.9050 μm, one obtains the shot noise current indicated in Table 1.19.

The actual spectral bandwidth that would be used in such a receiver would be a function of a number of design variables that are discussed in Sec. 1.7.4. Various options include wideband, 0.4- to 1.1-μm single channels (which could have 1.5 times as much noise as the wide visible wavelength band specified in the previous example) and arrays of spectrally narrow filters (as represented by the narrow-band example in the table).

For the situation where the sun is not in the field of view and the receiver is viewing solar-illuminated terrain, or sky, the incident irradiance is reduced by the sky/terrain reflectivity, which is typically between 0.5 to 0.01, and the reflecting terrain/sky should be treated as an area source.

Johnson Noise. Johnson noise results from the thermal excitation of the electrons in any resistor. The noise level in the current domain is specified by the equation

$$I_{\text{Johnson noise}} = (4kT)^{1/2}\left(\frac{\Delta f}{R_l}\right)^{1/2} \ , \tag{1.105}$$

where k is Boltzmann's constant, 1.38×10^{-23} J/K; T is the temperature in degrees Kelvin; R_l is the load resistance in ohms; and Δf is the electronic bandwidth in hertz.

Table 1.19 Noise Calculations for Sample Scenario

Noise	Assumed Parameters	Parameter Value	Noise Current (amperes)
Solar Shot (wide band, visible)	Optical Gain	1	
	Detector Area	0.0025 cm^2	
	Responsivity	0.65 A/W	
	Solar Irradiance, 0.45 to 0.7 μm	1200 W m^{-2} μm^{-1}	
	Optical Bandwidth	0.25 μm	
	Electronic Bandwidth	16.67 MHz	
	Pulse Width	30 x 10^9 s	
			1.61 x 10^{-8}
Solar Shot (narrow-band, near-IR)	Optical Gain	1	
	Detector Area	0.0025 cm^2	
	Responsivity	0.65 A/W	
	Solar Irradiance, 0.9050 μm	400 W m^{-2} μm^{-1}	
	Optical Bandwidth	100 Å (0.01 μm)	
	Electronic Bandwidth	16.67 MHz	
	Pulse Width	30 x 10^9 s	
			1.86 x 10^{-9}
Johnson	Temperature	300 K	
	Electronic Bandwidth	16.67 MHz	
	Pulse Width	30 x 10^9 s	
	Resistance	1000 Ω	
			1.66 x 10^{-8}
Detector	Detector Area	0.0025 cm^2	
	Responsivity	0.65 A/W	
	Electronic Bandwidth	16.67 MHz	
	Pulse Width	30 x 10^9 s	
	Detector D^*	3 x 10^{12} W^{-1} cm $Hz^{1/2}$	4.42 x 10^{-11}

Because typical laser warning receivers are electronically wideband, and the internal resistance of the detectors may, consequently, be low (of the order of 50 to 5000 Ω for silicon *p-i-n* detectors), Johnson noise can be a limiting system parameter. Assuming a room temperature silicon *p-i-n* detector with an internal resistance of 2000 Ω configured for maximum detection efficiency (matched filter with the load resistor equal to the internal detector impedance), this expression can be approximated by

$$I_{\text{Johnson noise}} = 2.88 \times 10^{-12}\left(\frac{1}{\Delta t}\right)^{1/2} \quad [\text{A}] \ . \tag{1.106}$$

Note that the detector internal resistance and the matched load resistor connected in parallel to it would correspond to an effective resistance of 1000 Ω in the configuration described.

The data in Table 1.19 indicate that the Johnson noise is of the order of the wideband solar shot noise and that it is significantly larger than the narrow-band solar shot noise for the conditions considered. Typically, the designer of such a narrow-band LWR would be inclined to consider an avalanche-type detector to obtain postdetection signal gain prior to the load resistor Johnson noise, thus approaching the more sensitive background-limited situation. Conversely, for the wideband case, the avalanche detector would not provide a significant sensitivity advantage because the system is initially background limited.

Internal Detector Noise in Visible-Band Systems. For visual band LWR applications, silicon detectors, of either the *p-i-n* or avalanche variety, are prime candidates. The detector noise is characterized by the detector D^*. The resultant detector noise current is given by the expression

$$I_{\text{detector noise}} = \frac{R_\lambda}{D^*}(A_d \Delta f)^{1/2} \ , \tag{1.107}$$

where R_λ is the detector responsivity, D^* is the specific detectivity in cm $\text{Hz}^{1/2}\ \text{W}^{-1}$, A_d is the detector area in square centimeters, and Δf is the electronic noise bandwidth in hertz.

Specific detectivity D^* is a term that includes the noise arising from all sources of incident background irradiance as well as the Johnson noise effect discussed in the preceding paragraphs (and Sec. 1.5.2.2). However, typical specification sheet values are often stated under conditions of negligible Johnson noise contributions and minimal background illumination. Thus, such numbers tend to characterize only the background radiation noise arising from the detector thermal background (D^*_{BLIP}, see Sec. 1.5.2.2) and any excess internal noises.

For the typical silicon *p-i-n* detector the "spec-sheet" D^* is of the order of 3×10^{12} cm $\text{Hz}^{1/2}\ \text{W}^{-1}$, the responsivity is about 0.65 A/W, and by assuming the circuit is a matched filter for the incident pulse one obtains

$$I_{\text{detector noise}} = 1.53 \times 10^{-13}\left(\frac{A_d}{\Delta t}\right)^{1/2} \quad [\text{A}] \ , \tag{1.108}$$

where A_d is in square centimeters and Δt is the pulse duration in seconds.

As can be seen from the resultant noise levels shown in Table 1.19, the internal noise is substantially smaller than the solar shot and Johnson noise terms and is seldom the limiting noise for visible, or near-visible, band laser warning receivers.

For avalanche-type detectors additional noise spikes are sometimes associated with the avalanche process. When such detectors are used to obtain the postdetection gain necessary to raise the operating regime above the load resistor Johnson noise or other preamplifier noise, these spikes may become the limiting system noise.

Noise in Mid- and Far-IR Systems. Laser warning receivers operating at wavelengths beyond 2.5 μm, or so, tend to be limited by the statistical fluc-

tuations in the thermal background and in the detector itself in the same way as missile warning receivers operating in these regions. Thus, most such detectors are cooled and employ internal cold filters and/or cold shields identical with those used in other, more traditional, infrared detection systems. The lasers in this spectral regime may also be of the short-pulse, or high-modulation-rate, variety so that Johnson noise may become a concern in this spectral range as it is in the visible.

1.7.3.5 False Alarm and Detection Probabilities

False Alarm Rate. The false alarm rate, expressed in terms of false alarms per second, is given by Eq. (1.38) in Sec. 1.4.2.1. Figure 1.55 is a plot of this expression in terms of false alarms per hour for an LWR with a 16.7-MHz bandwidth (matched to a 30-ns laser pulse). A false alarm rate of one per hour occurs for such a system at a threshold to noise ratio of approximately 7.

Sensitivity for the Sample Receiver. Table 1.19 presented a summary of the assumed parameters and resultant noise levels for the cases of a visible band silicon detector and one with a 100-Å filter centered in the near IR.

From the table it is apparent that the visible wideband system is limited by both solar shot noise and Johnson noise. Although there are a variety of potential wideband LWR configurations, this system is arguably typical, and its noise level is used as the basis for the sample problem.

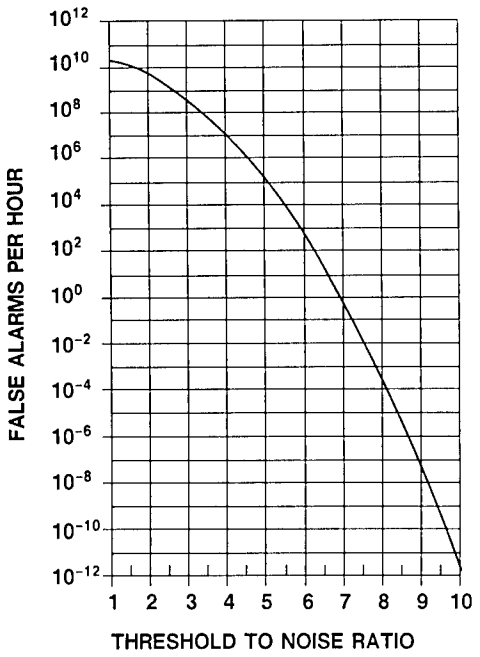

Fig. 1.55 False alarms per hour versus threshold-to-noise ratio for a typical laser receiver.

The nominal sensitivity of the LWR, expressed in terms of watts per square centimeter, is related to the limiting noise current and system threshold level by the relation

$$\text{sensitivity} = \text{TNR}\frac{I_N}{R_\lambda A_R} , \tag{1.109}$$

where TNR is the previously discussed threshold-to-noise ratio.

The total rms noise current used in this expression is obtained from the standard rms relation

$$I_{N\,\text{total}} = (I_a^2 + I_b^2 + \ldots)^{1/2} . \tag{1.110}$$

For the wideband LWR, the total rms noise is 2.31×10^{-8}, and the resultant sensitivity at a threshold to noise ratio of 7 (about one false alarm per hour) is 10^{-4} W/cm^2.

Detection Probability. The probability of detection is a function of the system TNR (established as a consequence of the system false alarm specification), the signal strength, and the noise level. Equation (1.36) and Fig. 1.31 in Sec. 1.4.2.1 present the relationships involved. A convenient approximation to this relationship is provided by the expression

$$P_D = \frac{1}{2}\left(1 + \text{erf}\frac{I_S - I_T}{\sqrt{2}I_N}\right) , \tag{1.111}$$

where erf is the standard error function tabulated in various mathematical and statistical references.[78]

This equation is plotted as a function of signal level, with the TNR as a parameter, in Fig. 1.56 for the noise level, detector area, and responsivity corresponding to the sample problem "typical" receiver. Note that the curve for a TNR of 7, corresponding to the previously computed nominal sensitivity, indicates a detection probability approaching 0.5 at the computed nominal sensitivity of 10^{-4}. Furthermore, this curve indicates that the incident irradiance must be approximately 1.17×10^{-4} W/cm^2 to result in a detection probability of 90%. (LWR systems are typically specified to have a probability of detection of at least 90%.)

SNR/Probability of Detection for Sample Problem. Table 1.20 presents a summary of the signal level data of Sec. 1.7.3.1 and the noise calculations of Sec. 1.7.3.4. The signal-level data for direct incidence and near-axis aerosol scatter is presented for laser to LWR ranges of 2 and 10 km for visibility ranges of 23, 10, and 2 km, respectively. The latter two visibility ranges are equal to the respective physical ranges and, hence, representative of the maximum attenuation situation experienced by visually directed threat lasers.

Note that the SNR for the directly incident signal is very high for a directly incident beam even though a spectrally wideband receiver has been assumed. The SNR is more than adequate to provide a large gain margin to allow for

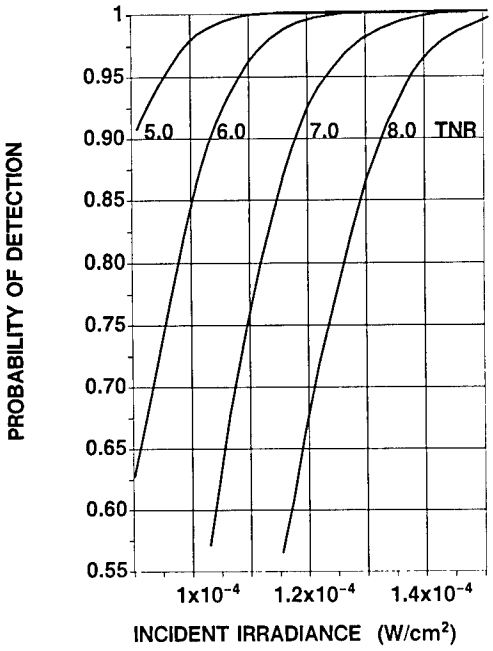

Fig. 1.56 Probability of detection versus incident irradiance with TNR as a parameter for a typical laser receiver.

Table 1.20 SNR for the Sample Scenario at 2- and 10-km Ranges (Scatter Intercept Values Computed at Four Times the Beam Radius)

Laser to LWR Range (km)	Visibility Range (km)	Detection Mechanism	Signal Level (W/cm^2)	SNR
2				
	23	Direct Beam	2.3×10^{3}	1.6×10^{8}
	23	Scatter Intercept (1 m offset)	1.3×10^{-2}	9.1×10^{2}
	2	Direct Beam	2.3×10^{2}	1.6×10^{7}
	2	Scatter Intercept (1 m offset)	3.4×10^{-2}	2.3×10^{3}
10				
	23	Direct Beam	5.6×10^{1}	3.9×10^{6}
	23	Scatter Intercept (5 m offset)	1.7×10^{-3}	1.2×10^{2}
	10	Direct Beam	1.9×10^{1}	1.3×10^{6}
	10	Scatter Intercept (5 m offset)	1.5×10^{-3}	1.1×10^{2}

atmospheric scintillation of the laser beam. Even when the visibility range is less than the laser-to-LWR range, this continues to be the case.

The aerosol scattered signal is much lower than the directly incident signal. However, even the lowest signal level, which corresponds to a scatter intercept 5 m off the axis of the laser with both the actual range and the visibility range equal to 10 km, produces an SNR of 110, which corresponds to a probability of detection higher than 0.999.

Although the directly incident signal is reduced by either an increase in distance or a reduction in the visibility range as might be expected, the more complex phenomenon of atmospheric scattering may exhibit apparent anomalies such as that indicated for the 2-km range in the table. In that case, the SNR for the scatter intercept is higher when the visibility is lower because the increase in scattered signal, for the assumed atmosphere, more than compensated for the loss incurred over that particular propagation distance.

1.7.3.6 Clutter and False Signals. Clutter, consisting of relatively static, local, background patterns, is the limiting parameter for the missile warning receivers discussed elsewhere in this chapter. Laser warning receivers are usually low-angular-resolution staring systems targeted against high-speed, transient laser pulses. As a result, clutter of the sort that drives the MWR design, is of minimal concern for the typical LWR. There are, however, two situations where clutter is of significant concern: (1) LWRs targeted against long-pulse, quasi-cw, lasers and (2) transient clutter with temporal characteristics similar to the desired laser sources.

Quasi-cw lasers tend to be found in weapon applications. They are usually high-power devices, and signal-to-clutter ratio is not a limiting issue for self-protection applications. In long-range ESM scenarios, static scene clutter may be of concern.

For the self-protection scenario, transient clutter, in the form of sun glint, lightning, and cosmic rays, is potentially an important factor. Such sources are usually treated as discrete, false signals rather than as a continuous clutter environment.

Sun glint intensity is often equal to, or greater than, the desired laser signal intensity. Many LWR concepts use temporal (i.e., rise time) discrimination, at least in part, to reject sun glint. The temporal characteristics of typical sun glints are illustrated in Fig. 1.43 and, as shown, sun glint rise times are slower than those of many military lasers. In addition to temporal processing, some LWRs employ coherence and spectral sun glint discrimination. The design issues relevant to such techniques are addressed in the following subsections.

1.7.3.7 Coherence Measurement Processing Issues. Detailed quantification of the degree of coherence of lasers and other sources involves careful laboratory techniques and is seldom attempted in field applications such as laser warning. Typically, when coherence is used as a discriminant in an LWR, the target lasers are highly coherent with regard to the incoherent sources to be rejected. In addition, some lasers with relatively low coherence are important militarily, so it is necessary to consider the discrimination ratios produced by these lasers in comparison to the incoherent sources.

1.7.4 Equipment Considerations

1.7.4.1 Wavefront versus Amplitude Division. Measurement of laser direction of arrival, wavelength, and sometimes, coherence are key to the successful operation of laser warning receivers. A variety of arrangements is available for each of these parametric measurements. Most of these measurements involve the dissection of the laser beam into several parts. There are two general options to dividing a beam of light: wavefront division and amplitude division, as illustrated in Fig. 1.57. (*Wavefront division* implies the use of adjacent sampling apertures, each receiving and operating on a different transverse segment of the beam. *Amplitude division* involves tapping off a portion of the wavefront by means of a beamsplitter.)

Many traditional measurement techniques, such as taking the ratio of different lens (antenna) outputs to determine direction of arrival, involve adjacent aperture (wavefront division) techniques. Moreover, issues of system simplicity, alignment simplicity, and so on, may tend to dictate adjacent aperture techniques for direction and coherence measurement.

In a scintillating atmosphere, the lateral amplitude variation induced by the atmosphere is superimposed on any adjacent apertures, or aperture arrays (wavefront division) from which multiple signals are extracted to determine direction, wavelength, or coherence. If the multiple apertures are smaller than, and closer together than, the structure of the atmospheric pattern this phenomenon is negligible. Unfortunately, this is frequently not the case.

This implementation problem with wavefront sampling techniques is generally recognized but often underestimated. On the premise that the "characteristic dimensions" of near-earth scintillation are "a few inches or so" and that this increases with altitude, systems consisting of centimeter-sized adjacent apertures have been implemented on the presumption that they were small with respect to the scintillation pattern. Such systems have usually failed because of the very steep intensity contours associated with typical scintillation patterns.

Figure 1.17 in Sec. 1.3.2.4 shows the lateral coherence dimensions for a representative situation. For a 5-km path at the ruby laser wavelength, the coherence dimension was determined to be about 5 cm. The allowable separation/diameter of adjacent apertures, from which the received power is compared in subsequent processing, is a function of the comparison accuracy required. Certainly, the sum of the aperture diameters and their separation must be substantially smaller than this coherence dimension. For some applications, it has been concluded that sampling apertures, or adjacent etalons (see Sec.

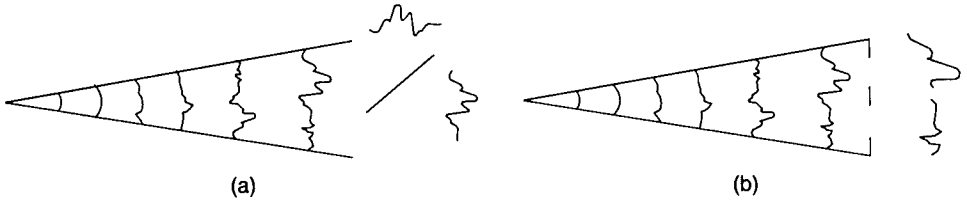

Fig. 1.57 Laser beam division: (a) amplitude and (b) wavefront configurations.

1.7.4.3), do not experience adequately similar intensity levels until the diameter and spacing are reduced to the order of 1/100 of this value, or 0.5 mm.

A variety of creative approaches have been successfully employed to permit the utilization of wavefront sampling techniques in practical systems. These include the use of arrays of very tiny apertures as well as homogenizing or integrating optical cavities that equalize the scintillation effects across several apertures. Alternatively, others have adopted amplitude sampling (beamsplitter) techniques instead of coping with the difficulties of wavefront division within the scintillating atmosphere.

1.7.4.2 Coincidence Circuit Rejection of False Signals

Cosmic Rays. Coincidence circuits, employed to reject cosmic ray events, rely on the fact that cosmic rays are statistically independent events and each ray strikes only one of the detectors. From a macroscopic point of view, the cosmic ray activity is a function of solar activity, the geographical location, and the local environment, all of which impact the local cosmic ray density incident on both of the coincidence channels. For purposes of estimating cosmic ray false alarm probability, it is reasonable to assume that the probability of a cosmic ray event is proportional to the detector area and receiver time constant and that the cosmic ray incidence on the individual detectors is statistically independent.

EMI. Standard EMI design practices of shielding, grounding, and so on, are required for LWR systems.[102] Moreover, because of the wide electronic bandwidth and the high sensitivity of the detector and preamplifier electronics, such systems are often particularly susceptible to EMI problems. Because the primary EMI false signal sources are often microwave fire-control radars with functions similar, or identical, to the laser, it is difficult to distinguish between them in subsequent processing. One successful approach to providing additional EMI suppression is the use of an optically blind channel in a coincidence arrangement with the optical channels. Successful implementation of this technique involves careful duplication of all the electronic and electronic coupling parameters of the "real" channels by the blind channel. This can include using an identical detector/preamplifier and mechanical arrangement for the "blind" channel.

Lightning. Because there is a large EMI impulse associated with a lightning flash, systems that employ an optically blind channel for EMI rejection also may utilize this channel to reject lightning-generated false signals.

1.7.4.3 Coherence Detection Techniques. There is seldom, if ever, a direct need to measure coherence for LWR applications. If the source exhibits the wavelength, intensity, and modulation characteristics of a known threat laser, it probably can do the job of the threat laser and determining its coherence *per se* may be of little consequence to any operational response. However, coherence is an excellent property for distinguishing threat laser radiation from other spurious sources of battlefield radiation. Consequently, binary (i.e., coherent/not coherent) discrimination techniques may be applied to LWR design. The primary reason for using coherence techniques within an LWR usually is to reject sun glint without restricting the spectral bandpass of the

system. Important secondary reasons include rejection of gun flashes, flares, flood lamps, aircraft beacons, and so on.

As indicated in Sec. 1.3, different lasers have different degrees of coherence. Although discrimination among lasers by means of their coherence is not usually a warning issue *per se*, the variation in coherence among lasers becomes a design parameter in developing an LWR that will properly characterize the lower coherence lasers and not reject them as incoherent false targets.

Two key issues drive the design of laser coherence discrimination techniques: (1) the common requirement for single pulse detection/analysis and (2) atmospheric scintillation effects. The transverse intensity variations associated with atmospheric scintillation can be expected to complicate any coherence measurements involving adjacent apertures (wavefront division), whereas single-aperture techniques (amplitude division) may rely on internal dynamic processes that are difficult to carry out during an individual pulse, which is only a few billionths of a second long, as would be required to obtain single pulse analysis. These issues are discussed further in the following.

There are at least three different coherence discrimination configurations potentially applicable to LWR design. These include (1) arrays of Fabry-Pérot etalons[103–105] (interferometers), (2) Michelson interferometers,[106–108] and (3) scattering surfaces.[109] The first two of these are the most common configurations considered, and their implementation within LWR applications is discussed in the following paragraphs. The third configuration, that employing scattering surfaces for coherence determination, has been proposed in the literature, but no implementations have been reported to date.

Figure 1.58 shows a two element Fabry-Pérot etalon array. The detectors following the array are connected in a differential amplifier arrangement. For light that has a coherence length significantly greater than the etalon internal dimension, the etalon transmission is determined by the internal resonance of the etalon and is a function of the etalon thickness and the wavelength of the light. Because the two etalons are constructed such that one is half a wavelength longer than the other, one output is always higher than the other; i.e., one is transmitting while the other is reflecting the incident light. Consequently, there is always a large output from the differential amplifier. Conversely, incident light with a coherence length substantially shorter than the etalon spacing does not resonate within either etalon, and the transmission of both is low (nominally equal to the transmittance squared of the etalon mirrors). Moreover, the output of both etalons is equal, resulting in a zero output from the differential amplifier.

Although typical atmospheric scintillation does not cause a significant reduction in the coherence length—i.e., an increase in the spectral linewidth [see Eqs. (1.6) and (1.7)]—of a laser beam, the resultant mottled pattern is a major perturbation in the transverse intensity of the beam. As a result, when this configuration is placed in such a wavefront, the atmospherically induced intensity modulations are superimposed on top of the etalon-induced spatial modulation and distort the coherence measurement process.

This measurement distortion can be readily visualized for the case in which the transmitting etalon falls in a scintillation null, whereas the reflecting etalon is at a scintillation peak. As a result, the mottled, coherent beam would yield low, possibly equal, signals on both channels, which could be erroneously classified as incoherent.

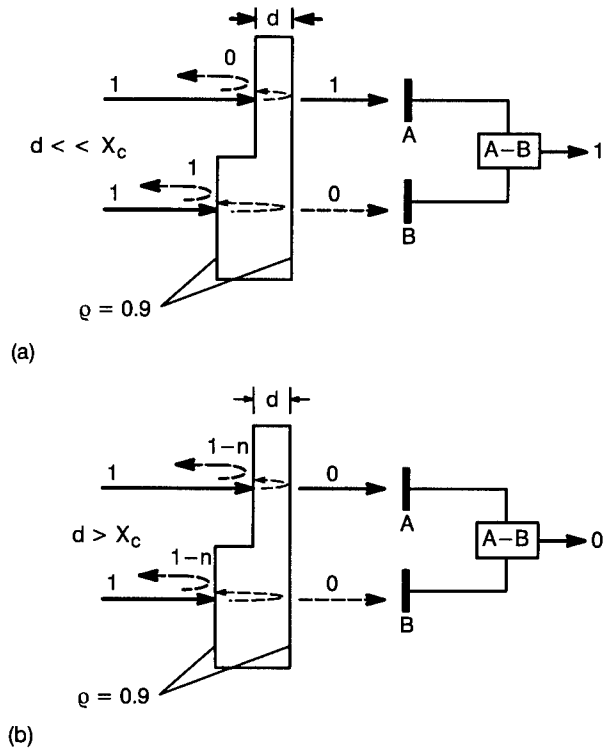

Fig. 1.58 Coherence discrimination with a two-step etalon: (a) coherent and (b) incoherent input beam.

As indicated in Sec. 1.7.4.1, this complication is not peculiar to the etalon approach to coherence discrimination, but is a characteristic of any wavefront sampling technique operating in a scintillating atmosphere. Similar problems exist when adjacent detectors are used in spectral ratio measurements and in angle ratio measurements.

Figure 1.59(a) is a reproduction from a U.S. patent[110] granted in 1982. The approach illustrated is an amplitude division approach involving pairs of etalons. Figure 1.59(b), from the same patent, shows two detectors, each with a picket fence shape, with the individual "pickets" interleaved in an interdigitized fashion. A Fabry-Pérot etalon is deposited over each individual picket or digit, and adjacent digits constitute etalon pairs. The scintillation effects in this wavefront division approach are avoided by keeping the digit size small, whereas the collection area is increased by combining many digits into a single detector unit.

Interferometric configurations involving amplitude-division techniques offer potential for LWR applications because of the relative immunity of such techniques to transverse scintillation effects. The basic Michelson interferometer, the archetype for such arrangements, is shown in Fig. 1.60.

The Michelson has a half-silvered beamsplitter that reflects half the incident power to the upper mirror and transmits the other half to the mirror on the far right. When the light is coherent and the optical paths to the two mirrors are adjusted so that the two equal amplitude retroreflecting beams are out of

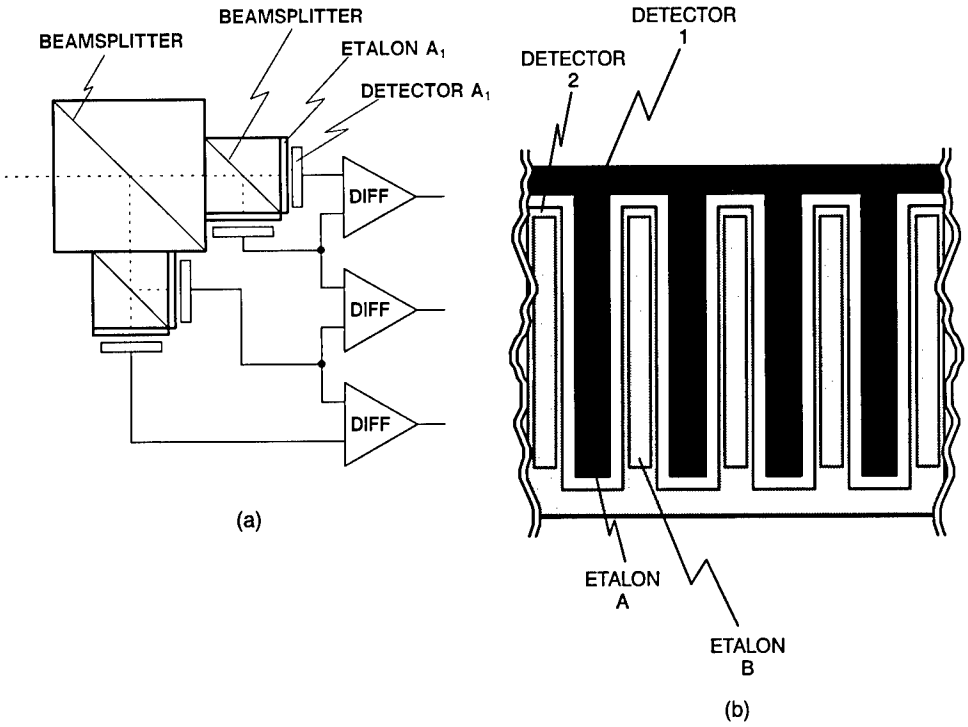

Fig. 1.59 Analyzer for coherent radiation: (a) beamsplitter, four-step etalon configuration, and (b) interdigitated two-step etalon-detector configuration.

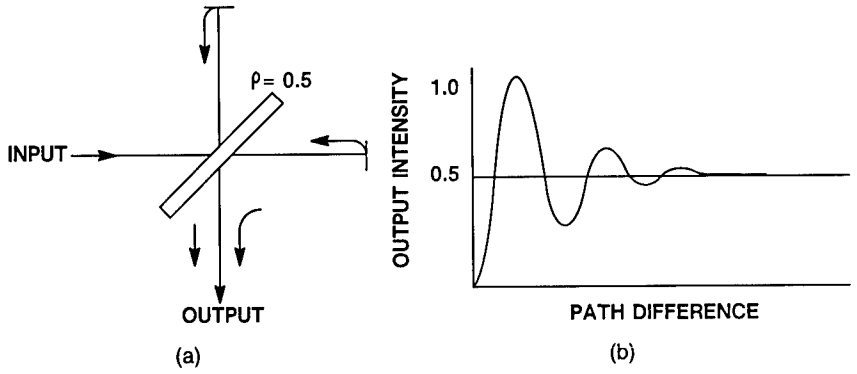

Fig. 1.60 Rapid continuous scan Michelson coherence measurement: (a) configuration and combining paths and (b) intensity versus path difference.

phase, they cancel, and the power delivered to the output port is zero. Conversely, when the optical paths are equal, the two beams combine in-phase, and the output is a maximum.

One could envision implementing a coherence length measurement technique by placing a detector in the downward beam path and moving one of the mirrors away from the equal path condition. Initially, the optical intensity would be modulated between 0 and 1, as shown in the figure. As the total path

differential between the two arms of the interferometer approaches and exceeds the coherence length of the light involved, the light intensity approaches a constant value.

The difficulty with the Michelson interferometer approach lies in the dynamics involved. Typical military fire-control lasers have durations of the order of tens of nanoseconds, and to sweep out an individual peak-to-null cycle, the mirror would have to be moving at a rapid rate. Such techniques implemented with electro- and acousto-optical modulators, rather than mechanical motion, have the potential for successful implementation in practical configurations.

1.7.4.4 Spectral Measurements. Some laser warning receivers do not use spectral measurements at all, but rely on other laser parameters (usually its temporal or coherence properties) to characterize its military function and/or to reject optical false signals. As a result, spectral discrimination techniques have had less research emphasis than other laser discriminants. In the future, as tunable lasers enter the military inventory, this parameter will grow in importance.

Laser warning receivers can perform direct spectral measurements on the received energy to recognize and characterize the laser source and its function. This differs from the spectral processing implicit in missile warning receivers that primarily implements a clutter discrimination function.

In the laser case, the spectral measurement circuits usually attempt to recognize a particular narrow-band laser and possibly to provide some sun glint, lightning, gunflash, or searchlight rejection. Most are implemented in one of the following forms:

- independent processing of parallel narrow-band optical channels [Fig. 1.61(a)]
- ratios of two linear spectral filter channels [Fig. 1.61(b)]
- spectroscopic techniques involving various types of gratings and detector arrays [Fig. 1.61(c)].

For the adjacent spectral band configuration, the resultant receiver may consist of 2 to 20 (or more) spectral channels across the visible silicon band and include one, or several, channel(s) covering the 3- to 5- and 8- to 12-μm atmospheric windows. Within the visible range, the spectral width of the individual channels not only provides spectral identification but also reduces solar clutter and solar shot noise. With this approach the designer must tradeoff between the number of apertures employed and the spectral resolution obtained.

There are spectral-band overlap problems in designing such an adjacent channel system. Part of the overlap problem is a consequence of the spectral/angle interrelationship of conventional interference filters. Another aspect of the overlap problem stems from the finite out-of-band response of all filters (spectral sidelobes). Such overlap can cause considerable confusion for a system that is trying to distinguish between intense narrow lines (which spill over into an adjacent band) and lower intensity wideband sources that naturally radiate in several bands. As a result, the location of spectral edges in such a system must be carefully coordinated with the wavelengths of expected lasers, the spectra of battlefield false targets, and the system processing logic.

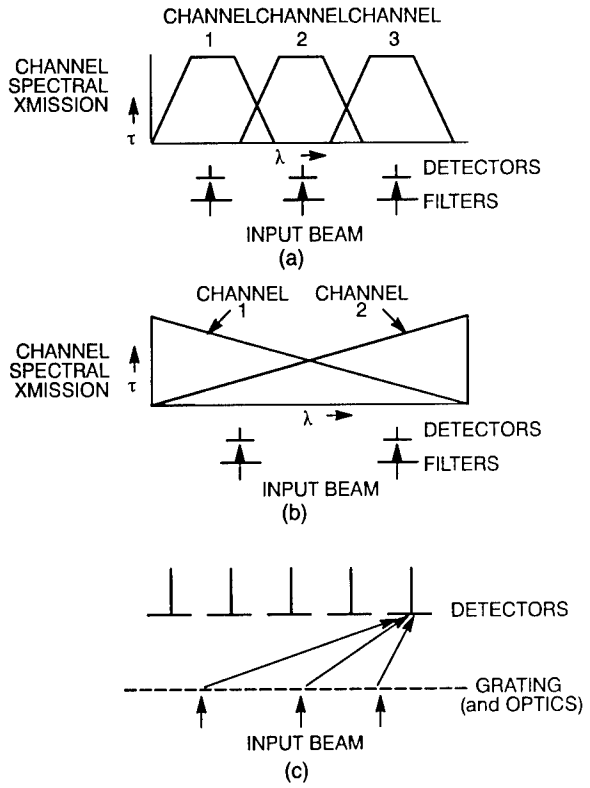

Fig. 1.61 Common spectral measurement configurations: (a) multiple spectral channels, (b) two-channel spectral ratio measurement, and (c) spectrometer (grating/prism).

If the system range of interest can be narrowed to several discrete lasers, ignoring all else, then a few narrow-band channels can be used. For instance, during the 1980s, ruby, Nd:YAG, and possibly doubled-Nd:YAG, channels would have been sufficient to cover most deployed threat lasers. More recently, the deployed laser types have increased, and during the 1990s, tunable lasers may enter deployment. As a result, this simple expedient may be negated by the expanding threat spectrum.

Laser warning receivers have been implemented using a pair of broad, overlapping channels with spectrally inverse wavelength responses. In such a system, the ratio between channel outputs can precisely characterize the incident wavelength. When implementing a spectral ratio system is is important to avoid wavefront division configurations because they result in atmospheric scintillation corruption of the spectral measurement.

Spectrometer approaches involving dispersive elements (prisms or gratings) placed in front of a detector array also can be used to measure source wavelength. Such arrangements may suffer from design problems with the detector array. In general, high-spatial-resolution detectors tend to block the temporal data on the signal, as a consequence of their low bandwidth; whereas high-speed detectors are difficult to implement in large arrays because of intra-element coupling problems (see Sec. 1.7.4.5).

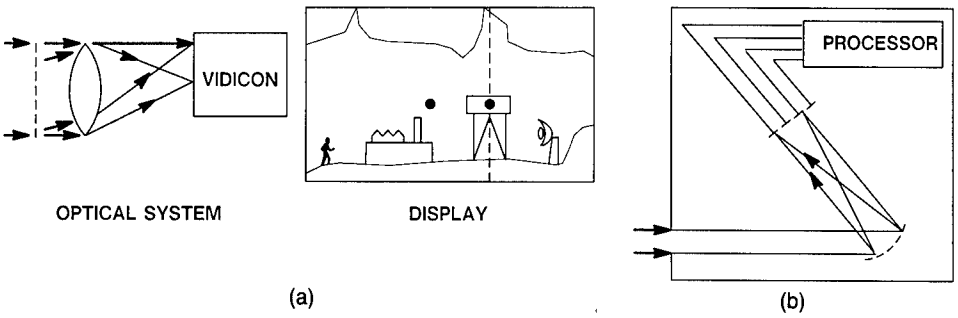

Fig. 1.62 Grating approaches to spectral measurements: (a) transmission grating/television configuration and (b) reflection grating/detector array configuration.

There are two primary spectrometer arrangements applicable to LWR applications. The first configuration, Fig. 1.62(a), consists of a simple transmission grating superimposed on a television (TV) system. The result is a bright source dot at the image location of the actual source and a second dot (i.e., the first-order spectra) displaced from it by a distance proportional to the source wavelength. The advantage of this approach is that it provides the location of the source as well as its wavelength. Of course, the loss of laser temporal data and superposition of the laser on the image clutter restricts this approach to high-intensity, direct-incidence scenarios.

The second spectrometer configuration, Fig. 1.62(b), is a reflective grating employed with a relatively high speed linear array. In this arrangement, temporal characteristics are preserved, and the potential number of spectral channels greatly exceeds that obtained with individual spectral apertures. Because this technique provides no inherent directional data, it must either be coupled with an adequate resolution angle measurement system and/or otherwise designed to minimize the angle/wavelength ambiguity inherent in grating spectrometers.

The normal incidence angular deviation of the first diffraction order for a simple transmission grating is expressed in terms of wavelength λ, grating spacing d_g, and the diffraction angle by

$$\lambda = d_g \sin\theta \ . \tag{1.112}$$

Wavelength *bins* are established in such a system by the angular subtense and placement of the detector array.

1.7.4.5 Angle-of-Arrival Techniques

Imaging Techniques. Most tactical and technical responses to warning of any sort require some knowledge about the direction of the threat.

Usually optical and infrared sensors are implicitly credited with high angular resolution that derives from their short wavelength. However, in spite of the inherently favorable wavelength-to-diameter ratio, there are difficulties in obtaining accurate threat direction from a LWR as a consequence of three specific issues: (1) the single pulse nature of some lasers, (2) the possible dif-

ference between the laser direction of arrival and the threat location, and (3) the impact of atmospheric wavefront distortion.

The difficulty with single-pulse direction finding, when the single pulse arrives without warning and lasts 30 ns, or less, is obvious: all measurements must be simultaneous and carried out within very wide bandwidth circuits. This differs substantially from the typical microwave RWR within which pulse trains are deinterleaved and processed for directional data.

The possibility of ambiguity between signal direction of arrival and the threat location is a consequence of the various propagation paths outlined in Sec. 1.7.1. For direct beam incidence on the LWR, the only issue is signal level saturation (not a trivial issue), and a variety of direction of arrival techniques are available. For splash intercepts, the photon source is an area on, or adjacent to, the LWR-protected platform, and its location has little direct relationship to the threat location. Similarly, for atmospheric scatter intercepts, the photon source is a line within the atmosphere that ends at the threat laser, but the photon origin, from the receiver perspective, may be 180 deg away from the physical location of the threat. Unfortunately, the latter two situations are potential circumstances for laser warning, thus calling into question the applicability of simple direction measurements in some scenarios.

Finally, the impact of atmospheric wavefront distortion on wavefront sampling configurations may degrade the angle data in various candidate angle measurement arrangements.

Figure 1.63 illustrates the classical approach to optical direction measurement. An area detector with internal spatial resolution is placed at the focus of a lens. The lens transforms the incident angular information into the spatial coordinates of the detector.

Such imaging systems are straightforward and, in other applications, implemented in a variety of ways. For the present application, laser warning involving pulsed lasers, our implementation options are limited to staring

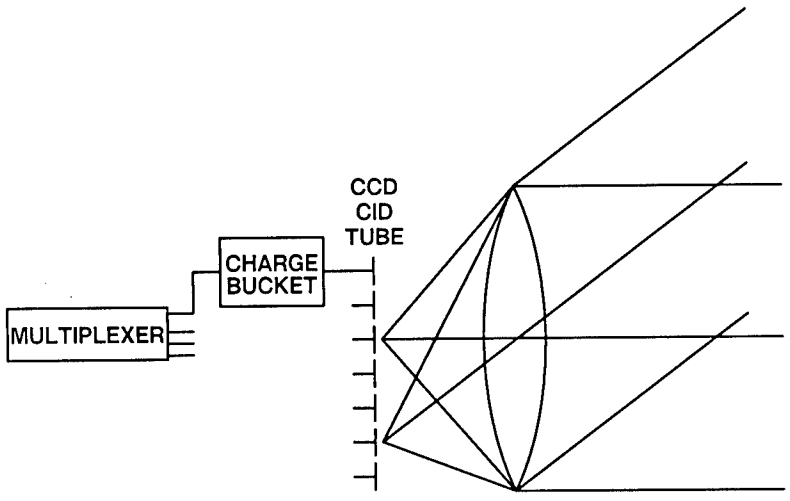

Fig. 1.63 LWR direction of arrival by conventional imaging on an area detector array.

configurations, because most scanning approaches have intolerable scan-on-scan problems and a consequently low probability of detection.

Candidate staring detectors, as utilized in LWR applications, can be categorized in terms of their response times and signal accumulation processes as either signal-integrating or real-time detectors.

Integrating detectors include conventional TV camera tubes, such as vidicons, as well as solid-state arrays, such as charge-coupled devices (CCDs) and charge-injection devices (CIDs). Such detectors inherently integrate and/or store, the received signal for a relatively long time, often $\frac{1}{30}$ s, during which each pixel is sequentially sampled by its multiplexing electronics. The multiplexed output from multiple pixels, as many as a million, is a wideband signal of several megahertz. However, the signal bandwidth of the individual pixel is the inverse of the integration time, or of the order of 30 Hz. Thus, the integration process eliminates much of the laser temporal structure.

Alternatively, the system could be constructed with wideband individual detectors. In that case, it is more likely to utilize 10 to 1000 resolution elements (i.e., channels) rather than a million, and the spatial resolution advantages of using an imaging-type system may be lost. In particular, when the LWR designer chooses to preserve pulse duration data, with the wide bandwidths that pulse shape preservation requires, interchannel coupling problems tend to occur, and practicality may dictate use of a small array (low angular resolution).

Separate subsystems can be used for the measurement of each parameter to avoid some of these design constraints. For instance, it may be possible to use a high-resolution imaging detector with a single, separate, high-speed (wideband) detector system whose sole function is to determine the temporal parameters of the pulse.

Another significant concern with imaging direction-of-arrival measurement is the wide field of view associated with most warning requirements, say 140 deg. When the necessary *fish-eye* lens is designed, it turns out to provide little, if any, effective optical gain. Thus, such a system, although incurring a potentially high cost for its optics, may exhibit the sensitivity of a detector with no lens at all. Therefore, the LWR designer may try other nonimaging, even nonlens, arrangements.

Mask Techniques. Figure 1.64 illustrates two approaches that have evolved for achieving reasonable angular resolution while minimizing the number of high-speed, wide-bandwidth electronic channels.

Figure 1.64(a) illustrates a brute force approach to nonimaging, shadowlike direction measurement. An array of long thin cells is placed behind a screen with a single long slit, parallel to the detectors, at its center. The positive shadow of the slit falls on different detectors for different angles of incidence. The one-dimensional arrangement shown is practical for many applications in that many scenarios require only azimuthal direction of arrival. However, the number of angular bins, say, seven within 140 deg, corresponds only to 20-deg resolution. To improve this to 2 deg involves a tenfold increase in parts count. Thus, although this may be practical for low resolution, it does not efficiently expand to the resolution desired for many practical applications.

Figure 1.64(b) shows a plan view of a similar configuration where the long thin detectors are orthogonal to the slit. (The drawing shows the shadow in

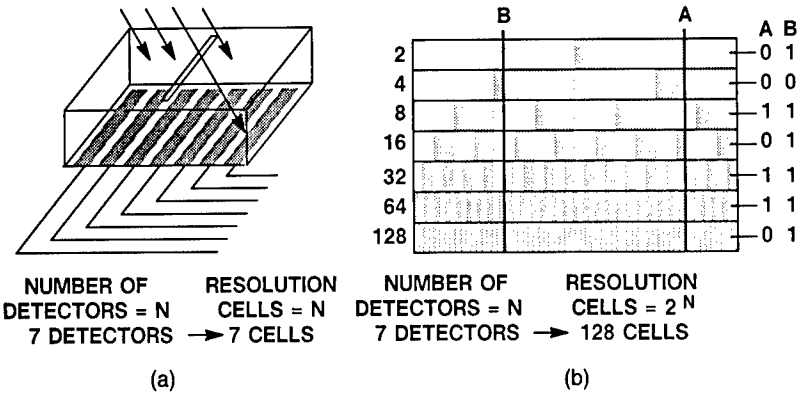

Fig. 1.64 LWR direction of arrival by mask techniques involving linear detector array: (a) slit aligned with detection array and (b) slit orthogonal to detection array and integral binary-coded mask.

two separate positions.) In addition to the slit, each detector is now covered by a partial mask that blocks portions of it. The top detector is half-blocked. The one below it is half-blocked, also, but the blockage is rearranged so that half the area blocked in the upper detector is now exposed, and half the area exposed is now blocked. This pattern is continued in this fashion for all the subsequent detectors. These blocking masks are, in fact, fashioned after a binary code. Note the detector outputs, indicated by 0 and 1, when the slit produces the positive shadow shown on the right; all outputs are zero except the third, fifth, and sixth detectors, producing a 0010110 digital position code. For a source angle illustrated by position B, the output detector code is 1011111. This approach produces 128 resolution cells from the same seven detectors—enough for many practical applications. At most, only one or two additional channels would be needed.

Such a system need not be limited to using this simple binary code. Other mask arrangements have other desirable properties. In particular, there is another binary code, the *gray code*, that minimizes positional ambiguity at the zone edges.

In the design of such a system, we cannot ignore scintillation; the length of the array must be less than the atmospherically induced intensity structure or the atmosphere will corrupt the angle encoding process.

1.7.4.6 Time-of-Arrival Techniques. Microwave and acoustic systems sometimes determine source direction by means of temporal measurements. If two detectors are positioned along a long baseline and both receive the signal simultaneously, it follows that the source is along a line perpendicular to the receivers. If the one on the right receives the signal first, the source is offset to the right at an angle proportional to the delay in the signal reaching the left receiver.

This approach is counterindicated for many LWR scenarios because of the limited lateral extent of the laser beam. The electronic bandwidth required to measure the time delay resulting from a specific angular displacement is pro-

portional to the baseline between the two receivers—for some scenarios this is limited by the threat beamwidth to less than a meter, whereas, for the microwave and acoustic situations this is limited by platform dimensions to 10 m, or more. In addition, such a process falls in the *wavefront division* category and would be detrimentally affected by the atmosphere.

1.7.4.7 Detector and Electronic Considerations

Detector Selection. Laser warning receivers may require individual detectors or detector arrays. LWR application-specific issues include dynamic range and transient response. In this application, maximum signal levels may be 4 to 10 orders of magnitude, or more, above the desired minimum detectable signal level, and desired pulse response time may be of the order of nanoseconds. At the higher signal levels it is necessary to consider the nonlinear transient response of the detector as well as its more commonly specified small-signal bandwidth. Few detectors, and/or their associated electronics, provide linear response over such a range of response times. Thus, it is necessary to select/design the postdetection circuitry in conjunction with the detector selection. The initial criterion is to avoid detector destruction, and the second is to maximize the dynamic range over which the signal is properly characterized. Finally, the concept of *graceful* degradation is invoked to ensure that, as the detector and its circuits stretch and/or clip the laser pulse, the processing circuits avoid catastrophically incorrect threat characterization.

Various LWR arrangements use linear, or two-dimensional, arrays to implement specific spectral, angular, and coherence measurement techniques. The detector types involved include television imaging tubes, such as vidicons; linear arrays of high speed detectors; and various integrating solid-state arrays, employing CCD, CID, and related readout techniques. LWR-specific concerns that should be considered include electronic and optical interelement coupling and the impact of temporal integration on LWR system processing options.

1.7.4.8 Electronic Circuit Selection/Design Issues

Matched Filter Design Concepts. Direct measurements of pulse duration, peak power, power at pulse 3-dB points, and so on, require that the detector and its electronics have a bandwidth sufficiently wide to replicate the pulse shape. For pulse rise times of 5 ns, this implies an electronic bandwidth greater than 200 MHz. This may be undesirable from a practical point of view for a laser warning receiver, for which the design objectives are usually driven by large-volume, low-cost applications. In addition to the costs involved, such wideband systems provide an excess noise bandwidth. When LWRs are driven to their radiometric limits by the need to detect atmospheric scatter and/or to function in low-visibility conditions, the design trade-offs usually favor the use of matched filter detection electronics. Such circuits are well known and discussed extensively in the radar and IR systems literature (see Sec. 1.4.2.2). A matched filter detection system exhibiting a spectral response equal to the complex conjugate of the pulse spectrum offers the maximum potential SNR.

When both high sensitivity and duration measurement are required, the duration measurement can sometimes be translated to a pulse bandwidth

assessment. The use of detection circuits involving a detector/preamplifier matched to the shortest expected pulse duration, in parallel with an array of similar matched filter/threshold circuits each matched to the pulse duration bins of interest is one of the most efficient implementations of duration binning from a radiometric signal-to-noise perspective. Other approaches involve detector/preamplifier front ends matched to the shortest duration pulse followed by an analog-to-digital conversion and digital processing.

Because the signal level of the temporally stretched, atmospherically scattered intercept is substantially lower than that of the directly incident beam, the designer may choose to match the electronics for the longer, weaker pulse when such scenarios are anticipated.

Finally, as much of the laser recognition process can often be accomplished by establishing that the laser duration is less than 100 ns, detector/preamplifier bandwidths as narrow as a few megahertz, or less, may be adequate for the pulsewidth discrimination required in some situations.

Wide Dynamic Range Impact/Design Overview. The wide dynamic range of incident signal intensity is a major factor in LWR circuit design and selection. Although many optical detectors have a large dynamic range of linear operation, the typical preamplifiers that follow them, as well as ancillary bias circuits, often operate linearly only over a maximum of three to four decades of current/voltage.

Historically, the semantics of dynamic range definition has been a cause for substantial confusion within the LWR design process. The dynamic range of the electronic circuits tends to be specified in terms of decibels according to the traditional definition of 20 times the common logarithm of the current or voltage ratio. Thus, a six-decade dynamic range of detected signal current is viewed at the electronic circuit level as 120 dB. However, this dynamic range also corresponds to an optical power level variation of six decades that, in the optical domain, is also legitimately characterized in terms of decibels according to the traditional definition of 10 times the logarithm of the power ratio. In these terms, the dynamic range would be stated as 60 dB. This apparent inconsistency is the result of the photon-to-electron detection process in which the optical power is linearly transformed to an electronic current (square-law detection). The semantic confusion arising from the inherent nature of optical direct detection, although philosophically trivial, should be considered whenever LWR specifications are established or interpreted.

LWR dynamic range is often established in three phases: first, the requisite sensitivity (i.e., the low end of the dynamic range) is established; then the sensitive detector/preamplifier is protected against damage by signals at the high end of the dynamic range; finally, the processing doctrine is selected such that proper laser characterization is obtained over the necessary range. If the dynamic range for the processor is less than the full system dynamic range, the processor should be designed for graceful degradation; whereby, the system alerts the operator to a potential threat and informs about the processing shortfalls. The term *catastrophic failure* should be reserved not for the situation when the detector burns out (and the operator is so notified) but rather for the situation where the processing fails and a potentially lethal situation is erroneously classified as safe.

Detector Protection. Detectors, alone, are relatively insensitive to laser destruction. In wide-field-of-view LWR systems that have little optical gain, the basic detector can withstand energy levels of the order[111,112] of 1 J/cm^2. However, the detector bias circuits and the preamplifier input circuits can be destroyed by the resultant current flow, or voltages, at levels substantially below this level. An arrangement often used to protect a silicon *p-i-n* detector and its preamplifier consists of a pair of back-to-back diodes in parallel with the protected components, biased to short any overload before it can destroy the component. The design issues involved in implementing such a circuit from a protection point of view are straightforward. The more subtle trade-off between the implementation of this protective circuit and the resultant system sensitivity is unique to the wide-dynamic-range LWR regime. In particular, the problem with such circuits is the additional noise potentially introduced by the protective diodes and its impact on the system sensitivity level.

Processing Dynamic Range. By establishing the appropriate feedback circuit, an amplifier with a linear dynamic range of three decades can be converted into a circuit in which the three decades becomes the dynamic range of the logarithm of the input.[113] Although such a circuit may provide an adequate dynamic range, it introduces various signal distortions that must be addressed in subsequent processing to properly characterize the incident laser.

The large-signal frequency response of nonlinear circuits is often characterized in terms of such parameters as slew rate rather than by the small-signal frequency response. Such circuits may have difficulty following the fall times of the laser pulse. Although they may replicate small pulses, and/or even the rise times of large pulses, they may "hang up" on the fall times of large signals; a factor that must be addressed in the laser recognition processing.

LWRs that involve adjacent spectral channels have an additional feature that complicates the processing dynamic range. Such systems inevitably have some optical leakage of signal through the spectral stop bands of adjacent channels. It is difficult to suppress this leakage optically to levels lower than six decades below the peak transmission of the adjacent, transmitting channel. For systems with a dynamic range requirement greater than six decades of optical power, the processing circuits must be designed to properly handle (i.e., dispose of) this out-of-band signal. The difficulty in such disposal arises from three issues: (1) temporal stretching by the electronics, (2) the need to properly characterize the wideband sources that naturally overlap into both channels, and (3) the potential for multiple laser intercepts. Distortion of the large pulse in the proper channel may make it difficult to compare the time of arrival and pulse shape to determine that it and the weaker signal "bleeding through" the out-of-band channel are from the same laser. Proper handling of this situation requires the generation of a processing *truth table* that includes all the possible combinations and distortions and ensures that, even when the processor has a potential for confusion, it never fails to alert the operator to a potentially lethal event, even at the risk of an occasional false alert.

Typical optical threshold circuits consist of a detector, a preamplifier, and a threshold circuit that triggers when the signal exceeds some preset threshold. Such circuits have been presumed during the prior discussions on signal detection and false alarm. However, an alternative circuit, termed a *hard limiter*,

finds common application in many radar systems. Its design principles and signal detection theory are well established. Hard limiters are attractive candidates for application to laser warning applications as they tend to have a large dynamic range and shield the subsequent circuitry from some of the aspects of the dynamic range requirement.

1.7.5 Testing

1.7.5.1 Overview.[b] The quickest and most cost effective way to evaluate laser warning receivers is to use a progressive series of laboratory, field, and vehicle tests. Because each subsequent test phase costs more than the previous one, solving the problems that can be solved in earlier test phases greatly reduces the total time and cost of testing. The types of problems to be solved in each test phase are summarized in Table 1.21.

In laboratory tests, the primary goal is to characterize the LWR as a radiometric receiver and to verify that the system's interfaces to the test equipment are working. The objectives of field tests are to determine the impact of natural backgrounds, atmospheric phenomena, and potential false alarm sources on LWR performance. Field tests are also used to test equipment compatibilities prior to vehicle testing. Vehicle (flight) tests are the ultimate test of the LWR where its probability of detection is measured over a parametric test matrix. Special measurement and testing concerns pertaining to the field and vehicle testing are now discussed briefly.

During field tests, one of the most important effects to characterize is scintillation. Because scintillation produces a statistical distribution of pulse intensities it can make an otherwise below-threshold average irradiance detectable for some fraction of the received pulses. Thus, it is crucial that the test designer provide a calibrated radiometer that can characterize the received signals next to the LWR. The radiometer should have a wide dynamic range (10^4), at least a 15-deg field of view, and should be at least an order of magnitude more sensitive than the LWR. A data acquisition system must be provided that can quantify the pulse-to-pulse intensity fluctuations.

To make irradiance or system performance predictions for particular test conditions, a variety of atmospheric parameters must be measured, including the aerosol size distribution and other meteorological parameters. Mie scattering codes and the AFGL FASCODE model are available for processing the meteorological data. Often aerosol scattering phase functions are measured with calibrated radiometers to compare with the predicted phase function. Considerable care must be taken to separate the port scatter radiation from the aerosol scatter, particularly in the forward scatter angles. A port scatter block can be placed between the radiometer and the laser port to eliminate this signal source. Collecting data to validate a system performance model is best accomplished during field tests. The system model can be used to extrapolate test results to new weather conditions, geometries, and scenarios as occur during the subsequent vehicle tests.

[b]This subsection was written by M. Neer, E. Newsom, and R. Preston, SciTec, Inc., Princeton, New Jersey.

Table 1.21 Key Aspects of the Four Phases of LWR Testing

Laboratory Tests	Field Tests	Vehicle Compatibility Tests	Performance Vehicle Tests
Sensor Detection Threshold - Wavelength Dependence - High Angular Resolution - Background Dependence	Impact of Atmospherics - Background Variations - Aerosol Scatter - Scintillation	Compatibility of Instrumentation Rack with LWR and Vehicle	Single and Multi-Pulse Probabilities of Detection
Dynamic Range	LWR Performance - "Shipped" Configuration	Compatibility of LWR with Vehicle - Switchology (EMC)	Susceptibility to False or Ambiguous Angle-of-Arrival from - Terrain Reflections
Min./Max. Pulsewidths	- Probability of Detection - Az, El, Miss Distance	- Radar Susceptibility (EMI) - Functional Performance (Lasers)	- Vehicle Reflections
Wavelength Coverage	- Multiple Lasers - Terrain Reflections	- Vehicle Compatibility Vibration/Dust	Multiple Laser Threats
Accuracy - Wavelength - Direction-of-Arrival	- Susceptibility to Optical False Alarms	Dress Rehearsal for Performance Vechicle Tests	Multiple Laser and Radar Threats
- PRF - Pulsewidth	Dress Rehearsal for Vehicle Tests		Compatibility with On-Board Systems - Avionics - Communications - Munitions - Electronic Warfare
Compatibility with Host RWR			
Dress Rehearsal for Field Test			Optical False Alarm Susceptibility

The three main categories of LWR vehicle (flight) tests are vehicle compatibility tests, system performance tests, and tactical performance tests. Compatibility tests are used to ensure that the installed LWR is compatible with the vehicle and the instrumentation rack. Performance tests are used to evaluate an LWR's effectiveness, including probability of detection, compatibility with other on-board systems, immunity to false alarms, reaction time, and human factors. Tactical performance tests are needed to test the LWR in tactically realistic scenarios. As an example, a system performance flight test may involve flying carefully programmed circular flight profiles at various roll angles for 90 min while the laser is fired at the system under test in machine gun fashion. Tactical performance tests of a helicopter system may involve laser engagements dominated by pop-up maneuvers associated with firing antitank missiles. Whereas the performance test involves a large number of elevation and azimuth angles in a rigorous fashion, the tactical performance test primarily involves forward aspect angles and zero elevation angle, typical of actual missions.

The support measurements for vehicle tests are often different from those of field tests. For instance, because scintillation varies so much with vertical profile, ground-level scintillation measurements normally do not apply to an integrated flight path, and aerosol size distributions and meteorological parameters are typically the only atmospheric measurements made during flight tests.

The most important parameters to measure during vehicle tests have to do with the laser beam pointing and the vehicle data. The laser beam pointing problem has been solved in recent years with the use of laser *indicator spots*. These laser indicator spots are visible to the laser operator and correspond precisely to the laser beam location.[114] A video record is made of the trans-

mitted laser pulses so that each pulse directed to the LWR can be counted and its miss distance measured. These data, combined, say, with an aircraft's roll, pitch, and yaw data are needed to determine actual direction of arrival to compare with the LWR reported value. Typically, a video record is made of the LWR results in the vehicle to correlate them with pulses recorded at the laser transmitter. For accurate pulse-to-pulse analysis both the threat simulator and the vehicle video system must be correlated using synchronized Inter-Range Instrumentation (IRIG) clocks.

1.7.5.2 Laboratory Testing[c]

General Considerations. The types of laser warning receiver parameters to be measured in the laboratory include sensitivity, field of view, dynamic range, pulse width coverage, wavelength coverage, direction of arrival accuracy, PRF accuracy, and wavelength accuracy.

Many laser warning receivers do not measure nor provide outputs for all of these parameters. For example, a radiometric receiver may use a minimum irradiance threshold together with a maximum pulse width threshold for detection and discrimination. However, for other receivers it may well be that neither pulse irradiance nor pulse width are actually measured, and if they are measured, they may not be provided as an output for testing. Conversely, some laser warning receivers not only measure these parameters but also produce digital threat words that quantify, although sometimes crudely, these measured values.

To measure the parameters of a laser warning receiver with high angular resolution across its field of view for a given laser wavelength and pulse width, it is usually necessary to have a computer-controlled test stand that, on command, rotates the sensor heads to a specified azimuth and elevation angle with respect to the incident radiation. To measure irradiance-dependent parameters, either the irradiance levels on the receiver can be varied at each incident angle direction or incident angles can be varied under the conditions of fixed irradiance levels. The latter method is usually preferred as it tends to produce field-of-view profiles for a number of discriminates directly. Because most parameters are best visualized as a function of field of view, emphasis is often placed on acquiring data in a raster format. Raster-formatted data is taken as stripes of azimuth or elevation points with successive increments of the orthogonal axis to produce data that traverse a pattern similar to a TV raster. Care should be taken to make sure that raster scan coordinates correspond to the receiver's field-of-view coordinates. Depending on the mechanical configuration of the scanning mechanisms, as well as the receiver's own direction-of-arrival detection scheme, coordinate transformations are sometimes required to account for coordinate system mismatches. These mismatches are not always obvious to the casual observer and are often ignored. Parametrically characterizing laser receivers over their entire fields of view while maintaining these considerations can be an extremely tedious procedure.

To further complicate matters, detection thresholds may vary as a function of background brightness because shot noise (proportional to the square root

[c]This subsection was written by J. H. Parker, U.S. Air Force Wright Laboratories, Dayton, Ohio.

of photoelectrons induced by solar background) vary greatly in bright sun versus nighttime backgrounds. Most laboratory testing validates performance for nighttime or low-level background conditions. To validate performance for bright sun conditions, solar radiation must either be "piped in" from outdoors or indoor solar simulators must be introduced into the test configuration. Otherwise, solar background testing must be reserved for the field. Another complicating, and often overlooked factor, is the polarization of the laser source, which, depending on the technique used for laser detection and discrimination, may affect receiver sensitivity. Polarization rotation devices introduced into the measurement configuration are often helpful in determining the receiver's susceptibility to polarization. An alternative method is to perform a few baseline tests in various mounting orientations to determine if there is a preferred receiver axis with respect to the laser's orientation.

Still another complicating issue is the receiver's susceptibility to atmospheric scintillation. Although field testing remains the ultimate proving ground for atmospheric effects, it is often desirable to isolate the contributions of atmospheric turbulence effects on laser propagation to evaluate how turbulence components affect receiver performance. Depending on the technique employed, atmospheric scintillation testing in the laboratory can be expensive and complex. Atmospheric scintillation simulation methods can take many forms. Most methods employ some fluid medium contained in an environment capable of maintaining specified thermal gradients across the medium. Alternative methods[116] utilize acoustically driven reflective membranes to modulate the intensity profile of reflected collimated laser light. With this method, various scintillation parameters, such as amplitude distributions, angle of arrival distributions, and phase front characteristics, can be manipulated to study their effects on receiver performance. Note also that scintillometers are required to monitor simulated turbulence during the testing process.

Terminology and Issues. The terminology and definitions commonly used in LWR laboratory tests are presented here.

Detection threshold: The units are watts or joules per square centimeter. The detection threshold is the irradiance level below which the LWR system does not detect any pulses and above which it detects all pulses. Note that because of various forms of system noise, most laser warning receivers have a finite range of irradiance values over which the percentage of pulses detected goes from 0 to 100% (beyond this value there is a large dynamic range of proper operation, which ends with the onset of detector or circuit saturation effects). For most systems, the range of ambiguous declaration is very small and the detection threshold is defined at the 100% point. Note also that actual detection threshold must be considered in the context of the desired field-of-view response. The threshold might also be specified as a percentage of field-of-view coverage. Sometimes the threshold is defined as the irradiance level that causes detections throughout the receiver's intended field-of-view profile. An additional note is that sensitivity must be specified at a particular laser wavelength, because most laser receivers do not have flat spectral response.

Field of view: Units are degrees. The field of view of the laser receiver is defined in terms of elevation and azimuth in platform coordinates. Zero azi-

muth and zero elevation is *nose-on*, whereas 180 deg azimuth and zero elevation is *tail-on*. An example of field-of-view specification for a laser warning receiver is 0 to 360 deg in azimuth and ± 60 deg in elevation. Note that field of view is more often than not a function of irradiance; therefore, field of view usually infers some baseline sensitivity.

Dynamic range: Dynamic range (which is unitless) is defined as the ratio of the maximum-to-minimum laser irradiance for which the system performs in a satisfactory manner. Although a unitless quantity, dynamic range is generally specified in terms of decades or decibels of optical power. An example of a dynamic range specification for a laser receiver might be four decades, implying a ratio of 10,000. In the case of very complex receivers having multiple discriminates and detector focal planes, dynamic range may have to be specified and measured for each discriminate.

Pulse width: Units are nanoseconds. Pulse width is defined as the full width at half maximum. Note, however, that for certain lasers, pulse shape considerations may complicate the interpretation of pulse width. Pulse width accuracy is defined as the difference between reported and actual pulse width divided by the actual pulse width. Thus, if a 50-ns pulse is recorded as 40 ns, the pulse width accuracy is 20%.

Wavelength coverage: Units are micrometers. Wavelength coverage is specified in terms of the spectral limits over which lasers can be detected. Spectral bandwidth is synonymous with the wavelength coverage. Wavelength accuracy is defined as the difference between reported and actual wavelength.

Direction of arrival (DOA): Units are degrees. The direction-of-arrival accuracy is defined as the rms difference between the reported direction of arrival and the actual direction of arrival. In laboratory testing, where the receiver sees only direct radiation, actual laser direction is that of the laser radiation itself. In this case, the geometric limitations of the particular receiver architecture are under measurement. Geometric limits are usually broken into two components, resolution and accuracy. As an example, a direction of arrival sensor might divide its 120 deg azimuth field of view into 10 sectors. This would imply a resolution of 12 deg. This 12-deg sector resolution might provide an accuracy of ± 6 deg. In the case of field testing, near off-axis radiation can create false directional vectors because of the atmospheric scattering components. In this case, the actual direction is a vector originating at the sensor and pointing directly at the laser location. For example, a field environment in which the laser is detecting off-axis aerosol scattered radiation, the centroid of the received radiation could be approximately 3 deg different from the actual direction of the laser threat. Therefore, the laser warning receiver reports the centroid of the aerosol scattered radiation as the direction of arrival, the DOA error is 3 deg. The field observations contain the errors resulting from both receiver architecture geometry and scattering.

PRF: Units are hertz. The PRF of the laser source is defined as the inverse of the time interval between pulses. Thus if two pulses are fired 50 ms apart, the PRF is 20 Hz. If 20 pulses are fired, all of which are 50 ms apart, over a 1-s period, the PRF is 20 Hz. If 3 of the 20 pulses fired during the 1-s period

are not detected because of scintillation, several time intervals between pulses varying from 50 ms (20 Hz) to 200 ms (5 Hz) could be observed during that 1-s period.

Typical Test Configuration. Figure 1.65 depicts an equipment configuration for laser receiver laboratory testing. The receiver under test resides on a two-axis rotary positioner. Positioner accuracy should be at least 0.1 deg for direction of arrival testing.

Laser sources are beam conditioned with a large off-axis collimator to simulate far-field propagation conditions. Selection of the expanding mirror is based on the focal length of the collimator and the beam uniformity requirements. Typically, laser beams have Gaussian power distributions. For large apertures, the expanding mirror should be selected to collimate only the central peak of the Gaussian beam, essentially "throwing away" much of the beam energy. It is also important that the collimator diameter be large enough to accommodate the size of the receiver aperture under test.

Optical attenuators inserted before the expanding mirror permit adjustment of the irradiance levels in the collimator. Fixed neutral density filters may

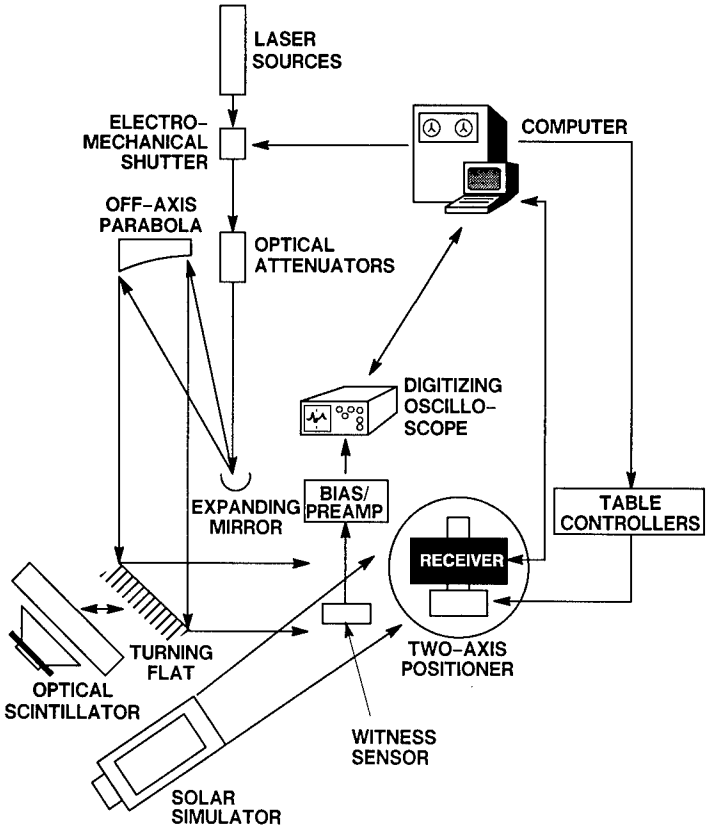

Fig. 1.65 Laser receiver testbed equipment configuration.

sometimes be used. Many commercially available filters introduce serious interference anomalies if stacked together to get the desired irradiance, and most introduce severe beam steering in the collimator. Circular variable neutral density filters are an option, but often produce beam gradients and beam-steering problems. Dually opposed, linearly variable neutral density filters have become available in recent years that are capable of producing good beam uniformity with negligible beam steering in the collimator.

The electromechanical shutter allows single-pulse testing with high-repetition-rate lasers by gating single pulses out of the continuous pulse train. This is often desirable for lasers of fixed PRF or for lasers that are more stable at higher PRFs. However, a shutter can create a timing anomaly if not properly synchronized to the laser. The temporal placement of the laser pulse within a fully open phase of the shutter's open cycle is not guaranteed without specialized timing circuitry. Spatially, the raw laser beam can be partially vignetted by a shutter blade caught in the process of opening or closing whenever a single laser pulse gates through the shutter. Any vignetting of the raw beam is greatly magnified by the collimator and can result in the partial shadowing of key sensor elements on the sensor head. This may cause anomalies or drop-outs in the receiver data. A shutter synchronization control circuit, properly locked to the laser PRF and shutter windowing time, always gates a test pulse through a known and fully open phase of the shutter cycle.

Witness sensors sample a portion of the collimated beam to monitor the irradiance levels on a pulse-to-pulse basis. Witness sensors should be selected to provide the largest collection area permissible while still maintaining sufficient rise time to faithfully permit pulse width measurements. Amplified witness sensor electrical pulses are captured on high-speed digitizing oscilloscopes for calculation of peak irradiance and pulse width. Radiometric calibrations in the test setup should include the photodetector, biasing, amplifiers, attenuators, and digitizers as a whole, and not rely solely on the photodetector manufacturer's detector calibrations.

Table controllers, oscilloscope data, laser firing, and receiver responses are all interfaced to a master computer. Data acquisition software manages the automation of table position, radiometry, laser firing, and receiver threat word interpretation. Where robust testing is desired, a solar simulator is shown that permits testing in intense solar background conditions. An atmospheric turbulence simulator is also shown for testing under atmospheric scintillation conditions.

1.8 TERMINOLOGY[d]

Aerosols: A two-phase system consisting of dispersed liquid or solid particles in a gas.

Amplitude division: Division of an electromagnetic beam into multiple beams by dividing the electromagnetic field into multiple parts and redirecting them into separate propagation paths, as accomplished by a "half-silvered" mirror.

[d]Some of these definitions are taken from standard dictionaries.[117]

The resultant individual beams all have the same scintillation-induced wavefront distortions at the plane of division.

Ascending node: The point on the line of nodes that the satellite passes through as it travels from below to above the equatorial plane.

Autocorrelation function: The convolution of a normalized one- or two-dimensional pattern with itself; an indication of spatial correlation between nearby intensity values in a background.

Bidirectional reflection distribution function: A function characterizing the directional reflective properties of a surface. It describes the fraction of radiation incident from a specified direction that is reflected into a unit solid angle centered about another specified direction as a function of incident and reflected angles from the surface normal.

Beam rider: A type of command-guided missile that flies along an electromagnetic beam deriving its guidance commands by means of a rear-looking receiver.

Binning: The process of coarse parametric measurement of laser (threat) parameters with the nonlinear parametric resolution tailored to distinguish among candidate threat categories.

Declaration: The output from a warning receiver processor that specifies a threat has been detected.

Deinterleaved: The process of separating multiple interleaved received pulse trains originating from separate sources, as in the radar warning receiver deinterleaving of pulse trains from individual radars prior to performing the individual threat characterizations.

Depth of modulation: The ratio of the maximum minus minimum light intensity to the sum of the maximum and minimum light intensity, namely, $m = (I_{\max} - I_{\min})/(I_{\max} + I_{\min})$.

Diffuse reflector: A reflecting surface that scatters radiation that is incident on it, thus producing diffuse reflection.

Directional reflectance: The fraction of incident radiation from a specific direction that is reflected into the hemisphere about the surface normal.

Dynamic range: The difference between the overload level and the minimum acceptable signal level in a system or transducer.

Excimer laser: A rare-gas halide or rare-gas metal vapor laser emitting in the ultraviolet (126 to 558 nm) that operates on electronic transitions of molecules.

Extinction coefficient: The coefficient α determining the exponential rate of attenuation of transmitted radiation with distance R when $(I/I_0) = \exp(-\alpha R)$.

Fabry-Pérot etalon: See Fabry-Pérot interferometer.

Fabry-Pérot interferometer: A multiple-beam interferometer consisting usually of two flat plates, with high reflectance.

False alarm: An erroneous target detection decision caused by noise or other interfering signals exceeding the detection threshold.

Field of regard: The total angular operational field of an optical system. For a gimballed system, the field of regard consists of the sensor field of view and the overall gimbal limits.

Field of view: The maximum area that can be seen through a lens or an optical instrument.

First-order spectra: The separate spectral lines formed by a diffraction grating that are characterized by one wavelength difference in path length between adjacent slits.

Fisheye lens: A type of lens that has a wide angular field.

Free-electron laser: A laser that produces stimulated emission by passing a beam of free—that is, not bound to an atom or molecule—electrons through an undulator or *wiggler*. The undulator creates a magnetic field of alternating polarity (in another version it guides the electrons along a helical path), causing the electrons to wiggle and thus radiate.

Gain margin: The allowance of additional system sensitivity to provide for maintaining the specified performance of a system despite the occurrence of various phenomena that may degrade its performance; as in a gain margin to allow for received power fluctuations resulting from atmospheric scintillation.

Graceful degradation: The concept of designing a system, or signal processor, such that its failure modes result in a gradual diminishment of capability rather than a catastrophic failure. As an example, allowing a warning receiver to designate an event with an indeterminate set of parameters as a possible threat, rather than as a nonthreat, if the processor determines that the parameters might have arisen from system saturation effects that could have been associated with a true threat.

In-phase: That state determining that two waves of like frequency will travel through their maximum and minimum values of the same polarity simultaneously.

Isotropic: Same for all directions.

Laser cavity: An optical resonant structure in which lasing activity begins when multiple reflections accumulate sufficient electromagnetic field intensity.

Latency: The time period between the initial acquisition of threat data by a warning receiver and its declaration that a threat exists.

Limiter circuits: A circuit of nonlinear elements that restricts the electric excursion of a variable in accordance with some specified criteria. Note that hard limiting is a limiting action with negligible variation in output in the range where the output is limited. Soft limiting is a limiting action with appreciable variation in output in the range where the output is limited.

Matched filter: A filter that maximizes SNR so that a waveform of known shape can be separated from random noise.

Measure of effectiveness: A parameter whose value gives some indication of the performance of the total system. Examples are probability of detection or false alarm rate.

Metamorphic snow: Snow that has been partially melted and refrozen, resulting in different radar and optical characteristics from fresh fallen snow. Also called refrozen snow.

Mie scattering: Scattering exhibited by particles about the same size as the wavelength of the radiation under consideration and with refractive index significantly different from that of the surrounding medium.

Monopulse: A radar technique in which information concerning the angular location of a source or target is derivable from each pulse or signal detection by comparison of signals received simultaneously in two or more antenna beams, as distinguished from techniques such as switching or scanning, in which angle information requires multiple pulses.

Noise equivalent irradiance: The radiant flux density (usually in watts per square meter) required for a system to produce an output signal equal to the noise; the input irradiance at which the SNR is unity.

Noise equivalent power: At a given modulation frequency, wavelength, and for a given effective noise bandwidth, the radiant power that produces an SNR of 1 at the output of a given detector.

Perigee: The least distant point from the center of the earth to an orbit around it.

Pixel: Contraction of picture element. A small element of a scene, often the smallest resolvable area, in which an average brightness value is determined and used to represent that portion of the scene.

Port scatter: Optical scatter from the fixtures, coatings, and optical lens at the output of a laser transmitter. Such scatter may be characterized by a low-intensity, wide-angle scattered beam with narrow specular components at random angles.

Pushbroom scanning: In imaging systems, a line of detectors scanned through object space by the motion of the platform.

Radiance: Radiant power per unit source area per unit solid angle. Usually it is expressed in $W\ m^{-2}\ sr^{-1}$.

Radiation efficiency: The ratio of (1) the total power radiated by an antenna to (2) the net power accepted by the antenna from the connected transmitter.

Rayleigh scattering: Scattering by particles very small compared to the wavelength of the radiation being considered. A feature of Rayleigh scattering is that the scattered flux is inversely proportional to the fourth power of the wavelength.

Reflectance: The ratio of the intensity of the total radiation reflected from a surface to the total incident on that surface.

Relaxation time: The time required for the deviation from equilibrium of some system parameter to diminish to $1/e$ of its initial value.

Rise time: Measurement of the time elapsed during the circuit output change from 10 to 90%.

Sensitivity: A measure of a receiver's (or detector's) ability to sense a small signal.

Sidelobes: A radiation lobe in any direction other than that of the intended lobe.

Slew rate: In general, the speed with which a system can execute a command to change its parametric state. For optomechanical systems this usually refers to angular position and is measured in degrees per second. For electronic circuits and components it refers to the speed with which the proper circuit output is established and is specified in terms such as volts per second.

Truth table: A table that describes a logic function by listing all possible combinations of input values and indicating the true output values for each combination.

Wavefront division: Division of an electromagnetic beam into multiple beams by directing adjacent portions of the beam through separate apertures. The resultant individual beams will have amplitude patterns and average intensities corresponding to the transverse amplitude distribution of the original beam at the plane of division and, hence, may be of dissimilar, random, intensity and spatial pattern.

White noise: The random noise having a spectral density that is substantially independent of the frequency over a specified frequency range.

References

1. R. P. Main, "Military lasers in Europe," *Lasers and Applications* **3**(6), pp. 85–89 (June 1984).
2. J. T. Lin, "New laser sources," in *Southcon/88 Conference Record,* Orlando, Florida, pp. 178–183 (1988).
3. F. X. Kneizys et al., "Atmospheric transmittance/radiance: computer code LOWTRAN 6," AFGL-TR-83-0187, Air Force Geophysics Laboratory, Hanscom Air Force Base, Massachusetts (1983).
4. C. I. Coleman, "Laser threat warning," *Proceedings of the Conference on Military Microwaves,* Brighton, England, pp. 21–26 (1986).
5. D. H. Pollock, "An introduction to electro-optical warfare," *Signal* **38**(8), 35–38 (April 1984).
6. David E. Schmieder, Georgia Tech Research Institute, Atlanta, GA, private communication (1992).
7. C. B. Ludwig et al., *Handbook of Infrared Radiation from Combustion Gas,* NASA SP-3080 (1973).
8. Richard D. Hudson, *Infrared System Engineering,* John Wiley & Sons, New York (1969).
9. W. E. Schnieder and G. H. Spaberg, "UV spectroradiometric output of an F404 turbojet," *Proceedings of the SPIE* **1109,** 169–185 (1989).
10. P. W. Kruse and L. D. McGlauchlin, *Elements of Infrared Technology: Generation, Transmission, and Detection,* John Wiley & Sons, New York (1962).
11. Dennis Blay, General Dynamics, Pomona, CA, private communication (1991).
12. M. Haney and D. Psaltis, "Measurement of the temporal coherence properties of pulsed single-mode laser diodes," *Applied Optics* **24**(13), 1926–1932 (1985).
13. M. Born and E. Wolf, *Principles of Optics,* 6th ed., Pergamon Press, New York (1985).
14. A. S. Marathay, *Elements of Optical Coherence Theory,* John Wiley & Sons, New York (1982).
15. L. Mandel and E. Wolf, "Coherence properties of optical fields," *Reviews of Modern Physics* **37,** 231 (1965).
16. M. J. Baron and G. B. Parrent, *Theory of Partial Coherence,* Prentice-Hall, New York (1964).
17. *1989 Laser Focus World Buyers Guide,* 24th ed., Tulsa, OK (1989).
18. W. J. Smith, *Modern Optical Engineering,* p. 138, McGraw-Hill, New York (1966).

19. J. C. Slater and N. H. Frank, *Electromagnetism,* p. 182, Dover, New York (1969). Original publication McGraw-Hill, 1947.
20. G. N. Watson, *Theory of Bessel Functions,* 2nd ed., Macmillan, New York (1945).
21. P. O. Overfelt and C. S. Kenney, "Comparison of the propagation characteristics of Bessel, Bessel-Gauss, and Gaussian beams diffracted by a circular aperture," *Journal of the Optical Society of America* **8**(5), 732–745 (1991).
22. D. R. Bjork, K. A. Klicker, and F. M. Cady, "Predicting laser port scatter," *Proceedings of the SPIE* **967,** 58–61 (Aug. 1988).
23. H. P. Smith et al., *FASCODE—Fast Atmospheric Signature Code (Spectral Transmittance and Radiance),* Air Force Geophysics Laboratory Report AFGL-TR-78-0081 (Jan. 1978).
24. L. S. Rothman et al., "The HITRAN database," *Applied Optics* **26**(19), 4058–4097 (1987).
25. F. X. Kneizys et al., "User's guide to LOWTRAN 7," AFGL Technical Report, TR-88-0177 (Aug. 1988).
26. E. M. Patterson and J. B. Gillespie, "Simplified UV and visible atmospheric propagation model," *Applied Optics* **28**(3), 425–429 (1989).
27. A. D. Sheffer et al., *GTVISIT Analyst Manual,* Georgia Tech Research Institute, Electro-Optics Laboratory, Atlanta (1991).
28. G. A. Findlay and D. R. Cutten, "Comparison of 3-5 and 8-12 micron IR systems," *Applied Optics* **28**(23), 5029 (1987).
29. L. J. Pinson, *Electro-Optics,* John Wiley & Sons, New York (1988).
30. F. X. Kneizys et al., "Linear absorption and scattering of laser beams," AFGL Technical Report No. TR-84-065 (Sep. 1984).
31. *RCA Electro-Optics Handbook,* Technical Series EOH, RCA Corporation, Harrison, NJ (1974).
32. E. M. Patterson, Georgia Tech Research Institute, Atlanta, private communication (1990).
33. A. Ishimaru, *Wave Propagation and Scattering in Random Media,* Academic Press, New York (1978).
34. A. Zardecki and A. Deepak, "Forward multiple scattering corrections as a function of detector field of view," *Applied Optics* **22**(19), 2970–2976 (1983).
35. L. R. Bissonnette, "Multiscattering model for propagation of narrow light beams in aerosol media," *Applied Optics* **27**(12), 2478–2484 (1988).
36. M. V. Kabanov et al., "Statistical model of directed light-scattering coefficients of coastal haze," *Journal of the Optical Society of America A* **2**(10), 1735–1738 (1985).
37. John C. Stover, *Optical Scattering Measurement and Analysis,* McGraw-Hill, New York (1990).
38. J. W. Strohbehn, Ed., "Laser beam propagation in the atmosphere," in *Topics in Applied Physics,* Vol. 25, Springer-Verlag, Berlin (1978).
39. W. K. Pratt, *Laser Communication Systems,* John Wiley & Sons, New York (1968).
40. P. H. Deitz, "Near earth propagation of optical beams," *Electronic Communicator* **2**(5), 15 (1967).
41. V. P. Kostin, "Assessment of the relative increase in laser power needed to compensate for atmospheric modulation noise," *Radiotekhnika* (1), 84–85, UDC 621.391.16 (Feb. 1987).
42. J. I. Davis, "Consideration of atmospheric turbulence in laser systems design," *Applied Optics* **5**(1), 139–147 (1966).
43. G. S. Campbell, *An Introduction to Environmental Biophysics,* Springer-Verlag, New York (1977).
44. H. Rose et al., "The handbook of albedo and thermal earthshine," ERIM, Ann Arbor, MI, Report 190201-1-T (1973).
45. United States Air Force, AFWAL, *Camouflage Handbook,* AFWAL-TR-86-1028 (1986).
46. R. B. Goldman and W. R. Owens, "Infrared signatures of land combat vehicles and environmental background," Report AFATL-TR-80-29 (1980).
47. Sherwood B. Idso and W. L. Ehrler, "Estimating soil moisture in the root zone of crops: a technique applicable to remote sensing," *Geophysics Research Letter* **3**(1), 23–25 (1976).
48. G. D. Kinzer and R. Gunn, "Evaporation, temperature, and thermal relaxation times of freely falling raindrops," *Journal of Metrology* **8**(2), 71–83 (1951).
49. C. Cox and V. Munk, "Measurements of the roughness of the sea surface," *Journal of the Optical Society of America* **44,** 838 (1954).

50. Marvin Cloud, "Contrast prediction model, user's manual," Analytics, Report for Contract F08635-83-C-0337 (1986).
51. Mikael Bramson, *Infrared Radiation, A Handbook for Applications,* Plenum Press, New York (1968).
52. K. Masuda et al., "Emissivity of pure & sea waters for IR model sea surfaces," *Remote Sensing in the Environment* **24,** 313 (1988).
53. H. W. O'Brien et al., "Red and near infrared spectral reflections of snow," U.S. Army Cold Region Research and Engineering Lab, Hansom, NH, CRREL, AD-A007732 (1975).
54. G. G. Gimmestad and Q. B. Zhou, "Directional IR optical measurements of natural snow surfaces," in *Proceedings of the Beijing International Symposium on Remote Sensing,* Beijing, China Association for Science and Technology, pp. 659–684 (Nov. 1986).
55. E. E. Bell, L. Eisner, J. Young, and R. A. Oetjen, "Spectral radiance of sky and terrain at wavelengths between 1 and 20 microns. II. Sky measurements," *Journal of the Optical Society of America* **50,** 1313–1320 (Dec. 1960).
56. Sherwood B. Idso, "A set of equations for full spectrum and 8–14 and 10.5–12.5 micron thermal radiation from cloudless skies," *Water Resources Research,* **17,** 295–304 (1981).
57. M. Martin and P. Berdahl, "Summary of results from spectral and angular sky radiation measurements," *Solar Energy* **33,** 241 (1984).
58. Y. P. Novosetsev, "Spectral reflectivity of clouds," *Spektrolnaya Otrazhatelnaya Oblakov* **152,** 186–191 (1964). (Translation by National Aeronautics and Space Administration, Washington, DC, NASA TT F-328.)
59. D. E. Schmieder and M. R. Weathersby, "Detection performance in clutter with variable resolution," IEEE *Transactions on Acoustics, Speech, and Signal Processing* **19**(4), 622 (1983).
60. D. L. Fried and R. D. Williams, "Signal processing for clutter rejection in quasi-staring sensor," *Proceedings of the SPIE* **197,** 48 (1979).
61. M. C. Hetzler, Georgia Tech Research Institute, Atlanta, GA, private communication (1988).
62. Lee K. Balick and Edwin L. Doak, "Directional effects on scene complexity in oblique thermal imagery and photographs of a deciduous forest," *Applied Optics* **27**(19), 3978 (1988).
63. N. Ben-Yosef, private communication presented in "Infrared clutter in thermal images: ground terrain," Tutorial T-21, SPIE (Feb. 1988).
64. M. A. Uman, *Lightning,* McGraw-Hill, New York (1969).
65. D. F. Smart and M. A. Shea, "Galactic cosmic radiation and solar energetic particles," in *Handbook of Geophysics and the Space Environment,* A. S. Jursa Ed., Air Force Geophysics Laboratory, National Technical Information Service, Springfield, VA, AD-A167000 (1985).
66. S. O. Rice, "Mathematical analysis of random noise," in *Selected Papers on Noise and Stochastic Processes,* N. Wax, Ed., Dover, New York (1954).
67. L. A. Williams, Jr., "Spectral discrimination for long range search/track infrared systems," *Proceedings of the SPIE* **292** (1981).
68. S. Watanabe, *Pattern Recognition, Human and Mechanical,* John Wiley & Sons, New York (1985).
69. D. H. Pollock, "Clutter rejection for infrared surveillance sensors," *Proceedings of the SPIE* **292,** 180–192 (1981).
70. C. W. Helstrom, *Statistical Theory of Signal Detection,* 2nd ed., Pergamon Press, New York (1968).
71. B. R. Hunt and T. M. Cannon, "Nonstationary assumptions of Gaussian models of images," *IEEE Transactions on Systems, Man and Cybernetics* 876–882 (Dec. 1976).
72. J. W. Strohbeln, Ed., "Laser beam propagation in the atmosphere," in *Topics in Applied Optics,* Vol. 25, Springer-Verlag, New York (1978).
73. D. L. Fried et al., "Measurements of laser-beam scintillation in the atmosphere," *Journal of the Optical Society of America* **57**(7), 787–797 (1967).
74. R. J. Hill et al., "Measured statistics of laser beam scintillation in strong refractive turbulence relevant to eye safety," *Health Physics* **53**(6), 639–647 (1987).
75. R. G. Frehlich and J. H. Churnside, "Probability density function for estimates of the moments of laser scintillation," *Proceedings of the SPIE* **926,** 32 (1988).
76. J. W. Strohbeln, Ed., "Laser beam propagation in the atmosphere," in *Topics in Applied Optics,* Vol. **25,** p. 60, Springer-Verlag, New York (1978).

77. J. H. Churnside, "Aperture averaging of optical scintillations in the turbulent atmosphere," *Applied Optics* **30**(15), 1982–1994 (1991).

78. C. D. Hodgman, *Handbook of Chemistry and Physics,* 42nd ed., The Chemical Rubber Publishing Co., Cleveland, OH (1960).

79. R. Illing, et al., "Image motion compensation using photon counting UV detector," *Proceedings of the SPIE* **932,** 246 (1988).

80. American Institute of Physics, "Directed energy weapons—CH 7, acquisition, tracking, and discrimination," *Reviews of Modern Physics* **59**(3), S145–S168 (1987).

81. D. Casasent et al., "Subpixel target detection and tracking," *Proceedings of the SPIE* **726,** 206–220 (1986).

82. C. David Wang, "Adaptive spatial/temporal/spectral filters for background clutter suppression and target detection," *Optical Engineering* **21**(6), 1033–1038 (1982).

83. T. J. Patterson et al., "Image processing for target detection using data from a staring infrared mosaic sensor in geosynchronous orbit," *Optical Engineering* **25,** 166–172 (1986).

84. K. J. Button and J. C. Wiltse, *Infrared and Millimeter Waves,* Vol. 4, Academic Press, New York (1981).

85. Darryl T. Gehly, "It's decision time for missile warning," *Journal of Electronic Defense* **14**(8), 33–39 (1991).

86. N. Bloembergen et al., "The science and technology of directed energy weapons," *Reviews of Modern Physics* **59**(2), S1–S201 (July 1987).

87. Curtis D. Cochran, Dennis M. Gorman, and Joseph D. Dumoulin, Eds., *Space Handbook,* Air University Press, Maxwell Air Force Base, AL (1985).

88. Roger R. Bate, Donald D. Mueller, and Jerry E. White, *Fundamentals of Astrodynamics,* Dover, New York (1971).

89. Wayne K. Davis, "Conceptual design and requirements of a pushbroom focal plane," in *Technical Issues In Focal Plane Development, Proceedings of the SPIE* **282,** 29–33 (1981).

90. *Advanced Scanners and Imaging Systems for Earth Observations,* NASA SP-335, Scientific and Technical Information Office, NASA, Washington, DC (1973).

91. W. B. Birtley, O. K. Kowallis, L. A. Molnar, T. J. Wright, "Development of Teal Ruby experiment radiometric requirements," *Proceedings of the SPIE* **282,** 15–28 (1981).

92. "Tracor receives trio of laser warning awards," *Journal of Electronic Defense,* p. 22 (Jan. 1990).

93. "Perkin-Elmer will build first military laser warning receiver," *Aviation Week & Space Technology,* p. 81 (Sep. 19, 1988).

94. E. Newsom and M. Neer, private communication, SciTec Inc., Princeton, NJ (Feb. 1991).

95. H. C. Van de Hulst, *Light Scattering by Small Particles,* John Wiley & Sons, New York (1957).

96. D. Deirmendjian, *Electromagnetic Scattering of Spherical Polydispersions,* RAND Corporation Report R-456-PR, American Elsevier Publishing, New York (1969).

97. S. A. Clough et al., "Atmospheric spectral transmittance and radiance: FASCODE 1B," *Proceedings of the SPIE* **277,** 151 (1981).

98. S. A. Clough et al., "FASCODE3: spectral simulation," in *Proceedings of the IRS '88: Current Problems in Atmospheric Radiation,* pp. 372–375 (1988).

99. R. C. Shirkey et al., *EOSAEL 87: Vol I, Executive Summary,* Army Atmospheric Sciences Laboratory, White Sands Missile Range, NM, Report ASL-TR-0221-1 (Oct. 1987).

100. J. Bastian, E. Blish et al., private communication, Ball Systems Engineering Division, Fairborn, OH (Feb. 1991).

101. E. P. Shettle and R. W. Fenn, *Models for the Aerosols of the Lower Atmosphere and the effects of Humidity Variations on Their Optical Properties,* U.S. Air Force Geophysics Laboratory Report AFGL-TR-79-0214 (Sep. 1979).

102. H. W. Ott, *Noise Reduction Techniques in Electronic Systems,* John Wiley & Sons, New York (1976).

103. R. Crane, Jr., "Laser detection by coherence discrimination," *Optical Engineering* **18**(2), 212–217 (1989).

104. E. T. Seibert, "Analyzer for coherent radiation," U.S. Patent 4,536,089 (Aug. 20, 1985).

105. W. T. Krohn et al., "Coherent radiation detecting apparatus," U.S. Patent 4,600,307 (July 15, 1986).

106. C. J. Duffey and D. Hickman, "A temporal coherence-based optical sensor," *Sensors and Actuators,* **18,** 17–31 (1989).

107. C. J. Duffey and D. Hickman, "An imaging system based on temporal coherence differences," *Journal of Physics D: Applied Physics* **21,** S56–S58 (1988).

108. P. Sutton, "A novel electro-optical remote-sensing technique based on bandpass coherence processing," *Journal of Physics D: Applied Physics* **22,** 379–384 (1989).

109. J. Jannson, T. Jannson, and E. Wolf, "Spatial coherence discrimination in scattering," *Optics Letters* **13**(12), 1060–1062 (1988).

110. E. T. Seibert, "Analyzer for coherent radiation," U.S. Patent 4,309,108 (Jan. 5, 1982).

111. F. Bartoli et al., "A generalized thermal model for laser damage in detectors," *Journal of Applied Physics* **47,** 2875–2881 (1976).

112. M. Kruer et al., "Laser damage in silicon photodiodes," *Optical and Quantum Electronics* **8,** 453–458 (1976).

113. R. S. Hughes, *Logarithmic Amplification,* Artech House, Norwood, MA (1986).

114. M. Neer, SciTec, Princeton, NJ, included in "Laser warning receiver methodology report," Defense Research Establishment Valcartier, Courcelette, Quebec (May 1991).

115. J. H. Parker, USAF Wright Laboratories, Dayton, OH, included in "Laser warning receiver methodology report," Defense Research Establishment, Valcartier, Courcelette, Quebec (Oct. 1991).

116. J. H. Parker, "Reflective membrane scintillation for laser receiver diagnostics," in *Proceedings of the SPIE* **999,** 281–297 (1988).

117. *The Photonics Dictionary,* Laurin Publishing, Pittsfield, MA (1991); *IEEE Standard Dictionary of Electrical and Electronics Terms,* John Wiley & Sons, New York (1978).

CHAPTER 2

Camouflage, Suppression, and Screening Systems

David E. Schmieder
Georgia Tech Research Institute
Atlanta, Georgia

Grayson W. Walker*
U.S. Army Belvoir Research, Development and Engineering Center
Fort Belvoir, Virginia

CONTENTS

*Author of Section 2.6.

2.1 INTRODUCTION

This chapter addresses the subject of low observables. It is a special application and extension of the scientific and engineering principles discussed in other chapters and volumes of this handbook. Examples of related topics include radiometry, detection theory, optical properties of materials, detection devices, atmospheric effects, and radiation sources. Many of those principles are repeated here in the special context of this application. However, the reader may find it useful to refer to those topics in other parts of the Handbook for supplementary treatments.

Table 2.1 gives the symbols, descriptions, and units for the terms that are used in this chapter.

Efforts to control signatures usually result in encountering some common terms such as camouflage, screening systems, signature suppression, low observable (LO), and very low observable (VLO). Most of these terms mean nearly the same thing. However, there are some differences that warrant clarification. The term *camouflage* is derived from the French word *camoufler,* which means to disguise. Thus, camouflage is the means by which an object is concealed by disguising and changing its appearance. Historically, camouflage has meant visible paint schemes, background matched nets, and leaf covers. A *screening system* usually implies camouflage in the form of a net. The terms *signature suppression* and *low observable* have evolved more recently to describe the concept of camouflage extended beyond the visible to multiple waveband regions. Finally, the term *very low observable* has emerged to describe platforms designed from the start to include low observable features as a major design goal rather than as a retrofit capability. These VLO vehicles typically achieve much lower signature levels.

2.2 TARGET SIGNATURES AND THREAT SENSORS

Low observable designs are driven by signature generation mechanisms and threat sensor characteristics. Unfortunately the signature generation process is complex in that it is driven not only by the vagaries of target emissions, but also by the vagaries of the immediate target background as well. The design process is even more demanding when it is realized that those generation mechanisms result in dramatically different results in different portions of the infrared spectrum and with differing levels of spatial detail. Definition of threat sensor types, with their operating bands and resolution capability, helps to focus signature control on the spectral regions and spatial dimensions of greatest interest. This section briefly addresses the major source generation processes. It also describes the key threat sensors, their operating bands, and their resolution implications.

Target signature generation mechanisms are of greatest interest when addressed in terms of discriminants. Discriminants are features that serve to separate the target signature from other confusing background objects. Signatures should include the composite of all discriminants. However, because the mechanisms potentially available for separation are numerous, signature description becomes complicated if it must accommodate all of them. Furthermore, the worst of it is that not all detection mechanisms of all sensors—

Table 2.1 Symbols, Nomenclature, and Units

Symbols	Nomenclature	Units
A	Area	cm^2
a	Absorbed fraction of incident irradiance	—
c	Velocity of light	cm s^{-1}
E_i	Incident irradiance	W cm^{-2}
E_r	Reflected irradiance	W cm^{-2}
f_r	Target in-band BRDF	sr^{-1}
H	Panel altitude above ground level	m
h	Planck's constant	W s^2
I	Plume radiant intensity	W sr^{-1}
I_o	Plume radiant intensity normalization value	W sr^{-1}
J_N	Normalized spectral radiant intensity	W sr^{-1} cm
J_o	In-band radiant intensity	W sr^{-1}
J_o'	Plume radiant intensity normalization value (same as I_o)	W sr^{-1}
j	Number of molecular oscillator frequencies	—
k_o	Absorption coefficient	m^{-1}
L	Directional radiance	W cm^{-2} sr^{-1}
L_r	Reflected radiance	W cm^{-2} sr^{-1}
L_b	Incident background radiance	W cm^{-2} sr^{-1}
L_{BB}	Planck blackbody radiance function	W cm^{-2} sr^{-1} μm^{-1}
L_{BBI}	Target blackbody radiance in-band	W cm^{-2} sr^{-1}
L_o	Immediate target background radiance	W cm^{-2} sr^{-1}
M	Mach number	—
m_e	Reduced mass	g
N	Number of atoms per unit volume	m^{-3}
NEI	Noise equivalent irradiance	W cm^{-2}
n_i	Index of refraction imaginary part	—
n_p	Refractive index of pigment	—
n_b	Refractive index of binder	—
n_c	Complex index of refraction	—
n_r	Index of refraction real part	—
P_i	Incident power	W
P_r	Reflected power	W
P_t	Total pressure	lb $in.^{-2}$
q_e	Charge on an electron	C
R	Range	cm
r	Recovery factor	—
SNR	Signal-to-noise ratio	—
s	Scattering coefficient	m^{-1}
T	Target surface absolute temperature	K
T_A	Spectral atmospheric transmission	—
T_a	In-band atmospheric transmission	—
T_o	Ambient air temperature	K
T_s	Skin temperature	K

Table 2.1 *(continued)*

Symbols	Nomenclature	Units
T_t	Total temperature	°F
ΔT	Panel temperature difference relative to ambient air temperature	°C
V	Velocity	ft^{-1}
$\propto$	Panel tilt angle	deg
γ_e	Free electron damping constant	—
γ_j	Bound electron damping constant	—
$\tilde{\nu}$	Wavenumber	cm^{-1}
λ	Wavelength	μm
ε	Emissivity	—
ε_d	Directional emissivity	—
ε_i	Target in-band directional emissivity	—
ε_o	Permittivity of free space	$C^2\ N^{-1}\ m^{-2}$
ε_r	Required emissivity	—
θ	Ray angle	rad
θ_i	Angle of incidence	rad
θ_r	Angle of reflectance	rad
ρ	Reflected fraction of incident irradiance	—
ρ_d	Total directional reflectance	—
ρ_{d1}	Target total directional reflectance	—
$\rho_\perp$	Amplitude reflectivity with electric field vector perpendicular to plane of incidence	—
$\rho_\parallel$	Amplitude reflectivity with electric field vector parallel to plane of incidence	—
τ	Transmitted fraction of incident irradiance	—
ϕ	Ray angle	rad
ϕ_i	Angle of incidence	rad
ϕ_r	Angle of reflectance	rad
Ω	Solid angle	sr
Ω_i	Solid angle of incidence	sr
Ω_r	Solid angle of reflectance	sr
ω	Angular frequency	$rad\ s^{-1}$
ω_{oj}	Molecular oscillator natural frequency	Hz

the human eye/brain is one example—are fully understood. If the detection mechanisms are not fully understood, it is difficult to describe the target features needed by those mechanisms.

Fortunately, these signature definition problems are manageable with the aid of various simplifying assumptions that can be tailored to fit various categories of threat sensors. One of the more common divisions is the separation based on so-called *imaging* versus *nonimaging* sensors. Imaging sensors are represented by the human eye and aids such as televisions, FLIRs (forward-looking infrared), and image intensifiers. These threats differ from nonimaging

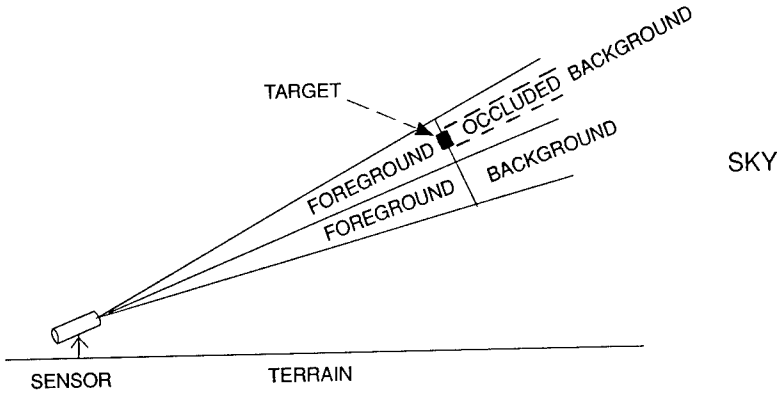

Fig. 2.1 An infrared contrast signature is the difference in radiation between a sensor pixel containing the unresolved target and an adjacent pixel.

sensors primarily in their ability to resolve and process silhouette and internal target pattern detail. Nonimaging sensors, on the other hand, typically see very little pattern detail and depend on target signal strength and coarse dimensions for background separation. Examples of the latter are conventional reticle missile seekers, IRSTs (infrared search and track), and terminally guided submunitions. The separation between signatures based on sensor is not clean because imaging sensors can be effective against targets at ranges beyond their ability to resolve detail. Ultimately, however, the definition of signature depends on whether the target will be resolved or unresolved in the signature suppression application.

Unresolved signatures are easiest to describe. They result simply from the difference between the signal received, in the sensor's instantaneous field of view, with the target present compared to that received with the target absent. The definition is illustrated in Fig. 2.1. Suppression design requires that the total radiation occluded by the target be supplied by the target. Spatial distribution of target emissions is not as important as the spatially integrated total emission level. The suppression goal is to minimize overall target contrast.

Resolved signatures are much more difficult to describe because of the importance of their spatial properties. They result from a long list of pattern-related features. Those features include not only the patterns of major recognizable components (wings, tails, turrets, hull, etc.) but also the texture internal to the components. Suppression design requires that such features be disguised. Successful disguises are those that eliminate recognizable shapes by redefining them and blending them into the background. The suppression goal is pattern deception.

2.2.1 Aircraft Signatures

Aircraft signatures are a composition of many processes. Any one of those processes can dominate in a given engagement scenario. Figure 2.2(a) shows the various generation mechanisms at work, whereas Fig. 2.2(b) shows example results in the 3- to 5-μm spectral band.[1] Four generation mechanisms

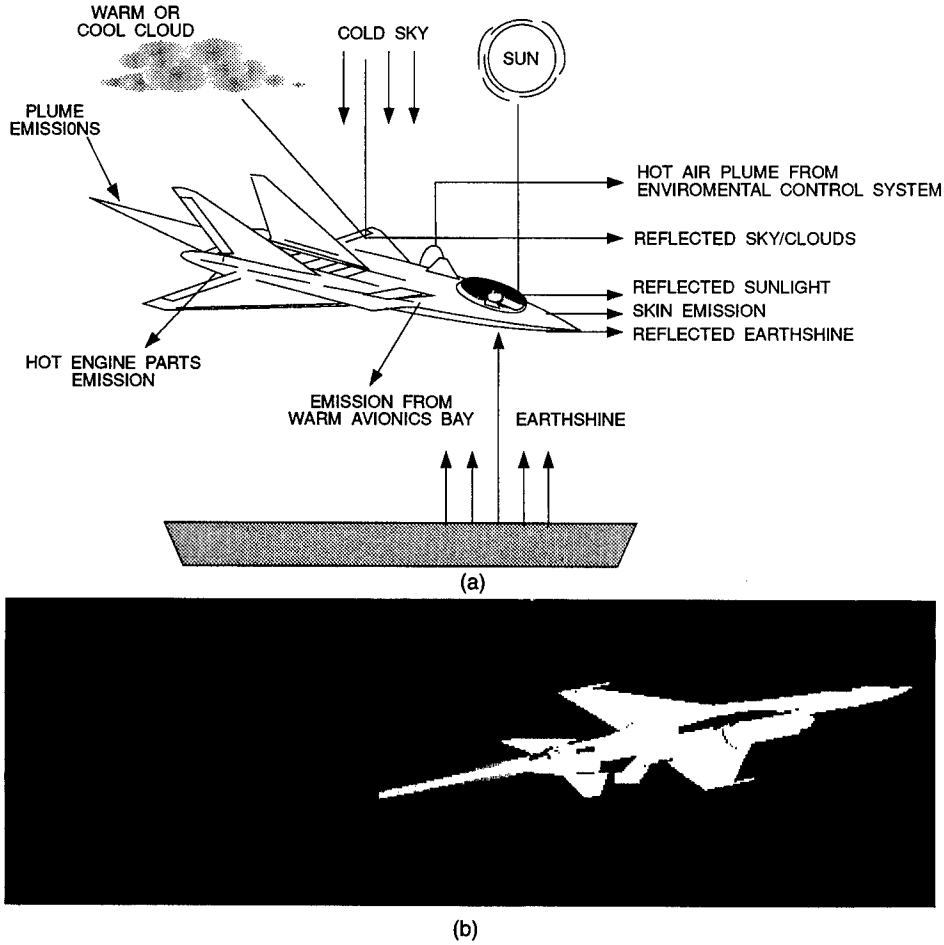

Fig. 2.2 (a) Aircraft IR signature elements. (b) Illustration of F-16 aircraft signature in the 3- to 5-μm spectral band as predicted by the IASPM computer code.[1] (Photo provided courtesy of Horizon Technology, San Diego, CA.)

show up clearly in the infrared photo of a jet fighter in Fig. 2.2(b). First, hot exhaust gases are clearly visible from the engine nozzle. Second, internally generated engine heat is seen as it conducts out to warm the outer aircraft skin. Third, the top of the aircraft is dark as a result of reflecting the cold sky off the top of the fuselage. Finally, the bottom of the fuselage appears to be warm because of reflections of the warm ground and horizon sky off the highly reflecting skin. Note that if that same aircraft skin were to have been coated with a low-reflectance, high-emissivity paint, the fuselage would have appeared uniformly white because of aerodynamically generated skin heating.

Of course, these are not the only mechanisms that can show up or even dominate the aircraft signature generation process. In the same 3- to 5-μm region, sun reflections can cause glint and glare. In the ultraviolet and visible spectral regions, the aircraft can appear to be a dark silhouette against a uniformly bright sky background. In the visible and near-infrared regions it

can also appear to be a positive, sunlit form against a darker sky background. Finally, in the nominal 1- to 3-μm region, the target can appear, at night, to be merely a circular two-dimensional disk because only the outlines of the hot nozzle can be seen when viewed from the rear in that band. (There is a contribution from hot water vapor in the combustion products, but it is strongly attenuated by water vapor in the atmosphere under nonafterburning engine conditions.) Ultimately, the target appearance that the suppression designer cares about is that seen by the threat sensor.

Threat sensors can more narrowly define the generation mechanisms of interest by their operating spectral bands. Table 2.2 summarizes the threats of concern for aircraft and shows their nominal spectral bands.

Visible band threats include the unaided eye and television sensors. The unaided eye is a threat in the form of acquisition and fire control for antiaircraft artillery (AAA) and airborne guns. Television sensors are used in the same way and cover the visible spectrum, but also respond in the near infrared when equipped, for example, with silicon sensors.

Infrared missile seekers are dominated by the response of cooled and uncooled lead sulfide (PbS) and lead selenide (PbSe) and cooled indium antimonide (InSb). Uncooled PbS equipped seekers, filtered to the 1.9- to 2.9-μm band, are spectrally well matched to jet engine hot tail pipe emissions, visible largely from the aircraft rear. However, when unfiltered, they respond over the larger passband of 0.7 to 3.0 μm and receive more significant solar reflections off the aircraft body. The latter are a result of both direct solar illumination of the target and indirect sky illumination from atmospheric scattering. More recent generation IR missile seeker threats use the 3- to 5-μm passband. The 3- to 5-μm band threats have the advantage of all aspect target lock-on ability. This ability results first from the strong plume emissions visible in that band and from skin emissions. Plume emissions extend well beyond the body and can be seen with little obscuration over all, but near nose-on, viewing angles. Body emissions also provide all-aspect lock-on capability. Here earthshine and self-emissions resulting from aerodynamic skin heating provide the body signature source. Future threat seekers are likely to use imaging focal plane arrays made of either silicon or platinum-silicide for spectral responses in the 0.4- to

Table 2.2 Aircraft Threat Types and Spectral Bands

Threat Type	Nominal Bands (μm)
Unaided eye	0.4–0.7
Television	0.4–0.7 0.4–1.1
Infrared missile seekers	1.9–2.9 0.7–3.0 1.0–4.0 3–5
Infrared search and track	3–5 8–12
Forward-looking infrared	8–12 3–5

1.1- and 1- to 5-μm bands, respectively, indium antimonide for the 3- to 5-μm band, and mercury cadmium telluride for the 8- to 12-μm band.

Infrared search and track (IRST) systems work mostly in the same 3- to 5-μm band as do missile seekers and look for the same signature sources. Older sensors used moderately cooled lead salt detectors (PbS/PbSe), which could get response in the nominal 1- to 5-μm band, but with poor sensitivity. The latter detectors were more dependent on solar reflections and engine hot parts than on plume and skin self-emissions. Future systems may include the 8- to 12-μm band, in addition to the 3- to 5-μm band, in an effort to obtain more skin signature.

Forward-looking infrared (FLIR) sensors are primarily used for target acquisition, including detection and recognition, with an operator. These systems are presently dominated by 8- to 12-μm mercury cadmium telluride (HgCdTe) detectors. Future FLIRs may use focal plane arrays that respond in either the 3- to 5- or the 8- to 12-μm bands.

The highest priority threat band for aircraft signature suppression is the 3- to 5-μm band. Engine signature generation mechanisms dominate at close ranges in this band. Multiple aspect aircraft target spectral signatures[2] are shown in Fig. 2.3. From the rear, a combination of graybody emissions from hot exhaust parts and plume line emissions are seen. Toward the front of the aircraft, hot parts become obscured, and the composite signature is dominated by the plume.

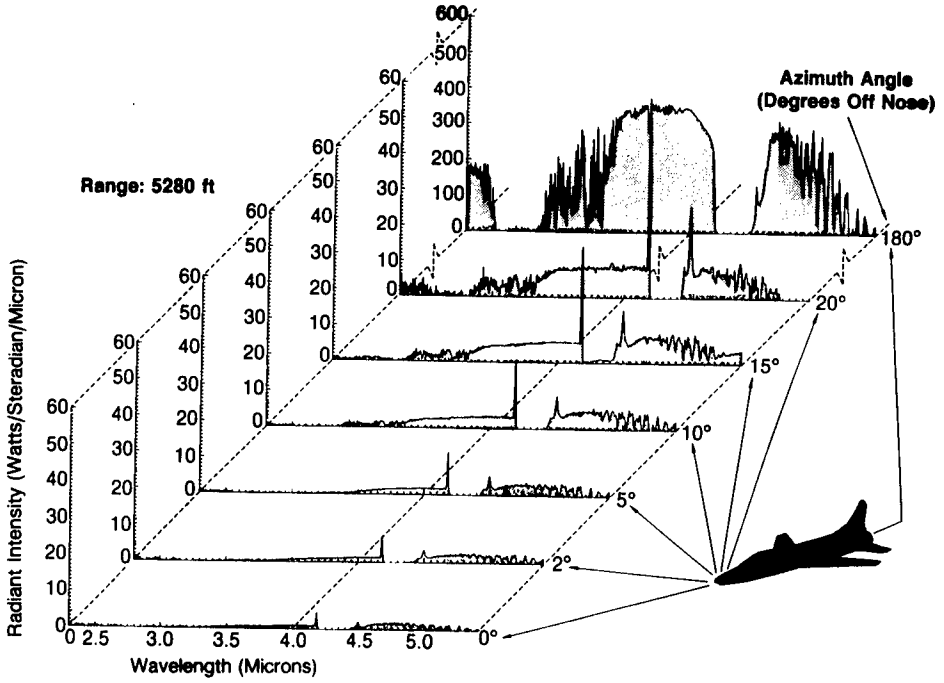

Fig. 2.3 Variation of aircraft spectral signatures over aspect angle.[2]

Plume emissions are arguably the highest priority source for aircraft suppression design. This is because plumes offer a near-all-aspect signature and, at the same time, provide a unique spectral distribution that separates them from natural background clutter. Plume signatures are predictable from the spectroscopy of gases. Reference 3 describes the characteristic line emissions resulting from combustion products and discusses their generation mechanisms. However, large quantities of high spectral resolution measurement data are also available. Much of the data presented here originates from the unpublished data collected by Dennis Blay and his associates at General Dynamics, Valley Systems Division, Ontario, California.

While plume signatures are potentially dominant, they are heavily attenuated by the atmosphere. Figure 2.4 shows the appearance of the plume spectra at various propagation ranges. It is often of interest to be able to compute

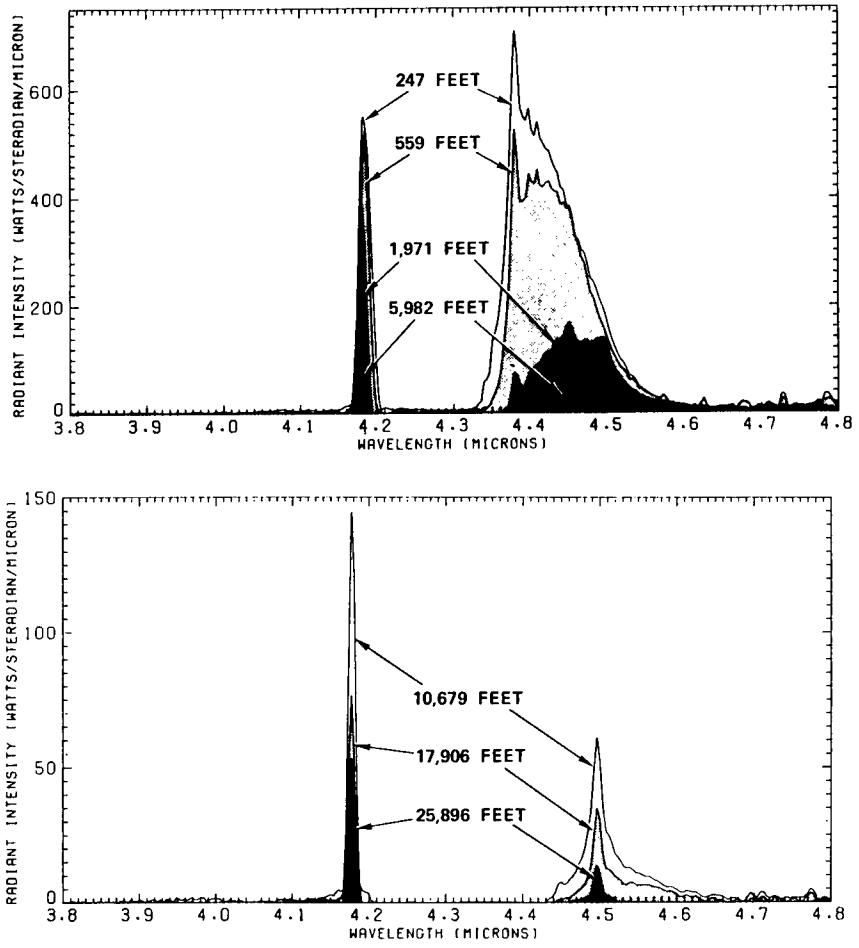

Fig. 2.4 Variation of plume spectra with propagation range.[2] (Temperature: 71°F; humidity: 18%; H_2O concentration: 0.35 cm/km; altitude: 2160 ft; date: 3-29-71.)

plume spectral signatures under other conditions, atmospheric conditions, and slant paths by using one of the atmospheric transmission computer models, such as Lowtran.[4] This is difficult to do from plots of engine plume spectra because of the extreme accuracy required relative to absorption/emission band edges. Plots typically cannot be read with sufficient accuracy for purposes of further analysis. Table 2.3 shows tabular values of representative unsuppressed turbine engine spectra that may be useful for such applications. Section 2.5 gives examples of corresponding suppressed plume data and shows how such tabular data can be used to predict propagated signatures.

The values in Table 2.3 are measured data[2] recorded for a Skyhawk Wright J65-W-4 turbojet plume operating under conditions of 100% throttle, nonafterburning, with an associated exhaust gas temperature (EGT) of between 650 and 680°C. This engine produces a static thrust of 7800 lb. The aircraft was mounted for static operation on a ground test stand at an altitude of 2160 ft above sea level. Care was taken in these side aspect measurements to exclude airframe body and engine hot parts contributions. Measurements were taken at a range of 247 ft. The data includes atmospheric attenuation effects over that range but excludes background radiation, i.e., the data represent target-to-background contrast. (Note that wavelength intervals are nonuniform to preserve key features while using a minimum number of data points.)

Plume spectra can differ greatly for different engines, cycles, operating conditions, and environments. However, these data are representative of plume spectra at this temperature and can be used for signature propagation estimation purposes. Note, however, that gas temperature has a major impact on both plume source intensity and propagation effects. Lowering plume temperature can dramatically reduce both intensity and propagation distance. For that reason, plume temperature reduction is a major focus in the design of suppressed signature turbine engines. These latter effects are discussed in more detail in Sec. 2.5.

An important issue regarding plume propagation is how much spectral resolution is required. A "rule of thumb" that has been used[2] is that the atmospheric transmission model should use a resolution level comparable to the resolution of the measurement data. If the analyst wants to avoid a high-resolution calculation, he should first "thin" the data by averaging spectral intensity values over the resolution band of interest and then operate his transmission model at that thinned resolution. Mismatches between measurement data resolution levels and propagation resolution can result in large computation errors. When matched, however, it is estimated that plume and transmission model resolution levels as low as 20 cm^{-1} can be used with a band average plume intensity error of 20% or less in most circumstances.

Even if there were no signature contributions resulting from the propulsion system, sources associated with aircraft skins would still present large apparent emissions. This is mostly caused by aerodynamically heated skin radiance, solar loading, and reflections of the surrounding environment. Methods for assessing reflections are discussed in Sec. 2.3. Solar loading is offset by convective cooling above speeds of approximately Mach 0.2. Aerodynamic skin heating and convective cooling are the dominant remaining concerns.

Aerodynamic skin heating results from the friction of air molecules as they come to rest on the surface. It is balanced by convective, conductive, and

Table 2.3 Measured Values of Turbine Engine Spectral Radiant Intensities (from Ref. 2)

WAVELENGTH (microns)	SPECTRAL RADIANT INTENSITY ($Wsr^{-1}\mu m^{-1}$)		WAVELENGTH (microns)	SPECTRAL RADIANT INTENSITY ($Wsr^{-1}\mu m^{-1}$)
3.799	7.93		4.194	252.42
3.818	10.16		4.196	134.74
3.850	7.93		4.201	28.25
3.892	5.69		4.202	7.93
3.934	5.69		4.202	5.69
3.964	7.93		4.210	10.16
3.986	5.69		4.219	5.69
3.998	7.93		4.229	10.16
4.025	3.36		4.248	5.69
4.050	7.93		4.271	5.69
4.076	10.16		4.297	3.36
4.091	5.69		4.317	3.36
4.108	7.93		4.331	19.21
4.123	5.69		4.337	57.72
4.138	7.93		4.341	64.53
4.150	10.16		4.346	134.74
4.155	12.50		4.347	143.79
4.162	16.97		4.359	247.85
4.165	44.20		4.366	347.53
4.170	116.65		4.371	472.02
4.174	209.43		4.374	605.64
4.175	311.26		4.378	702.99
4.179	431.27		4.379	680.33
4.180	515.10		4.381	635.11
4.182	549.04		4.385	562.65
4.185	542.23		4.386	551.28
4.188	487.87		4.391	540.00
4.190	381.47		4.396	558.08
4.400	528.62		4.550	30.59
4.403	510.53		4.563	23.78
4.406	535.42		4.567	30.59
4.410	508.29		4.575	16.97
4.417	487.87		4.594	10.16
4.422	483.39		4.602	7.93
4.433	444.88		4.607	12.50
4.437	415.51		4.611	5.69
4.440	410.94		4.619	21.54
4.444	381.47		4.624	5.69
4.447	381.47		4.639	5.689
4.454	324.87		4.658	7.93
4.459	318.06		4.661	5.689
4.462	299.98		4.666	14.73
4.467	295.50		4.673	14.73
4.472	247.85		4.680	5.69
4.477	241.14		4.685	3.36
4.494	177.73		4.690	10.16
4.503	123.36		4.693	5.69
4.511	93.99		4.700	12.50
4.516	89.42		4.715	3.36
4.521	66.76		4.719	28.25
4.527	62.29		4.722	30.59
4.535	44.20		4.727	5.69

radiative cooling, in steady-state operation, to result in thermodynamic equilibrium. Of these cooling mechanisms, convection is usually the most significant. Conduction of heat into the airframe is minimal, after the skin reaches its steady-state temperature, because conventional aircraft provide few conductive heat dissipation mechanisms. Radiative skin cooling is not large at the low skin temperatures experienced during subsonic flight. It can be significant, however, at higher speeds unless low-emissivity coatings are used to suppress this unwanted observable.

Hudson[5] relates aerodynamically heated skin temperature T_s to ambient air temperature T_o (both in kelvins) with the formula

$$T_s = T_o(1 + 0.2rM^2) , \tag{2.1}$$

where

r = recovery factor
= 1.0 at stagnation point (where air stream comes to a complete rest)
= 0.87 for turbulent flow
= 0.82 for laminar flow

M = Mach number.

Equation (2.1) ignores the extra cooling that would occur with radiative heat transfer and, instead, considers only convection. More thorough treatments can be found in Ref. 6.

2.2.2 Ground Vehicle and Equipment Signatures[a]

The term *ground vehicles and equipment* encompasses the mobile tactical equipment employed by military forces engaged in ground combat. It includes trucks, tanks, self-propelled field and air defense artillery, command and communications equipment, and portable electric power generators. Although most such equipment belongs to the army, similar equipment used by Air Force and Marine Corps units is also included. Fixed installation equipment and facilities are not included except in cases where an identical item (such as a diesel-engine-driven generator) performs the same function in either the fixed or mobile role.

Sensors that pose threats to this equipment fall into the category of visual, image intensifier equipped, television, infrared linescan mappers, and, more recently, FLIRs, imaging seekers, and terminally guided submunitions (including sensor fuzed weapons). Lasers also pose a threat from the standpoint of range finders and designators but these weapons are usually only employed after the vehicle is detected. Laser radar is an exception, but is not yet widely deployed.

Visual, image intensified, and television sensors are dependent on ambient illumination for signature generation. They depend both on a reflectance difference between the target and the background to create contrast and on the

[a]Includes material from Grayson W. Walker, U.S. Army Belvoir Research, Development and Engineering Center, Ft. Belvoir, Virginia.

availability of sufficient reflected ambient illumination to create an adequate signal level.

Given adequate illumination, visible and near-infrared signatures ultimately depend on the spectral reflectivity differences between the target and the background in the sensor response band. Visual sensors can use photopic color differences as a discriminant. Image intensifiers extend the visual spectrum out to approximately 0.9 μm or into the near infrared. So do television sensors that can use silicon detectors with response out to approximately 1.1 μm. These near-infrared sensors can exploit the high reflectivity of live foliage and the low reflectivity of conventional paints to see a large negative contrast difference between the vehicle and its background. Figure 2.5 shows example plots of total spectral reflectances for several common terrain backgrounds and conventional camouflage paint. These visual and near-infrared signature components are an important element that continue to require careful control.

Mappers and emerging FLIRs, infrared imaging seekers, and infrared submunitions see signatures mostly originating from heat generated self-emissions.

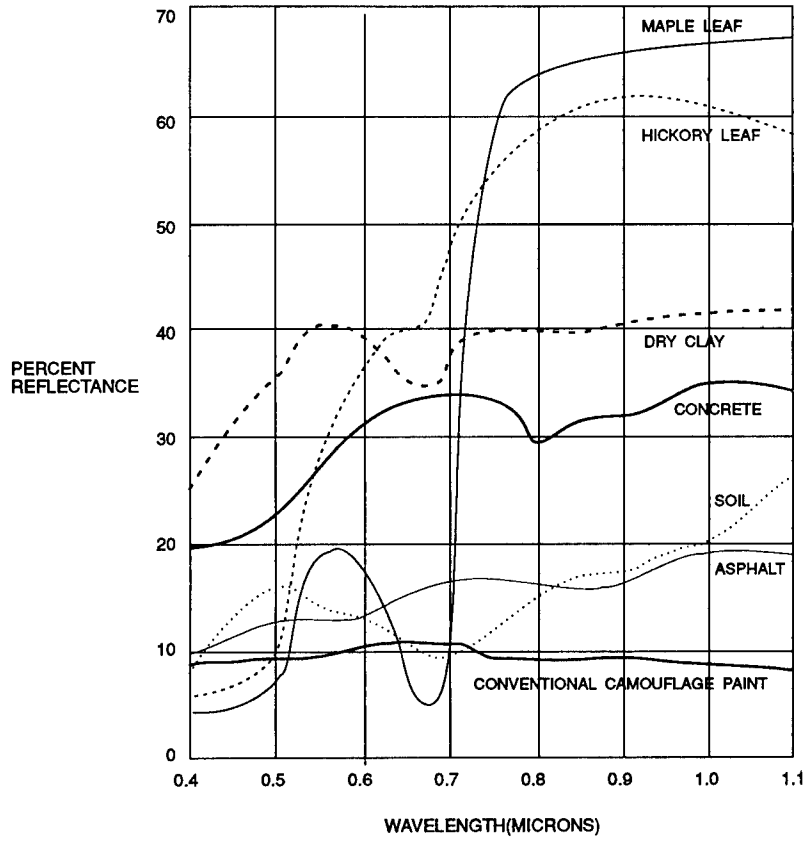

Fig. 2.5 Examples of typical spectral reflectance for common surfaces.

These sensors nominally work in the 3- to 5- or 8- to 12-μm bands. In the 3- to 5-μm band, the sun is still a significant contributor of reflected radiation. Mappers, FLIRs, and imaging seekers are capable of seeing internal target detail with temperature differences less than a degree Celsius. However, they detect targets at long ranges by seeing their hot-spot emissions. Submunitions and sensor fused weapons rely solely on unresolved hot spots to find the target autonomously in clutter. Self-emissions offer the possibility for long-range detection and standoff attack, day or night, by human-assisted infrared imaging equipped systems or by autonomous munitions. This fact gives impetus to understanding ground vehicle infrared signature generation mechanisms.

Each of the described equipment items, if not protected, emits a set of signatures because of its design and configuration. Although this set of signatures is unique to the equipment type, each of the signatures can be described generically to assist in devising protective techniques.

Internally Generated. These sources include the propulsion system, drive train, and auxiliary power equipment. Virtually all of the items under consideration have a main engine that provides motive or generating power; a few are gasoline fueled, most are diesel fueled, and the M-1 tank fleet is unique with its turbine engines. Friction and combustion heating raise engine compartment temperatures to the region of 120°C. Much of this heat leaks to heat the compartment sides and cover.

Engine exhaust gases are led through a muffler system to the open air. In all cases there is a resulting exhaust gas "plume" whose size and temperature varies with the size of the engine. In most cases the muffler system is exposed to the air and is in itself a detectable signature.

The vast majority of the engines discussed (i.e., all except tank turbines and small gasoline engines) are liquid cooled, and incorporate radiators to cool the circulating liquid. Radiators by their nature are exposed to the air and thus also present detectable signatures, although not of the magnitude of the engine or exhaust.

Trucks and tracked vehicles, when driven, generate friction heat in their running gear—tires on trucks and the entire system of road wheels and tracks on tracked vehicles. The resulting signatures remain evident over extensive elapsed time following a halt.

Most tracked vehicles and many communications systems are equipped with small power units auxiliary to the main engine, to permit low-power operation of communications (and some personnel cooling/heating) equipment. Such auxilliary power units (APUs) do generate thermal signatures, but they are of concern primarily at night, when all other elements of the system are quiet and cool.

Solar Heating. A second component of the thermal signature is that caused by exposure to the sun. The effects are solar heat loading and diurnal variations. The solar heating phenomenon begins with the fact that most mobile tactical equipment is first, made of metal, and second, is dark in color for camouflage reasons. As a result, when such equipment is exposed to the sun, it absorbs heat quickly and retains the heat throughout exposure. The speed and degree of heating are directly related to the construction of the specific equipment. Consider a line of vehicles that includes an M-52 cargo truck with

canvas cover, an M-2 fighting vehicle with relatively light aluminum armor, an M-1 tank with heavier armor, and an M-60 tank with its very heavy steel armor, all exposed to the same sun conditions. The truck heats most rapidly and the M-60 least rapidly. Concerning stable temperature after exposure, however, the line-up is reversed; the M-60, with its far greater mass of metal, attains and retains the highest temperature with the others in order down to the cargo truck.

The solar heating problem is further complicated by changes in exposure conditions from day to day and throughout the day. It seems obvious that a day of clouds and rain is a day without a skin-heating problem, whereas a day of bright sun produces the previously described results. On the day of bright sun, most equipment items begin the day stable from overnight cooling and continue to warm through the day until sunset, when they begin to cool slowly. Figure 2.6 illustrates a typical diurnal heating cycle for both light and heavy armor types. Overnight cooling varies with ambient temperature and equipment type; in a warm climate the heavy-mass, tanklike item may never fully cool. Between the extremes of the fully gray day and the full sun day, intermittent clouds or rain can interrupt the warming cycle and produce an erratic

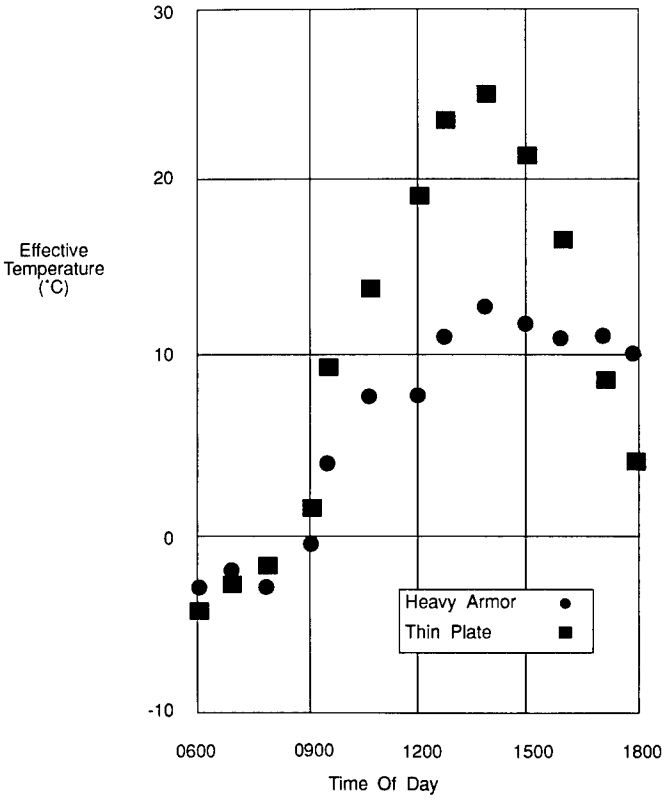

Fig. 2.6 Diurnal variation of vehicle skin temperature during July in Rome, NY.

warming curve. Figure 2.7 shows an illustration of diurnal effects on both operating and nonoperating vehicles at various times of the day. Images shown were predicted from a thermal model[7] for an assumed location in Florida during November. The sun rises from the bottom right hand corner of the photo and sets in the direction of the upper left corner.

Secondary Heating. A third component of the overall thermal signature of a military unit is the influence of equipment on the adjacent ground and air. Ground tracks, exhaust emissions, and dust clouds are the major considerations.

As the mobile equipment items transit their area of operations, wheels and tracks impinge upon the ground and disturb the ground surface. This action results in a heated ground track, which can be detected by thermal sensors after the passage of the equipment, in addition to its availability as a classic visual cue to military activity.

When the transit is made under dry conditions, it is also common that the movement action generates dust, which is thrown up into the exhaust cloud and floats with it. Depending on air temperature and wind conditions, this exhaust gas/dust cloud can linger in the area and present a thermal signature after passage of the equipment.

2.2.3 Background and Clutter Effects

Target signature almost always results from the difference, or contrast, between the target and its immediate background. It is therefore often just as important to understand the background's emission characteristics as it is the target's.

Background effects are also determined by threat sensors. Nonimaging sensors can be defeated by reducing target total emissions to match the background. The dilemma is determining what constitutes a "match." Ideally, contrast should be reduced to some level related to the sensor's internal noise level. That relation is driven by the application. For instance, if the application is protection from IR missile seekers, the relation to sensor noise is determined from the minimum acceptable lock-on range. However, if the background is not uniform, different criteria can apply.

A nonuniform background can have two effects relative to nonimaging threat sensors. First, it can defeat efforts to match contrast because no one target emission level may now result in acceptably low contrast against each background location. Second, it can enhance efforts to hide by introducing a variation—clutter—which provides confusing objects among which it is difficult for the seeker to find the true target. Both background effects must be taken into consideration when defining the target's signature and the suppression requirement. Thus, unresolved target signatures depend on background intensity mean values as well as on the intensity variations. Clutter size effects are most important when they are on a scale comparable to or larger than the target dimensions.

Backgrounds affect resolved target signatures differently than they do unresolved signatures. Imaging sensors see internal target detail and external shape detail. Therefore, target signatures are defined by their pattern features. Those features are unique only to the extent that their properties differ from those in the background. Resolved signatures are primarily defined in terms

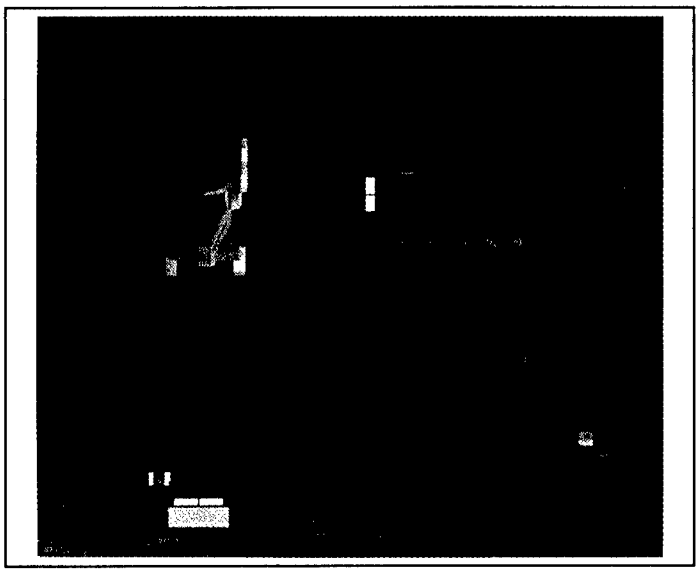

9:00 AM

Larger thermal mass of tanks exhibit slower response to morning solar load.

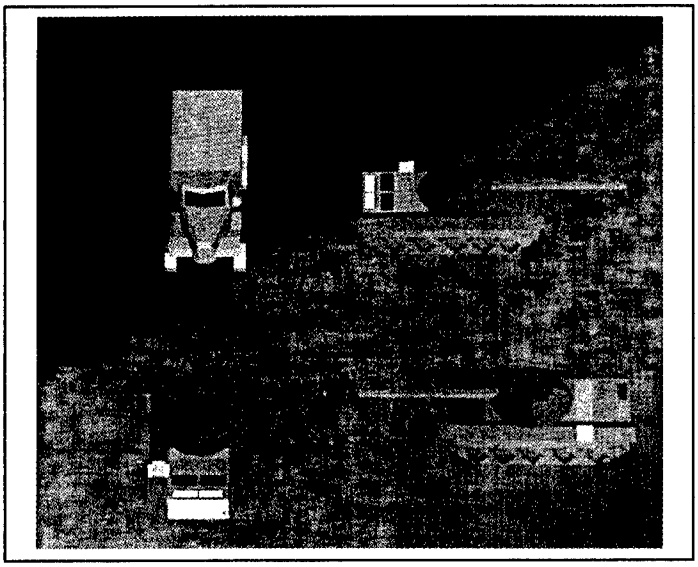

12:00 NOON

Target signatures illustrate the solar heating effects due to position and material class.

Fig. 2.7 Diurnal effects on target signatures in the 8- to 12-μm band (see Ref. 7).

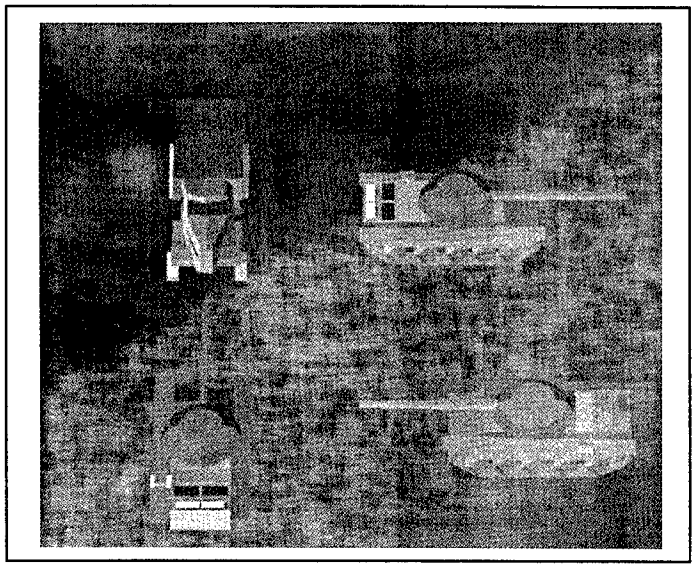

3:00 PM
Signature reversals are beginning during period of decreasing solar load.

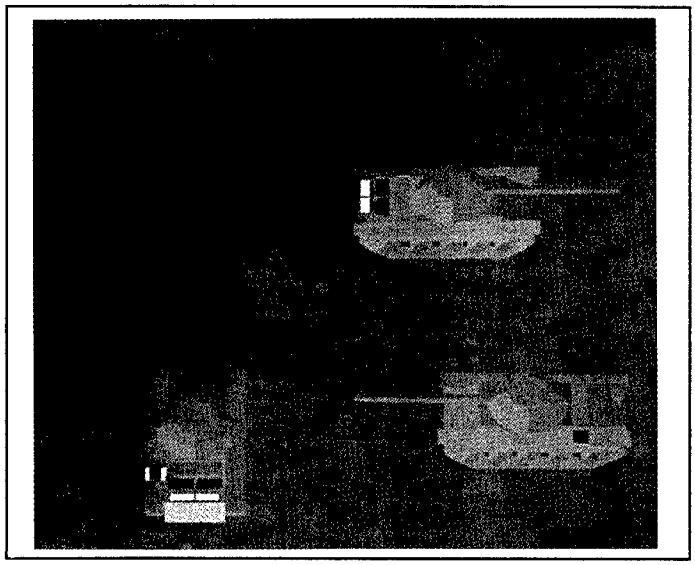

6:00 PM
Positive contrast exhibited by tanks, while truck shows negative contrast, illustrate thermal lag effects.

Fig. 2.7 (continued)

of texture and component contrasts. Thus, resolved target signatures depend on background intensity mean values as well as on clutter intensity variations on a size scale comparable to internal target detail. Background spatial, spectral, and intensity characteristics are key to target signature generation and signature suppression. Many of their properties are described elsewhere in this handbook.

2.3 SYSTEM FRAMEWORK FOR REFLECTIVITY AND EMISSIVITY

Surface characteristics, including material properties and structural shape, are key elements in the control of signature. However, the final signature is as much a result of the operating environment as of surface characteristics. It is essential to be able to relate the signature both to the external environment and to the underlying material properties. Reflectivity and emissivity are the quantities that make the needed connection.

This section constructs a framework for defining the meaning of the terms reflectivity and emissivity. It then extends the framework in two directions. First, given a signature goal, it shows how the environment constrains emissivity and reflectivity. Second, given a required emissivity and reflectivity, it shows how these requirements relate to fundamental, but still broadly defined, material properties. The result is a framework for relating system requirements and material properties to reflectivity and emissivity.

2.3.1 Fundamental Relationships

Key surface properties of interest to the signature control designer are bidirectional reflectivity and directional emissivity. However, these quantities have historically had many definitions and it is necessary to have a common framework of interpretation. Fortunately, one has evolved based on the bidirectional reflectivity distribution function (BRDF), which is capable of adequately describing both bidirectional reflectivity and directional emissivity. Much of the foundation for this framework is based on the work of Nicodemus.[8]

Concepts relating reflectivity to emissivity are founded in energy conservation principles, Kirchhoff's law, and Helmholtz's reciprocity theorem. It follows from energy conservation principles that for power incident on a surface

$$a + \rho + \tau = 1 \ , \tag{2.2}$$

where

a = absorbed fraction
ρ = reflected fraction
τ = transmitted fraction.

However, Kirchhoff's law states that

$$a = \varepsilon \ , \tag{2.3}$$

where ε is the emissivity defined as the ratio of the radiant emittance of the surface to the radiant emittance of a blackbody at the same temperature. Then for an opaque surface, $\tau = 0$, and

$$\varepsilon = 1 - \rho \ , \tag{2.4}$$

where, in general, all terms are spectrally dependent hemispherical averages, but here are considered to be band averages as well, and there are no constraints on the direction of incident radiant power.

Consideration of the directional properties of these terms results in the definition of other derivative terms and concepts. Simplified surfaces can be described that obey special laws. For instance, perfect mirror surfaces obey Snell's law: Angle of reflection equals angle of incidence. Perfectly diffuse surfaces obey Lambert's law: Reflected radiance is independent of angle. However, few natural surfaces fit either category well, but instead, fall somewhere between them.

The general case is well treated with the concept of a BRDF, which is defined for a flat surface element dA as

$$f_r(\Theta_i,\phi_i,\Theta_r,\phi_r) \equiv \frac{dL_r(\Theta_r,\phi_r)}{dE_i(\Theta_i,\phi_i)} \ , \tag{2.5}$$

where (Θ_i,ϕ_i) and (Θ_r,ϕ_r) define incident and reflected ray directions, respectively, per Fig. 2.8, and where $dE_i(\Theta_i,\phi_i)$ is the incident irradiance on dA from the Θ_i,ϕ_i direction and $dL_r(\Theta_r,\phi_r)$ is the reflected radiance from dA in the Θ_r,ϕ_r direction. Note that BRDF is a ratio of two *different* quantities. It expresses the ratio of reflected radiance, i.e., W cm^{-2} sr^{-1}, to incident irradiance, i.e., W cm^{-2}. Accordingly, it has units of inverse steradians and can assume infinite values. Its virtue is that it expresses the directional dependence of reflectivity on the geometry of both incident and reflected angles.

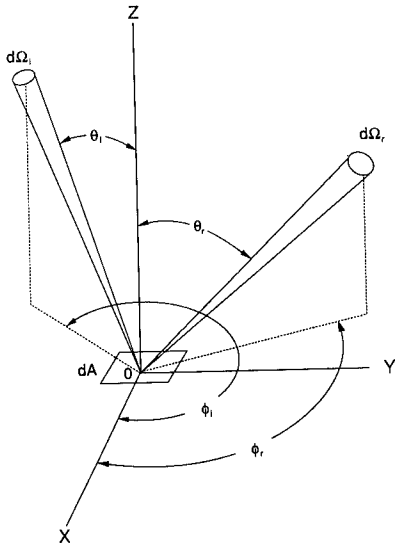

Fig. 2.8 Definition of incident and reflected directions.

Total directional reflectance is related to BRDF but is defined as the ratio of two *similar* quantities:

$$\rho_d(\Theta_i,\phi_i) \equiv \frac{dP_r}{dP_i(\Theta_i,\phi_i)} = \int_{\text{hemisphere}} f_r \cos\Theta_r \, d\Omega_r \ , \tag{2.6a}$$

or

$$\rho_d(\Theta_i,\phi_i) \equiv \frac{dP_r(\Theta_r,\phi_r)}{dP_i} = \int_{\text{hemisphere}} f_r \cos\Theta_i \, d\Omega_i \ , \tag{2.6b}$$

where

dP_i = total power incident from all directions
$dP_i(\Theta_i,\phi_i)$ = element of power incident from Θ_i,ϕ_i
dP_r = total power reflected into the hemisphere
$dP_r(\Theta_r,\phi_r)$ = element of power incident from Θ_r,ϕ_r
$d\Omega_{r,i}$ = element of solid angle in spherical coordinates.

Total directional reflectance contains no reflected (incident) directional information because it is the integral of reflected (incident) rays over the whole hemisphere.

Helmholtz's reciprocity theorem shows no difference between incident and reflected directions such that

$$\rho_d(\Theta_i,\phi_i) = \rho_d(\Theta_r,\phi_r) = \rho_d(\Theta,\phi) \ , \tag{2.7}$$

and subscripts on Θ and ϕ can be dropped.

Finally, directional properties of emissivity can also be determined from Helmholtz's reciprocity theorem, which allows us to rewrite Eq. (2.4) in terms of angles and total directional reflectance ρ_d:

$$\varepsilon_d(\Theta,\phi) = 1 - \rho_d(\Theta,\phi) \ . \tag{2.8}$$

The BRDF dependency of emissivity follows from Eq. (2.6):

$$\varepsilon_d(\Theta,\phi) = 1 - \int_{\text{hemisphere}} f_r \cos\Theta \, d\Omega \ . \tag{2.9}$$

Thus, knowledge of a surface's BRDF is sufficient information to quantify directional reflectance and directional emissivity.

Figures 2.9 and 2.10 illustrate the appearance[9] of representative BRDF functions for glossy paint and diffuse paint, respectively, on an aluminum substrate. These functions were measured with monochromatic light at 10 and 3.8 μm. The logarithmic scale exaggerates the diffuse component in each figure. It is interesting to note that the glossy paint has a glint lobe or beamwidth (beamwidth at half intensity) of approximately 2 deg, whereas the diffuse paint is far from being Lambertian. On the other hand, glossy paint concentrates most of the reflected energy in a narrow beam much like one would expect of

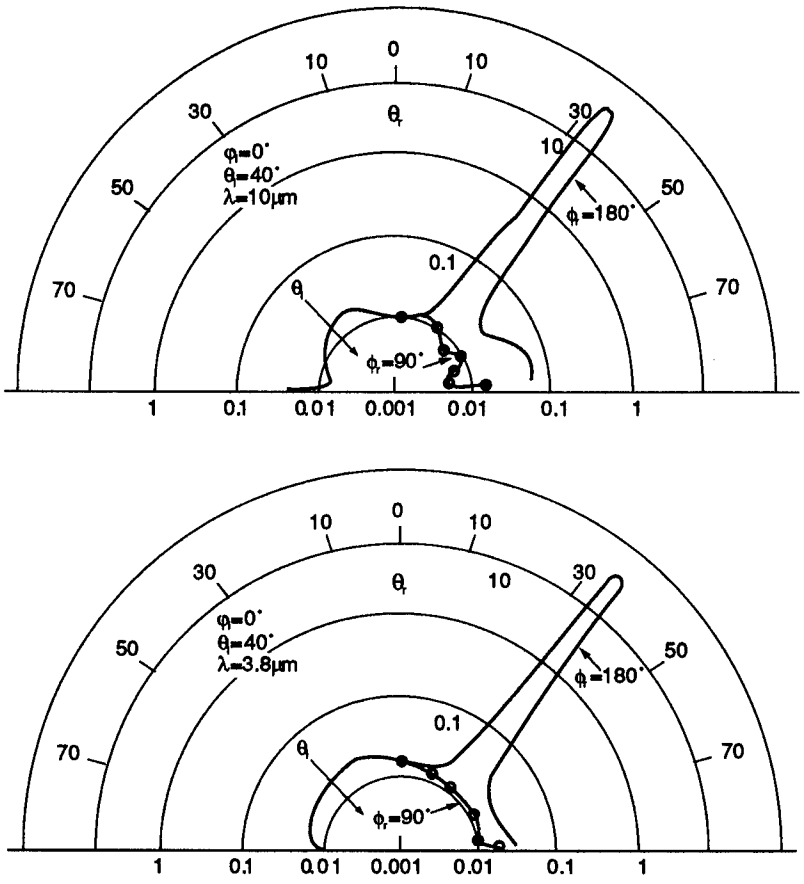

Fig. 2.9 Representative BRDFs for glossy paint.[9]

a specular surface. In examining the signature of planar painted surfaces due to reflected source irradiation, it is probably safe to approximate glossy surfaces as being perfectly specular when dealing with sources of several degrees or more. But, when dealing with diffuse surfaces, much more attention must be paid to the source extent and irradiation geometry before simplifying assumptions can be made.

Even with real BRDFs special cases are of interest. For instance, it can be shown that for perfectly diffuse surfaces

$$f_r = \frac{\rho}{\pi}, \tag{2.10}$$

where ρ, the total reflectance dP_r/dP_i, is a constant. Similarly, for perfectly specular surfaces it can be shown that

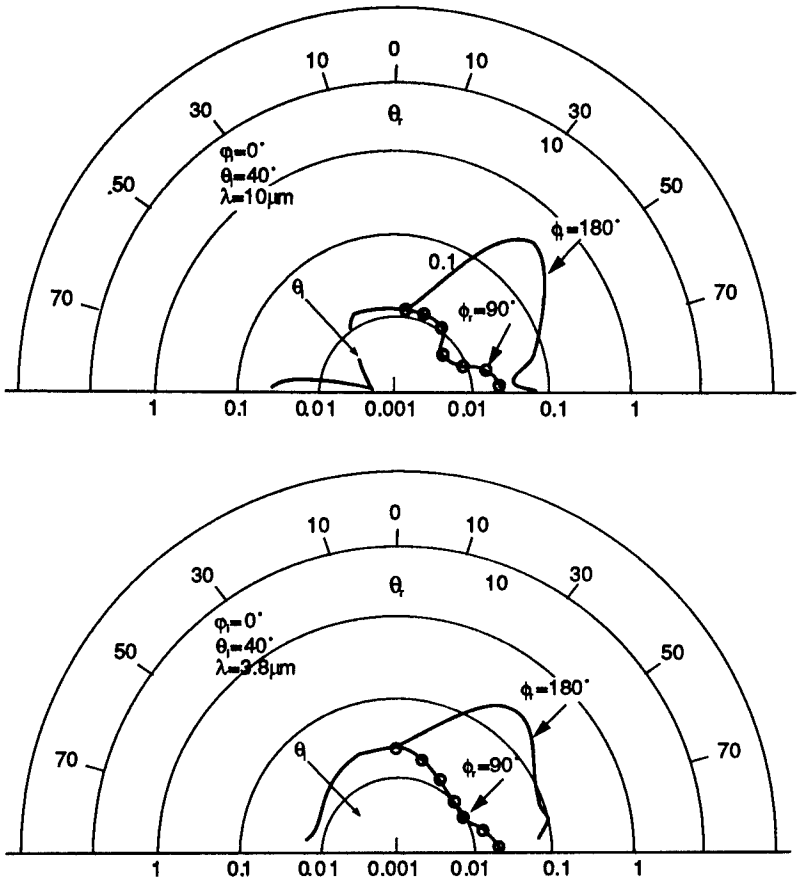

Fig. 2.10 Representative BRDFs for flat paint.[9]

$$f_r(\Theta_i,\phi_i,\Theta_r,\phi_r) = 2\rho_d(\Theta_i,\phi_i)\delta(\sin^2\Theta_r - \sin^2\Theta_i)\delta(\phi_r - \phi_i \pm \pi) \ , \qquad (2.11)$$

where δ denotes the Dirac delta functions and ρ_d is again the total directional reflectance but may vary with angle. It then follows from Eq. (2.9) that the directional emissivity for diffuse surfaces viewed from any angle, or for specular surfaces viewed at angle (Θ,ϕ) is

$$\text{diffuse:} \quad \varepsilon_d = 1 - \rho \ , \qquad (2.12a)$$

$$\text{specular:} \quad \varepsilon_d = 1 - \rho_d(\Theta,\phi) \ , \qquad (2.12b)$$

Eqs. (2.11) and (2.12b) are used next to show representative real-world directional emissivity requirements for specular low observable coatings.

2.3.2 System Requirements

Coatings offer the potential to reduce heat-induced self-emissions by reducing surface emissivity. However, one of the problems encountered with that approach is that reductions in emissivity are accompanied by increases in reflectivity. In fact, situations often can arise where reduced emissivity actually increases apparent surface emissions because the increase in reflected background radiance more than offsets the reduction in self-emissions. Accordingly, it is important to examine the requirements that various backgrounds and viewing geometries impose on emissivity.

In general, surface graybody directional radiance $L(\Theta,\phi)$ (in units of W cm^{-2} sr^{-1}) for a planar target surface at absolute temperature T in Kelvins is

$$L(\Theta,\phi) = \varepsilon(\Theta,\phi)\int_{\Delta\lambda} L_{BB}(\lambda,T)\, d\lambda + \int_{\text{hemisphere}} f_r(\Theta,\phi,\Theta_i,\phi_i) L_b(\Theta_i,\phi_i) \cos\Theta_i\, d\Omega_i \ , \tag{2.13}$$

where

$L_{BB}(\lambda,T)$ = Planck blackbody spectral radiance function, or

$$L_{BB}(\lambda,T) = \frac{2hc^2}{\lambda^5} \frac{1}{\exp(ch/\lambda kT) - 1} \ [\text{W cm}^{-2}\ \text{sr}^{-1}\ \mu\text{m}^{-1}] \tag{2.14}$$

h = 6.6256×10^{-34} W s^2, Planck's constant
c = 2.9979×10^{10} cm s^{-1}, velocity of light
k = 1.3805×10^{-23} W s K^{-1}, Boltzmann's constant
λ = wavelength, in micro- or centimeters
$\Delta\lambda$ = spectral band of interest
$L_b(\Theta_i,\phi_i)$ = incident background radiance on the surface, in band, from direction (Θ_i,ϕ_i)
$d\Omega_i$ = elemental solid angle of incidence from direction (Θ_i,ϕ_i).

The first term in Eq. (2.13) is the surface's self-emission component and the second term is the reflected component.

This form, although difficult to evaluate, is of broad general interest. However, it is argued in later sections that, for signature control, planar surfaces with highly specular reflectances are desirable for reducing the intercept probability against solar and other point source reflectors. In the latter case, Eq. (2.11) can be used to rewrite the reflectance term in Eq. (2.13) as

$$\int_{\text{hemisphere}} f_r L_b \cos\Theta_i\, d\Omega_i = L_b \rho_d \ , \tag{2.15}$$

and from Eq. (2.12b)

$$L_b\rho_d(\Theta,\phi) = L_b[1 - \varepsilon(\Theta,\phi)] \ . \tag{2.16}$$

Then Eq. (2.13) becomes

$$L = \varepsilon L_{\mathrm{BBI}}(\lambda,T) + L_b(1 - \varepsilon) \ , \tag{2.17}$$

where

$$L_{\mathrm{BBI}}(\lambda,T) = \int_{\Delta\lambda} L_{\mathrm{BB}}(\lambda,T)\, d\lambda \ , \tag{2.18}$$

and where the notation showing explicit functions of angle has been dropped to simplify the nomenclature.

Emissivity requirements come from contrast suppression criteria. If L_0 is the immediate target background radiance, then target contrast is

$$L - L_o = \varepsilon L_{\mathrm{BBI}}(\lambda,T) + L_b(1 - \varepsilon) - L_o \ . \tag{2.19}$$

One criterion for signature suppression is that the target contrast be zero, or

$$\varepsilon L_{\mathrm{BBI}}(\lambda,T) + L_b(1 - \varepsilon) - L_o = 0 \ . \tag{2.20}$$

The required emissivity ε_r is then found by solving Eq. (2.20) for emissivity, or

$$\varepsilon_r = \frac{L_o - L_b}{L_{\mathrm{BBI}} - L_b} \ , \tag{2.21}$$

where L_b is the radiance specularly reflected off the target panel and into the sensor. Panel temperature is assumed to be invariant with emissivity.

Equation (2.21) can be evaluated to determine example required emissivities by postulating a target platform position and a threat sensor viewing geometry. Figure 2.11 illustrates one case of general interest. Panel tilt angle (α) deter-

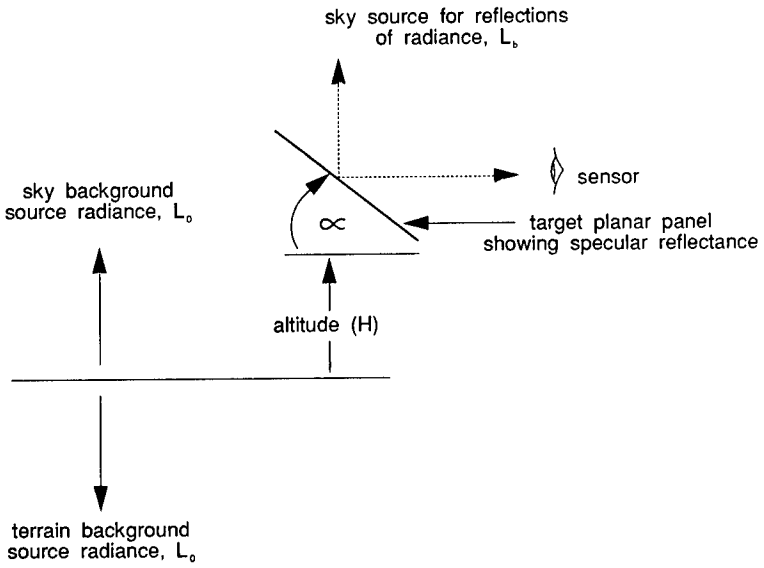

Fig. 2.11 Surface position and specular reflector-viewing geometry.

mines the source direction for specular reflection into the sensor. Thus, for $\alpha = 45$ deg, the sensor "sees" the cold zenith sky radiance times the surface specular reflectivity. For increasing tilt angle, as α goes to 90 deg, the sensor sees increasingly warm sky radiance until the source direction approaches the horizon sky. At tilt angles greater than 90 deg the sensor sees the terrain.

Required target emissivities under these viewing conditions are shown in Figs. 2.12 and 2.13 for several target minus background physical temperature differences (ΔT's). Figures 2.12(a) and 2.12(b) show the case where the panel is viewed against the horizon sky background, whereas Figs. 2.13(a) and 2.13(b) show results for an assumed terrain background. Both cases are for a ground level panel ($H = 0$). Sky radiances were calculated from LOWTRAN 6 under night sky conditions using the 1962 U.S. Standard Atmosphere Model. Terrain radiances were calculated by assuming the terrain to be at air temperature (288 K) and having unity emissivity.

In these figures, target minus background ΔT's were computed from the relation $\Delta T = T(\text{target}) - T(\text{background})$. Both target and background tem-

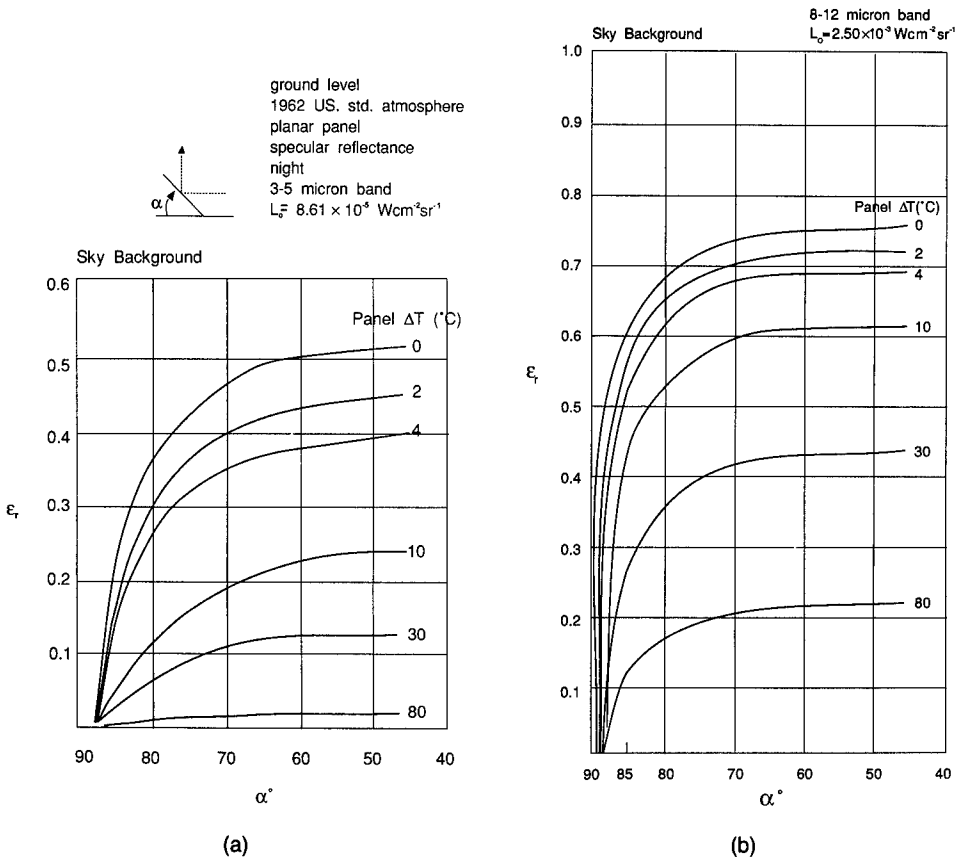

Fig. 2.12 Emissivity required for zero contrast as a function of panel tilt angle when viewed against horizon sky: (a) 3- to 5-μm band and (b) 8- to 12-μm band.

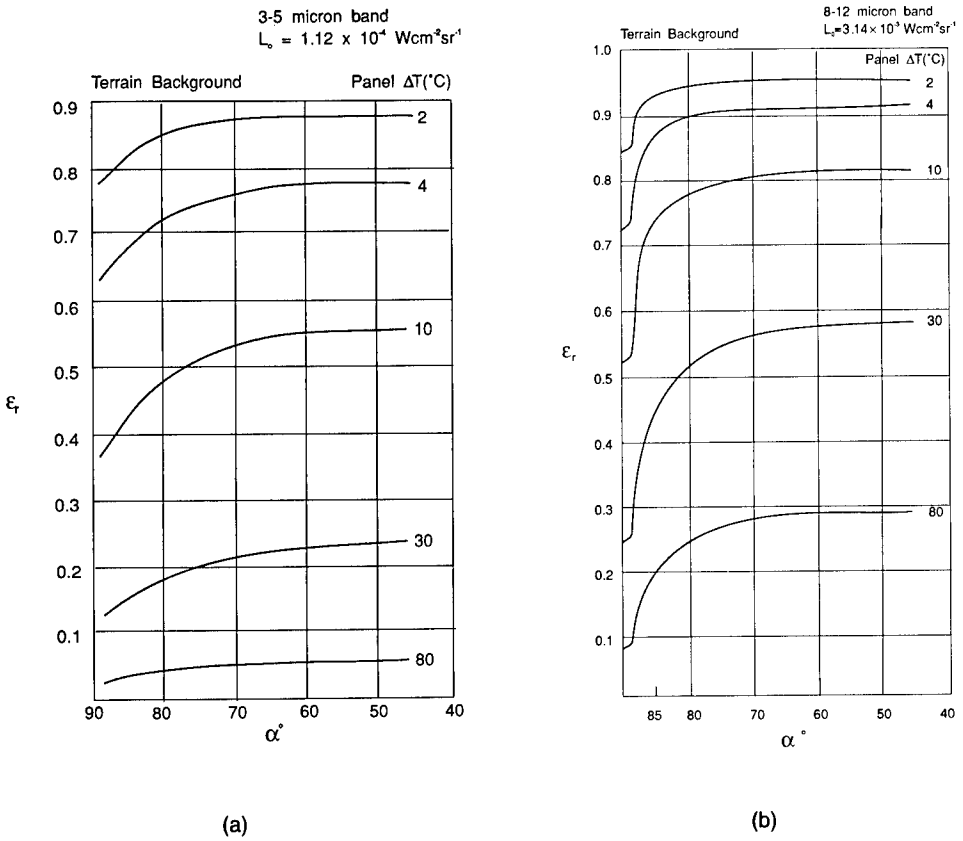

Fig. 2.13 Emissivity required for zero contrast as a function of panel tilt angle when viewed against terrain: (a) 3- to 5-μm band and (b) 8- to 12-μm band.

peratures were physical temperatures. For terrain, background physical temperature was 288 K and, because unity emissivity was assumed, this was also the apparent background blackbody radiant temperature. However, for the sky background, apparent radiant temperature was lower than its 288 K physical temperature. Accordingly, apparent radiant ΔT's for the sky background cases would have been greater than the physical ΔT's shown.

Figure 2.14 shows LOWTRAN sky radiance values, as a function of zenith angle, at ground level. Of course, sky and ground radiances can vary considerably under different assumptions. Required emissivities would vary also.

Examination of these emissivity plots shows expected trends. Some of these trends result from the assumption of a warm, high-emissivity terrain background. For instance, a warmer terrain background allows higher emissivities, for a given target ΔT, than does a horizon sky background. This is because the sky is less dense, and although the lowest layer has the same temperature as the ground, one can see through the inner layers to the cooler outer atmospheric layers. Thus, the vehicle must reflect more of the cold zenith sky to overcome the comparatively cool horizon sky background.

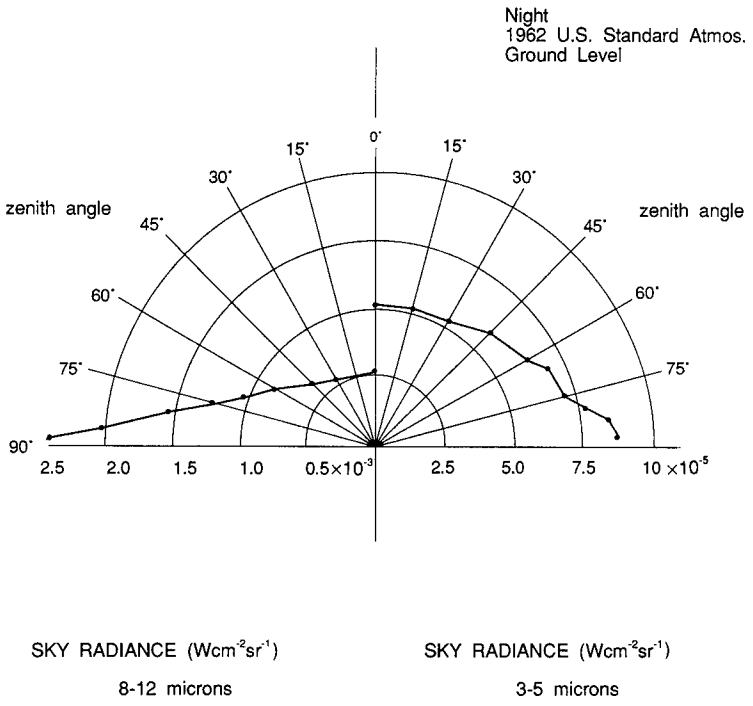

Fig. 2.14 Sky radiance level as computed from LOWTRAN 6.

Less reflectance (higher emissivity) is required in the 8 to 12-μm band than in the 3- to 5-μm band because, as is seen in Fig. 2.13, the ratio of zenith sky to horizon sky radiance is much higher in the 8- to 12-μm band. Therefore, comparatively less reflectance is needed in the longer wave band to compensate for self-emissions. Because higher emissivities are easier to attain than lower emissivities, one could conclude that suppression is easier in the longwave band. This conclusion is even more likely when it is realized that natural backgrounds tend to have higher emissivities in the 8- to 12-μm band than they do in the 3- to 5-μm band. The assumption here of unity emissivity is unrealistic against many terrain backgrounds because common terrain types can have emissivities as low as 0.5 in the 3- to 5-μm band. Lower emissivity backgrounds, of course, result in the requirement for lower emissivity coatings. Ultimately, lower background emissivities can result in Eq. (2.21) requiring a negative emissivity. This means that the suppression goals may not be met with coatings alone, but may require active cooling techniques as well.

Required emissivities in the 3- to 5-μm band vary much less, with panel tilt angle, against the terrain background than they do against the sky background. This is because the sky background is cooler than terrain and requires relatively more panel reflectance. At large tilt angles, the reflected horizon sky approaches the radiance of the target's sky background. Thus, comparatively greater reduction in panel emissivity is needed.

Note that required emissivity changes very slowly with panel tilt angle in both the 3- to 5- and 8- to 12-μm bands against terrain backgrounds. This is an advantage to the suppression designer. The lack of sensitivity to tilt angle gives more latitude to slant vehicle skin with other design considerations in mind.

In summary, required skin emissivity can be expected to vary considerably as a function of target temperature, viewing geometry, and background emissivity when striving for "zero" contrast suppression levels. However, although it was not discussed here, background clutter can be expected to relax these requirements. Clutter provides a source of "confusing objects" that will tend to obscure the target. Specific requirements for suppression in the presence of clutter are determined from detection theory and are not discussed further in this chapter.

This completes the framework that relates surface emissivity and reflectivity to system signature goals. Results shown here are germane to ground vehicle and low-altitude helicopter surface applique requirements. Equivalent requirements for high-speed fixed-wing aircraft at various altitudes are discussed in Sec. 2.5.

2.3.3 Material Properties

Required emissivities and reflectivities can be related to underlying material property requirements. This is done in summary only here to show the general functional forms and variables involved. Very limited material types are considered. The next section goes into more detail on a broader array of material designs. The references to this chapter provide detailed discussions.

For linear, isotropic, homogeneous, and weakly magnetic media, the specular reflectivity from a smooth surface is given by the Fresnel equations,[10] or

$$\rho_{\perp}(\Theta_{i,t}) = \left(\frac{n_i \cos\Theta_i - n_t \cos\Theta_t}{n_i \cos\Theta_i + n_t \cos\Theta_t}\right)\left(\frac{n_i \cos\Theta_i - n_t \cos\Theta_t}{n_i \cos\Theta_i + n_t \cos\Theta_t}\right)^{*} , \tag{2.22}$$

$$\rho_{\|}(\Theta_{i,t}) = \left(\frac{n_t \cos\Theta_i - n_i \cos\Theta_t}{n_i \cos\Theta_t + n_t \cos\Theta_i}\right)\left(\frac{n_t \cos\Theta_i - n_i \cos\Theta_t}{n_i \cos\Theta_t + n_t \cos\Theta_i}\right) , \tag{2.23}$$

where the result is independent of ϕ because of the material assumptions made. The angles Θ_i and Θ_t are defined by Fig. 2.15 and $n_{i,t}$ is the index of refraction of incident and transmitting media, respectively. For natural radiation,

$$\rho(\Theta_{i,t}) = \frac{\rho_{\perp} + \rho_{\|}}{2} . \tag{2.24}$$

In general, the index of refraction is a complex quantity

$$n_c = n_R - in_I , \tag{2.25}$$

where n_R and n_I are the real and imaginary parts, respectively. However, the imaginary part depends on material conductivity and is high for metals but

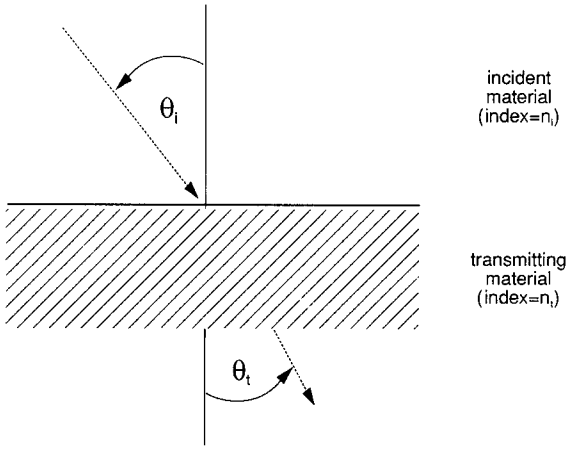

Fig. 2.15 Definition of angles used in Fresnel equations.

diminishes for materials with a low dielectric constant. One of the most general forms for the index of refraction, be it metal, semiconductor, or dielectric, is[10]

$$n_c^2(\omega) = 1 + \frac{Nq_e^2}{\varepsilon_o m_e}\left(\frac{f_e}{-\omega^2 + i\gamma_e\omega} + \sum_j \frac{f_j}{\omega_{oj}^2 - \omega^2 + i\gamma_j\omega}\right), \tag{2.26}$$

where

ω = angular frequency of incident light
N = number of actions per unit volume
q_e = charge on an electron, 1.6×10^{-19} C
ε_o = permittivity of free space (dielectric constant), 8.8542×10^{-12} $C^2\,N^{-1}\,m^{-2}$
ω_{oj} = molecular oscillator natural frequency of j'th molecule
m_e = reduced mass of effective charge or dipole
f_e = number of conduction electrons, with no natural frequencies
f_j = material molecular oscillator strengths
j = number of molecular natural oscillator frequencies in material
γ_e = free electron damping constant
γ_j = bound electron damping constant.

Equation (2.26) expresses the theory that when light interacts with matter, the incident electric field can interact with both free and bound electrons. The strength of the interaction is a frequency-dependent function of the mass of the charged elements, their density, and their characteristics as oscillators.

Equation (2.26) is useful as an indicator of the general physical properties that affect the interaction of light with matter. However, it does not apply to many materials needed for signature-control coatings because these materials are often neither homogeneous nor isotropic. Section 2.4 discusses representative material properties for the more diverse materials employed in signature control applications.

2.4 GENERAL SUPPRESSION METHODS

Signature suppression can be accomplished with a variety of methods and the choice depends on the specific application. Methods available can usually be fit into one of the following categories:

- obscuration
- shape tailoring
- surface appliques
- self-illumination
- active cooling
- wake control.

These methods are seldom mutually exclusive and are usually most effective when used in combination. Moreover, it is difficult to prioritize control methods without referring to both the specific vehicle type and the environment in which it will be operating. However, obscuration is the most common thread found in low observable designs and is closely followed by the use of surface treatments. Shape tailoring is often useful in combination with surface treatments. Self-illumination can be useful when reflectivity control is less effective, whereas active cooling is common in designs for engine suppression. Wake control gets more attention as success is achieved in controlling the more direct signature contributors and is not discussed further in this section. In every case, the technique chosen must be compatible with signature control in other bands with the most important being the radio frequency (rf) band. It is usually of little value to accomplish electro-optical (EO) signature control if it comes, for instance, at the expense of radar cross section. Each technique is described here together, when appropriate, with requirements for compatibility with radar cross section reduction (RCSR) methods.

2.4.1 Obscuration

It is often easier to hide a signature source than to eliminate it. Accordingly, obscuration is one of the more common suppression techniques. Obscuration can take many forms. It can range from a simple baffle, designed to obstruct the line of sight to a hot part, to a camouflage net thrown over the entire vehicle. It is usually done with the theory that the object accomplishing the obscuration will be easier to control than the object it hides. Thus, obscuration does not necessarily complete the signature suppression goal because suppression must still be implemented on the masking device. Specific obscuration techniques are discussed later in vehicle application sections.

2.4.2 Shape Tailoring

Shape is a direct signature control approach and should be considered in combination with RCSR design. Shape is likely to be a primary RCSR technique that the IR suppression design will need to be compatible with. Accordingly, the shape should be chosen for the synergism it can provide to a well-integrated rf/IR design.

Fortunately, shaping effects in rf signature reduction are very similar to those in EO reduction and compatibility is relatively easy to achieve. The goal in both domains is simply to avoid reflections directed toward the threat re-

ceiver. Compatibility results from the fact that the primary rf signature generation mechanism in vehicles is the geometric optics reflection mechanism.[11] Thus, the reflected component of both IR and rf signatures should be subject to the same shape considerations.

However, geometrically reflected signature components in the IR and visible domains are subject to a major additional constraint over those in the rf domain: source location. Radar threat sources are almost always monostatic, i.e., they are collocated with the receiver. Passive external EO sources are almost always bistatic in that they result from natural illumination sources such as the sun and the earth, which are typically located at an angle away from the threat receiver. These passive bistatic sources constrain the shape options available to the EO suppression designer.

The most common bistatic EO illumination source is the sun. It can yield a large reflected contribution from the visible to the mid-infrared region of the spectrum. Shape design can play a major role in avoiding a reflected component from this large signature source. Reflections can be loosely lumped into the four categories illustrated in Fig. 2.16.

These categories roughly represent the continuum of reflection conditions that are encountered from target surfaces. They are all heavily driven by surface roughness and shape. Most are also a function of viewing position. The most commonly encountered condition is the pseudo-diffuse condition, which generally gives a dim surface, if reflectivity is low, but can still give a significant signature as a result of large surface areas. Arguably the least desirable condition is wide-angle glint because it can be seen from many viewing positions and is typically very bright. Glare is less undesirable because it has a narrow beam, but is to be avoided because the beam can still be unacceptably large and can appear intense because of high brightness and large surface area. Glare is really just a special case of pseudo-diffuse reflection where the observation point is now located in the mainlobe instead of in the diffuse region. Narrow-angle glint reflections are often the "lesser evil" because, although they can be seen and can be very bright, their beam is so narrow that the probability of continuous intercept under dynamic conditions is low.

Of course these illustrations are only special cases of a very wide range of surface reflection conditions. Moreover, they neglect the fact that secondary solar radiation from atmospheric scattering can contribute approximately[12] 20% to total object solar irradiance in the visible to near infrared and must be considered in a total solution. Still, the former phenomena represent first-order solar reflection effects and require control in both the visible and infrared spectral regions.

Techniques for controlling point source reflections are illustrated in Fig. 2.17. These techniques depend heavily on both shape and surface properties. It is important to note that they ignore self-emission aspects of signature control and that they may not be compatible with a well-integrated design that must consider all IR signature sources. The combination of low reflectances with roughened surfaces can greatly reduce diffuse and specular reflections. Shaping should strive to eliminate doubly curved surfaces in favor of either flat or singly curved surfaces. A flat surface directs the specular lobe of a reflection into a narrow angle with consequent reduction in intercept probability and tracking continuity. Likewise, a singly curved surface directs the

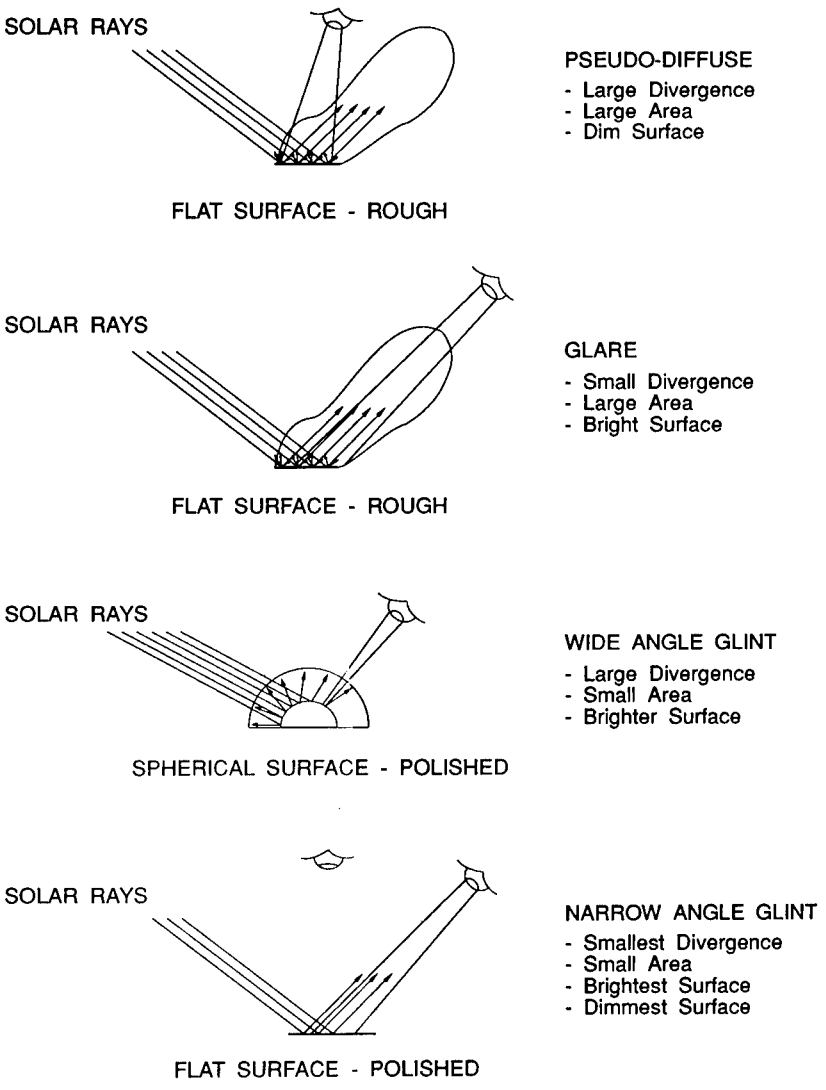

Fig. 2.16 Illustration of four representation reflection categories.

specular component into a thin curved surface instead of into a large solid angle and similarly results in reduced intercept probability. Strakes or baffles might offer some reflectivity control but generally introduce corners that can result in stronger reflections from other angles for both EO and rf sources.

These techniques can be used in combination but care must be exercised to consider the total effect. For instance, the highly directional properties of flat segment surfaces would be partially defeated if combined with a diffusely reflecting paint. Contrarily, it may be necessary to use the combination of flat segment surfaces and diffuse coatings if the diffuse coating, on a doubly curved surface, still offered a broad-angle specular component of unacceptable intensity. Final choices depend on the application scenario and viewing geometry.

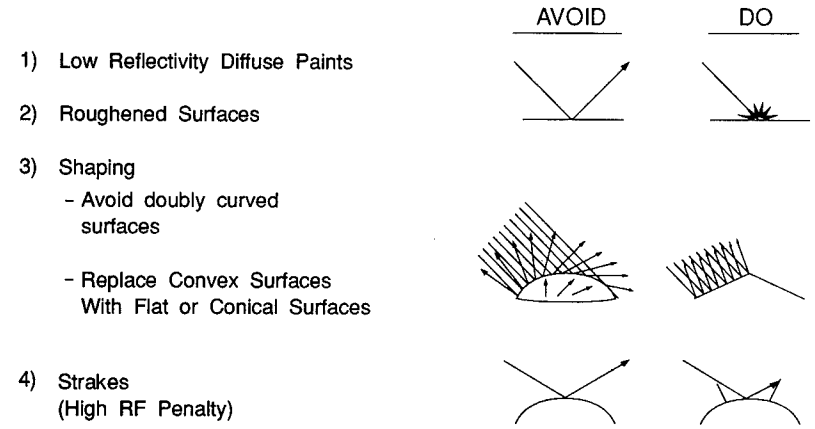

Fig. 2.17 Techniques for glint and glare reduction.

2.4.3 Surface Appliques

Coatings offer the potential to alter apparent surface characteristics by modifying their reflection, self-emission, and directional properties. They are a major tool for the design of low observable systems in the visible and infrared spectrum.

Effects of surface appliques can be addressed separately in the visible and infrared spectral regions, although they must be compatible. In the visible region they are dominated by the scattering and absorption properties of subsurface pigments and dyes, whereas in the infrared they are dominated by the reflection and self-emission properties of surfaces (such surfaces may still be the submerged surfaces of pigments). Although there is little difference in the fundamental physics involved in these two regions, their technology sometimes differs, and it is possible to discuss each region separately. However, in the final coating product, visible, infrared, and radar reflectance properties must be meshed for multispectral signature control.

2.4.3.1 Visible Coatings. Mechanisms at work are illustrated in Fig. 2.18. Conventional paints may have one to three separate layer types and can consist of a primer, undercoat, and topcoat. The main purpose of the primer is usually

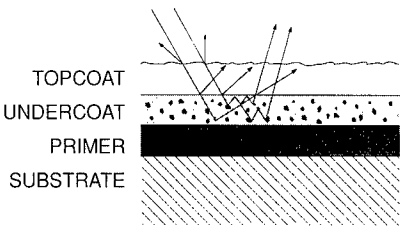

Fig. 2.18 Paint composition.

to provide a mechanism for successive layers to adhere to the surface but it also can serve to passivate metal substrates against electrochemical corrosion effects[13] and to isolate substrates from other reactive chemicals. The primer can also perform the same reflection control functions of top coatings, but there is a limit to the functions one can practically accomplish in one layer type. The undercoat (which is the topcoat if there is no additional layer) contains the primary pigment designed to control spectral reflectivity. A transparent topcoat can be added to control surface roughness, provide abrasion resistance, and provide contamination protection.

Paint constituents and optical properties are described in terms of the undercoat, although most of these properties can be made to apply to primers and top coats as well. Table 2.4 describes the major constituents and their functions. Key ingredients are the pigments and the binder. Binders hold the pigment particles together after the paint has dried. Main optical properties of binders are their transparency and index of refraction. Likewise, the main optical properties of pigments are their index of refraction and opacity. Pigment controls reflectivity by offering a high index of refraction relative to the binder medium. In general, reflectivity is computed from Eq. (2.24) for a homogeneous medium. For normal incidence it becomes

$$\rho = \frac{[n_p(\lambda) - n_b(\lambda)]^2}{[n_p(\lambda) + n_b(\lambda)]^2} , \tag{2.27}$$

where n_b is the refractive index of the binder and n_p is the refractive index of the pigment.

One of the most common pigments in general use[13] is titanium dioxide (TiO_2), which has a refractive index of approximately 2.8. Most binders are made from oils or polymers that offer a refractive index near 1.5. Because reflections occur at the interface between two media having different refractive indices, it is clear that this opportunity arises with paint at least at the interface between air (refractive index = 1) and the binder and at the interface between the binder and the pigment. Thus, common paints reflect approximately 4% at the surface with air and 9% between the binder-pigment boundary. Reflection off the binder-substrate is driven by overall coating transmission as well as by the refractive index of the substrate. Transmission is determined by the opacity and volume density of the pigmentation and by the thickness

Table 2.4 Paint Constituents

Pigments (filler)	Primary material used to impart color; remains insoluble; provides protection hardness: weatherability; provides roughness: grind size
Dyestuff	Secondary material used to impart color; soluble in solvent and/or binder; transparent in thin coats; limited usage
Binder (polymers)	Holds pigment particles together, to substrate; transparency needed
Solvent	Provides application mobility; evaporates
Additives	Driers; wetting, antisag, flattening, and similar agents

of the coating. Most pigments are opaque in the wavelength region they are designed to control. Substrate reflections then depend on pigment density and coating thickness. These are typically chosen to eliminate substrate reflections completely. Clearly, total coating reflectivity is determined by a variety of surface and internal scattering mechanisms. Determination of apparent paint reflectivity is too complex to be described by Eq. (2.27). Appropriate relationships are discussed later.

Dyes also control spectral reflectivity, but are far less common. Unlike pigments that remain insoluble, dyes are soluble and are dissolved in the binder. Reflectivity control is accomplished by absorption of the undesired wavelengths. Dyes can be added to coating formulations that already contain pigments and can serve special purposes. Their application to signature suppression is potentially useful for the control of discrete laser lines. Dyes can potentially add laser line attenuation without affecting the overall broadband signature control strategy.

Binders impact the optical properties of coatings but also strongly determine other important physical properties including durability and temperature tolerance. It is important to note that the utility of coatings for signature control is as much driven by factors such as durability, maintainability, and adherability as it is by their optical properties. Most binders are polymers (sometimes called resins), defined as large organic molecules where simple repeating units are joined by covalent bonds.[14] They are formed in nature by the oxidation of vegetable oils and can also be synthesized in the laboratory. Many different types of polymers can be found. They include thermoplastic and thermoset types. Historically, vegetable oils derived from oilseeds such as linseed, cottonseed, etc. have constituted the largest category of resins. These natural oils can be polymerized by thermal or oxidative methods. Some of the more common polymer binders are alkyds (polyester-based), polyesters, epoxy resins, polyurethanes (or simply urethanes), silicone resins, and acrylics. In general, all of these binders can have uses in signature control coating formulations. However, some have unique properties worth noting. For instance, epoxy resins and polyurethanes offer a high degree of flexibility, toughness, abrasion resistance, and resistance to chemicals. In addition, they offer good weather resistance and adhesion to metals. Silicone provides high levels of heat resistance that is generally only limited by the pigment. With ceramic pigments, silicone paints can be formulated to withstand temperatures to 750°C; with aluminum, serviceability can go to 650°C. Normal enamels, on the other hand, can typically withstand temperatures[13] between 200 and 300°C. Silicone also offers good weathering qualities because of its water repellency. Although these properties are important, camouflage paint binders must still meet the optical property requirements discussed later.

Solvents are used as an application medium in paints that dry by evaporation. These are primarily limited to lacquers and latex paints. Solvents are eliminated in the drying process and have no effect on the optical properties of the paint. Other paints, such as epoxies, urethanes, and baking enamels form dry films by chemical reaction and do not contain solvents.

Certain additives can impart special optical properties to paints. Among the most important are the flattening agents. One type of flattening agent reduces specular reflections by adding particles of a grain size that is large compared

to the wavelength. These large particles increase internal scattering. A special case of the large particle additive is the transparent glass sphere or bead additive. Glass spheres can result in large scattering angles, but they have the side effect of producing a large retroreflectivity. This is desirable for some applications such as for transportation road signs, but is obviously undesirable when trying to protect military vehicles against active illumination sources such as laser illuminators and search lights. Still, they are often found in military instrument panel paints where they are effective in reducing glare. Another type of flattening agent adds a ripple to the top surface of the coating. The ripple diffuses specular reflections by increasing the range of incidence angles apparent to the incoming light. It has the same effect on exiting internally reflected light.

Pigment particle size also affects gloss. Pigment grind sizes that are both large in comparison to the wavelength of light and formulated in dense concentrations appear rough to incident light. Large grind sizes can also increase surface roughness but surface scattering effects are typically secondary to internal scattering. Small particle sizes in dense concentrations, on the other hand, appear uniformly smooth to longer wavelength incident light for a more glossy appearance. Thus, particle sizes can be used to provide diffuse scattering properties in the visible and yet provide a more specular appearance in the longer wavelength infrared region. As is seen later, this is exactly what is wanted to simultaneously control solar reflections in the visible and infrared when used on planar surfaces.

Most paints are composites of several material types. Therefore, the simple formulas that predict reflectivity for homogeneous materials do not directly apply. According to Starr[15] the prediction of coating reflectivity for composites can be derived from the properties of the medium and the suspended particulate materials by dividing the problem into four cases.

Case I. Particle Size Is Much Less Than the Wavelength. Effective medium theory (EMT) can be applied[16] when the particle sizes are less than 20% of the wavelength and when the particles are a small volume fraction of the total. Specifically, the Maxwell-Garnett (MG) approach can be used. This approach calls for modifying the material properties contained in expressions for homogeneous materials to impart small changes because of the presence of the particulates. Expressions for reflectivity, such as Eq. (2.27), would then still apply.

Case II. Particle Size Is Much Greater Than the Wavelength. Kubelka-Munk theory[17] explains diffuse reflectivity when the media has a high volume fraction of particulates or when particles are large relative to the wavelength. This theory relates reflectance to two factors: a scattering coefficient s and an absorption coefficient k. Reflectivity is then given by the equation

$$\rho = \frac{1 - [k_0/(k_0 + 2s)]^{1/2}}{1 + [k_0/(k_0 + 2s)]^{1/2}} , \tag{2.28}$$

where s is the scattering coefficient, and k_0 is the absorption coefficient. The absorption coefficient is equivalent to the Beer-Lambert extinction coefficient

and is easily computed from the components' concentration weighted absorption coefficients. However, the scattering coefficient has a complex relationship to component properties. Details can be found in Ref. 17.

Case III. Particle Size Is Comparable to the Wavelength and Volume Concentration Is Low. Material optical properties are complex in this range of particle sizes. No one theory appears to satisfactorily apply.

Case IV. Composites Consisting of Layers. Composites consisting of layers that have thicknesses much larger than the wavelengths involved show few interference effects. However, thin layers offer the potential for coatings to show reflective spectral selectivity through optical interference. When these layers are homogeneous, reflectivity is highly directional and is easily predicted as a function of incidence angle.[18] However, when the particles are composed of layers, the prediction of reflectivity is much more difficult and has not been widely addressed.

As might be imagined by the complexity of some of the analytical approaches, many of the reflective properties of coatings are determined from direct measurement. The formulations that produce the desired colors often result from empirical investigations. The pigment formulations of many camouflage paints are also heavily empirical. Table 2.5 shows a summary of the pigment types that result[19,20] in various camouflage paint colors. Of particular interest are formulations for various army greens. These paints are representative of a series of military camouflage paints designed to give a visual as well as near-infrared match to the reflectivity of foliage. Figure 2.19 shows a plot of the spectral reflectivity limits[19] for field green, light green, forest green, dark green, and olive drab.

2.4.3.2 Infrared Coatings. Of course, ideal coatings treat both the visible and infrared requirements as well as rf needs. Compatibility requirements between bands are discussed as these issues arise.

Equations (2.12), derived earlier, showed the important relation between emissivity and reflectivity. A major connotation of this equation to signature control is that a low emissivity surface must have a high reflectivity and that, conversely, low surface reflectivity results in high emissivity. A practical implication is that, when placing a high-temperature object in its natural environment, low-emissivity coatings may reduce self-emissions but still result in significant overall apparent emissions because of reflections. A logical consequence is that situations can arise where no emissivity, or surface applique, can, by itself, provide the desired signature control levels. These situations then require the application of other techniques, which are discussed elsewhere in this chapter. Figures 2.12 and 2.13 previously showed representative emissivities required for signature control when such control was possible using surface appliques.

In general, spectral reflectivity requirements are application and scenario dependent. However, nominal requirements can be stated from signature generation principles and knowledge of typical vehicle usage. Table 2.6 shows nominal requirements by major spectral region. Visible region reflectivities are driven by the desire to match the immediate background, which are often low reflectivity (0.05 to 0.20) materials. Near infrared (NIR) reflectivities need

Table 2.5 Pigmentation (from Ref. 19)

Light Green Dark Green Forest Green Olive Drab Green 383	Acid insoluble green pigment predominately composed of cobalt, zinc, and chromium oxides with other oxides permitted, carbazole dioxazine violet, yellow iron oxide, red iron oxide, chromium oxide, permanent maroon, light stable organic yellow, magnesium/iron oxide.
Field Drab Earth Yellow Desert Sand	Yellow iron oxide, red iron oxide, chromium oxide, titanium dioxide, carbon black.
Aircraft Green Olive Drab 34087	Yellow iron oxide, red iron oxide, carbon black, black iron oxide.
Earth Brown Earth Red Brown 383	Yellow iron oxide, red iron oxide, titanium dioxide, carbon black, chromium oxide, brown iron oxide, carbazole dioxazine violet.
Sand	Yellow iron oxide, red iron oxide, chromium oxide, titanium dioxide, carbazole dioxazine violet.
Black Aircraft Black 37038 Interior Aircraft Black	Carbon black, black iron oxide.
Aircraft White 37875	Titanium dioxide.
Aircraft Red 31136	Titanium dioxide, light stable organic red. Titanium dioxide, light stable organic red.
Aircraft Gray Interior Aircraft Gray 36231	Titanium dioxide, carbon black, yellow iron oxide.
Aircraft Insignia Blue 35044	Copper phthalocyanine blue, carbon or lampblack, titanium dioxide.

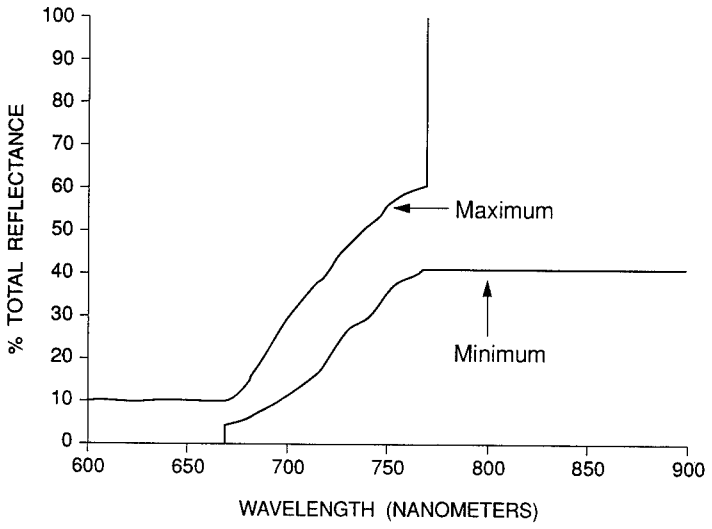

Fig. 2.19 Allowable spectral reflectivity range for various green camouflage paints.[19]

to be dramatically higher (0.4 to 0.7) against live foliage backgrounds. In the mid- and long-wave infrared, reflectivities need to be high on higher temperature parts so that the resulting low emissivities can reduce self-emissions. Required emissivity values, as shown earlier in Sec. 2.3, can easily range from 0.05 to 0.6. These low emissivities can result in high daytime solar reflections as well as high day and night ground reflections. So in some cases, as with high-altitude aircraft, reflectivities must be kept low and other means, such as active cooling techniques, must be used to control the mid-infrared and long-wave infrared self-emissions.

Table 2.6 Nominal Spectral Reflectivity Requirements

OBJECT	VISIBLE 0.4 - 0.7 micron	NIR 0.7 - 1.0 micron	MWIR 3 - 5 micron	LWIR 8 - 12 micron
Turbine nozzle	low	low (vs. internal reflec.) high vs. hot parts	low vs. internal reflec.) high vs. hot parts	low (vs. internal reflec.) high (vs. hot parts)
engine housing	high-bottom view low-top view	high-bottom view low-top view	high	high
muffler	low	high (vs. foliage)	high	high
armor hull	low	high (vs. foliage)	moderate	moderate
aircraft body (subsonic) — low alt. — high alt.	low-top high-bottom low	low-top high-bottom low	high low (w/cooling)	high low (w/cooling)
(supersonic) — high alt.	low	low	high	high
helicopter body — low alt.	low	high (vs. foliage)	moderate (w/shape) low (w/cooling)	moderate (w/shape) low (w/cooling)

Standard military paints mostly offer only high-infrared emissivities because of their use of titanium dioxide pigments, or more recently, tungsten trioxide pigments. Most conventional pigments show low-infrared reflectance when packed at high densities. Thus, conventional pigments are useful for modifying otherwise high-reflectance infrared coatings and offer the opportunity to accomplish visible coloring in the process. Unfortunately, lower emissivities are needed for most signature control requirements.

Conventional methods for obtaining infrared reflectivity control have historically centered on the use of metals. Figure 2.20 shows an example[21] of the broadband control that is achieved with aluminum having various surface conditions. Metals are generally used to achieve a low emissivity because they contain free electrons that provide for high refractive indices, as governed by Eq. (2.26), over broad bands. Reflectivities can be decreased, at shorter wavelengths, by increasing surface roughness. A rough surface causes multiple bounces of incident light waves. Even though each bounce may experience a high reflectivity, the combination of many bounces, with each bounce having a slight attenuation, eventually results in a lower overall effective surface reflectivity. This effect is wavelength dependent because surface roughness is inversely proportional to wavelength. Moderate to high infrared reflectivity can be achieved with metal surfaces, but a transparent top coat may be required to preserve surface oxidation and roughness state.

Less reflectivity and more spectral shaping can be accomplished by going to lower conductivity materials. Semiconductors show less conductivity than metals. Their lower electron density causes semiconductors to have a high refractive index, with corresponding high reflectivity, at long wavelengths. However, they become transparent at shorter wavelengths where refractive index and extinction coefficient drop off. This effect can be controlled by varying the population of charge carriers, but is then temperature and composition dependent. Figure 2.21 shows an example[15,22] of the spectral reflectivity that can be obtained with lead selenide.

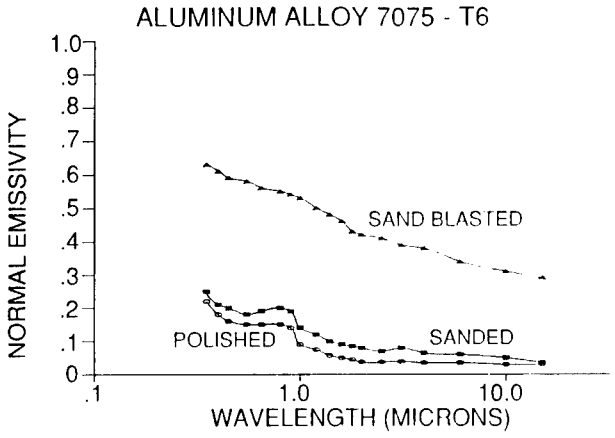

Fig. 2.20 Effects of surface finish on emissivity.

Still more spectral reflectivity tailoring can be achieved by going to a multiple layer approach. This technique is comparable to the approach used to make interference filters and has some of the same spectral tailorability advantages as well as angular dependency limitations. Figure 2.22 shows the results of efforts to create a coating with low visible reflectance and high infrared reflectance with a cut-on wavelength near[23] 3.0 μm. This result was achieved with a pigment consisting of a 17-layer, 3-μm-thick structure of silicon, silicon oxynitride, and silicon dioxide.

In general, one can achieve much more control over surface reflectivity by applying the desired material in the form of loose particles with variable densities. In addition, if the particles do not touch, they will effectively be transparent to rf wavelengths because the configuration would be nonconducting. Such control is available, for instance, by grinding the desired metals, semiconductors, or layered composites into flakes and mixing them into a binder as is done with paint pigments for visible signature control. Of course,

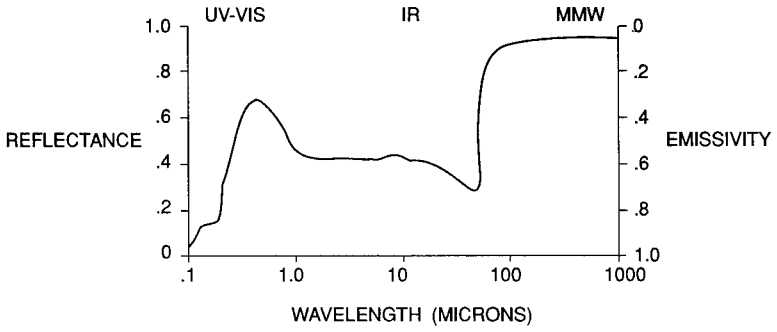

Fig. 2.21 Lead selenide (PbSe) semiconductor reflectivity (see Refs. 15 and 22).

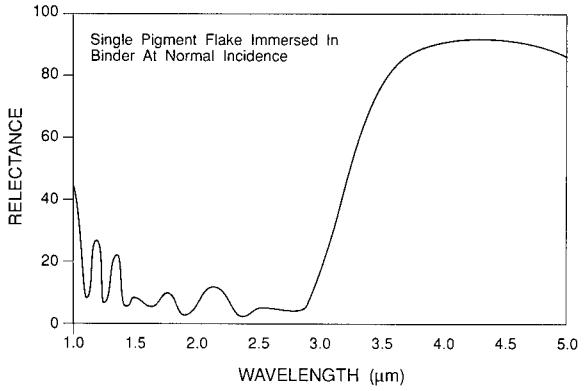

Fig. 2.22 Theoretical spectral performance of pigment design with emissivity transition[23] at 3 μm.

this process requires a binder that is suitably transparent over the spectral region of interest.

Figure 2.23 shows the infrared spectral reflectance achieved when silver coated glass microspheres[15] were used as pigmentation. Likewise, the spectrally tailored reflectance plot shown previously in Fig. 2.22 was the result of suspending layered flakes in a transparent binder.

Material properties for use in binder formulations are of interest if spectrally tailored pigments are to be successfully suspended. Here the designer needs materials that exhibit weak interactions with electromagnetic waves. Some polymers are good candidates because of their high toughness and flexibility. Because polymers are a class of molecular solids, they exhibit the desired weak electromagnetic interaction except in relatively narrow absorption bands. Figure 2.24 shows[24] the location of absorption bands[25] for several candidate polymeric binders. Note that these absorption bands potentially offer the coating designer an additional control, in the form of binder selection, for further tailoring coating spectral reflectance. Transmission spectra for other candidate polymers can be found in an infrared spectra atlas such as Ref. 24.

2.4.3.3 Future Technologies. The coating technologies described thus far produce fixed properties such as color, reflectivity, and emissivity. The resulting camouflage patterns, by necessity, have fixed properties, which means that the camouflage is an average or "best guess" design based on the most likely background conditions.

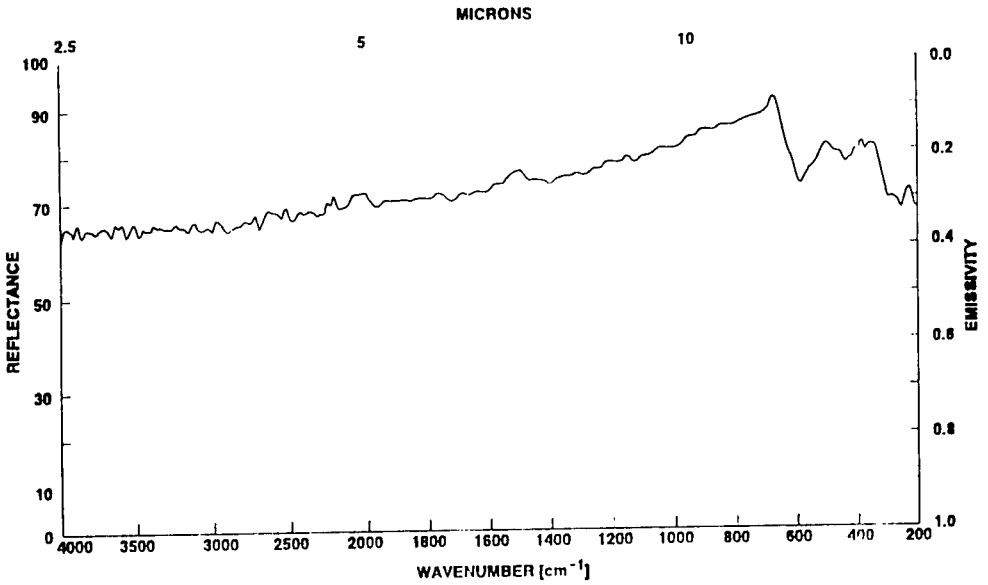

Fig. 2.23 Reflectance of silver pigment paint (see Ref. 15).

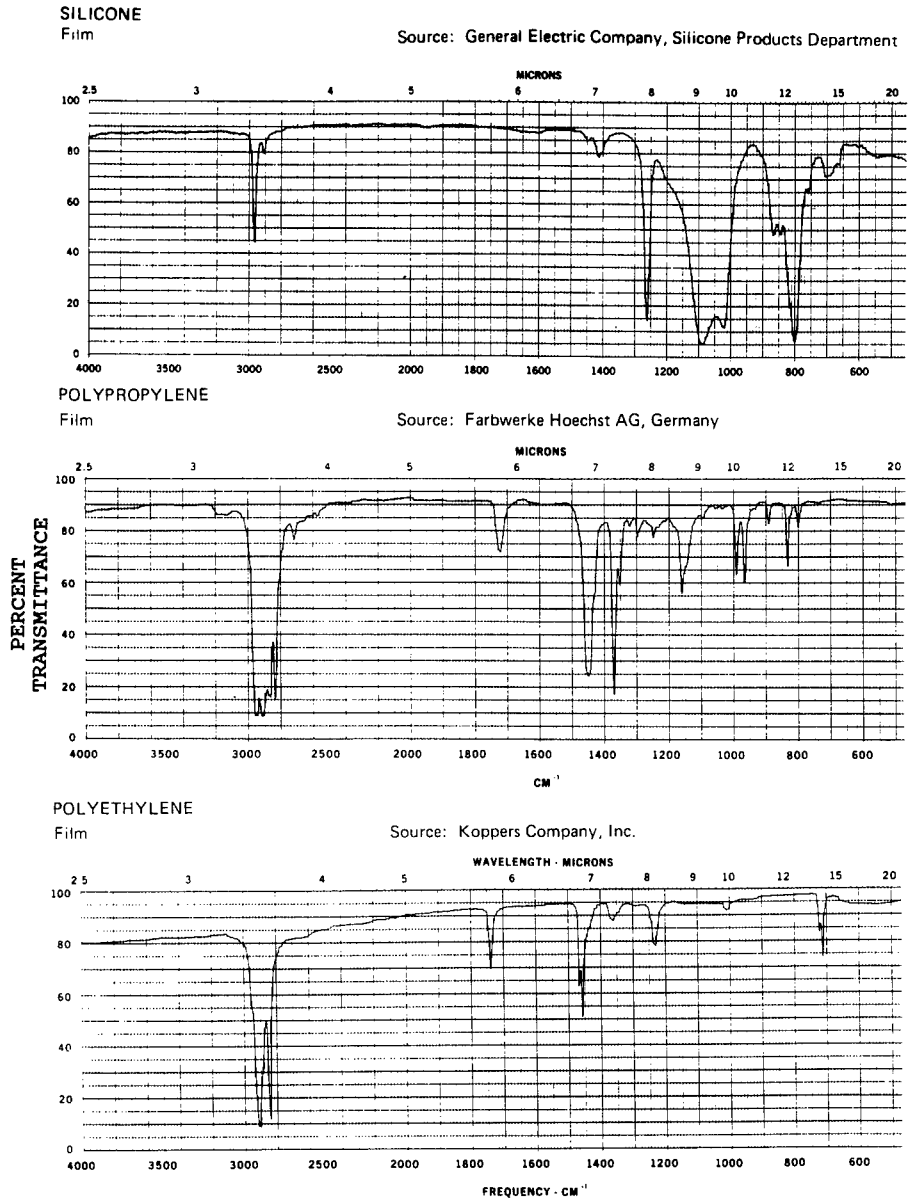

Fig. 2.24 Absorption bands for candidate polymeric binders.[24]

Ideal camouflage coatings would offer the opportunity for near real-time reflectivity adaptation to the background. This requirement is driven, in part, by target motion, which changes the part of the background that it reflects. It is also driven by target operating conditions, which can change the requirement for internal heat masking. Finally, it is driven by diurnal environmental effects in both the target and the background.

Some technologies offer opportunities for adaptive signature control. Passive and active technologies are available for visible and infrared applications that could be used to better match background conditions over the long term. Application of these technologies to camouflage requirements is in its infancy but the general principles are discussed.

Adaptive coatings can be grouped into categories named for the mechanism responsible for the adaptation process. Materials whose optical properties are subject to change by the application of external stimuli are called *chromogenics*. Camouflage application of chromogenics has benefitted from the large amount of research conducted on these materials by the solar energy industry. Some of the major chromogenic materials are:

- *thermochromics*—optical properties are reversible under the influence of temperature
- *electrochromics*—optical properties are reversible under the influence of an electric field
- *photochromics*—optical properties are reversible under the influence of incident radiant flux.

There are others, but the most mature and relevant are the thermochromics and electrochromics. Good surveys of chromogenics are provided in books edited by Granqvist,[26] Lampert and Granqvist,[27] and by others.[28–31]

Other techniques for signature control are required when coatings alone are insufficient. Emissivity control methods fail when the scenario dictates that cooling is required (Table 2.6), when the environment is too dirty or too harsh for coatings to last, or when there is insufficient ambient illumination in the desired directions. Alternative methods can be roughly categorized as either self-illumination or heat transfer. Self-illumination involves on-board light sources and are discussed later in the aircraft body signature suppression section. Heat transfer techniques involve an attempt to eliminate the source of heat (or cold) responsible for thermal contrast.

A wide range of heat transfer techniques are available[32] and are typically well known in various industrial applications. Most modern engineering textbooks[33] on the subject of thermodynamics treat the operating principles and analysis methods in detail. Table 2.7 summarizes conventional cooling methods. Heating is typically either not required, because most platforms generate waste heat as a by-product of propulsion, or is easy to supply by reversing the listed cooling processes. In general, the application of these technologies to camouflage can be as varied as they are in other industrial and civilian applications. Their major drawbacks are their bulk, complexity, power requirement, and cost compared to other coatings techniques.

Table 2.7 Summary of Major Conventional Cooling Techniques

GENERAL TECHNIQUE	SPECIFIC IMPLEMENTATION	TYPICAL COOLANT TYPE	APPROX. * EFFICIENCY (%)
Compression refrigeration	vapor compression	fluorochloro-carbons	200-300
	air compression	air	10-30
absorption refrigeration		ammonia-water lithium bromide-water	40-80
convection (forced)	impingement transpiration recirculation	air air, water, glycol " " "	600 + (high temp)
convection (free)	fin attachment	air	passive
conduction	thermal contact		passive
radiation	surface control	—	passive
state change	evaporation (transpiration)	water, glycol	passive
capillary action & vapor diffusion	heat pipe	water, glycol, sodium	passive
Peltier effect	thermoelectric	—	50-2000 (low temp)

* 100 x (heat power removed/drive power input)

2.5 AIRCRAFT SYSTEMS

2.5.1 Propulsion Design

Turbine engines dominate aircraft power plant designs because they offer a high power to weight ratio. Observable control for turbines must address plume and hot parts signature generation mechanisms. However, smoke and contrail signatures can also be significant by-products of turbine propulsion systems. This section addresses the control of plume and hot parts because they are the major engine signature contributors seen by modern threat seekers and IRSTs.

2.5.1.1 Gas Turbines. Jet propulsion engines use an open Brayton cycle for power generation.[33] The turbojet engine uses an ideal Brayton cycle, whereas turbofan and turboprop engines use the Brayton cycle in a modified form.

Figure 2.25 illustrates turbofan operation. It is the most common power plant in use for both military and commercial aircraft because of the favorable balance it achieves in efficiency, thrust, and speed. Turbofans differ from turbojets by providing rotating fan blades in front of the compressor that extend radially beyond the compressor. Fan air bypasses the compressor, burner, and turbine sections to provide direct thrust. Bypass air can be immediately expelled or ducted to the rear of the engine. The ratio of fan air mass bypassing the compressor to mass flowing through the compressor is a cycle parameter called the *bypass ratio*. This ratio is approximately proportional to the area ratio of the fan inlet duct to the compressor inlet duct. Bypass air can be used, with compressor and inlet bleed air, to cool internal hot parts and can also be mixed with the exhaust plume to cool the hot gases. In most other respects, turbofans resemble turbojets.

Figure 2.26 illustrates operation of a turbojet gas turbine cycle in terms of total pressure P_t and total temperature T_t. Note that the term *total* is used to

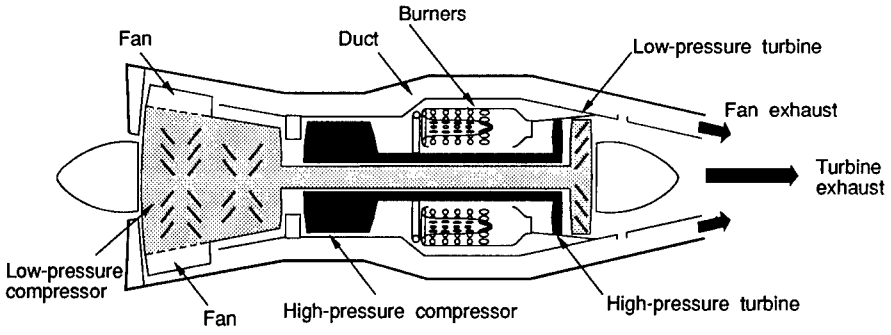

Fig. 2.25 Turbofan engine stages.

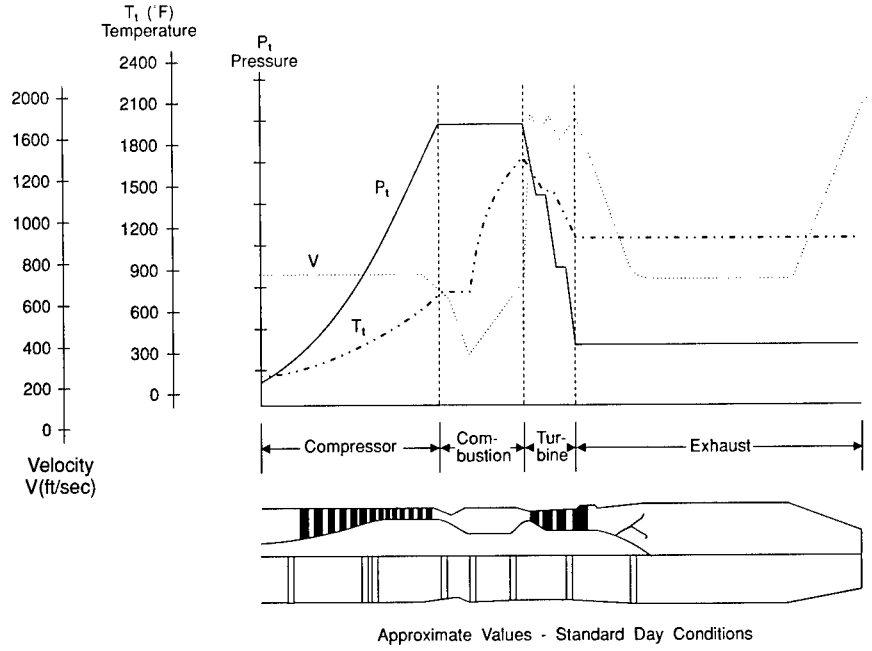

Fig. 2.26 Turbojet gas turbine cycle.

describe both pressure and temperature to differentiate them from *static* pressure and temperatures. A total pressure includes both a dynamic and a static effect as does a total temperature. Only the static temperature component contributes to gaseous radiant emissions.

In Fig. 2.26, the compressor stage compresses inlet air and raises the pressure, which also raises temperature, but velocity remains unchanged. This air is mixed with fuel and burned in the combustors. Combustion dramatically increases temperature but pressure stays the same. High-temperature compressed gas enters the turbine stage where energy is extracted to drive the

compressor. This process lowers both pressure and temperature but greatly increases velocity. Finally, high-velocity gases enter the exhaust where pressure and temperature remain unchanged but the nozzle forces an increase in exit velocity. The latter increase accounts for the engine's thrust.

Variations in the basic Brayton cycle are common. They include the mentioned turbofan and turboprop (similar to turboshaft engines used for helicopters) categories, but also include many variations within each category. Example cycle effects are bypass ratio changes, temperature and pressure modifications, afterburning, and air/plume mixing percentages. These variations can be used to optimize engine power, fuel consumption, and observables.

2.5.1.2 Plume Suppression. Some of the techniques for plume suppression are

- engine size reduction
- cycle tailoring
- plume/air mixing
- nozzle shaping
- obscuration.

Each is discussed here.

Engine size can clearly affect plume radiant emission levels. However, size is also clearly constrained by airframe size, speed, and payload requirements. If any of those requirements can be reduced, so can plume observables.

Cycle tailoring involves the choice of basic cycle configuration (turbojet, fan, prop, etc.) as well as specific configuration choices within each basic type. Fighter and bomber fixed-wing aircraft are already driven to turbofan cycles for the mentioned reasons. Likewise, helicopters use turboshaft and transports often use turboprop designs because of the greater thrust they produce at lower platform speeds. It is desirable to retain these cycle choices but adapt them for low observables.

Turbofans illustrate the design choices for all categories because turboprops and turboshafts can be thought of as turbofans with extra high bypass ratios. Internal design features determine local temperature and pressure profiles. These profiles can be adjusted to tailor gas temperatures, which ultimately affect the observed exhaust plume. Increases in bypass ratio result in a greater percentage of the engine thrust originating from cool fan air rather than from heated exhaust gases. This effect alone does not lower plume temperature but can reduce emissions. In addition, however, bypass ratio can be increased to give comparably greater air for internal exhaust nozzle cooling. In general, higher bypass ratios yield greater air for cooling purposes. However, the larger duct openings associated with high bypass ratios can be expected to cause higher radar cross sections (RCSs) as well. Final choice for bypass ratio must be a compromise among these potentially conflicting multispectral requirements. Figure 2.27 illustrates the available configuration choices. Only the mixed flow configurations offer significant opportunity for plume cooling with dilution from outside air.[34]

Mixing effects on plume temperature and resultant radiant emissions can be studied from the principles of fluid mechanics and gaseous combustion.[35] Figure 2.28 illustrates the reduced radiant emissions predicted[36] from these principles when cooling the plume of a turbofan engine equipped with an

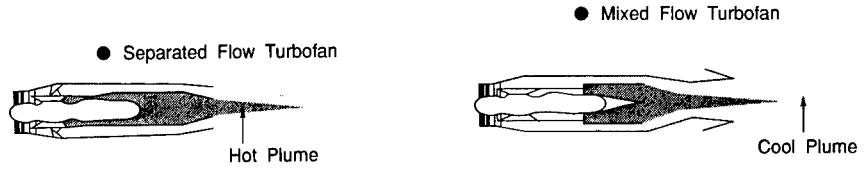

Fig. 2.27 Example turbofan configurations.

axisymmetric nozzle. Cooling is assumed to occur as the result of ideally mixing the exhaust gases with fan bypass air and further mixing those gases with free stream air in an ejector. These figures show the effects of plume cooling on both signature and signature propagation in the 3.5- to 5-μm band. Results show plume normalized radiant intensity plotted as a function of range for a broadside plume view. Apparent plume radiant intensity would decrease with angle, in the direction of the tail, because of absorption of the line emissions by cooler down-stream plume gases. However, apparent hot parts emissions would likely increase because of their greater exposure. All radiant intensity values are normalized to the peak value achieved at the altitude of 30 kft. Thrust levels were kept nominally the same, at a given altitude, whereas exhaust plume temperature was allowed to vary. The turbine was assumed to be operating at military throttle on an aircraft moving at Mach 0.9. Table 2.8 summarizes some of the engine conditions that go with these results. Note that engine thrust decreases with increasing altitude, at a given throttle setting and airspeed, because of the reduction in air density with altitude.

The computational procedure involved six steps. First, a self-consistent engine operating design was selected. Here, a turbofan engine design with mixed exhaust was patterned after a sample design given by Mattingly et al.[37] Engine exit properties, including static temperature, pressure, and velocity, were computed from his cycle deck programs ONX and OFFX. Second, gas combustion species were calculated from standard chemical equilibrium techniques. Here the NASA developed CE71 computer code[38] was used to perform the computations. Third, mixer nozzle exit conditions, for the desired exit total temperature, were computed using equations given by Mattingly et al. Fourth, after-nozzle plume flow fields were calculated using the presented engine exit properties. To compute plume radiant emissions, flow field properties of interest were static temperature, pressure, and species. The flow fields were computed from the parabolized Navier-Stokes equations described in Ref. 35. Fifth, plume emissions at close range were determined. This was done for a horizontal path using the computer code[39] EXPIRT. Finally, radiant intensity attenuation losses were predicted over the ranges of interest. The APART computer code was used for this task,[40] although LOWTRAN could have been used as well. A horizontal propagation path was assumed using the 1962 U.S. standard atmosphere.

Results can, of course, change considerably for different engine design and operating assumptions. Trade-offs involve cycle, mixer, and nozzle designs. Choices affect engine thrust and fuel consumption as well as size, weight, cost, and reliability. Changes in these variables can cause large differences in radiant emissions.

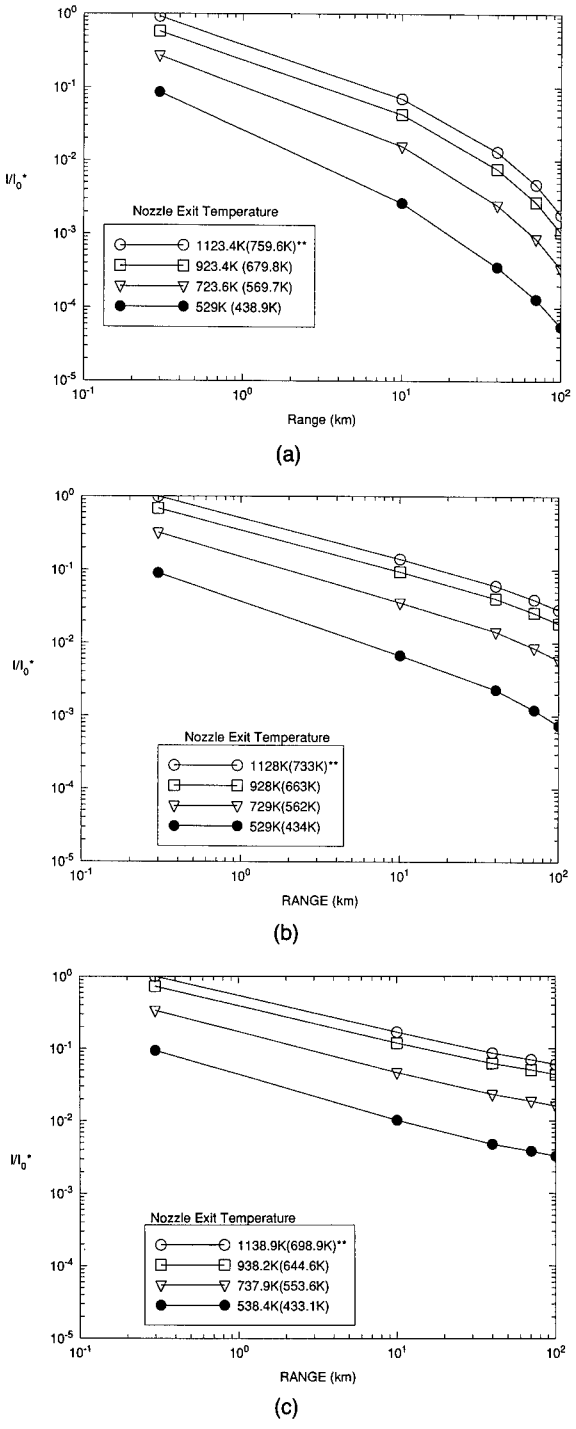

Fig. 2.28 Predicted plume radiant emissions (3.5 to 5.0 μm) for various nozzle exit temperatures at altitudes of (a) 2000 ft, (b) 15,000 ft, and (c) 30,000 ft. Mach 0.90 at U.S. standard atmosphere.

Table 2.8 Engine Operating Characteristics Summary

Engine type	Turbofan
Bypass ratio	0.3
Fan pressure ratio	3.5
Overall pressure ratio	16.0
Throttle	Military power
Air speed	Mach 0.9
Thrust at air speed:	
@ 2 kft altitude	15,900 lbs
@ 15 kft altitude	12,532 lbs
@ 30 kft altitude	9,208 lbs
Sea-level static thrust	17,881 lbs
Sea-level static air flow	200 lbs
Emissions @ 300 m range (3.5-5 microns)	
@ 2 kft altitude	142 (w/sr)
@ 15 kft altitude	153 (w/sr)
@ 30 kft altitude	153 (w/sr)
Fuel type	JP4
Nozzle area at exit plane	475 in^2
Plume temperature profile	flat

However, results show expected trends. Lower plume static temperatures cause them to radiate at lower levels. Moreover, lower plume temperatures cause comparatively greater transmission losses than do hotter plumes. The effect can be seen by comparing the emissions of the 759.6-K plume with those of the 438.9-K plume in Fig. 2.28(a). At 300 m, the cooler plume radiates approximately 1/10 as much, but at 10 km it appears to radiate only 1/30 as much. This is expected because the cooler plume emission lines undergo less broadening and overlap atmospheric absorption lines more. Suppression of plumes by lowering their temperature improves signature control by both reducing total emissions and by degrading their propagation through the atmosphere.

Example Calculation. An example calculation is useful to show the utility of Fig. 2.28 in estimating the vulnerability reduction achieved by cooling exhaust plumes. The sensitivity required for a sensor to track a target at range R on a uniform background is given by

$$\text{NEI} = \frac{J_o T_a}{\text{SNR}\, R^2} , \tag{2.29}$$

where

J_o = in-band target radiant intensity in watts per steradian, contrast at zero range
T_a = effective in-band atmospheric transmission
SNR = signal-to-noise ratio required for track
NEI = sensor noise equivalent irradiance in watts per square centimeter.

In the parlance of Fig. 2.28,

$$I = J_o T_a \tag{2.30}$$

and

$$I_o = J_o \ , \tag{2.31}$$

evaluated at a 30-kft altitude and 300-m range (J'_o), or

$$I_o = J'_o \ .$$

Then

$$J_o T_a = J'_o \left(\frac{I}{I_o} \right) \ , \tag{2.32}$$

and the required NEI becomes

$$\text{NEI} = J'_o \frac{(I/I_o)}{\text{SNR}\, R^2} \ . \tag{2.33}$$

Required NEI for sensor tracking of a suppressed plume at a given range can be found from Eq. (2.33) and Fig. 2.28 by assuming an unsuppressed plume signature J'_o and a required SNR. Figure 2.29 shows the apparent plume

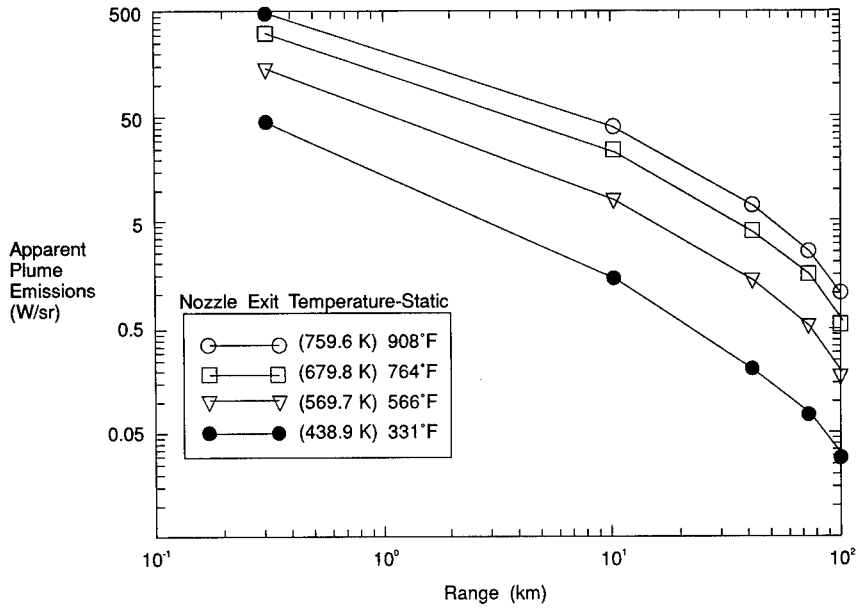

Fig. 2.29 Example plume signatures at various temperatures. Mach 0.90 at 2000-ft altitude and U.S. standard atmosphere.

signature that results over a horizontal path at a 2-kft altitude for an assumed 500 W sr^{-1} value for J_o'. Figure 2.30 shows the required sensor NEI for an SNR of 3. The latter is representative of the SNRs required for missile seeker launch. Again, these results assume a uniform background. Lower NEIs and enhanced sensor signal processing would likely be required if the plume were viewed against a cluttered background.

Table 2.9 provides a listing of normalized high-resolution plume spectral radiant intensities for the discussed exit nozzle temperatures. These may be used for studies of plume propagation effects over other sensor viewing paths and atmospheric conditions of interest. For instance, apparent target radiant intensity J_oT_a for a given band, range, engagement path, and atmosphere is the integral of the transmission weighted source spectral intensity. That integral can be approximated as

$$J_oT_a \simeq \rho \sum_{j=m}^{n} J_N(\tilde{\nu}_j)T_A(R,\tilde{\nu}_j)\Delta\tilde{\nu} \ , \tag{2.34}$$

where

ρ = total in-band plume radiant intensity at 300 m (user selected)

$J_N(\tilde{\nu}_j)$ = normalized plume spectral radiant intensity (Table 2.9) at wavenumber $\tilde{\nu}_j$

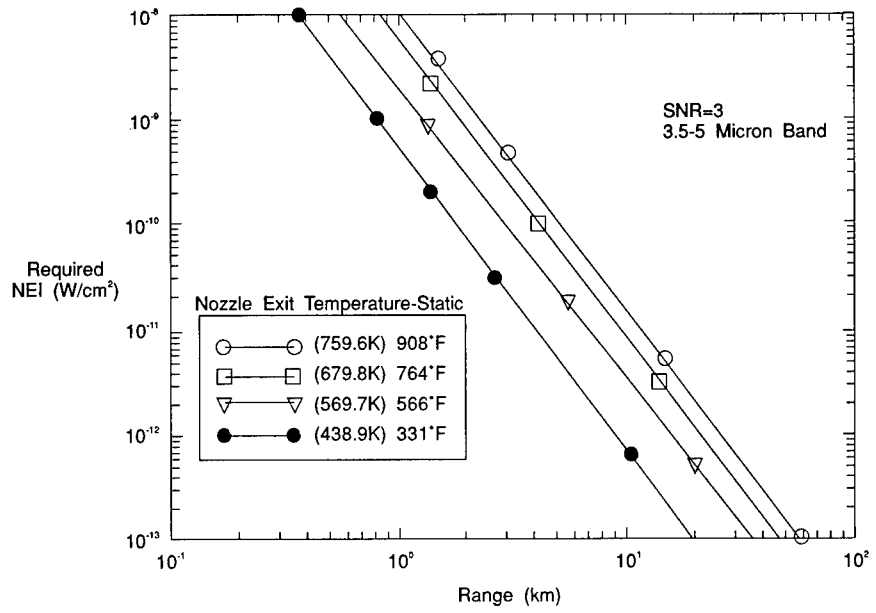

Fig. 2.30 Required sensitivity for tracking plumes. Mach 0.90 at 2000-ft altitude and U.S. standard atmosphere.

$\tilde{\nu}_j$ = wavenumber corresponding to j'th wavelength; $10{,}000/[\lambda_j(\mu m)]$

$T_A(R,\tilde{\nu}_j)$ = range and environment dependent spectral transmission of the atmosphere (LOWTRAN) at wavenumber $\tilde{\nu}_j$

$\Delta\tilde{\nu}$ = wavenumber increment, 5 cm^{-1}.

To evaluate the summation in Eq. (2.34), one would first compute spectral values for $T_A(R,\tilde{\nu})$ at a resolution of 5 cm^{-1} (i.e., the same resolution as in Table 2.9) in the spectral band of interest. Code predictions from LOWTRAN could be used for this purpose. The equation would then be easiest to evaluate by reading both J_N and T_A tabular values into files and performing the summation on a computer.

Again, it must be remembered that changes in engine design can yield large changes in radiant emissions at a given thrust. Emission values for specific engine designs are necessary for most purposes.

Lower signatures can be obtained with the same plume temperatures indicated above if nonaxisymmetric nozzle shapes are used. Nonaxisymmetric or two-dimensional (2-D) rectangular nozzles are pictured in Figure 2.31 for comparison to conventional axisymmetric or round nozzles. The 2-D nozzles are described in terms of aspect ratio, i.e., length-to-width ratio. These 2-D nozzles promote more rapid plume mixing with free stream external air. The result is a shorter plume core length after it exits the nozzle and a correspondingly lower plume radiant intensity. Another advantage they offer is more obscuration of the internal engine plume and hot parts. It is more difficult to see into the interior of a high-aspect-ratio nozzle unless the sensor is viewing it on axis. Here the 2-D nozzle is illustrated in combination with a serpentine *S-duct*. The S-duct is an additional suppression feature that prevents direct observation into the hot engine core area. Finally, note that high-aspect-ratio 2-D nozzles are compatible with RCS reduction in that, when long and narrow, they tend to direct rf energy into a narrow return beam rather than scatter it over wide angles.

Analysts should be aware that 2-D nozzles affect radiant emission propagation characteristics. Cooler outer layers of plume gases absorb emissions from hot inner layers. Therefore, plume shape and viewing geometry can affect propagation results.

A final treatment used to control plume signatures is the use of an airframe deck behind the exhaust nozzle.[41] A deck is an extension of the airframe body intended to obstruct the view to both nozzle hot parts and plume. Low-altitude aircraft would use decks on their upper surface above the engine to prevent higher altitude sensors from seeing these signature contributors. High-altitude aircraft would use the deck on the lower side of the engine to provide obscuration from below.

Table 2.9 Normalized Plume Spectral Radiant Intensities

Altitude=15 kft, Flight Mach number=0.9 90° off nozzle, 300 m range					
		$J_N(\varphi$ or $\lambda)$			
λ μm	$\tilde{\nu}$ cm^{-1}	1128 K	928 K	729 K	529 K
5.000	2000.	0.0600200	0.0442643	0.0206190	0.0046453
4.988	2005.	0.0547300	0.0389794	0.0114297	0.0006523
4.975	2010.	0.0573700	0.0424467	0.0202610	0.0048775
4.963	2015.	0.0606500	0.0472733	0.0306084	0.0156085
4.950	2020.	0.0565300	0.0427980	0.0239249	0.0086493
4.938	2025.	0.0529500	0.0392926	0.0191324	0.0048516
4.926	2030.	0.0459600	0.0325185	0.0084186	0.0003311
4.914	2035.	0.0447300	0.0320145	0.0109917	0.0010514
4.902	2040.	0.0472800	0.0359552	0.0212086	0.0088383
4.890	2045.	0.0418400	0.0307085	0.0146725	0.0036445
4.878	2050.	0.0358900	0.0251870	0.0069446	0.0003731
4.866	2055.	0.0339000	0.0237665	0.0067130	0.0003929
4.854	2060.	0.0342100	0.0248280	0.0113455	0.0025648
4.843	2065.	0.0352200	0.0269129	0.0169635	0.0083701
4.831	2070.	0.0278200	0.0192912	0.0048642	0.0002113
4.819	2075.	0.0270400	0.0193828	0.0083723	0.0016864
4.808	2080.	0.0257800	0.0183747	0.0076605	0.0014047
4.796	2085.	0.0247500	0.0176721	0.0077321	0.0016122
4.785	2090.	0.0244900	0.0180463	0.0100442	0.0038237
4.773	2095.	0.0208200	0.0145562	0.0054495	0.0007796
4.762	2100.	0.0192100	0.0133572	0.0048936	0.0006535
4.751	2105.	0.0177600	0.0122345	0.0040935	0.0004349
4.739	2110.	0.0167300	0.0114861	0.0037860	0.0003929
4.728	2115.	0.0168400	0.0120360	0.0060560	0.0018791
4.717	2120.	0.0144700	0.0098594	0.0032175	0.0003336
4.706	2125.	0.0136000	0.0093172	0.0034449	0.0004979
4.695	2130.	0.0125700	0.0084466	0.0023289	0.0001977
4.684	2135.	0.0132900	0.0094088	0.0046999	0.0014467
4.673	2140.	0.0123600	0.0085764	0.0037566	0.0008376
4.662	2145.	0.0117800	0.0081029	0.0034070	0.0006857
4.651	2150.	0.0109400	0.0073010	0.0023542	0.0002372
4.640	2155.	0.0107500	0.0071712	0.0028006	0.0004831
4.630	2160.	0.0105900	0.0069573	0.0029438	0.0006523
4.619	2165.	0.0104000	0.0064991	0.0023457	0.0003645
4.608	2170.	0.0107000	0.0062929	0.0018446	0.0001804
4.598	2175.	0.0118200	0.0065297	0.0015835	0.0001013
4.587	2180.	0.0148900	0.0079883	0.0021604	0.0002335
4.577	2185.	0.0193900	0.0101420	0.0027669	0.0003682
4.566	2190.	0.0258000	0.0130975	0.0028848	0.0001915
4.556	2195.	0.0357200	0.0180769	0.0040092	0.0002743
4.545	2200.	0.0494500	0.0252022	0.0055675	0.0003953
4.535	2205.	0.0687600	0.0356039	0.0083301	0.0006931
4.525	2210.	0.0953100	0.0503281	0.0125121	0.0011008
4.515	2215.	0.1370400	0.0739876	0.0193177	0.0018000
4.505	2220.	0.1946100	0.1078579	0.0307474	0.0034518
4.494	2225.	0.2773800	0.1578729	0.0481657	0.0061303
4.484	2230.	0.3494500	0.2048025	0.0685025	0.0105259
4.474	2235.	0.4383700	0.2659675	0.1009682	0.0204379
4.464	2240.	0.5528000	0.3442319	0.1369714	0.0296147
4.454	2245.	0.6956800	0.4450331	0.1874997	0.0444783
4.444	2250.	0.7452600	0.4934290	0.2318710	0.0692056
4.435	2255.	0.8589300	0.5795366	0.2732563	0.0779760

Table 2.9 *(continued)*

λ μm	$\tilde{\nu}$ cm^{-1}	1128 K	928 K	729 K	529 K
4.425	2260.	0.8080300	0.5613070	0.2865138	0.0958219
4.415	2265.	0.8418700	0.5970636	0.3128224	0.1065270
4.405	2270.	0.8206900	0.5924967	0.3141069	0.1049938
4.396	2275.	0.9030800	0.6636968	0.3521863	0.1099986
4.386	2280.	0.9919600	0.7418390	0.3924304	0.1095415
4.376	2285.	1.0000000	0.7637038	0.4211394	0.1235440
4.367	2290.	0.7112200	0.5559382	0.3287204	0.1160980
4.357	2295.	0.4988400	0.3959957	0.2443030	0.0959331
4.348	2300.	0.3881500	0.3115148	0.1980029	0.0838505
4.338	2305.	0.2209400	0.1786838	0.1168325	0.0539640
4.329	2310.	0.1467400	0.1189851	0.0785551	0.0374548
4.320	2315.	0.0494600	0.0401326	0.0269024	0.0135466
4.310	2320.	0.0394500	0.0321137	0.0216213	0.0108966
4.301	2325.	0.0048100	0.0038796	0.0026069	0.0013676
4.292	2330.	0.0018500	0.0014969	0.0010107	0.0005387
4.283	2335.	0.0035200	0.0028333	0.0018951	0.0009822
4.274	2340.	0.0010000	0.0007943	0.0005348	0.0002829
4.264	2345.	0.0026000	0.0020773	0.0013855	0.0007141
4.255	2350.	0.0151100	0.0120360	0.0078879	0.0038694
4.246	2355.	0.0005700	0.0004582	0.0003032	0.0001569
4.237	2360.	0.0015000	0.0012067	0.0008044	0.0004114
4.228	2365.	0.0014400	0.0011532	0.0007665	0.0003892
4.219	2370.	0.0154100	0.0122116	0.0079385	0.0038682
4.211	2375.	0.0820300	0.0648079	0.0414022	0.0192778
4.202	2380.	0.4305700	0.3352889	0.2014773	0.0809336
4.193	2385.	0.6782600	0.5150418	0.2866359	0.0979531
4.184	2390.	0.5952200	0.4319433	0.1939642	0.0360761
4.175	2395.	0.2028400	0.1226890	0.0310590	0.0017481
4.167	2400.	0.0010900	0.0007943	0.0004464	0.0001952
4.158	2405.	0.0008700	0.0006339	0.0003580	0.0001507
4.149	2410.	0.0007000	0.0005040	0.0002695	0.0001124
4.141	2415.	0.0005800	0.0004048	0.0002064	0.0000852
4.132	2420.	0.0004800	0.0003360	0.0001642	0.0000655
4.124	2425.	0.0004200	0.0002826	0.0001348	0.0000519
4.115	2430.	0.0003600	0.0002444	0.0001137	0.0000408
4.107	2435.	0.0003200	0.0002138	0.0000927	0.0000321
4.098	2440.	0.0002800	0.0001833	0.0000758	0.0000259
4.090	2445.	0.0002500	0.0001604	0.0000632	0.0000198
4.082	2450.	0.0002300	0.0001451	0.0000547	0.0000161
4.073	2455.	0.0002200	0.0001375	0.0000505	0.0000136
4.065	2460.	0.0002000	0.0001298	0.0000421	0.0000111
4.057	2465.	0.0001900	0.0001222	0.0000421	0.0000099
4.049	2470.	0.0001800	0.0001146	0.0000421	0.0000086
4.040	2475.	0.0001700	0.0001069	0.0000295	0.0000062
4.032	2480.	0.0001700	0.0000993	0.0000295	0.0000049
4.024	2485.	0.0001700	0.0000993	0.0000337	0.0000062
4.016	2490.	0.0001600	0.0000916	0.0000253	0.0000037
4.008	2495.	0.0001600	0.0000916	0.0000337	0.0000062
4.000	2500.	0.0000600	0.0000305	0.0000126	0.0000037
3.992	2505.	0.0000600	0.0000305	0.0000126	0.0000025
3.984	2510.	0.0000600	0.0000305	0.0000126	0.0000025
3.976	2515.	0.0000600	0.0000305	0.0000126	0.0000025
3.968	2520.	0.0000600	0.0000305	0.0000126	0.0000037
3.960	2525.	0.0000600	0.0000305	0.0000126	0.0000025
3.953	2530.	0.0000600	0.0000305	0.0000126	0.0000025

(continued)

Table 2.9 *(continued)*

λ μm	$\tilde{\nu}$ cm^{-1}	1128 K	928 K	729 K	529 K
3.945	2535.	0.0000600	0.0000305	0.0000126	0.0000037
3.937	2540.	0.0000600	0.0000305	0.0000126	0.0000025
3.929	2545.	0.0000600	0.0000382	0.0000126	0.0000037
3.922	2550.	0.0000700	0.0000382	0.0000126	0.0000037
3.914	2555.	0.0000700	0.0000382	0.0000126	0.0000025
3.906	2560.	0.0000800	0.0000458	0.0000168	0.0000025
3.899	2565.	0.0000900	0.0000535	0.0000211	0.0000062
3.891	2570.	0.0000900	0.0000535	0.0000211	0.0000037
3.883	2575.	0.0001000	0.0000535	0.0000211	0.0000049
3.876	2580.	0.0001100	0.0000611	0.0000295	0.0000074
3.868	2585.	0.0001100	0.0000687	0.0000211	0.0000037
3.861	2590.	0.0001200	0.0000764	0.0000295	0.0000086
3.854	2595.	0.0001300	0.0000764	0.0000337	0.0000086
3.846	2600.	0.0001400	0.0000840	0.0000295	0.0000062
3.839	2605.	0.0001500	0.0000916	0.0000379	0.0000111
3.831	2610.	0.0001500	0.0000916	0.0000421	0.0000111
3.824	2615.	0.0001500	0.0000916	0.0000337	0.0000062
3.817	2620.	0.0001700	0.0001069	0.0000463	0.0000148
3.810	2625.	0.0001700	0.0001069	0.0000463	0.0000148
3.802	2630.	0.0001700	0.0001069	0.0000379	0.0000074
3.795	2635.	0.0001800	0.0001146	0.0000505	0.0000148
3.788	2640.	0.0001800	0.0001146	0.0000547	0.0000161
3.781	2645.	0.0001900	0.0001146	0.0000463	0.0000111
3.774	2650.	0.0001900	0.0001222	0.0000547	0.0000161
3.766	2655.	0.0002000	0.0001222	0.0000547	0.0000148
3.759	2660.	0.0002100	0.0001298	0.0000505	0.0000124
3.752	2665.	0.0002200	0.0001375	0.0000590	0.0000173
3.745	2670.	0.0002100	0.0001222	0.0000337	0.0000025
3.738	2675.	0.0002300	0.0001451	0.0000632	0.0000161
3.731	2680.	0.0002400	0.0001451	0.0000632	0.0000173
3.724	2685.	0.0002400	0.0001375	0.0000421	0.0000037
3.717	2690.	0.0002500	0.0001527	0.0000547	0.0000086
3.711	2695.	0.0002600	0.0001604	0.0000674	0.0000161
3.704	2700.	0.0002600	0.0001527	0.0000463	0.0000049

Table 2.9 *(continued)*

$\lambda\ \mu m$	$\tilde{\nu}\ cm^{-1}$	1128 K	928 K	729 K	529 K
3.697	2705.	0.0002800	0.0001680	0.0000547	0.0000074
3.690	2710.	0.0003000	0.0001833	0.0000674	0.0000136
3.683	2715.	0.0003300	0.0001986	0.0000800	0.0000185
3.676	2720.	0.0003600	0.0002215	0.0001095	0.0000383
3.670	2725.	0.0003600	0.0002215	0.0000969	0.0000259
3.663	2730.	0.0003600	0.0002138	0.0000716	0.0000111
3.656	2735.	0.0003700	0.0002138	0.0000632	0.0000074
3.650	2740.	0.0003800	0.0002291	0.0000758	0.0000111
3.643	2745.	0.0003900	0.0002291	0.0000674	0.0000062
3.636	2750.	0.0004100	0.0002444	0.0000800	0.0000111
3.630	2755.	0.0004400	0.0002597	0.0000969	0.0000173
3.623	2760.	0.0004400	0.0002597	0.0000716	0.0000062
3.617	2765.	0.0004800	0.0002902	0.0001053	0.0000198
3.610	2770.	0.0005100	0.0002978	0.0001095	0.0000185
3.604	2775.	0.0005200	0.0003055	0.0001011	0.0000136
3.597	2780.	0.0005300	0.0003131	0.0001011	0.0000136
3.591	2785.	0.0005500	0.0003284	0.0001221	0.0000247
3.584	2790.	0.0005600	0.0003284	0.0001179	0.0000210
3.578	2795.	0.0005600	0.0003284	0.0001053	0.0000148
3.571	2800.	0.0005800	0.0003360	0.0001221	0.0000235
3.565	2805.	0.0005900	0.0003360	0.0001011	0.0000124
3.559	2810.	0.0006100	0.0003513	0.0001137	0.0000148
3.552	2815.	0.0006400	0.0003742	0.0001348	0.0000235
3.546	2820.	0.0006500	0.0003742	0.0001221	0.0000161
3.540	2825.	0.0006700	0.0003895	0.0001263	0.0000185
3.534	2830.	0.0005800	0.0003284	0.0001053	0.0000148
3.527	2835.	0.0004900	0.0002749	0.0000842	0.0000111
3.521	2840.	0.0004000	0.0002215	0.0000716	0.0000111
3.515	2845.	0.0003100	0.0001680	0.0000590	0.0000111
3.509	2850.	0.0002100	0.0001146	0.0000379	0.0000062
3.503	2855.	0.0002300	0.0001222	0.0000379	0.0000062
3.497	2860.	0.0002400	0.0001298	0.0000379	0.0000049

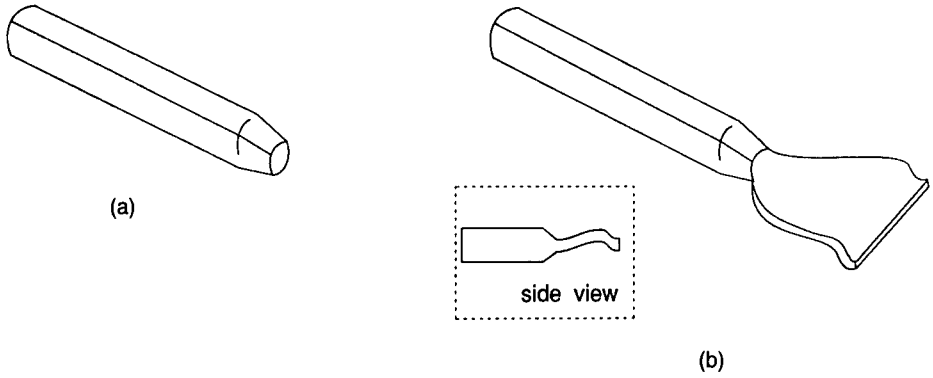

Fig. 2.31 High-aspect-ratio 2-D configuration for turbine engine signature reduction: (a) conventional axisymmetric nozzle and (b) nonaxisymmetric 2-D nozzle.

2.5.1.3 Hot Parts Suppression. Techniques for turbine engine hot parts suppression include

- obscuration
- cooling
- emissivity control
- physical size reduction.

These techniques are compatible with plume-cooling methods and, in some cases, have been already discussed.

Unlike plumes, hot parts are already greatly obstructed from view over large angles. Their visibility can be reduced further by the use of a serpentine duct or with the use of a plug in the exhaust nozzle. These items can prevent viewing into the hot turbine section but must themselves be cooled. Methods for cooling visible hot parts again exploit turbine fan air as well as inlet and compressor bleed air. The air can be used to convection cool the back side of hot nozzle parts, perform transpiration cooling by bleeding through small perforations in the liner, provide film cooling by flowing through slots along the liner to form a cooler confluent boundary layer, and by directly bathing the hot surfaces. Louvers, slots, and holes increase the risk of clogging with contaminants.[34] Direct cooling with large amounts of bypass air is most effective.

Hot parts cooling methods are only broadly compatible with RCS reduction goals. Louvers, slots, and holes as well as large air ducts can increase RCS. But the cooler surfaces they provide allow a wider selection of radar absorbing materials (RAM) for use as liners.

Emissivity control must be done with thorough knowledge of hot spot locations and is not a cure-all. A low-emissivity coating is able to reflect other hot surface emissions and should be used with that in mind. It is most effective when used in locations that reflect only emissions from cooler surfaces into viewable regions. A combination of cooling and emissivity control often works best. Cool parts should have the higher emissivities.

2.5.2 Aircraft Body Signature Suppression

Aircraft skin signatures are major contributors to total aircraft observables almost regardless of the contribution made by the propulsion system. Skin signatures are viewable over all aspects in numerous spectral regions and are better matched to atmospheric transmission windows than are propulsion system plume signature components. Aircraft can often be observed over great distances because of their altitude, which often provides long unobstructed lines of sight and, sometimes, uniform backgrounds. Fortunately, for the suppression designer, the skin seldom provides significant spectral discriminants to separate it from natural background clutter. Aircraft body signature characteristics are dominated by broadband intensity and spatial pattern effects.

Viewable characteristics are a strong function of range. At the longer ranges, threat sensors can often detect targets but cannot easily resolve target detail. At those ranges, the only signature aspect that matters is the match of the spatially integrated radiance, in the spectral band of interest, with the background. At the shorter ranges, however, detail can be resolved and it is then important to match the spatial characteristics with the background as well. These differences drive the signature control strategy to different approaches depending on threat sensor resolution. Accordingly, control strategies are discussed in terms of target resolution.

2.5.2.1 Resolved Aircraft. Aircraft are considered to be resolved when the observer is sufficiently close to be able to see distinguishing pattern detail such as silhouette shape or internal pattern structure. Short-range signature control technology is dominated by visible and near-visible band imagery because infrared sensors are less prolific and have lacked the resolving power of television and visible band telescopic sensors. Although this may be changing, the strategies used in the visible band can be studied and applied, as needed, to the infrared bands as well. Visible-band camouflage techniques are the result of many decades of design experience and are as applicable today as they have been in the past.

The camouflage strategy pursed when the aircraft will be resolved is one that can be loosely described as *feature fallout.* Goals are driven by the psychophysics of human perception. One of the ways observers detect targets is by recognition of expected target features. Thus, an aircraft could be detected by first recognizing some combination of key structural features such as the tail, fuselage, wing, etc. A strategy for reducing detectability is then to mask these features.

Opportunities for aircraft feature masking can be categorized as

- contrast reduction
- reshaping
- texture matching
- desensitizing.

Contrast reduction is matching the surface spectral radiance to the background to make the feature, or entire target, disappear. Reshaping is making characteristic feature shapes look like unrelated objects by blending portions of features into the background or into other features. Texture matching is related to reshaping in that the technique matches internal texture of the target—a

key feature in itself—to that of the background. Desensitizing simply tries to raise the observer's threshold of detectability above that of the target contrast. These techniques work best when used in combination.

Control over observer sensitivity was suggested by Doll et al.[42] when it was discovered how the eye processes scene spatial information. Processing is apparently done by dividing scenes into spatial frequency ranges where each range is processed in parallel.[43,44] When confronted with strong repetition of certain spatial frequencies, Doll postulated that the channel reduces its *gain,* or sensitivity to contrast. It would appear to be nature's way of adapting to strong spatial stimuli much like it adapts to strong intensity stimuli. If this theory is correct, camouflage designers could exploit the physiology of the eye by reinforcing strong patterns already found in the target background. The theory suggests that finding targets in clutter may not just be a matter of contending with confusing objects, but may be one of contending with reduced contrast sensitivity as well.

Figure 2.32 shows a photo[45] of aircraft with camouflage patterns that use many of these principles. For instance, internal texture is designed to match

Fig. 2.32 Illustration of camouflage principles for resolved targets.

the texture of the cultivated farm fields below. In this case, overall contrast reduction is difficult because the background presents so many varied intensities that it would be impossible to match them at all target locations. However mean target reflectance has been chosen to match mean background reflectance as a way to reduce overall contrast. Moreover, feature fallout is possible with contrast reduction, in this example, because of the varied intensities presented within a given aircraft feature. For instance, it is seen that various areas of the wings, fuselage, and tail are well matched to certain background intensities. At locations on these features where intensities match the background, boundaries disappear and the shape of the feature is extended to include the boundary of the background. Such blended target and background boundaries no longer present the shape expected of a wing or fuselage and they are difficult for an observer to recognize. Internal feature structure is also reshaped by matching intensities between portions of the wing, fuselage, and tail. Finally, the strong periodic structure in both the target and the background make it possible that visual channel contrast response is less for the spatial frequencies predominant in these target structures than it would be for targets dominated by other frequencies. A synergism of effects is at work in this example to minimize detectability.

Although these principles are illustrated for a visual image, the same concepts apply in the infrared. There, the only difference would be the differing background contrast levels presented and the techniques used to achieve pattern definition on the target features. A range of internal contrasts can be produced with varying emissivity surface coatings or with the active heat transfer techniques discussed in the previous section. Results should minimize detectability by imaging infrared sensors.

2.5.2.2 Unresolved Aircraft. The goal with unresolved targets is to match the total radiant intensity of the body with that presented by the occluded background. Several methods are available for accomplishing this goal. They include surface reflectivity and emissivity control, active cooling and heating, and self-illumination.

Visible signature control techniques emulate the countershading strategy often found in nature. For instance, lizards, alligators, wolves, and deer are equipped with relatively dark skins or fur on their tops and much lighter skins or fur on their bellies.[46] A darker treatment on top counteracts the illumination that predominates on top, whereas a lighter reflectivity underneath counteracts the reduced illumination characteristic of underside shadows. Aircraft camouflage paint treatments employ the same countershading strategy. The objective is to better match their surroundings in the presence of strong directional illumination from the sun and hemispherical illumination from the sky. This typically calls for more than just uniformly decreased reflectivity on the top and increased reflectivity on the bottom. Rather, it requires lightening areas on either side subject to shadows.

Many considerations must go into the selection of the scheme and the reflectance levels.[45] For instance, target maneuverability and threat sensor engagement viewing angles are important inputs to the decision process. Roll maneuvers that expose a light underside to direct solar illumination can cause countershading to backfire. The same can be said for using a reflectance, or

color, chosen to match one geographic area, in a different area. Color is usually not important at long ranges because light scattered into the viewing path tends to dilute apparent colors to a gray appearance anyway. Altitude is important because the amount of sky radiance diminishes with increasing altitude because of the lower density of molecular scatterers. That is one reason why high flying surveillance platforms, such as the SR-71 Blackbird, are typically all black. At very high altitudes, the background is ultimately the blackness of deep space. Reference 45 provides tables of visible camouflage paint reflectances and patterns required for various missions and geographical areas.

In many situations there is not enough light illuminating the target. This happens, for instance, in an air-to-ground defense suppression, or close air support, mission where a low-altitude aircraft is viewed against a bright sky background. The aircraft underside may be the only aspect visible to the sensor. Even a 100% reflecting underside may not be enough reflectance to make the shadowed areas appear as bright as the sky background. In this scenario the target will likely appear as a high-negative-contrast object. Here the suppression designer can add light in the form of active illumination[47] to raise the apparent brightness of the dark shadowed regions. Reference 48 reports that this was apparently done with some success during World War II when spot lights, referred to as *Yaheudi lights,*[47] were attached to the underside of Avenger bombers to reduce their detection range.

In addition to the preceding diffuse illuminance skin sources, the suppression designer must consider sources of glint and glare associated with solar reflections. There are several options for controlling them. Applicable methods refer to the shaping and applique techniques discussed in the earlier section on general suppression methods:

1. Avoid doubly curved surfaces.
2. Use planar or singly curved segments with polished finishes.
3. Use planar or singly curved segments with matte finishes.
4. Use baffles.
5. Use doubly curved surfaces only with matte finishes.

One of the most difficult sources of glint has historically been the aircraft canopy. Pilots prefer seamless hemispherically shaped canopies to avoid blind spots. Nothing could be worse from the standpoint of glint susceptibility. Solar illumination is so bright that a glint reflectivity of only a few percent is still a major visual cue.

Options are limited by the need to see through the canopy under low as well as high ambient brightness conditions. Antireflection coatings are usually only effective over small angles. Absorption coatings work, but also limit canopy light transmission to the pilot. The best control strategy appears to be the use of planar or singly curved surfaces to confine glint reflections—of visual, IR, and radar wavelengths—to narrow angles.

Very similar arguments apply to other portions of the aircraft body. Visual techniques must be compatible with IR and rf considerations, yet the energy balance equation is very complicated. Solar glint and glare signature components must be reconciled with diffuse components. Infrared self-emissions must be balanced with reflections of earth, sky, and solar irradiance. In the multispectral scenario, the designer must be mindful that the sun is a strong

potential source of both aircraft heat loading and reflections. Finally, the atmosphere is an altitude-dependent influence that is capable of determining self-emissions. It supplies a cold air sink as well as a source of speed-dependent aerodynamic heating. Flat or singly curved body surfaces are a useful element for multispectral signature control against all of these sources.

Planar surfaces are desirable primarily because they provide control of reflected solar signatures while still allowing control of self-emissions with high-reflectivity coatings. Strong self-emissions can originate from aerodynamic- or propulsion-related sources of body heating. At high subsonic and supersonic speeds, skin heating is considerable. Therefore, low surface emissivities are desirable for reducing this signature contributor. Yet the resulting high surface reflectivities can cause a strong contribution from solar reflections. Use of matte finishes would not help because they tend to spread solar reflections over broad angles. A high-reflectance, glossy, planar surface is an attractive solution because it both offers low emissivity and confines solar-reflections to narrow angles.

Many operational conditions have to be satisfied for a given strategy to work. For instance, when operating at high altitudes, a low-emissivity skin offers the opportunity to reflect earthshine at many viewing angles—especially with up-looking sensors. This effect can again be moderated, to some extent, by body shape. Ultimately, however, some viewing conditions can arise where no combination of reflectance or shape can match the apparent infrared body emissions to the cold background of a high-altitude sky. These cases might require some form of active cooling with the techniques described earlier.

Still another operational condition can place the aircraft at low altitudes where it could be seen by higher altitude, down-looking, airborne sensors. These sensors could see it against a warm earth background. In this case, the high-reflectivity surfaces can reflect the cold sky and cause the aircraft to show a strong negative contrast against the ground. These cases show the strong dependence of signature control strategies on scenario and emphasize the utility of adaptive chromogenic appliques.

The amount of aircraft skin emissivity required for zero contrast with the background can be calculated from the equations derived in Sec. 2.3. Equation (2.21) showed the required surface emissivity for a specularly reflecting planar panel to be

$$\varepsilon_r = \frac{L_0 - L_b}{L_{\mathrm{BBI}} - L_b}\,, \tag{2.21}$$

where

L_0 = background radiance immediately behind the target
L_b = radiance specularly reflected by the panel toward the threat sensor
L_{BBI} = Planck blackbody radiance.

This equation was shown to account for target self-emissions and reflected environmental irradiances. Figure 2.33 shows the resulting aircraft skin emissivities required in the 3.0- to 5.0-μm spectral band for a planar specularly

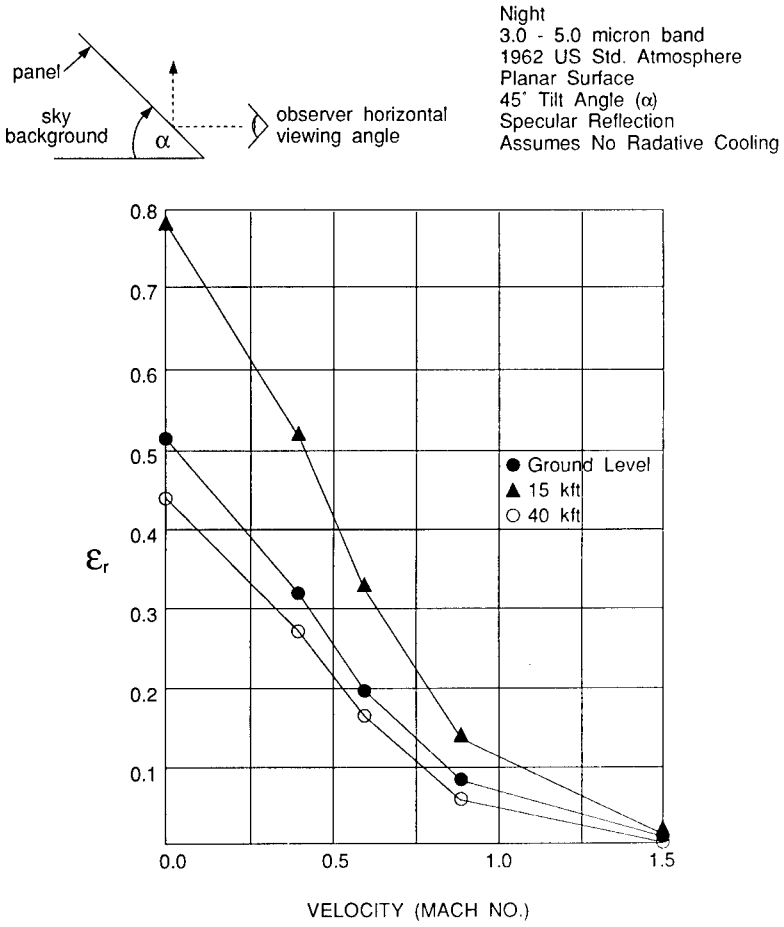

Fig. 2.33 Skin emissivity required versus velocity when viewed horizontally against sky background.

reflecting panel tilted upward at a 45-deg angle. Here the observer is assumed to be viewing the panel along a horizontal line of sight against a sky background. This geometry is near optimum for infrared signature suppression because the panel reflects the coldest part of the sky and, therefore, allows the highest skin temperatures.

Skin temperatures were computed from Eq. (2.1) in Sec. 2.2. These temperatures were assumed to result from laminar flow aerodynamic heating with no radiative cooling regardless of emissivity. The latter assumption causes the emissivity requirement to be slightly lower than shown in the figure. It was further assumed that the recovery factor $r = 0.82$. Values for air temperature were taken from plots of air temperature versus altitude from Ref. 4 for a 1962 U.S. standard atmosphere and are repeated here in Fig. 2.34.

Background sky radiances L_b were computed for night operations from LOWTRAN 6, also using the 1962 U.S. standard atmosphere. Plots of these sky radiance values were shown previously in Fig. 2.14.

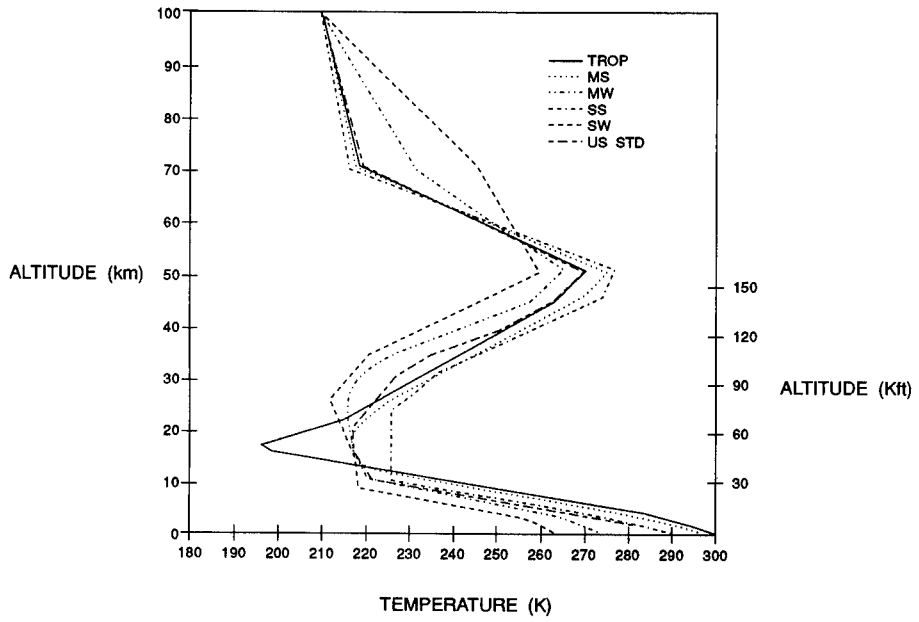

Fig. 2.34 Temperature versus altitude for six LOWTRAN model atmospheres.[4]

As expected, Fig. 2.33 shows that decreasing skin emissivities are required to suppress increasing emissions due to increased aircraft velocity. Emissivity requirements for day signature suppression would be slightly lower because of increased sky radiance from solar effects.

It is interesting to note the variability of required emissivity with altitude. In particular, operation at the moderate altitude of 15,000 ft requires a higher emissivity than operation at either ground level or at 40,000 ft. This effect can be explained, with the geometry illustrated, by comparing the ratio of the radiance of the vertical sky to that of the horizontal sky at various altitudes. Among the three altitudes considered, that ratio is the highest at 15,000 ft. Likewise, the ratio of target self-emissions to immediate background emissions is a consideration. In the plots of Fig. 2.33, both ratios are highest at the 15,000-ft altitude. Because high emissivities are generally easier to attain than low emissivities, this result suggests that operation at moderate altitudes is preferred. Of course, other atmospheres can lead to different conclusions. Similarly, small changes in viewing geometry can dramatically affect results.

Viewing geometry effects are partially illustrated in Fig. 2.35 for two vehicle velocities. Here the panel tilt angle α is allowed to vary from 45 deg, where it reflects the cold zenith sky, to 90 deg, where it reflects the warmer horizon sky. Again, reflectivity is assumed to be specular and the observation point is coaltitude for a near horizontal viewing path (the horizontal viewing condition is allowed to vary upward by approximately 2 deg, at low altitudes, to place the target against the warmest sky background location predicted by LOWTRAN 6. LOWTRAN 6 does not predict maximum sky radiance to occur at the expected 90-deg zenith angle but, instead, predicts the maximum to occur at an angle slightly above the horizon. Measured data[49,50] do not support this

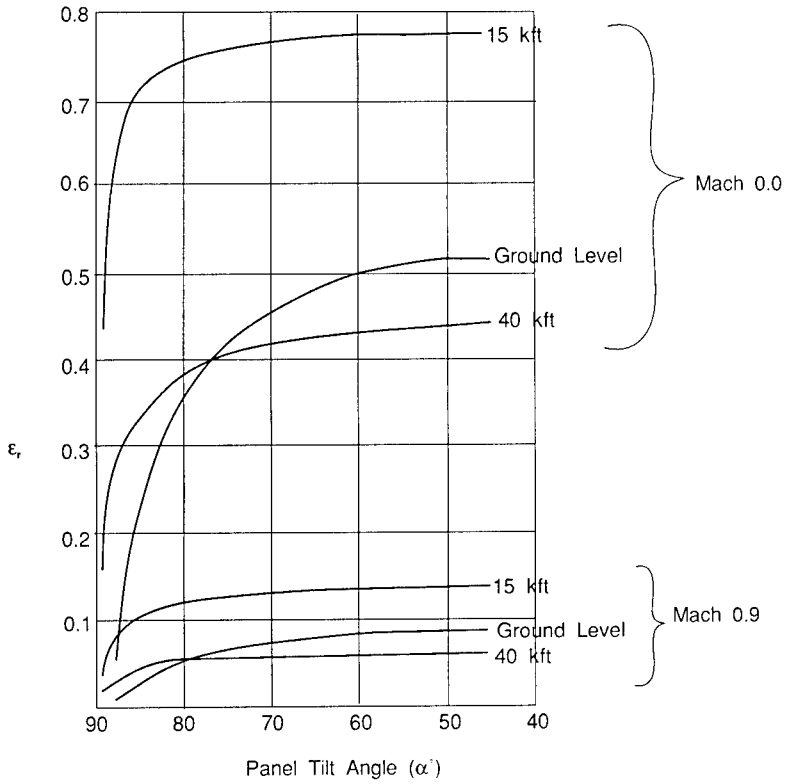

Fig. 2.35 Emissivity required for zero contrast as a function of panel tilt angle when viewed against horizon sky.

dip at low elevation angles and suggest that it may be due to a discrepancy in the LOWTRAN radiance prediction code.

The Mach 0.9 velocity plots show that aircraft skin emissivity is relatively insensitive to panel tilt angle at this speed. The reason is that almost every sky background location that reflects off the panel is much cooler than the aerodynamically heated skin. This appears to make the aerodynamic design easier in that skin shape can then be driven with more attention to aerodynamic design issues than with observables. However, the same cannot necessarily be said for sensitivity to altitude since the mid-altitude case requires an emissivity of more than double the high-altitude condition. It would appear that the latter effect is easier to address because skin emissivity can, in principle, be more easily adapted in flight—with the aid of chromogenics—than can skin shape. Of course, other viewing geometries such as those that place the target against a terrain or zenith sky background can significantly change these conclusions.

The Mach zero speed case broadly typifies helicopter, slow moving fixed-wing, or balloon operations. Again, the suppression designer's job is apparently eased by the relative insensitivity of required skin emissivity to panel tilt angle. It is also eased by the comparatively higher emissivities required. Higher emissivity coatings are both easier to achieve and more compatible with visible

and near-infrared pigments. It was seen earlier that typical visible pigments have high emissivities in the infrared.

Differing backgrounds can sometimes result in significantly different requirements. For instance, if the panels were to tilt more than 90 deg, as would be the case for most lower fuselage locations, the panels would reflect terrain radiance. Because terrain is usually slightly warmer than a horizon sky background and significantly warmer than a high-altitude sky, negative emissivities could be required. This would indicate the need for some other type of signature control strategy such as active cooling. However, that conclusion is not straightforward because, for example, some terrain types also have low emissivities and, even though warmer, they may reflect less radiance off of the aircraft skin than cooler sky background types. Clearly, scenarios, including threat sensor viewing geometries and background types, determine suppression requirements. If the system cannot be designed for the scenario, perhaps the scenario can be designed for the system.

Finally, it is worth noting that the "required" emissivities, shown in Figs. 2.33 and 2.35, were selected based on the criteria that they yield zero contrast, against the target background, at zero range to the target. Background clutter and atmospheric transmission effects over extended target-sensor ranges ordinarily work to increase both tolerable contrast levels and resulting emissivity requirements. The magnitude of these effects ultimately depends on threat sensor characteristics. The more relaxed requirements can be computed with the techniques used to predict sensor acquisition and lock-on performance, as discussed in other volumes of this Handbook.

2.6 GROUND VEHICLES AND EQUIPMENT[b]

2.6.1 Suppression Goals

The basic idea of any camouflage scheme is to cause the protected item to become indistinguishable from its background, in the view of the sensor, at some range. During the 1970s, the U.S. "camouflage community" conducted extensive parametric analyses in efforts to determine how much is enough for a variety of targets, backgrounds, and sensors. Application of this work for the thermal infrared region was followed in the early 1980s by field measurements and tests. One major conclusion, generally accepted by the community, was that if the apparent temperature of the item could be held within $\pm 4°C$ of its background, the desired blending effect could be achieved. This statement therefore became a *design goal* for infrared camouflage. Similar, although less quantitative, goals exist for the visible and near-infrared spectral regions.

Given an infrared design goal that appears to meet the need, two areas of concern immediately surface if the goal is to be met and a protection system work. These concerns involve target temperature characterization and diurnal variations. It is a relatively simple matter to place a temperature measuring and/or recording device on the surface of the target area and measure the temperature of that section of the surface. It is more complex to use any single

[b]This section was written by Grayson W. Walker, U.S. Army Belvoir Research, Development and Engineering Center, Ft. Belvoir, Virginia.

measurement to characterize the entire target; material, color, shade, and angle to the sun all can cause surface temperatures to vary from one section to another. These complexities are magnified when the subject is the background. Issues include background size and type (soil, vegetation, sky, man-made materials). As suggested in Sec. 2.2, the temperature of the target item varies from day to day and within the diurnal cycle. Background temperatures also vary, except that in most cases, the range of variation for the background is not as great as that for the target. The result is that if a curve of diurnal temperature variation for a target is superimposed upon a similar curve of background temperature, not only do both vary throughout the day, but their differences also vary. This compounds the signature suppressor's task.

In the modern era of reconnaissance systems that operate in more than one region of the electromagnetic spectrum, the design goal concept expands to become multispectral camouflage; i.e., to cause the protected item to become indistinguishable from its background in the view of a designated set of sensors at some set of designated ranges. Since about 1970, camouflage systems, mostly screens or nets, have incorporated protection in visual, near-infrared, and radar spectral ranges, and are thus multispectral to a degree. The main element missing to date is some treatment of the 3- to 5- and 8- to 12-μm infrared spectral region. The camouflage community, both U.S. and international, has acknowledged the existence of this gap since the mid-1970s. A great deal of work has been done to bound the problem and attempt to solve it. Efforts have involved internal design and external countermeasures.

2.6.2 Nonhardware Signature Suppression

Before entering into a detailed discussion of the technical alternatives involved in countersurveillance, there are a number of techniques available to the soldier in the field to reduce the illumination of the target, minimize its silhouette, or disrupt the characteristic shape of the target.

One elementary technique is to use the natural shadows to hide from detection. This approach is effective for the visual, near-infrared, and thermal infrared wavebands. The low light in the shadows makes both unaided and aided visual detection much more difficult, and the low contrast background minimizes any silhouetting of the target. This technique applies equally well against near IR detectors because these too rely on reflected radiation. The case with thermal IR detectors is somewhat different. Hiding in the shadows does not diminish the signature from a heat producing source such as an internal combustion engine. However, parking a vehicle in the shadows does limit or sometimes eliminate the solar heating effects. The thermal signature can be reduced by simply aligning the vehicle so that primary signatures, such as the exhaust, do not point toward the threat sensor. In the particular case of engine exhaust, it is important not to let the exhaust impinge on the surrounding foliage or other vehicles because the exhaust would cause secondary heating effects.

The use of natural foliage applied to vehicles has been a time-honored technique because using materials from the surrounding area obviously produces a good match to the background. In addition, the textured structure of the foliage breaks up the outline of the target, which makes it particularly useful

as open field camouflage. In some countries, netting is attached to the vehicle to give an anchor point for attaching freshly cut foliage. Natural foliage is excellent multispectral (visual, infrared, and radar) camouflage, but the effectiveness of this camouflage, especially in the infrared and radar regions, quickly degrades as the foliage dies.

Application of mud is another technique of utilizing natural materials to blend with the background. Mud is particularly effective against the radar threats but is much less effective against visual and thermal IR threats and does not provide a disruption to the target's shape.

The most effective and long-lasting camouflage techniques are the ones engineered into the vehicle itself. From a visual standpoint it is desirable to minimize shadows cast by sections of the vehicle and eliminate any oddly shaped structures that make it stand out from natural shapes. This last requirement is probably the hardest to achieve. In the case of thermal IR suppression, a number of engineering techniques can significantly reduce a target's signature. Insulation of the outer skin from internally generated heat is an obvious solution but care must be taken to avoid exacerbating the solar heating effects. Double-walled designs with air flow between the walls is a very effective method of reducing both the radiant transfer of heat from internal parts to the vehicles surface and to reduce the solar heating effects.

2.6.3 Hardware Suppression Systems

The primary camouflage techniques in use by military forces today are camouflage screening systems (camouflage nets) and disruptive camouflage pattern painting. Both the screen and the paint come in several color schemes to meet the variety of environments (i.e., woodland, desert, and snow) in which military forces must operate. The green colors in the woodland patterns of the screen and paint systems are tailored to match the chlorophyll reflectance curve of natural foliage, which exhibits sharp rises in reflectance at approximately 650 to 700 nm. However, neither camouflage system is currently designed to reduce the signatures produced by the thermal emissions resulting from internal heating or solar loading of the equipment.

Prior to the application of exterior countermeasures, the effects of the internal workings of the vehicle on its signature need to be considered. It is in the total integral design of a vehicle that the most economical, operationally useful, and long-lasting signature reduction steps will be realized.

2.6.3.1 Integral Vehicle Designs. The designer of a signature suppressed vehicle needs to consider the physical size of the vehicle, the radiative and conductive effects of engine heating, waste heat removal (exhaust), frictional heating of the treads or tires, and the operational effects of weapons or other functional actions of the vehicle.

Physical size of the vehicle is directly related to acquisition range. The Johnson[51] criteria describes the relationship between resolution and target detection/identification ranges. Doubling the height of the target doubles the acquisition range because sensor acquisition is determined by the number of resolution cycles on the target. In designing the vehicle the height of the vehicle should be minimized.

The type of engine and the design and placement of that engine in the vehicle are critical factors influencing the thermal signature. Diesel engines are much more efficient in terms of waste heat output compared to turbine engines; therefore, designs incorporating diesel engines rather than turbine engines generally reduce the thermal signatures of vehicles.

Because observation of vehicles on the battlefield is generally from the frontal quadrant, positioning the engine in the rear of the vehicle, e.g., M1 or M60 tank, usually produces a lower infrared threat signature. However, in cases where engines are located in the front of the vehicle, the thermal signature can be minimized by constructing the engine compartment to make the best use of the intake air to cool the internal components. An example of a low-signature configuration is the M2/M3 engine compartment layout shown in Fig. 2.36. Ambient air is used to internally cool the engine (i.e., radiator), reduce the outer skin temperature of the engine, and to flush the engine compartment of accumulated waste heat. By locating the muffler in the path of the engine-cooling air flow and routing the exhaust gas to the very back of the vehicle, the frontal signature is greatly reduced. The addition of louvered grills and double-walled air intake and exhaust ducts have also been used to reduce direct observation of hot engine/exhaust components and produce cool outer surfaces on vehicles. Whether the vehicle has a rear engine or forward engine, thermal insulation of the engine and the engine compartment from the rest of the vehicle further reduce the thermal signature by minimizing the effects of conductive and radiative heating.

Exhaust gas and the impingement of that gas on other objects is a serious problem. The exhaust gas should be directed so that it does not strike any part of the vehicle other than the exhaust grill. The exhaust can produce significant secondary signatures when it reacts with the surrounding environment. When exhaust strikes the ground it can produce a hot spot on the ground adjacent

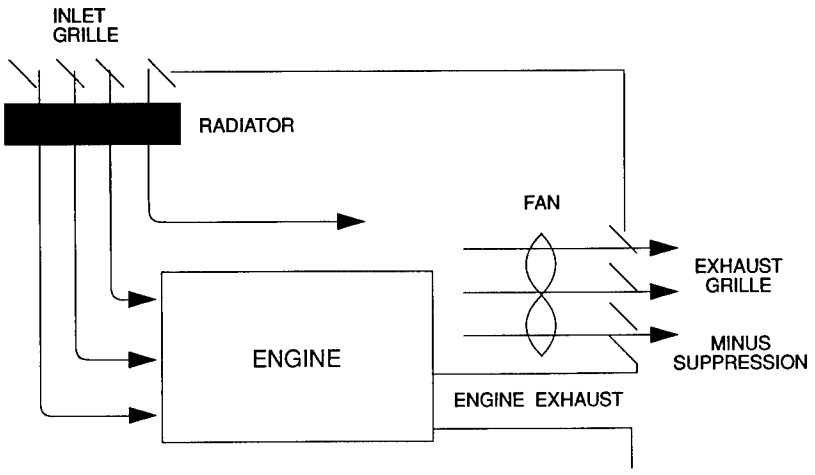

Fig. 2.36 Engine compartment layout for optimized thermal signature.

to the vehicle and a hot airborne dust cloud. The hot dust cloud is an obvious detection cue for threat sensors. However, the hot spot on the ground can be a beneficial false aiming point for top attack munitions. In general, vehicles that produce large, very hot exhaust flows should have their exhaust flows directed up where the gas can cause little harm.

Other infrared sources on military vehicles, although generally less significant than engine heating, can produce infrared signature cues that increase vulnerability. Examples of other sources are road wheels, tracks, and main guns. Frictional forces between the vehicle and the roadway cause the tracks on armored vehicles and the rubber road wheels on standard military vehicles to project fairly unique signature cues. In addition, rubber road wheels are very susceptible to solar loading and produce a distinctively unnatural donut-shaped heat pattern for each wheel. In both cases, track skirts and wheel covers can be designed to effectively hide the tracks and wheels from view and to produce little or no direct solar loading. The track covers are also effective in reducing the radar signature, which is produced by the multiple bounce returns so common from the tank wheels.

Firing of a tank's main gun also produces a rather distinctive silhouette, which aids in target recognition. A number of countries have developed ventilated barrel covers to produce convective cooling of the barrel. This procedure also minimizes barrel warping caused by the effects of nonuniform solar heating.

These integral design features are attractive because they are in operation at all times, require no troop training, produce no additional burden for the soldier during maneuvers, and are less vulnerable to the external environment.

2.6.3.2 Camouflage Screens. The camouflage screen is the mainstay of camouflage for countries throughout the world. The screen is produced in two basic system concepts: three-dimensional and two-dimensional. The most common are the 3-D systems produced by the United States, Great Britain, Sweden, France, Belgium, Netherlands, and several Warsaw Pact countries. They are characterized by a color-coated material (garnish) attached to a fish net substrate for strength. The garnish is incised to produce visual texture and movement (i.e., similar to leaf movement).

The U.S. Army has a camouflage screen called Lightweight Camouflage Screening System (LCSS). The LCSS is manufactured in three color combinations (woodland, desert, and snow) and two basic types (radar scattering and radar transparent). It is packaged and issued in "modules"; each module contains a hexagon-shaped and a diamond-shaped garnished screen, a support system of poles and spreaders, and a repair kit. A single module provides about 900 ft^2 (or 100 m^2) of coverage; any edge of any screen section can be mated with any other edge to form multimodule canopies. As examples, one module can cover a 30-kW generator, and two modules can cover an M-113 APC; but it takes several modules to adequately drape an M-1 tank. The incision pattern of the LCSS yields about 50% open space when erected.

An issue of concern is screen thermal effects. Simply covering an object with this screen provides some protection against solar loading because the incised screen reduces the amount of solar energy impinging on the object, similar to the effect of a tree canopy. However, the 50% open space severely limits the effectiveness of the screen in protecting heat generating targets against ob-

servation by thermal IR sensors. Extreme care must be exercised when operating heat producing equipment under a screen because significant secondary heating effects can be produced by the emitted hot exhaust gases, which increases the vulnerability of the equipment to detection. Prolonged emission of hot gases under the screen elevates the overall temperature of the screen and can produce a particularly hot spot where the exhaust impinges directly on the screen (Fig. 2.37). Because the screen covering a target is generally two to three times bigger than the target itself, the whole object (equipment plus screen) can become a significantly bigger infrared target compared to the uncovered target. In addition to the visual effects of texture and motion, and to some extent a radar Doppler effect produced by the incision pattern, the open area serves to minimize the effects of accumulated rain, sleet, snow, and noxious exhaust gases when equipment is operated under the screen.

A second type of camouflage screen design is the 2-D screen used by Israel and currently being evaluated by Germany and the United States. This screen has a visual camouflage pattern printed directly on an open weave material. Although this design does not have the large open areas present in the 3-D design, the woven textile material is porous enough to allow easy observation of hot objects under the screen. There is some evidence that these 2-D screens are less likely to solar load because the open weave provides for faster convective heat transfer of the solar energy to the surroundings. At this time it is not known how these 2-D screens hold up in sleet, snow, and heavy wind conditions, or if exhaust gases accumulate under the screen.

Partial thermal solutions are possible. It is doubtful whether either the 2-D or 3-D camouflage screens, which meet such a wide variety of spectral and

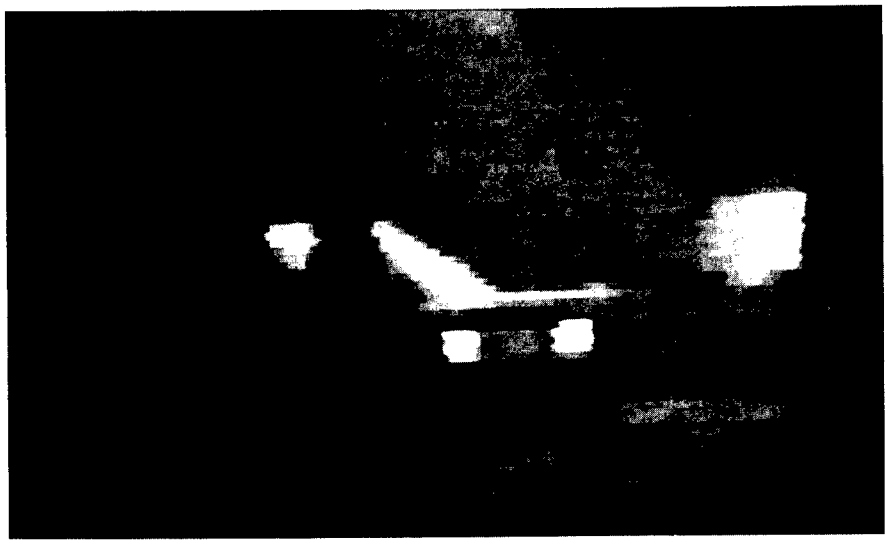

Fig. 2.37 An 8- to 12-μm band thermal image illustrates net heating. The object on the right is an operating generator without a screen: the object on the left is a generator covered with a screen that is being heated by exhaust impingement. Two foreground objects are reference sources.

operational military requirements, will be effective in hiding the thermal signature produced by internally generated heat. However, the secondary signature effects from exhaust gas heating and solar loading can be minimized. The camouflage screen can be deployed in such a way that it does not cover the entire object, but is left open around the area of the engine exhaust ports. Alternatively, the exhaust gas is channeled to the screen so that the air under the screen is not heated and the minimum hotspot is produced on the screen itself. Solar loading of the screen can be minimized by placing the screen in a position where it receives as little solar radiation as possible.

A more technically advanced alternative is to coat the screen with low-emissivity pigments, which reduce the apparent temperature (i.e., the observed temperature of the object as determined by the sensor compared to the actual surface temperature) of the screen relative to its background. Barracuda of Sweden, the largest producer of camouflage materials outside the United States, is currently experimenting with low-emissivity coatings applied uniformly or in patterns to its camouflage screens. The low-emissivity pattern gives an added dimension to thermal camouflage by producing a texture or clutter on the screen, thereby enabling the screen to more effectively blend into the thermal clutter observed in natural backgrounds.

Care must be taken when using a low-emissivity coating because, as discussed earlier, low emissivity generally means high thermal reflectivity. The more reflective the material, the more likely is the situation where the object is projecting the apparent temperature of the surroundings rather than the apparent temperature of the object itself. What is actually detected by the sensor is dependent on the viewing angle and the orientation of the viewed surface (i.e., vertical, angled up, or horizontal). From elevated viewing angles, vertical surfaces usually reflect the natural vegetation surrounding the object, whereas horizontal surfaces reflect sky conditions. From a ground-based-sensor perspective, vertical surfaces reflect either natural surroundings or other equipment in the vicinity of the observed target. Vertical surfaces again reflect sky conditions. Reflection of the natural surroundings is usually advantageous because the object then takes on the appearance of the surroundings and background matching is achieved. Reflection of the sky conditions off the angled or horizontal surfaces usually produce unwanted results because the cold sky (60 K from a clear sky) or, in the case of a 3- to 5-μm sensor, the hot sun can create equal or bigger contrasts with the background compared to the untreated, hot target object.

2.6.3.3 Tarps or Blankets. An alternative method of hiding the thermal signature of a vehicle is to place a thermal barrier directly between the heat producing object and the sensor. In the mid-1970s the United States experimented with a thermally insulating blanket system to suppress the signature of a generator while in operation. The blanket covered the hotspots on the generator and the insulation retarded the transfer of heat from the generator to the blanket itself. The problem with this system was that it was bulky and eventually the blanket reached some equilibrium temperature with the generator, which was higher than that of the surrounding temperature.

Another Swedish camouflage producer, FFV, has developed a thermal insulating system similar to the thermal blanket concept. The system incorpo-

rates a paper bladder, which is filled with insulating foam material and placed around the hot object to hide thermal emissions from observation. After prolonged operation, the bladder can either be replaced or refilled. Little is known of the operational efficiency of this system, however, its drawbacks would appear to include its bulkiness and the limitation of access to the equipment for operation or maintenance. The problem of equipment accessibility is paramount in fielding a useful as well as effective camouflage system. It cannot be stressed too much that any design of a thermal suppression system must consider how the system is integrated into the overall vehicle.

The British have recently fielded a thermal tarp, which will be draped over objects in the field. The tarp is green in color and has a surface emissivity of 0.5 on both sides. Theoretically the tarp could reach the same physical temperature as the object it is covering, however, the low emissivity surface will produce a lower apparent temperature with respect to the sensor. Because the tarp could melt if placed over a very hot surface, such as an exhaust grill, they are fielding a separate insulating mat that will be placed directly on these very hot surfaces and the tarp will be placed over the mat. A tarp with an emissivity of 0.5 will give significant sky reflections; therefore, the tactics employed with the tarp will have to be considered carefully. When the equipment is deployed in open areas, a camouflage screen should be employed over the tarp to diffuse the sky reflections.

In certain applications, a standoff tarp system is an alternative to the draped tarp. This system would incorporate a frame to support a standoff distance between the system and the tarp. The advantages of this system are that the radiative heating of the tarp and the likelihood of physical damage from direct contact with very hot objects would be reduced. The lower temperature of the tarp could allow a higher surface emissivity to be used, thereby lessening the effects from sky reflectivity. A two-sided tarp, incorporating a moderate emissivity outer surface and a very low emissivity inner surface is another method of reducing radiative heating of the tarp. The reflective nature of the inner surface limits the heating of the tarp itself and the moderate emissivity of the outer surface reduces the apparent temperature of the tarp from both the internal heat and solar loading effects. The disadvantage to the two-sided tarp is that the user has to ensure that the tarp is deployed in the proper orientation, which under night or battlefield conditions could pose problems.

2.6.3.4 Disruptive Pattern Painting. There are almost as many camouflage paint patterns as there are armies to use the patterns and the design rationale for these colors and patterns are just as numerous. Just as in the case of the camouflage screens, camouflage paint has been developed to adapt military equipment to the three major terrain environments, woodland, desert, and snow. Urban areas also constitute a terrain for camouflage paint consideration, however, the colors and shapes of the patterns are so different from the requirements of natural terrains, that only limited work has been done in the area. There appear to be two major philosophies governing the use of camouflage paint; one is to blend the equipment into the background in terms of coloration and texture, and the other is to provide a pattern that disrupts the characteristic shape of the vehicle so that the tell-tale silhouette of the vehicle is changed.

References

1. W. Kreiss, W. Lanich, and E. Niple, "E-O aerial targeting workstation," *NAECON89,* J. L. Morris, Ed., May 22–24, 1990, Dayton, OH, IEEE, New York (1990).
2. Dennis Blay, General Dynamics, Valley Systems Division, Pomona, CA, private communication (June 1990).
3. C. B. Ludwig, W. Malkmus, J. E. Reardon, and J. A. L. Thompson, *Handbook of Infrared Radiation from Combustion Gases,* NASA SP-3080, National Aeronautics and Space Administration, Washington, DC (1973).
4. F. X. Kneizys, E. P. Shettle, W. O. Gallery, J. H. Chetwynd, Jr., L. W. Abreu, J. E. A. Selby, S. A. Clough, and R. W. Fenn, "Atmospheric transmittance/radiance: computer code Lowtran 6," AFGL-TR-83-0187, U.S. Air Force Geophysics Laboratory (Aug. 1983).
5. R. D. Hudson, *Infrared System Engineering,* John Wiley & Sons, New York (1969).
6. C. C. Lin, Ed., *High Speed Aerodynamics and Jet Propulsion,* Vol. V, *Turbulent and Heat Transfer,* Princeton University Press, NJ (1957).
7. K. R. Johnson and W. R. Owens, "TCM2—A new medium resolution thermal contrast model," U.S. Air Force Avionics Laboratory Report AFWAL-TR-87-105A, Georgia Tech Research Institute (1987).
8. F. E. Nicodemus, "Directional reflectance and emissivity of an opaque surface," *Applied Optics* 4(7), 767–773 (1965).
9. B. P. Sandford, "Infrared reflectance of aircraft paints," AFGL-TR-84-0307, U.S. Air Force Geophysics Laboratory, Hanscom AFB, MA (1984).
10. E. Hecht and A. Zajac, *Optics,* Addison-Wesley, Reading, MA (1979).
11. E. Knott, J. Schaffer, and M. Tuley, *Radar Cross Section,* Artech House, Norwood, MA (1985).
12. L. D. Jones and H. R. Condit, "Sunlight and skylight as determinants of photographic exposure," *Journal of the Optical Society of America* **38**(2), 123–178 (1948).
13. *Surface Coatings,* Vol. I, 2nd ed., Tafe Educational Books, Oil and Colour Chemists' Association, Kensington, Australia (1983).
14. I. M. Ward, ed., *Structure and Properties of Oriented Polymers,* Applied Science Publishers, London, England (1975).
15. T. L. Starr, Georgia Institute of Technology, private communication (1989).
16. L. E. Murr, *Solar Materials Science,* Academic Press, New York (1980).
17. W. M. Wendlandt and H. G. Hecht, *Reflectance Spectroscopy,* Interscience Publishers, New York (1966).
18. W. J. Smith, *Modern Optical Engineering,* McGraw-Hill, New York (1966).
19. Military Specification MIL-C-53039 (ME) (16 April 1984).
20. Military Specification MIL-C-46168C (ME) (28 March 1984).
21. D. K. Edwards and I. Catton, "Radiation characteristics of rough and oxidized metals," in *Advances in Thermophysical Properties of Extreme Temperatures,* S. Cratch, Ed., American Society of Mechanical Engineers (1965).
22. Federal specification MIL-L-19538C (11 May 1990).
23. E. D. Palik, Ed., *Handbook of Optical Constants of Solids,* Academic Press, Orlando, FL (1985).
24. M. E. Krisl, R. Shimshick, and N. Boling, "Multilayer dielectric pigment for IR emissivity modification," Product Brochure, Deposition Sciences, Inc., Santa Rosa, CA (1989).
25. *The Infrared Spectra of Monomers and Polymers,* 2nd ed., Sadtler Research Laboratories, Philadelphia, PA (1983).
26. C. G. Granqvist, *Spectrally Selective Surfaces for Heating and Cooling Applications,* Vol. TT01, SPIE Optical Engineering Press, Bellingham, WA (1989).
27. C. M. Lampert and C. G. Granqvist, *Large-Area Chromogenics: Materials and Devices for Transmittance Control,* Vol. IS04, SPIE Optical Engineering Press, Bellingham, WA (1988).
28. C. N. Berglund, "Thermal filaments in vanadium dioxide," *IEEE Transactions on Electron Devices* **ED-16**(5), 432–437 (1969).
29. F. J. Morin, "Oxides which show a metal-to-insulator transition at the Neel temperature," *Physical Review Letters* **3,** 34–36 (1959).
30. J. B. Goodenough, "Direct cation-cation interactions in several oxides," *Physical Review* **117**(6), 1442–1451 (1960).

31. G. Soward et al., "Prototype all-solid lithiated smart window devices," *Proceedings of the SPIE* **823,** 90 (1987).
32. *ASHRAE Handbook, Fundamentals,* American Society of Heating, Refrigerating and Air Conditioning Engineers, Atlanta, GA (1989).
33. Z. B. Black and J. G. Hartley, *Thermodynamics,* Harper & Row, New York (1985).
34. G. E. Varney, GE Aircraft Engines, Cincinnati, OH, private communication (1989).
35. D. A. Anderson, J. C. Tannehill, and R. H. Pletcher, *Computational Fluid Mechanics and Heat Transfer,* Hemisphere Publishing, New York (1984).
36. D. M. Brani and C. R. Hewitt, unpublished internal research, Georgia Tech Research Institute (1990).
37. J. D. Mattingly, W. H. Heiser, and D. H. Daley, *Aircraft Engine Design,* AIAA Education Series, Washington, DC (1987).
38. S. Gordon and B. McBride, "Computer program for calculation of complex chemical equilibrium compositions," NASA Lewis Research Center, Report NASA SP-273 (1976).
39. B. V. Shetler and W. M. Cornette, "Exhaust plume infrared radiative transfer (EXPIRT) code," Photon Research Associates, La Jolla, CA (1987) (unpublished).
40. S. D. Jandrall and W. M. Cornette, "Atmospheric propagation and radiative transfer (APART) computer code," Photon Research Associates, La Jolla, CA (1987).
41. N. S. Gowadia, private communication (1988).
42. T. J. Doll, J. M. Cathcart, and S. S. Steadman, "An operator based methodology for infrared countermeasure evaluation," FMC Contracts 164582K and 168387M, Georgia Tech Research Institute, Atlanta, GA (1989).
43. A. P. Ginsberg, "Visual information processing based on spatial filters constrained by biological data," AMRL-TR-78-129, U.S. Air Force Armstrong Medical Research Laboratory, Wright-Patterson Air Force Base, OH (1978).
44. R. De Valois and K. De Valois, "Spatial vision," *Annual Review of Psychology* **31,** 304–341 (1980).
45. A. Akerman and H. Hammill, *Camouflage Handbook,* U.S. Air Force Avionics Laboratory Report AFWAL-TR-86-1028, U.S. Air Force Avionics Laboratory, Calspan Corporation (1986).
46. E. Sloane, *Camouflage Simplified,* Devin-Adair, New York (1942).
47. B. Sweetman, "Stealth in service," Interavia Aeropsace Review No. 042(002)39 (1987).
48. *Disguises of War,* NOVA Television Program, Journal Graphics, New York (1989).
49. A. Ben-Shalom, B. Barzilai, D. Cobib, A. D. Devir, S. G. Lipson, and U. P. Oppenheim, "Sky radiance at wavelengths between 7 and 14 microns: measurements, calculation, and comparison with Lowtran 4 predictions," *Applied Optics* **19,** 838–839 (1980).
50. F. G. Wollenweber, "Impact of atmospheric layering on Lowtran 6 radiance calculations," *Applied Optics* **29**(34), 5177–5181 (1990).
51. J. Johnson, "Analysis of image forming systems," in *Proceedings of the Image Intensifier Symposium,* ASTIA, Document AD220160 (1958).

CHAPTER 3

Active Infrared Countermeasures

Charles J. Tranchita
Kazimieras Jakstas
Robert G. Palazzo
Northrop Electronic Systems Division
Rolling Meadows, Illinois

Joseph C. O'Connell
U.S. Army CECOM
Fort Monmouth, New Jersey

CONTENTS

3.1 INTRODUCTION

The goal of active infrared countermeasures (IRCM) is quite simple: add modulated infrared energy to the infrared signature of an aircraft to counter infrared guided missiles. Yet the system engineer who suddenly is tasked with the understanding, design, or production of active IRCM systems soon becomes aware of the many complexities it presents. Aircraft power limitations, aircraft signatures, mission analysis, infrared missile signal processing, infrared sources, and missile-target simulation each play a critical role in the success of an active IRCM system. The goal of this chapter is to show how these disciplines interrelate.

3.1.1 Active IRCM

An infrared missile tracks on the infrared signature produced by the target aircraft. Early nonimaging seekers tracked by having the missile optics and reticle produce modulated IR energy at a detector. The missile signal processing is used to determine the position of the target with respect to the missile and guide its course to interception. When presented with multiple IR targets, these seekers track the one with the highest radiant intensity.

Active IRCM was first operationally employed during the Vietnam conflict. Active IRCM exploits the signal processing of the missile electronics. By adding modulated IR energy to that of the platform, the active jammer adds spurious signals to the missile processing electronics. These signals can cause the seeker to lose the target completely—a condition known as optical breaklock (OBL)—or alter the trajectory of the missile such that it never intercepts the target.

Presently, active IRCM modulation is done either electronically or mechanically, depending on the IR source in the jammer. Arc lamps, which are filled with alkali metal vapors or inert gases, are modulated electronically. The amplitude of the radiation produced is temporal, i.e., it is a function of the instantaneous power applied to the lamp. Mechanical modulation is used with fuel-fired sources or electrically heated sources. The radiation amplitude of the source itself is constant. The modulation is produced by having an opaque or spectrally filtered chopper in the optical train.

In general, several advantages are gained with present active IRCM. It provides continual protection. It can act as a stand-alone system. It is made to be visually covert.

The disadvantages of present active IRCM systems include auxiliary power requirements, size, weight, and a trend to be threat specific. Specific advantages and disadvantages peculiar to electronically and mechanically modulated systems are discussed in Sec. 3.4.

3.1.2 Methodology in the Design of Active IRCM

This chapter is concerned with active IRCM for fixed- and rotary-wing aircraft against passive detection IR missiles. This class of missiles includes surface-to-air missiles, air-to-air missiles, surface-to-surface missiles, and air-to-surface missiles.

In the design and analysis of active IRCM, a methodology has been used that provides prediction for the success of active IRCM. The methodology begins with a determination of the aircraft signature and its mission. From the mission analysis, the types of threats that the aircraft may encounter are determined. The required techniques are defined. The selected jammer source capabilities are compared to the technique definition. Aircraft constraints—including available power, installation sites, and operational requirements—then complete the system definition. The system performance is simulated, either digitally or semiphysically, and the design is iterated. The system is constructed, field tested, and then put into operation. An overview of the methodology is shown in Fig. 3.1.

A listing of the symbols and definitions used throughout this chapter is given in Table 3.1.

3.2 AIRCRAFT SIGNATURES

The atmosphere has windows where the infrared transmission is high and relatively uniform. Several detectors exist whose spectral response peaks in these transmission bands. A convention has grown that categorizes missiles by band. For the purpose of discussion, the following bands are defined:

band α = 1.9 to 2.9 μm
band β = 3.0 to 5.0 μm.

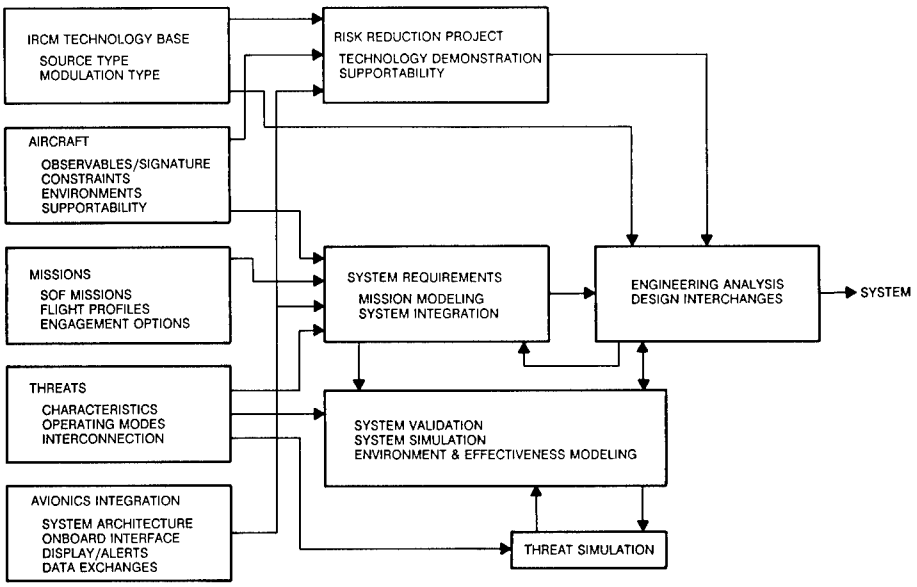

Fig. 3.1 IRCM methodology flow.

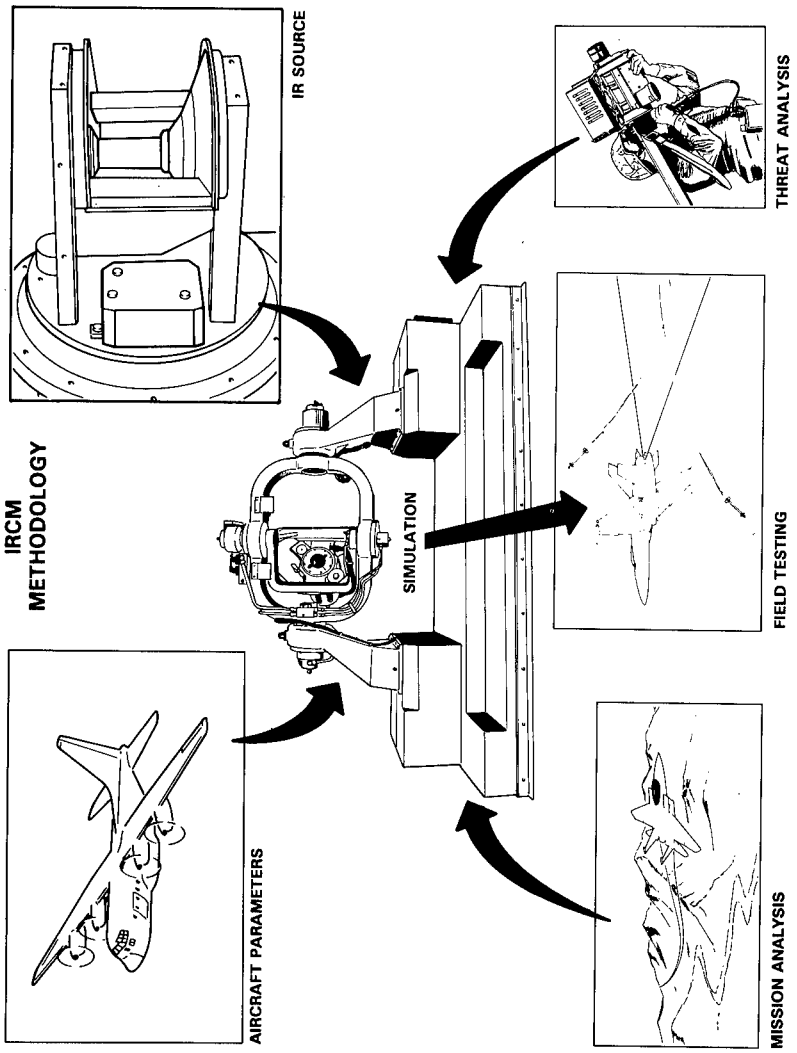

Fig. 3.1 *(continued)*

Table 3.1 List of Symbols

A	target radiation power falling on the reticle
A_0	on-axis illuminated area
A_c	effective collecting area of the seeker
A_d	area of detector
a_n	commanded missile lateral acceleration in the guidance plane
A_P	projected source area
A_{p_i}	projected area of an element
A_{ref}	projection system aperture
B	peak jammer power
band α	1.9 to 2.9 μm
band β	3.0 to 5.0 μm
C_1	1.191×10^4 W cm^{-2} μm^4 sr^{-1}
C_2	1.438×10^4 μm K
c_n	Fourier series coefficient
d	diameter of engine exhaust port
d_k	jammer waveform Fourier series coefficient
DOM	depth of modulation
E_d	damage threshold irradiance for detector
$E_{j\lambda}(\lambda)$	jammer spectral irradiance at the seeker
$E_{t\lambda}(\lambda)$	target spectral irradiance at the seeker
E_o	laser damage threshold irradiance
f_1, f_2	spin frequencies of two scanning elements
I	signature (in-band radiant intensity)
I_I	interpulse in-band radiant intensity
I_J	jammer radiant intensity
I_P	peak in-band radiant intensity
I_{ac}	platform radiant intensity
I_{dc}	average of the waveform (in excess of interpulse contribution)
I_α, I_β	on-axis radiant intensity in band α, band β
$\frac{J}{S} \equiv \frac{I_J}{I_{\text{ac}}}$	ratio of jammer intensity to platform intensity
$(J/S)_{\text{elec}}$	effective J/S ratio in the missile electronic band
L	source radiance
L_{band_i}	in-band radiance of each area element
$m(t)$	image dwell modulation
$m_r(t)$	reticle modulation function
$m_t(t)$	carrier gating function (a square wave)
N	a proportionality constant
P_e	laser power on optical element
P_j	instantaneous jammer power
P_l	laser power
$P(t)$	seeker driving signal
$P_d(t)$	radiation power falling on detector
$P_j(t)$	time-modulated jammer power arriving at the reticle
P_{band}	in-band power
P_{elec}	electrical power
P_{input}	total electrical power input

Table 3.1 *(continued)*

P_{rad}	radiated power
R	range from laser to seeker
$S(t)$	combined jammer and target radiation power
$s_c(t)$	carrier amplifier output
$S_e(t)$	effective signal waveform
$s_e(t)$	envelope of carrier signal modulation
S_i	signals detected by quad cell elements
t	time
T_d	dwell time on target
T_j	jammer waveform period
T_m	reticle (or gyro) spin period
T_o	jammer pulse duration
T_r	image dwell time on the reticle
T_s	relative time delay between jammer and reticle modulation
T_{HP}	temperature of hot parts
T_{body}	temperature of body skin
V_m	magnitude of missile velocity vector
y	distance of turbine plate from exhaust port
Greek:	
α	ratio of the radius of the image location (or the tracking error) to the radius of the reticle that provides a simplified measure of the modulation efficiency ($0 \leqslant \alpha \leqslant 1$)
α_m	jammer interpulse modulation ratio
$\beta(t)$	differential phase angle
$\Delta\omega$	difference in angular frequencies between the jammer modulation and the gyro spin
ε	tracking error magnitude
ε_i	emissivity of each area element
$\varepsilon_{\text{band}}$	in-band efficiency
ε_{rl}	right-left tracking error
ε_{ud}	up-down tracking error
θ	angle with respect to the normal of the exhaust port
θ_i	instantaneous FOV
θ_t	total FOV
λ	wavelength
λ_1,λ_2	wavelength limits of the band
λ_{mid}	midpoint wavelength in the band
ξ_{band}	conversion efficiency factor
ρ_j	jammer duty cycle
ρ_m	reticle modulation duty cycle
ρ_s	fractional time delay of jammer pulse relative to reticle modulation
$\dot{\sigma}$	LOS rotation rate
τ	irradiation time
τ_a	atmospheric transmission factor
τ_o	optical transmission factor
$\tau_o(\lambda)$	spectral transmission of the seeker
$\varphi_j(t)$	jammer waveform phase angle
$\dot{\bar{\varphi}}(t)$	tracking-error-rate phasor
ω_c	carrier frequency
ω_j	jammer angular frequency

(continued)

Table 3.1 *(continued)*

ω_m	angular frequency of reticle spin
ω_r	rate of rotation of the projection system
Ω	solid angle into which radiation is projected
Ω_l	spatial substense of the beam

3.2.1 Signature Estimation

Active IRCM analysis is concerned with the signature of the platform as sensed by the missile. Often the signature is not known and the analyst is forced to make an estimate.

Consider a target that subtends a small angle to the missile. The target can be broken down into n area elements where the radiance is uniform over each element. The radiant intensity that is emitted by the aircraft (i.e., its signature) is

$$I = \sum_{i}^{n} \varepsilon_i L_{\text{band}_i} A_{p_i} \ , \tag{3.1}$$

where

I = the signature (in-band radiant intensity)
ε_i = the emissivity of each area element
L_{band_i} = the in-band radiance of each area element
A_{p_i} = the projected area of the element.

The many radiation sources—plume, hot parts, skin, reflected skyshine, reflected earthshine, reflected clouds, etc., and their temporal and spatial variations—make an exact determination of the signature for an arbitrary aircraft virtually impossible.

For a nontactical aircraft it is possible to make several simplifying assumptions that can give a reasonable estimation of the signature for bands α and β. The platform is assumed to radiate as a graybody. In addition, the assumption is made that the emissivity for all elements of the aircraft is unity. The number of radiation sources is limited to the hot parts and body skin. Furthermore, the temperature is assumed to be uniform over each source. Thus, Eq. (3.1) can be simplified to

$$I = L(T_{\text{HP}})_{\text{band}} \sum_{\text{hot parts}} A_{p_i} + L(T_{\text{body}})_{\text{band}} \sum_{\text{body}} A_{p_i} \ , \tag{3.2}$$

where T_{HP} is the temperature of the hot parts and T_{body} is the temperature of the body skin. Using these assumptions, analysis of several aircraft measurements[1] has shown that T_{HP} can be estimated as falling into the 750 to 800-K range. For most nontactical aircraft, aerodynamic heating effects are neglected. The parameter T_{body} is estimated to be within a few degrees of ambient temperature.

At any particular azimuth and elevation angle, the projected area of the body can be found from a sketch, photograph, or even a toy model. The esti-

mation of the pattern of the radiation produced by the hot parts can be found[2] by using the following relationship:

$$I(\theta) = L(T_{HP})_{band} \frac{\pi d^2}{4} \cos^{\left(\frac{y}{d}+1\right)}\theta \ , \tag{3.3}$$

where

d = the diameter of the engine exhaust port
y = the distance of the turbine plate from the exhaust port
θ = the angle with respect to the normal of the exhaust port.

Figure 3.2 shows three radiation patterns for different values of the ratio y/d. The values of y and d can be obtained by examining diagrams of the aircraft engine. These can be obtained from several sources, most notably Ref. 3.

The evaluation in Eq. (3.2) requires the computation of the in-band radiance. The spectral width of the bands and the temperature of the component elements allow for further approximations to simplify the computation.

The radiance over the band is

$$L_{band} = \int_{\lambda_1}^{\lambda_2} L(\lambda)\, d\lambda \ , \tag{3.4}$$

where λ_1,λ_2 = the wavelength limits of the band. Since the bands are at most 2 μm in width, one can approximate Eq. (3.4) by

$$L_{band} = (\lambda_2 - \lambda_1)L(\lambda_{mid}) \ , \tag{3.5}$$

where $\lambda_{mid} = (\lambda_2 + \lambda_1)/2$.

The radiance can be determined from the Planck function

$$L(\lambda,T) = \frac{C_1}{\lambda^5[\exp(C_2/\lambda T) - 1]} \ , \tag{3.6}$$

where $C_1 = 1.191 \times 10^4$ W cm^{-2} μm^4 sr^{-1} and $C_2 = 1.438 \times 10^4$ μm K. For the values of λ and T of interest (e.g., $\lambda = 4.0$ μm and $T = 800$ K), the exponential factor $\exp(C_2/\lambda T)$ is much greater than unity; i.e.,

$$\exp(C_2/\lambda T) = 89.6 \gg 1 \ ,$$

allowing the simplification of Eq. (3.6) to

$$L(\lambda,T) = \frac{C_1}{\lambda^5 \exp(C_2/\lambda T)} \ . \tag{3.7}$$

If higher accuracy is needed, Eq. (3.4) can be integrated analytically using the approximation in Eq. (3.7).

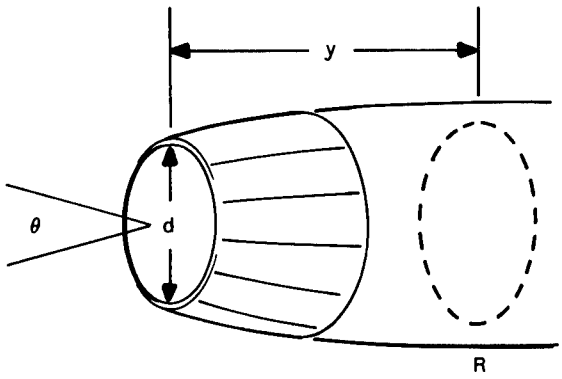

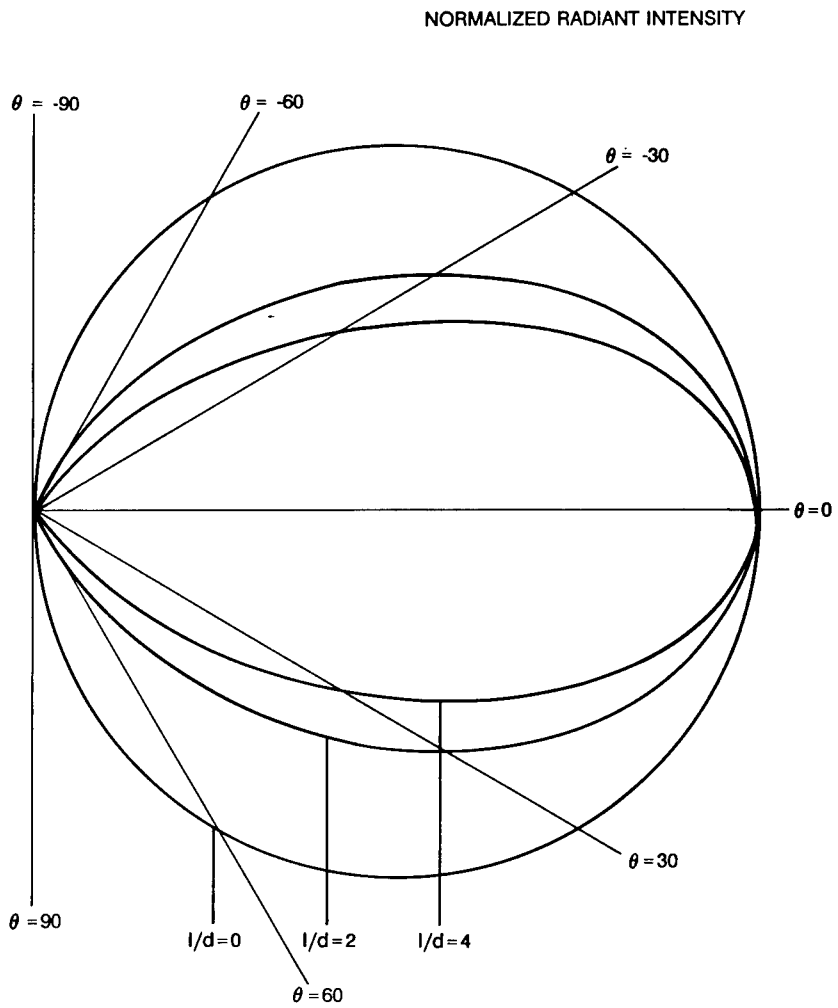

Fig. 3.2 Hot parts: radiation patterns.

Table 3.2 Example Calculation

	Band $\alpha(\lambda_{mid} = 2.4\ \mu m)$	Band $\beta(\lambda_{mid} = 4.0\ \mu m)$
$L(T_{HP})_{band}$ (W cm^{-2} sr^{-1})	$1 \times 0.05 = 0.05$	$2 \times 0.0961 = 0.192$
$L(T_{body})_{band}$ (W cm^{-2} sr^{-1})	$1 \times 3.14 \times 10^{-7} = 3.14 \times 10^{-7}$	$2 \times 7.22 \times 10^{-5} = 1.44 \times 10^{-4}$

Table 3.3 Typical Projected Areas On-Axis

	$A_{p\ engine}$	$A_{p\ body}$
Helicopter	3000 cm^2	6×10^5 cm^2
Cargo aircraft	5000 cm^2	2×10^6 cm^2

3.2.1.1 Example Calculation. Consider a helicopter and a cargo aircraft. For both aircraft, let the estimate of the engine temperature be 750 K and of the body temperature be 300 K. Thus, Table 3.2 can be generated from Eqs. (3.5) and (3.7). Typical projected areas on-axis with the engine are given in Table 3.3.

Therefore, by multiplying appropriate elements of each matrix, we can evaluate Eq. (3.2) for the helicopter:

$$I_\alpha = (0.050 \times 3000) + (3.14 \times 10^{-7} \times 6 \times 10^5) = 150.2\ \text{W sr}^{-1}\ ,$$

$$I_\beta = (0.192 \times 3000) + (1.44 \times 10^{-4} \times 6 \times 10^5) = 662.4\ \text{W sr}^{-1}\ .$$

Likewise for the cargo aircraft:

$$I_\alpha = (0.050 \times 5000) + (3.14 \times 10^{-7} \times 2. \times 10^6) = 250.6\ \text{W sr}^{-1}\ ,$$

$$I_\beta = (0.192 \times 5000) + (1.44 \times 10^{-4} \times 2. \times 10^6) = 1248\ \text{W sr}^{-1}\ ,$$

where I_α, I_β = the on-axis radiant intensity in band α, band β. For both aircraft, the results show that the contribution to the band α signature from the body is less than 1 W sr^{-1}. Thus, it is usually safe to exclude the body contributions from the estimation of I_α.

3.2.2 Signature Measurement

A more precise estimate of the signature can be gained from a measurement of the aircraft. Measured values of the platform radiation are dependent on the conditions under which the measurement is performed; they are a strong function of several factors, including the background, background temperature, engine temperature, and aircraft velocity. These effects can be particularly large in the long-wavelength band β.

3.2.2.1 Spectral Measurements. Several types of radiometers, such as the Fourier transform radiometer (FTR) and circular variable filter radiometer (CVFR),[4] can give an accurate spectral measurement of the aircraft signature alone. The FTR uses a Michelson interferometer, as shown in Fig. 3.3. A collimated beam is split into two parts, each part traveling a separate path to a reflecting mirror. The separate beams are recombined at the beam splitter and reflected to a detector. Fringes will occur because of interference. The amplitude of the central fringe depends on the difference in length that each portion of the beam has traversed. For a monochromatic source, the detected amplitude varies sinusoidally as one mirror is moved with respect to the other at a constant velocity. The amplitude of the oscillation is dependent on the strength of the source. The frequency of the oscillation is a function of the velocity of the mirror and the source wavelength. For a polychromatic source, the detected voltage is a complex function of time. The detected voltage is the sum of each frequency response caused by each wavelength. The Fourier transform decomposes the time response into the component frequency responses. Thus, the Fourier transform of the detector voltage is proportional to the spectrum of the source.

The CVFR moves a filter wheel in front of a detector. Each position of the wheel allows transmission about a center wavelength with a width approximately 0.05 μm. Each wavelength-dependent signal is found by rotating the wheel until the corresponding wavelength position is in front of the detector. The wheel is paused for a small amount of time (or rotated slowly) and the detected voltage is measured. When the response has been found for all the filters, the spectrum is complete.

Assuming the source remains constant over the measurement time, the FTR usually can provide a higher-resolution spectrum with less radiated power and in less time than a CVFR.

For the spectral measurement of the jammer, the CVFR is the more useful instrument. The jammer produces pulses of radiation. It is often of interest to find the spectrum produced when the pulse is at its peak. If the source is

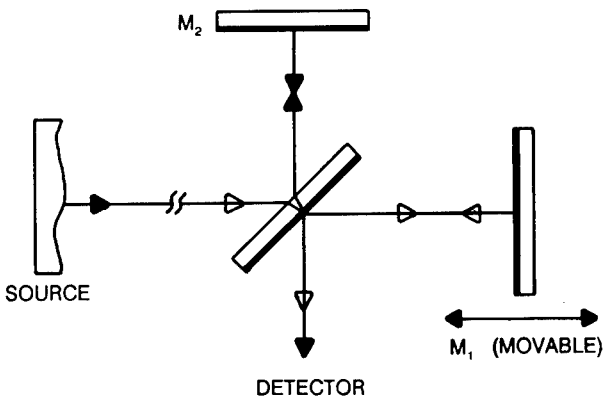

Fig. 3.3 Block diagram of the Fourier transform radiometer.

pulsating, the FTR will not yield the correct spectrum of the modulated radiation. The CVFR can be synchronized with the pulse train and the CVFR can be used to obtain the spectrum of the pulse at its peak. If the pulse amplitude varies, the CVFR yields the average pulse peak amplitude.

3.2.2.2 Bandpass Measurements. Since the missile acts as a bandpass radiometer, the bandpass measurement of the combined value of the aircraft signature and the jammer is often done. The bandpass filter and detector are matched as well as possible to that of the missile. A typical experimental configuration is shown in Fig. 3.4.

The radiometer consists of collecting optics, a chopper, a bandpass filter, and a detector. The output of the detector is sent to an oscilloscope. By mechanically chopping the combined jammer and aircraft signature radiation, the jammer-to-aircraft signature ratio (J/S) can be found directly from the oscilloscope trace. This is shown in Fig. 3.5.

3.3 JAMMING TECHNIQUES AGAINST IR MISSILES

3.3.1 A Functional IR Missile Description

An IR missile utilizes energy radiated or reflected by a target, such as an aircraft or a ground vehicle, for passive homing. Homing IR missiles invariably employ proportional navigation to intercept the target. The reason for this is the relative simplicity of the proportional navigation concept and its implementation. To achieve an intercept using proportional navigation guidance, the missile must have a range closure (negative range rate) and must control the line-of-sight (LOS) rotation rate. A simplified relation that embodies proportional navigation can be stated as

$$a_n = NV_m\dot{\sigma} \ , \tag{3.8}$$

where

a_n = the commanded missile lateral acceleration in the guidance plane
N = a proportionality constant
V_m = the magnitude of the missile velocity vector
$\dot{\sigma}$ = the LOS rotation rate.

The guidance plane is defined as the plane containing the relative range **R** and the relative velocity vector **V**, as shown in Fig. 3.6. The optimal direction for the missile acceleration $\mathbf{a_n}$ is in the guidance plane and normal to the relative range vector **R**. In a practical implementation of proportional navigation, various compromises are made, depending on the available sensor information and missile thrust or acceleration control. The LOS rotation rate is usually obtained by sensing the target direction via the seeker and by driving the seeker tracking loop to maintain the seeker boresight on the target. Ignoring the transients, the seeker angular rate in tracking the target provides a direct measure of the LOS rotation rate. IR jamming techniques are aimed at disrupting or deceiving the seeker tracking function, which in turn affects the missile guidance function.

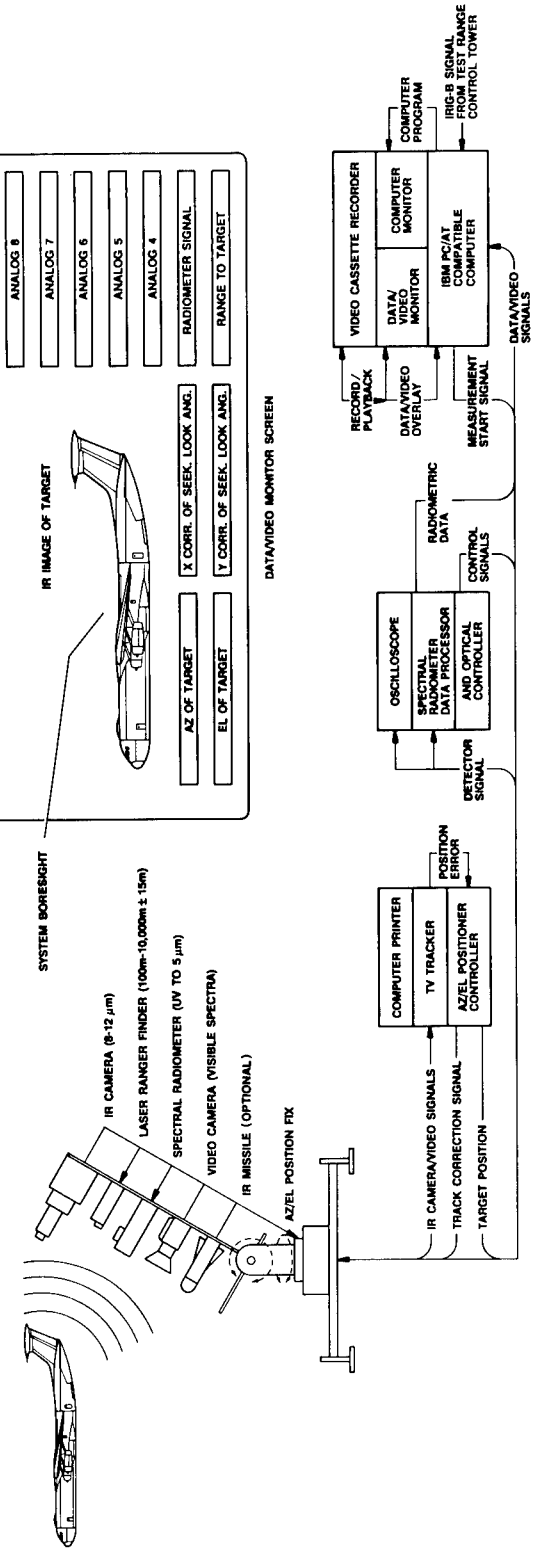

Fig. 3.4 Tracking radiometer and IR seeker.

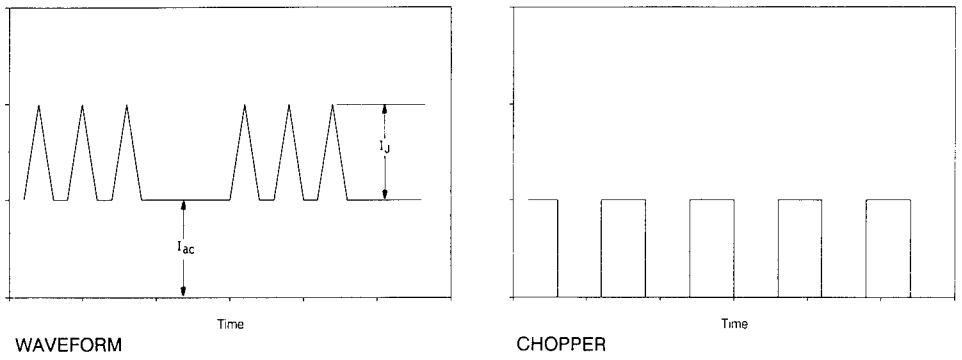

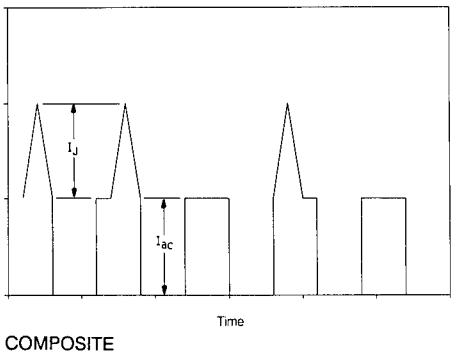

Fig. 3.5 *J/S* values from oscilloscope.

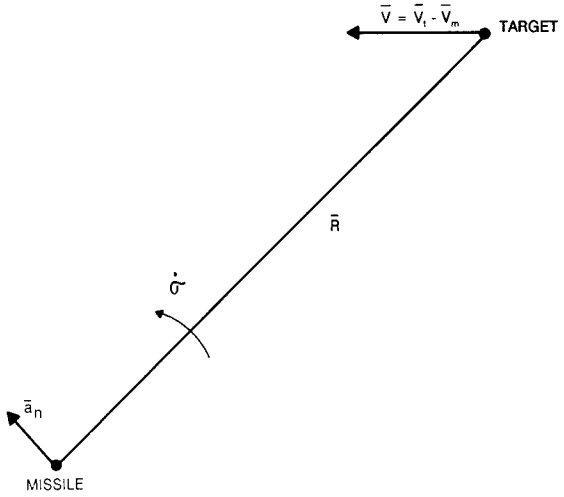

Fig. 3.6 Guidance plane geometry.

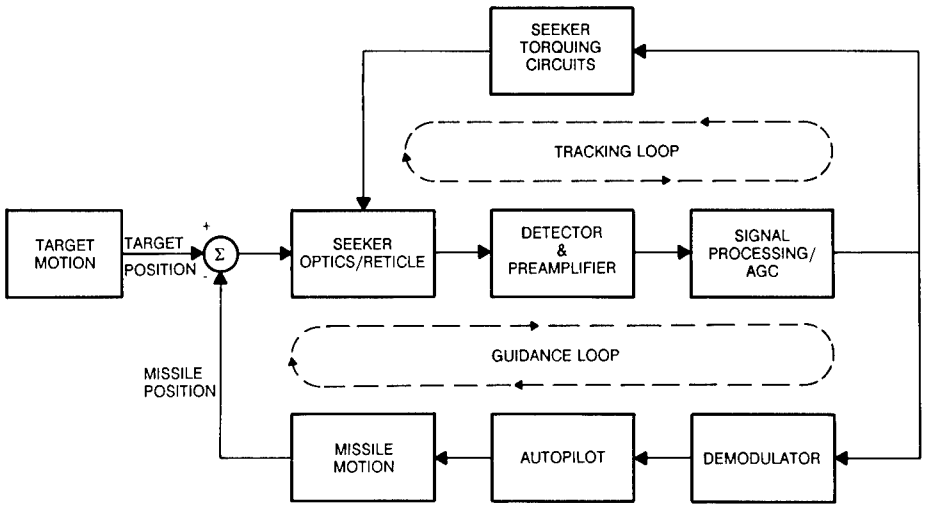

Fig. 3.7 A typical missile block diagram.

A typical IR missile block diagram is presented in Fig. 3.7 showing the basic tracking and missile guidance loops. The driving inputs stem from the target motion and the target radiation as seen through the atmosphere at the seeker. The seeker is represented by a gimbaled gyro or in some cases by a nonspinning platform supporting some optics. In the spinning gyro case, the target may be imaged on a spinning reticle (spin-scan modulation) or the target image may be nutated on a stationary reticle (conical scan, or conscan, modulation). The reticle consists of a pattern of transparent and opaque regions, and the motion of the target image relative to the reticle provides a modulation of the target radiation signal.

The modulated target radiation is sensed by a detector that converts it into an electrical signal that is processed to generate appropriate signals for driving the seeker to close the tracking loop and is further demodulated to drive the appropriate missile control surfaces as commanded by the autopilot to generate the necessary missile turning rates.

3.3.2 Detectors and Spectral Response

A detailed theory of detectors and associated electronics may be found elsewhere in this handbook. The discussion here is limited to the characteristics of the detectors, i.e., their spectral response, as it pertains to their interaction with the target and jammer radiation.

The spectral response of a missile seeker is determined by its optical elements, i.e., dome, mirrors, lenses, filters, etc., and its detector. The seeker spectral region is determined by the target radiation spectrum and by the available detectors.

Early IR missile seekers were designed with uncooled PbS detectors operating in band α. This effectively limited missile attack capability against typ-

ical aircraft to the rear aspect where the hot engine parts may be seen. As the detector technology advanced and cooling of the detectors became practical, the operating spectral region of the seekers began to shift toward the mid-IR region, band β. Since typical aircraft with jet engines emit a significant amount of plume radiation in this region, most modern missiles are capable of attacking aircraft at all aspects. However, because of shielding, cooling, and other factors, aircraft signatures may not be adequate at many aspect angles for the missile seeker to lock on, especially at long ranges.

For in-band jamming, the jammer must radiate a sufficient amount of power in the spectral band of the seeker to compete with the radiation produced by the target. The effective instantaneous jammer power P_j in the seeker spectral band collected by the detector may be estimated using the following relationship:

$$P_j = A_c \int E_{j\lambda}(\lambda)\tau_o(\lambda)\, d\lambda \ , \tag{3.9}$$

where

A_c = the effective collecting area of the seeker
$E_{j\lambda}(\lambda)$ = the jammer spectral irradiance at the seeker
$\tau_o(\lambda)$ = spectral transmission of the seeker
λ = wavelength.

Similarly, the effective target power falling on the detector can be defined as follows:

$$P_t = A_c \int E_{t\lambda}(\lambda)\tau_o(\lambda)\, d\lambda \ , \tag{3.10}$$

where $E_{t\lambda}(\lambda)$ = the target spectral irradiance at the seeker.

3.3.3 Seeker Scanning and Signal Processing

To gain insight into how a seeker tracking loop may be disrupted, it is essential to examine the methods used in the seekers for scanning, modulation, and tracking-loop signal processing. Among the more common scanning detection techniques are

1. spin-scan
2. conscan
3. rosette
4. focal-plane array (FPA)
5. quadrant.

The spin-scan and conscan seekers utilize reticles for signal modulation. A rosette-scan seeker scans a small instantaneous field of view (IFOV) subtended by a detector in a rosette pattern. A focal-plane-array seeker may scan a linear array detector in a raster or bar fashion over the image of the target scene in the focal plane or it may utilize a two-dimensional detector mosaic, the elements of which are read out periodically to determine the image of the scene. A quadrant detection scheme employs a set of four detectors on which a defocused target image is projected.

3.3.3.1 Spin-Scan Seeker. A spin-scan seeker usually consists of a spinning gyro with a telescope and a reticle placed in the focal plane of the collecting optics. The reticle spins with the gyro and modulates the projected target scene. A classical spin-scan reticle (sometimes referred to as the rising-sun reticle) is shown in Fig. 3.8. A point target is projected onto the reticle as a blur circle, the size of which corresponds approximately to the width of one of the spokes at some radius (e.g., midpoint). This matching is done for the purpose of generating a near-optimal (sinusoidal) carrier signal. A sample waveform is shown for the case where the image is a point source. As the image blur circle moves toward the center, the modulation efficiency decreases and is zero at the center. The half of the reticle with the circular rings provides 50% transmission (gray sector) and is used to determine the phase angle of the demodulated waveform relative to a reference waveform generated by the spinning gyro magnet in the seeker reference coils.

The modulated radiation collected on the detector is converted to an electrical signal, amplified, and processed through a bandpass amplifier. The passband of this amplifier is centered on the carrier frequency. This frequency is equal to the number of spoke pairs times the spin frequency times two (to

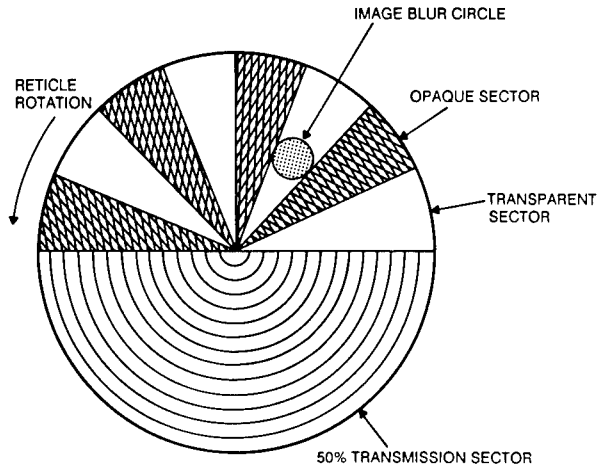

(a)

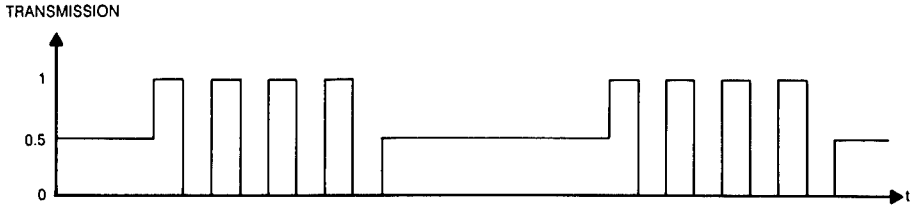

(b)

Fig. 3.8 Illustration of a spin-scan reticle: (a) rising-sun reticle pattern and (b) reticle modulation function.

account for the fact that the carrier waveform pulses are generated in one-half revolution). The gain level of the amplifier or preamplifier may be controlled by an automatic gain control (AGC) circuit. The signal is then rectified and passed through an envelope detector and a synchronous or a bandpass filter, providing a signal suitable for driving the tracking and the guidance loops.

One of the drawbacks of spin-scan seekers is the lack of carrier signal when the image is on boresight. When the image is near the center, the AGC operation and tracking may be susceptible to noise.

3.3.3.2 Conscan Seeker. In a conscan seeker the reticle is stationary, and the target image is nutated on the reticle by a wedge or a canted mirror that spins with the gyro. A typical reticle may be a spoked wagon wheel, as shown in Fig. 3.9(a), or a variant thereof. When the target image is on boresight, a constant carrier signal is generated, as shown in Fig. 3.9(b). For small tracking errors the generated modulation is frequency modulation (FM), and for large tracking errors the modulation is basically amplitude modulation (AM).

Signal processing in a typical conscan seeker consists of a bandpass amplifier with a limiter and with AGC followed by an FM discriminator or a high-pass filter and an envelope detector. The output of the envelope detector drives a precession amplifier and a guidance demodulator.

In comparison to the spin-scan seeker, the conscan seeker generates a constant amplitude carrier signal at zero tracking error, thus making the AGC and tracking more stable.

3.3.3.3 Rosette-Scan Seeker. A rosette-scan seeker scans a small IFOV subtended by a single detector in a rosette pattern in space about the target. The rosette pattern consists of a number of loops, or petals, that originate at a common center, as shown in Fig. 3.10. This pattern can be achieved by two counterrotating optical elements (wedges or mirrors). The pattern is closed if the ratio of the spin frequencies of the two elements is rational.

A noteworthy property of this pattern is that the center gets traversed once for each petal, while each petal is traversed only once per frame. In effect, this pattern may be considered as providing tracking information for images in the center and updates once per frame outside the central region. Time gating may be utilized to exclude detected signals from tracking considerations outside a prescribed radius of the pattern. Because of its small IFOV, a rosette-scan seeker is able to resolve multiple sources in its total FOV. Also, the dwell time on target during each pass of the detector is relatively short. Using the relationships developed in Ref. 5, the dwell time on target T_d can be approximated by the following relationship:

$$T_d = \frac{2\theta_i}{\pi(f_1 + f_2)\theta_t}, \tag{3.11}$$

where

θ_i = the instantaneous FOV (rad)
θ_t = the total FOV (rad)
f_1, f_2 = the spin frequencies of the two scanning elements (Hz).

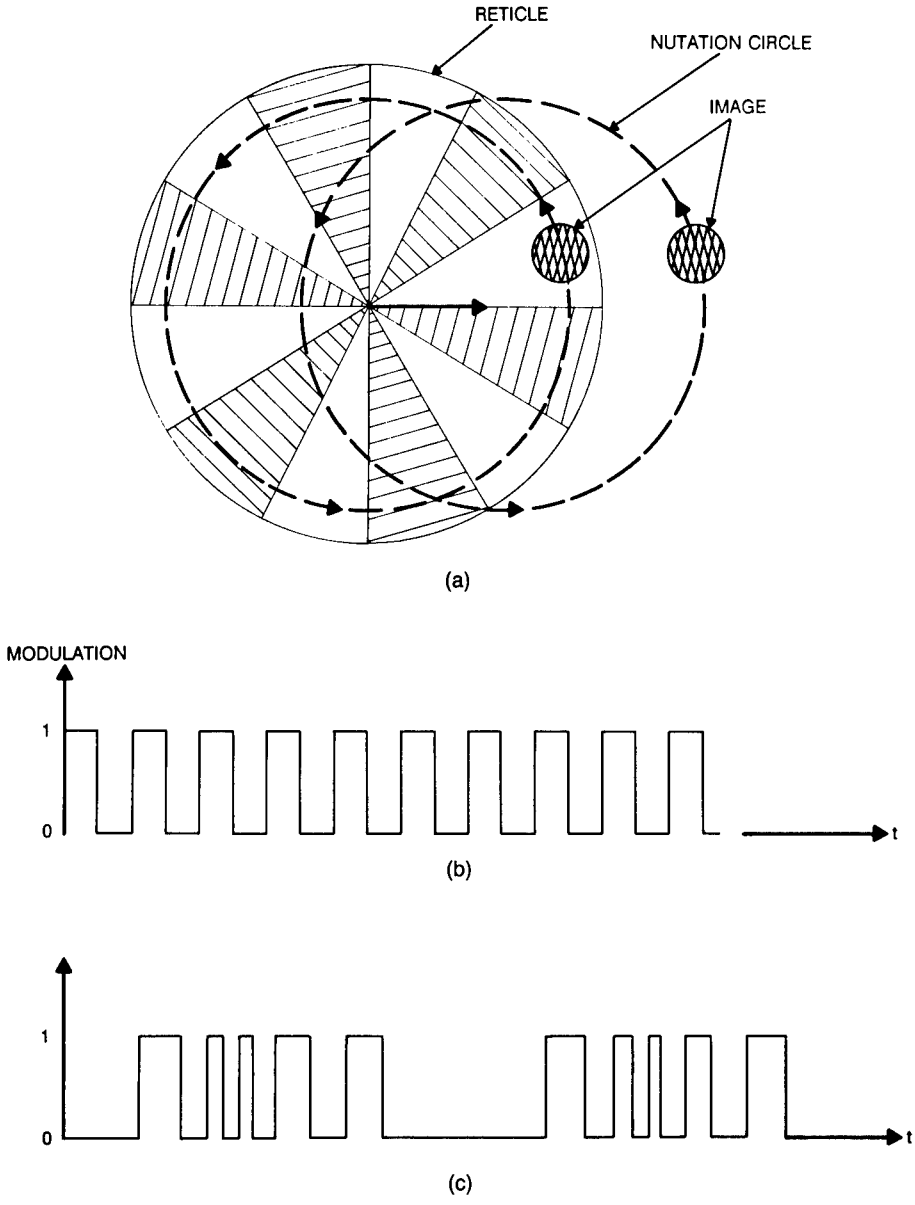

Fig. 3.9 Conscan reticle: (a) wagon-wheel reticle and image nutation, (b) modulation function for on-axis image, and (c) modulation function for off-axis image.

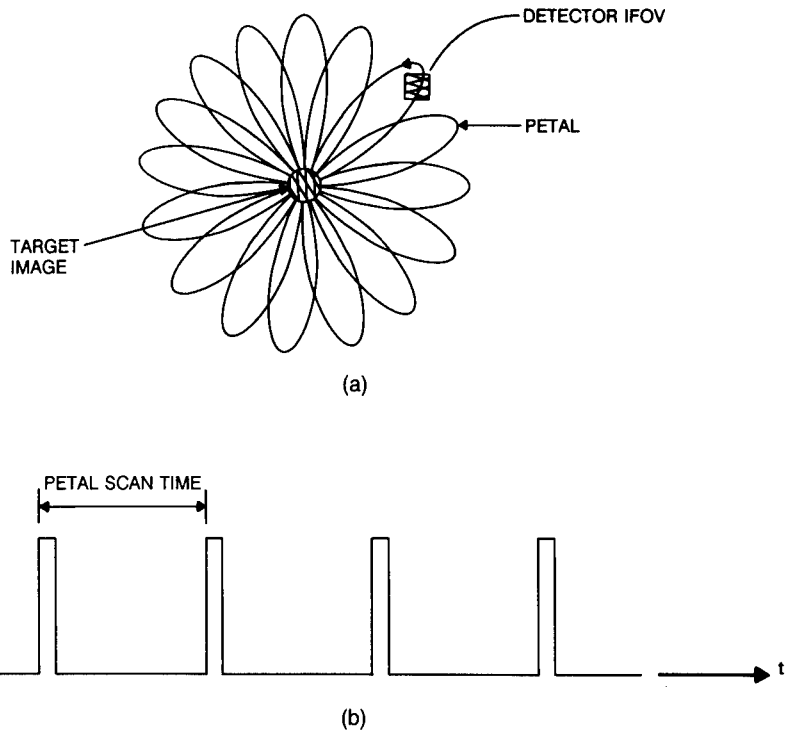

Fig. 3.10 (a) Rosette scanning pattern and (b) normalized signal pulse sequence for on-axis image.

Since the time to traverse one petal is $1/(f_1 + f_2)$, the percentage of the dwell time to the petal scan time is

$$T_d(f_1 + f_2) = \frac{2\theta_i}{\pi\theta^t} \times 100 \ . \tag{3.12}$$

As an example, let $\theta_i = 2$ mrad and $\theta_t = 36$ mrad. Then

$$T_d(f_1 + f_2) = 3.5\% \ ,$$

which is a small fraction of the petal scan time.

3.3.3.4 Focal-Plane-Array Seeker. New seekers are being developed that are based on multielement detectors. These concepts may include a scanning linear array or a two-dimensional mosaic detector. The target scene is imaged on the detector in the focal plane of the seeker optical system. This is illustrated in Fig. 3.11.

Various algorithms may be employed by FPA seekers to process the information contained in the detected image to determine a tracking point in the scene, e.g., an engine on an aircraft, an edge on a tank, etc. The tracking algorithm may select the maximum intensity point, the intensity weighted or the geometric centroid of the image points, an edge of the projected image of

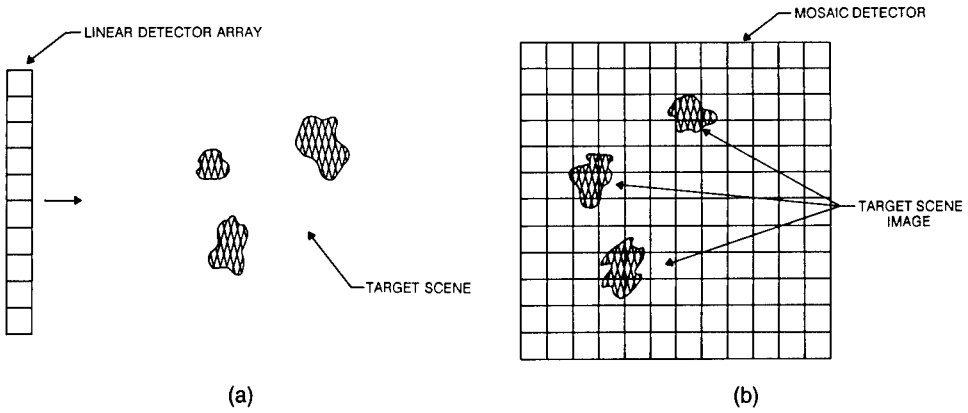

Fig. 3.11 Illustration of focal-plane detectors: (a) linear detector scanning of a target scene and (b) mosaic detector and target scene.

the target, or a point arrived at by correlating a reference image with the detected image. Thresholding may be employed by each detector element. The level of the threshold may be controlled by an AGC determined, for example, by the sum of the intensities of the total image or by the maximum intensity in the image distribution.

In comparison with the reticle-type seekers, FPA seekers provide better resolution of the image scene. This spatial-resolution feature can be used for implementing various discrimination algorithms against such expendables as flares, chaff, etc.

3.3.3.5 Quadrant-Detector Seekers. A class of seekers employs an arrangement of four detectors known as a quadrant-detector set. The image of the target is defocused on purpose, resulting in a relatively large blur circle on the detector elements, as shown in Fig. 3.12(a). The signal detected by each element of the quad is proportional to the area of the blur image falling on the element. Tracking of the target is achieved by balancing the signals of the four quad elements. The tracking error as a function of the offset of the blur circle is depicted in Fig. 3.12(b). The tracking error in the up-down direction is formed as

$$\varepsilon_{ud} = \frac{(S_1 + S_2) - (S_3 + S_4)}{\sum_{i=1}^{4} S_i}, \tag{3.13}$$

where S_i is the signal detected by the i'th element. Similarly, the tracking error in the right-left direction is computed as

$$\varepsilon_{rl} = \frac{(S_2 + S_3) - (S_1 + S_4)}{\sum_{i=1}^{4} S_i}. \tag{3.14}$$

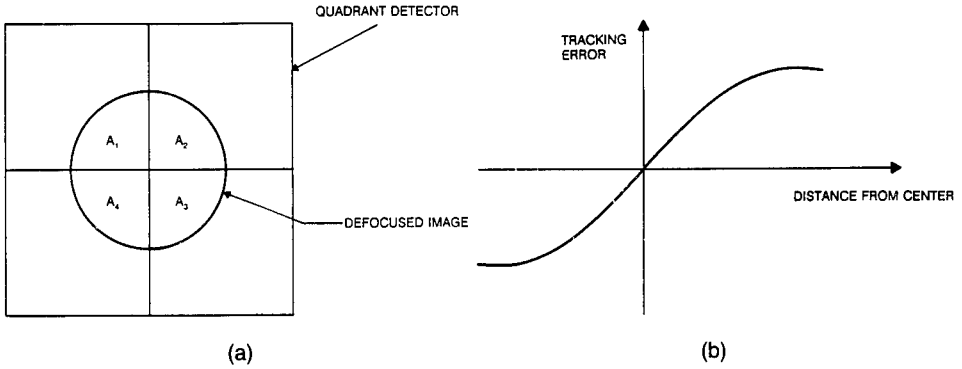

Fig. 3.12 Quadrant detection tracking: (a) quadrant detector and image and (b) tracking error.

3.3.3.6 Counter-Countermeasure (CCM) Techniques. After the appearance of the first-generation (spin-scan and conscan) IR missiles and their success against aircraft targets in the Korean and later in the Vietnam conflicts, a need for countermeasures against these missiles emerged. A simple countermeasure against these seekers is an expendable, i.e., an IR flare that can be deployed from the aircraft under attack. The intensity of the flare is usually several times that of the target radiation. Both the spin-scan and conscan seekers bias their tracking points toward the more intense source. The seeker thus tracks a separating flare and loses track of the target. As the flare became a versatile and relatively effective CM, missile designers began to develop techniques to reduce and/or offset the effectiveness of the flare. IR missiles began to emerge with some "fixes," or CCM techniques, against the simple flare CM.

IRCCM techniques against the IR flare may be based on the following differences between the target and the IR flare characteristics:

1. temporal signal changes
2. spectral differences
3. trajectory differences (relative kinematics)
4. spatial size and distribution.

Thus, a rapid increase in the seeker signal amplitude could be indicative of a flare deployment. However, signal fluctuations also could be caused by intentional or unintentional target radiation level changes.

There may exist spectral differences between the target and the flare. For example, spectral radiation of the aircraft is more characteristic of a lower-temperature emitter compared to a flare, which radiates like a relatively hot blackbody. The seeker may discriminate against the flare by detecting target and flare radiation in more than one spectral band and by comparing the detected signals. The differences in the target and flare trajectories in space also may be exploited for flare-discrimination purposes. The aircraft is a powered vehicle moving along some established trajectory, i.e., a straight-line

course or a turning maneuver, or it may be in a stationary mode, such as a hovering helicopter. On the other hand, when a flare is deployed from the aircraft, it travels in a ballistic trajectory as affected by the gravitational and drag forces. As viewed from the seeker, the LOS rotation rates with respect to the target and the flare may be different and could serve as a basis for flare discrimination.

Spatial size and/or distribution of the target image compared to the image of a flare may be different, depending on the target type and engagement conditions, i.e., range-to-go or aspect angle, and could be employed for flare-discrimination purposes.

To exploit the temporal, spectral, kinematic, or spatial differences between a given target or a class of targets and a flare, the seeker must have the necessary means for detecting these differences in one form or another. For example, to utilize the spatial size differences, the seeker must be capable of resolving the target and flare images, as may be the case for scanning and imaging (FPA) seekers.

The CCM techniques against the flare CM that have been, or may be, incorporated in some of the advanced IR seekers also may influence the effectiveness of other IRCMs, e.g., IR jamming with active onboard sources. Active countermeasure design must consider the possible impact of such CCM features on the effectiveness of the specific jamming waveforms.

3.3.4 IR Jamming Techniques

Some general approaches for active onboard IR jamming are discussed briefly. The requirements for effective IR jamming may include

1. a suitable IR source (a lamp or a laser) collocated with the target
2. effective temporal modulation of the source (jamming waveform)
3. missile launch and location detection and identification if necessary
4. an optical device to project jammer energy onto the missile.

The function of active IR jamming is to cause the missile to miss its intended target by disturbing the seeker tracking process. The active IRCM acts in such a way as to cause either a complete loss of target tracking (optical breaklock, or OBL) or to degrade target tracking in such a manner that the guidance of the missile is affected adversely. Obviously, an early OBL is preferable since it usually implies a large miss distance; however, an early OBL may not always be achievable, and a sufficiently large miss distance beyond the lethal range of the missile warhead may be the next best objective for IR jamming.

3.3.4.1 Jamming of Spin-Scan Seekers. As discussed in Sec. 3.3.3.1, a typical spin-scan seeker has a reticle pattern with a 50% phasing sector. Typical modulation waveforms obtained for a constant radiation level target are shown in Fig. 3.13. The waveforms consist of an amplitude-modulated (AM) carrier. Signal processing removes the carrier and recovers the envelope of the waveform, which is at the reticle rotation (spin-scan) frequency. The phase angle of this waveform relative to some reference determines the angular direction in which the seeker is driven to bring the target image to the center. Thus, a null point, where zero torque is applied, is obtained at the center of the reticle pattern since no modulation (carrier or spin) is generated there.

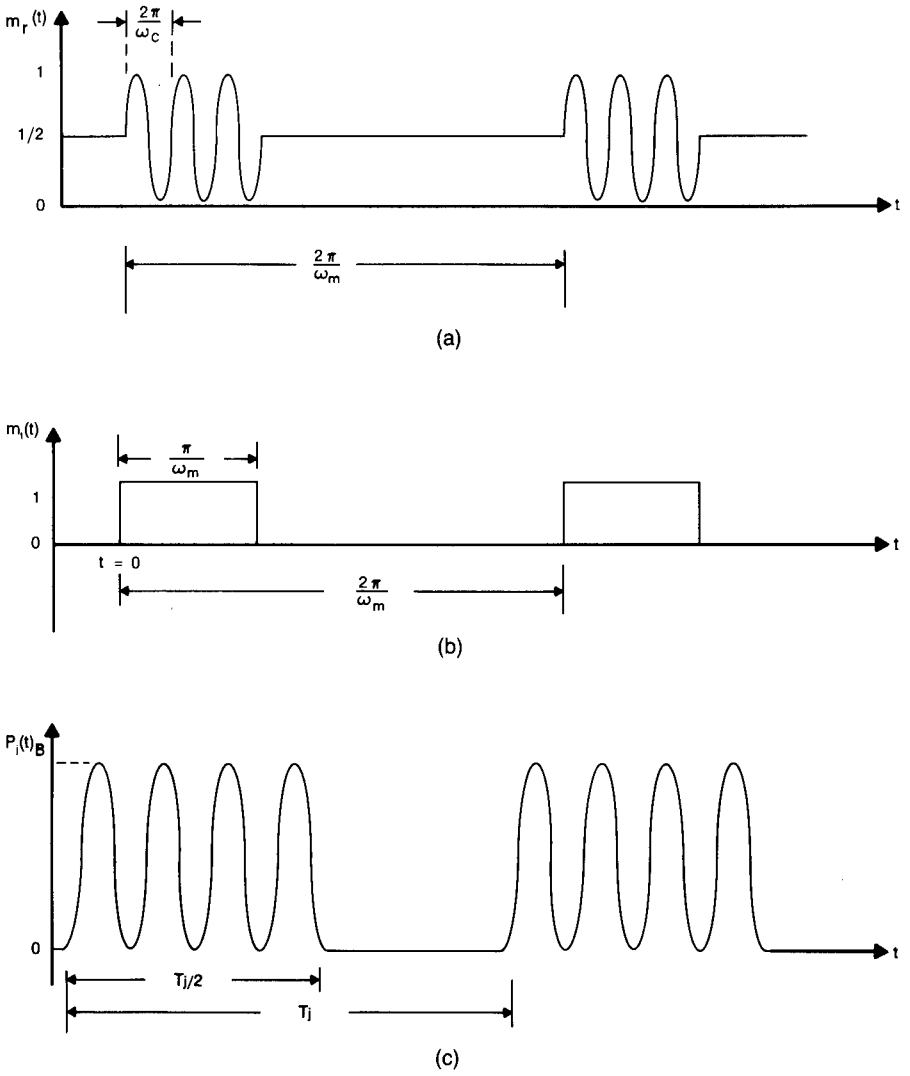

Fig. 3.13 Spin-scan modulation waveforms: (a) typical spin-scan modulation waveform, (b) carrier modulation function, and (c) jammer modulation waveform.

Consider a general case of a target with a collocated jammer that is modulated in time. The radiation power seen at the detector $P_d(t)$ may be represented by

$$P_d(t) = [A + P_j(t)]m_r(t) \ , \tag{3.15}$$

where

A = the target radiation power falling on the reticle
$P_j(t)$ = the time-modulated jammer power arriving at the reticle
$m_r(t)$ = the reticle modulation function.

The reticle modulation is periodic at the angular frequency of ω_m and can be represented by a Fourier series:

$$m_r(t) = \sum_{n=-\infty}^{\infty} c_n \exp(j\omega_m t) \ , \tag{3.16}$$

where

$$c_n = \frac{1}{T_m} \int_0^{T_m} m_r(t) \exp(-jn\omega_m t)\, dt \ , \tag{3.17}$$

$$T_m = \frac{2\pi}{\omega_m} \ . \tag{3.18}$$

If the jammer waveform is also periodic at the angular frequency of ω_j, $P_j(t)$ can be represented by

$$P_j(t) = \sum_{k=-\infty}^{\infty} d_k \exp(j\omega_j t) \ , \tag{3.19}$$

where

$$d_k = \frac{1}{T_j} \int_0^{T_j} P_j(t) \exp(-jk\omega_j t)\, dt \ , \tag{3.20}$$

$$T_j = \frac{2\pi}{\omega_j} \ . \tag{3.21}$$

Substitution of Eqs. (3.16) and (3.19) into (3.15) yields

$$P_d(t) = \left[A + \sum_{k=-\infty}^{\infty} d_k \exp(j\omega_j t)\right] \sum_{n=-\infty}^{\infty} c_n \exp(j\omega_m t) \ . \tag{3.22}$$

At the detector, $P_d(t)$ is converted into a voltage or current and is processed through a carrier amplifier, an envelope detector, and precession amplifier circuits before the signal is applied to drive the seeker. To get an insight into the jammer and seeker interaction, consider the following example, where the reticle modulation function is as shown in Fig. 3.13(a); i.e.,

$$m_r(t) = \frac{1}{2}[1 + \alpha m_t(t) \sin\omega_c t] \ , \tag{3.23}$$

where

α = the ratio of the radius of the image location (or the tracking error) to the radius of the reticle that provides a simplified measure of the modulation efficiency ($0 \leq \alpha \leq 1$)

$m_t(t)$ = a carrier gating function (a square wave), as shown in Fig. 3.13(b)
ω_c = the carrier frequency.

The Fourier series representation of $m_t(t)$ is

$$m_t(t) = \frac{1}{2} + \frac{2}{\pi}\sum_{n=0}^{\infty}\frac{(-1)^n}{2n+1}\sin[(2n+1)\omega_m t] \ . \tag{3.24}$$

Assume that the jammer modulation $P_j(t)$ also has the form of a carrier at the frequency ω_c and is gated at the frequency ω_j, as shown in Fig. 3.13(c); i.e.,

$$P_j(t) = \frac{B}{2}m_j(t)(1 + \sin\omega_c t) \ , \tag{3.25}$$

where $m_j(t)$ has the same form as $m_t(t)$ except that ω_m is replaced by ω_j and B is the peak jammer power. The Fourier series representation for $m_j(t)$ is

$$m_j(t) = \frac{1}{2} + \frac{2}{\pi}\sum_{k=0}^{\infty}\frac{(-1)^k}{2k+1}\sin\{(2k+1)[\omega_j t + \varphi_j(t)]\} \ , \tag{3.26}$$

where φ_j is an arbitrary phase angle relative to $m_t(t)$. For this special case Eq. (3.15) becomes

$$P_d(t) = \frac{1}{2}\left[A + \frac{1}{2}Bm_j(t)(1 + \sin\omega_c t)\right][1 + \alpha m_t(t)\sin\omega_c t] \ . \tag{3.27}$$

Assuming that the carrier amplifier passes signals at or near the carrier frequency only, the output of the carrier amplifier may be approximated by

$$s_c(t) \approx \alpha\left[A + \frac{1}{2}Bm_j(t)\right]m_t(t)\sin\omega_c t + \frac{1}{2}Bm_j(t)\sin\omega_c t \ . \tag{3.28}$$

The envelope of the carrier modulation in Eq. (3.28) is

$$s_e(t) \approx \alpha A m_t(t) + \frac{B}{2}m_j(t)[1 + \alpha m_t(t)] \ . \tag{3.29}$$

The envelope signal $s_e(t)$ is further processed by a precession amplifier, which is tuned around the spin frequency ω_m. Assuming that ω_j is close to ω_m, the seeker driving signal is given by

$$P(t) \approx \alpha\left(A + \frac{B}{4}\right)\sin\omega_m t + \frac{B}{2}\left(1 + \frac{\alpha}{2}\right)\sin[\omega_j t + \varphi_j(t)] \ . \tag{3.30}$$

The driving signal torques a spinning gyro (rotating magnet). The interaction of the rotating magnet and the seeker torquing signal results in the seeker precession rate proportional to the product of $P(t)$ and $\exp(j\omega_m t)$. Since the

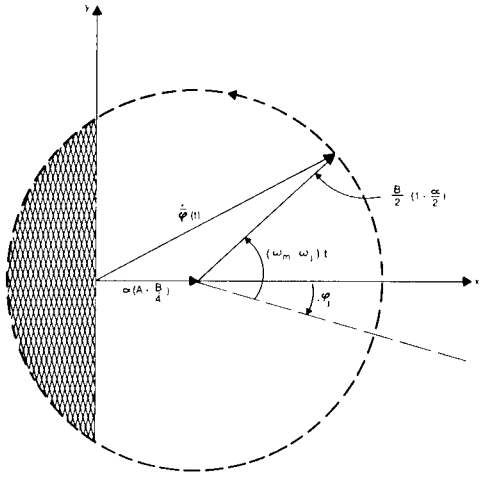

Fig. 3.14 Phasor diagram under jamming.

gyro effectively responds to a dc or slowly varying component of this product, the tracking error rate phasor (magnitude and phase angle) is proportional to

$$\dot{\bar{\varphi}}(t) \approx \alpha\left(A + \frac{B}{4}\right) + \frac{B}{2}\left(1 + \frac{\alpha}{2}\right) \exp[j\beta(t)] \ , \tag{3.31}$$

where $\beta(t) = (\omega_m - \omega_j)t - \varphi_j(t)$. A diagram of this phasor is shown in Fig. 3.14. Without the presence of the jammer ($B = 0$), the image point is driven toward the center along the in-phase direction with a rate proportional to αA, where it reaches an equilibrium ($\alpha = 0$). The presence of the jammer modulation introduces sinusoidal perturbation, in addition to the constant in-phase component. There is no longer an equilibrium point in the center. During a part of the phasor $\dot{\bar{\varphi}}\ (t)$ revolution, the image is pulled toward the center. When $\dot{\bar{\varphi}}\ (t)$ is in the cross-hatched region in Fig. 3.14, the image is pushed away from the center. This condition is reached if $B > 2\alpha A$. If the rate of change of the angle $\beta(t)$ is sufficiently slow, the image may be driven off the reticle. This depends on the target and jammer radiation signals, the jammer waveform parameters, and the seeker parameters.

3.3.4.2 Jamming of Conscan Seekers. Unlike the spin-scan seeker, a conscan seeker utilizes a circularly symmetrical reticle that generates a constant carrier signal when the target image is on boresight. The conscan seeker produces frequency modulation at small tracking errors and amplitude modulation at large tracking errors when the nutation circle of the target image is off the reticle during a part of the scan cycle. Relative phase information for the tracking error is provided by the direction in which the center of the nutation circle moves relative to the reticle, as shown in Fig. 3.15. If there is no LOS rotation rate, the seeker reaches an equilibrium point when the nutation circle is centered on the reticle. With some LOS rotation rate present, the nutation circle is offset from the center until the tracking error produces

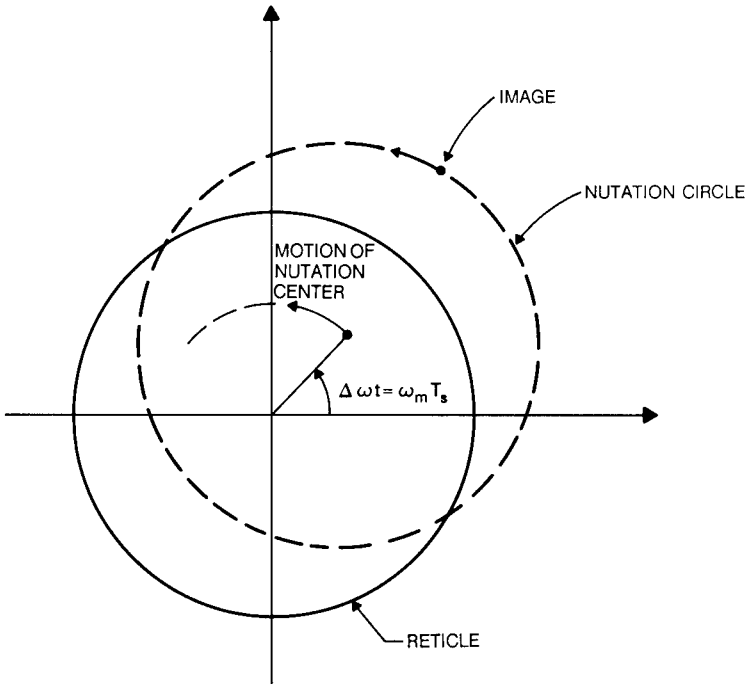

Fig. 3.15 Motion of nutation circle.

the necessary seeker driving torque to follow the LOS rotation rate. This is the principle of the equilibrium in the tracking loop; i.e., the tracking point (or the center of the nutation circle) is displaced on the reticle until the torque generated to drive the seeker balances the LOS motion. A typical tracking rate versus the tracking-error characteristic for a conscan seeker with a wagon-wheel reticle is shown in Fig. 3.16.

If a jammer with some modulation were superimposed on the target, the seeker would attempt to establish a new equilibrium point. Such an equilibrium point may or may not be stationary on the reticle, depending on the jamming waveform. To get some insight into this equilibrium process, consider a case where the jammer is on during a part of the scan cycle and off during the remainder. Such a jammer waveform is illustrated in Fig. 3.17. The jammer period T_j is the same as the scan period T_m. The following reasoning indicates that for this case a pseudoequilibrium is established by the seeker at a point where a part of the nutation circle during the time the jammer is turned on is off the reticle. If the nutation circle were to be pushed further out until the jammer modulation were no longer on the reticle, a tracking error would exist that would tend to pull the nutation circle toward the center of the reticle. As the circle is pulled toward the center, the jammer modulation produces an error that in turn pushes the circle outward. Thus, a pseudoequilibrium point (zero seeker torque) is reached where the jammer-induced error counterbalances the error produced by the offset target.

If the jammer period deviated slightly from the scan period, the nutation circle would revolve on the reticle at the difference frequency. This may be

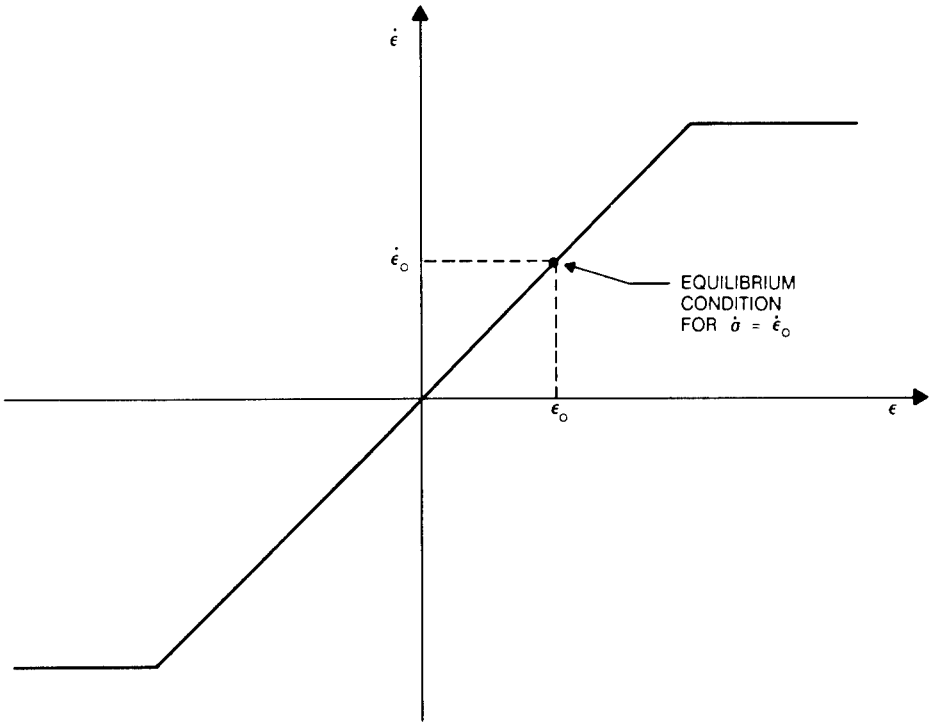

Fig. 3.16 Tracking-error characteristics.

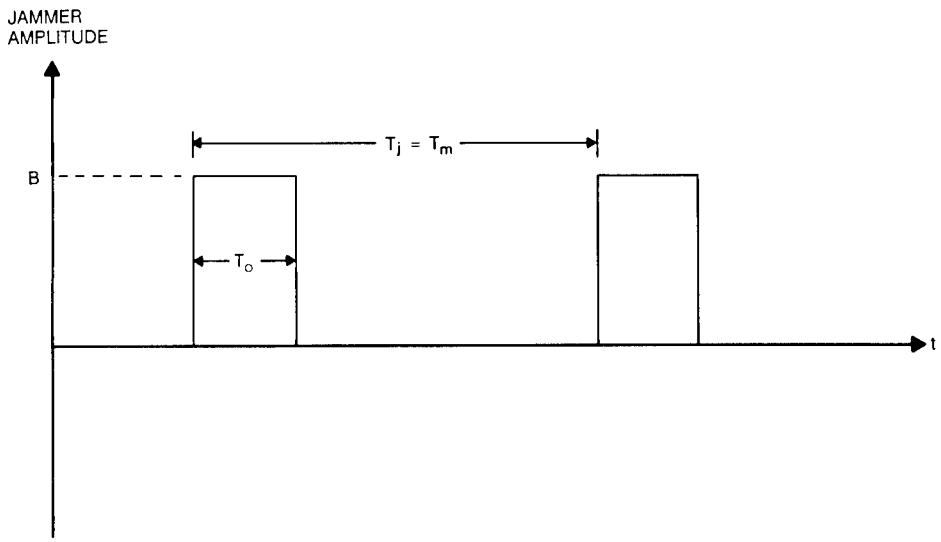

Fig. 3.17 Typical jamming waveform.

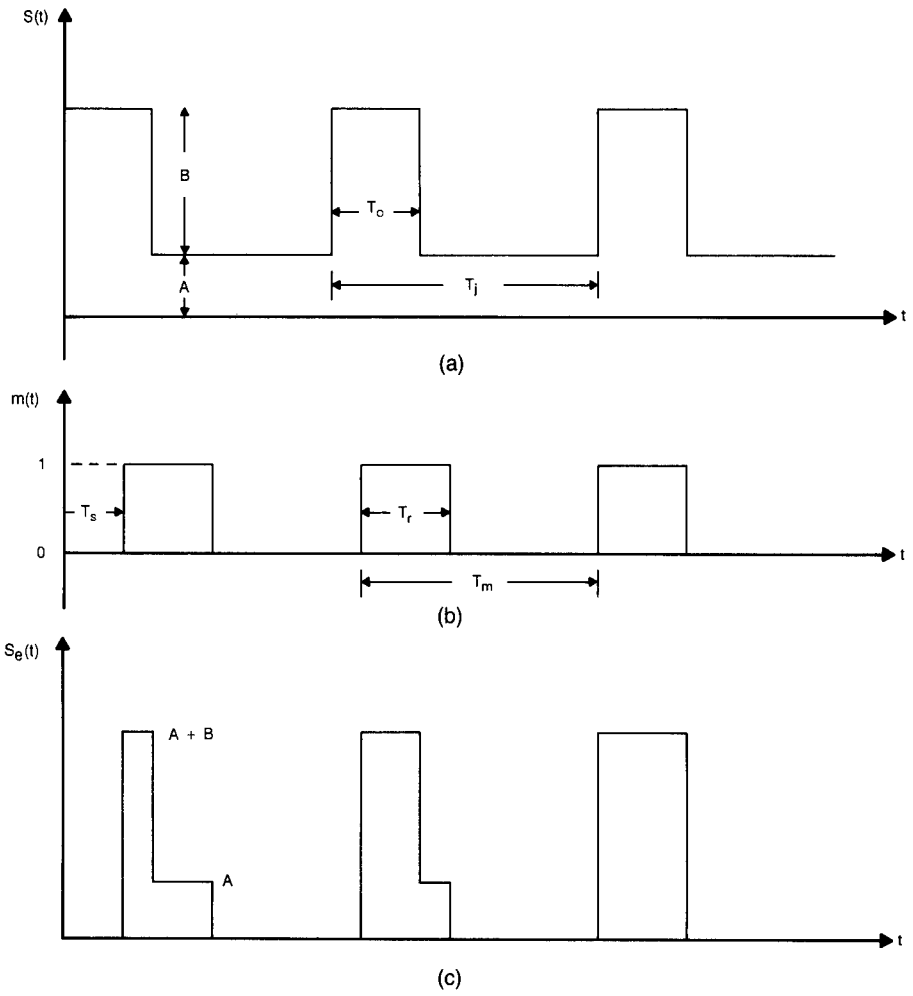

Fig. 3.18 Effective target and jammer waveforms: (a) combined target and jammer waveform, (b) reticle modulation function, and (c) effective signal waveform.

shown using the following simplified example. Let the combined jammer and target radiation be given by $S(t)$, where $S(t)$ is shown in Fig. 3.18(a) and may be represented by the following Fourier series:

$$S(t) = A + \sum_{n=-\infty}^{\infty} c_n \exp(jn\omega_j t) \ , \tag{3.32}$$

where

$$c_n = \frac{jB}{2\pi n}\left[\exp\left(-j2\pi n\frac{T_o}{T_j}\right) - 1\right] \ , \tag{3.33}$$

A is the target radiation power, B is the jammer radiation power, T_o is the jammer pulse duration, and T_j is the jammer waveform period ($\omega_j = 2\pi/T_j$).

The reticle modulation function represents the relative dwell time T_r of the image on the reticle, and T_s is the relative delay, or $\omega_m T_s$ is the phase angle of the center of the nutation circle in reticle coordinates relative to the start of the jammer pulse. This is illustrated in Fig. 3.15. The reticle dwell modulation $m(t)$ is shown in Fig. 3.18(b) and has the following Fourier series representation:

$$m(t) = \sum_{k=-\infty}^{\infty} d_k \exp[jk\omega_m(t - T_s)] \ , \tag{3.34}$$

where

$$d_k = \frac{j}{2\pi k}\left[\exp\left(-j2\pi k\frac{T_r}{T_m}\right) - 1\right] \ , \tag{3.35}$$

T_r is the time the image is on the reticle, and T_m is the scan period ($\omega_m = 2\pi/T_m$).

Note that for simplification the carrier-signal generation is implicitly assumed and has been omitted from consideration. Also, any nonlinearities (such as limiters) also have been ignored. For this reason, the inferences reached here may or may not be valid for specific conscan seekers, depending on the details of their signal processing.

The seeker tracking will be influenced by the signal frequency components at or near ω_m. A diagram of the effective waveform is shown in Fig. 3.18(c). An approximate form of this modulated waveform at the detector may be obtained by considering

$$S_e(t) \approx S(t)|_{\text{dc}}\, m(t)|_{\text{ac}} + S(t)|_{\text{ac}}\, m(t)_{\text{dc}} \ , \tag{3.36}$$

where $|_{\text{dc}}$ indicates the dc-component of the waveform and $|_{\text{ac}}$ is the fundamental frequency component of the waveform. Using Eqs. (3.32) through (3.35) in Eq. (3.36) yields

$$\begin{aligned} S_e(t) \approx\ & (A + B\rho_j)\sin(\pi\rho_m)\cos(\omega_m t - 2\pi\rho_s - \pi\rho_m) \\ & + B\rho_m \sin(\pi\rho_j)\cos(\omega_j t - \pi\rho_j) \ , \end{aligned} \tag{3.37}$$

where

$$\rho_j = \frac{T_o}{T_j} \ , \quad \rho_m = \frac{T_r}{T_m} \ , \quad \rho_s = \frac{T_s}{T_m} \ . \tag{3.38}$$

Assuming that a scaled version of $S_e(t)$ is processed to represent the seeker torquing signal, the low-frequency component of its interaction with the spinning gyro magnet has the following form:

$$\begin{aligned} S_e(t)\exp(j\omega_m t)|_{\text{LF}} \approx\ & (A + B\rho_j)\sin(\pi\rho_m)\exp[j\pi(2\rho_s + \rho_m)] \\ & + B\rho_m \sin(\pi\rho_j)\exp[-j(\Delta\omega t - \pi\rho_j)] \ , \end{aligned} \tag{3.39}$$

where $\Delta\omega = \omega_j - \omega_m$. In response to this drive signal, the seeker tracking loop will adjust T_r and T_s to keep the average seeker tracking rate at zero. If the jammer period is slightly off from the scan period, the nutation circle will revolve on the reticle at the difference frequency $\Delta\omega$. This seeker nutation due to jamming is superimposed on the LOS rotation rate. The seeker thus tracks the target in the average sense over a complete cycle of the difference frequency.

For the case of synchronous jamming ($\Delta\omega = 0$) the following equilibrium condition must hold:

$$(A + B\rho_j)\sin(\pi\rho_m)\exp[j\pi(2\rho_s + \rho_m)] + B\rho_m \sin(\pi\rho_j)\exp(j\pi\rho_j) = 0 \ . \tag{3.40}$$

This implies that

$$(A + B\rho_j)\sin(\pi\rho_m) = B\rho_m \sin(\pi\rho_j) \ . \tag{3.41}$$

Condition (3.41) is satisfied by adjusting T_r. The other condition involves T_s and is

$$\rho_s = \frac{1}{2}(\rho_j - \rho_m + 1) \ , \tag{3.42}$$

where ρ_s ranges from 0 to 1.

The approximations involved in the above analysis are better suited for the cases where the reticle modulation factor ρ_m and the jammer modulation factor ρ_j are near 0.5. Away from this region, the accuracy of this analysis may degrade rapidly.

The disturbances introduced by the jammer in the seeker tracking loop also may be propagated into the guidance loop and affect the performance of the missile, ultimately resulting in increased miss distance. Because of the complex and nonlinear nature of this problem, digital computer or physical simulations are necessary to assess the impact of postulated jamming approaches and to select the best jamming method against a specific missile or class of missiles.

3.3.4.3 Other Active CM Techniques

3.3.4.3.1 Jamming the AGC. The automatic gain control in the seeker signal processing performs the function of maintaining the signal level at some constant value. The dynamic range of the received signal is dependent on the particular target, its signal variation with aspect angle, and the engagement range. The AGC time constant for adjusting the gain may be based principally on the need to follow the signal growth due to range closure. A general approach for jamming the AGC may consist of turning the jammer radiation fully on and turning it off, with the on-time and the off-time corresponding in some way to the response times of the AGC. The goal of this type of jamming is to deny the seeker proper target tracking signal for as large a duty cycle as possible. When the jammer radiation is abruptly turned off, the seeker must increase the level of the gain to bring the target signal up into the operating range. When the jammer is turned on again, the seeker signal is driven into

saturation. If the jammer radiation level is large relative to the target, AGC jamming may cause significant disruption of the seeker tracking and missile guidance functions. The effectiveness of such jamming depends on the *J/S* ratio, the AGC time constants for increasing and decreasing signals, the type of signal processing, etc.

3.3.4.3.2 Saturation/Blinding Jamming. The objective of this countermeasure is to inject large jammer signals into the seeker to saturate the signal-processing circuits, preferably the detector preamplifier circuits. Such saturation of the signal may be more detrimental to the seekers that process amplitude-dependent information, such as the spin-scan seekers. It may be difficult and impractical to saturate the signal in a seeker with relatively large dynamic AGC range (10^5 or so). For example, if the noise equivalent input (NEI) level of the seeker is of the order of 10^{-11} W cm^{-2}, such a seeker may begin to saturate at a signal level of 10^{-6} to 10^{-5} W cm^{-2}. The jammer intensity needed to deliver this level of irradiance at the seeker from a 2 km range is at least 40 to 400 kW sr^{-1}. This signal level may be possible with highly directional sources only. Saturation jamming may have little effect against seekers that process FM modulation, such as the conscan seekers.

3.3.4.3.3 Impact of Seeker Dwell Time on Jamming. When jamming IR seekers, an important characteristic is the dwell time (or the duty cycle) of the seeker on the target. In the case of spin-scan seekers, the target is being viewed continuously, except for the opaque modulation sectors on the reticle. This means that the window for onboard jamming opportunity is open all the time. In the case of conscan seekers, the window for jamming may be reduced because the jammer disturbance forces the nutation circle to go off the reticle during a part of the scan cycle.

Consider now a single-detector scanning system such as a rosette-scan seeker. The dwell-time factor of such a seeker on the target is usually very small (a few percent of the scan time). It follows, therefore, that the opportunity for jamming in such a case is drastically reduced.

Furthermore, scanning seekers utilize pulse processing, which further limits the jammer effectiveness. The jammer may be able to introduce an occasional disturbance in the pulse amplitude. Generally, one does not anticipate that a somewhat random pulse will affect the seeker performance. There is a chance that the pulse may disturb the operation of the automatic gain control of the seeker and possibly degrade the performance of the seeker and the missile but the probability of such effect is small. Similar considerations may be extended to linear scanning array seekers.

In the case of FPA seekers, the window for jamming is open all the time; however, the target image may be moving from one element to another while jamming is in progress. In general, jamming of scanning or imaging seekers may not affect the seeker tracking function directly, such as by causing an error in the computation of the target location. The basic aim in jamming these seekers may be to achieve a general disruption of the operation of the seeker, such as causing signal saturation, perturbation of the AGC, etc. The effectiveness of such jamming approaches may depend on the particular seeker signal-processing implementation.

3.3.5 High-Power Jamming and Damage

One of the jamming approaches may be to direct a sufficiently large amount of radiation at the seeker so as to cause physical damage to some of its sensitive components to impair or deny the seeker tracking function. These components include the detector, reticle, filters, and possibly the dome. The power levels required to inflict such damage are very high, and the only suitable source device for achieving this is a laser. The laser power must be concentrated in a narrow beam, and the beam must be directed at the seeker for a sufficiently long period of time to inflict the desired damage. If the laser is to damage one of the internal components of the seeker, e.g., the detector or the reticle, the laser radiation must be able to penetrate all the optical elements in front of the element to be damaged. If dome damage is the goal, the laser energy must be absorbed by the dome, which requires an out-of-band laser.

The laser power impinging on an optical element P_e may be calculated using the following relationship:

$$P_e = \frac{P_l \tau_a \tau_o A_c}{\Omega_l R^2} , \tag{3.43}$$

where

P_l = laser power
Ω_l = angular subtense of the beam
τ_a = atmospheric transmission factor
τ_o = optical transmission factor
A_c = effective collecting area of the seeker
R = range from laser to seeker.

3.3.5.1 Detector Damage. Thresholds for thermal damage in IR detectors depend on damage mechanisms, irradiation time, beam diameter, laser wavelength, optical and thermal properties of the materials used in detector construction, quality of thermal coupling to the heat sink, etc. The susceptibility of IR detectors to intense laser radiation has been investigated in considerable detail at the U.S. Naval Research Laboratory.[6] The results of this investigation show that for short irradiation times ($\tau < 10^{-5}$ s) the laser damage threshold E_o (irradiance in watts per square centimeter) varies inversely as τ. For intermediate irradiation times (10^{-5} s $< \tau < 10^{-2}$ s) E_o varies inversely to the square root of the pulse time. For $\tau > 10^{-2}$ s, E_o approaches a constant. For short irradiation times the energy density required to raise the surface of the detector to the melting point is inversely proportional to the absorption coefficient and directly proportional to the specific heat and the increase in surface temperature necessary to melt the detector material.

For the IR detector materials of interest (e.g., PbS, PbSe, InSb, photoconductive and photovoltaic), the range of E_o for a pulse length of 10^{-7} s is 10^6 to 10^7 W cm^{-2}. This corresponds to a fluence level of 0.1 to 1 J cm^{-2}. In general, the thin-film PbS and PbSe detectors have higher absorption coefficients and thus lower fluence values (0.1 J cm^{-2}) than the other detector materials. The thresholds for HgCdTe, PbSnTe, and InSb materials are very similar (1 J cm^{-2}).

For irradiation pulses shorter than 10^{-7} s, electric breakdown in IR detector materials may become important; however, this effect has not been studied sufficiently, and thus few results are known.

Consider now an example calculation for the laser power required to damage a seeker detector at an engagement range of 2 km. Let the damage threshold for the detector, E_d be 10^7 W cm^{-2} and the detector area A_d be 10^{-4} cm^2. In addition, assume the following values:

$$A_c = 10 \text{ cm}^2$$

$$\tau_a = 0.9$$

$$\tau_o = 0.7$$

$$\Omega_l = 10^{-8} \text{ sr} .$$

The power collected by the detector is

$$P_e = A_d E_d = 10^{-4} \times 10^7 = 10^3 \text{ W} .$$

The laser power needed to produce this power level on the detector is

$$P_l = \frac{P_e \Omega_l R^2}{\tau_a \tau_o A_c} = \frac{10^3 \times 10^{-8} \times (2 \times 10^5)^2}{0.9 \times 0.7 \times 10} = 63.5 \text{ kW} .$$

Thus, a pulsed laser with a pulse length of 100 ns, a beam width of approximately 0.1 mrad, and a pulse power of 64 kW would be required to damage this detector. To deliver this energy on the detector, the laser must be pointed to within one-half of the beamwidth or less, i.e., 5×10^{-5} rad, which may be no small task on a stationary platform, let alone on a moving platform.

3.3.5.2 Reticle Damage. If the seeker utilizes a reticle for modulation, the reticle is placed in the focal plane. Since the detector is not in the focal plane, it may require less energy to damage the reticle than the detector. When this is the case, the effects of such reticle damage on the performance of the missile may be of concern. While detector damage may be catastrophic regarding the seeker's ability to track the target, burned out or scarred areas on the reticle are not expected to lead to such catastrophic failure unless these damaged areas comprise a significant portion of the useful reticle area. The energy threshold level required to damage a reticle depends on its materials and construction. Coatings or films deposited on the reticle substrate material may require damage levels comparable to those for damaging thin-film detectors.

3.3.5.3 Dome Damage. The seeker dome may be damaged with an out-of-band high-power laser. Thermal stress induced by high-power-laser energy may lead to cracking of the seeker dome. To produce such an effect, energy density levels a few orders of magnitude higher than those needed to damage detectors may be required. The damage threshold for the dome is strongly dependent on the absorption coefficient of the material. The large energy levels

required to damage seeker domes imply that only ground-based laser systems may be suitable for this type of countermeasure.

3.4 JAMMER SOURCES AND MODULATION

Depending on the system concept, either incoherent or coherent sources are amenable to active IRCM. At the present time, active IRCM systems employ incoherent sources. While several coherent sources are being considered for active IRCM, none are yet in operation. A brief discussion of coherent sources is included for completeness.

3.4.1 Incoherent Sources

The active IRCM jammer must produce pulses of radiation to defeat the incoming missiles. The amplitude of the radiation produced by the source can be varied by some mechanical means, or the source itself can be "flashed." Thus, it is convenient to class incoherent sources into two categories: mechanically modulated sources and electronically modulated sources. In either case, the radiant intensity produced is a function of the source and an accompanying reflector.

Sources that are fuel-fired or electrically heated lend themselves to mechanical modulation. The radiator in the fuel-fired source is a ceramic cavity heated by the combustion of fuel. Electrically heated sources can be hermetically sealed carbon rods or tungsten. The sources can be characterized as high-emissivity graybodies that have a temperature between 1700 to 3000 K. For all practical purposes these sources produce a constant radiance that depends only on their temperature. The modulation element is either a filter or mechanical chopper that lies in the optical path between the source/reflector and missile.

Electronically modulated sources—or arc lamps—consist of an anode, cathode, vapor fill, and a surrounding envelope. A voltage difference between the anode and cathode causes an arc that ionizes the vapor. The resulting current causes free electrons to collide with the elements in the vapor. While emissions resulting from interlevel transitions occur, the primary emission mechanism for IRCM arc-lamp radiation is acceleration (bremsstrahlung) of free electrons.

Both alkali metal (cesium) and inert gas (xenon) filled lamps have been proposed for active IRCM. Alkali-metal lamps can be characterized as high-emissivity graybody emitters. When pulsed, alkali-metal lamps have an effective temperature between 2000 to 4000 K. Xenon has an effective temperature between 5000 to 6000 K.

The band efficiency is defined as

$$\varepsilon_{\text{band}} = \frac{P_{\text{band}}}{P_{\text{input}}}, \tag{3.44}$$

where

$\varepsilon_{\text{band}}$ = the in-band efficiency
P_{band} = the in-band power
P_{input} = the total electrical power input.

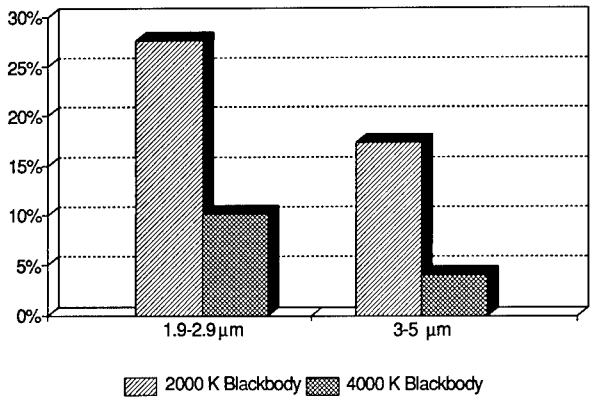

Fig. 3.19 Relative band efficiencies of blackbody sources.

The Planck function can be used to determine efficiencies of each source (see Fig. 3.19). While the lower-temperature source is more efficient, the radiance levels produced by the higher-temperature source are greater (see Table 3.4).

The jamming waveform characteristics chosen are a function of the source as well as the threat to be defeated. For example, the optimum waveform duty cycle is source dependent. A large duty cycle is preferred with a mechanically modulated source since the chopping of the source necessitates some inefficiencies; i.e., the radiation produced by the source when it is blocked must be dissipated. Electronically modulated systems, however, are more efficient with a lower duty cycle waveform. They have a lower-power standby mode and a high-power pulsed mode. Power is conserved if the duty cycle is low.

Other trade-offs can be made. The simplicity of the mechanical modulation is appealing, but it places limits on the waveforms that can be achieved by such a system; i.e., the jamming code is difficult to change in real time. Electronically modulated systems offer greater versatility. Electronically modulated systems "have the advantage of flexible code modulation, code selectability from microprocessor controlled, stored-code libraries and rapid code change with minor impact on the hardware system."[7]

Table 3.4 Radiance Level

Blackbody Temperature	Band α	Band β	TOTAL $\left(\frac{\sigma T^4}{\pi}\right)$
2000 K	7.99 W cm^{-2} sr^{-1}	5.0 W cm^{-2} sr^{-1}	28.9 W cm^{-2} sr^{-1}
4000 K	46.8 W cm^{-2} sr^{-1}	18.7 W cm^{-2} sr^{-1}	462 W cm^{-2} sr^{-1}

3.4.1.1 Source Effects on Jammer-to-Signature Ratio. The function of active IRCM is to add spurious pulses of radiation to the platform signature to degrade the performance of the missile. In adding radiation, the active IRCM adds to the signature of the aircraft since the jammer radiation never goes completely to zero between pulses. This effect is more pronounced in arc-lamp sources, but some interpulse radiation is still present with mechanically modulated systems. This effect can be quantified by defining a depth of modulation (DOM) as

$$\text{DOM} = \left(1 - \frac{I_I}{I_P}\right) \times 100\% \ , \tag{3.45}$$

where

DOM = the depth of modulation
I_I = the interpulse in-band radiant intensity
I_P = the peak of the in-band radiant intensity.

For several arc-lamp sources, the amount of interpulse radiance is linearly proportional to the peak of the jammer pulse [see Fig. 3.20(a)]. Equation (3.45) can be written as

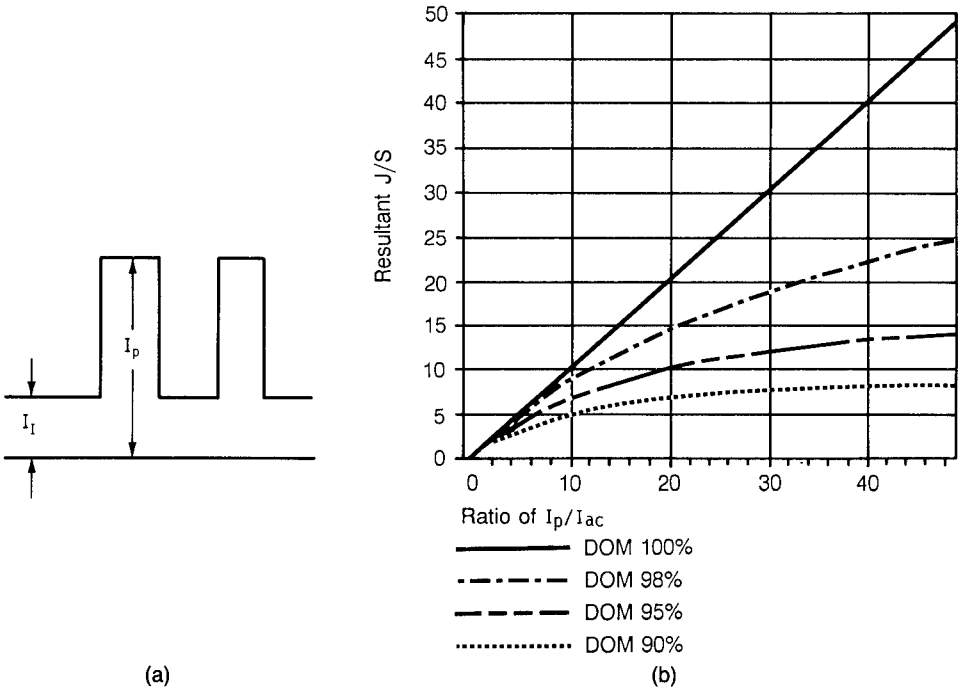

Fig. 3.20 Depth of modulation: (a) jammer parameter definitions and (b) resultant J/S versus I_P/I_{ac}.

$$\begin{aligned} \text{DOM} &= \left(\frac{I_P - \alpha_m I_P}{I_P}\right) \times 100\% \\ &= (1 - \alpha_m) \times 100\% \ , \end{aligned} \tag{3.46}$$

where $\alpha_m = I_I/I_P$ $(0 \leq \alpha_m \leq 1)$. The J/S ratio produced by the source and reflector is defined as

$$\frac{J}{S} = \frac{I_P}{I_{ac} + I_I} \ , \tag{3.47}$$

or using $\alpha_m I_P$ for I_I in Eq. (3.47) yields

$$\frac{J}{S} = \frac{I_P}{I_{ac} + \alpha_m I_P} \ , \tag{3.48}$$

where I_{ac} is the platform radiant intensity. Note that Eq. (3.48) sets a limit on the maximum J/S ratio that a source can achieve. Assume that

$$I_P \gg I_{ac} \ . \tag{3.49}$$

Then, Eq. (3.48) becomes

$$\frac{J}{S} = \frac{I_P}{\alpha_m I_P} = \frac{1}{\alpha_m} \ . \tag{3.50}$$

When I_P is very large, the effectiveness of the jammer is limited by its own interpulse radiation. The constant α_m can be as small as 0.005 or as large as 0.15. Figure 3.20(b) shows the J/S ratio as a function of I_P/I_{ac} for several different values of α for a fixed aircraft signature level. Thus, the peak radiant intensity that a source can produce is not the sole parameter in determining the J/S ratio.

As a final note, the effective J/S ratio that reaches the missile processing electronics is a function of the duty cycle of the jamming waveform. The detector senses the product of reticle modulation with the aircraft signature and the jammer modulation. The product of two modulation schemes causes new frequencies to be generated. These new frequencies are the sum and difference of the component frequencies of each modulation scheme. The passband of the signal-processing electronics eliminates most of these new frequencies except those near the carrier frequency. One such frequency near the carrier frequency that is generated is produced by the reticle "beating" with the dc term of the jammer. Thus,

$$\left(\frac{J}{S}\right)_{\text{elec}} = \frac{I_P}{I_{ac} + I_I + I_{dc}} \ , \tag{3.51}$$

where

$(J/S)_{elec}$ = the effective J/S ratio in the missile electronic band
I_{dc} = average of the waveform (in excess of interpulse contribution).

3.4.2 Coherent Sources

The application of laser sources to IRCM is very appealing. Lasers are inherently high-radiance sources and can be coupled fairly easily into pointing systems. At present, production of coherent radiation in the mid-IR regime is difficult to achieve in a safe manner or with high conversion efficiencies. In addition, most lasers produce radiation at a single wavelength. Thus, they can be countered in the IR missile by the use of a blocking filter.

A laser system that has spectral agility for a good active IRCM is hydrogen fluoride/deuterium fluoride (HF/DF). It produces many lines of radiation in both the α and β bands. The HF/DF system uses a chemical reaction and therefore has a high electrical-to-radiated-power efficiency. However, the HF/DF system is not amenable to an operational environment. The constituent chemicals of the laser medium are exceptionally caustic and constitute a danger to personnel and materials. It is doubtful that any fielded system concepts will employ an HF/DF laser.

With the advances in diode laser pumps for solid-state lasers (primarily Nd:YAG), gas lasers and frequency converters (i.e., Raman cells) have become less attractive to IRCM developers. Solid-state systems, because of their attractive size, efficiency, and reliability qualities, are now of great interest. These systems use a two-step process: a solid-state laser supplies radiation at one frequency to a crystalline material. The nonlinear interaction of the incident radiation with the crystal produces radiation of another frequency. Several candidates for conversion are possible in theory—although slight deviations in material composition can reduce their efficiency. A variety of programs, supported by government contract or internal research and development, are underway with the goal of producing a viable IRCM laser source. These include

- Ho:YAG/YLF or Tm:YAG/YLF lasers with $AgGaSe_2$ optical parametric oscillators (OPOs)
- a CO_2 rf-excited laser with a Tl_3AsSe_3 up-converter
- a Nd:YAG laser with both a KDP and a CDS OPO (two conversions).

3.5 SYSTEM CONCEPTS

The active IRCM system must present modulated radiation to an attacking missile. Input power availability, the spectral sensitivity of the threat, power output requirements, size, and weight are all determining factors in the system chosen. The concepts reviewed here are the wide-beam system, the spatially modulated system, the directed system, and closed-loop jamming.

3.5.1 Wide-Beam Systems

The ideal active IRCM system would provide protection against the known heat-seeking missiles and produce a radiation pattern that overlapped the signature of the platform. While not a necessary condition, it would be preferable that an ideal active IRCM system caused an optical breaklock (OBL) in the attacking missile. In addition, the ideal system would require no auxiliary input for warning, be power efficient, be visibly covert, and would be easily adapted to any new threat.

In the early days of active IRCM, most missile threats encountered were limited to sensing radiation produced in band α. The IRCM systems produced to counter these missiles were nearly ideal. The active IRCM system reflector design matched the band α radiation pattern produced by a platform. The band α radiation pattern is due to the hot parts. Thus, the missile was constrained to attack only the aft portion of the aircraft. The IRCM system for these aircraft uses a reflector that points the jammer radiation in a wide-field-of-view pattern to the aft, neglecting any forward coverage. Since the jammer radiation pattern was large and overlapped the aircraft signature pattern, no auxiliary system was required for missile launch detection. The band α threats generally were simple spin-scan systems that underwent OBL when successfully jammed. The radiance of the incoherent sources—either alkali-metal-vapor arc lamps or carbon rods—was high in this band. Thus, the jammers were efficient in this band. The active IRCM system was made visually covert by placing a spectral filter in the optical path. Upgrading the system to handle different IR threats was done by time sharing of waveforms.

These systems saw service during the Vietnam era and are still resident on several platforms. They are inexpensive, easy to operate, and their stand-alone operation is virtually automatic. The advent of complex band β threats has proven that limitations exist, but this should not be construed to mean that the death knell has sounded for these systems. Thus, the wide-beam active IRCM system has many years of service ahead of it.

3.5.2 Spatially Modulated Systems

The active IRCM system must produce temporal modulation as detected by an incoming missile. It has been discussed how active IRCM systems produce temporal modulation directly either by electronic or mechanical modulation of a source.

The source itself, however, need not be modulated in time to produce a temporal modulation. Several everyday examples exist of sweeping a source by an observer: a lighthouse, a search light, a police light, etc. In these systems, a constant radiance source illuminates a reflector, which projects a beam into a small solid angle. The reflector rotates and causes the beam to rotate with it. To an observer fixed in space, the amplitude of the radiation detected is modulated. The period of the modulation is a function of the rate of rotation of the reflector.

Active IRCM systems have successfully used spatial modulation. These systems consist of a cylindrical source that is centrally located with respect to a projection system. The projection system consists of either lenses or reflectors and produces a pinwheel pattern of radiation (see Fig. 3.21). Through rotation

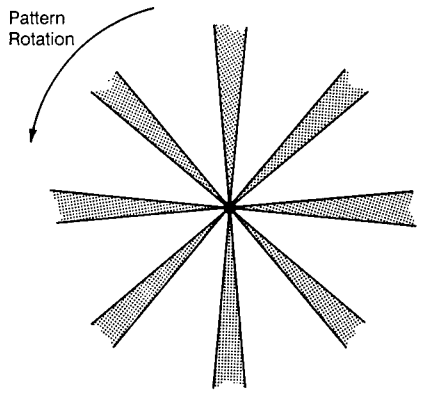

Fig. 3.21 Pinwheel radiation pattern.

of the projection system the missile is illuminated by pulses of radiation. The radiant intensity is

$$I = LA_p \ , \tag{3.52}$$

where L = source radiance and A_p = projected source area. The rate of change of I is

$$\frac{dI}{dt} = L\frac{dA_p}{dt} \ . \tag{3.53}$$

For example, assume that the projected area has the following form:

$$A_p = A_0 \cos^3\omega_r t \ . \tag{3.54}$$

Then

$$\left|\frac{dA_p}{dt}\right| = A_0\left|\frac{d\cos^3\omega_r t}{dt}\right| = 3A_0\omega_r \cos^2(\omega_r t)\sin(\omega_r t) \ , \tag{3.55}$$

where ω_r = the rate of rotation of the projection system, A_0 = the on-axis illuminated area, and t = time.

It may be advantageous to modulate temporally the source in conjunction with spatial modulation to insert higher frequency component waveforms.

3.5.3 Directed Systems

The advent of band β missile systems has placed severe requirements on active IRCM system design. The efficiency of conventional sources (arc lamps and carbon rods) decreases in the long-wavelength region, while the signature of the platform tends to increase. In addition, the band β missile systems have

improved scanning systems—conical and rosette—and several have sophisticated CCM circuitry.

These considerations have led to the directional IRCM (DIRCM) system concept. Instead of radiating the IR energy to all points in space, the DIRCM system concentrates the energy where it is effective—at the missile. The most promising method of directing the IR energy toward the missile is simply to point a reflector at it.

However, the DIRCM system is inherently more complex than the wide-beam system. The DIRCM system must be cued to the presence of a threat, the reflector slued toward it, and the jamming energy maintained on the missile independent of the motion of the platform. A missile launch detector or warning receiver alarms the IRCM system to the presence of a threat missile. It also provides the directional pointing vector to steer and point the jamming reflector. A pointing and tracking system is an integral part of the DIRCM system.

An approximation to the radiated power is given by

$$P = LA_{\text{ref}}\Omega \ , \tag{3.56}$$

where A_{ref} is the aperture of the projection system and Ω is the solid angle into which the radiation is projected.

The power required for the active IRCM system is dependent on the solid angle into which the system radiates. For a given source and aperture size, reduction of the solid angle directly reduces the required radiated power and, in turn, the input power for the active IRCM system. A DIRCM system's main advantage over the wide-beam system is that DIRCM requires less power. This is because the DIRCM concentrates the power into a smaller projected solid angle of radiation. Thus, it is possible to construct the DIRCM system providing a higher radiant intensity than its wide-beam counterpart using the same input power.

The radiant intensity produced by the jammer (on-axis) is

$$I_{\text{in-band}} = L_{\text{in-band}}A \ . \tag{3.57}$$

The radiance L is largely a function of the physical characteristics of the source. The exit area A of the aperture is a function of the reflector design. To increase the on-axis radiant intensity over its wide-beam counterpart, the DIRCM system must increase the radiance or the aperture area or both. Yet with most incoherent sources, the peak radiance they can achieve varies slowly with input power.

Since the J/S ratio is of paramount importance in defeating threats, the DIRCM system designer must be aware of the limits of the in-band radiance of the source. The required jammer power coupled with a small available in-band radiance may require a correspondingly large radiating aperture. The reflector required to produce the aperture may be such that it becomes a burden to the DIRCM system, since it implicitly requires a complex (and heavier) pointing system.

If a small radiating aperture is desired or required, a high band-β radiance source is needed. High radiance sources in band β, however, are extremely

inefficient. To keep the input power required at a practical value, the projected solid angle must shrink. In general,

$$P_{\text{elec}} = \frac{P_{\text{rad}}}{\xi_{\text{band}}} \tag{3.58}$$

$$= \frac{LA_{\text{ref}}\Omega}{\xi_{\text{band}}}, \tag{3.59}$$

where

P_{elec} = the electrical power
P_{rad} = the radiated power
ξ_{band} = conversion efficiency factor.

The size of the beamwidth (Ω) determines the accuracy required of the pointing and tracking system.

3.5.4 Closed-Loop Jamming Systems

The system concepts described so far are open-loop jamming systems; i.e., the jamming waveform parameters are selected *a priori.*

If the modulation format is incorrect, the jammer can be ineffective and, in a worst case, may enhance the vulnerability of the aircraft.

Closed-loop jamming offers a method of determining a more optimum jamming waveform. "Closed loop jamming systems use either a laser or a thermal source to interrogate the missile to be jammed. Critical information on the operating frequencies of the missile seeker can be deduced by monitoring the reflected energy from the missile seeker and fed to the modulator of a high-power jammer. This jamming signal has a higher probability of being effective against the missile than an equivalent open loop jammer modulated in preset program of frequencies." [8]

3.6 TEST AND EVALUATION

Active countermeasure system development is an evolutionary process. Key to the realization and survival of a countermeasure system is test and evaluation. Modeling and simulation are cost-effective methods of evaluating design concepts and excellent laboratory tools. Field use requires further testing of system design: prototype and operational systems can be mounted on a platform and tested. Seekers can be held captive while the effects of the jammer are observed. Finally, the system can be tested by a live firing of the missile against a drone or cable car equipped with the active IRCM system.

3.6.1 Jammer Intensity Tests

The verification of the jammer performance often requires laboratory tests of the jammer. The radiant intensity produced by the jammer alone is measured rather simply, though some care must be taken to ensure that a far-field measurement is done (a long hallway has proven to be quite useful in this regard). As noted previously, the spectral characteristics are determined by

using a CVFR and associated electronics synchronized with the jamming pulses. Usually, the radiant intensity of the jammer is measured with the aid of a small, diffuse gold reflector (see Fig. 3.22). This allows for a portion of the emitted energy to be sampled and the operation of the radiometer to be well away from its saturation point. Usually, the spectral characterization is done at a single point in space with respect to the jammer (i.e., 0 deg elevation and 0 deg azimuth). Once the spectral characterization of the jammer is complete, a complete spatial characterization of the jammer is done for a particular band of interest. This is achieved by having the jammer rotated in both azimuth and elevation with respect to the gold reflector.

The measurement of the jammer includes both the source and the reflector. It is sometimes useful to measure the source independent of the reflector. The measurement of the source as it operates in the jammer, though, can be quite complicated. This is because the reflector geometry can affect the air flow near the lamp and hence the lamp temperature. In particular for arc lamps, it can be very difficult to reproduce the temperature distribution of the lamp.

3.6.2 Simulation

Simulation provides quick and cost-effective assessment of technique and system effectiveness. Simulation can be divided into three classes. The first, digital simulation, uses a digital model of the missile. The second class, analog (or signal injection), uses an electronic model of the missile. The third, semiphysical, uses actual seeker hardware in the simulation.

3.6.2.1 Digital Simulation. Often the IRCM system designer is working without access to the missile he is trying to counter. Even if the missile is available, some components and the corresponding circuits may not be accessible—or the number of tests required of the seeker may degrade substantially its performance. Digital simulation provides the means to obtain detailed information about the seeker response.

This type of simulation encompasses computer modeling of missile components, circuitry, active IRCM, fly-out patterns, six degrees of freedom (DOF) motion analysis, and IR signatures. Mathematical analysis is applied to all facets of the active IRCM system design to predict system performance.

To perform a digital simulation, the designer of active IRCM must have a highly detailed database of the missile in question. Active IRCM techniques, especially against advanced seekers, involve consideration of various nonlinear portions of the missile signal-processing elements. Simple models that use true/false estimates of jammer worthiness often given erroneous results. Since the fidelity of the digital model must be high, the simulation is slow. Although this is a function of the computer used, run times of 50× to 100× real time are typical.

3.6.2.2 Analog (Signal-Injection) Simulation. The method employed in the analog simulation is to model both the electromechanical and electrical portions of the missile electronically. Analog simulation begins with missile tracking and guidance circuits being breadboarded. Key to the simulation is the electronic representation of the scanning system. An oversized reticle mask is mounted on the face of a cathode-ray tube (CRT), which displays the target

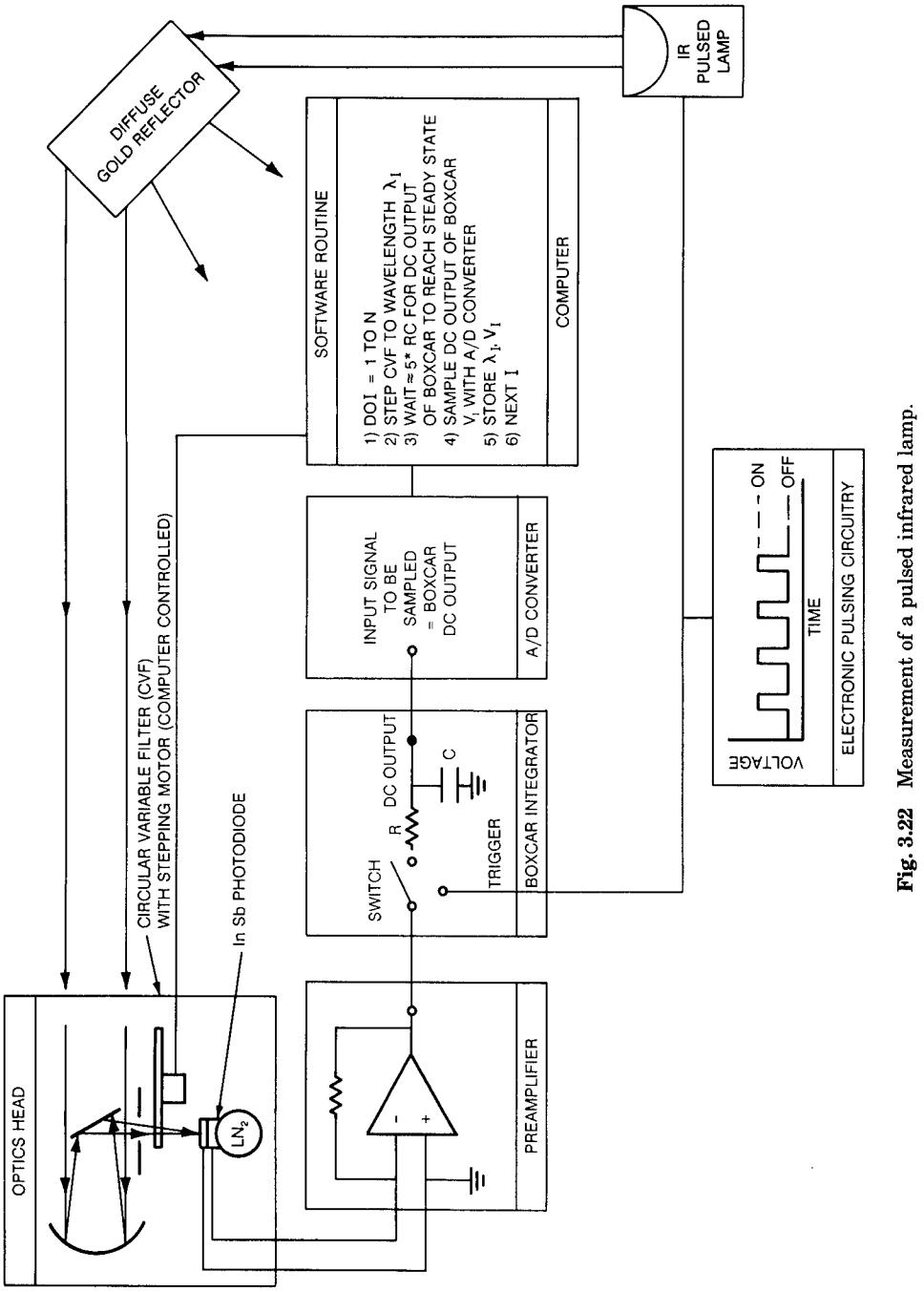

Fig. 3.22 Measurement of a pulsed infrared lamp.

image. The interaction of the target image with the reticle is captured by an optical detector operating in the visible spectrum. The detector output is injected into breadboarded guidance circuitry. The amplitude modulation of the jammer is done by direct modulation of the amplitude of the image on the CRT tube. An analog or digital computer can be used to close the simulation loop. The computer calculates the aerodynamic forces on the missile and solves the equations of motion.

This type of simulation allows access to various circuit nodes during the operation of the missile flight. It can run in real time and be automated for successive runs. A great deal of data is required for the simulation to ensure that the breadboarded circuits are operating correctly.

3.6.2.3 Open-Loop Simulation. Open-loop simulation is a single degree of freedom test using actual seeker hardware. An artificial line of sight is generated, and seeker response is measured. The simulation is termed open loop since only the tracking loop is tested without closing the guidance loop.

The generation of the artificial line of sight is done by the rotation of the table. The seeker head is mounted on the table. A collimated beam is aligned with the seeker body axis. The gyro is allowed to track the target. When the table and the missile body are rotated, the gyro attempts to maintain its fixed direction in space. This causes a relative displacement between the gyro axis (seeker boresight) and the source. This error drives the seeker gyro to follow the rotation of the table as if there were a true line-of-sight rotation between the source and the seeker.

The open-loop simulation measures the response of the tracking loop to a stimulus. The tests are more useful when dealing with spin-scan seekers, since optical breaklocks can be measured directly. Open-loop simulation requires access to a seeker. Little seeker specific data, however, are required to perform the open-loop simulation except for power requirements. It must be remembered that seekers are not designed to be used as laboratory measurement devices. The continual operation of the seeker can severely degrade its performance and inadvertently influence results. A photograph of a typical open-loop simulation configuration is shown in Fig. 3.23.

3.6.2.4 Closed-Loop Simulation. Closed-loop simulation is a full six-DOF hardware-in-the-loop (HWIL) simulation. The use of actual radiating sources and missile hardware defines the missile simulation. The six degrees of freedom are missile angular motion and the missile spatial motion with respect to the target. Missile angular motion is accomplished by a three-axis missile positioning table that rotates the missile in pitch, roll, and yaw. The target motion is done by moving a collimated infrared beam in azimuth and elevation with respect to the missile. The closure of range is simulated by changing the radiance of the collimated beam. Target generation usually includes aircraft targets, backgrounds, and IRCM, both active and expendable. The loop is closed with an analog or digital computer that calculates the moments and forces on the missile. The computer then drives both the target motion system and the missile rotation system.

Closed-loop simulation is particularly useful for the evaluation of countermeasure systems against advanced missiles. Since optical breaklock is difficult to achieve, the simulation aids in determining the miss distance that the CM

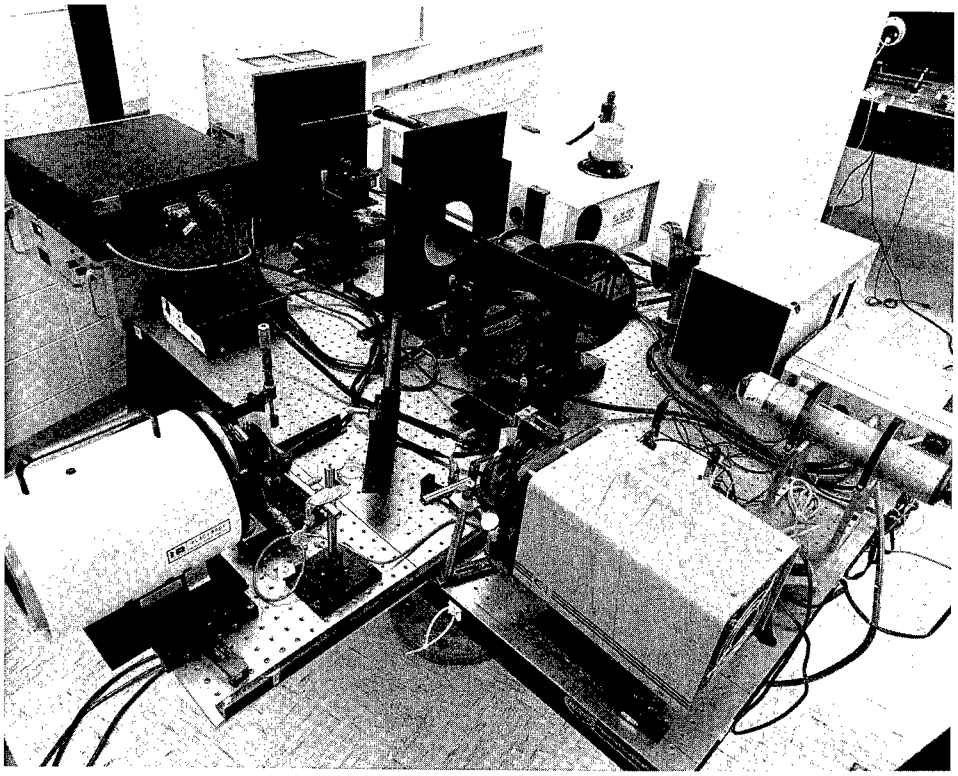

Fig. 3.23 Open-loop simulation.

produces. The simulation operates in real time. Since a run is on the order of 10 s, large amounts of data may be generated in a short time. Little information about the seeker is required; however, missile aerodynamic forces must be modeled. The simulation can explore a number of different scenarios in a highly controlled environment. Since the simulation uses actual missile seekers, care must be taken to ensure that the missile performance is not degraded through excessive testing. A photograph of a typical closed-loop simulation configuration is shown in Fig. 3.24.

3.6.3 Captive Testing

Captive testing employs the seeker, active IRCM system, and the platform. The seeker is mounted in a gimbal either on the ground or on a chase aircraft. The platform, complete with active IRCM, flies by the seeker. A video camera, either IR or visible, is boresighted with the seeker body axis. The direction at which the gyro is pointed is monitored through a video overlay. A circular ring in the video screen gives the instantaneous field of view of the gyro. The center of the circular ring moves with the gyro pointing direction. In this fashion, the scene the missile gyro is sensing can be viewed.

Captive testing is particularly useful for seekers where optical breaklocks may occur. Jammer-produced perturbations can be seen directly, in real time.

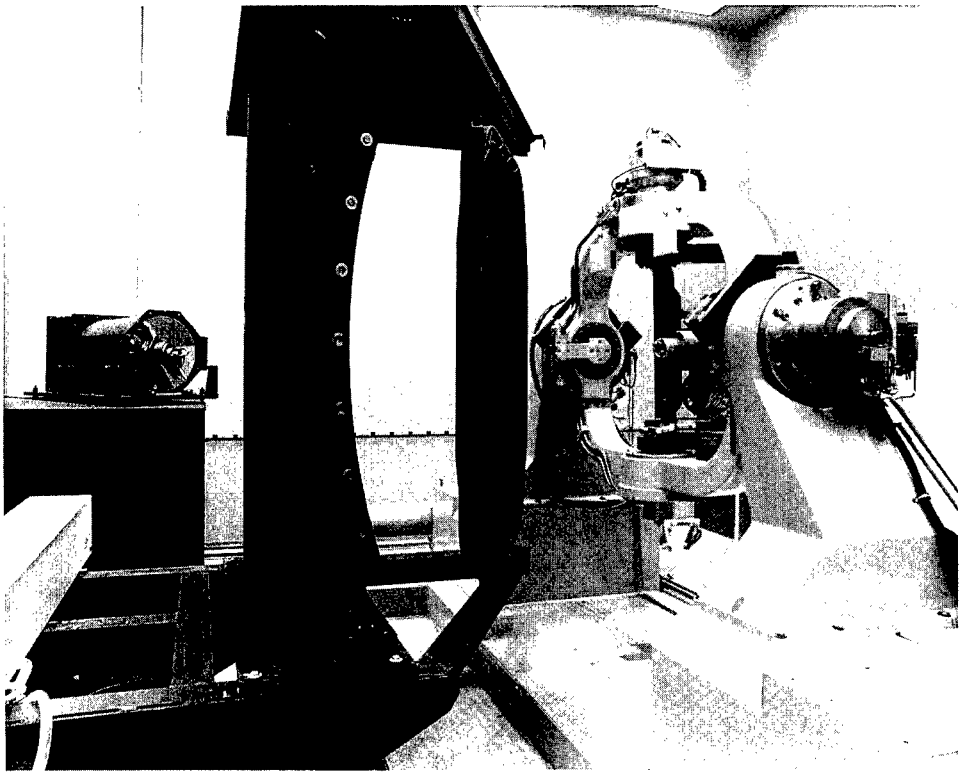

Fig. 3.24 Closed-loop simulation.

If optical breaklock does not occur, it may be difficult to estimate jammer effectiveness via captive testing alone.

3.6.4 Live Firings

Short of the battlefield, live firings are the most credible method of determining an active IRCM's effectiveness. In a live firing, the IRCM system is mounted on a drone or cable car and the missile is fired at it. The live firing provides a rather spectacular demonstration of the system's success or failure.

Live firings are expensive; hence, the number of firings against a particular jammer system are small. The small sample size makes it difficult to obtain statistical inference on the system performance. It can be difficult to control such items as platform specifics (altitude, velocity, trajectory), environment (wind, ambient temperature, background), and missile integrity. As a result, live firings do not lend themselves to system development—they are reserved for verification of system performance.

3.7 REAL-WORLD ISSUES

Fundamental to any active IRCM system is its ability to operate in the real world. The jammer must not affect the performance of the platform or its

subsystems. Certain electronic modulation schemes switch large currents that can, if not shielded, cause electromagnetic interference.

The system must be reliable. For active IRCM systems, the jammer source tends to be the component most likely to fail. Thermally induced stress in both arc lamps and carbon rods are inherent in the operation of IRCM systems. Other reliability issues are electronic components, motor bearings, etc.

The designer must be cognizant of these deficiencies and plan for their service in the field. In particular, source replacement must be done easily and with a minimum effort by personnel.

Acknowledgments

The authors thank Dr. Gerald Griffith for his patient reading and correction of the manuscript, Mr. Ian Agard for his technical contribution to the figures, Mr. George Schwind for his interest and contribution to this effort, Mr. Dino Goegan for preparation of the figures, and Ms. Sharon Padal for the preparation of the manuscript.

References

1. C. Link, Northrop Corporation, private communication (1990).
2. C. Link and M. Maas, Northrop Corporation, private communication (1990).
3. *Jane's All the World's Aircraft.* Jane's Information Group, Surrey, UK (1990).
4. F. Grum and R. Becherer, *Radiometry—Optical Radiation Measurements,* Vol. 1, Academic Press, New York (1979).
5. W. L. Wolfe and G. J. Zissis, Eds., *The Infrared Handbook,* pp. 22–55, Environmental Research Institute of Michigan, Ann Arbor, MI (1978).
6. F. Bartoli, L. Esterowitz, M. Kruer, and R. Allen, "Irreversible laser damage in IR detector materials," *Applied Optics* **16,** 2934 (1977).
7. K. S. Drellishak, "EO/IR countermeasures: countering the (in) visible threat," in *The International Countermeasures Handbook,* 11th ed., EW Communications, Palo Alto, CA (1986).
8. H. S. Eustace, "IR/EO in EW: an assessment of technology," in *The International Countermeasures Handbook,* 4th ed., EW Communications, Palo Alto, CA (1978).

Bibliography

Alward, J., "Spatial-frequency filtering," Infrared Laboratories, University of Michigan (1965).

Bartoli, F., L. Esterowitz *et al.,* "Irreversible Laser Damage in IR Detector Materials," *Applied Optics* **16,** p. 2934, November 1977.

Biberman, L. M., M. R. Holter, S. Nudelman, G. Suits, W. L. Wolfe, and G. J. Zissis, "Infrared design problems illustrating the use of reticles," in *Fundamentals of IR Technology,* Macmillan, New York (1962).

Biberman, L. M., *Reticles in Electro Optical Devices,* Pergamon Press, New York (1965).

Born, M., and E. Wolf, *Principles of Optics,* Pergamon Press, New York (1970).

Churchill, R., *Fourier Series and Boundary Value Problems,* McGraw-Hill, New York (1941).

Cox, A., *A System of Optical Design,* The Focal Press, New York (1964).

Drellishak, K. S., "EO/IR countermeasures: countering the (in)visible threat," *The International Countermeasures Handbook,* 11th ed., EW Communications, Palo Alto, CA (1986).

Due, C. T., and L. M. Peterson, *IRIA State-of-the-Art Report: Optical Mechanical Active/Passive Imaging Systems,* Vol. I, Environmental Research Institute of Michigan, Ann Arbor, MI (1982).

Fisher, D. W., R. F. Leftwich, and H. W. Yates, "Survey of infrared trackers," *Applied Optics* **5**(4), 507–515 (1966).

Garbuny, M., *Optical Physics,* Academic Press, New York (1965).

Hudson, Jr., R. D., *Infrared Systems Engineering,* Wiley-Interscience, New York (1969).

"The IR/EO EW basis," *The International Countermeasures Handbook,* 3rd ed., EW Communications, Palo Alto, CA (1977).

"IR/EO in EW: an assessment of technology," *The International Countermeasures Handbook,* 4th ed., EW Communications, Inc., Palo Alto, CA (1978).

Jamieson, J. A., R. H. McFee, G. N. Plass, R. H. Grube, and R. G. Richards, *Infrared Physics and Engineering,* McGraw-Hill, New York (1963).

Jane's All the World's Aircraft, Jane's Information Group, Surrey, UK (1990).

Jenkins, F., and H. White, *Fundamentals of Optics,* McGraw-Hill, New York (1950).

Lawrence, R. S., and J. W. Strohbehn, "A survey of clean-air propagation effects relevant to optical communications," *Proceedings of the IEEE* **58,** 1523–1545 (1970).

Levinstein, H., "Infrared detectors," *Physics Today* **30**(11) (Nov. 1977).

Lipson, S., and H. Lipson, *Optical Physics,* Cambridge University Press, Cambridge, U.K. (1969).

Lloyd, J., *Thermal Imaging Systems,* Plenum Press, New York (1975).

Malacara, D., *Optical Shop Testing,* John Wiley & Sons, New York (1978).

Montgomery, W. D., "Periodic reticle for optical classification," *Journal of the Optical Society of America* **55**(9), 1082–1085 (1965).

Montgomery, W. D., and Broome, P. W., "Spatial filtering," *Journal of the Optical Society of America* **52**(11) (1962).

Pohl, R., *Optik und Atomphysik,* Springer, Berlin (1958).

Powell, R. W., "Infrared tracking," *Am. Rocket Soc. J.* **29**(12), 973–980 (1959).

Smith, W., *Modern Optical Engineering,* McGraw-Hill, New York (1966).

Tartarski, V. I., *The Effects of the Turbulent Atmosphere on Wave Propagation,* Israel Program for Scientific Translations, Jerusalem (1971).

Titchmarch, E. C., *Theory of Fourier Integrals,* Oxford Press, Oxford, UK (1937).

Ulrich, J., D. Montgomery, and J. Alward, "Analysis of reticle systems," Report 6054-2-T, The University of Michigan, Ann Arbor, MI (1965).

Welford, W., *Aberrations of Symmetrical Optical Systems,* Academic Press, New York (1980).

Wiener, N., *Fourier Integral and Certain of Its Applications,* Dover, New York (1959).

Williams, C., and O. Becklund, *Optics, A Short Course for Engineers,* John Wiley & Sons, New York (1972).

Wolfe, E., Ed., *Handbook of Military Infrared Technology,* U.S. Government Printing Office (1965).

Wolfe, W. L. and G. J. Zissis, Eds., *The Infrared Handbook,* Environmental Research Institute of Michigan, Ann Arbor, MI (1978).

Yariv, A., *Introduction to Optical Electronics,* 2nd ed., Holt, Rinehart and Winston, New York (1976).

CHAPTER 4

Expendable Decoys

Neal Brune
Tracor Aerospace, Inc.
San Ramon, California

CONTENTS

4.1 INTRODUCTION

Infrared decoys are widely used to protect combat systems from IR tracking threats. The most widespread example is that of IR flares used to protect aircraft from heat-seeking missiles. However, IR decoys are also gaining wide acceptance for the protection of ships against certain types of antishipping missiles. Active developments are underway to evaluate various decoy and IR clutter technologies for application to ballistic missile and space systems.

Decoys are used with one of three tactical objectives: seduction, distraction, or dilution. Applications of these tactics are discussed next.

The nomenclature used throughout this chapter is given in Table 4.1.

Seduction. The best-known objective is disengaging an actively tracking threat sensor. This technique, often referred to as *seduction,* is accomplished by presenting the radiant characteristics sought by the tracking system in a manner such that the decoy is preferred to the original target. Usually this requires radiating a stronger signal than that of the target in the tracker's band of interest. Because many trackers home on the brightest source, the original target is quickly ignored and the decoy accepted. Properly employed against a vulnerable threat, a single seduction decoy can provide a very high probability of survival.

Distraction. This tactic requires the decoy to be deployed before the threat is tracking the target. The decoy is placed so that it is acquired before the threat has the opportunity to observe the target. This is a common tactic for shipboard applications. Often, more than one decoy is required because of greater uncertainty in the threat's location and time of arrival. This tactic has the desirable feature of avoiding direct comparison between the target and the decoy.

Distraction decoys need not exceed the target signature, rather they need only be credible to the threat. Most threats can be relied on to home on the first credible target encountered. More sophisticated threats may employ multiple discriminants and call for more sophisticated decoys. Each application must be addressed by considering the expected threat selection criteria, the operational environment, the mission, and the target value.

Dilution. Dilution tactics are less desirable than either seduction or distraction. Dilution is used when the target and decoys may be observed simultaneously for relatively long periods of time. Such threats usually have either an imaging system or a track with scan capability sufficient to track and observe several potential target characteristics.

Dilution decoys must exhibit signature features within the acceptable range of target characteristics. The intent is to force the threat to attack all potential targets to achieve its goal. In general, the dilution tactic affords at best an $n/(n + 1)$ survival probability when n decoys are used against a single threat.

4.2 GENERAL DESIGN REQUIREMENTS

The derivation of decoy performance requirements must always start with a definition of the threat. The threat is the weapon system of concern to the

Table 4.1 Symbols, Nomenclature, and Units

Symbol	Description	Units
a	Burn rate constant	$cm\ s^{-1}$
C_1	First radiation constant	$3.7415 \times 10^4\ W\ cm^{-2}\ \mu m^4$
C_2	Second radiation constant	$1.4388 \times 10^4\ \mu m\ K$
C_d	Drag coefficient	
d_e	Static radiant emittance factor	
d_s	Plume shape factor	
d_w	Wind stream degradation factor	
E_λ	Specific intensity in the wave band of interest	$J\ g^{-1}\ sr^{-1}$
$F_{\lambda,T}$	Fraction of total radiation in the band of interest	
g	Gravitational acceleration constant	$m\ s^{-2}$
H_c	Fuel heat of combustion	$J\ g^{-1}$
I	Radiant intensity (pointance)	$W\ sr^{-1}$
I_b	Calibration standard intensity	$W\ sr^{-1}$
L_λ	Flux density at the wavelength λ	$W\ sr^{-1}\ cm^{-2}$
$\dot{m}$	Fuel combustion rate	$g\ s^{-1}$
n	Burn rate exponent	
r	Burning surface recession rate	cm^{-1}
P	Ambient pressure	Pa
R_e	Radiometer responsivity	$W\ sr^{-1}\ m^{-2}\ V^{-1}$
S	Burning surface area	cm^2
T	Temperature	K
t	Time	s
v	Velocity	$m\ s^{-1}$
V_b	Radiometer voltage during calibration	V
V_s	Radiometer voltage during measurement	V
W	Flare weight	N
Greek:		
β	Ballistic coefficient	$N\ m^{-2}$
ε	Average emissivity	
ε_λ	Emissivity at the wavelength λ	
λ	Wavelength	μm
ρ_a	Air density	$kg\ m^{-3}$
ρ_f	Fuel density	$g\ cm^{-3}$
σ	Stefan-Boltzmann constant	$5.6697 \times 10^{-12}\ W\ cm^{-2}\ K^{-4}$

platform that is to be protected by the decoy. This discussion is concerned with those threats that are either aimed or guided to their targets by means of IR sensors.

Before the design process can begin, assumptions must be made about the threat's method of guidance or tracking and the conditions under which it operates. Various non-IR factors, such as warhead lethality, help to define the

required miss distance. Either the launch or the detection range helps define decoy persistence. Often an understanding of the environment helps define decoy requirements. For example, the atmospheric transmission characteristics may eliminate several wavelengths from concern. Other requirements may be shaped by analysis of the technology available to the threat designer or cost considerations.

By its very nature, an expendable decoy must be smaller, lighter, and cheaper than the protected target. Implementations require a compromise between dispensing system capacity, cost, and performance. Several design considerations are illustrated in Fig. 4.1. For example, a small source can radiate as much energy as a larger one if it is at a higher temperature or has a higher emissivity. However, certain threats reject targets that have a spectral distribution associated with an unrealistically high temperature. Other threats may attempt to reject decoys on the basis of physical size, shape, or position. The more target characteristics are simulated, the larger and more expensive the decoy becomes. Successful designs have always come about from acceptance of the risk that some potentially observable target characteristics must be ignored in the interest of decoy producibility. Continued decoy success requires that threat characteristics be regularly reviewed for new performance requirements.

A particularly common design problem is illustrated in the spectral intensity versus wavelength plot of Fig. 4.2. The figure shows the relative spectral distribution of a small, hot source such as a decoy, and a large, relatively cool source, such as an aircraft target. The relative signatures have been adjusted so that their signatures in a common threat seeker band are equal. Clearly the two could be easily distinguished if the threat had simultaneous access to data in other wavelength bands. The decoy is substantially brighter at the shorter wavelengths and noticeably less bright at the longer wavelengths. In general, the longer the wavelength of interest, the more difficult the decoy design problem. Shipboard decoy applications impose similar design issues at longer wavelengths to those of the illustration.

Key requirements for specification development are summarized in Table 4.2. Each of these aspects is discussed in more detail in the following.

Peak Intensity. This is normally the most important requirement. Decoys must radiate with sufficient intensity in the band of interest to at least be credible. In most applications, the decoy must exceed the intended target's radiant intensity in all of the threat bands. This requires large amounts of stored energy at the greatest possible density. If the radiant intensity requirements are not chosen with care, the relatively low energy conversion efficiency associated with inexpensive decoys, such as flares, may place a severe burden on other system characteristics, such as weight, volume, and cost. Typically, a conventional aircraft IR flare consumes from 0.5 to 1 MW of power for each 1000 W sr^{-1} of in-band radiant intensity at flight conditions.

Rise Time. Aircraft decoys must reach an effective level of intensity prior to leaving the seeker field of view, even in the face of severe aerodynamic deceleration. These decoys may be subject to an aerodynamic deceleration as great as 300 m s^{-2}. The diameter of the threat field of view at the time of decoy deployment is usually less than 200 m. This means that effective op-

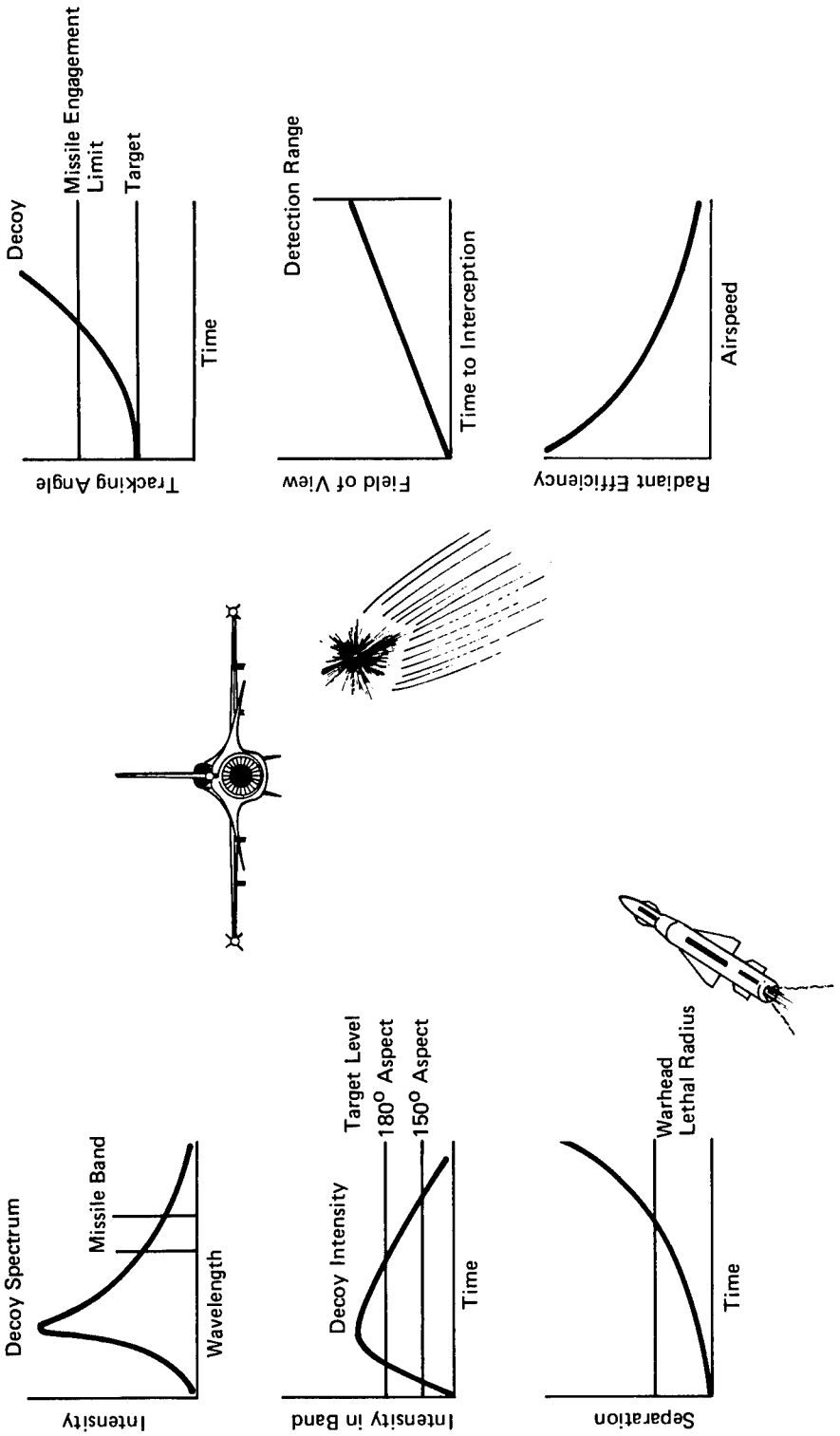

Fig. 4.1 Decoy design considerations.

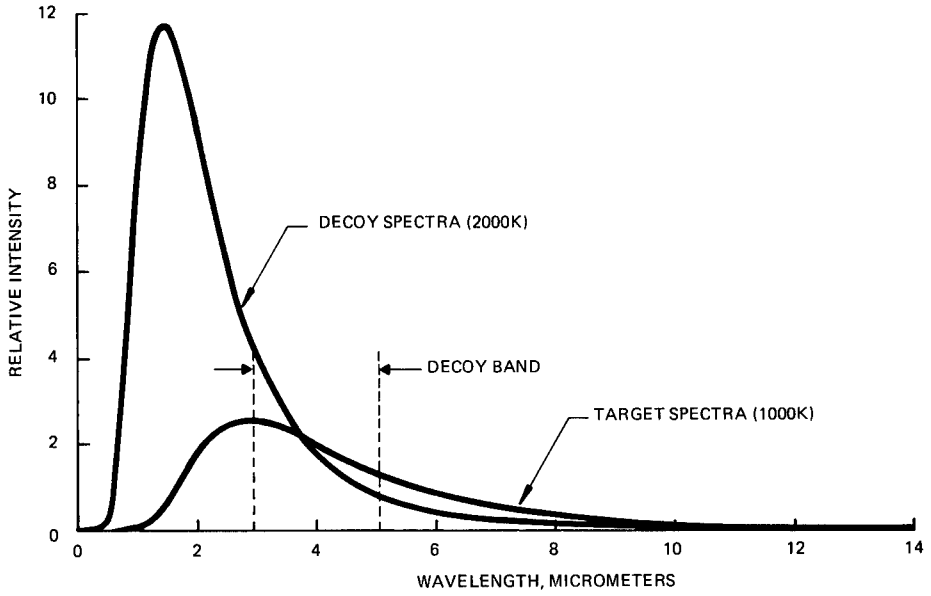

Fig. 4.2 Typical decoy/target spectra.

Table 4.2 Key Decoy Performance Requirements

PERFORMANCE CHARACTERISTIC REQUIREMENT	TYPICAL OBJECTIVE	DESIGN ISSUES
Peak Intensity	Exceed Target Platform Signature to Attract Target.	Primary Driver for Decoy Weight, Volume, and Cost.
Initiation Rise Time	Achieve Effective Intensity Quickly Enough to Capture Seeker before Leaving Field of View.	Usually Requires Special Ignition Materials Excessively Rapid Rates may Trigger Counter-Countermeasures.
Spectral Characteristics	Differences between Decoy and Target may be Exploited by Target.	Dependent on Threat Characteristics. Often Difficult to Verify. May have Severe Effect on Choice of Fuel and Radiation Mechanism.
Function (Burn) Time	Maintain Credible Signature Until Target is No Longer in Threat Field of View.	Also Strong Impact on Weight, Volume, and Cost.
Ejection Velocity	Generate Sufficient Separation Rate from Target so that Threat is Decoyed beyond Lethal Radius.	Launcher must be able to withstand Recoil
Aerodynamic Properties	Maintain Credible Trajectory to Avoid Rejection by Threat.	Some Threat Imposed Requirements have Substantial Impact on Complexity and Decoy Size.

erational intensity levels must be achieved in a fraction of a second. However, some threat seekers may interpret a rapid increase in signal level as evidence that a decoy is present in the field of view. In such cases, the designer must decide whether to attack the decoy rejection scheme or to attempt to avoid it.

Other types of engagements may unfold more slowly. Shipborne decoys are usually in the same field of view for several seconds before the threat must make a tracking decision. This means that the decoy may take a longer period of time to reach operational intensity.

Spectral Characteristics. Most decoys are chemically heated sources that radiate in accordance with black- or graybody characteristics. The smaller physical size of the decoy is best overcome by operating at a higher temperature for greater radiant efficiency. In most applications, this conflicts with the desire to match the spectral characteristics of the target.

The ability to resolve temperatures depends greatly on both the decoy and target temperatures and the threat observation wavelengths. Further insight can be gained from Figs. 4.3(a) and 4.3(b). These illustrate selected spectral ratios in the temperature range associated with typical hot targets [Fig. 4.3(a)], such as aircraft, and cooler targets [Fig. 4.3(b)], such as ships. The data are derived from Planck's law and therefore represent the ideal. Temperature estimation schemes must rely on the relative signal level in two different wavelengths or wave bands. Measurement uncertainty and background variations make it difficult to distinguish between ratios differing by less than 20%.

As shown in the figures, the wider the separation of the measurement bands, the greater the rate of change of the ratio with temperature. Widely separated wavelengths require multiple detectors, which is an additional complication for the threat. Closely spaced wavelengths such as 4 and 5 μm can be measured using a single detector with different filters.

Spectral matching requirements severely affect aircraft decoy performance. Spectral matching often requires that the relative signal level of the decoy in specific, threat-imposed, wavelength bands must be within the normal variation of the target characteristics. This can be accomplished by more carefully controlling the decoy temperature, but most spectral design efforts focus on the use of selective emitters. Selective emitters allow a higher temperature decoy to appear to closely resemble a lower temperature target. Emitters are used that have a relatively high emissivity in the band of interest and a significantly lower emissivity in those bands where the target intensity is low. Certain gaseous combustion products, such as carbon dioxide, radiate strongly in certain bands, whereas they are transparent in others. More elaborate selectively emissive surfaces can be multilayer optical coatings.

Function Time. It is preferred that a decoy persist long enough to ensure that no possibility of target reacquisition remains. Otherwise, the risk of reacquisition makes it necessary to deploy a second decoy. The desired minimum function time is that interval that ensures that the original target is no longer in the threat field of view. More often it is desirable for the decoy to function until the threat has passed the target or is no longer able to maneuver to the target. This is also a critical performance factor for high-intensity decoys, such as aircraft flares. Generally weight, volume, and unit cost are closely related to function time.

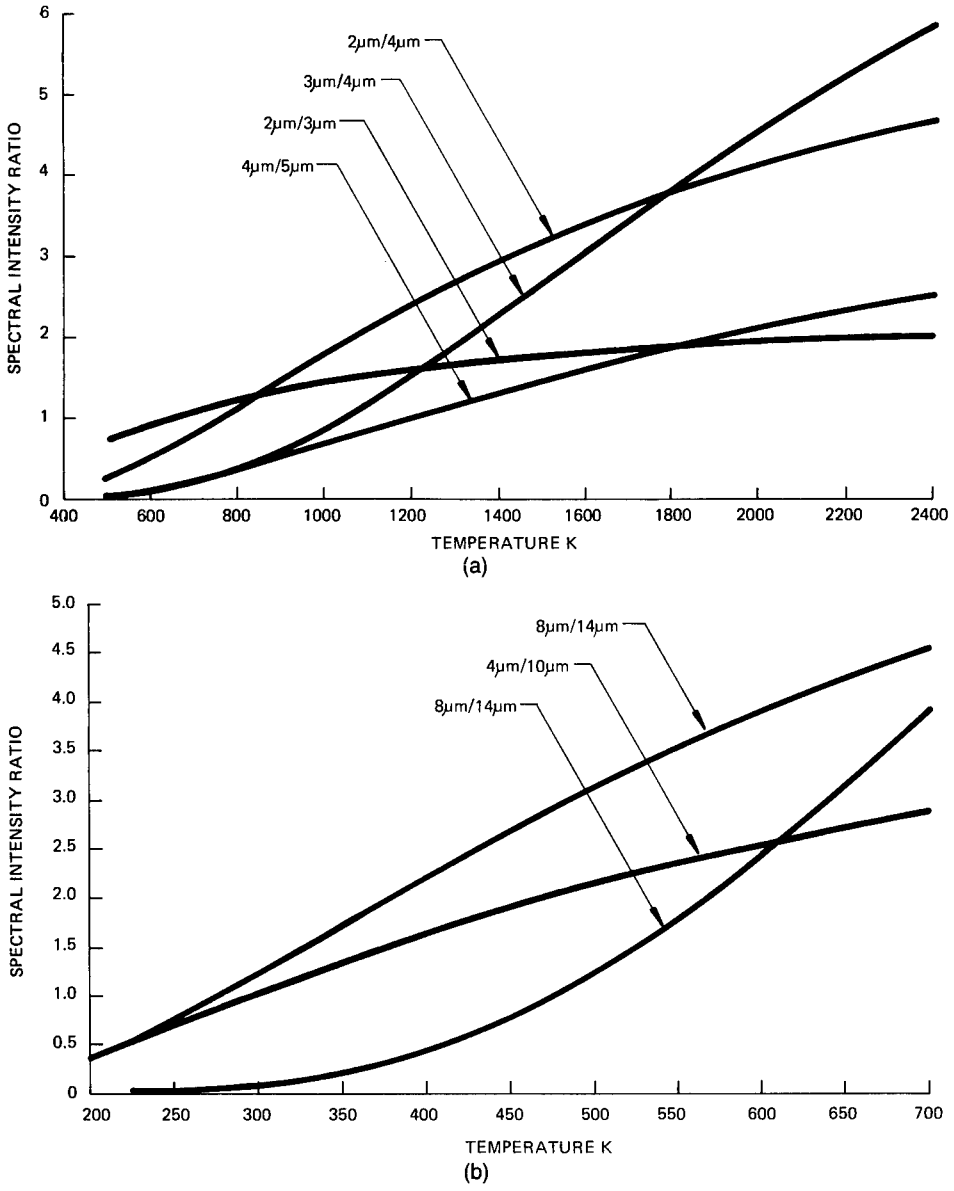

Fig. 4.3 Selected spectral ratios for (a) hot targets and (b) cooler targets.

Ejection Velocity. Seduction decoys must be placed in a location where they can be readily observed by the threat and then separate from the target at a rate within the threat kinematic tracking limit. This may also require knowledge of the threat bearing and field of view. Most decoys are ejected from the target in a direction chosen so that they generate the greatest possible angular separation rate consistent with the tracker's capability and the target's credibility. A credible decoy separation rate can generally be greater than the maneuvering capability of the target.

Aerodynamic Characteristics. The continued separation of the decoy from the target is strongly influenced by its aerodynamic characteristics and the

relative wind at deployment. This is particularly true for aircraft decoys but is often important for shipborne decoys.

4.3 AIRCRAFT DECOYS

Aircraft IR decoys are solid pyrotechnic flares that are ejected either in response to a cue from missile warning system or as a precaution against possible attack. Figure 4.4 shows several flares shortly after ejection. Each flare is contained in a cartridge that includes the IR source itself, an ejection charge, and an ignition mechanism. Some flares are ignited by the ejection charge but most rely on a secondary source that also provides protection from ignition prior to the flare being ejected from the aircraft.

4.3.1 Requirements

The most significant requirements for aircraft decoys are the rapid development of a high-intensity source. The flare must ignite and reach a level exceeding that of the target before leaving the seeker field of view. Most operational flares reach effective intensity in less than 1 s and persist for less than 5 s. The decoy must also have sufficient ballistic density to avoid rapidly falling

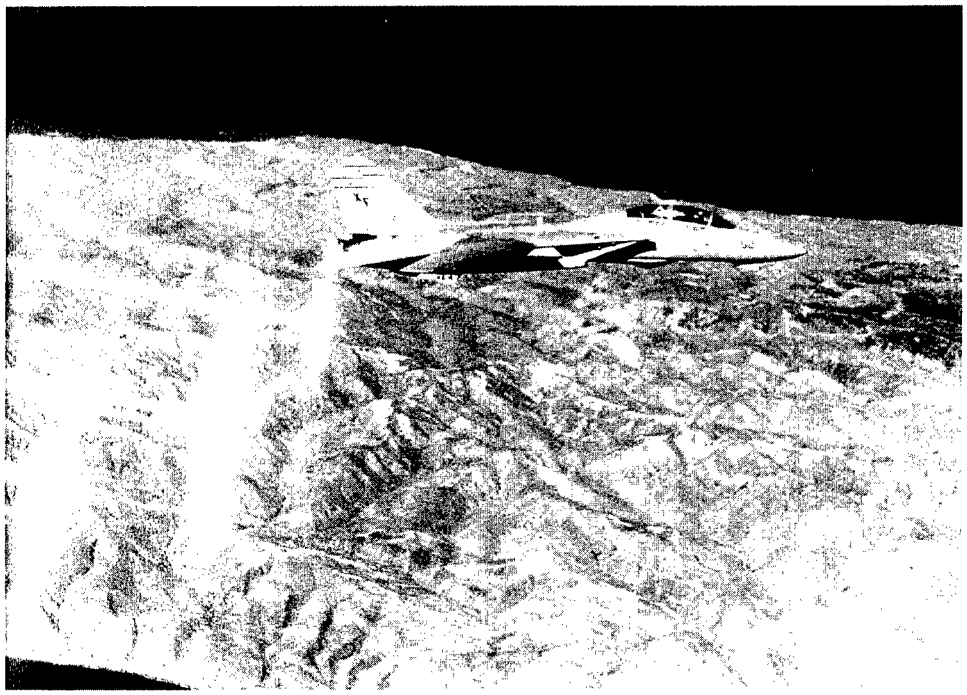

Fig. 4.4 Aircraft IR decoys.

Table 4.3 Typical Signature Levels

Aircraft Type	Intensity (W sr^{-1})	
	2–3 μm	3–5 μm
Rotary wing	10–100	100–300
Fixed wing (propeller)	20–200	200–500
Jet fighter	50–1,000	100–10,000
Jet transport	100–1,000	100–5,000

out of the field of view. Certain threats may also have a capability for flare rejection. This often places additional requirements in the form of the flare's spectral content and kinematic behavior.

Target Characteristics. A typical range of platform signature levels is shown in Table 4.3. These values are not necessarily representative maxima or minima but are intended to illustrate the likely range of consideration for the decoy designer. The signature is the sum of several contributions. These are illustrated in Fig. 4.5. Solar reflection can be significant during daylight conditions. Radiation from a jet engine exhaust plume is substantial in the CO_2 and H_2O bands and is a primary source at side aspects. The hot metal parts of a jet fighter dominate the signature at tail-on aspects. These hot metal parts usually form the basis for the flare specification. Use of the afterburner can increase the signature of a jet fighter by an order of magnitude.

Variation with Aspect. The target aircraft signature, particularly that of jet aircraft, can vary greatly in terms of both intensity and spectra as a function of the viewing aspect from nose to tail. An example of this is shown in Fig. 4.6.

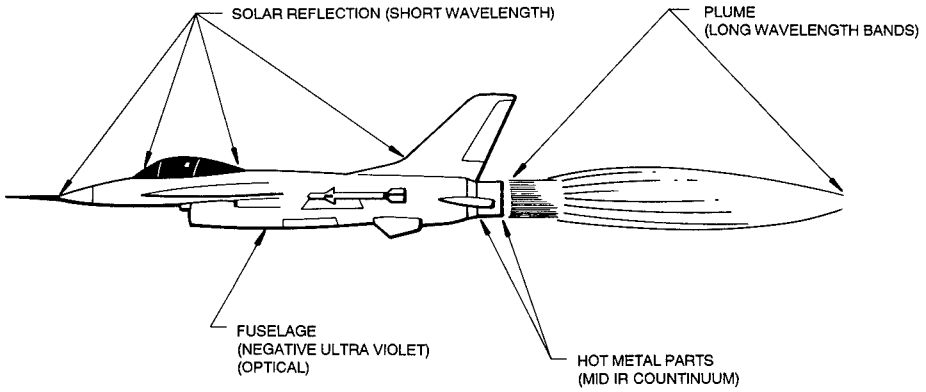

Fig. 4.5 Aircraft IR signature components.

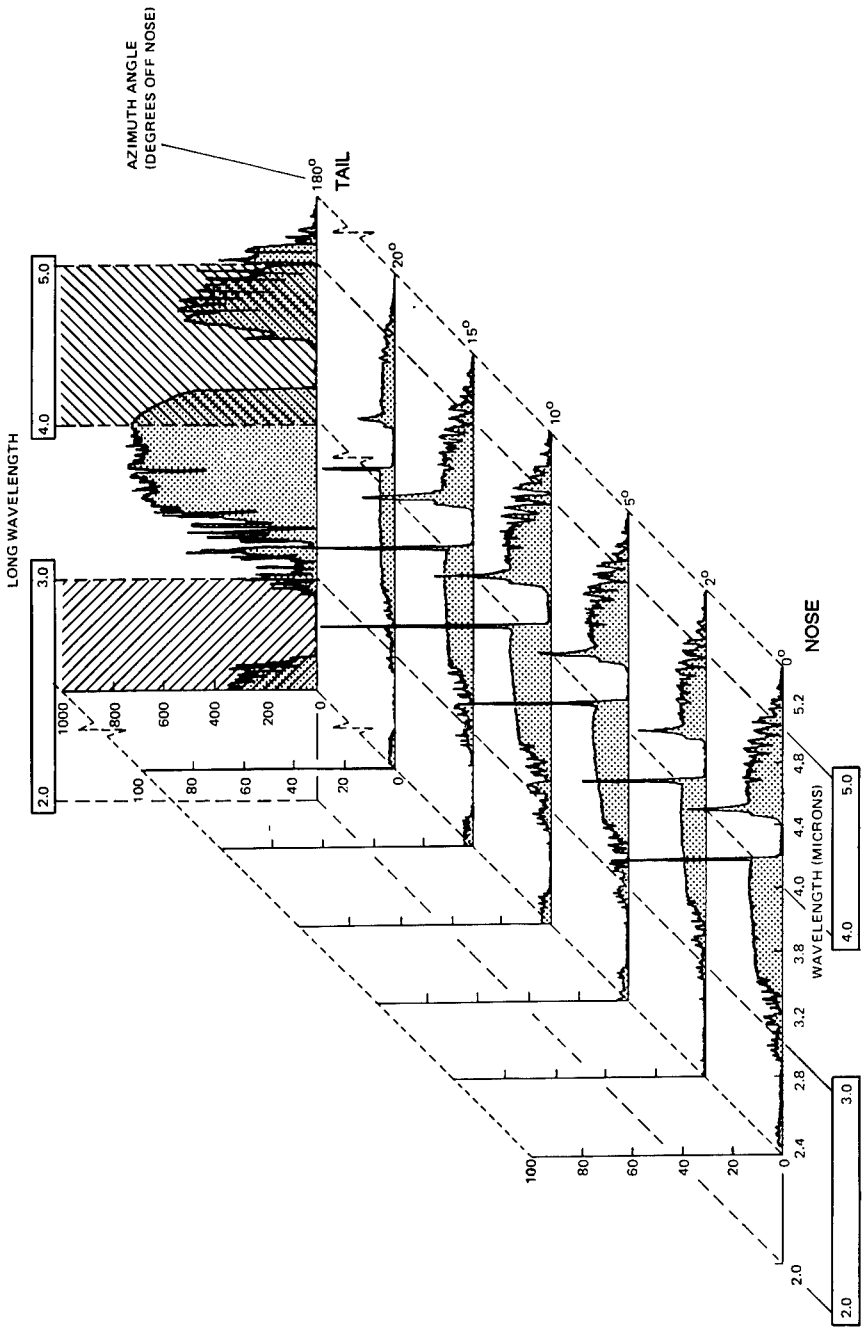

Fig. 4.6 Variation of aircraft signature with aspect angle.

4.3.2 Design Techniques

An example of a solid pyrotechnic IR flare is shown in Fig. 4.7. The purpose of the major components shown are as follows: The cartridge case provides environmental protection for the flare prior to ejection and serves as ejection tube. The ejector charge is contained in the pressure cartridge and is usually an electrically initiated commercial gunpowder charge. All modern flare ejector cartridges can withstand at least 1 W of power indefinitely without firing.

The obturating piston seals the expulsion gases behind the pellet and also prevents premature ignition. The safing and initiating mechanism ignites the flare after it clears the case. The end cap retains the flare in the case and serves as an environmental seal.

Flare Chemistry. The energy radiated by the flare's plume is provided by a pyrotechnic reaction. Pyrotechnics provide a high energy density and good storage life at a moderate cost. The most commonly used pyrotechnic composition is made of atomized magnesium powder and polytetrafluoroethylene (PTFE) resin. This is a very high energy fuel with solid combustion products for good radiation efficiency. The combustion reaction in the absence of air is generally considered to be

$$2Mg + C_2F_4 \rightarrow 2MgF_2 + 2C + \text{heat} .$$

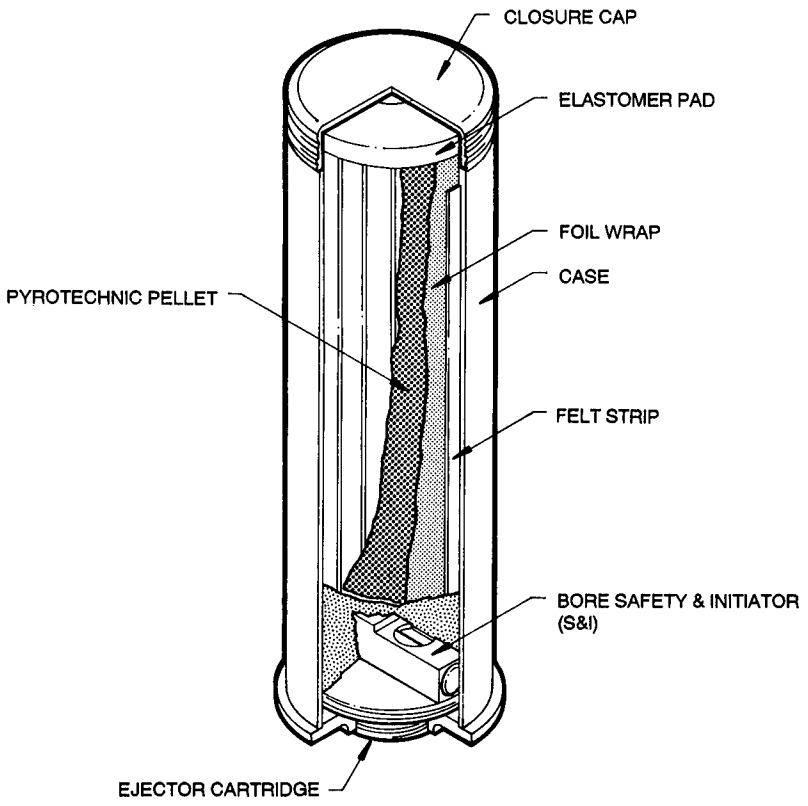

Fig. 4.7 Components of a conventional flare.

The flare composition is formulated with an excess of magnesium fuel. The excess magnesium reacts with atmospheric oxygen to produce magnesium oxide and additional heat energy. A typical fuel formulation would have a heat of combustion of about 7500 J g^{-1} in the absence of air and about twice that when burned in air. Under certain conditions, a portion of the carbon may be oxidized to either CO or CO_2.

Approximately twice the magnesium that would be normally required for a stoichiometric ratio is often used. The excess magnesium is vaporized by the initial reaction and subsequently consumed by reaction with atmospheric oxygen. Fuel-rich mixtures also burn more predictably at low pressures. Atomized magnesium powders are the most widely used because of their uniformity of shape and minimal surface oxidation. Ground magnesium particles can be used in ignition mixes for a faster burn rate and occasionally in the basic flare material itself.

The PTFE resin is a commercially available molding powder. The PTFE particle size has a significant effect on burn rate. This is the only significant performance consideration when choosing the oxidizer.

Synthetic rubber compounds or other polymers are added to bind the flare materials together more firmly after consolidation. Consolidation can be accomplished either by compression of the dry powder in a die cavity or extrusion. In either case, dry powdered flare material is formed into a solid grain by pressures exceeding several hundred atmospheres. Solvent casting techniques, such as those used in the preparation of large solid propellant rockets, are also occasionally used to form flare pellets.

Binder compounds may also be chosen because they contribute to the flare performance by providing hydrocarbons for additional atmospheric combustion. Fluoroelastomer binders contribute to the anaerobic reaction by donating fluorine to the magnesium. In other applications, the binder may contribute high-emissivity particulates to enhance radiant efficiency.

Certain fabrication methods, such as extrusion, also require greater amounts of the binder to serve as lubricant during consolidation. Flares made this way are usually stronger than pressed flares. They are also slightly less energetic because the additional binder must displace either fuel or oxidizer. Most applications require a minimum tensile strength of the order of 1 MPa to withstand the flight environment.

Figure 4.8 shows the components of a functioning flare in flight. After the formation of the initial anaerobic combustion products, the magnesium vapor oxidation takes place in mixing region at the surface of the luminous zone. The luminous zone is the region where the hot combustion products yield their thermal energy via mixing with the atmosphere and radiation. The radiant performance characteristics can be approximated by those of continuum radiation in accordance with the well-known Planck equation:

$$L_\lambda = \frac{1}{\pi\lambda^5} \frac{C_1}{\exp\,(C_2/\lambda T) - 1}\,, \tag{4.1}$$

where

L_λ = flux density per unit solid angle per unit area at the wavelength λ (sterance)

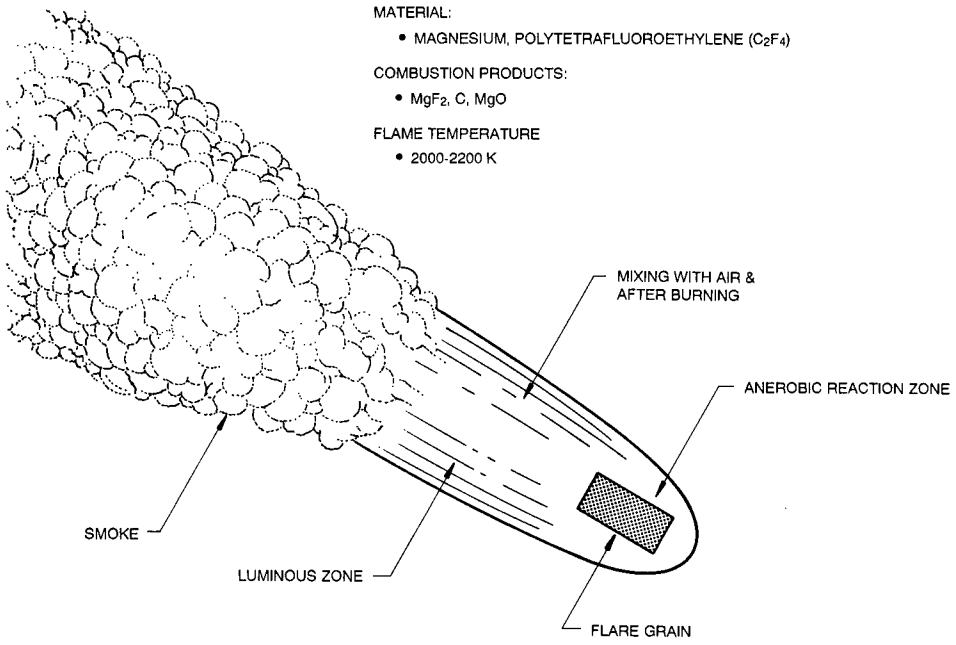

Fig. 4.8 Flare in airstream.

C_1 = first radiation constant, 3.7415×10^4 W cm^{-2} μm^4
C_2 = second radiation constant, 1.43879×10^4 μm K
λ = wavelength in micrometers
T = temperature in kelvins.

Because the particulate combustion products are still present in the flare's wake after cooling, they appear as smoke. This smoke is an unavoidable by-product of efficient chemical flares.

At high speeds, the combustion heat loss is dominated by atmospheric mixing and dilution, whereas under slow speeds or static conditions the heat loss is primarily through radiation. Chemical flares are extremely inefficient radiation sources at most aircraft speeds. It is only their high energy density that makes them the decoy radiation source of choice.

A representative spectrum of a Mg/PTFE decoy is shown in Fig. 4.9. The slight bulge in the spectrum in the CO_2 radiation band results from partial oxidation of the carbon in the binder. This effect can be slightly enhanced through the use of certain additives.

Intensity Estimates. Although Eq. (4.1) could be used to predict the performance of a flare in flight, it is difficult to use because the radiating surface area is rarely known. A more useful empirical relation for the intensity (pointance) is derived from energy considerations and has the following form:

$$I = \dot{m} E_\lambda \ , \tag{4.2}$$

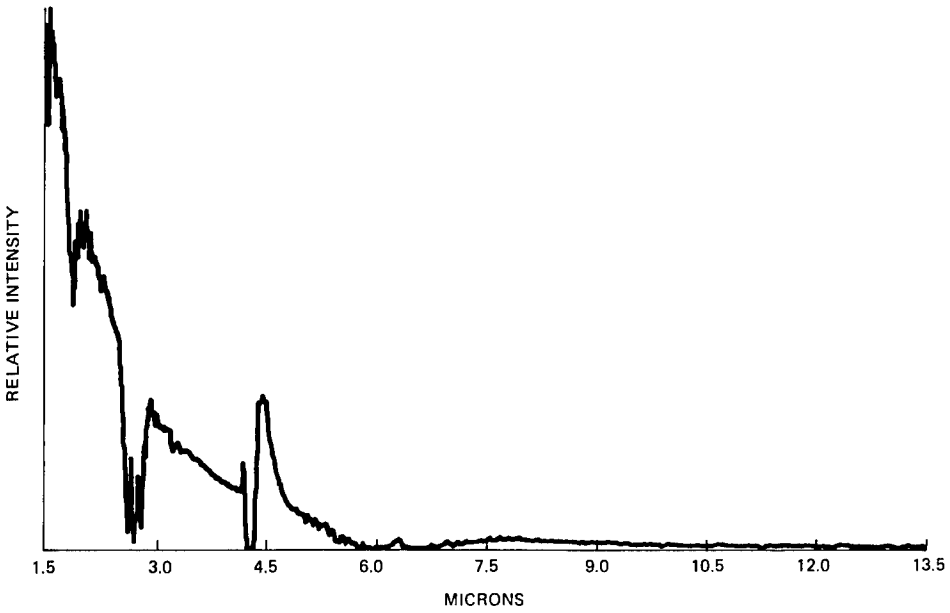

Fig. 4.9 Typical Mg/PTFE spectral distribution.

where $\dot{m}$ is the fuel combustion rate in grams per second and E_λ is the specific intensity in J g^{-1} sr^{-1}:

$$E_\lambda = \frac{1}{4\pi} H_c F_{\lambda,T} d_e d_w d_s \ , \tag{4.3}$$

where H_c is the fuel heat of combustion in joules per gram and d_c is the static radiant emittance factor. Under many circumstances it is about 0.75.

The windstream degradation factor d_w has been experimentally derived for a variety of flight conditions. It is most commonly expressed as the ratio of the peak static intensity to the peak dynamic intensity. This value may range from 0.1 at near sonic speeds to 1.0 at static conditions. It is further discussed in the section on "Wind-Stream Effects on Intensity."

The plume shape factor d_s relates the observed intensity as a function of aspect angle. It is roughly the ratio of the projected radiant area at the viewing angle to the tail aspect radiant area. It usually ranges from about 2.0 to 1.0 for conventional flares. It is sometimes combined with the wind-stream factor.

The function $F_{\lambda,T}$ is the fraction of the total radiation in the band of interest. For most flares, it approximates the integral of Plank's formula in the band of interest divided by that of the Stefan-Boltzmann law:

$$F_{\lambda,T} = \frac{1}{\varepsilon\sigma T^4} \int \frac{\varepsilon_\lambda C_1}{\lambda^5} \frac{1}{\exp(C_2/\lambda T) - 1} \, d\lambda \ , \tag{4.4}$$

where

ε = the average emissivity (usually assumed to be 1.0)
ε_λ = emissivity at the wavelength λ
σ = the Stefan-Boltzmann constant 5.6697×10^{-12} W cm^{-2} K^{-4}.

By way of example, a typical pyrotechnic fuel might have a combustion energy of 15,000 J g^{-1}. Assuming its spectral distribution corresponds to that of a blackbody at 2000 K, $F_{\lambda,T} = 0.176$ for the 3- to 5-μm band. Using $d_c = 0.75$, $d_w = 0.1$, and $d_s = 1.0$, the hypothetical specific intensity is

$$E_\lambda = \frac{1}{4\pi} \times 15{,}000 \times 0.176 \times 0.75 \times 0.1 \times 1.0 = 15.8 \text{ J g}^{-1} \text{ sr}^{-1}. \quad (4.5)$$

Chemical flares waste a vast portion of their combustion energy, however, they still represent the most efficient source available. A typical energy storage density is of the order of 15,000 J g^{-1}. A density of the order of 1.7 g cm^{-3} yields a volumetric storage efficiency of 25,000 J cm^{-3}. A typical flare for a fighter aircraft consumes its fuel at a rate of more than 100 g s^{-1}. This means more than 2.5 MW of energy is produced before convective heat losses.

Figure 4.10 shows the heat of reaction of some other high-energy pyrotechnic mixtures that can be considered for decoy applications. A Mg/PTFE compo-

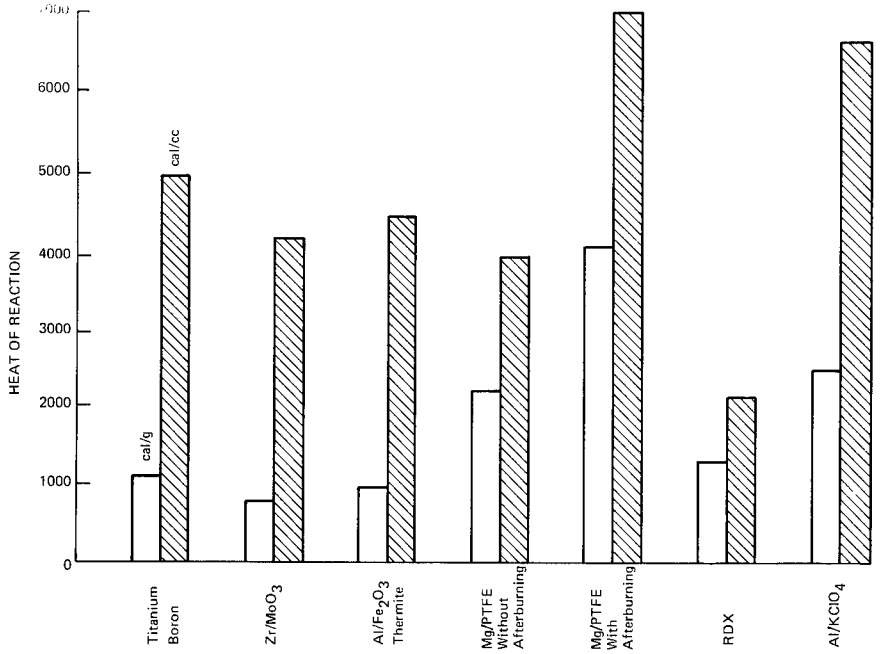

Fig. 4.10 Selected reaction energies.

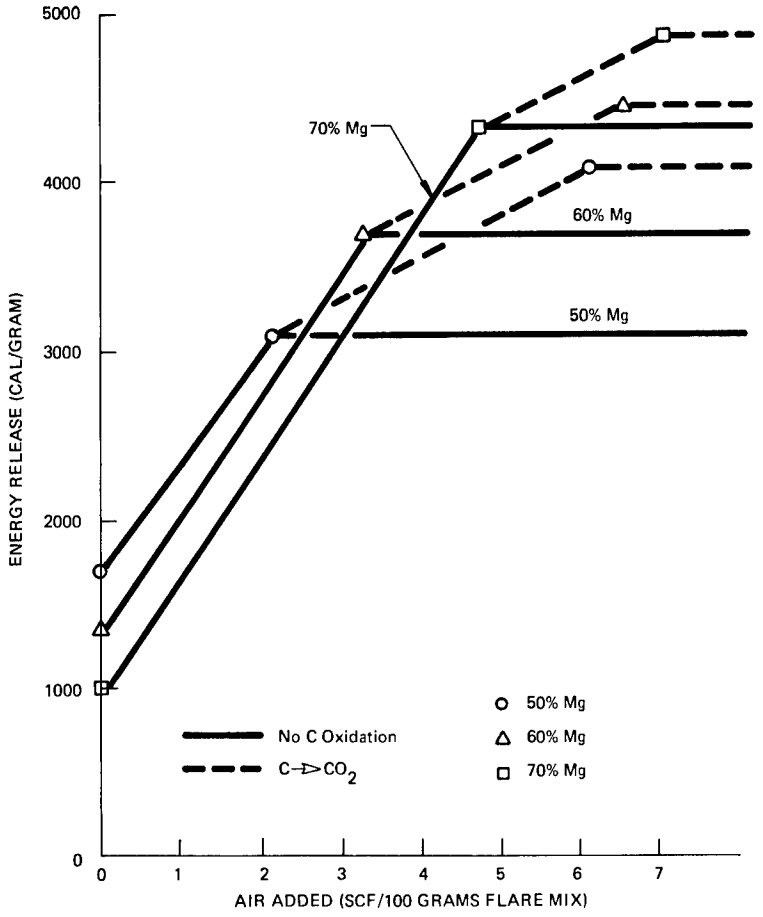

Fig. 4.11 Energy release as a function of air added for Mg/PTFE fuels.

sition with and without afterburning has been included for comparison. The other mixtures are stoichiometric.

The effect of afterburning of the excess magnesium is illustrated for three representative compositions of that type in Fig. 4.11. The figure shows the amount of ambient air mixing for a given flare fuel quantity. The choice of formulation is influenced by the application. Low-altitude, low-speed applications can rely greatly on ambient air for the required oxidizer, and combustion proceeds until nearly all of the available fuel is consumed. At higher altitudes and speeds, the combustion is less likely to proceed all the way to completion. Therefore, compositions with a higher portion of their oxidizer included in formulation become a better choice at high altitude.

Altitude Effects. In addition to the combustion efficiency issue, other factors affect flare performance at high altitudes. The term $\dot{m}$ from Eq. (4.2) can be determined by the following relation:

$$\dot{m} = \rho_f S r \ ,$$

where

ρ_f = fuel density in the pyrotechnic pellet
S = burning surface area
r = linear rate of recession of the burning surface

Flare fuels, like other solid pyrotechnics, burn at a rate that is also influenced by ambient pressure. In general, these fuels follow the relationship:

$$r = aP^n \ ,$$

where

r = the linear burn rate
a = an empirical constant
P = the ambient pressure
n = an empirical constant.

The variable n is also referred to as the *burn rate exponent.* It is usually less than unity. Reported values of the burn rate exponent range from 0.1 to 0.8. Most flare compositions have a linear burn rate in the range of 2.5 to 7.5 mm s^{-1}. Although the lower ambient temperature may have some effect on the afterburning reaction in the luminous zone, the primary effect of increasing altitude is considered to be the reduction in burn rate caused by the reduced ambient pressure. This reduced burn rate translates directly into a reduced fuel consumption rate and hence a reduced rate of energy release. The burning rate exponent is strongly affected by particle size of both of its major ingredients. High-altitude flare compositions use finer particle sizes of magnesium, not more than 100 μm, and coarser PTFE particles, 200 μm or more, to minimize the effect.

The burn rate at high altitudes is complicated by the fact that the forward surface of the flare experiences stagnation pressure equal to $\frac{1}{2}\rho_a v^2 + P$, where ρ_a and P are the ambient density and pressure, respectively. This may have the net effect of slightly increasing the burn rate on a portion of the surface at high speed. This effect is rarely noticed in flight tests because the flare slows down too quickly. However, the increase in burn rate with dynamic pressure has been observed in wind tunnel tests.

Wind-Stream Effects on Intensity. The wind-stream effects have the most dramatic impact on flare performance. The performance degradation is roughly in accordance with the curve shown in Fig. 4.12. This performance leads to the normal rule of thumb that conventional flares are designed so that their performance at sea level under static conditions is 10 times the required intensity under dynamic conditions. The apparent radiation temperature of the continuum radiation generally increases slightly with wind speed. This is attributed to the stripping away of the cooler radiating particles at the outer edge of the plume, leaving only the hotter core. Note that this increase in apparent temperature is observed only with respect to the spectral characteristics of the flare. The overall radiant intensity is severely degraded by wind speed at all wavelengths.

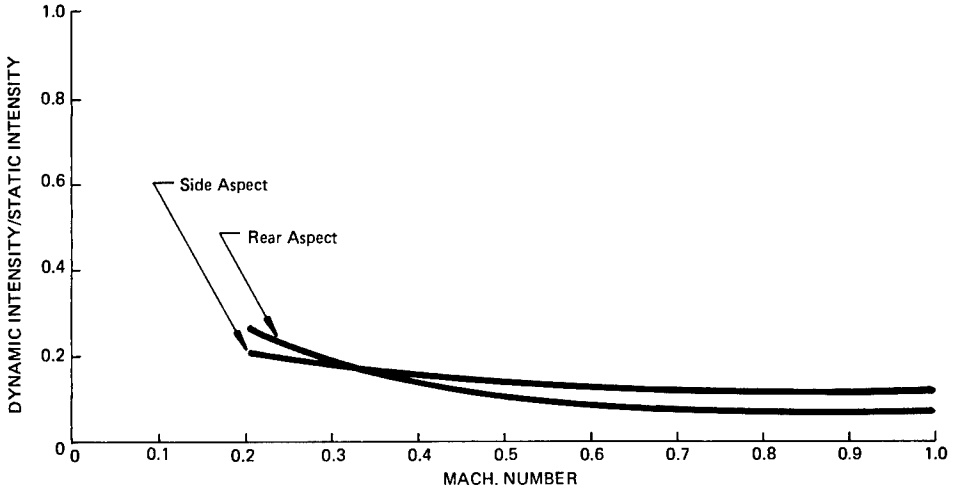

Fig. 4.12 Wind factor versus Mach number radiometer, parallel orientation.

Conventional Flare Trajectories. The deceleration of a flare can be represented by the equation

$$\frac{dV}{dt} = \frac{\rho_a g v^2}{2\beta} , \tag{4.6}$$

where dv/dt is the drag deceleration, ρ_a is the atmospheric density, v is the velocity, and β is the ballistic coefficient, which is defined as

$$\beta = W/C_d A_{\text{ref}} ,$$

where W is the flare weight, C_d is the drag coefficient, and A_{ref} is the reference area for the drag coefficient.

Flare separation relative to the dispensing aircraft is shown for a variety of flight conditions in Figs. 4.13(a) through 4.13(d). These estimates are for a cylindrical flare with a mass of 500 g, 30 m s^{-1} downward ejection, and a burn time of 4 s. Those characteristics are similar to many operational flares. The data were generated by numerical integration of Eq. (4.6) with continuous correction for the change in β as the flare burns. The value β was also adjusted for the change in drag coefficient when the decoy transitioned from supersonic to subsonic flow. This method has shown agreement to within 10% of flight measurements. Flare trajectory calculation is strongly affected by the burn time because the deceleration is very high near burnout. Therefore, the examples shown are not useful for flares with burn times greatly different from 4 s. All of the variations are smooth and interpolation between plots can be expected to provide data suitable for preliminary analyses. Heavier flares than the example do not slow down as quickly, therefore, the rate of separation is slower. Trajectories for flare masses other than 500 g can be estimated by

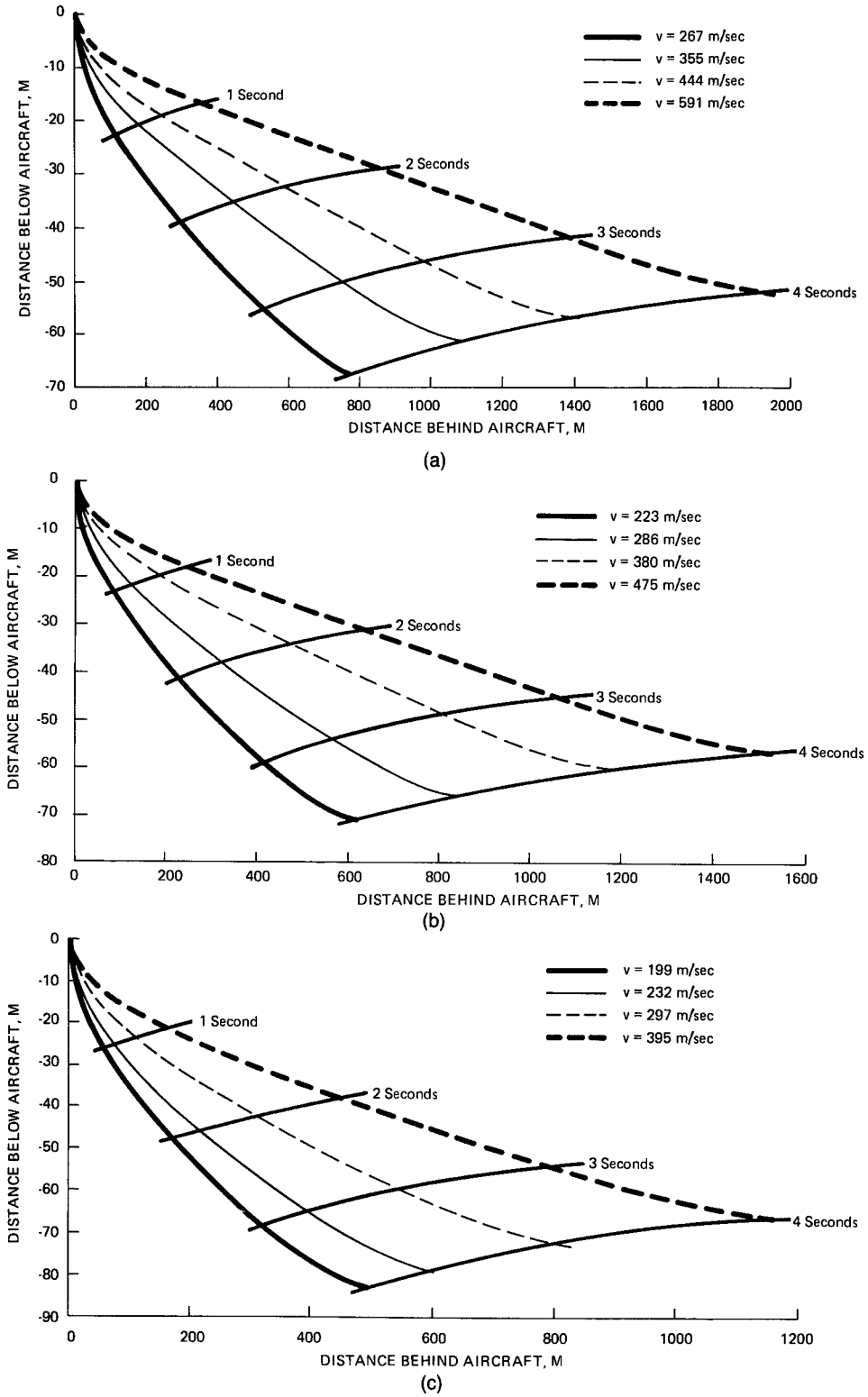

Fig. 4.13 Flare separation for selected airspeeds at altitudes of (a) 12 km, (b) 6 km, (c) 3 km, and, on following page, (d) 1.5 km.

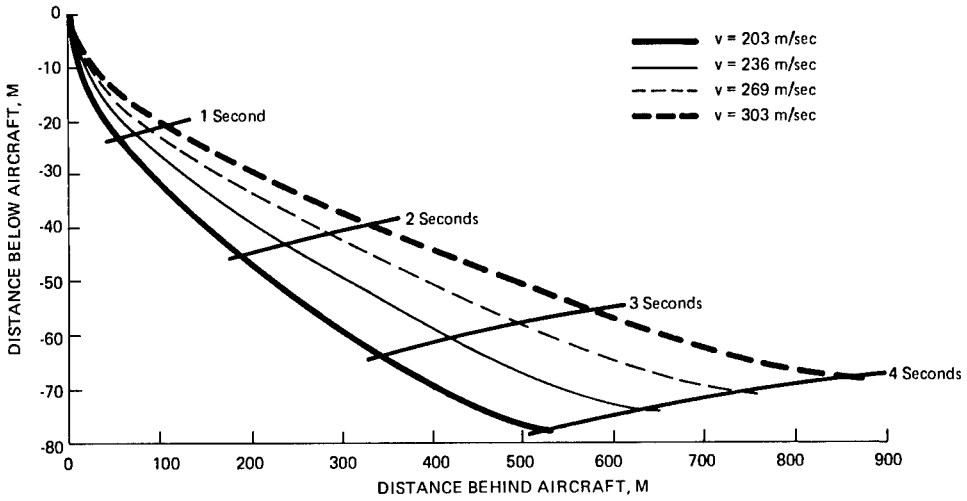

(d)

Fig. 4.13 *(continued)*

choosing a curve corresponding to the same velocity but at a different altitude so that the ratio of air density and flare mass remains the same.

Aerodynamic Designs. A significant improvement in flare trajectory performance can be obtained by orienting the flare into a lower drag orientation and increasing its weight. Aerodynamic and propelled flares are being developed to overcome the potential discriminant of the flare rapidly falling behind the aircraft. One method of achieving improved aerodynamic performance is shown in Fig. 4.14. In this example, the flare fuel is burned internally in a rectangular cylinder. The combustion products are ducted out through a shroud that serves as a mount for the stabilizing fins. The trajectory is enhanced by the reduction in drag area, which is achieved by orienting the flare pellet parallel to the wind stream. Further benefits come from the increased mass of the metal structure. Also, the base drag is reduced by venting the flare products aft into the wake.

Another advanced design uses a separate rocket motor to propel the flare. This design also has metal fins for stability, but incorporates an internal solid propellant rocket motor. An aerodynamic contour is applied to a metallic nose to reduce the aerodynamic drag. The rocket provides sufficient propulsion to accelerate the flare ahead of the aircraft even at near sonic speeds.

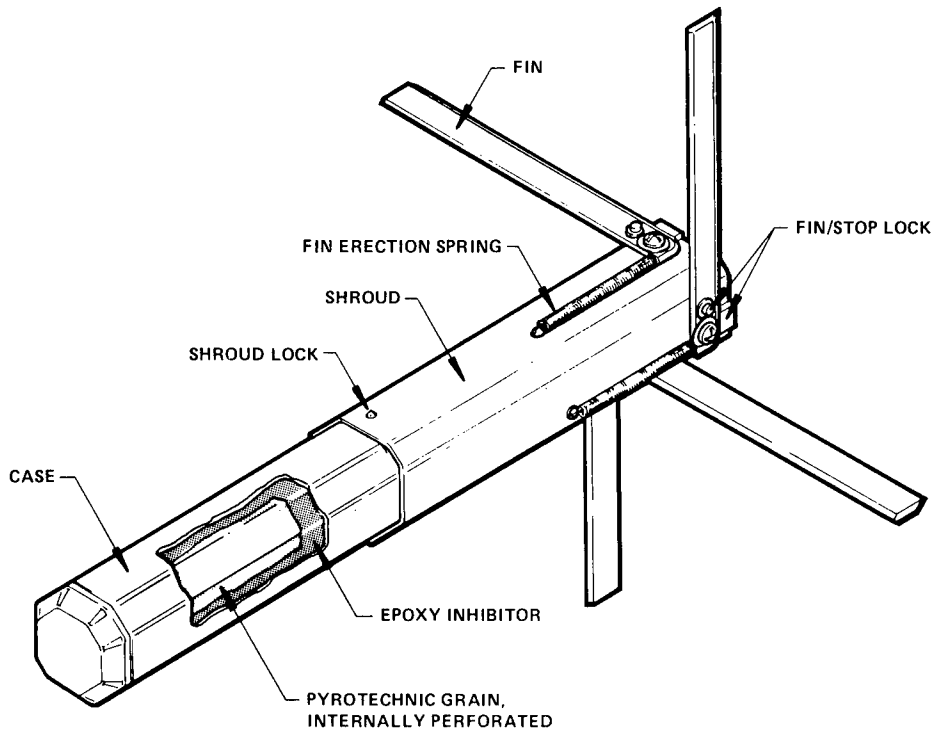

Fig. 4.14 MJU-31/B aerodynamic flare.

4.3.3 Development Process

During the development process performance measurements are made over a wide variety of conditions. Initially flare concepts are subjected to sea-level static intensity measurements as a matter of convenience. These serve the primary purpose of confirming the burn rate history of the fuel. Such tests are generally followed by wind-stream measurements to determine performance under simulated flight conditions. After confirmation of the flare safety, flight tests are conducted to quantify decoy performance under operational conditions. Flight tests normally encompass in-flight IR measurements, verification of safe separation, and decoy effectiveness.

A common intermediate step in the development process consists of test launching the flares from a high-speed rocket sled. This test is particularly useful to verify the trajectory of less conventional designs, such as aerodynamic flares or upward firing dispensers. The rocket sled provides an opportunity to determine flare performance under realistic high-speed flight conditions without risking an aircraft. The drawbacks to sled tests are that the per unit test cost is higher than that of aircraft flight testing and that high-altitude conditions cannot be simulated.

Static Tests. Performance requirements always include a particular radiant intensity history as a function of time. Early in the development process, it is

more useful to perform the measurements in a manner that allows the evaluation of design changes rather than to determine the absolute performance under flight conditions. Typically, flare designs evolve based on static performance measurements as a matter of convenience. During that time, Eq. (4.2) is used to estimate performance. The static performance requirement is related to the flight performance with the aid of Eq. (4.3). The factor d_w is chosen to be 0.1 for most developments but may be further refined if specific performance data is available.

Several complications make even static measurements less precise. Many of these are not encountered during IR measurements of other types of sources. Because the radiation of the flare comes from the luminous plume rather than the pellet itself, it is necessary to test under conditions that allow for consistent flow of the combustion products away from the flare. Otherwise, variations in either the plume shape or smoke obscuration may introduce measurement-to-measurement variations that may overcome design variations.

The flare is destroyed during the process, therefore no test can be exactly duplicated. Each flare has slightly different burn characteristics. Several flares of a similar configuration must normally be tested before conclusions can be drawn. This can be time consuming and expensive.

Another problem unique to the flare development process is the fact that the flare intensity changes rapidly with time. Many commercially available radiometers do not have adequate frequency response. Measurements are normally made with fixed band radiometers. However all band measurement methods result in further approximations. For example, the radiometer in general has a different relative sensitivity across the band of interest than that of either the threat or any subsequent instrument used.

If performance is specified in more than one band, simultaneous measurements can be made using one radiometer for each band. Filter wheel scanning radiometers can also be used for multiband measurements at some loss in intensity history. High-speed Fourier transform spectrometers (FTSs) are becoming more available, resulting in greater usage of this type of instrument during the development process. Figure 4.8 was generated using such an instrument.

The requirements for flare measurement are unique in the IRCM community. The hazardous nature of the test specimen and the enormous quantities of smoke generated prevents measurement in the typical optical laboratory. These measurements are either performed out of doors or in test tunnels with extensive forced air ventilation. Careful attention to the development of efficient and uniform air flow is required in indoor test facilities to avoid obscuration of the flare plume by smoke. Additional care must also be taken to avoid the measurement of reflections from the test tunnel walls. Normally, the flare pellet is removed from the ejection cartridge and mounted on a test stand. Ignition is accomplished with an electric match. The protective tape wrappings are left on the flare pellet prior to ignition.

The transient nature of the flare radiation and the presence of very intense signals generally can be measured best using thermal detectors. Most static measurements are made using pyroelectric radiometers. These radiometers generally incorporate fixed band interference filters to restrict the instrument sensitivity to the band of interest. Because a wide field of view, typically 10

to 15 deg, is required to observe all of the plume simultaneously, no collective optics are used. The field of view is generally defined by the instrument aperture and the detector geometry. Because most aircraft decoy measurements are made at wavelengths of 5 μm or less, the background is essentially constant for both calibration and measurement, and no special precautions are necessary.

The radiometer can be calibrated by comparing the measurement of a blackbody reference source to that of the flare. Most laboratory calibration sources are limited to a maximum temperature of 1273 K (1000°C), a small error is introduced by the fact that the source temperature of the flare is closer to 2000 K. This variation is likely to be constant from one static specimen to the next. Again, the primary purpose of static measurements is to develop a consistent and conveniently reproducible comparative measurement procedure.

The instrument is calibrated by the following procedure. The quantity R_c is determined by

$$R_e = \frac{I_b}{V_b r^2} , \tag{4.7}$$

where

R_e = instrument responsivity in W sr^{-1} m^{-2} V^{-1}
I_b = intensity of the calibration standard in W sr^{-1}
r = distance from the source to the detector in meters
V_b = radiometer voltage recorded when viewing the source.

During the calibration process, care should also be taken to verify the instrument linearity. This can be done by determining the quantity R_c as a function of either several different values of I_b or for several different values of r^2. The preferred method is to fix the measurement distance and change the source intensity using a reference source with an adjustable aperture.

After calibration, the apparent decoy intensity is determined by the following relation:

$$I_d = R_e V_s r_d^2 , \tag{4.8}$$

where r_d is the radiometer to decoy range and V_s is the voltage associated with the decoy measurement.

Multiple instruments can be used in parallel when data in different bands are required. It is desirable to locate these as close together as possible to ensure that the same plume aspect is observed by each instrument. Other radiometers incorporate spinning filter wheels.

The orientation of the flare pellet affects the shape of the flare plume when flares are tested in still or slowly moving air, because the velocity of the combustion products leaving the surface of the flare is large relative to the airstream. Thus, the plume extent is greatest in a direction normal to those facets of the flare with the greatest surface area. Flares should be tested in a consistent orientation relative to the airflow and the radiometers. Specific requirements for the mounting of the flare pellet during static measurements should be included in written test procedures.

Atmospheric absorption can significantly alter the apparent radiation intensity of the flare for measurements over a path of 100 ft or more. The situation can also occur over shorter measurement ranges when the band of interest encompasses an atmospheric absorption band, as is often the case in the 4- to 5-μm region. Correction is usually made using transmission coefficients obtained via one of the LOWTRAN series of absorption models.

Flight Tests. Flight tests are essential to the verification of a flare design's in-flight signature, trajectory, and decoy effectiveness. This is generally performed over an ordnance range using a chase aircraft carrying specialized instrumentation. The flight instrumentation is usually installed in an aircraft pod, which is mounted on an external stores station of a two-seat aircraft. Because of the expense of flight tests, several instruments are mounted in the instrumentation pod. Normally, this instrumentation consists of one or more radiometers, an automatic tracking device, and several captive missile seeker heads. On-board recording equipment is used to record the flare signature and the captive seeker tracking behavior. Control of the instrumentation is carried out by a dedicated operator in the second cockpit of the aircraft.

An example of such a system is the Supersonic Airborne Infrared Measurement System. This pod, developed by the U.S. Air Force Armament Division at Eglin Air Force Base, Florida, is shown in Fig. 4.15. The radiometers and tracking equipment are mounted behind a sapphire dome. The captive missile seekers are mounted external to the pod structure parallel to the flight

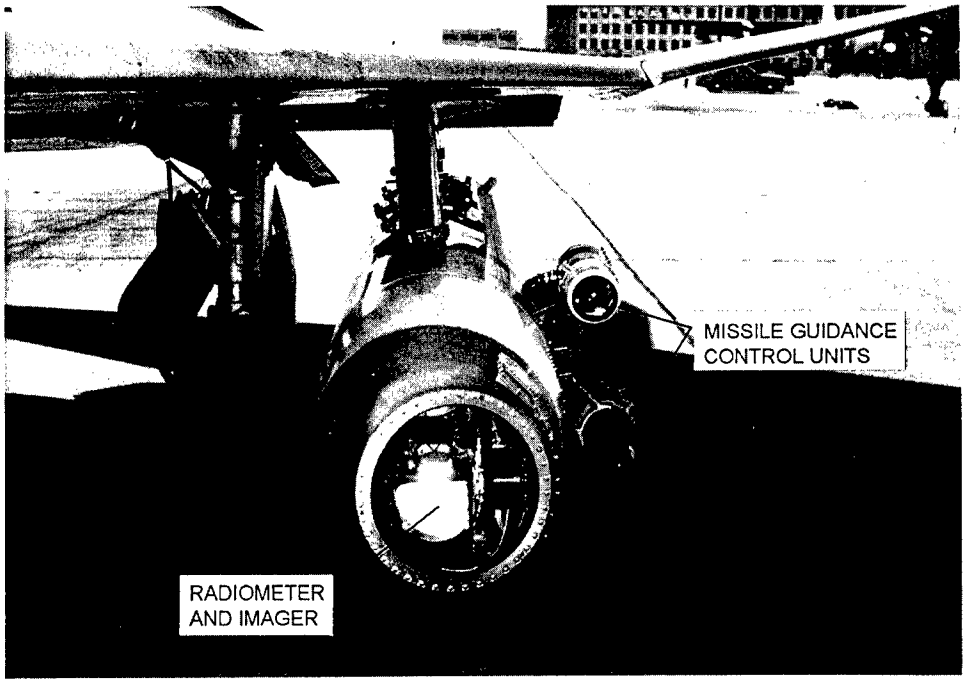

Fig. 4.15 Supersonic airborne infrared measurement system.

direction. Such an arrangement provides for good measurement capability of aircraft and flare signatures near tail aspect. The pod can be mounted backward on the instrumentation aircraft to make measurements from the forward aspect. However, measurements are somewhat difficult at other than fore and aft aspects with this type of configuration. This is particularly true for the captive seekers, which are mounted in a fixed orientation relative to the flight path. This results in an unrealistic geometry for seeker angles of more than about 30 deg.

The preferred approach for measurements at larger aspects is to mount all of the instruments in a large turret at the front of the pod. A well-known example of this approach is the U.S. Navy's ATIMS 3 pod.

Accurate range information is essential to relate the intensity at the airborne radiometer to source radiant intensity. A laser rangefinder mounted on the instrumentation pod provides the most direct measurement of the range to the flare dispensing aircraft. Alternatively, the flight test can be conducted over an instrumented range so that either ground-mounted radar or photographic instrumentation can be used.

Laser rangefinders and radar systems are suitable for measuring the separation between the dispensing and measurement aircraft, but they are not suitable for determining the range between the flare and the measurement aircraft. Various methods have been used with varying degrees of success to estimate the flare-to-radiometer distance during flight tests. A widely used method is to dispense the flare within sight of a ground-based photometric system. This allows accurate determination of the flare trajectory relative to the dispensing aircraft for a particular flight condition. Extrapolations to other flight conditions are then made using digital trajectory models with compensation for different altitudes and air speeds. Once a flare's trajectory is characterized, computation of the source signature can proceed using the trajectory model and the measured aircraft separation at flare launch.

The flare's in-flight performance characteristics are then estimated using the apparent radiant intensity, the calculated flare trajectory, the calculated measurement range, and the calculated atmospheric absorption, again using the LOWTRAN atmospheric absorption model. This process introduces several opportunities for errors when it is necessary to derive actual metric data. Often it is difficult to get close agreement between different test series and even harder to get agreement with different test instrumentation and facilities.

Although the standard practice for reporting aircraft measurements is on logarithmic scales, inflight flare measurements should be reported on linear scales. Flight measurements of flares are used to evaluate the efficiency of candidate designs during the development process. Generally, this includes numeric integration of the flare intensity as a function of time. This is made substantially more difficult by reporting the data in a logarithmic format.

A more useful test may be to evaluate the flare's breaklock performance rather than its absolute intensity. This requires that the flare be dispensed under realistic flight conditions from its intended aircraft host. Captive seekers mounted either on ground-based tracking platforms or on airborne pod instrumentation, as previously described, can be used for this purpose. The primary shortcoming of captive seeker tests is that they do not simulate the changing geometry of the engagement as the missile closes on the target

complex. This results in increasingly unrealistic decoy-to-target signature ratios as the two sources separate. Also, the rate of apparent angular separation is different from the perspective of the approaching missile during captive seeker tests. This makes evaluation of the possible reacquisition of the aircraft by the seeker after flare burnout difficult. However the results become increasingly more accurate at longer ranges. These tests are usually supplemented by computer simulations of the missile performance based on known characteristics and measured flare performance.

Live firings against either drone aircraft or other simulated targets are carried out in those situations that warrant the expense. Such tests are useful for verifying actual decoy performance under specific conditions and may also provide design feedback when enlightened by further analysis.

4.3.4 Tactical Implementation

Ideally, decoys are launched at the precise time and location to maximize the threat miss distance. This condition can only be obtained with specialized warning systems or tactics wherein the decoys are dispensed only when a threat is known to be imminent.

Launch Warning. The limited quantity of expendables that can be carried on most combat aircraft requires that they be efficiently employed. Ideally, decoys would only be launched when a threat is imminent. Occasionally, the aircrew may visually acquire the threat in time to launch the decoy, but normally reactive dispensing in the presence of a threat can be accomplished only with the aid of an automatic warning system. The key figures of merit for a warning system to initiate decoy dispensing are warning time and false alarms. Warning times greater than the burn time of the decoy are not necessary, but most decoy systems require at least 1 to 2 s of warning prior to intercept. Without this minimum warning it may not be possible to place a functioning decoy in a trajectory that will preclude missile intercept in time to be effective. Current aircraft decoy dispenser installations vary in capacity from 15 to 480 flares. Most combat aircraft loadings are between 30 and 60 flares. This means that most operational installations can tolerate only a few false alarms.

Often the tactical situation is such that other warning resources are available. For example, a threat fighter aircraft may first use a radar or laser rangefinder to verify if a target is within range. If the target is equipped with suitable radar or laser warning, then decoys may be efficiently used even if an IR-guided missile has not been specifically detected.

Prophylactic Deployment. It is also possible to dispense decoys in anticipation of an IR, missile threat if sufficient stores and knowledge of the threat's likely location are available. The best example of this is the dispensing of flares at timed intervals while attacking heavily defended targets. Attack aircraft often dispense flares at intervals approximately equal to the burn time. Such a tactic may either break track or deny acquisition by the missile seeker.

4.3.5 Dispensers

Most flares are ejected pyrotechnically. The storage canister also serves as the ejection chamber. The flare cartridges are loaded into a magazine that is mounted

to a breech plate, which in turn is mounted to the aircraft structure. A typical dispensing system is the AN/ALE-47 countermeasures dispenser. This dispenser is also capable of dispensing a variety of other types of decoys, such as chaff or rf expendables. The system incorporates electronic controls and computational algorithms to optimize the dispensing rate as a function of the tactical situation. The dispenser processor interfaces with both missile and radar warning systems. It also obtains flight conditions directly from the aircraft Military Standard 1553 data bus.

4.4 SHIPBORNE DECOYS

The adaptation of IR seekers to antishipping missiles encouraged the development of IR decoys to protect ships. A wide variety of IR decoy types have been developed for shipboard use. Some of the techniques and tactics used are similar to those of aircraft decoys. Others are substantially different because the threat has additional modes of operation and the target signature is more complex.

4.4.1 Threat Considerations

The launch range of many antishipping missiles is greater than the tracking range of the seeker. These threats rely on some other form of guidance such as radar or inertial navigation to place the IR seeker in position to acquire the target. The IR guidance can then take over in the terminal phase after the target is confirmed. This technique makes possible long-range missiles with the terminal accuracy of IR guidance.

Acquisition after launch provides additional tactical deception opportunities because decoys can be used to avoid target lockon. With adequate warning, it is possible to place a decoy in a position where it is more likely to be acquired by the threat than is the intended target. This tactic, called *distraction,* is an important complement to the seduction tactics, which can only be used after the target is acquired. Risk to the target is avoided by distracting the seeker prior to lockon.

The seduction countermeasure approach can still be used later in the engagement if distraction efforts are unsuccessful. Seduction techniques seek to transfer the threat aim point from the target to decoy. Seduction techniques utilize decoys that provide a more attractive set of signature characteristics to the seeker. Seduction tactics can be made more effective if the direction and time of arrival of the threat is known.

Threat seekers can utilize either mid- or long-wavelength bands. More sophisticated seekers may try to compare signatures in two different bands and preferentially attack targets with a predetermined spectral intensity ratio. Typically, scanning detectors are used for the tracking function. These can operate in either the 3- to 5-μm band or the 8- to 14-μm band. The shorter wavelength seekers can more easily detect hot spots, such as the exhaust stack or equipment areas that generate heat. Longer wavelength seekers may sense the entire superstructure of the vessel.

The threat tracker often incorporates some form of automatic gain control to adapt to the background level. The target may then appear as either positive

or negative in contrast to that background, depending on the target history and the environment.

4.4.2 Decoy Requirements

Signature Considerations. Ship signatures can be estimated using blackbody equations. The accuracy of the calculations for any specific situation can be improved by partitioning the target into radiant facets when precise knowledge of the surface temperatures and emissive properties is available. Some portion of the background will nearly always be in the seeker's field of view. Because the detectable signal level is the contrast between the target and the background, it can be assumed that the apparent signature will be influenced by the instantaneous field of view and the signal processing. Both target and background can vary widely in signature magnitude and spectral content. This means that the seeker must accept as targets a wide range of signals.

Reflections from the ocean surface have the effect of altering the apparent shape or spectral content of the target. Reflections can occur in calm seas and in certain solar geometries.

Signature variations complicate matching of the target characteristics by the decoy. These same variations make discrimination against decoys more difficult. Decoy rejection may be particularly difficult during the acquisition phase when a distraction decoy may be the only object in the field of view.

Most ship signatures in the 3- to 5-μm range are less than 1000 W sr^{-1}. This mid-IR signature requirement is similar to that for an aircraft decoy. Such a signature level can be easily obtained with an aircraft style point source flare. Fuel efficiency is much greater in the relatively still wind conditions associated with the sea environment. Point source decoys can be useful against simple threats with poor spatial resolution. More sophisticated area decoys have been developed that provide a more realistic source size.

Both the ship and the surrounding ocean radiate strongly in the 8- to 14-μm band. The contrast is likely to be relatively small compared to the absolute magnitude of either source. The ship is usually warmer than the sea, but the discernible contrast level varies greatly with environmental conditions. For a given level of detector sensitivity, the maximum detection range is driven by the contrast level, the target size, and the seeker's instantaneous field of view. A large field of view includes a substantial amount of background radiation, which serves to dilute the target signature, thereby reducing detection range.

Under most conditions the contrast signature of a combat ship is less than 10,000 W sr^{-1} in the 8- to 14-μm band. This signature level can often be several times that of the 3- to 5-μm band. Decoy design requirements can be conservatively estimated from the ship's surface area, temperature, and emissivity by using blackbody calculations.

Decoy Placement. Distraction decoys should be placed where they are likely to be observed first by the threat seeker. If the direction and approximate time of arrival are known, it is generally effective to place the decoy 1 k or more from the target in the direction of the threat. If accurate threat bearing information is not available, distraction decoys should be positioned in multiple locations generally in the direction of the threat. Consideration must be given

to the ship's direction of travel, and in some cases the relative wind, so that the decoy remains in an effective location for the longest possible time.

Seduction decoys are placed so that they quickly appear in the seeker field of view. This is necessary to capture the attention of the seeker. After the seeker has transferred track to the decoy, the ship and decoy must separate in bearing relative to the seeker to avoid impact after overflight of the decoy. For floating decoys, the ship speed through the water and the threat bearing relative to the ship can be used to predict the rate of angular separation.

Decoy Persistence. Persistence requirements are driven by the missile time of flight and available warning. Seduction decoys can be effective with as little persistence as 20 s. Twice that time is often required for distraction decoys. Because fuel weight is normally directly proportional to function time, the decoy persistence requirement must be traded off against payload volume and cost.

4.4.3 Design Techniques

Many shipboard IR decoys rely on chemical combustion sources for their radiant energy. Existing designs encompass both solid and liquid fuel sources.

Chemical flares, similar to those used to protect aircraft, can decoy simple threats that track only in the mid-wavelength bands. The efficiency of flare fuels in the shipboard environment is much better than in the airborne situation because combustion and radiation take place at sea level in relatively modest wind conditions. This permits these simple decoys to be similar in size to aircraft decoys because the increased burn time requirement is largely offset by the greater radiant efficiency available in the ship-launched environment.

More sophisticated threats may require more accurate spectral matching. This usually is achieved at the expense of a lesser radiant efficiency. A decoy for a small combat ship, such as a coastal patrol vessel, may need as little as 1 kg of fuel. A larger combatant, such as a frigate or destroyer, may have a greater detection range and thus require greater decoy persistence and signature magnitude. Large ship decoys might easily require 10 to 20 times as much fuel.

Liquid-Fueled Decoys. These tend to have very good IR signature characteristics but are complicated. A pyrotechnic gas generator is used to expel the fuel through a nozzle where it is then ignited. The fuel burns in a plume that may extend several meters above the decoy. The decoy is supported on the ocean surface by a flotation assembly.

The fuel can be either a simple hydrocarbon or a more complicated chemistry, which has been chosen for its radiation spectral distribution. Most liquid fuels have a caloric output on the order of 30,000 to 40,000 J g^{-1} of fuel when burned in air. If 5% of the radiant energy is in the band of interest and if the decoy radiates in all directions, the efficiency of such fuels may be of the order of 150 J g^{-1} sr^{-1}. This suggests that a 10,000 W sr^{-1} decoy with a 30-s persistence would require about 2000 g of fuel.

The operational efficiency of floating decoys is further reduced by wind effects. The greater the wind speed, the greater the amount of air that is mixed with the flare plume. Overmixing of air results in poor combustion and cooling of the plume.

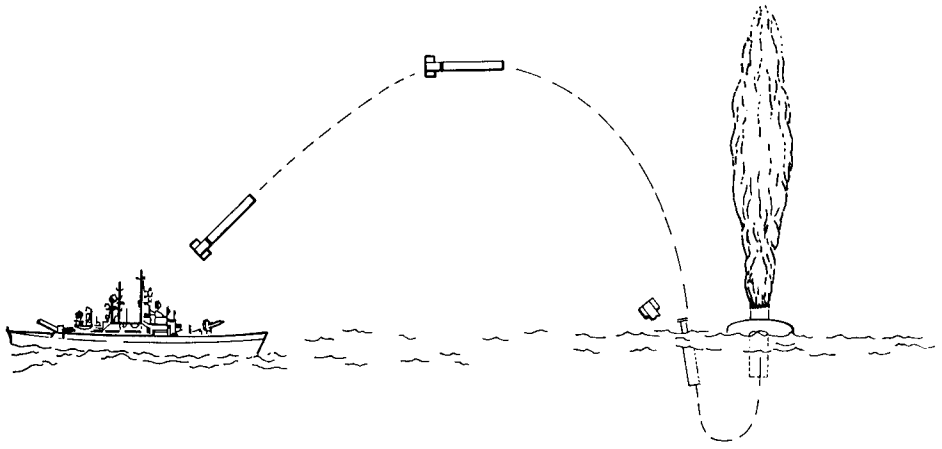

Fig. 4.16 Torch decoy.

The best-known example of a liquid-fueled decoy is the U.S. Navy MK 186 "Torch." This decoy is launched from the MK 36 Launching System. The decoy is interchangeable with the shipboard chaff rounds, which may also be launched from the same system. The deployment is consistent with that of a mortar-type system and therefore relatively close to the ship. The decoy function is illustrated in Fig. 4.16.

Floating Solid Fuel Decoys. These decoys are substantially easier to design and manufacture. The solid fuel combustion rate is determined by the burning characteristics of the fuel and does not require dispensing and regulation as in the case of the liquid-fueled decoys. These decoys float on the ocean and project a radiant plume of combustion products upward, as in the case of the liquid-fueled decoys.

The simplest solid fuel decoys use a magnesium fluorocarbon (Mg/PTFE) fuel similar to that used in airborne applications. This provides a good level of intensity in the 3- to 5-μm band but has not been found useful in the 8- to 14-μm band. The radiation from a burning Mg/PTFE plume in slow moving air is essentially that of a blackbody at about 2000 K. Therefore, only a small fraction of the combustion energy is radiated in the long wavelengths.

Other solid fuels have been developed that are much more efficient in terms of both their spectral shape and radiant efficiency in the longer bands. Most of these compositions use metallic fuels. Carbon compounds are generally avoided in those fuels. The presence of a strong radiator such as carbon in a flare plume results in a spectral distribution that resembles a high-temperature graybody.

The hydrated oxides of phosphorus are a modest radiator in the 8- to 14-μm band. A sufficiently dense cloud of phosphorus combustion products provides an efficient signature in both the mid- and long-wavelength bands. Often, the long-wavelength signature persists well after combustion is complete. This radiation comes from the residual smoke cloud. If the smoke cloud is sufficiently dense, its signature may resemble that of a graybody at the ambient air temperature.

The radiation mechanism of a phosphorus flame is more complicated than that of the Mg/PTFE plumes and does not resemble a blackbody. The level of visual radiation is comparatively low for the amount of mid- and long-wavelength emission. Many chemical compositions used in phosphorus-fueled decoys resemble those of obscurants such as smoke pots. Most of the mid-wavelength IR signature of phosphorus flares comes from the flame. Thus, the spectral content of the decoy signature changes with time if the smoke remains in the field of view. To remain effective in the 3- to 5-μm band, combustion must continue for the entire decoy function time.

Aerodynamically Suspended Decoys. Some solid fuel decoys are sufficiently light in weight that they can be suspended in air for useful time periods with the aid of parachutes or by appropriate aerodynamic shaping. The phosphorus fuels can be formed into thin flakes or applied as a coating to thin films. The fuel burn rate can be modified through the use of chemical inhibitors so that a lightweight, long-burning element is produced. The fall rate of these decoys should be less than 5 m/s so that they have a useful persistence when deployed at altitudes of 50 to 100 m. The average fall rate can be expected to be about half the initial value for those decoys that are completely consumed by combustion. An aerodynamically suspended decoy is shown in Fig. 4.17. The decoy cloud in the figure is formed by the air burst of a canister of phosphorus flakes.

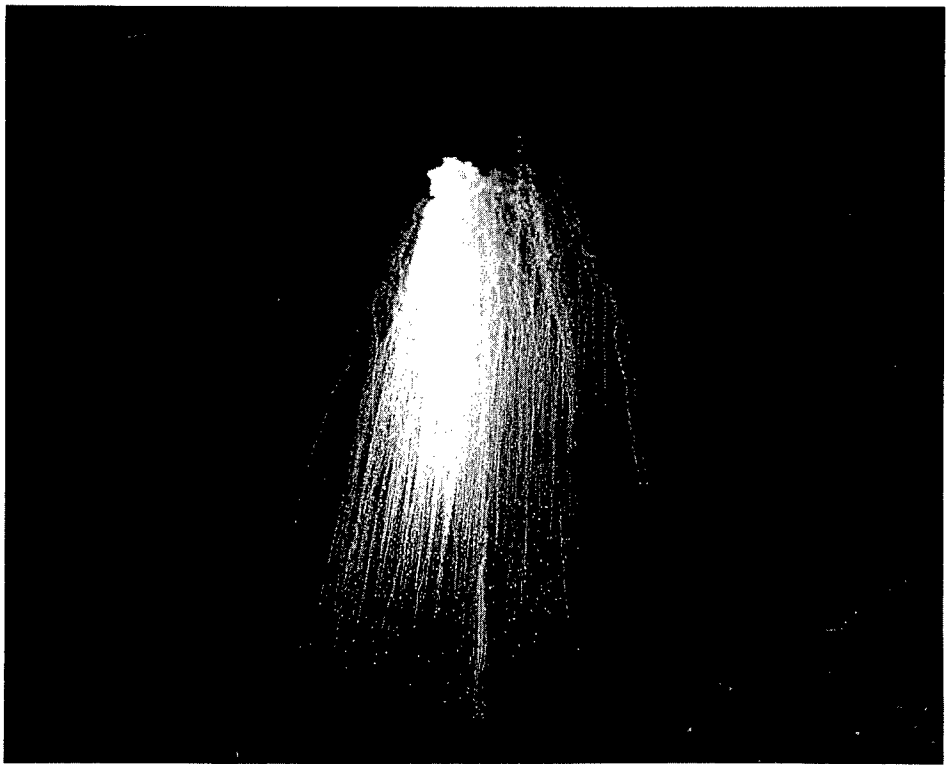

Fig. 4.17 Aerodynamically suspended decoy.

Aerodynamic suspension of the decoy has several benefits. The cloud formed from the combustion products provides a radiant surface much larger than the characteristic "hot spot" of the floating decoys. With careful attention to the design of the deployment mechanism, this *area decoy* provides spatial characteristics more like that of a ship.

The burn rate of Mg/PTFE fuels is much greater than that of phosphorus fuels. Therefore, useful burn times are not available from Mg/PTFE fuels when formed in particles light enough to have useful fall rates. These decoys are suspended from parachutes. The fuel is formed in a large pyrotechnic grain, which is shaped so as to provide the required burn time. The fall rate of parachute decoys can be made similar to that of the lightweight particles.

4.4.4 Measurement Methods

Radiant performance in the 3- to 5-μm band can be measured by standard radiometry. Reasonable care is required to avoid the presence of other sources in the background, however, the decoy signal is usually much greater than the background. Because shipboard decoys are used under sea-level ambient conditions, wind-stream facilities are not required for decoy evaluation. As with other types of flares, care must be taken to avoid obscuration of the decoy signature by smoke when conducting measurements at short ranges. Smoke can also affect the observed intensity at long ranges and should be noted during acceptance testing to maintain measurement consistency.

Measurements in the 8- to 14-μm band are more difficult because of the presence of background radiation. The preferred method is to use an infrared imaging system and perform posttest processing on each pixel of the recorded image. The effect of background radiation can be reduced by testing at night.

A spectral scanning instrument, such as a Fourier transform interferometer, is a useful tool to evaluate compositions. Such a device can be used to obtain spectral data as a function of time and position in the cloud.

Decoy performance is evaluated in a manner similar to that for aircraft decoys. Both distraction and seduction tactics can be evaluated by launching the decoy in the operational manner and observing the response of the surrogate threat seeker in the course of flight to the target. The seeker can be mounted in an aircraft pod for evaluation under simulated engagement conditions.

Simpler decoy evaluations can be conducted where the ship and decoy are readily observed from land. The seekers and radiometric equipment can be more conveniently mounted and operated in a shore facility.

4.4.5 Dispensers

Two types of launchers are used to place shipboard decoys in tactically useful positions.

Mortar-launched systems are relatively simple and low cost. They are limited to short-range deployment and can impart substantial recoil forces to the ship deck. A typical launch velocity is about 70 m s^{-1}. Initiation of the decoy occurs after a suitable time delay, usually when the round is near the peak of its trajectory. The most widely used mortar system is the U.S. Navy MK 36 Decoy Launch System. This system fires a variety of 130-mm-diam payloads.

A typical payload mass is about 20 kg and about 1200 mm in length. Rocket-powered decoys are also launched from the system when longer ranges are required.

Rocket-launched systems are used when it is desirable to deploy the decoy at a longer range. Most rocket designs are intended for distraction applications and deploy decoys at ranges beyond 1 km. Rockets can also be used for short-range seduction decoys, particularly where launcher weight and recoil forces transmitted to the deck are important.

Acknowledgments

I would like to thank Dr. Bernard E. Douda of the Naval Surface Warfare Center, Crane, Indiana, and Mr. Joseph Koesters of the Air Force Wright Laboratory, Wright Patterson AFB, Ohio, for their reviews of this manuscript. I extend my thanks also to Dr. Carl E. Dinerman of Tracor Aerospace, Inc., who served as a contributor.

Bibliography

Final Report: The Aircraft Infrared Measurements Guide, Joint Logistics Commanders Joint Technical Coordinating Group on Aircraft Survivability (March 1983).

Hoerner, Sighard F., *Fluid-Dynamic Drag,* Midland Park, NJ: Sighard F. Hoerner (1958).

McLain, Joseph Howard, *Pyrotechnics,* Philadelphia, PA: The Franklin Institute Press (1980).

U.S. Army Armament Munitions and Chemical Command, *Project Manager Smoke/Obscurants, Informal Report on the Transmissometry Workshop 11–13 December 1984,* Ronald H. Kohn & Associates (May 1985).

Zissis, G. J. and W. W. Wolfe, Eds., *The Infrared Handbook,* Infrared Information and Analysis Center, Environmental Research Institute of Michigan, Ann Arbor, MI (Revised 1985).

CHAPTER 5

Optical and Sensor Protection

Michael C. Dudzik
Environmental Research Institute of Michigan
Ann Arbor, Michigan

CONTENTS

The material in this chapter was prepared and reviewed under the Security Classification Guide for Laser Protection, dated 5 Jan. 1988, US Army Laboratory Command SLCSM-AA, under Section 4, Chapter II, AR 380-5. The information in this chapter is generic and does not represent current or proposed military sensor systems.

5.1 INTRODUCTION

Central to any optical design problem is the discovery of unplanned parameters that influence design performance or response. In recent years, the evolution of active electro-optic weapon systems to include laser rangefinders/designators, laser radar, and laser weapons has become of increased concern to the electro-optics community. Laser energy, when focused or in some instances unfocused by optical or ocular elements, poses unique hazards to both a sensor system and the human eye. This chapter addresses the impact of laser radiation on optical and sensor systems and highlights the generic protection technologies available to reduce hazard susceptibility.

It is important to note that this area of electro-optic technology is relatively new and grew from the foresight of individuals who recognized the critical nature of the hazardous laser-interaction phenomena. Several key government organizations provided leadership, while government laboratories, commercial industry, and academia responded to the challenge by developing a significant understanding of the problem as well as multiple technical responses and cost-effective implementation processes. Due to restrictions on information classification, this chapter presents laser hazard protection in a generic manner without endorsement or disapproval of any protection technology. This area of electro-optics technology has been developed by many researchers, only some of whom are referenced in this chapter. This technology will continue to grow as concepts mature and new developments occur. The reader is encouraged to monitor the literature for awareness of these developments.

5.2 MODERN LASER HAZARDS

The hazards of laser radiation have long been known and documented.[1] The highly collimated nature of laser light allows it to be focused effectively if the wavelength is within the spectral bandpass of the human eye or the collecting sensor. Focusing raises the peak intensity of the pulse or the integrated continuous-wave (cw) illumination, increasing the likelihood and extent of induced damage. However, intense laser radiation at wavelengths outside the spectral bandpass of the eye or the sensor system also can represent a significant hazard that must be accounted for in any hazard reduction plan. The laboratory use of lasers for alignment, experimentation, and medical and photochemical applications is accompanied by stringent laser safety procedures. Laboratory exposure limits are set by laser safety standards that are based on ANSI Z-136.1, Standard, Safe Use of Lasers.[2] Military regulations also prescribe safe laser practices (for example, see US Army AR40–46).

Laboratory laser hazards represent a distinct class of protection problems. Laboratory lasers are use dependent and represent both continuous-wave and pulsed laser sources. Likewise, the spectral domains of operation vary from the ultraviolet to the far-infrared. In all cases, laboratory personnel must use safety eyeware that provides the correct spectral coverage and optical density for adequate protection to ensure conformance with ANSI Z-136.1. Conformance to safety procedures and standards is the responsibility of the organizational laser safety engineer, and enforcement is the responsibility of organizational management. However, each individual must take the time to understand and practice laser safety in day-to-day activities.

Military laser hazards can occur from both intentional and unintentional laser exposure during military operations.[1,3] Unintentional laser exposure may result from sources such as target reflections (sometimes termed target splash) or from the sweep beam of a laser radar (ladar). Intentional exposure may be incidental to ranging or designating or the result of a purposeful attack on sensors.

The extensive proliferation of lasers for laboratory and military use makes hazard awareness critical for ocular and sensor protection. The remainder of this chapter addresses protection methodology and generic protection technologies available for hazard elimination.

5.3 EXPOSURE ANALYSIS

5.3.1 Sensor Susceptibility

The susceptibility of electro-optic sensors to laser radiation effects can be predicted and measured with a reasonable degree of accuracy. The analysis consists of methodically tracing a collimated light source through the optical path from the collecting aperture to the image focus and properly accounting for attenuation. Furthermore, each sensor type may utilize different detector/electronic designs for image processing and display. Therefore, no single hazard analysis is valid for all designs of the same sensor category. In effect, each new sensor design will require a separate hazard analysis even if several common components are used in the various designs.

5.3.2 Exposure

5.3.2.1 On-Axis Exposure Effects. On-axis exposure effects present the greatest technical challenge for electronic imaging sensors, especially if the laser hazard falls within the spectral bandpass of the sensor system. Under this condition, the illuminating laser radiation is received and acted upon by the sensor optics in exactly the same manner as the spectral scene information. However, the effect of on-axis, in-band laser radiation on sensor system response is intensity, fluence, and time dependent as well as a function of the image readout electronics. The irradiance level dependence produces interaction spanning from a veiling glare effect at low levels, up to detector saturation, and at extreme levels the possibilities of catastrophic laser-induced damage to one or more of the sensor elements.

For far-field laser radiation sources, the sensor collecting aperture can be considered to be completely filled by a plane wave of uniform intensity distribution. Collimated light from a distant point source passing through a limiting aperture will not image as a point, but as a result of diffraction will appear as an Airy disk surrounded by concentric, circular rings, as shown in Fig. 5.1(a).[4] A well-designed optical receiver will allow for Fraunhofer diffraction in the focal plane, and the magnitude of the resulting diffraction pattern will vary in magnitude for on-axis and off-axis illumination. Under ideal conditions, the diffraction-limited focusing optics (aberration-free) will act to produce a concentric Airy disk pattern. An ideal focus distribution is shown in Fig. 5.1(b) with the largest relative intensity in the central ring (83.9%).[5]

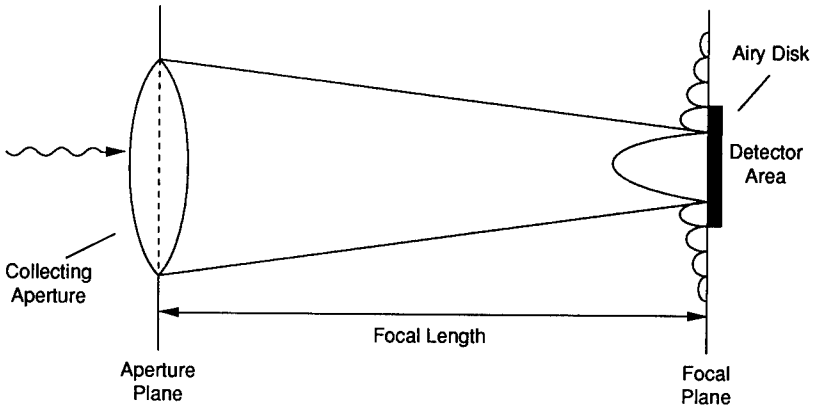

(a)

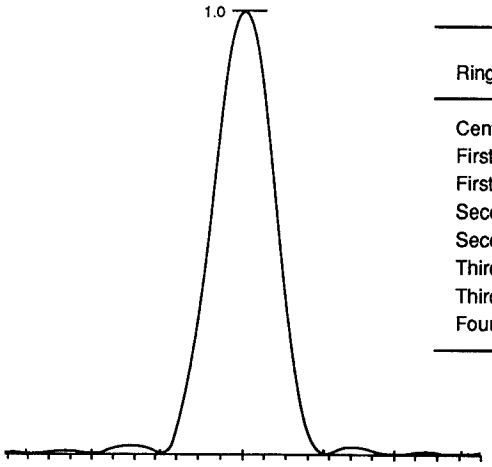

Ring	Amount of Light in Ring (%)
Center	83.9
First Dark	—
First Bright	7.1
Second Dark	—
Second Bright	2.8
Third Dark	—
Third Bright	1.5
Fourth Dark	—

(b)

Fig. 5.1 Formation and intensity distribution of an Airy disk pattern. (a) Airy disk formation by sensor optics. (b) Intensity distribution.

The ideal focus distribution is distorted by atmospheric effects. Optical aberrations and chromatic focus also can effect the shape and diameter of the focus distribution on the sensor image plane. For the purpose of an ideal susceptibility analysis, the worst-case scenario always will be that resulting from ideal focus conditions.

Example: Sensor System Susceptibility Analysis. For demonstration purposes only, assume a simplified electronic imaging sensor is under development, as shown in Fig. 5.2. The system optical designer can perform a first-order laser hazard analysis to determine the susceptibility of the sensor to expected in-band and out-of-band laser radiation. One constituent part of this analysis is conducted through a ray-trace program. The example sensor system is a staring

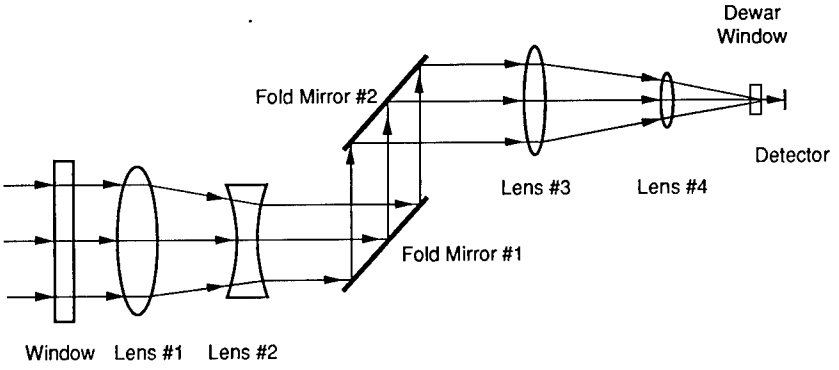

Fig. 5.2 Example sensor design.

8- to 12-um sensor. The optical design and component features are presented in Table 5.1.

To perform a first-order sensor susceptibility analysis the following procedure can be used:

1. Identify the sensor system optical parameters, including
   a. optical element material
   b. bulk material and mirror absorption coefficients
   c. transmission path thickness of optical elements
   d. anti-reflection coating loss per surface
   e. optical ray bundle diameter on each element surface.
2. Calculate the sensor transmission related values:
   a. optical gain at each surface
   b. optical attenuation at each element
   c. energy density as a function of position within the optical design.

An illustration of the overall procedure is shown in Appendix II.

The positions of high optical gain are a good indicator of problem locations within a design. Components located in these positions require careful analysis of laser-induced phenomena. Note the high optical gain on this example detector. However, once a high-gain location is isolated, the energy density at that gain point must be evaluated in terms of laser-induced-damage values at that location.

Loss mechanisms for bandpass radiation are attenuation through scattering and absorption. These mechanisms are very predictable and are shown in Fig. 5.3. □

For energy transmission, the wavelength-dependent absorption and reflection losses for each element and surface must be determined. Approximate bulk absorption values can be obtained from the material manufacturer. However, optical coatings are design and production-process dependent and usually are measured for exact values, but a typical rule of thumb is assumed to be within 1% to 3% per surface within the central portion of the spectral bandpass.

Table 5.1 Example Sensor Characteristics

Component	Material	Alpha (cm)	Thickness (cm)	Surface	AR Coating Loss	Optical Diameter (cm)	Cum Optical Transmission	Optical Gain	Cum Optical Gain	Cum Trans Gain
Window	ZnSe	0.004	1.0	1st	0.022	10	0.978	1.0	1.0	0.97
				B	—	—	0.974	—	—	—
				2nd	0.022	10	0.952	1.0	1.0	0.95
Lens #1	Ge	0.020	2.5	1st	0.018	10	0.935	1.0	1.0	0.93
				B	—	—	0.889	—	—	—
				2nd	0.018	9.5	0.873	1.1	1.1	0.96
Lens #2	Ge	0.020	1.75	1st	0.020	5.0	0.850	3.61	3.96	3.36
				B	—	—	0.820	—	—	—
				2nd	0.020	4.0	0.800	1.51	5.97	4.77
Mirror #1	PC	1%	—	1st	0.015	4.0	0.790	1.0	5.97	4.71
Mirror #2	PC	1%	—	1st	0.015	4.0	0.780	1.0	5.97	4.65
Lens #3	Ge	0.020	1.2	1st	0.018	4.0	0.766	1.0	5.97	4.57
				B	—	—	0.747	—	—	—
				2nd	0.018	3.0	0.734	1.78	10.64	7.80
Lens #4	Ge	0.020	0.3	1st	0.018	1.0	0.721	9.0	95.79	69.06
				B	—	—	0.716	—	—	—
				2nd	0.018	0.4	0.703	6.25	598.70	420
Dewar Window	ZnSe	0.004	0.2	1st	0.022	0.10	0.688	16	9579.31	6590
				B	—	—	0.687	—	—	—
				2nd	0.022	0.05	0.672	4	3.83×10^4	2.5×10^4
Detector	MCT	—	—	1st	—	0.02	0.672	6.25	2.4×10^5	1.6×10^5

PC—Pyroceramic Mirror
MCT—HgCdTe Abbreviation

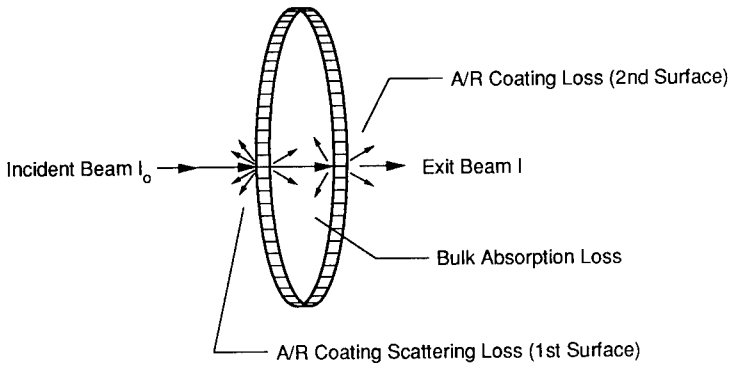

Fig. 5.3 Optical loss mechanisms.

Coating absorption or rejection characteristics away from the central frequency of the spectral bandpass must be specified or measured. The detector/electronic system response to laser hazard radiation is a function of the laser characteristics and incident irradiance. For the purpose of the example, the imaging properties of the sensor convert all incident in-band photons into an image. Therefore, all in-band hazard radiation is imaged along with background scene information. In classical optical analysis, the laser hazard would be imaged as if it were a point source located at infinity. In practice, as incident laser irradiance values increase, internal scattering and electronic saturation of the amplifier electronics occur. The internal scattering is caused by backscatter from optical surfaces. A large percentage of reflected radiation is generated at the dielectric interface between the antireflection coating and the bulk material of the optical element. Scratches, pits, and mechanical damage points on the optical element surface contribute significantly to the presence of optical scattering. The visible camera industry compensates for this phenomenon, sometimes referred to as veiling glare, through changes in the optomechanical design features of the camera. Internal scattering can cause several detector elements to reach the state of saturation even though the original laser hazard is imaged as a spatial point source.

The second phenomenon in sensor susceptibility analysis is catastrophic optical element failure due to laser-induced damage. Element failure can occur at either the coating surface or in the bulk material of the optical element.

The optical absorption phenomenon has been studied by many researchers.[6–12] In the thermal-induced optical damage process, optical absorption produces localized heating, which in turn increases as the temperature dependence of the absorption coefficient, which in turn increases until thermal runaway occurs and the material undergoes a mechanical fracture. This effect is fundamental to cw laser-induced optical damage.

Pulsed damage is related to the peak irradiance as well as the energy distribution within the pulse. Single-pulse and multiple-pulse exposures produce different damage thresholds.

Representative damage thresholds of some commonly used optical materials at wavelengths of common laser hazards are provided in Tables 5.2 and 5.3. Figure 5.4 provides experimental representative damage data for common detector materials. (Note: material absorption coefficients can change with material purity and crystal structure, and therefore it is necessary to consult the material manufacturer for exact values if absolute detail is required.) Continuous-wave damage thresholds must relate to exposure time as well as intensity. Pulsed-laser damage thresholds are both pulse-length and repetition-rate dependent. In general, it is an accepted engineering practice to always measure the specific elements for damage values rather than to rely on tabular values for other than simple models. Tabular material damage values are useful for estimating approximate order of magnitude for component failure. When measurements are conducted on actual components, the damage value measured is representative of the element and the process by which the element was manufactured. Damage thresholds for elements are dependent on the bulk material as well as the antireflection coating used and on the surface preparation technique used to prepare the substrate.

Table 5.2 Measured Damage Thresholds for Various Optical Glass Types (from Ref. 6)

Glass Type	Threshold* (J/cm^2)	Range** (%)	Glass Type	Threshold* (J/cm^2)	Range** (%)
FK 1	155, 175	17, 3	KF 6	70	86
FK 3	30	10	KF 9	90	131
FK 5	125, 60	34, 17	BaLF 3	80	20
FK 6	165	4	BaLF 51	90	21
FK 51	35	54	SSK 1	90	7
PK 2	95	17	SSK N8	80	23
PK 3	90	4	LaK N7	60	42
PK 50	135	7	LaK 8	40	41
PSK 2	95	35	LaK 10	8	100
PSK 3	105	9	LaK 11	8	0
PSK 50	110	95	LaK 16	5	60
PSK 51	105	12	LaK N16	6	57
PSK 52	15	93	LaK N18	25	15
PSK 53	50	117	LaK 19	20	52
BK 1	140, 165	44, 3	LaK 21	65	3
BK 4	155	8	LLF 1	130	19
BK 5	155	40	LLF 2	125	40
BK 6	120	13	BaF 4	55	4
BK 7	135, 80, 150	24, 17, 14	BaF N10	30	10
BK 8	150, 150	16, 27	LF 5	50	14
BK 10	130	20	LF 7	95	0
BK 13	145, 125	25, 33	F 2	30	44
BK 50	150, 155	19, 31	F 7	35	3
UBK 7	120	45	BaSF 52	5	0
BaLK 1	95	16	LaF N3	30	10
BaLK 3	100	22	LaF 24	10	55
K 3	100	23	SF 1	15	12
K 4	125	4	SF 2	25	21
K 5	100	24	SF 4	15	0
K 7	110	15	SF 6	10	0
K 10	100	19	SF 50	30	38
K 11	95	30	SF 57	8	14
K 50	105	17	SF 58	7	14
UK 50	115	8	SF 59	6	0
ZK 1	80, 140	2, 18	TiK 1	140	44
ZK 2	120	25	TiF 2	125, 80	24, 34
ZK 5	120	15	TiF 3	125, 63	51, 30
ZK N7	110	16	KzF 1	85	0
BaK 2	110	0	KzF 2	95	30
BaK 3	80	29	KzF 4	60	73
BaK 4	85	27	KzF 5	95	17
SK 8	85	21	KzF 6	95	21
SK 16	60	28	KzFS 2	15	19
SK N18	10	14	KzFS 6	45	17
KF 1	100	29	KzFS 7	6	0
KF 2	70	24	KzFS 5	< 4	
KF 3	70	111			

*Lowest level among several tests for which damage was observed by the unaided eye.
**There is a finite probability of damage at any level. The range shown here is the region between highest exposure without damage and lowest exposure with damage, as a percentage of the latter, observed in these particular measurements.

Table 5.3 Damage Values for Selected Optical Materials for CO_2 Laser Radiation

CW Damage Thresholds — Exposure (W/cm^2)

Material	1 s	10 s
Germanium	1E+3	1E+2
Polyceramic Mirrors	2E+3	6E+2
ZnS	1E+3	1E+2
ZnSe	5E+3	1E+3

Pulsed Damage Thresholds — Exposure (J/cm^2)

Material	10^{-6} s	10^{-9} s
Germanium	10	4
Polyceramic Mirrors	3	1
ZnS	—	—
ZnSe	50	2

Example continued. Assume that the operating sensor is accidentally exposed to an eye-safe CO_2 laser of 10 $\mu J\ cm^{-2}$ incident on the front window of the sensor, a CO_2 laser weapon of 1000 $\mu J\ cm^{-2}$, and a Nd:YAG laser rangefinder of 20 $\mu J\ cm^{-2}$.

It must be noted that both CO_2 lasers (10.6 μm) are well within the spectral bandpass of the staring sensor and that the laser radiation will be transmitted along with the normal scene information. Therefore, a detailed understanding of the radiation interaction is required. However, the Nd:YAG laser radiation is not transmitted owing to the transmission characteristics of the optics. Since the Nd:YAG exposure level is less than that required for optical damage to the ZnSe and Ge optical elements, the sensor is not susceptible to this radiation wavelength. Tables 5.4 and 5.5 provide a comparison of damage thresholds against incident radiation for this example. Note that the laser weapon did produce laser hazard damage, whereas the laser rangefinder did not damage the sensor system. □

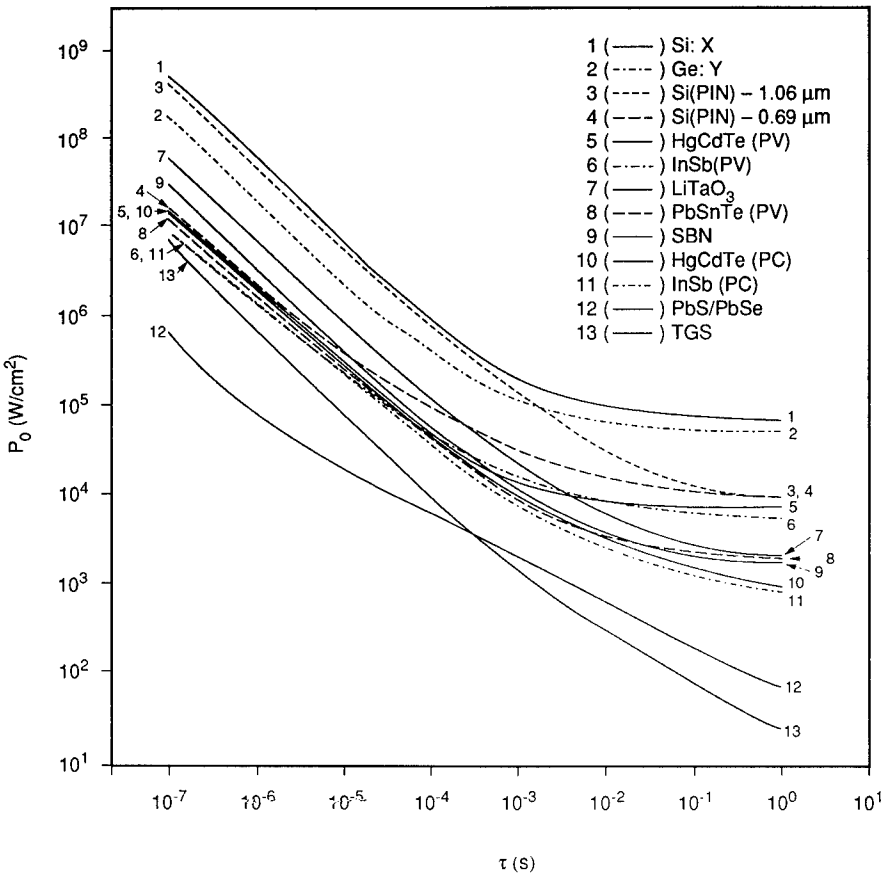

Fig. 5.4 Experimental thresholds P_0 for onset of laser damage in IR detector materials. P_0 (W cm^{-2}) is plotted as a function of irradiation time τ. Wavelengths of lasers used: curves 1, 2, 5, 7–10, and 13—10.6 μm; curves 6 and 11—5.2 μm; curves 3 and 12—1.06 μm; curve 4—0.69 μm (from Ref. 8).

Table 5.4 Example Hazard Radiation Interaction from 10×10^{-6} J/cm^2 10.6-μm CO_2 Laser Radiation for a 1×10^{-6} s Pulse

Component	Cum Trans Gain	Cum Hazard Exposure Level J/cm^2	Material Damage Threshold J/cm^2	Damaged
Window	0.97	9.7×10^{-6}	50	No
	0.95	9.5×10^{-6}	50	No
Lens #1	0.93	9.3×10^{-6}	10	No
	0.96	9.6×10^{-6}	10	No
Lens #2	3.36	3.3×10^{-5}	10	No
	4.77	4.7×10^{-5}	10	No
Mirror #1	4.71	4.7×10^{-5}	3	No
			3	No
Mirror #2	4.65	4.6×10^{-5}	3	No
			3	No
Lens #3	4.57	4.5×10^{-5}	10	No
	7.80	7.8×10^{-5}	10	No
Lens #4	69.06	6.9×10^{-4}	10	No
	420	4.2×10^{-3}	10	No
Dewar	6590	6.6×10^{-2}	50	No
Window	2.5×10^4	2.5×10^{-1}	50	No
Detector	1.6×10^5	1.6	4	No

Table 5.5 Example Hazard Radiation Interaction from 1000×10^{-6} J/cm^2 10.6-μm CO_2 Laser Radiation for a 1×10^{-6} s Pulse

Component	Cum Trans Gain	Cum Hazard Exposure Level J/cm^2	Material Damage Threshold J/cm^2	Damaged
Window	0.97	9.7×10^{-4}	50	No
	0.95	9.5×10^{-4}	50	No
Lens #1	0.93	9.3×10^{-4}	10	No
	0.96	9.6×10^{-4}	10	No
Lens #2	3.36	3.3×10^{-3}	10	No
	4.77	4.7×10^{-3}	10	No
Mirror #1	4.71	4.7×10^{-3}	3	No
			3	No
Mirror #2	4.65	4.6×10^{-3}	3	No
			3	No
Lens #3	4.57	4.5×10^{-3}	10	No
	7.80	7.8×10^{-3}	10	No
Lens #4	69.06	6.9×10^{-2}	10	No
	420	4.2×10^{-1}	10	No
Dewar	6590	6.59	50	No
Window	2.5×10^4	25	50	No
Detector	1.6×10^5	160	4	Yes

5.3.2.2 Off-Axis Effects. Off-axis laser hazard effects to electronic imaging sensors are design dependent. However, the phenomena of detector/electronic saturation and optical element damage are possible and must be accounted for in any complete analysis. The effects of off-axis laser hazards are functions of incident irradiance, total energy, and exposure time.

Analysis of off-axis effects is generally obtained by direct testing and measurement since computer models historically cannot duplicate all of the multiple path features of stray-light radiation scattering in all but simple optical systems. Furthermore, direct testing of these effects can be conducted with a high degree of certainty at less cost than an unvalidated computer model.

5.3.3 Ocular Susceptibility

The human eye is one of the most remarkable sensors in its ability to provide resolution, depth of focus, color sensitivity, and operation under a variety of light conditions.[1] These unique attributes, however, are of prime concern with respect to the loss of vision associated with acute exposure to laser radiation. Laser light characteristics, including wavelength, pulse length, pulse energy, peak irradiance, and exposure time, are potential factors in determining ocular susceptibility. The purpose of this section is to provide the reader with a fundamental understanding of the ocular hazard phenomena. Several exceptional references are provided at the end of this chapter and the interested reader is encouraged to consult these authors and their organizations for further detailed information.

Figure 5.5 provides a diagram of the human eye. For laser hazard analysis several important features of the physiology of the eye merit attention. First, the human eye has an optical gain. For general analysis one may assume a

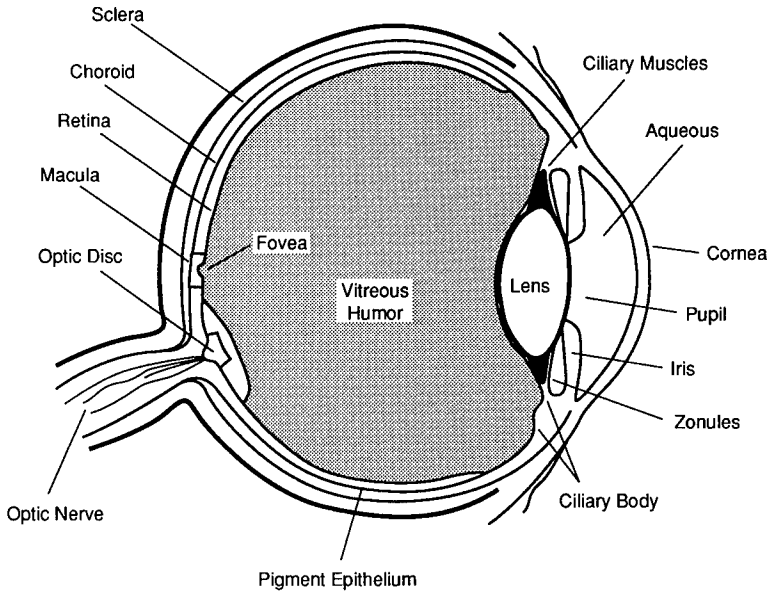

Fig. 5.5 The human eye.

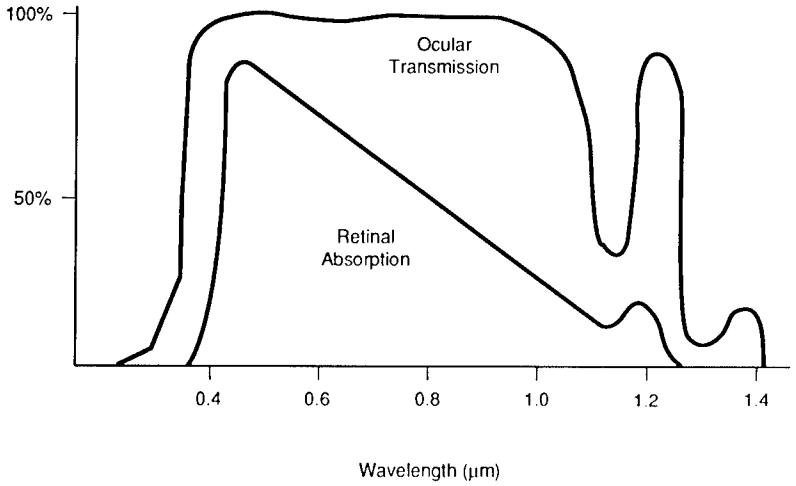

Fig. 5.6 Ocular transmission and retinal absorption of the human eye.

gain of approximately 200,000. Experimental data indicate that this value tends to remain approximately constant for pupil diameters between 4 and 7 mm. The image on the retina is the result of propagation of refracted light through the lens and the vitreous humor and is defined by an Airy disk pattern. In addition, the human eye is capable of spectral ocular transmission to the retina and corresponding retinal absorption across a wide spectral bandwidth, as shown in Fig. 5.6. Discussions of the interaction mechanisms of the laser hazard radiation with the retina and the thresholds for induced physiological damage are beyond the scope of this chapter. However, more detailed information can be found in Ref. 1.

The effects of incident laser radiation across the broad spectrum of laser wavelengths from UV to the far-IR must be examined against the maximum permissible exposure (MPE) levels for those wavelengths and exposure conditions. The MPE is defined by ANSI Z-136.1[2] as "the level of laser radiation to which a person may be exposed without hazardous effect or adverse biological changes in the eye or skin." The actual MPE values vary according to laser wavelength and exposure duration. The process for determining MPE values is described in ANSI Z-136.1 for multiple examples. In addition to ocular MPE values, ANSI Z-136.1 also provides MPE values for skin exposure. Criteria and procedures for determining MPE from ANSI Z-136.1 are as follows:

- Identify the wavelength of the laser.
- Identify the exposure duration.
- Identify the interaction type as intrabeam, extended source, or irradiance to the skin.
- Determine MPE value for the interaction type from Tables.
- Apply correction factors as required.

Ocular susceptibility to laser radiation is a function of multiple parameters, including wavelength, exposure duration, exposure level, repetition of exposure, and direct or diffuse exposure.[2,13,14] ANSI Z-136.1 was developed for the

unaided eye. In this regard, if the hazard situation under analysis is composed of a dual problem such as that of an individual looking through a pair of binoculars, then the problem must be divided such that the exposure value incident on the eye is that value corresponding to the exit of the binocular eyepiece and not the value incident on the binocular entrance optics.

Personal protective equipment, especially protective eyeware, must provide sufficient protection to ensure that the MPE value is not exceeded during the hazardous situation. In laboratory safety procedures, the laser safety engineer calculates the worst-case situational exposure values along the optical path and provides protective eyeware with sufficient optical density (OD) to meet appropriate MPE requirements. For military situations, the eyesafe controlled use of laser systems is not always realistic. Conversely, laser safety during training activities is tightly controlled. However, during actual combat operations, individuals are susceptible to laser hazards from intentional and unintentional sources. Currently, the US military has ongoing programs to provide protective eyeware and training to reduce the hazards associated with battlefield lasers.

Ocular hazard effects can be grouped generally into three categories: flash effects, retinal burns, and corneal burns.[13] Flash effects occur when light entering the eye is below the MPE levels and interferes with visual perception through a loss of the eye's ability to perceive brightness, contrast, or color. Flash effects degrade with time and do not result in permanent injury to the individual exposed. Retinal burns are the result of radiation focused on the retina at exposure levels above MPE, resulting in physical injury. Optical radiation from 0.4 μm to 1.4 μm can penetrate the ocular media and focus on the retina. This focused radiation, either pulsed or cw, if in excess of MPE will cause either thermal or photochemical injury to the retina. Figure 5.7(a) illustrates the condition for this effect of visible and near-IR radiation. Studies have suggested that retinal damage, especially to the fovea region, effect color perception and cause spatial vision degradation. Damage mechanisms range from initial peripheral edema and swelling of the photoreceptor in the foveal region to large foveal lesions and hemorrhage into the vitreous humor of the eye.

For laser wavelengths longer than approximately 1.5 μm, radiation tends to be absorbed on or within the cornea and vitreous humor. Corneal damage produces a loss of transparency or surface irregularity on the cornea. The damage mechanism to the cornea results from absorption heating of the surface and can produce effects ranging from minimal corneal lesions to full corneal loss. Corneal exposure is represented in Fig. 5.7(b).

5.3.4 Optical Retroreflection

All objects have phenomenologically based signatures. Two of the most common signatures are passive emission and reflection. Passive emission is a temperature-related phenomenon, whereas reflection signatures are dependent on parameters such as surface reflectivity and object orientation.

Consider an object that is illuminated by a plane wave front of laser radiation. The incident energy can be transmitted, reflected, or absorbed at the surface:

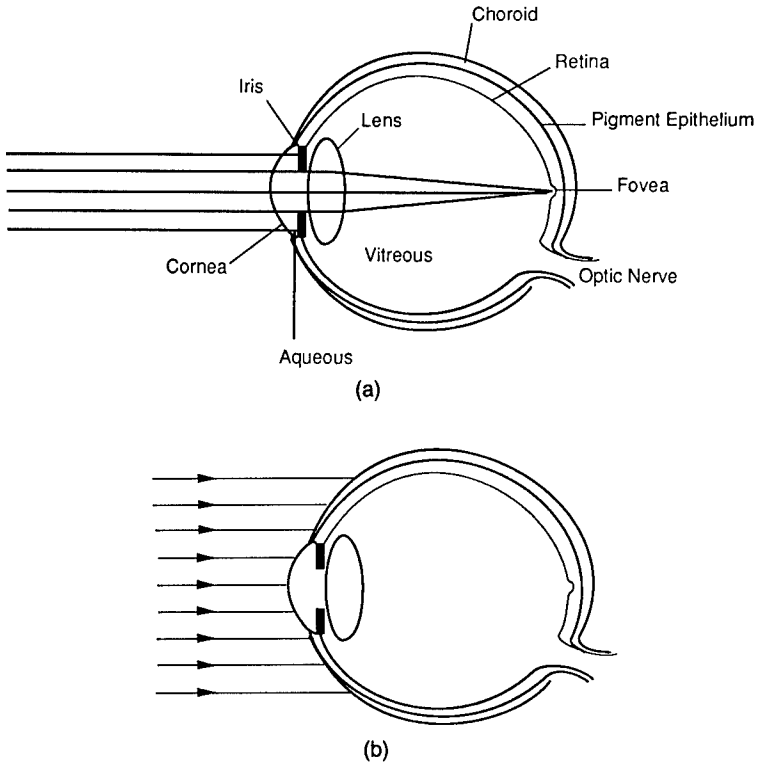

Fig. 5.7 Ocular exposure. (a) Retinal exposure. (b) Corneal exposure.

$$\rho + \tau + \alpha = 1 \ , \tag{5.1}$$

where ρ is the reflectivity, τ is transmission, and α is the absorption. If an object is assumed to be opaque, some energy will be lost owing to absorption, while the remainder is reflected in either a specular or diffuse fashion. The spatial distribution of the reflected radiation forms the basis for detection of the object against its background.

The distribution of radiation reflected by an object or target can be referred to as cross section. Simply stated, cross section is the amount of radiation being reflected from an object surface divided by the solid angle over which the radiation is reflected. Cross section is defined in simple form as

$$\sigma = \rho \frac{A}{\omega} \ , \tag{5.2}$$

where A is the area of the reflecting object surface and ω is the solid angle of the reflected energy, and ρ is the object reflectivity. Often there exists a substantial variation of ρ with wavelength.

There exists a class of reflective targets that have small physical size but have the ability to reflect incident radiation over a small incident angle. These are often referred to as retroreflective targets and consist of corner cubes, corner reflectors, reflex prisms, and retroreflectors. By design, these objects have lim-

ited size but provide a highly directive return. A practical example is the reflection one observes from a bicycle reflector or a cat's eye when illuminated by a bright light at night. When properly illuminated, some electro-optical sensors can exhibit retroreflective properties. Consider, for example, the presence of "solar glint" from binoculars used by troops in the field (by analogy this could also be a TV camera, direct view optic, or other sensor). The presence of the solar glint can inadvertently reveal operational presence and position. Reducing binocular solar glint is achieved via a combination of both optical coatings and binocular orientation when not in use. This combination therefore reduces both the source of retroreflection and the accessibility of the sensor.

5.4 PROTECTION TECHNOLOGIES

5.4.1 Generic Protection Technology

Protection against laser hazards is a continuously evolving science. Many of the current technologies are both novel and elegant. However, it remains the choice of the systems designer to identify and implement a hazard protection concept for ocular and electro-optic sensors. Design trade-offs must consider the impact of cost, performance, and reliability of the protection technology when specifying protection performance.

Protection technology can be categorized into six distinctive types:

1. spectral bandpass selection
2. mechanical shutters
3. fixed filters
4. tunable filters
5. limiters
6. optical switches.

In general, fixed filters and limiters are thought of as being passive (i.e., not requiring external electrical power), while tunable filters and switches are active forms of protection technology. In each case, performance penalties and hazard susceptibility reduction are critical design goals.

5.4.1.1 Spectral Bandpass Selection. The use of spectral bandpass selection, either via wavelength rejection or absorption filtering media, is a primary means of protecting a sensor from unwanted laser hazards. This technique has long been used by the optical industry for removing unwanted wavelengths from the sensor optical bandpass. The intrinsic use of optical elements made from materials with bandpass cutoff characteristics is a simple and reliable method of optical systems protection. This technique often is preferred where applicable in that it remains independent of response time and laser operating characteristics. It must be noted that to use this technique, a complete material damage analysis must be performed on the optical design and verified by testing such that the maximum exposure level of out-of-band radiation will not produce component damage.

The optical systems designer can obtain optical material properties from the manufacturer. Key parameters for selecting a material for protection are the optical density at the wavelength in question in conjunction with the

material thickness required to obtain the desired total optical protection, and the material damage threshold. If the material properties, especially damage threshold, are not known, it is required that proper experimental protocol be used to ensure repeatability and consistency with other measured data. The author acknowledges the excellent experimental protocol developed by the US Naval Research Laboratory for conducting material and detector damage threshold measurements (see Appendix I).

5.4.1.2 Mechanical Shutters. Mechanical shutters, positioned internally or externally, can prevent unwanted hazard transmission when a sensor is not operational. Shutters are currently used for environmental protection of optics from mechanical surface damage. Shutters offer simple hazard protection but lack rapid response time against single-pulse laser hazards.

5.4.1.3 Fixed-Filter Concepts. Fixed filters use the properties of reflection or absorption and are centered about a single wavelength.[15] A typical fixed-filter response curve is shown in Fig. 5.8 for wide bandpass, narrow bandpass, and notch rejection. Filter properties to absorb or reflect laser hazard radiation will differ by design and manufacturing process. Fixed filters are a form of passive laser hazard protection in that they are always present in the optical system. This can be both an advantage and a disadvantage. Fixed filters are functional against both cw and pulsed-laser hazard radiation until the filter damage threshold is reached. Technical specifications applicable to fixed filters analysis are filter width, optical density, and spectral transmission (both peak and average).

Filter width is an important parameter for the optical system designer to consider because of the performance impact. Filter width is most often specified as bandwidth at the half-power points. Optical density provides a measure of the filter's capability to prevent laser radiation at a fixed wavelength from passing through the filter. The spectral transmission must be specified for both peak and average transmission. It is important to monitor the design relationship between peak and average transmission values for fixed filters and its impact on sensor performance over the spectral range of operation. A rule of thumb is that interference filters can provide high optical densities often at the expense of average transmission, whereas absorption filters provide lower optical densities at better average transmission values. Significant advances are being made in interference filter designs that allow for an increase in the average transmission value over the spectral bandpass. The system designer must be careful to note the value of average transmission when making a filter selection.

The absorption filter often is based on molecular or atomic absorption. A limitation to this concept is that these filter characteristics are only as effective as the population of absorbing molecules or atoms present. When the photon flux exceeds a critical threshold (which is a function of absorption cross section and the number of active absorbers), the filter has reached what is often termed the "bleaching" point. Absorption filters can be used in two modes—fail open and fail closed. In the fail-open mode, the "bleaching" removes the absorbing population and allows specific wavelengths to pass. In the fail-closed mode, absorption can eliminate an optical property of an element and halt further transmission within the sensor. Absorption filters offer great advantage in

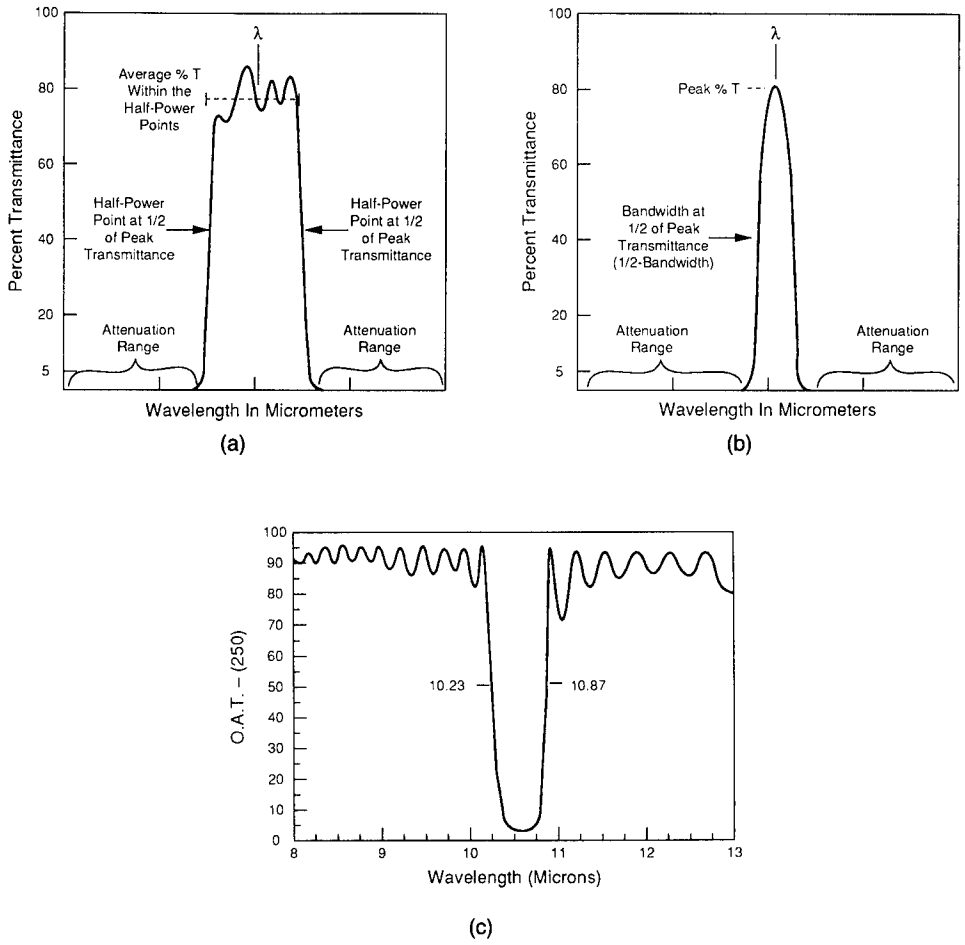

Fig. 5.8 Fixed-filter concepts. (a) Typical wide bandpass filter performance. (b) Typical narrow bandpass filter performance. (c) IR notch filter. (Data courtesy of Optical Coating Laboratory, Inc.)

that they are simple and inexpensive, although mass-produced dielectrics can achieve cost parity. Materials are available in solid, liquid, or gaseous forms that provide absorptive characteristics in various regions of the visible and infrared spectrum. A systems designer also must be aware of the filter substrate material, especially when considering damage threshold analysis.

Interference filters are the most common form of filters used to reject unwanted wavelengths.[15] They are composed of multilayer stacks of dielectric materials deposited on a substrate material. Interference filters are used for laser hazard protection as

1. *Bandpass filters:* filters used to define a spectral bandpass different from that of the optical materials.
2. *Cutoff filters:* filters used to cut off the spectral bandpass at either the high end or low end of the operating spectrum of the sensor.
3. *Narrow-band filters:* filters used to reject specific wavelengths.

These filter designs are typically capable of higher optical densities for hazard rejection than most absorption filters; however, these optical components have an angle sensitivity that has a negative impact on overall filter operating performance, depending on placement within the optical chain. Interference filters are well understood by the optical industry and can be produced at reasonable cost. When used for hazard protection, interference filters must be measured for laser damage susceptibility. Once damaged, the laser hazard protection of the filter is negated. From a practical standpoint, interference filters also must be checked for durability and flaws such as pinholes. Failure of the filter in an electronic imaging sensor is undesirable, but failure of the filter in a direct-view optical sensor that is used for viewing by a human eye can be catastrophic.

Other types of fixed filters are also available for laser hazard protection. Filter choice will be a trade-off between optical density, spectral impact to the sensor due to performance loss, filter cost, reliability, and durability. The optical designer should be aware of the effects of angular sensitivity and of wavelength shift as a function of temperature in considering filter selection for systems operating under a wide range of temperatures.

5.4.1.4 Tunable Filters. Tunable filters are active media that allow the optical bandpass to be controlled as a function of time against wavelength. Like fixed filters, tunable filters are based on either absorption or reflection phenomena and function against pulsed or cw laser hazard radiation.[17–19] Tunable filters have technical specifications similar to fixed filters, with additional conditions of volume, response time, and power consumption. Some examples of tunable filters are scanning Fabry-Pérot etalons, tunable Bragg-cell filters, and acousto-optic tunable filters. Tunable filters are currently the focus of extensive research and development activities.[19] The advantage of tunable-filter technology is that one filter element can provide hazard protection against one or more wavelengths of laser hazard. The disadvantages of older tunable-filter designs were a result of the significant broadband insertion losses within the sensor optical bandpass, narrow field of view, and finite activation times in the microsecond to millisecond range, which is unacceptable against submicrosecond laser pulses. Examples of tunable filters are shown in Fig. 5.9.

5.4.1.5 Limiters. Limiters are a broad class of materials that provide sensor protection. Most limiter devices are dependent on the peak irradiance (power) of the laser pulse. Other limiter concepts operate by refractive-index changes induced by thermal heating of a material. Limiter technology is based on both active and passive concepts.[20] Active concepts are characterized by optical devices that must be triggered externally or receive energy in some form from a source outside the laser pulse in the optical path. Conversely, passive devices are triggered by the pulse itself and often are described as self-induced limiters.

Many of the limiter concepts being reported are based on the nonlinear response of matter to incident electromagnetic radiation fields. The nonlinear laser-induced response is the result of an intensity-dependent variation of the propagation characteristics of the material to the incident laser radiation.[21] Nonlinear effects can take place in solids, liquids, and gases. A Taylor series

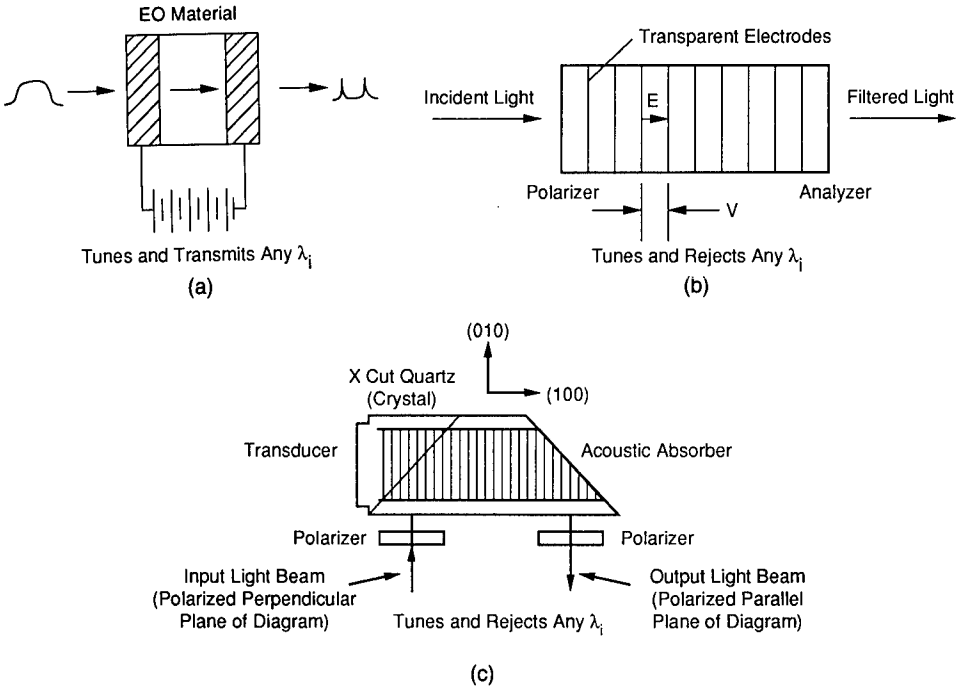

Fig. 5.9 Tunable-filter concepts. (a) Scanning Fabry-Pérot filter. (b) Tunable Bragg-cell filter. (c) Acousto-optic tunable filter.

expansion often can be used to express a material response by expanding the optical polarization $\mathbf{P}$ in terms of electric field $\mathbf{E}$ as

$$\mathbf{P} = \mathbf{X}^{(1)}\mathbf{E} + \mathbf{X}^{(2)}\mathbf{E}^2 + \mathbf{X}^{(3)}\mathbf{E}^3 + \ldots , \tag{5.3}$$

where the first-order susceptibility tensor $\mathbf{X}^{(1)}$ is related to the optical linear domain of the material, which includes the linear index of refraction, linear absorption, and magnetic permeability of the material. Susceptibility tensor values beyond $\mathbf{X}^{(1)}$ generally decrease in increasing order. As a result, most optical phenomena can be described accurately by using only the first three terms of the equation. The second-order term has components that oscillate at sum and difference combinations of the incident frequencies as well as a component that does not oscillate. Second-order term effects are phase matching, frequency mixing, and parametric generation. The second-order term can describe a materials photorefractive effects. The third-order term can provide a description of two-photon absorption, self-focusing and self-defocusing, and saturable absorption. System engineering advantages of self-induced nonlinear devices for laser hazard protection are

- activation by a broad range of wavelengths
- large dynamic range of protection
- response within the pulse duration
- wide field of view
- high spectral transmission at low intensities.

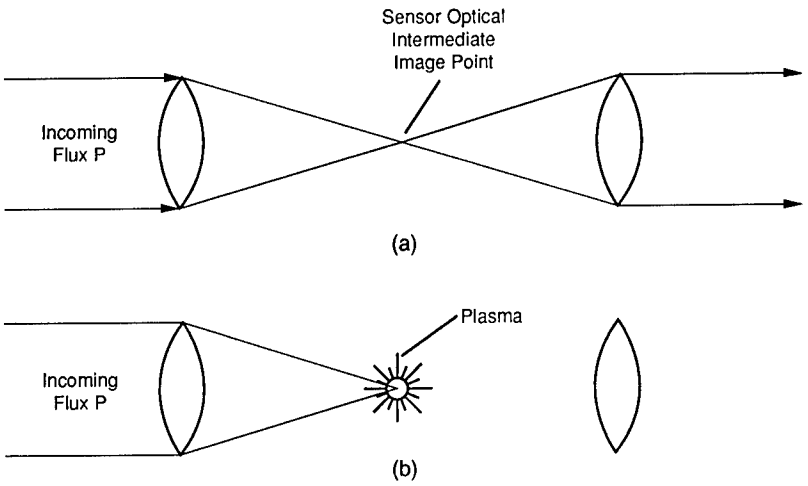

Fig. 5.10 Optical limiter concept. (a) No plasma attenuation for $P < P_0$ (no breakdown). (b) Plasma attenuation for $P > P_0$ (breakdown).

Passive devices developed from nonlinear theory often are termed optical limiters to preclude confusion with electrical current limiting devices.

Optical power limiters are nonlinear devices in which, once activated by the pulse, the remainder of the pulse is substantially attenuated. In this device, incident radiation is brought to focus in a gas, liquid, or solid.[20,22–24] When the electric field strength of the focused pulse reaches an activation threshold, limiting action of the remaining pulse will occur. In a gas limiter, for example, an ionization-induced plasma is produced. This process is shown in Fig. 5.10. When activated by the laser hazard pulse, the plasma will interact with the remainder of the pulse via absorption, refraction, and scattering. Once activated, ideal optical limiters develop optical density as fast as fluence increases. However, in reality this linear increase is not always possible owing to optical and mechanical properties of the limiter. The linearity of the limiter response must be understood before selecting a particular design for application. Figure 5.11 illustrates the switching intensity of an ideal optical limiter.

5.4.1.6 Optical Switches. An optical switch is also a nonlinear device[25] that is capable of being switched externally or induced to switch from the incident laser hazard radiation. Typically, an optical switch changes from a transparent optical component to an opaque optical component upon activation.

Optical switches have been developed from both vanadium oxide (V_xO_y) and chalcogenide mixtures; however, new materials also are under investigation. Optical switches exhibit sharp reproducible switching properties and have been applied onto substrates for use in broadband hazard protection applications. Figure 5.12 provides the switching characteristics of an ideal switch.

Depending on the material used, nonlinear switch coatings can be applied to both flat and curved surfaces. This aspect allows the designer application choices within an optical design. Also, a nonlinear switch can be incorporated in a tandem fashion with other protection concepts to provide protection against pulsed and cw laser hazards.

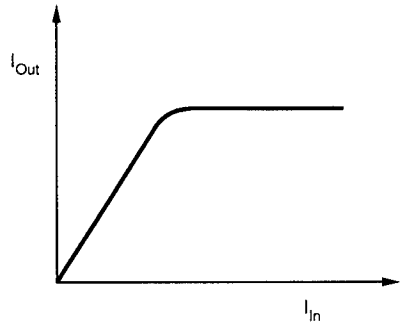

Fig. 5.11 Optical limiter response to incident radiation.

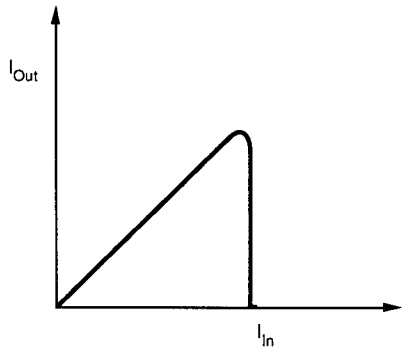

Fig. 5.12 Optical switch response to incident radiation.

Important design parameters to consider when selecting an optical switch are insertion loss, switching time, optical density, and material damage thresholds for both the substrate and the switch. Active switch concepts may require external power consumption and environmental constraints. Ongoing research is providing continued performance improvements in these hazard protection devices.

5.4.2 Emerging Concepts in Protection Technologies

Emerging concepts in protection technologies are attempting to solve both frequency-specific and frequency-agile hazard problems.[26–28] These emerging concepts are based on both linear and nonlinear material properties. This section briefly describes several promising concepts. As these technologies are applied to produce component hardware, the same engineering selection criteria described in the previous sections will be applicable to design requirements.

5.4.2.1 Ablative/Sacrificial Materials. For high-energy broadband hazard protection applications where short operating timelines exist, ablative material protection or sacrificial optical element concepts are useful. This technique allows direct heating and damage of an optical substrate earlier in the optical chain than the critical element requiring protection, without the total failure of the sensor. Ablative/sacrificial materials can be static or dynamic. A dynamic device allows fresh material to be continuously inserted into the optical path to restore the hazard protection performance. Ablative materials are used in a manner analogous to reentry vehicle materials, which are acted upon and discarded by the frictional heating of the earth's atmosphere during reentry without damage to the vehicle structure or components. In this manner, concepts have been proposed using ablative shields, sacrificial optical elements, and optical fuses. These concepts lend themselves to broadband hazard protection requirements for both pulsed and cw laser hazards. An ablative/sacrificial material concept is shown schematically in Fig. 5.13.

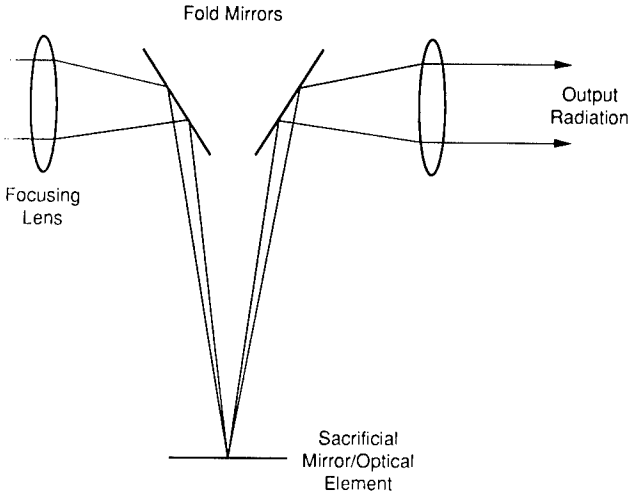

Fig. 5.13 Ablative/sacrificial element concept.

5.4.2.2 Rugate Filters. Rugate is defined in Webster's as "to crease or wrinkle." In terms of a hazard protection concept, a rugate filter is a dielectric spectral filter composed of a sinusoidal refractive-index profile in a direction normal to the plane of the film. The period of the index of modulation is one-half of an optical wavelength such that the filter produces a Bragg reflection through interference of multiple reflections. Rugate theory provides that multiple wavelengths can be rejected by superimposing several sinusoidal index modulations of different periods in the filter design.[16]

Ideally, a rugate filter can have high peak reflectivity in a very narrow bandwidth. The rugate filter concept is very attractive in that it has the potential to provide an almost unlimited number of spectral protection lines against laser hazards. Transmission loss over the operating spectral bandpass will, however, be dependent on filter thickness and material composition properties. Another unique feature of a rugate filter is that owing to its homogeneous composition and lack of physical interfaces between dissimilar materials, the filter can provide negligible scattering properties. Figures 5.14(a) and (b) illustrate the spectral-transmission and refractive-index characteristics of a typical rugate filter design. Figure 5.14(c) provides typical characteristics of an actual four-line rugate filter.

5.4.2.3 Self Focusing/Defocusing Limiters. The concept of self-focusing or self-defocusing limiters is based on a positive or negative third-order susceptibility term in Eq. (5.3) for a given material.[20,21] The phenomenon is a power-dependent process. If positive (self-focusing), the material will display focusing properties, that will cause a focused beam to focus further, thereby increasing the power density in the beam spot within the limiter but broadly defocusing in the remainder of the sensor optics. If the term is negative (self-defocusing), the material will display defocusing properties causing the focused beam to expand, thereby lowering the power density in the spot and also causing further defocusing.

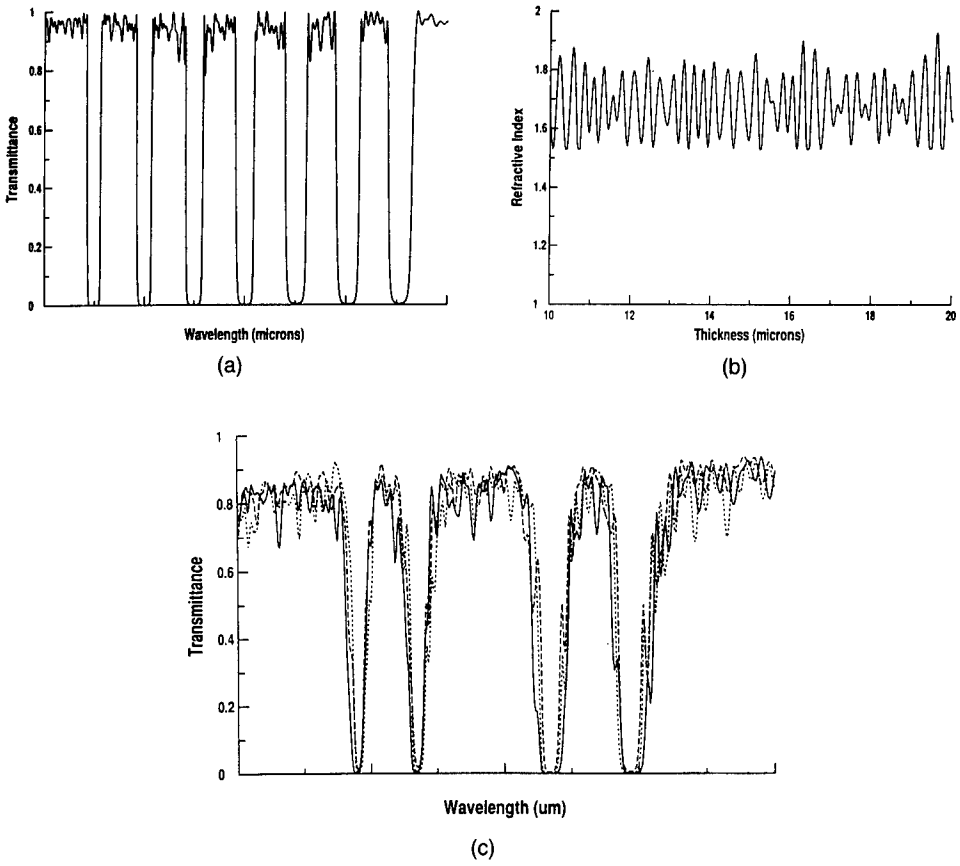

Fig. 5.14 Multiline rugate filter. (a) Rugate-filter concept. (b) Portion of refractive-index profile. (c) Actual four-line rugate filter. (Data courtesy of Rockwell International Science Center.)

The self-focusing/defocusing limiter has application in the visible and the infrared portions of the spectrum. Since this phenomenon is a power-dependent process, these limiters have the potential to operate on the leading edge of the laser pulse and can be used for application against both pulsed and cw laser hazard radiation. Figure 5.15 shows the concept of self-defocusing and self-focusing in an in-line optical path. The material providing the nonlinear index change for this phenomena may be either solid or liquid.

5.4.2.4 Thermal Lensing Limiters. Most optical materials exhibit temperature-induced index-of-refraction changes. Under specific conditions a material can be induced to act as a thermal lens such that the beam size is expanded, which will reduce the laser power density at that location and at optical component locations downstream in the optical design.[20,21] Since thermal-lensing effects are time-dependent phenomena (owing to the positive feedback associated with optical-induced heating in a substrate), thermal-lensing limiters show potential for cw laser hazard protection applications.

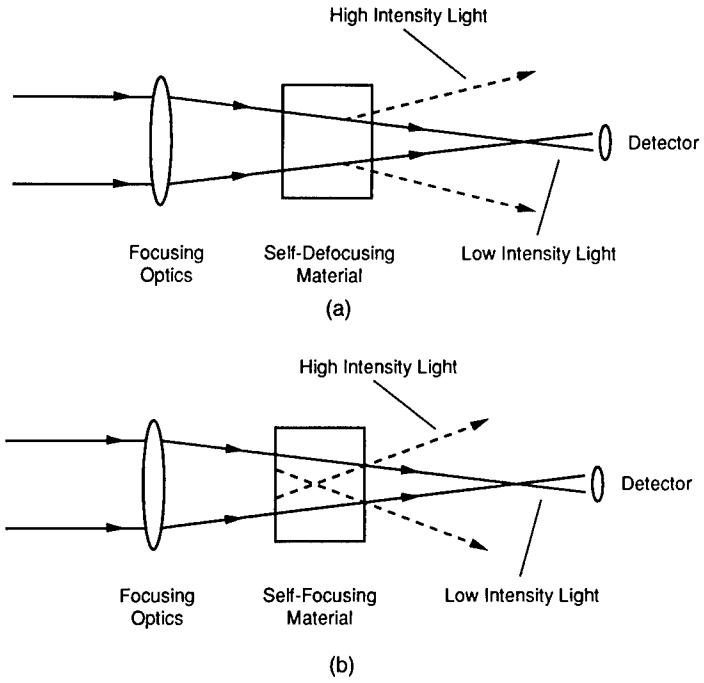

Fig. 5.15 Self-focusing/defocusing limiter concepts. (a) Self-defocusing concept. (b) Self-focusing concept.

5.4.2.5 Photorefractive Limiters. The photorefractive effect can produce a nonlinear-based limiter for laser hazard protection.[20] As laser radiation passes through a crystalline material, free charges are liberated and will be distributed into a space-charge field that effectively modifies the index of refraction. Under proper conditions when multiple beams are present, the space-charge field produces a volume grating. This generated volume grating is a result of constructive and destructive interference, which allows energy coupled between different beams to spread in an asymmetrical manner from the crystal. The photorefractive effect, also known as beam fanning, is shown in Fig. 5.16.

Design factors important to photorefractive limiters are damage threshold and photorefractive speed. Damage threshold is a material characteristic and depends on pulse length and irradiance. Photorefractive speed is a result of its basic host crystal and optical characteristics, dopant, internal electric-field strength, and incident laser intensity.

5.4.2.6 Holographic Filters. Holographic filters are a rapidly emerging laser hazard protection technology.[28] Currently, holographic notch and supernotch filters are fabricated by recording interference patterns between two mutually coherent laser beams on an optically sensitive media. This is different than conventional interference filters, discussed in Sec. 5.4.1.3, which are fabricated by deposition of materials with dissimilar indices of refraction. Holographic filters can be designed with high optical densities and extremely narrow spectral bandwidth. Holographic-filter designs can provide sharper edge cutoff than

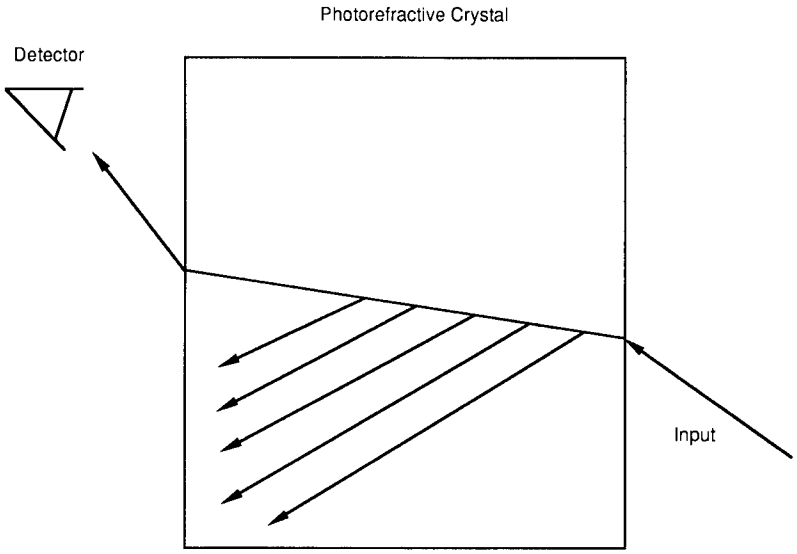

Fig. 5.16 Photorefractive limiter concept.

conventional dielectric filters. This feature removes unwanted artifacts of conventional filter construction and decreases insertion loss in the operating spectral bandpass of the sensor.

The optical density of holographic filters at specific wavelengths is angle sensitive with regard to incident radiation. Therefore, the optical systems designer must ensure placement of the filter within the optical chain to maximize the optical density without adverse impact from off-axis radiation. However, the filter will continue to perform blocking functions against internal scattered radiation within the cone angle of the filter design. Holographic notch filters can be used against visible and near-infrared laser hazards and are currently under development for the far-infrared spectral regions. Figure 5.17 shows typical transmission, optical density, and angle dependence of holographic notch and supernotch filters.

5.4.2.7 Nonlinear Photon Localization/Nonlinear Mirror. A promising phenomenon for hazard protection is the combination of photon localization and nonlinear optics into a one-dimensional multilayer dielectric system.[3] As incident radiation intensity increases, the refractive indices of the nonlinear material layers change, creating the reflection of the incident laser radiation. Higher intensities result in higher values of reflection. The advantage of this concept is that it can be a broad-spectrum reflector while transmitting normal scene information. However, laser-induced damage thresholds of the multilayer materials must be determined.

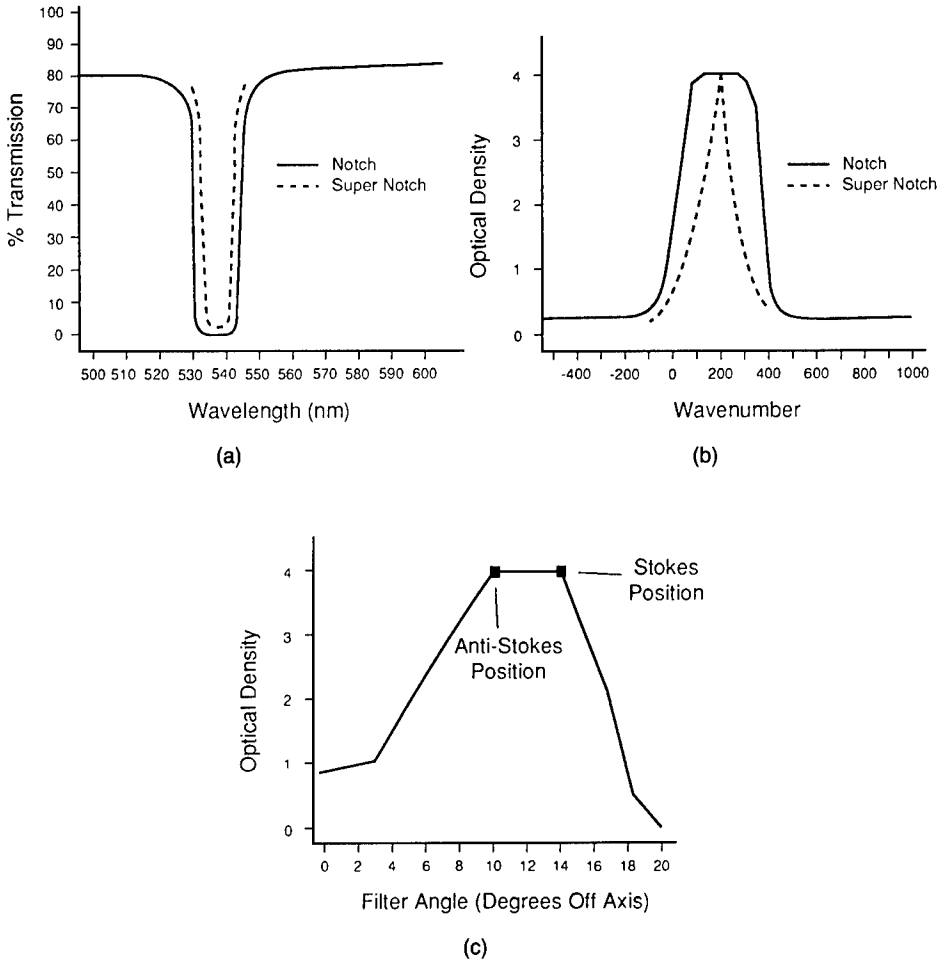

Fig. 5.17 Holographic notch filter features. (a) Transmission versus wavelength. (b) Optical density versus wave number. (c) Optical density versus filter angle. (Data courtesy of Kaiser Optical Systems.)

5.4.3 Protection Example

To illustrate the principles of laser hazard protection, several technologies will be applied to the sensor system described in the previous example (see Sec. 5.3.2.1).

To protect the sensor of the previous example against the 10.6-μm laser-weapon hazard, one possible combination of protection technologies is shown in Fig. 5.18.

First, the designer has placed a mechanical shutter mechanism on the exterior optical entrance aperture. The purpose of this device is to protect the sensor against accidental exposure when the sensor is not in use. A secondary use is to prevent the sensor window from receiving mechanical damage to the coatings and substrate during normal operational use and storage. Note that

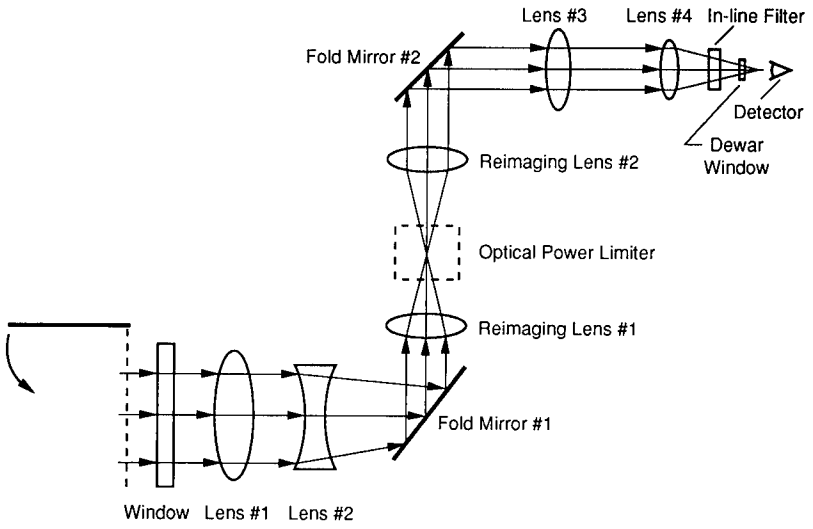

Fig. 5.18 Protection example.

a closed shutter when placed in this location protects the entire sensor from all laser hazard wavelengths.

Second, the designer inserted an optical power limiter in the sensor to provide pulsed laser hazard protection. By passing the high-energy (above threshold) pulsed laser hazard radiation through an intermediate image point within the optical limiter, the pulsed hazard can be attenuated from the optical path before more sensitive downstream optical components can be damaged.

Third, the designer has placed a single notch filter behind the last lens of the imager to remove low-level (subdamage) pulsed or cw radiation from falling onto the detector.

Assume the following protection technology characteristics:

- *Optical Power Limiter (OPL):*
  0.5 J cm^{-2} activation energy, pulse length independent
  5% overall spectral performance degradation
- *Filter:*
  O.D. 4 at peak
  ZnSe substrate
  10% overall spectral performance degradation.

Table 5.6 provides a hazard protection analysis of the protected sensor. Note that the optical elements upstream from the OPL remain susceptible to pulsed laser hazard radiation. Furthermore, the optical filter material damage threshold now becomes the critical value against cw 10.6-μm radiation owing to its placement at a high-gain point in the optical system.

Table 5.6 Example Sensor Protection Performance against 10.6-μm Pulsed Laser Hazard of 1000 × 10^{-6} J/cm^2

Component	Cum Trans Gain	Cum Hazard Exposure Level J/cm^2	Material Damage/ Activation Threshold J/cm^2	Damaged
Window	0.97	1.0 E–3	50	No
	0.95	9.5 E–4	50	No
Lens #1	0.93	9.3 E–4	10	No
	0.96	9.6 E–4	10	No
Lens #2	3.36	3.3 E–3	10	No
	4.77	4.7 E–3	10	No
Mirror #1	4.71	4.7 E–3	3	No
			3	No
Reimaging Lens #1	4.71	4.7 E–3	10	No
	2.00	2.0 E–3	10	No
Intermediate Image Point	9 E5	900	2	Activated
Reimaging Lens #2	2.00	Hazard Radiation Is 450 Times Greater Than Optical Power Limiter Activation Threshold. Therefore downstream optics are protected against **pulsed laser induced damage**.		No
	4.71			No
Mirror #2	4.71			No
Lens #3	4.71			No
	4.50			No
Lens #4	41.0			No
	245			No
In-Line Filter	1000			No
Dewar Window	3920			No
	1.5 E4			No
Detector	1.6 E5			No

5.5 APPENDIXES

5.5.1 Appendix I: Resources

Many organizations are available to assist the optical systems engineer in laser hazard susceptibility analysis protection technologies. A partial list is provided for the interested reader.

ANSI Z-136.1
American National Standards Institute, Inc.
1430 Broadway
New York, NY 10018

Ocular Interactions
Director
USAMRD
Brooks AFB, TX 78235
ATTN: SGRD-UWB

Protection Technologies
Director
US Army Survivability Management Office
2800 Powder Mill Road
Adelphi, MD 20783

or

Commander
USAF Wright Laboratories
Materials Laboratory (WL/MLPJ)
Wright-Patterson AFB, OH 45433

Material Damage Threshold Measurement Protocol
Commander
US Naval Research Laboratory
4555 Overlook Ave.
Washington, DC 20375
Attn: Mr. Filbert Bartoli, Bldg. 30, Code 6551

5.5.2 Appendix II: Illustrative Example of Energy-Density Calculation

The purpose of this appendix is to demonstrate the process of calculating the energy density within an example optical system for pulsed-laser radiation. Continuous-wave hazard radiation calculations can be conducted in a similar manner. The reader is reminded that if the human eye is a component in the calculations, the protocol of ANSI Z-136.1 is followed in determining safety thresholds.

Assume the optical system shown in Fig. 5.19. The optical designer has provided the optical bundle diameters at each surface of each element, as shown in Table 5.7. To calculate the optical gain at each linear position within the optical system, the optical gain at that location from a previous location in the system is calculated by

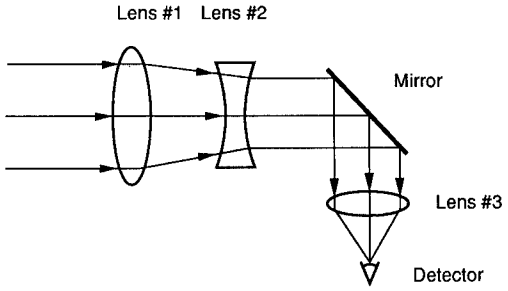

Fig. 5.19 Simple optical sensor.

Table 5.7 Example Sensor Design Characteristics

Component	Surface	Bundle Diameter (cm)
Lens #1	1st	2.00
	2nd	1.75
Lens #2	1st	1.00
	2nd	0.50
Mirror	1st	0.50
Lens #3	1st	0.50
	2nd	0.20
Detector		5×10^{-3}

Table 5.8 Example Sensor Optical Gain Values

Component	Surface	Cumulative Optical Gain
Lens #1	1st	1.00
	2nd	1.30
Lens #2	1st	4.0
	2nd	16.0
Mirror	1st	16.0
Lens #3	1st	16.0
	2nd	100.0
Detector		1.6×10^5

$$\text{optical gain} = \frac{\text{bundle area on the 1st surface}}{\text{bundle area on the 2nd surface}} . \tag{5.4}$$

The optical gain on the first surface of the first element is always considered to be unity by definition. In our example, the lens provides magnification such that the exiting beam diameter is smaller than the entering beam diameter. Referring to Table 5.7, the optical gain on the second surface of the first lens is

$$\text{optical gain} = \frac{2 \times \pi(2)^2}{2 \times \pi(1.75)^2} = 1.30 .$$

Second-surface gain values are necessary to understand energy density in the bulk and energy density on the second-surface antireflection coating. More sophisticated models will incorporate gain values within the layers of the antireflection-coating design.

The same calculation process is used to calculate the gain values on each component in the optical system. These values are shown in Table 5.8. The optical gain of the entire sensor from front aperture to the detector is the product of the gain at each element or the ratio of the clear aperture (in this case the first-surface bundle diameter) to the focus spot diameter on the detector:

$$\text{geometrical optical gain} = \frac{\frac{\pi}{4} \times (2.0)^2}{\frac{\pi}{4} \times (5 \times 10^{-3})^2} = 1.6 \times 10^5 .$$

Table 5.9 Optical Sensor Material Properties

Component	Material	Thickness (cm)	Attenuation Coefficient	Measured A/R Coating Loss	
				1st Surface	2nd Surface
Lens #1	Woodallium	1.00	0.20	0.03	.003
Lens #2	Huberium	0.75	0.10	0.02	0.02
Mirror	Zimmermanium	—	—	0.05	—
Lens #3	Millerium	1.25	0.15	0.02	0.02
Detector	Perrymanium	—	—	—	—

By following the optical gain values from the entrance aperture to focus positions, the optical designer can determine areas of high gain and therefore potential problem areas for laser hazard radiation induced component damage.

To calculate the optical damage induced by pulsed radiation, the energy density as a function of location must be known. To calculate the energy density, the attenuation of each optical element as a function of the wavelength in question must be analyzed.

Assume that the optical sensor is composed of the mythical materials with the properties and antireflection coating reflectivities listed in Table 5.9. Attenuation loss through the first lens element can be calculated in the following manner. The energy density (joules per square centimeter) incident on the first surface coating is assumed to be from a plane wave front from a source located at infinity. This initial energy will be attenuated by the first antireflection coating on the outside lens. From Table 5.9, this coating has a 3% loss per surface. Therefore, the energy passing through the coating and into the bulk material is

$$E_{\text{Bulk}} = (1 - 0.03) \times E_0 \ .$$

The energy attenuated by the bulk material of the optical component can be approximated by Beer's law:

$$E = E_0 \exp[-(\mu x)] \ . \tag{5.5}$$

From the example data,

$$E = (1.0 - 0.03)\, E_0 \exp[-(0.2 \times 1.0)] = 0.79 E_0 \ .$$

In a focusing lens, the energy density will increase with increasing linear position. Therefore, the energy density will be higher, especially on the back

surface of the lens than on the front surface. There also will be an analogous situation for cw laser radiation. However, for critical optical components the amount of energy attenuated per unit length in the optical component becomes a factor for susceptibility of the component to laser-induced damage if the predominant mechanism is through absorption.

The energy density at the rear surface of the lens is the product of the energy passing through the component and the gain:

$$\text{energy density}_{\text{rear}} = 0.79E_0 \times 1.30 = 1.027E_0 \ .$$

Finally, the energy density exiting the lens in this example is attenuated by the antireflection coating:

$$E_{\text{out}} = (1.0 - 0.03) \times 1.027E_0 = 0.99E_0 \ .$$

If one assumes that the air space between optical elements has no real appreciable attenuation of the energy, then the next location of interaction is the second lens in the design. Using the same process as was used in lens 1, the attenuation by the coating will be 2%, the bulk absorption will be 8%, and the attenuation by the second antireflection coating is 2%.

For the case of collimated optical spaces, the geometrical optical gain is unity by definition. However, energy-loss mechanisms from mirror surfaces, unity windows, and other nongain components must be considered in the energy-loss budget.

The energy-density calculations are completed for this example in Table 5.10. The reader is asked to check the values independently as an exercise.

Table 5.10 Energy-Density Calculations

Element/Surface	Attenuation	Cumulative Transmission	Cumulative Optical Gain**	Energy Density*
Lens #1				
1st	0.03	0.97	1.0	0.97
B	0.19	0.79	—	—
2nd	0.03	0.76	1.30	0.99
Lens #2				
1st	0.02	0.75	4.0	3.0
B	0.08	0.69	—	—
2nd	0.02	0.68	16.0	10.89
Mirror	0.05	0.64	16.0	10.24
Lens #3				
1st	0.02	0.63	16.0	10.08
B	0.17	0.52	—	
2nd	0.02	0.51	100	51.00
Detector	—	0.51	1.6×10^5	8.16×10^4

*As a fraction of energy incident on front surface
**Gain at the surface

Tables 5.4 and 5.5 were derived using this same analysis methodology but for a more complicated optical design.

The above analysis can be written for PC spreadsheet analysis of sensor designs with a reasonable degree of accuracy. However, the reader again must be cautioned that while the analysis is straightforward, the correct values used for absorption, scattering, and laser-induced damage must be derived from actual experimental data. Experimental or measured data are of highest value in the analysis. Their importance is based on the fact that the values represent the manufacturing process (surface finish, surface cleanliness, bulk material impurities) used to create the element as well as the antireflection-coating design. Also, analysis that considers only the geometrical optical gain factor from the front aperture to the detector focus will not account for the attenuation parameters of the design and will be misleading. By conducting analysis of optical attenuation, the reader also will gain an appreciation of the inherent losses associated with complex optical sensors, especially refractive-based optical designs. Extensive optical loss within traditional refractive optical systems makes recent advances in reflective and binary optical technology relevant to new optical systems.

References

1. D. Sliney and M. Wolbarsht, *Safety with Lasers and Other Optical Sources,* Plenum Press, New York (1980).
2. American National Standards Institute, Publication ANSI Z-136.1 (1986).
3. K. Yoo and R. Alfano, "Nonlinear photon localization for high intensity laser protection systems for photodetectors and eyes," *Optics Letters* **16**(23), 1823–1825 (1991).
4. R. Gagliardi and S. Karp, *Optical Communications,* R. E. Krieger Publishing Co., Malibar, FL (1988).
5. Dr. P. Perryman, Texas Instruments, personal conversation (1989–90).
6. W. B. Alexander, "Specifying glass for laser applications," in *Electro-Optical System Design,* pp. 12A–22A (1975).
7. H. Hack and N. Neuroth, "Resistance of optical and colored glasses to 3-nsec laser pulses," *Applied Optics* **21**(18), 3239 (1982).
8. F. Bartoli, L. Esterowitz, M. Kruer, and R. Allen, "Irreversible laser damage in IR detector materials," *Applied Optics* **16**(11), 2934–2937 (1977).
9. F. Bartoli, L. Esterowitz, R. Allen, and M. Kruer, "A generalized thermal model for laser damage in infrared detectors," *Journal of Applied Physics* **47**(7), (1976).
10. M. Kruer, L. Esterowitz, F. Bartoli, and R. Allen, "Optical radiation of SBN materials and pyroelectric detectors at 10.6 μm," *Journal of Applied Physics* **46**(3), (1975).
11. J. Meyer, M. Kruer, and F. Bartoli, "Optical heating in semiconductors: laser damage in Ge, Si, InSb, and GaAs," *Journal of Applied Physics* **51**(10), (1980).
12. H. E. Bennett *et al.,* Eds., *Laser Induced Damage in Optical Materials: 1989,* Proc. Boulder Damage Symposium, NIST Publication 801 (1990).
13. H. Zwick, K. Bloom, D. Lund, and E. Beatrice, "Laser ocular flash effects," *Proceedings of Army Science Conf.* (1982).
14. J. Wolfe, "Laser retinal injury," Report #177, Letterman Army Institute (1984).
15. W. Wolf and G. J. Zissis, Eds., *The Infrared Handbook,* Environmental Research Institute of Michigan, Ann Arbor, MI (1985).
16. R. L. Hall, Rockwell International Science Center, personal conversation (1992).
17. *Laser Focus* **14,** 110 (1978).
18. P. Yeh and W. Gunning, *Proceedings of the SPIE* **202,** 2–15 (1979).
19. I. Kaminow, *An Introduction to Electro-optical Devices,* Academic Press, New York (1974).

20. G. Wood, W. Clark III, M. Miller, G. Salamo, and E. Sharp, "Evaluation of passive optical limiters and switches," *Proceedings of the SPIE* **1105,** 154–180 (1989).

21. J. F. Reintjes, *The Optics Source Book, Nonlinear Optics,* S. P. Parker, Ed., pp. 236–239, McGraw-Hill, New York (1988).

22. J. Davis, A. Smith, C. Giranda, and M. Squicciarini, "Laser induced plasma formation in Xe, Ar, N and O at the first four Nd:YAG harmonics," *Applied Optics* **30**(30), (1991).

23. T. Bunning, L. Natarajan, M. Schmitt, B. Epling, and R. Crane, "Optical limiting in solutions of diphenyl polyenes," *Applied Optics* **30**(30), (1991).

24. K. Aron, R. Lytel, G. Lipscomb, M. Stiller, J. Altman, J. Thackara, and A. Ticknor, "Nonlinear organic tunable filters, switches and shutters," *Proceedings of the SPIE* **1105,** 52–60 (1989).

25. D. P. Partlow, "Switchable vanadium oxide films by a sol-gel process," *Journal of Applied Physics* **70**(1), 443–452 (1991).

26. K. Nashold, R. Brown, D. Walter, and R. Honey, "Temporal and spatial characterization of optical breakdown in a suspension of small absorbing particles," *Proceedings of the SPIE* **1105,** 78–90 (1989).

27. "Security classification guide for laser protection," Department of the Army, U.S. Army Laboratory Command (1988).

28. Kaiser Optical Systems product brochure, Ann Arbor, MI (1992).

CHAPTER 6

Obscuration Countermeasures

Donald W. Hoock, Jr.
Robert A. Sutherland
Battlefield Environment Directorate
U.S. Army Research Laboratory
White Sands Missile Range, New Mexico

CONTENTS

6.1 INTRODUCTION

6.1.1 Concept of CCD and Obscuration (CCD-O)

According to one American dictionary, the word *obscuration* is defined in terms of the verb *obscure* as "that which applies to something that is perceived with difficulty; either because it is hidden or veiled or because of obtuseness on the part of the observer." This definition is closely related to the concepts defined elsewhere in this volume if one replaces the word hidden with concealed, the word veiled with camouflaged, and the word obtuseness with deception. In fact obscuration concepts can be described in the same terms as those established for camouflage, concealment, and deception (CCD).

A major difference between airborne obscurant countermeasures (smoke, dust, etc.) and directly applied countermeasures (paints, foliage, etc.) is that the former modify target and background signatures indirectly and sometimes inadvertently through propagation effects. Although the two concepts are often treated separately, it often happens in real-world applications that the two types of countermeasures complement each other, sometimes in a synergistic manner.[1,2] For this reason the new, somewhat redundant, acronym CCD-O is coined for the combination of CCD and the obscuration effects treated in this chapter.

Obscuration is not well defined quantitatively in the literature. According to the *Glossary of Meteorology*,[3] obscuration can be linked to the term *(vertical) visibility*. However, this is much too narrow an interpretation and not really appropriate for most CCD-O applications. In this chapter, we treat obscuration as any process that specifically modifies electromagnetic propagation through the intervening medium between an object and observer.

6.1.2 Scope of the Chapter

This chapter focuses on obscurants and the combined effects of the propagation medium, meteorological conditions, and illumination conditions on the propagation of electromagnetic radiation. The electromagnetic spectrum from the ultraviolet through the infrared is emphasized, although some of the concepts are also applicable at longer wavelengths.

This chapter considers man-made aerosols and obscurants that are manufactured specifically for CCD-O applications. It also includes other anthropogenic sources including soil-derived dust and fire-produced smoke. It does not include rain, snow, or similar adverse weather phenomena, although in most respects these can be treated as obscurants using a similar methodology. We use the term *aerosol* to refer generically to both dry and wet particles dispersed and suspended in air, although distinctions are sometimes made between aerosols as liquid-based suspensions and particulates as dry suspensions. Some suspensions contain both solid and liquid phases.

A typical obscuration scenario is sketched in Fig. 6.1. The different propagation effects shown are summarized in Sec. 6.1.3 and are discussed in detail in subsequent sections. As shown in Fig. 6.1, propagation processes are generally categorized as transmission, scattering, absorption, and emission of electromagnetic radiation (of any wavelength) by the obscuring medium. The goal is to estimate, model, simulate, or otherwise predict these effects on spectral

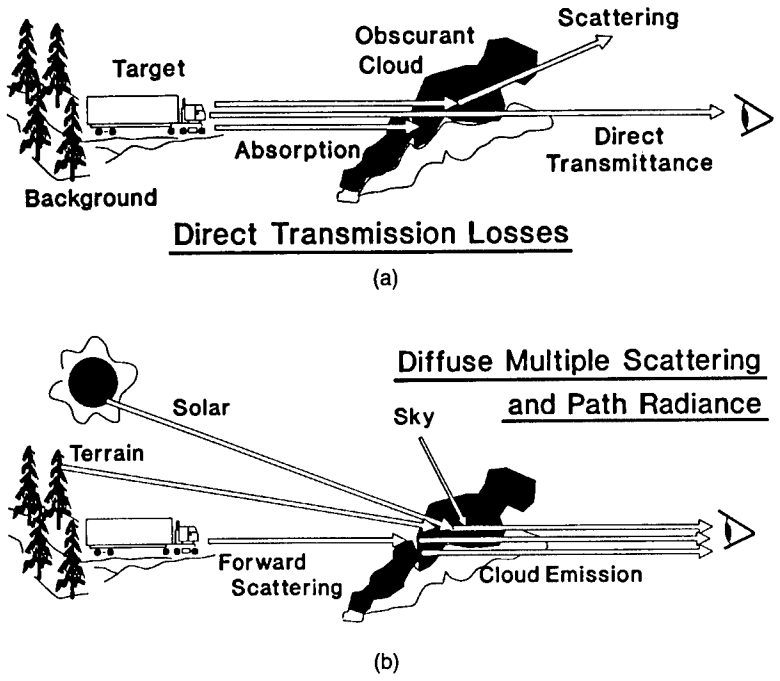

Fig. 6.1 A typical obscuration scenario includes both (a) transmission losses from the target and (b) radiance received from scattering and emission from the obscurant itself.

signatures, target contrast with its background, background clutter, etc. The final sections of this chapter describe obscuration properties and propagation effects on perception and signal-processing algorithms for human and machine-based target acquisition.

6.1.3 Overview of Propagation Mechanisms

Different processes by which an obscurant cloud alters electromagnetic radiation propagation are shown in Fig. 6.1. In direct transmission processes, absorption and scattering remove some radiation coming directly from targets and from other scene elements within the observer's field of view. Scattering within the obscurant introduces radiation from beam sources and localized point sources, such as the sun and flares that may or may not be within the field of view themselves. Spatially extended radiance sources such as sky, natural cloud cover, and terrain are also sources of diffuse multiply scattered radiation. This produces the radiant signature of the obscurant cloud itself. Thermal emission of radiation from atmospheric and aerosol clouds within the field of view can similarly contribute to this cloud radiance. Finally, optical turbulence through the natural atmosphere and forward scattering by aerosol particles can reduce available resolution and scene detail.

Electromagnetic propagation also depends on specific properties of the aerosols and their environment. Aerosol properties include mass concentration, size distribution of particles, vapor condensation and liquid droplet evaporation

parameters, optical scattering and absorption efficiencies, particle shape effects, and, for hygroscopic materials, the chemical potential of the obscurant. Environmental factors include wind, temperature, turbulence, relative humidity (RH), terrain effects on the obscurant cloud, and the ambient radiation environment (sun, sky, clouds, etc). In addition, the methods by which aerosol clouds are generated can influence aerosol particle production rates, particle settling, and various time and spatial fluctuations in propagation effects.

6.1.4 Chapter Outline

The following sections describe each of the mechanisms in some detail. Table 6.1 defines the various symbols and their SI units. Section 6.2 is devoted to basic electromagnetic propagation and obscurant properties. Section 6.3 details the effects of forward scattering on radiant intensity. Section 6.4 covers general radiative transfer theory and concepts more or less well established in the scientific community. Section 6.5 presents expressions for contrast and contrast transmission. Section 6.6 describes meteorological factors that influence obscuration effectiveness. Section 6.7 examines obscuration influences on some of the more fundamental acquisition and perception processes.

Table 6.1 Symbols, Nomenclature, and Units

Symbol	Definition	SI Units
$I(\lambda,\mathbf{r};\Omega)$	Spectral radiance, radiant intensity	$W\ m^{-2}\ sr^{-1}\ \mu m^{-1}$
λ	Wavelength	μm
$\mathbf{r}$	Line-of-sight position vector	m
s	Distance along the propagation path	m
Ω	Solid angle in direction θ,ϕ	sr
θ	Zenith angle from the vertical	rad
μ	$\mu = \lvert\cos(\theta)\rvert$, θ a zenith angle	dimensionless
ϕ	Azimuth angle clockwise from north	rad
τ	Optical depth	dimensionless
T	Transmittance	dimensionless
$c(\mathbf{r})$	Mass concentration at position $\mathbf{r}$	$kg\ m^{-3}$
α	Mass extinction coefficient	$m^2\ kg^{-1}$
α_{scat}, α_{abs}	Mass scattering, absorption coefficient	$m^2\ kg^{-1}$
CL	Concentration length	$kg\ m^{-2}$
K_{ext}, γ_{ext}	Volume extinction coefficient	m^{-1}
σ_{ext}	Particle extinction cross section	$m^2\ particle^{-1}$
Q_{ext}	Particle extinction efficiency	$particle^{-1}$
Q_{scat}, Q_{abs}	Scattering, absorption efficiency	$particle^{-1}$
a	Particle radius	μm
$n(a)$	Number distribution by particle size	$number\ m^{-3}\ \mu m^{-1}$
$m(a)$	Mass distribution by particle size	$kg\ m^{-3}\ \mu m^{-1}$

(continued)

Table 6.1 *(continued)*

Symbol	Definition	SI Units
ρ	Bulk density	kg m^{-3}
$m = n - ik$	Complex refractive index	dimensionless
a_w	Water activity	dimensionless
$\mu_h(a_w)$	Hanel growth factor	dimensionless
f	Relative humidity (RH)	dimensionless
S	Surface tension	N m^{-1}
V_m	Molar specific volume	m^3
R	Universal gas constant	J kg^{-1} K^{-1}
ω_0	Single-scattering albedo	dimensionless
N_0	Total particles per unit volume	particles m^{-3}
M_0	Total mass per unit volume	kg m^{-3}
a_{gn}	Log-normal geometric mean radius	μm
a_{gm}	Log-normal mass median radius	μm
σ_g	Log-normal standard deviation	dimensionless
$n_L(a)$	Number distribution by log-radius	m^{-3} (ln μm)$^{-1}$
$m_L(a)$	Mass distribution by log-radius	kg m^{-3} (ln μm)$^{-1}$
$a_{\text{mode},n}$	Number mode radius	μm
Y_f	Smoke mass yield factor	dimensionless
$P(\boldsymbol{\Omega},\boldsymbol{\Omega}')$	Scattering phase function	sr^{-1}
$P_n(\mu)$	Legendre polynomial	—
g	Henyey-Greenstein asymmetry factor	dimensionless
x	Scattering phase parameter	dimensionless
k	Propagation wavenumber	μm^{-1}
E, A	Electric field and amplitude	V m^{-1}
$G(\mathbf{r},\mathbf{r}')$	Free-space Greens function	—
$G\uparrow, G\downarrow$	Surface irradiance	W m^{-2}
B	Vertical optical depth	dimensionless
t_k	Temperature	K
σ	Stefan-Boltzmann constant	W m^{-2} K^{-4}
$B(\lambda,t_k)$	Planck blackbody spectral emittance	W m^{-2} sr^{-1} μm^{-1}
$e(\lambda,t_k)$	Spectral emittance	W kg^{-1} sr^{-1} μm^{-1}
$J(\lambda,\mathbf{r}';\boldsymbol{\Omega})$	Optical radiance source function	W m^{-2} sr^{-1} μm^{-1}
F_0	Solar beam irradiance	W m^{-2}
G_0	Global irradiance	W m^{-2}
D_0	Diffuse sky irradiance	W m^{-2}
A_0	Surface albedo	dimensionless
R, T	Reflectance, transmission operators	dimensionless
UR, UT	First-order R, T moments	—
URU, UTU	Second-order R, T moments	—
E_3	Third-order exponential integral	—
$C(\mathbf{r})$	Contrast observed along LOS at $\mathbf{r}$	dimensionless
I_t, I_b	Target, background radiant intensity	W m^{-2} sr^{-1}

Table 6.1 *(continued)*

Symbol	Definition	SI Units
I_p, I_s	Path radiance, path radiance limit	W m^{-2} sr^{-1}
I^*, I^d	Diffuse, direct radiance	W m^{-2} sr^{-1}
T_c	Contrast transmittance	dimensionless
ε	Emissivity	dimensionless
D^*	Duntley factor	dimensionless
S_g	Sky-to-ground ratio	dimensionless
f	Spatial frequency	cycles $mrad^{-1}$
h, R	Height and range to target	m, km
$M(f)$	Modulation transfer function	dimensionless
γ, β	Spatial, angular beam divergence	m^{-1}, rad^{-1}
MRC (f)	Minimum resolvable contrast	dimensionless
MRT (f)	Minimum resolvable temperature	K
$K(f)$	Lens MTF	dimensionless
$D(\lambda f)$	Atmospheric structure function	dimensionless
V	Visibility or visual range	km
$N(I)$	Intensity histogram	—
m_{pq}	pq'th image moment	—
M_{pq}	Central pq'th image moment	—
N_{pq}	Range invariant pq'th image moment	—
W_{ij}, G_{ij}	Gradient and edge image operators	—
S	Normalized image entropy	—
$D(i)$	Image distribution separation	—
$\mathbf{u}(z)$	Horizontal wind velocity with height	m s^{-1}
u_*	Wind friction velocity	m s^{-1}
z_r	Terrain surface roughness	m
L	Monin-Obukhov length scale	m
e_0	Partial pressure of water vapor	mbar

6.2 ELECTROMAGNETIC PROPAGATION AND BASIC OBSCURANT CHARACTERISTICS

6.2.1 The Spectral Radiance Function

Radiant flux (measured in units of energy per unit time) is the rate at which energy is transferred from one surface or region to another by electromagnetic radiation fields. *Radiant exitance* is the flux per unit area leaving a source of radiation, and *irradiance* is the flux per unit area received by a real or imaginary surface. *Radiance* refers to the radiant flux density (measured in units of energy per unit area per unit time) *per unit solid angle* incident on a surface with inward normal in the direction of propagation (i.e., on a surface oriented perpendicular to the direction of propagation). *Spectral radiance* refers to the

same quantity but for a specific wavelength. This quantity is also sometimes referred to as the *radiant intensity* or often simply as the *intensity*. However, this usage can be confused with other works that define intensity in terms of a radiant flux per unit solid angle as opposed to a radiant flux density per unit solid angle. Radiance should also not be confused with the term *luminance,* which is reserved for photometric quantities, which include the wavelength-dependent response function of the eye.[4,5]

With these basic radiometric quantities defined, we use Chandrasekhar's convention[6] $I(\lambda,\mathbf{r}_0;\mathbf{\Omega})$ to represent the spectral radiance or radiant intensity at a point in space designated by a position vector $\mathbf{r}_0$ for a component of electromagnetic radiation propagating along a unit vector in the direction $\mathbf{\Omega}$ at a monochromatic wavelength λ. The direction $\mathbf{\Omega}$ can be specified in a scenario coordinate system by a zenith angle θ and an azimuthal angle ϕ. It can also be specified as the direction of a unit vector from position $\mathbf{r}_0$ to another position $\mathbf{r}$.

6.2.2 Basic Obscurant Interactions with Propagating Radiance

Applications for CCD often require computing the radiant intensity $I(\lambda,\mathbf{r};\mathbf{\Omega})$ at position $\mathbf{r}$ relative to its value at some position $\mathbf{r}_0$. To determine the radiance arriving at the given point $\mathbf{r}$ from its several origins can require consideration of several different processes.

6.2.2.1 Fraction of Radiance that Arrives Undisturbed at r. A major obscuration effect is to partly reduce radiance. It is desirable to quantify how much of the "original" radiant intensity emanating from an object survives transmission through an obscurant with its direction, phase, and resolution properties intact. By definition, this surviving fraction quantifies the *direct transmittance* of the obscuring medium. It is computed using Beer's law, as discussed in Sec. 6.2.3.1. Quantities important in determining transmittance are the concentration of obscurant and its extinction coefficient. The latter combines the absorption and scattering losses of photons for the distribution of different-sized particles in the aerosol. Transmittance is important in its own right in many problems where obscuration results in significant energy loss from passive or active sources.

6.2.2.2 Fraction of the Original Energy that is Detectable at r. Sometimes it is important to quantify the total radiant intensity detectable at $\mathbf{r}$ that originated at $\mathbf{r}_0$. Direct transmission is only one contributing factor. An optically thick, highly scattering obscurant, for example, can effectively reduce the directly transmitted power from a strong active source to zero. Yet the source might still be detectable because some energy from $\mathbf{r}_0$ reaches $\mathbf{r}$ after scattering one or more times in the obscurant. This scattered fraction of original energy is not included in the direct transmittance calculated from Beer's law. The additional optical quantities that impact this *forward scattering* contribution to the radiance from $\mathbf{r}_0$ are the obscurant's single scattering albedo and its angular pattern of scattering, called the *phase function.* The scattering function for particles that have a dimension much larger than the wavelength of the radiation is usually highly peaked in the forward direction. Particles large compared to the wavelength thus contribute significantly to this effect. Forward scattering is also important if a detector at $\mathbf{r}$ looking in the direction

of $\mathbf{r}_0$ has a large area or a wide field of view so that many scattered photons contribute to the received power. Then higher order multiple scattering processes could need to be included.

6.2.2.3 Total Radiance Received at r Regardless of Source. Not all photons arriving at $\mathbf{r}$ provide a radiance or *signal* coming directly from an object to be imaged or a source to be detected. Some of the received radiance results when photons from the ambient electromagnetic radiation environment scatter multiple times by the obscurant and arrive at $\mathbf{r}$. This is called *diffuse radiance* or *path radiance*. Some radiance also results from photons emitted from the obscurant itself, as in the case of thermal emission. This overall effect can be an important background interference, or noise, both steady and fluctuating, added to a desired signal. The path radiance contribution is required, for example, to calculate contrast and contrast transmittance (which differs from direct transmittance). Diffuse radiance also provides the appearance and signature for the obscurant cloud itself. For CCD applications it is desirable to have a highly detectable obscurant for some purposes and an obscurant with low signature for others. The calculation of the diffuse radiance component is influenced by the spatial distribution or geometries of the obscurant concentrations, the distribution and strength of illumination sources, the environmental state of the obscurant medium, and the availability of suitable mathematical tools for solving multiple scattering problems to sufficient accuracy.

6.2.2.4 Spreading and Fluctuation Effects on Radiance. A process important to some applications is how the scattering of photons from aerosol particles alters the coherence and phase information in the received signal. This decreases the ability to focus point objects through the obscurant to the diffraction or sensor limit present in clear conditions. The spreading effect is similar to that of optical turbulence, but it depends more on the sizes of particles than on the sizes of turbulent eddies that produce refractive fluctuations.

A different fluctuation effect on radiance is induced by aerosol concentration inhomogeneities over the target-to-observer lines of sight (LOS). Concentration inhomogeneities are generated over a broad range of scales by turbulent processes in the atmosphere. They can be important as a form of correlated noise across a partly obscured image or as a source of intermittency in received radiance.

6.2.3 Quantities for Computing Transmittance

The transmission of radiant energy through a propagation medium depends significantly on the concentration of aerosol and the optical properties of the aerosol. Beer's law quantifies the basic attenuation over a line of sight.

6.2.3.1 Direct (Beer's Law) Transmittance. Radiant intensity that survives intact after passing from $\mathbf{r}_0$ to $\mathbf{r}$ through an obscuring medium of optical depth $\tau(\lambda;\mathbf{r},\mathbf{r}_0)$, also called the *optical thickness,* is given by the Beer-Bouguer-Lambert attenuation process,[7] often referred to simply as Beer's law:

$$I(\lambda,\mathbf{r};\boldsymbol{\Omega}) = I(\lambda,\mathbf{r}_0;\boldsymbol{\Omega}) \exp[-\tau(\lambda;\mathbf{r},\mathbf{r}_0)] \ , \tag{6.1}$$

where

$$T(\lambda;\mathbf{r},\mathbf{r}_0) = \exp[-\tau(\lambda;\mathbf{r},\mathbf{r}_0)] \tag{6.2}$$

is called the *direct transmittance,* or often just the *transmittance.* This simple expression is useful for determining the total fraction of radiance absorbed and scattered by an obscurant cloud as illustrated in the upper part of Fig. 6.1. Beer's law does not completely describe, however, the total radiant intensity reaching **r.** Some photons from $\mathbf{r}_0$ can scatter multiple times and still reach **r.** Additional photons also scatter into the path from other sources.

Hypothetical Example. To make this statement clearer, consider the example of a two-path monostatic laser radar system wherein a laser beam travels to a target, is reflected, and returns along the same path to a detector. What optical depth τ of obscurant is required according to Beer's law to remove 99.95% of the power that would propagate back to the detector under clear conditions? Is it possible for the return power to be 0.0010 of the clear air power when an obscurant cloud is present with an optical depth of 4.5?

Answer. From Eq. (6.2) one finds that an obscurant optical depth τ of 3.8 produces a transmittance T of 0.0224. The original radiant intensity from the source is reduced by this factor in reaching the target, as indicated by Eq. (6.1). Any reflected radiant intensity is also reduced by this factor on its return trip through the obscurant to the detector. The total expected reduction factor is thus $(0.0224)^2 = 0.0005$. An obscurant with optical depth of 3.8 that is traversed twice should therefore be sufficient to remove 0.9995 of the original radiant intensity through scattering and absorption.

The second part of this hypothetical example points out, however, an important limitation in using Eq. (6.1). In this example of a two-path traverse of the obscurant, an optical depth τ of 4.5 is sufficient to scatter and absorb all but about 0.0001 of the original clear air power according to Eq. (6.1). However, if a total power of 0.0010 of the clear air value is still being received, then one can conclude that some of the laser energy scattered by the obscurant is also reaching the detector. Equation (6.1) computes only the fraction of the radiance that traverses the obscurant without undergoing any interactions. It tells us nothing about what subsequently happens to any scattered and absorbed power. Other propagation processes must thus also be considered. These depend on the properties and placements of the obscurant and sensor and are considered in the following.

6.2.3.2 Definitions of Line of Sight Versus Path of Propagation. Generally, $\mathbf{r}_0$ is a position vector to any physical point along a path of propagation at which the radiance is known. It does not need to coincide with a physical object. In many applications, however, $I(\lambda,\mathbf{r}_0;\Omega)$ is taken to be the radiant intensity originating from some solid object located at $\mathbf{r}_0$ such as a target or a background. The position vector **r** can similarly be the position of an observer or sensor. This chapter uses the term *propagation path* as the direction along which the radiation is traveling, i.e., from $\mathbf{r}_0$ to **r.** The line of sight (LOS), however, is in the reverse direction, i.e., the path from which an observer at **r** seeks to observe an object at $\mathbf{r}_0$. For some quantities, such as optical depth τ, this difference in the direction is irrelevant. However, many processes, such as solar scattering, involve distinct asymmetries in direction. Care is thus

needed to avoid confusion. A second potential point of confusion concerns the use of the term LOS in some CCD applications to mean any optical path that is unobstructed by terrain and vegetation and over which an object at $\mathbf{r}_0$ is thus viewable by an observer at $\mathbf{r}$. In this chapter, LOS means simply a straight line from an observer to an object. No guarantee is implied by the term LOS that an object at $\mathbf{r}_0$ is in fact perceivable from $\mathbf{r}$ under given obscuration conditions.

6.2.3.3 Optical Depth in Terms of Extinction and Concentration. Between any two position vectors $\mathbf{r}_0$ and $\mathbf{r}$, the length of the propagation path can be defined as $s = |\mathbf{r} - \mathbf{r}_0|$, also called the *range*. Points on this path can be parameterized by a scalar s' along a unit vector in the direction $\boldsymbol{\Omega}$ pointing from the position $\mathbf{r}_0$ to $\mathbf{r}$:

$$\mathbf{r} = \mathbf{r}_0 + s'\hat{\boldsymbol{\Omega}}, \quad 0 \leq s' \leq s \ . \tag{6.3}$$

In Eq. (6.2), the optical depth or optical thickness $\tau(\lambda;\mathbf{r},\mathbf{r}_0)$ can be defined over this optical path as

$$\tau(\lambda;\mathbf{r},\mathbf{r}_0) = \int_0^s \alpha(\lambda;s')c(s')\, ds' \ , \tag{6.4}$$

where $c(s')$ is the obscurant concentration at each point s' along the path from $\mathbf{r}_0$ to $\mathbf{r}$. The mass extinction coefficient $\alpha(\lambda,s')$ is a wavelength-dependent optical property of the obscurant material. It can also depend on the particle size distribution, particle composition, and shape (often assumed to be spherical). The effects of these factors on optical properties are addressed later.

To a good approximation, one often assumes that obscurant material properties are essentially uniform in an aerosol cloud, with major variations only in obscurant concentration. In that case, the optical depth is generally written

$$\tau(s) = \alpha\int_0^s c(s')\, ds' = \alpha \mathrm{CL} \ , \tag{6.5}$$

where the term *concentration length* (CL) or *CL-product* is used for the total mass density integrated over the LOS. For vertical columns, optical depth is sometimes denoted as B in later sections.

Hypothetical Example. A transmissometer is used to monitor obscurant transmittance over an LOS at a CCD test. A mixture of obscurants is released into a narrow cloud in front of a target. To estimate CL, obscurant concentrations are monitored across the cloud at several points along the LOS. At one particular moment the CL is 0.0030 ± 0.0006 kg m^{-2}, and the obscurant cloud transmittance is 0.350 ± 0.005. What is α at that moment? How can error in estimating α be reduced if obscurant concentration varies but not its composition?

Answer. The total direct transmittance through a medium is the product of the transmittances of different components that make up the medium. In this example, the transmittance over the LOS through the natural atmospheric gases, haze, and other ambient aerosols can be designated T_{air}. The trans-

mittance through the released obscurants alone over the same LOS can be designated T_{obsc}. Then the total direct transmittance over the LOS (at a given wavelength) is

$$T_{total} = T_{air}T_{obsc} \ . \tag{6.6}$$

The transmissometer in this example measures T_{obsc} as the ratio of total transmittance through the obscurant to a reference measurement of total transmittance in "clear air." Using Eqs. (6.2), (6.5), and (6.6), the obscurant mass extinction coefficient is thus estimated from

$$\alpha = -\frac{\ln(T_{obsc})}{CL} \ , \tag{6.7}$$

so that α is approximately 350 $m^2\ kg^{-1}$. The estimated uncertainty in this value is $\pm 75\ m^2\ kg^{-1}$, with more than 90% of the error in α resulting from measurement uncertainty in CL. This follows from the equation for propagated error with uncertainties ΔT_{obsc} of 0.005 and ΔCL of 0.0006:

$$|\Delta\alpha| \approx \frac{1}{T_{obsc}CL}|\Delta T_{obsc}| - \frac{\ln(T_{obsc})}{(CL)^2}|\Delta(CL)| \ . \tag{6.8}$$

The uncertainty in α might be reduced by averaging many values of α determined over time. However, if the relative fractions of different obscurants and their optical properties remain constant in time, then it is simpler to collect a time-integrated concentration or *dosage* of obscurant at several points along the LOS. A dosage integrated over the LOS can then be divided by time-integrated log-transmittance to estimate a value for α:

$$\alpha = \frac{-\int_0^t \ln[T_{obsc}(t')]\,dt'}{\int_0^L \left[\int_0^t c(t';s')\,dt'\right] ds'} \ . \tag{6.9}$$

This method is sometimes used to measure α in the field. However, even for obscurant mixtures where only the concentration varies in time, this method can be inaccurate if the extinction varies significantly with wavelength. The average of several monochromatic α values over a band of wavelengths does not necessarily equal the single value of α that results from Eqs. (6.7) or (6.9) using a single, wavelength-averaged transmittance. This error is further considered in a later section.

6.2.3.4 Obscurant Extinction, Scattering and Absorption Coefficients. Extinction is quantified in different ways. In obscuration problems it is common to use the extinction per unit obscurant concentration integrated over the entire size distribution of airborne particles. This mass extinction

coefficient $\alpha(\lambda)$ is also referred to as the *specific extinction coefficient.* It can be related to other forms for quantifying extinction including the volume extinction coefficient $K_{ext}(\lambda,s)$ or $\gamma_{ext}(\lambda,s)$, the single-particle or molecular extinction cross section $\sigma_{ext}(\lambda,a)$, and the single-particle extinction efficiency $Q_{ext}(\lambda,a)$. Useful conversions between these representations of extinction coefficients are provided, assuming spherical particles, by

$$\begin{aligned}\alpha(\lambda) &= \frac{K_{ext}(\lambda,s)}{c(s)} = \frac{\gamma_{ext}(\lambda,s)}{c(s)} \\ &= \frac{\int \sigma_{ext}(\lambda,a)n(a)\,da}{\rho\int (4\pi/3)a^3 n(a)\,da} \\ &= \frac{3\int Q_{ext}(\lambda,a)a^2 n(a)\,da}{4\rho\int a^3 n(a)\,da}\ ,\end{aligned} \tag{6.10}$$

where ρ is the bulk density of the obscurant material, a is the particle radius, and $n(a)$ is the number of particles of radius a per unit volume in the radius interval a to $a + da$.

The volume extinction coefficient K_{ext}, sometimes written γ_{ext}, is most useful when the obscurant concentration is uniform. It then represents an optical depth per unit distance through the aerosol, as can be derived from Eq. (6.5).

The single-particle extinction efficiency Q_{ext} is the dimensionless ratio of the optical extinction cross section per particle σ_{ext} to the geometrical particle cross-sectional area. This is often calculated from theory as discussed in subsequent sections.

The integrated quantities in the denominators of Eq. (6.10) are the volume of material per unit volume of air times the bulk mass density of the obscurant material. This is equivalent to obscurant concentration. Thus, the mass extinction coefficient is equivalent to particle extinction cross sections integrated over all sized particles per unit mass concentration of aerosol in the air.

The extinction coefficient quantities are each the sum of two parts: one to account for scattering and one to account for absorption. For example,

$$\alpha(\lambda) = \alpha_{scat}(\lambda) + \alpha_{abs}(\lambda)\ , \tag{6.11}$$

where absorption, scattering, and extinction all share common units.

Note that purely as a matter of convenience, traditional literature and system test specifications often use non-SI units in CCD obscuration applications. Typically α is given in units of $m^2\ g^{-1}$, for example; K_{ext} is often reported in km^{-1}; concentrations are measured in $g\ m^{-3}$; bulk density is given in centimeter-gram-second (cgs) system units of $g\ cm^{-3}$ or as a dimensionless specific gravity; and particle dimensions are cited in micrometers. The reason for these non-SI units is that numerical values for these quantities then tend to fall into convenient ranges of about 0.001 to 100 in practical problems. Proper SI unit conventions are cited in Table 6.1, however.

6.2.4 Physical and Optical Properties for Scattering Coefficients

The number or mass of particles of different sizes, the refractive index at each wavelength, the particle shapes, and their orientations (if the particles are not spherical) affect the transmittance and related optical properties of aerosols.

6.2.4.1 Particle Size Distributions. Scattering, absorption, and extinction functions depend, in part, on the ratio of the particle or droplet dimension (e.g., radius) to the wavelength of the incident electromagnetic radiation. Nearly monodisperse (single-sized) distributions of particles exist, such as polystyrene microspheres that are used for optical calibration. However, most natural aerosol clouds contain particles of many different sizes. Some obscurants, in particular soil-derived dust and fire smokes, have particles that range in size from hundredths to hundreds of micrometers in radius. Therefore, a weighted average over the number of particles of each size times the optical properties at each size must be performed to obtain the overall bulk optical properties for clouds of these materials.

It is common to fit actual measured data on the number or mass of particles of each size to one of the many types of smooth size distribution functions. Depending on the type of function selected, the data are reported in terms of a few relevant parameters: the minimum, maximum, and mean radii; the standard deviation or power law exponent; and the total number or mass of particles per unit volume of medium (i.e., total number density or mass concentration).

Log-Normal Number Distribution. A distribution of particles by size having a log-normal probability distribution is one example. It can be defined for the number of particles per unit volume $n(a)$ per radius a in the interval a to $a + da$. This is formally the derivative of the cumulative number distribution $N(a)$, which defines the total number of particles per unit volume with radii smaller than a:

$$n(a) = \frac{dN(a)}{da} = \frac{N_0}{\sqrt{2\pi}a \ln\sigma_g} \exp\left[-\frac{1}{2}\left(\frac{\ln a - \ln a_{gn}}{\ln\sigma_g}\right)^2 \right] . \tag{6.12}$$

The distribution parameters are the *geometric mean radius* a_{gn}, the *geometric mean standard deviation* σ_g, and the total number of particles per volume of air N_0. The *number median radius* is also a_{gn}, with half of the total number of particles smaller than this radius. Plotted with radii on a logarithmic scale, $n(a)$ is symmetrical about a peak at

$$a_{\text{mode},n} = a_{gn} \exp[-(\ln\sigma_g)^2] , \tag{6.13}$$

where it has the value

$$n(a_{\text{peak}}) = \frac{N_0}{\sqrt{2\pi}a_{gn} \ln\sigma_g} \exp\left[+\frac{1}{2}(\ln\sigma_g)^2 \right] . \tag{6.14}$$

One also commonly encounters the log-normal distribution written as $n_L(a)$, the number of particles per unit volume of radius a in the interval $\ln a$ to

$\ln a + d(\ln a)$. This distribution is Gaussian and symmetrical when plotted with a logarithmic radius scale:

$$n_L(a) = \frac{dN(a)}{d(\ln a)} = \frac{N_0}{\sqrt{2\pi}\,\ln\sigma_g} \exp\left[-\frac{1}{2}\left(\frac{\ln a - \ln a_{gn}}{\ln\sigma_g}\right)^2 \right] . \tag{6.15}$$

It peaks at the mode radius, which is also a_{gn}, with the value

$$n_L(a_{gn}) = \frac{N_0}{\sqrt{2\pi}\,\ln\sigma_g} . \tag{6.16}$$

It is easy to see that the logarithm of the *geometric mean radius* a_{gn} equals $\ln a$ averaged over $n(a)$, i.e., the *number mean log-radius*:

$$\frac{1}{N_0}\int (\ln a) n(a)\, da = \frac{1}{N_0}\int (\ln a) n_L(a)\, d(\ln a) = \overline{\ln a} = \ln a_{gn} . \tag{6.17}$$

Note, however, that a_{gn} does not equal the *number mean radius,* because

$$\ln\left[\frac{1}{N_0}\int a n(a)\, da\right] = \ln\bar{a} = \ln a_{gn} + \frac{1}{2}(\ln\sigma_g)^2 . \tag{6.18}$$

This relationship and other moments of the distribution are easily derived by transforming the distribution to log-radii using

$$\begin{aligned} a^p n(a)\, da &= a^p n_L(a)\, d(\ln a) = \exp(p \ln a) n_L(a)\, d(\ln a) \\ &= \frac{N_0}{\sqrt{2\pi}\,\ln\sigma_g} \exp\left[+ \frac{1}{2}p^2(\ln\sigma_g)^2 + p \ln a_{gn} \right] \\ &\quad \times \exp\left(- \frac{1}{2}\left\{ \frac{\ln a - [p(\ln\sigma_g)^2 + \ln a_{gn}]}{\ln\sigma_g} \right\}^2 \right) d(\ln a) , \end{aligned} \tag{6.19}$$

so that Eq. (6.18) follows from Eq. (6.19) with $p = 1$, and Eqs. (6.13) and (6.14) are based on $p = -1$. Additional discussion of log-normal distribution parameters can be found in Ref. 8, with the caution that $\ln\sigma_g$ is simply termed σ_g in that work.

Log-Normal Mass Distribution. In calculating mass extinction it is also useful to express the log-normal size distribution by mass:

$$\begin{aligned} m(a)\, da &= m_L(a)\, d(\ln a) = \frac{4}{3}\pi\rho a^3 n_L(a)\, d(\ln a) \\ &= \frac{M_0}{\sqrt{2\pi}\,\ln\sigma_g} \exp\left[-\frac{1}{2}\left(\frac{\ln a - \ln a_{gm}}{\ln\sigma_g}\right)^2 \right] d(\ln a) , \end{aligned} \tag{6.20}$$

where the *mass median radius* a_{gm} is related to the *geometric mean radius* a_{gn} through Eq. (6.19) with $p = 3$:

$$\ln a_{gm} = \ln a_{gn} + 3(\ln\sigma_g)^2 \ . \tag{6.21}$$

The log-normal *mass mean radius* is related to a_{gm} similar to Eq. (6.18):

$$\ln\left[\frac{1}{M_0}\int am(a)\,da\right] = \ln\overline{a_m} = \ln a_{gm} + \frac{1}{2}(\ln\sigma_g)^2 \ , \tag{6.22}$$

where the total mass per unit volume M_0 can be determined from

$$\begin{aligned} M_0 &= \frac{4}{3}\pi\rho N_0(a_{gn})^3 \exp\left[+\frac{9}{2}(\ln\sigma_g)^2\right] \\ &= \frac{4}{3}\pi\rho N_0(a_{gm})^3 \exp\left[-\frac{9}{2}(\ln\sigma_g)^2\right] \\ &= \frac{4}{3}\pi\rho N_0(\overline{a_m})^3 \exp[-6(\ln\sigma_g)^2] \ . \end{aligned} \tag{6.23}$$

The peak in $m(a)$ is at the mode radius

$$a_{\text{mode},m} = a_{gm} \exp[-(\ln\sigma_g)^2] \ . \tag{6.24}$$

Measured particle size distributions are often reported as a cumulative distribution of the percentage number $N(a)$ or mass $M(a)$ of particles smaller than radius a and the median radius or diameter at the 50% point in the cumulative distribution. To determine if there is a fit to a log-normal distribution, however, the cumulative data should be transformed to $n_L(a)$ and $m_L(a)$ to find positions of peaks and σ_g. Measurements often cover only a finite band of radii that might not capture the very smallest or very largest particles. Thus, the reported median from the cumulative size distribution by number or by mass might not be a good estimate of a_{gn} or a_{gm}, particularly if there is more than one peak indicating a superposition of more than one *mode.*

Hypothetical Example. Suppose an aerosol is truly log-normal with a single mode having geometric mean radius a_{gn} of 0.9 μm, standard deviation σ_g of 2.3, specific gravity of 1.6 (i.e., a bulk density ρ of 1.6 g/cm^3), and airborne concentration of 5.3×10^{-4} kg m^{-3}. Characterize the plotted distributions and consider the implications to using a size distribution measurement device that has particle size limits of 1 to 30 μm.

Answer. The total mass in the sample volume M_0 is 5.3×10^{-4} kg m^{-3}. The bulk density ρ is 1600 kg m^{-3}. Using Eq. (6.23) with a_{gn} expressed in meters, N_0 is thus 4.8×10^9 particles m^{-3}. A plot of $n_L(a)$ will peak at a_{gn} of 0.9 μm with a peak value according to Eq. (6.16) of 2.3×10^9 particles m^{-3} (ln μm)$^{-1}$. The $n_L(a)$ distribution falls to $1/e$ of its peak value according to Eq. (6.14) at 0.28 and 2.9 μm.

Equation (6.19) shows that, when multiplied by any power of the radius, a log-normal distribution remains a symmetrical Gaussian on a logarithmic radius scale. It maintains the same width but shifts vertically and to larger or smaller radii. For example, if $n(a)$ is plotted instead of $n_L(a)$, the distribution

peak shifts according to Eq. (6.13) to a mode radius of 0.45 μm. The 1/*e* values shift to smaller radii compared to $n_L(a)$ by the same factor of 0.5, i.e., to 0.14 and 1.5 μm. This can be checked with Eq. (6.12). The peak value of $n(a)$ is 3.6 $\times$ 10^9 particles m^{-3} μm^{-1}, from Eq. (6.14).

Although the number mean radius from Eq. (6.18) is 1.3 μm, neither the $n(a)$ nor the $n_L(a)$ distributions peak in the measurement range of 1 to 30 μm. In fact, 55% of the total number of particles are smaller than the 1-μm lower limit of the proposed measurement device.

However, suppose the measurement and analysis can be performed in terms of mass. From Eq. (6.21), the mass distribution $m_L(a)$ peaks at a mass median radius a_{gm} of 7.2 μm with a value according to Eq. (6.20) of 2.5 $\times$ 10^{-4} kg m^{-3} $(\ln \mu m)^{-1}$. From Eq. (6.20), $m_L(a)$ falls to 1/*e* of its peak value at 2.2 μm and 23 μm, well within the device's range. The distribution $m(a)$ peaks at a mode radius of 3.6 μm with the value of 5.0 $\times$ 10^{-5} kg m^{-3} μm^{-1}. It falls to 1/*e* of the peak at 1.1 and 12 μm. The mass mean radius, from Eq. (6.22), is 10 μm, and more than 99.1% of the total mass particles is contained in the 45% of the total number of particles that have a radius larger than 1 μm. The device limits are thus appropriate for characterizing the mass distribution.

When presented with plotted size distribution data, one should first determine whether data represent $N(a)$, $M(a)$, $n(a)$, $n_L(a)$, $m(a)$, or $m_L(a)$ by examining the units along the vertical axis. Conversion between number and mass size distributions can aid in determining size distribution parameters.

Measured Log-Normal Distributions. Tables 6.2 and 6.3 cite representative values and references for measured and modeled airborne log-normal size distributions of some typical obscurants. The representative values in Table 6.2 are for standard screening smokes, natural blowing dust, vehicular dust, and high-explosive- (HE)-generated dust. Table 6.3 provides best estimates for carbonaceous smokes including acetylene soot, wood fire smoke, and petroleum fire smoke. The tables list the geometric mean radius; the geometric standard deviation; the quartile mass radii for 25, 50 (mass median), and 75% cumulative mass; the mode radius or position of the peak in $m(a)$; the mean radius for $m(a)$; a representative specific gravity or particle mass density; and the mass fraction partitioned among bimodal distributions.

Specific Gravity and Bulk Particle Mass Density. Particle-specific gravities and bulk densities are presented in Tables 6.2 and 6.3 and in later tables and figures. These mass densities represent typical values or ranges of values for *in situ* airborne particles and agglomerates as they might be found in obscurant clouds. Thus, soil-derived dust lofted from vehicles and explosions and also certain very porous carbonaceous smoke particles can have an average mass of material per unit particle volume that is much smaller than that of uniform solid or liquid droplets. For example, soil-derived dust particle densities can range from below 1.5 g/cm^3 (lightly cemented surface silt and clay aggregates) up to 2.6 g/cm^3 (quartz and granite sand grains).[9] Carbonaceous smokes can similarly range from less than 0.2 g/cm^3 (porous aggregates with low particle to void ratios) up to 1.87 g/cm^3 (bulk carbon).[10] Note that these densities are primarily important in balancing the available mass of original soil or smoke materials with the eventual airborne mass

Table 6.2 Airborne Aerosol Log-Normal Size Distributions for Phosphorus Smoke, Fog Oil Smoke, Hexachloroethane Smoke, Natural Dust, Vehicular Dust, and Explosive-Produced Dust

Obscurant	a_{gn}	σ_g	$m_L(a)$ Quartiles a_{25}	a_{gm}	a_{75}	m(a) a_{mode}	a_{mean}	Density (g/cc)	Mass %
Phosphorus 17% Rel. Hum.	0.24	1.45	0.28	0.36	0.47	0.31	0.39	1.62	100
Phosphorus 50% Rel. Hum.	0.27	1.45	0.32	0.41	0.53	0.36	0.44	1.44	100
Phosphorus 90% Rel. Hum.	0.37	1.45	0.44	0.56	0.72	0.49	0.60	1.18	100
Fog Oil	0.142	1.8	0.27	0.40	0.60	0.28	0.48	0.89	100
Hexachloroethane 85% RH	0.42	1.45	0.50	0.64	0.82	0.56	0.69	1.22	100
Dust: Blowing (heavy)	0.48	2.2	1.82	3.10	5.27	1.66	4.23	1.5-2.6	53
(Ref. 17)	26.1	1.37	28.4	35.1	43.4	31.8	36.9	1.5-2.6	47
Dust: Blowing (sandy)	1.02	2.05	2.95	4.79	7.77	2.86	6.19	1.5-2.6	7
(Ref. 16)	21.0	1.68	33.2	47.1	66.8	36.0	53.9	1.5-2.6	93
Dust: Desert (heavy)	0.50	2.25	2.08	3.60	6.21	1.87	5.00	1.5-2.6	33
(Ref. 19)	15.0	1.60	21.2	29.1	40.0	23.3	32.5	1.5-2.6	67
Dust: Vehicular (Sandy)	0.84	2.06	2.47	4.03	6.55	2.39	5.23	1.5-2.6	21
(Ref. 16)	27.0	1.57	36.7	49.7	67.4	40.6	55.0	1.5-2.6	79
Dust: Vehicular (Silty)	2.55	1.95	6.19	9.72	15.3	6.22	12.1	1.5-2.6	78
(Ref. 16)	19.0	1.59	26.5	36.2	49.5	29.2	40.3	1.5-2.6	22
Dust: HE (composite)	0.50	2.60	4.06	7.73	14.7	3.10	12.2	1.5-2.6	25
(Ref. 20)	22.5	1.87	47.8	72.9	111.	49.3	88.7	1.5-2.6	75
Dust: HE (damp soil)	0.10	3.7	7.02	17.0	41.1	3.07	40.0	1.5-2.6	36
(Ref. 20)	17.0	2.0	45.0	71.9	115.	44.5	91.4	1.5-2.6	64
Dust: HE (wet soil)	0.12	3.8	10.2	25.2	62.0	4.24	61.4	1.5-2.6	2
(Ref. 20)	60.0	1.6	84.8	116.	160.	93.0	130.	1.5-2.6	98

Table 6.3 Best Estimates of Log-Normal Particle Size Parameters for Various Fire-Produced Smokes

Obscurant	a_{gn}	σ_g	$m_L(a)$ Quartiles a_{25}	a_{gm}	a_{75}	m(a) a_{mode}	a_{mean}	Density (g/cc)	Mass %
Acetylene Soot (Ref. 22)	0.05	1.78	.092	.136	.200	.097	.160	Varies	100
Wood Fire Smoke: (Ref. 25)	.010 .060	1.32 1.58	.010 .083	.013 .112	.015 .153	.012 .091	.013 .125		Var
Wood Fire Smoke: Other Measured Ranges (Ref. 26)	.10 to .15	Not Available							
Petroleum Fire Smoke (Ref. 10)	0.10 0.10	1.50 4.35	.125 24.3	.164 65.5	.215 177.	.139 7.54	.178 193.		Var
Petroleum Fire Smoke Other Large-Mode Ranges (Ref. 29)	0.10 to 0.15	3.5 to 4.5	4.76 48.2	11.1 133.	25.8 367.	2.31 13.8	24.3 412		Var

in the final obscurant cloud. They do not affect the relative shape and size parameters given for the size distributions.

Screening Smoke. White phosphorus (WP) and red phosphorus (RP) burn to produce a hygroscopic smoke containing phosphoric acids. Hexachloroethane (HC) is a hygroscopic zinc chloride smoke produced when zinc oxide and hexachloroethane are burned in the presence of an aluminum catalyst.[11] These smokes are composed of spherical liquid particles that grow with relative humidity to an equilibrium size by absorbing ambient moisture that depends on ambient relative humidity. Size parameters in Table 6.2 are based on analysis of limited measured data[12] and on modeled hygroscopic particle growth.[13]

Fog Oil Smoke. Fog oil is a highly refined oil composed of long-chain hydrocarbons of approximate molecular weight of 100. It is vaporized at high temperatures and expelled by a generator to condense into small droplets in the air. It forms a white cloud that is particularly efficient at obscuring wavelengths in the visible band, indicative of very small particles.[14] Data in Table 6.2 are based on limited measurements and refinements to provide a very good fit to measured extinction data. Droplet sizes vary somewhat with the efficiency and temperature of the liquid vaporization process and the cooling rate of the vapor, however.

Locally Generated Dust Clouds. Airborne soil-derived dust contains particles of many sizes and nonspherical shapes. It can contain multiple mineral components with different morphologies, such as fine platelet clay particles and large angular sand particles. The effects of mixtures of different compositions on optical properties have been studied[15] as have the effects of shape on mass extinction.[16] Table 6.2 provides a number of measured size distribution data sets for dust with heavy mass concentrations or airborne within a few tens of meters of the sources. These should be interpreted as representing effective radii of spherical particles producing the same measured response as the nonspherical dust particles. The different examples are provided to illustrate somewhat the variations in measured values.

Soil-derived dust size distribution data taken at different measurement sites show common qualitative features, including the presence of two log-normal modes. A low-visibility (heavy mass loading) size distribution measured for blowing dust is shown in Table 6.2 under the entry "blowing (heavy)."[17,18] The result of several measurements of airborne dust from particularly sandy soil is listed under "blowing (sandy)."[16] A low-visibility, blowing-dust size distribution is listed as "desert (heavy)."[15,19]

Measured airborne distributions for explosive-generated dust[20] and for vehicular-generated dust[16] also show two modes. Log-normal size distribution parameters for dust raised by a tracked vehicle in a very sandy soil in New Mexico, designated as "vehicular (sandy)," shows quartile mass radii similar to but somewhat larger than those for blowing dust. Measurements of vehicular dust from a tracked vehicle on a relatively silty soil (having many more fine particles than in the sandy soil) in Colorado are characterized under "vehicular (silty)" in Table 6.2.

Size distribution data for explosive-generated dust[20] have also shown a general commonality between airborne dust size distributions at widely sep-

arated locations. An overall fit to clay, sandy clay, and sandy soil dispersed into the air by small high-explosive (HE) charges is listed as "HE (composite)" in Table 6.2. These measurements were performed a few tens of meters downwind of the detonations. This distribution shows the presence of much larger radii in the large-particle mode compared to the vehicular and blowing dust distributions. Two specific examples of measurements are also given for moisture effects on HE-generated dust[20] in slightly damp and wet soils at a location in the southern United States. The shift to larger particles with soil moisture might not simply represent moist dust grain agglomeration. The HE dust data contain the carbonaceous residue of the explosion, and in the wet soil tests the cloud appeared to be mainly a dark gray smoke.

Best Estimates for Carbonaceous Smokes. Any real-world fire event is a complex process involving the production of numerous complex aerosols and gases. In some cases, the aerosols are comprised of organic oil-like liquids and thus form nearly spherical droplets as in the case of some vegetative fire products.[21] At the other extreme, the aerosols can be comprised of long carbon chain structures that can overlap and entwine to form large porouslike agglomerates. Moreover, the particle morphology, composition, and size distribution can be a highly fluctuating function over both space and time and very dependent on fire type, fire intensity, and ambient conditions. In spite of the difficulties, there have been substantial measurements carried out in both the laboratory and the field. Table 6.3 displays some of the values of particle size parameters and extinction coefficients that are used in modeling.

The data for soot are well documented in a series of laboratory measurements by Roessler et al.[22] and Roessler and Faxvog.[23] The actual shape of soot particles depends on the source and can form either a coral-like structure with an overall spherical shape or can consist of agglomerated carbon spheres also forming an overall spherical shape having particle-to-void ratios[24] between 0.20 and 0.40.

For wood fire smokes the particle size distribution is a function of time and also depends on whether the fire source is flaming or smoldering. The values in Table 6.3 represent overall gross averages. For smoldering sources, the fraction of particles in the small size mode tends to increase with time and for flaming conditions tends to decrease with time according to Helsper et al.[25] The measurements in Table 6.3 by Mulholland and Oldemiller[26] were obtained under controlled laboratory conditions and for smoldering fires. For nonflaming conditions, these authors report smaller particles of the order of 0.005- to 0.02-μm radius.

Petroleum-based fire smokes produce a thick black smoke comprised of both organic-based carbon (mostly hydrocarbons) and nonorganic carbon agglomerates. Estimates of the organic-to-nonorganic ratio[10,27,28] vary from 4 to 20%. The measurements of particle size for petroleum-based fire smokes in Table 6.3 are based on data obtained in the field on small-scale test fires of burning diesel fuel obtained by Pinnick et al.[29] The particle size parameters reported by Sutherland et al.[10] in Table 6.3 are based in part on measured data and in part on the assumption that the small mode is comprised of unburned hydrocarbons. Other studies indicate that the unburned hydrocarbon fraction is attached to the large-mode carbon agglomerates over all sizes.[28] Another anal-

ysis of burned fuel oils using acousto-optics has also been performed by Bruce and Richardson.[27,30]

Other Size Distributions. Other forms of size distribution functions, including combinations of power laws and exponentials can be found in the literature. Most of these are for ambient atmospheric haze, fog, rain, snow, and other natural phenomena that are not considered here. Of particular note, however, are power laws for very large particle dust and ballistic soil agglomerates from large explosions. Power law fall-off in particle number is sometimes used to account for these very large particles, pebbles, and soil agglomerates as a separate large particle tail in the size distribution with typical power law radius exponents ranging from -3 to -3.5.

Size distributions are sometimes based on analyses of filter samples, surface deposits, and soil. Such data must be used with caution. A deposition sample might not reflect the smaller particles that are carried off by the wind, for example. Soil sample analysis uses sieving that includes detergent breakup of fine particles that might not represent actual airborne agglomerates.

6.2.4.2 Obscurant Indices of Refraction. As can be seen from plotted values[31] in Fig. 6.2, the change in refractive index of phosphoric acid droplets with relative humidity is most pronounced at infrared wavelengths in the 8- to 12-μm range. Table 6.4 lists the refractive indices of phosphorus smoke over the band of wavelengths from 0.2 to 14 μm at relative humidities of 10, 50, and 90%. At other relative humidities these indices can be determined as part of the hygroscopic growth process detailed below.

Table 6.5 lists refractive indices for water,[32] fog oil smoke, and smoke from vegetative fires[21] at 0.2- to 14-μm wavelengths. Table 6.6 lists refractive indices of graphite and brass[33] and for soot from diesel oil fires[34] at 0.2- to 14-μm wavelengths. Recent data on diesel soot refractive indices and mass extinction coefficients[28] indicate a possible importance of glassy carbon as a component of diesel oil fire soot. It has refractive indices intermediate to those of measured diesel oil soot[34] and graphite.[33]

Table 6.7 lists refractive indices for clay minerals montmorillonite, kaolinite, and illite[35] at 0.2- to 2.6-μm wavelengths. Clay minerals form into small platelets of sizes in the submicrometer to micrometer range, although agglomerates of clays can form larger particles or stick to sand grains. Table 6.8 continues the refractive indices for montmorillonite clay[36] and includes Saharan dust[37] and andesite[38] at 3.0- to 12.0-μm wavelengths. Table 6.9 lists refractive indices for limestone[39] and birefringent quartz[40,41] at 0.2- to 12-μm wavelengths. Quartz, andesite, limestone, and similar minerals are components of soil textural classes called silt ($1 < a < 37$ μm) and sand (74 μm $< a$), which are size classes larger than clay ($a < 1$ μm).

6.2.5 Computed and Measured Obscurant Extinction Coefficients

For certain ideal obscurant particle geometries, the optical scattering and absorption properties can be calculated exactly from electromagnetic theory. In particular, for an individual, homogeneous sphere, the rigorous Mie theory[42] provides exact absorption, scattering, and extinction coefficients based only on particle radius, mass density, and refractive index.

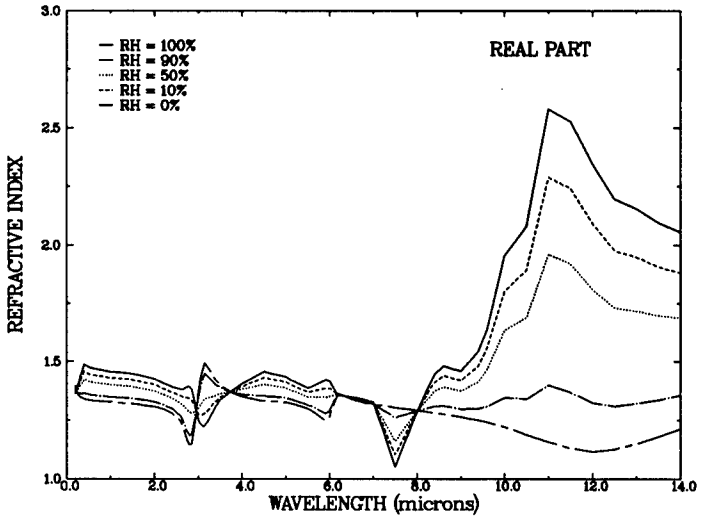

(a)

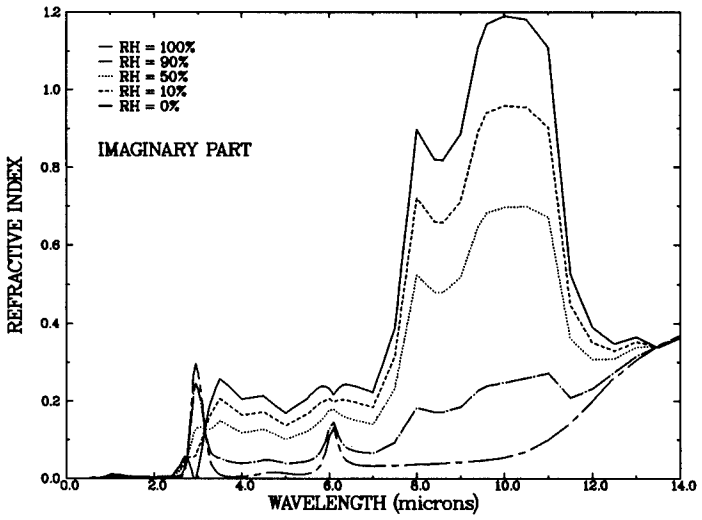

(b)

Fig. 6.2 Refractive indices of white phosphorus smoke for relative humidities of 0, 10, 50, 90, and 100%: (a) real component and (b) imaginary component.

Table 6.4 Refractive Indices of White Phosphorus Screening Smoke at Wavelengths from 0.20 to 14.0 μm and Relative Humidities of 10, 50, and 90%

Wavelength	RH=10%		RH=50%		RH=90%	
(μm)	N	K	N	K	N	K
.200	1.369	.225E-07	1.377	.476E-07	1.390	.910E-07
.225	1.377	.100E-07	1.376	.212E-07	1.374	.405E-07
.250	1.387	.685E-08	1.380	.145E-07	1.367	.277E-07
.275	1.398	.481E-08	1.385	.102E-07	1.364	.194E-07
.300	1.409	.327E-08	1.392	.693E-08	1.362	.132E-07
.325	1.421	.221E-08	1.399	.468E-08	1.362	.893E-08
.350	1.433	.133E-08	1.407	.281E-08	1.363	.538E-08
.375	1.445	.716E-09	1.415	.152E-08	1.364	.289E-08
.400	1.457	.380E-09	1.423	.805E-09	1.365	.154E-08
.425	1.454	.266E-09	1.421	.563E-09	1.363	.108E-08
.450	1.452	.209E-09	1.419	.442E-09	1.362	.844E-09
.475	1.449	.191E-09	1.417	.405E-09	1.361	.773E-09
.500	1.446	.205E-09	1.414	.433E-09	1.359	.827E-09
.525	1.445	.584E-03	1.413	.416E-03	1.358	.127E-03
.550	1.444	.117E-02	1.412	.832E-03	1.357	.254E-03
.575	1.443	.175E-02	1.411	.125E-02	1.357	.381E-03
.600	1.442	.234E-02	1.410	.167E-02	1.356	.508E-03
.625	1.441	.234E-02	1.410	.167E-02	1.356	.508E-03
.650	1.440	.200E-02	1.409	.143E-02	1.355	.436E-03
.675	1.439	.159E-02	1.408	.113E-02	1.355	.345E-03
.700	1.438	.117E-02	1.408	.832E-03	1.354	.254E-03
.725	1.437	.146E-02	1.407	.104E-02	1.353	.318E-03
.750	1.437	.175E-02	1.406	.125E-02	1.353	.381E-03
.775	1.436	.205E-02	1.405	.146E-02	1.353	.445E-03
.800	1.436	.234E-02	1.405	.167E-02	1.352	.508E-03
.825	1.435	.292E-02	1.404	.208E-02	1.352	.635E-03
.850	1.433	.350E-02	1.403	.250E-02	1.352	.762E-03
.875	1.433	.409E-02	1.403	.291E-02	1.351	.890E-03
.900	1.432	.467E-02	1.402	.333E-02	1.351	.102E-02
.925	1.431	.555E-02	1.402	.396E-02	1.350	.121E-02
.950	1.430	.642E-02	1.401	.458E-02	1.349	.140E-02
.975	1.430	.730E-02	1.400	.520E-02	1.349	.159E-02
1.000	1.429	.818E-02	1.400	.583E-02	1.349	.178E-02
1.200	1.427	.749E-02	1.397	.534E-02	1.346	.164E-02
1.400	1.424	.481E-02	1.394	.347E-02	1.343	.115E-02
1.600	1.417	.349E-02	1.388	.251E-02	1.339	.826E-03
1.800	1.409	.349E-02	1.381	.252E-02	1.333	.848E-03
2.000	1.401	.332E-02	1.373	.268E-02	1.327	.158E-02
2.200	1.384	.439E-02	1.359	.321E-02	1.315	.118E-02
2.400	1.369	.521E-02	1.343	.399E-02	1.299	.188E-02
2.600	1.352	.284E-01	1.320	.212E-01	1.266	.867E-02
2.650	1.349	.394E-01	1.311	.300E-01	1.247	.138E-01
2.700	1.346	.489E-01	1.301	.403E-01	1.222	.255E-01
2.750	1.345	.537E-01	1.291	.553E-01	1.198	.579E-01
2.800	1.340	.559E-01	1.283	.729E-01	1.185	.102E+00
2.850	1.332	.557E-01	1.279	.928E-01	1.189	.157E+00
2.900	1.316	.548E-01	1.283	.116E+00	1.226	.222E+00
2.950	1.294	.609E-01	1.293	.129E+00	1.292	.246E+00
3.000	1.273	.758E-01	1.301	.132E+00	1.350	.229E+00
3.050	1.272	.898E-01	1.316	.133E+00	1.392	.207E+00
3.100	1.273	.107E+00	1.329	.131E+00	1.425	.173E+00
3.150	1.281	.125E+00	1.342	.128E+00	1.447	.133E+00
3.200	1.287	.141E+00	1.342	.127E+00	1.436	.103E+00
3.250	1.297	.155E+00	1.346	.128E+00	1.430	.813E-01
3.300	1.308	.167E+00	1.349	.130E+00	1.419	.652E-01
3.350	1.319	.178E+00	1.351	.134E+00	1.407	.591E-01
3.400	1.329	.187E+00	1.355	.139E+00	1.400	.560E-01
3.450	1.339	.197E+00	1.360	.144E+00	1.395	.532E-01
3.500	1.348	.206E+00	1.363	.150E+00	1.389	.522E-01
3.600	1.359	.198E+00	1.366	.143E+00	1.379	.472E-01
3.700	1.368	.190E+00	1.369	.137E+00	1.373	.442E-01

Table 6.4 *(continued)*

Wavelength	RH=10%		RH=50%		RH=90%	
(μm)	N	K	N	K	N	K
3.800	1.377	.181E+00	1.373	.130E+00	1.367	.421E-01
3.900	1.386	.173E+00	1.377	.124E+00	1.363	.405E-01
4.000	1.394	.164E+00	1.382	.118E+00	1.360	.393E-01
4.100	1.402	.166E+00	1.386	.120E+00	1.358	.405E-01
4.200	1.410	.168E+00	1.390	.122E+00	1.357	.419E-01
4.300	1.417	.170E+00	1.394	.123E+00	1.355	.435E-01
4.400	1.424	.171E+00	1.398	.125E+00	1.354	.453E-01
4.500	1.431	.173E+00	1.403	.127E+00	1.354	.481E-01
4.600	1.427	.166E+00	1.399	.122E+00	1.351	.475E-01
4.700	1.423	.158E+00	1.396	.117E+00	1.350	.467E-01
4.800	1.419	.151E+00	1.394	.112E+00	1.349	.446E-01
4.900	1.416	.144E+00	1.390	.107E+00	1.347	.420E-01
5.000	1.412	.137E+00	1.387	.101E+00	1.344	.395E-01
5.100	1.402	.143E+00	1.379	.105E+00	1.339	.398E-01
5.200	1.394	.150E+00	1.372	.109E+00	1.334	.404E-01
5.300	1.386	.156E+00	1.365	.114E+00	1.328	.415E-01
5.400	1.377	.162E+00	1.357	.118E+00	1.321	.432E-01
5.500	1.370	.167E+00	1.349	.123E+00	1.314	.455E-01
5.600	1.373	.178E+00	1.349	.131E+00	1.307	.498E-01
5.700	1.377	.188E+00	1.348	.140E+00	1.299	.568E-01
5.800	1.381	.197E+00	1.347	.150E+00	1.288	.686E-01
5.900	1.386	.203E+00	1.347	.162E+00	1.278	.928E-01
6.000	1.385	.206E+00	1.351	.178E+00	1.291	.129E+00
6.100	1.371	.199E+00	1.356	.179E+00	1.330	.146E+00
6.200	1.358	.203E+00	1.360	.170E+00	1.362	.113E+00
6.300	1.355	.204E+00	1.355	.162E+00	1.356	.890E-01
6.400	1.351	.203E+00	1.350	.157E+00	1.348	.792E-01
6.500	1.347	.200E+00	1.345	.154E+00	1.341	.742E-01
6.600	1.343	.197E+00	1.340	.151E+00	1.336	.708E-01
6.700	1.339	.194E+00	1.336	.148E+00	1.331	.686E-01
6.800	1.334	.192E+00	1.331	.145E+00	1.326	.671E-01
6.900	1.330	.187E+00	1.327	.143E+00	1.323	.659E-01
7.000	1.325	.184E+00	1.323	.140E+00	1.319	.650E-01
7.100	1.281	.210E+00	1.290	.159E+00	1.307	.707E-01
7.200	1.236	.236E+00	1.258	.178E+00	1.295	.765E-01
7.300	1.191	.262E+00	1.225	.196E+00	1.283	.823E-01
7.400	1.146	.289E+00	1.192	.215E+00	1.272	.881E-01
7.500	1.102	.315E+00	1.160	.234E+00	1.260	.939E-01
7.600	1.139	.396E+00	1.186	.292E+00	1.267	.112E+00
7.700	1.176	.477E+00	1.211	.350E+00	1.272	.130E+00
7.800	1.213	.558E+00	1.237	.408E+00	1.279	.148E+00
7.900	1.249	.640E+00	1.262	.466E+00	1.284	.166E+00
8.000	1.286	.721E+00	1.288	.524E+00	1.290	.184E+00
8.200	1.350	.690E+00	1.331	.502E+00	1.300	.178E+00
8.400	1.413	.660E+00	1.375	.481E+00	1.310	.172E+00
8.600	1.440	.658E+00	1.392	.480E+00	1.311	.172E+00
8.800	1.429	.685E+00	1.383	.499E+00	1.304	.179E+00
9.000	1.419	.712E+00	1.374	.519E+00	1.296	.186E+00
9.200	1.451	.801E+00	1.394	.583E+00	1.298	.207E+00
9.400	1.482	.890E+00	1.415	.647E+00	1.298	.228E+00
9.600	1.560	.940E+00	1.468	.683E+00	1.309	.240E+00
9.800	1.682	.949E+00	1.552	.690E+00	1.327	.244E+00
10.000	1.804	.958E+00	1.636	.697E+00	1.346	.248E+00
10.500	1.895	.954E+00	1.691	.699E+00	1.340	.259E+00
11.000	2.288	.902E+00	1.962	.671E+00	1.400	.272E+00
11.500	2.241	.448E+00	1.920	.360E+00	1.368	.209E+00
12.000	2.092	.351E+00	1.810	.307E+00	1.324	.232E+00
12.500	1.977	.329E+00	1.731	.309E+00	1.309	.274E+00
13.000	1.949	.353E+00	1.718	.339E+00	1.321	.315E+00
13.500	1.907	.338E+00	1.698	.340E+00	1.336	.342E+00
14.000	1.882	.365E+00	1.689	.366E+00	1.356	.369E+00

Table 6.5 Refractive Indices of Water, Fog Oil Screening Smoke, and Vegetative Fire Smoke at Wavelengths from 0.20 to 14.0 μm

Wavelength	Water		Fog Oil		Vegetative Aerosol	
(μm)	N	K	N	K	N	K
.200	1.396	.110E-06	1.475	.100E-06	1.470	.000E+00
.225	1.373	.490E-07	1.475	.100E-06	1.470	.000E+00
.250	1.362	.335E-07	1.475	.100E-06	1.470	.000E+00
.275	1.354	.235E-07	1.475	.100E-06	1.470	.000E+00
.300	1.349	.160E-07	1.475	.100E-06	1.470	.000E+00
.325	1.346	.108E-07	1.475	.100E-06	1.470	.000E+00
.350	1.343	.650E-08	1.475	.100E-06	1.470	.000E+00
.375	1.341	.350E-08	1.475	.181E-03	1.470	.000E+00
.400	1.339	.186E-08	1.475	.660E-04	1.470	.000E+00
.425	1.338	.130E-08	1.475	.140E-04	1.470	.000E+00
.450	1.337	.102E-08	1.475	.800E-05	1.470	.000E+00
.475	1.336	.935E-09	1.475	.400E-05	1.470	.000E+00
.500	1.335	.100E-08	1.475	.300E-05	1.470	.000E+00
.525	1.334	.132E-08	1.475	.200E-05	1.470	.000E+00
.550	1.333	.196E-08	1.475	.200E-05	1.470	.000E+00
.575	1.333	.360E-08	1.475	.200E-05	1.470	.000E+00
.600	1.332	.109E-07	1.475	.200E-05	1.470	.000E+00
.625	1.332	.139E-07	1.474	.200E-05	1.470	.000E+00
.650	1.331	.164E-07	1.474	.200E-05	1.470	.000E+00
.675	1.331	.223E-07	1.474	.200E-05	1.470	.000E+00
.700	1.331	.335E-07	1.474	.200E-05	1.470	.000E+00
.725	1.330	.915E-07	1.474	.100E-05	1.470	.000E+00
.750	1.330	.156E-06	1.474	.100E-05	1.470	.000E+00
.775	1.330	.148E-06	1.474	.100E-05	1.470	.000E+00
.800	1.329	.125E-06	1.474	.100E-05	1.470	.000E+00
.825	1.329	.182E-06	1.474	.100E-05	1.470	.000E+00
.850	1.329	.293E-06	1.474	.100E-05	1.470	.000E+00
.875	1.328	.391E-06	1.474	.100E-05	1.470	.000E+00
.900	1.328	.486E-06	1.474	.100E-05	1.470	.000E+00
.925	1.328	.106E-05	1.474	.200E-05	1.470	.000E+00
.950	1.327	.293E-05	1.474	.100E-05	1.470	.000E+00
.975	1.327	.348E-05	1.474	.100E-05	1.470	.000E+00
1.000	1.327	.289E-05	1.474	.100E-05	1.470	.000E+00
1.200	1.324	.989E-05	1.474	.190E-04	1.470	.000E+00
1.400	1.321	.138E-03	1.474	.160E-04	1.470	.000E+00
1.600	1.317	.855E-04	1.473	.500E-05	1.470	.000E+00
1.800	1.312	.115E-03	1.473	.640E-04	1.470	.000E+00
2.000	1.306	.110E-02	1.473	.420E-04	1.470	.000E+00
2.200	1.296	.289E-03	1.472	.820E-04	1.462	.648E-04
2.400	1.279	.956E-03	1.472	.736E-03	1.456	.172E-03
2.600	1.242	.317E-02	1.471	.394E-03	1.439	.366E-03
2.650	1.219	.670E-02	1.470	.347E-03	1.435	.444E-03
2.700	1.188	.190E-01	1.470	.291E-03	1.425	.550E-03
2.750	1.157	.590E-01	1.469	.261E-03	1.409	.834E-02
2.800	1.142	.115E+00	1.469	.208E-03	1.399	.194E-01
2.850	1.149	.185E+00	1.468	.215E-03	1.390	.400E-01
2.900	1.201	.268E+00	1.468	.250E-03	1.389	.627E-01
2.950	1.292	.298E+00	1.467	.297E-03	1.397	.853E-01
3.000	1.371	.272E+00	1.466	.337E-03	1.416	.103E+00
3.050	1.426	.240E+00	1.464	.358E-03	1.436	.111E+00
3.100	1.467	.192E+00	1.462	.512E-03	1.456	.112E+00
3.150	1.493	.135E+00	1.460	.854E-03	1.470	.106E+00
3.200	1.478	.924E-01	1.457	.910E-03	1.484	.999E-01
3.250	1.467	.610E-01	1.451	.206E-02	1.490	.878E-01
3.300	1.450	.368E-01	1.441	.420E-02	1.485	.803E-01
3.350	1.432	.261E-01	1.415	.192E-01	1.469	.848E-01
3.400	1.420	.195E-01	1.436	.925E-01	1.489	.104E+00
3.450	1.410	.132E-01	1.521	.705E-01	1.523	.909E-01
3.500	1.400	.940E-02	1.518	.466E-01	1.524	.842E-01
3.600	1.385	.515E-02	1.500	.260E-02	1.526	.533E-01
3.700	1.374	.360E-02	1.490	.203E-02	1.520	.478E-01

Table 6.5 *(continued)*

Wavelength	Water		Fog Oil		Vegetative Aerosol	
(μm)	N	K	N	K	N	K
3.800	1.364	.340E-02	1.486	.170E-02	1.515	.394E-01
3.900	1.357	.380E-02	1.484	.108E-02	1.514	.331E-01
4.000	1.351	.460E-02	1.482	.701E-03	1.512	.284E-01
4.100	1.346	.562E-02	1.481	.669E-03	1.508	.220E-01
4.200	1.342	.688E-02	1.480	.680E-03	1.504	.167E-01
4.300	1.338	.845E-02	1.480	.644E-03	1.495	.107E-01
4.400	1.334	.103E-01	1.479	.528E-03	1.489	.894E-02
4.500	1.332	.134E-01	1.479	.504E-03	1.481	.759E-02
4.600	1.330	.147E-01	1.478	.487E-03	1.476	.518E-02
4.700	1.330	.157E-01	1.477	.413E-03	1.469	.347E-02
4.800	1.330	.150E-01	1.477	.390E-03	1.460	.238E-02
4.900	1.328	.137E-01	1.477	.415E-03	1.449	.101E-02
5.000	1.325	.124E-01	1.476	.357E-03	1.442	.717E-03
5.100	1.322	.111E-01	1.476	.370E-03	1.428	.953E-03
5.200	1.317	.101E-01	1.475	.552E-03	1.416	.124E-02
5.300	1.312	.980E-02	1.475	.640E-03	1.398	.155E-02
5.400	1.305	.103E-01	1.475	.585E-03	1.377	.191E-02
5.500	1.298	.116E-01	1.474	.524E-03	1.336	.227E-02
5.600	1.289	.142E-01	1.474	.680E-03	1.240	.367E-01
5.700	1.277	.203E-01	1.473	.867E-03	1.286	.226E+00
5.800	1.262	.330E-01	1.473	.964E-03	1.372	.184E+00
5.900	1.248	.622E-01	1.473	.100E-02	1.398	.207E+00
6.000	1.265	.107E+00	1.472	.102E-02	1.418	.221E+00
6.100	1.319	.131E+00	1.470	.135E-02	1.459	.212E+00
6.200	1.363	.880E-01	1.469	.304E-02	1.458	.211E+00
6.300	1.357	.570E-01	1.471	.260E-02	1.510	.214E+00
6.400	1.347	.449E-01	1.469	.159E-02	1.535	.171E+00
6.500	1.339	.392E-01	1.466	.180E-02	1.511	.136E+00
6.600	1.334	.356E-01	1.462	.340E-02	1.464	.139E+00
6.700	1.329	.337E-01	1.456	.734E-02	1.482	.137E+00
6.800	1.324	.327E-01	1.444	.309E-01	1.420	.169E+00
6.900	1.321	.322E-01	1.491	.426E-01	1.470	.214E+00
7.000	1.317	.320E-01	1.493	.106E-01	1.491	.210E+00
7.100	1.314	.320E-01	1.482	.534E-02	1.504	.222E+00
7.200	1.312	.321E-01	1.468	.116E-01	1.527	.213E+00
7.300	1.309	.322E-01	1.490	.225E-01	1.561	.213E+00
7.400	1.307	.324E-01	1.488	.851E-02	1.568	.190E+00
7.500	1.304	.326E-01	1.485	.711E-02	1.563	.169E+00
7.600	1.302	.328E-01	1.483	.649E-02	1.554	.162E+00
7.700	1.299	.331E-01	1.483	.626E-02	1.545	.168E+00
7.800	1.297	.335E-01	1.482	.546E-02	1.532	.183E+00
7.900	1.294	.339E-01	1.482	.529E-02	1.560	.191E+00
8.000	1.291	.343E-01	1.485	.491E-02	1.545	.188E+00
8.200	1.286	.351E-01	1.480	.446E-02	1.583	.216E+00
8.400	1.281	.361E-01	1.480	.475E-02	1.600	.194E+00
8.600	1.275	.372E-01	1.480	.552E-02	1.613	.173E+00
8.800	1.269	.385E-01	1.480	.443E-02	1.564	.173E+00
9.000	1.262	.399E-01	1.480	.407E-02	1.606	.282E+00
9.200	1.255	.415E-01	1.479	.453E-02	1.701	.213E+00
9.400	1.247	.433E-01	1.479	.472E-02	1.699	.190E+00
9.600	1.239	.454E-01	1.478	.536E-02	1.725	.194E+00
9.800	1.229	.479E-01	1.480	.550E-02	1.768	.139E+00
10.000	1.218	.508E-01	1.479	.509E-02	1.760	.871E-01
10.500	1.185	.662E-01	1.479	.557E-02	1.721	.323E-01
11.000	1.153	.968E-01	1.479	.467E-02	1.694	.000E+00
11.500	1.126	.142E+00	1.479	.714E-02	1.657	.000E+00
12.000	1.111	.199E+00	1.478	.620E-02	1.640	.000E+00
12.500	1.123	.259E+00	1.483	.753E-02	1.627	.000E+00
13.000	1.146	.305E+00	1.481	.898E-02	1.604	.000E+00
13.500	1.177	.343E+00	1.486	.110E-01	1.643	.119E-01
14.000	1.210	.370E+00	1.489	.571E-02	1.617	.000E+00

Table 6.6 Refractive Indices of Graphite, Brass, and Diesel Oil Fire Smokes for Wavelengths from 0.20 to 14 μm

Wavelength	Graphite		Brass		Diesel Soot	
(μm)	N	K	N	K	N	K
.300	1.535	.840E+00	1.388	.173E+01	3.421	.143E+02
.400	1.585	.768E+00	1.445	.181E+01	3.216	.126E+02
.500	1.629	.881E+00	.686	.225E+01	3.029	.111E+02
.600	1.673	.889E+00	.455	.325E+01	2.861	.968E+01
.700	1.714	.792E+00	.446	.411E+01	2.710	.840E+01
.800	1.768	.105E+01	.473	.489E+01	2.576	.724E+01
.900	1.809	.113E+01	.523	.565E+01	2.457	.620E+01
1.000	1.857	.122E+01	.603	.637E+01	2.353	.527E+01
1.500	2.162	.160E+01	1.044	.981E+01	2.022	.205E+01
2.000	2.477	.185E+01	1.711	.131E+02	1.925	.668E+00
2.500	2.691	.204E+01	2.458	.161E+02	1.949	.340E+00
3.003	2.917	.226E+01	3.227	.191E+02	1.989	.321E+00
3.509	3.142	.241E+01	3.852	.211E+02	2.017	.314E+00
4.000	3.337	.255E+01	5.077	.247E+02	2.038	.310E+00
4.505	3.528	.268E+01	6.097	.274E+02	2.056	.305E+00
5.000	3.681	.280E+01	7.097	.299E+02	2.068	.312E+00
5.495	3.891	.288E+01	8.190	.326E+02	2.084	.299E+00
6.024	4.040	.295E+01	9.041	.347E+02	2.074	.308E+00
6.494	4.163	.302E+01	10.103	.371E+02	2.104	.334E+00
6.993	4.277	.308E+01	11.291	.394E+02	2.114	.342E+00
7.519	4.378	.314E+01	12.468	.415E+02	2.132	.355E+00
8.000	4.456	.322E+01	13.375	.433E+02	2.162	.375E+00
8.547	4.562	.330E+01	14.164	.452E+02	2.196	.375E+00
9.009	4.631	.337E+01	15.051	.475E+02	2.224	.361E+00
9.523	4.721	.345E+01	15.971	.496E+02	2.237	.349E+00
10.000	4.791	.351E+01	16.878	.516E+02	2.249	.340E+00
10.526	4.874	.360E+01	17.932	.537E+02	2.256	.330E+00
10.989	4.935	.365E+01	18.880	.556E+02	2.249	.331E+00
11.494	4.977	.374E+01	19.912	.575E+02	2.268	.338E+00
12.048	5.061	.382E+01	21.006	.595E+02	2.274	.345E+00
12.500	5.124	.390E+01	21.916	.612E+02	2.290	.335E+00
12.987	5.186	.397E+01	22.867	.630E+02	2.287	.339E+00
13.514	5.240	.404E+01	23.884	.648E+02	2.319	.345E+00
14.085	5.296	.413E+01	24.982	.668E+02	2.403	.195E+00

Table 6.7 Refractive Indices for Clay Minerals Montmorillonite, Kaolinite, and Illite at 0.2- to 2.6-μm Wavelengths

λ	Montmorillonite		Kaolinite		Illite	
(μm)	n	k	n	k	n	k
0.20	1.542	.0021	1.496	.0010	1.441	.0023
0.30	1.523	.0006	1.514	.0011	1.401	.0018
0.40	1.525	.0002	1.490	.0002	1.423	.0012
0.50	1.526	.00005	1.493	.0001	1.415	.0010
0.60	1.520	.00004	1.493	.00004	1.411	.0007
0.70	1.525	.0001	1.497	.0001	1.394	.0012
0.90	1.528	.0001	1.501	.0001	1.391	.0012
1.0	1.530	.0002	1.502	.0002	1.387	.0012
1.2	1.530	.0002	1.502	.0002	1.387	.0012
1.4	1.530	.0001	1.502	.0003	1.387	.0012
1.6	1.530	.0002	1.502	.0003	1.387	.0013
1.8	1.530	.0003	1.502	.0005	1.387	.0014
2.0	1.530	.0005	1.502	.0006	1.387	.0013
2.2	1.530	.0006	1.502	.0012	1.387	.0019
2.4	1.530	.0008	1.502	.0016	1.387	.0020
2.6	1.530	.0010	1.502	.0043	1.387	.0023

Table 6.8 Refractive Indices for Montmorillonite Clay, Saharan Dust, and Andesite at 3.0- to 12-μm Wavelengths

λ	Montmorillonite		Saharan Dust		Andesite	
(μm)	n	k	n	k	n	k
3.0	1.48	.0032	1.475	.032	1.46	.0056
4.0	1.44	.0038	1.47	.0045	1.43	.0063
5.0	1.40	.0045	1.50	.013	1.40	.0086
6.0	1.32	.01	1.43	.045	1.35	.012
7.0	1.24	.03	1.45	.11	1.26	.028
8.0	1.04	.125	1.18	.085	1.06	.10
8.2	0.93	.20	1.11	.13	.99	.15
8.4	0.76	.31	1.09	.17	.91	.23
8.6	0.73	.52	1.07	.23	.83	.32
8.8	0.77	.79	1.65	.33	.78	.56
9.0	0.92	.87	1.87	.44	.77	.85
9.2	0.80	1.17	2.17	.52	.97	.88
9.4	1.29	1.84	2.80	.61	1.20	.90
9.6	2.12	1.68	3.07	.70	1.37	.96
9.8	2.49	1.17	2.86	.77	1.49	1.02
10.0	2.59	.625	2.59	.92	1.60	1.10
10.2	2.25	.30	2.77	.88	1.73	.99
10.4	2.04	.18	1.82	.70	1.87	.91
10.6	1.90	.18	1.70	.60	1.98	.78
10.8	1.86	.20	1.79	.37	2.06	.60
11.0	1.85	.25	1.84	.31	2.16	.42
11.2	1.81	.15	1.83	.29	2.08	.33
11.4	1.77	.15	1.82	.26	2.00	.28
11.6	1.74	.13	1.82	.23	1.93	.18
11.8	1.70	.13	1.81	.20	1.88	.15
12.0	1.69	.13	1.80	.18	1.83	.13

Table 6.9 Refractive Indices for the Minerals Limestone and Quartz at 0.2- to 12-μm Wavelengths, (O) Ordinary and (E) Extraordinary Rays

λ	Limestone		Quartz (O Ray)		Quartz (E Ray)	
(μm)	n	k	n	k	n	k
0.20	1.277	.472	1.650	10^{-7}	1.690	10^{-7}
0.30	1.569	.034	1.580	10^{-7}	1.590	10^{-7}
0.40	1.548	.052	1.558	10^{-7}	1.568	10^{-7}
0.50	1.566	.037	1.548	10^{-7}	1.557	10^{-7}
0.55	1.562	.040	1.546	10^{-7}	1.555	10^{-7}
0.60	1.565	.045	1.543	10^{-7}	1.552	10^{-7}
0.70	1.556	.025	1.541	10^{-7}	1.550	10^{-7}
0.80	1.552	.041	1.538	10^{-7}	1.547	10^{-7}
0.90	1.554	.044	1.537	10^{-7}	1.546	10^{-7}
1.00	1.562	.052	1.535	10^{-7}	1.544	10^{-7}
2.0	1.571	.070	1.520	10^{-7}	1.528	10^{-7}
3.0	1.535	.066	1.500	1×10^{-6}	1.500	1×10^{-6}
3.5	1.534	.057	1.485	1×10^{-5}	1.485	1×10^{-6}
4.0	1.518	.061	1.472	.00013	1.476	.00014
4.5	1.481	.068	1.426	.00066	1.432	.00073
5.0	1.441	.064	1.412	.00079	1.419	.00091
6.5	0.403	.645	1.235	.0042	1.248	.0049
8.0	1.860	.211	0.4298	.1383	0.3908	.1438
8.5	1.775	.195	0.1126	1.2506	0.0855	1.2160
9.0	1.732	.199	0.1746	2.597	0.2291	3.0416
9.5	1.703	.195	4.515	.3977	3.904	.2304
10.0	1.681	.187	2.665	.0519	2.572	.0440
10.5	1.627	.169	2.238	.0243	2.200	.0222
11.0	1.497	.174	2.013	.0174	2.000	.0159
11.5	2.286	.407	1.834	.0188	1.850	.0153
12.0	1.713	.148	1.565	.0469	1.683	.0237

6.2.5.1 Mie Theory. The exact Mie solution for scattering from spheres is well documented[43] and has been extensively studied. It is not described in detail here. FORTRAN computer programs for Mie calculations on both homogeneous and layered *onion skin* spheres are readily available.[43] Scattering and absorption cross sections for particle sizes, density, and refractive index can be combined with particle size distributions through Eqs. (6.10) and (6.11) to compute mass extinction, scattering, and absorption coefficients.

The following examples use a Mie scattering code to illustrate various dependences of extinction coefficients on particle size and refractive index. The refractive indices and particle densities, shown in Table 6.10, were used in Mie calculations for fog oil, soil-derived dust, and carbon. The results for fog oil and for dust (with additional calculations over other intermediate wavelengths) are compared later in the section to measured extinction coefficients.

For fog oil calculations, the refractive indices were taken from Table 6.5, and the particle mass density was taken from Table 6.2. Fog oil particles are spherical droplets of uniform density, and the Mie theory should work well. (As we see in a later section, agreement with directly measured mass extinction for fog oil is reasonable.)

For dust, the refractive indices in Table 6.10 were chosen to represent a hypothetical composite of minerals present in soil. An effective particle mass density of 1.7 g/cm^3 was chosen (somewhat arbitrarily) as a value typical of the soil producing an airborne dust cloud. For other mass densities ρ, the plotted mass extinction values in Fig. 6.3 are adjusted upward or downward by the ratio $1.7/\rho$. In principle, Mie theory should not be applied to dust particles because of their nonspherical shapes. Analysis of the difference between treating dust as spherical particles versus treating the particles as spheroids (with length to diameter ratios of up to 1.5) suggests that mass extinction predictions can be expected to differ by up to 50% based on shape assumptions.[16] The spherical assumption is used here because the measured size distributions cited earlier are for equivalent spheres and to illustrate similarities and differences from fog oil.

The carbon calculations in the examples use the refractive indices from Table 6.6 (graphite) and a particle mass density of 0.2 g/cm^3. As with dust, the computed mass extinction values can be adjusted for other densities ρ by multiplying by the factor $0.2/\rho$. This very low density was chosen based on analysis by Chylek et al.[24] for acetylene smoke particles. The Mie example for carbon particles is presented here mainly as a high-absorption example to contrast with the highly scattering fog oil smoke.

Mie Example Results. Results from the Mie calculations were combined and plotted in such a way that the separate effects of particle size and refractive index on extinction are illustrated. The Mie computer code was first used to calculate the Mie efficiencies Q_{abs}, Q_{sca}, and Q_{ext} for approximately 20,000 different radii ranging from 0.01 to 1000 μm, distributed uniformly over a logarithmic radius scale. Mass extinction values α_u were then determined per unit particle mass for a flat, uniform size distribution by mass (subscript u) by averaging over each of 200 log-radius intervals of similar size:

Table 6.10 Properties Used for Fog Oil, Dust, and Carbon Mie Calculation Examples

	Fog Oil	Dust	Carbon
Specific Gravity:	0.89	1.70	0.20
Refractive Index:			
λ = .55 μm	1.475 -i .000002	1.524 -i .00067	1.65 -i 0.885
λ = 1.06 μm	1.474 -i .000015	1.519 -i .00057	1.89 -i 1.26
λ = 3.4 μm	1.436 -i .0925	1.465 -i .0035	3.10 -i 2.38
λ = 4.5 μm	1.479 -i .0005	1.446 -i .0040	3.53 -i 2.682
λ = 8 μm	1.485 -i .0049	0.405 -i .141	4.45 -i 3.22
λ = 10.6 μm	1.479 -i .0056	2.21 -i .023	4.89 -i 3.60
λ = 12 μm	1.478 -i .0062	1.62 -i .035	5.06 -i 3.82
94 GHz		2.00 -i .035	

$$\alpha_{u,\mathrm{ext}}(\lambda,a) = \frac{\int_{\ln a_1}^{\ln a_2} Q_{\mathrm{ext}}(\lambda,a)\pi a^2 \, d(\ln a)}{\int_{\ln a_1}^{\ln a_2} (4/3)\pi\rho a^3 \, d(\ln a)} \, . \tag{6.25}$$

Such averaging intentionally smooths out the effects of very fine oscillations to improve later numerical integration over the particular size distributions. Similar tables of mass scattering and mass absorption coefficients were also produced for this uniform mass distribution, as shown in Figs. 6.3, 6.4, and 6.5.

Figure 6.3 plots the resulting extinction, absorption, and scattering coefficients at each wavelength in Table 6.10 for uniform dust size distribution by mass. The main features of these extinction curves are a flat response at small radii, a maximum contribution in some radius interval that shifts to larger sizes with longer wavelengths, and a convergence at large radii to a common value that decreases linearly (on this log-log scale) with increasing radius.

Examination of Fig. 6.3 shows that the flat extinction at small radii results completely from absorption contributions. Scattering decreases as radius decreases in this small-particle regime. Lorentz's analysis of small particles[44] showed that

$$\alpha_{u,\mathrm{abs}}(a) \approx -\frac{6\pi}{\lambda\rho}\mathrm{Im}\left(\frac{m^2-1}{m^2+2}\right) \quad \text{and}$$

$$\alpha_{u,\mathrm{sca}}(a) \approx \frac{32\pi^4 a^3}{\lambda^4\rho}\left|\frac{m^2-1}{m^2+2}\right|^2 \tag{6.26}$$

for sufficiently small radius, where m is the complex refractive index, λ is the wavelength, a is the particle radius, and ρ is the material density. Absorption thus becomes independent of radius and inversely proportional to wavelength for very small particles. The scattering, however, varies as radius cubed over wavelength to the fourth power for small particles.

Note that refractive indices also vary with wavelength and thus share in importance in these equations. Dust usually decreases in the real part and increases in the imaginary part of the refractive index at wavelengths near 8 μm. Figure 6.3 shows the different nature of the dependence of extinction on radius at 8 μm as compared to the visible region at 0.55 μm. (A region of high absorption is present in many minerals in the 7- to 9-μm wavelength region, although not always at the same wavelength.) The dependence on wavelength can also be seen for fog oil smoke in Fig. 6.4, where the imaginary part of the refractive index is smaller than for dust.

For sufficiently large particles (geometric optics limit) Q_{ext} approaches 2. Mass extinction becomes independent of wavelength and refractive index, and it falls off linearly with radius:

$$\alpha_{u,\mathrm{ext}}(a) \approx \frac{3}{2\rho a} \, . \tag{6.27}$$

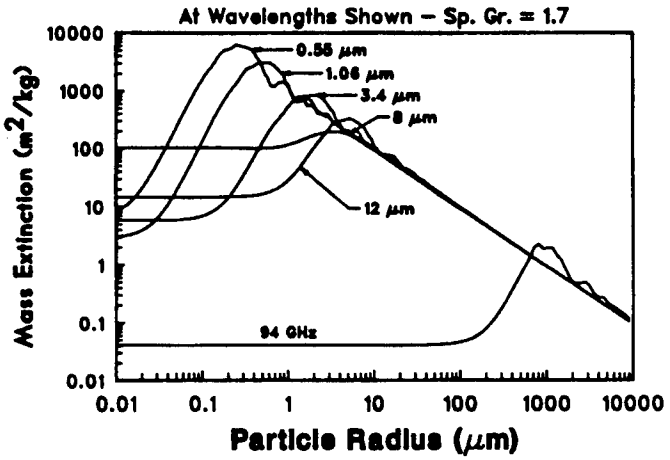

(a)

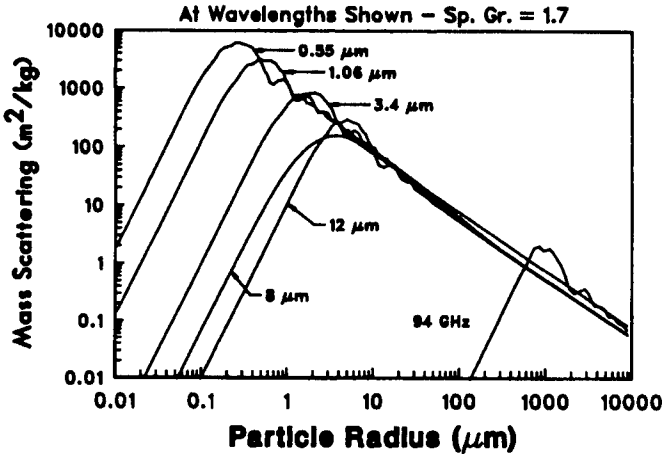

(b)

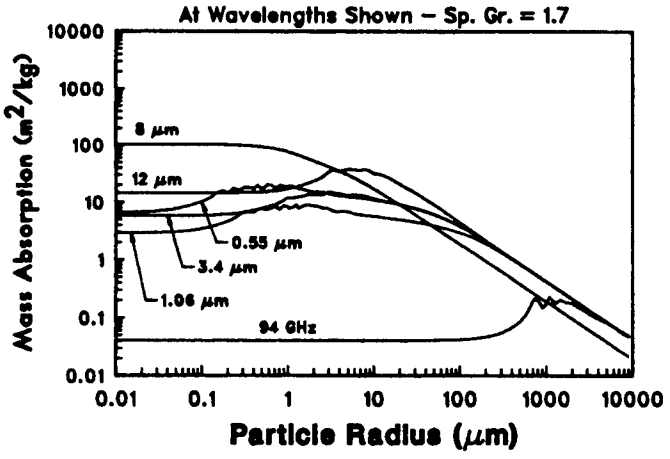

(c)

Fig. 6.3 (a) Extinction, (b) scattering, and (c) absorption per unit mass as a function of radius for HE dust at specific wavelengths from visible through millimeter wavelengths.

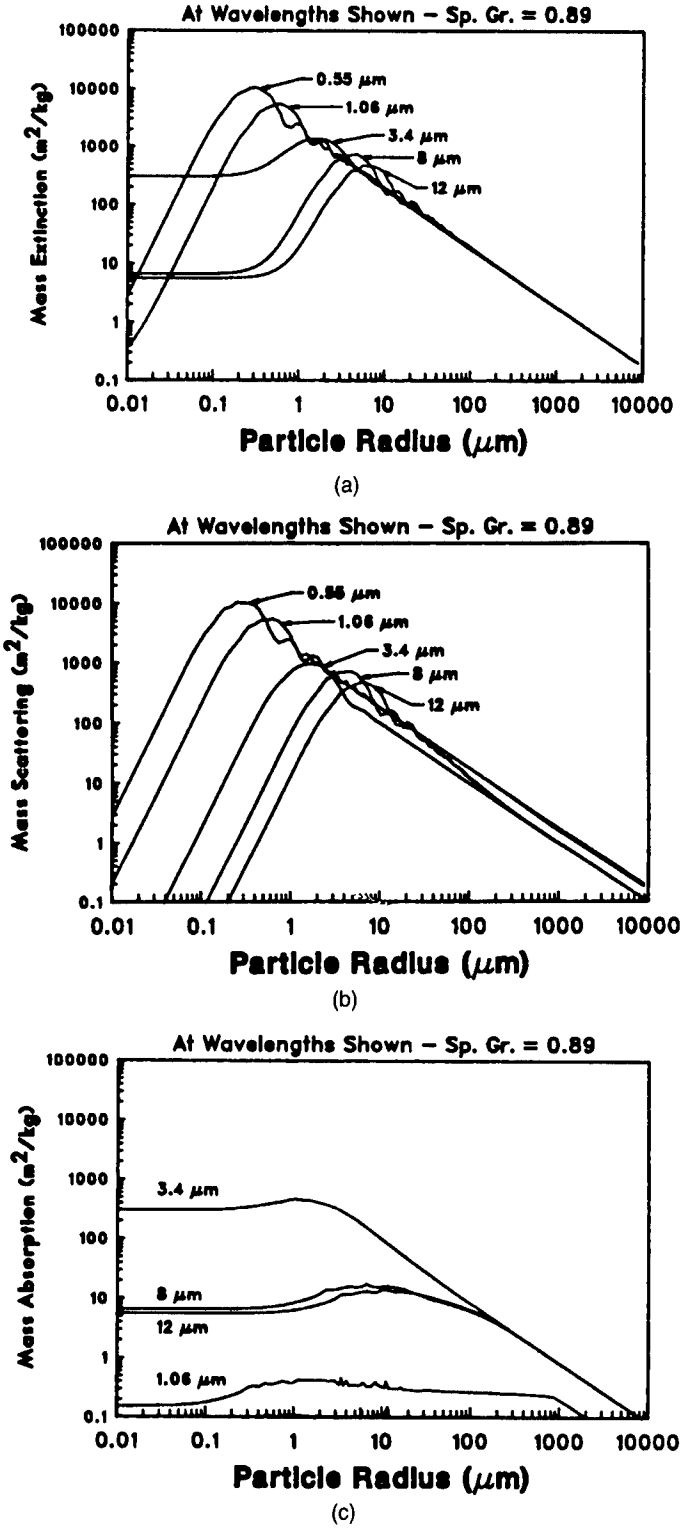

Fig. 6.4 (a) Extinction, (b) scattering, and (c) absorption per unit mass as a function of radius for fog oil screening smoke at specific wavelengths from visible through the infrared.

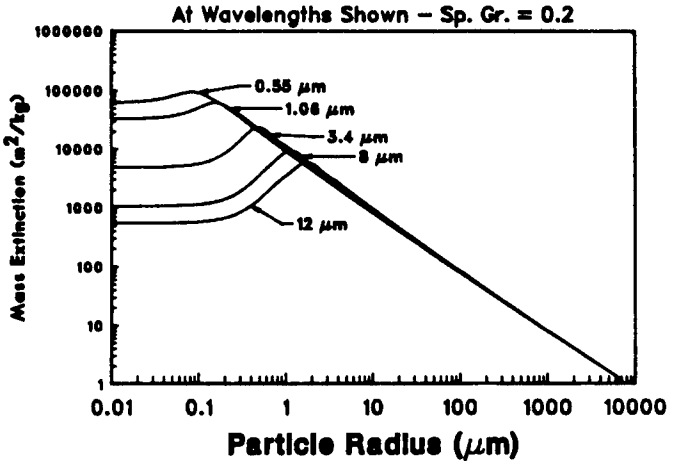

(a)

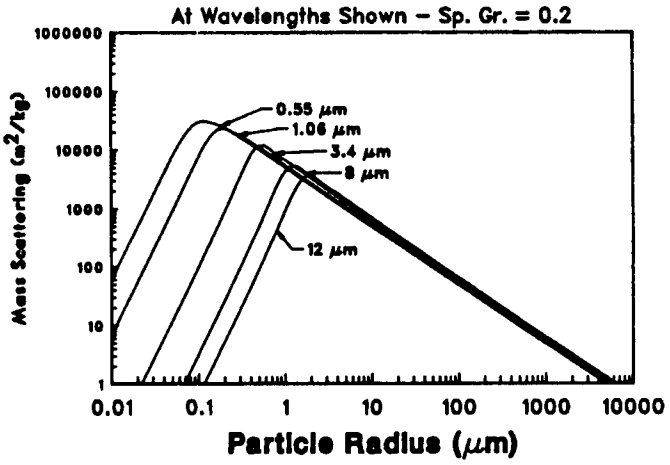

(b)

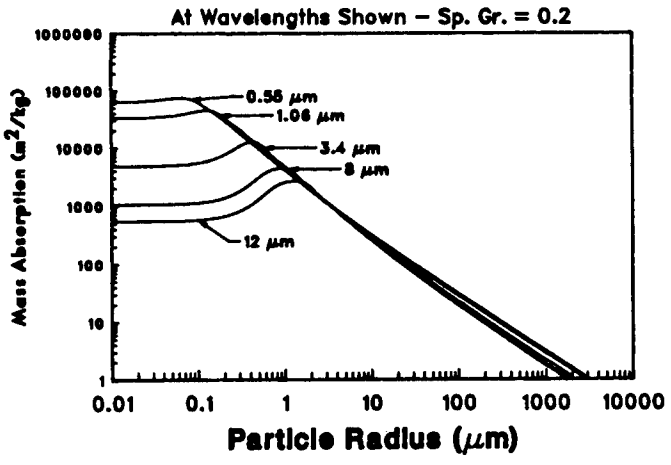

(c)

Fig. 6.5 (a) Extinction, (b) scattering, and (c) absorption per unit mass as a function of radius for carbon particles at specific wavelengths from visible through the infrared.

For particles with sizes comparable to the wavelength, a full Mie calculation is necessary to determine the scattering properties. Figure 6.5 shows the absorption, scattering, and extinction for carbon particles having the refractive indices in Table 6.10 and with mass uniformly distributed over all radii considered. The large imaginary refractive index of carbon results in a smoother, flatter response with particle size compared to fog oil. For obscurants with strong absorption, the peak extinction occurs approximately at the radius $\lambda/(2\pi)$. For obscurants with a small imaginary refractive index and a real part close to unity, the peak occurs[44] approximately at the radius $\lambda/[\pi(m - 1)]$.

A peak in extinction has an obvious implication in the selection of obscurant materials. For a given total mass of material available to be released as an aerosol, the obscuration at each wavelength is most efficient if the particle size matches the radii near the peak extinction for that wavelength. Particles that are large compared to the wavelength are less efficient because they contribute a large fraction to the mass concentration of the obscurant but contribute a relatively smaller fraction to the obscuration effects.

Example. This is illustrated for dust at the millimeter wavelength (3192 μm) associated with the frequency of 94 GHz. The computed extinction is low, 4×10^{-2} m^2 kg^{-1}, for all particle sizes smaller than 1 mm. It peaks at 2.3 m^2 kg^{-1} at about an 800-μm radius. Thus, whereas soil grains and clumps of all sizes produced by an explosion do contribute to the millimeter-wavelength extinction, a rapid fallout of larger particles close to the explosion has a correspondingly rapid effect on the recovery of millimeter-wavelength transmittance.

Infrared mass extinction for dust, however, is much larger than millimeter-wavelength extinction for all particles except for those of the order of a millimeter or larger. As long as those small dust particles are present, infrared extinction shows a much less dramatic response to the loss of large dust particles and ballistic soil that fall out of the cloud immediately after an explosion.

6.2.5.2 Effects of Hygroscopic Growth on Obscurants. In the preceding formulations it is assumed that the bulk material refractive indices needed in the Mie theory to compute Q_{ext}, Q_{scat}, and Q_{abs} are known. In some cases, the refractive indices can be calculated from first principles using concepts of theoretical molecular physics. However, in most practical applications these data are available only from measurement.

In particular, the refractive indices for water have been measured in several studies.[32] The water indices are quite important in modeling the optical properties of haze and certain hygroscopic screening smokes, in particular white phosphorus and hexachloroethane. In the atmosphere, initial nuclei grow by absorbing ambient moisture. This hygroscopic growth has a twofold effect on obscuration: first an increase in aerosol mass and droplet size resulting from absorption of atmospheric moisture and second a modification of the refractive indices of the composite water-solute complex. Overall, the effects on a hygroscopic aerosol are summarized in a first approximation using the formulation of Hanel.[13] The relevant parameters can be determined[12] from the following relationships:

droplet radius a:

$$a = a_0\left[1 + \frac{\rho_s}{\rho_w}\mu_h(a_w)\left(\frac{a_w}{1-a_w}\right)\right]^{1/3}, \tag{6.28}$$

bulk density ρ:

$$\rho = \rho_s\left[1 + \mu_h(a_w)\left(\frac{a_w}{1-a_w}\right)\right]\left[1 + \frac{\rho_s}{\rho_w}\mu_h(a_w)\left(\frac{a_w}{1-a_w}\right)\right]^{-1}, \tag{6.29}$$

real refractive index n:

$$n = n_w + (n_s - n_w)\left[1 + \frac{\rho_s}{\rho_w}\mu_h(a_w)\left(\frac{a_w}{1-a_w}\right)\right]^{-1}, \tag{6.30}$$

imaginary refractive index k:

$$k = k_w + (k_s - k_w)\left[1 + \frac{\rho_s}{\rho_w}\mu_h(a_w)\left(\frac{a_w}{1-a_w}\right)\right]^{-1}, \tag{6.31}$$

where subscript s and w refer, respectively, to solute and solvent (water) in the composite solution, a_0 is the dry solute radius, a_w is the water activity, and $\mu_h(a_w)$ is the Hanel growth factor defined strictly in terms of a water uptake equation as

$$M_w = M_s\mu_h(a_w)\left(\frac{a_w}{1-a_w}\right). \tag{6.32}$$

For equilibrium growth the water activity a_w is related to the relative humidity f and droplet radius a as

$$f = a_w \exp\left(\frac{2SV_m}{RT_k}\frac{1}{a}\right), \tag{6.33}$$

where the physical constants are molar specific volume V_m, surface tension S, universal gas constant R, and droplet temperature T_k.

For an ideal solution the Hanel factor $\mu_h(a_w)$ is a constant and can be calculated from first principles. However, for practical applications, the factor is determined from measurements of equilibrium vapor pressure as a function of solute mass fraction using one form or another of Eq. (6.32). For phosphorous smokes, the Hanel factor can be represented by the following empirical relationship[31]:

$$\mu_h(f) = \begin{cases} 1.477[\exp(-13.0f) + \exp(-1.80f)] & f < 0.80 \\ 1.350[1 - 0.41\exp(+0.726f)] & f \geq 0.80 \end{cases}. \tag{6.34}$$

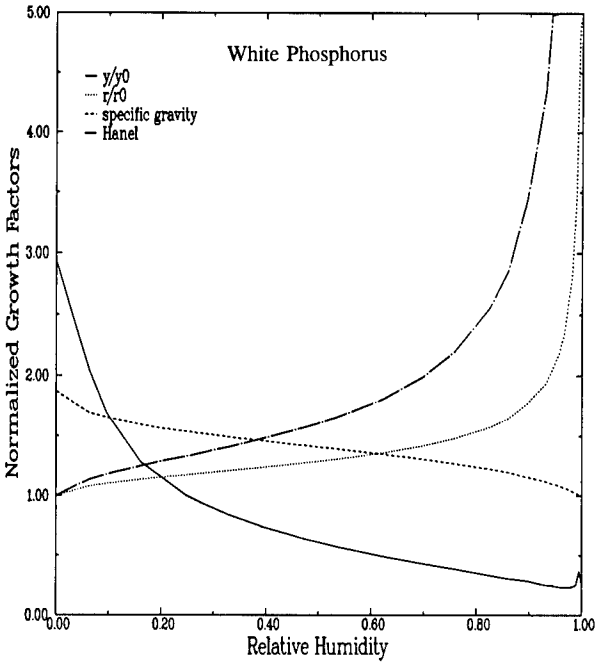

Fig. 6.6 Plot of the hygroscopic growth factors for white phosphorus screening smoke, including the Hanel factor $\mu_h(a_w)$, specific gravity, relative increase in radius, and relative increase in mass per particle.

Examples of the effects of hygroscopic growth on white phosphorus obscurant with relative humidity are shown in Fig. 6.6. These include the decrease in the Hanel factor and specific gravity of the particle with increasing relative humidity. As the particle absorbs more water, the specific gravity changes from that for the initial phosphorus particle to that of water. The relative increases in radius and in mass (called the *obscurant yield factor* Y_f) are also shown in Fig. 6.6 for increasing relative humidity.

6.2.5.3 Computed and Measured Mass Extinction Coefficients

Phosphorus Smoke. Using hygroscopic growth effects from Eqs. (6.28) through (6.31) and Mie calculations, the mass extinction for white phosphorus smoke can be determined. Results depend somewhat on the initial ("dry") values assigned to the smoke, especially at visible wavelengths near 0.55 μm. This is shown in Figs. 6.7 and 6.8, where mass extinction as a function of wavelength is plotted assuming a log-normal size distribution with σ_g of 1.5; three initial geometric mean radii of 0.1, 0.2, and 0.3 μm; and three relative humidities of 10, 50, and 90%.

Note in Figs. 6.7 and 6.8 that the mass extinction coefficient in the visible wavelength band, 0.4 to 0.7 μm, actually decreases at high relative humidities as the particle size distribution shifts to larger radii and the refractive index decreases. The strong dependence on relative humidity at approximately 3-μm wavelength and in the 8- to 12-μm band results from water absorption as evidenced by the peak in the imaginary refractive index in Fig. 6.2. When

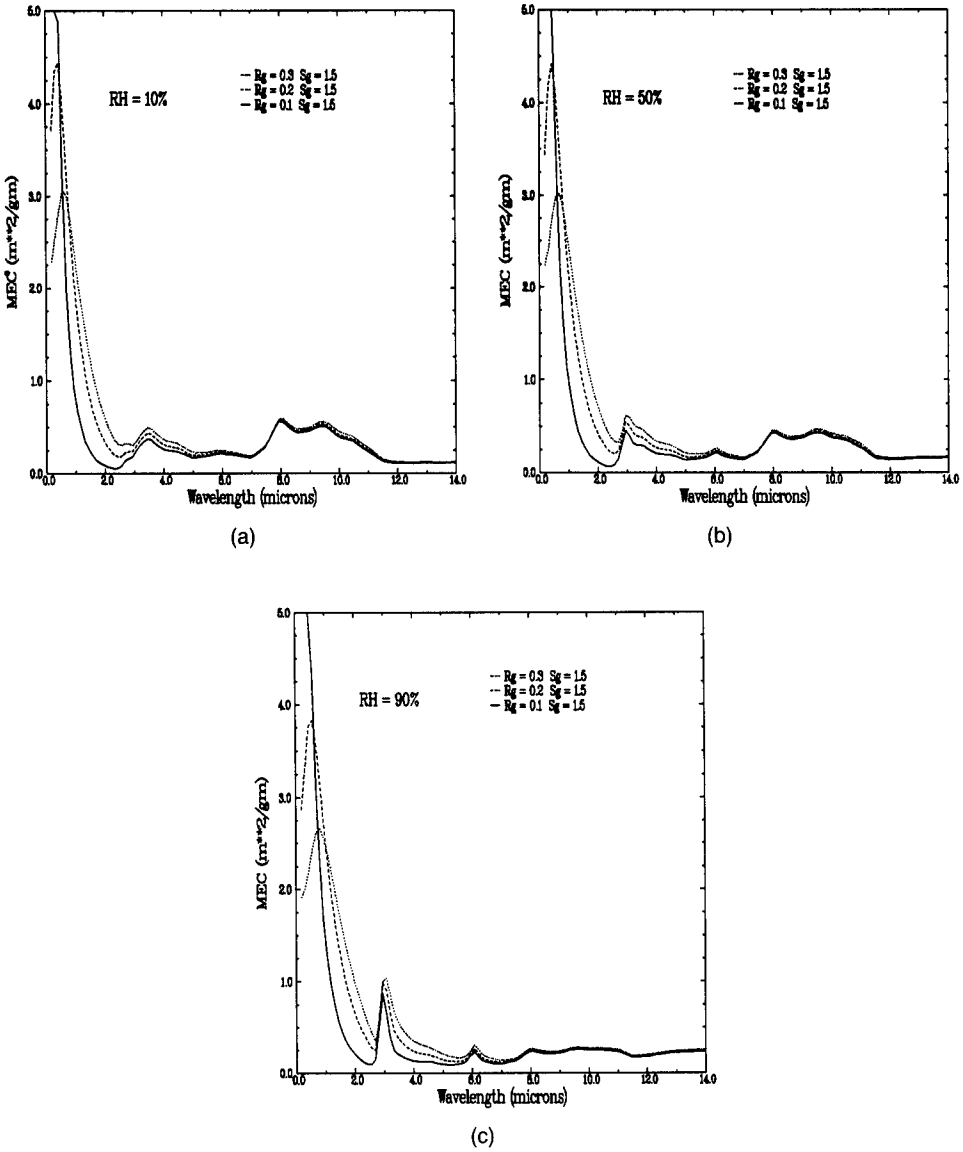

Fig. 6.7 Plots of the white phosphorus mass extinction coefficient as a function of wavelength using three values for initial droplet radii a_{gn} (0.10, 0.20, and 0.30 μm); standard deviation σ_g of 1.5; and three values of relative humidity: (a) RH = 10%, (b) RH = 50%, and (c) RH = 90%.

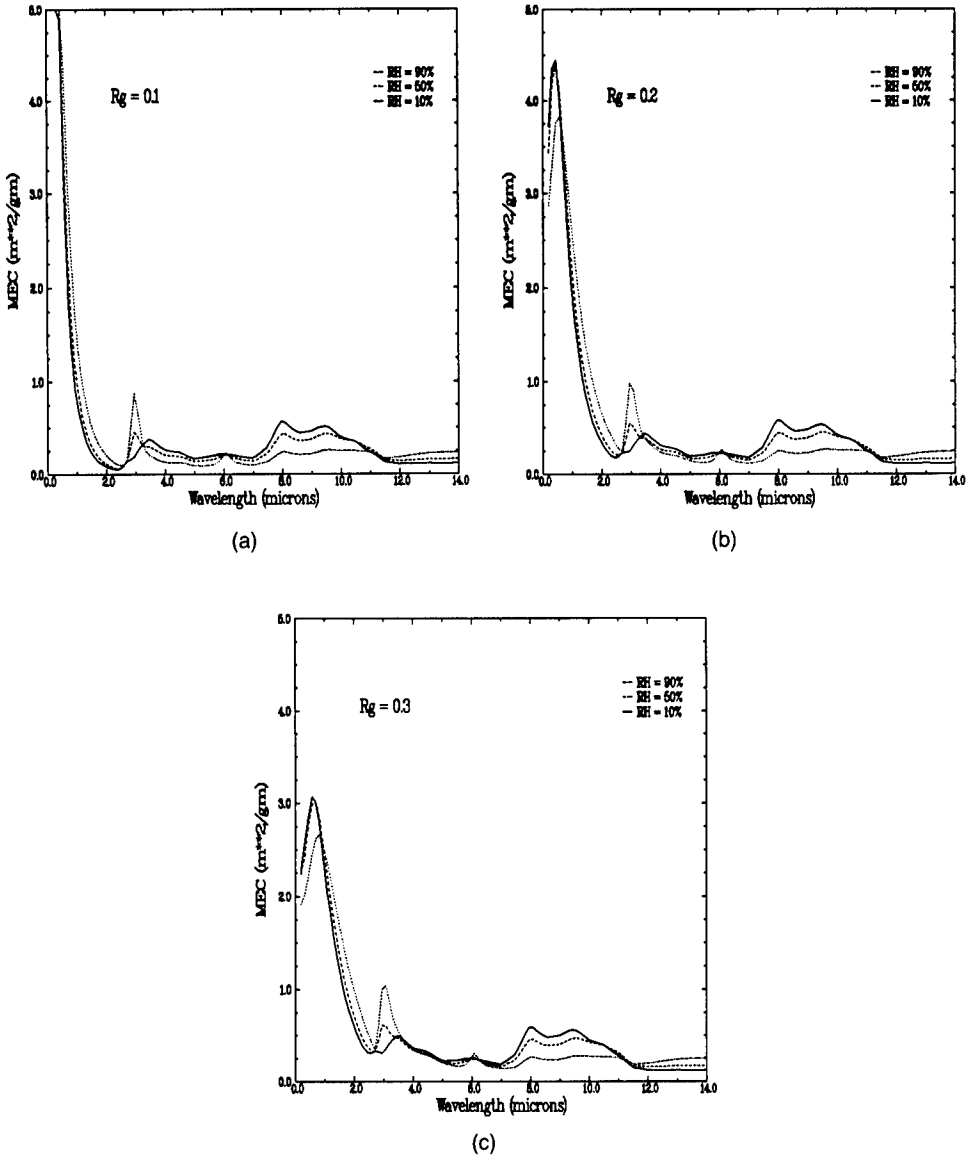

Fig. 6.8 Plots of the white phosphorus mass extinction coefficient as a function of wavelength using three values of relative humidity, 10, 50, and 90%, and three values for initial droplet radii: (a) $a_{gn} = 0.10$, (b) $a_{gn} = 0.20$, and (c) $a_{gn} = 0.30$; $\sigma_g = 1.5$.

compared against mass extinction measured in the laboratory and in the field, reasonable agreement is obtained when an initial dry radius of 0.225 μm is assumed.[19]

Fog Oil and Dust. One can combine the relevant size distributions from Table 6.2 with the curves for extinction per unit mass in Figs. 6.3 and 6.4 to compute mass extinction coefficients for fog oil and for dust. The particle size distribution by mass is used as a weight factor in integrating over the table of values from Eq. (6.25):

$$a_{\text{ext}}(\lambda) = \frac{\int_{a_{\min}}^{a_{\max}} m(a)\alpha_{u,\text{ext}}(\lambda,a)\, da}{\int_{a_{\min}}^{a_{\max}} m(a)\, da}, \tag{6.35}$$

where $a_{\min}$ and $a_{\max}$ are minimum and maximum radii, discussed in the following.

Table 6.11 compares mass extinction coefficients computed in this way with measured values. Band-averaged values were obtained by computing extinction over 20 wavelengths in each band and averaging. The results for fog oil are particularly straightforward because the particles are nearly spherical. The full range of size distribution radii were used with the log-normal distribution of Table 6.2 and the mass extinction from Fig. 6.4. Comparisons with measured data[19,45] are reasonable as shown in Table 6.11.

The rapid falloff in fog oil extinction with increasing wavelength can be understood by examining Fig. 6.9, which plots the product of the extinction per unit mass $\alpha_{u,\text{ext}}(\lambda,a)$ times the logarithmic mass size distribution $m_L(a)$. The logarithmic mass distribution $m_L(a)$ is used instead of $m(a)$ so that the apparent area under each curve on the logarithmic radius scale is proportional to the mass extinction. From the figure one can see that only near the visible band from 0.4 to 0.7 μm do both the peak in the size distribution and the peak in the mass extinction curves significantly overlap. The small absorption for fog oil implies that the mass extinction for particles much smaller than the wavelength is caused mainly by scattering. This falls off rapidly with decreasing radius, as shown in Fig. 6.4 and Eq. (6.26). Thus, the mass extinction of standard fog oil smoke is small for infrared wavelengths.

Dust mass extinction coefficients have been measured at several field experiments using transmittance and mass dosage over the LOS, as discussed earlier in the method[46] of Eq. (6.9). The range of measured values for several data sets are shown in Table 6.11. Within the spread in data there is little variation in dust mass extinction from visible through infrared wavelengths. Although dust transmission data often indicate a slight decrease in mass extinction with longer wavelengths and although absorption spectra of very fine dust particles show structure in infrared absorption, the band-averaged extinction of dust is fairly "neutral" from the visible through the infrared.

Measured dust mass extinction is compared in Table 6.11 with Mie calculations. The latter were obtained from the high-explosive dust (composite) and vehicular dust (sandy) size distributions of Table 6.2 combined with extinction per mass of Fig. 6.3. An effective soil grain density of 2 g cm^{-3} was used. Note

Table 6.11 Comparisons of Mass Extinction Coefficients for Fog Oil, Explosive-Produced Dust, and Vehicular Dust Computed from Mie Theory with Measurements at Several Wavelengths and Wavelength Bands

Wavelength (μm)	Mass extinction Coefficients (m^2 kg^{-1})						
	Fog Oil Smoke		Dust Field/Lab	HE Dust (Composite) Computed		Vehicle Dust (Sandy) Computed	
	Measured	Computed	Measured	a=0-10 μm	10-100 μm	a=0-10 μm	10-100μm
0.55		6510		259	20	297	18
0.4 - 0.7 band	6850-7730	6450	250-410	253	20	321	18
1.06	3480-3500	3500	230-350	271	21	349	19
3.0 - 5.0 band	245-270	219	250-320	272	21	332	19
10.6	18	12		274	22	325	20
8.0 - 12. band	14-20	15	210-330	196	22	214	20
94 GHz				0.03	0.03	0.03	0.03
Mass %	100	100		15.2	61.7	18.8	81.2
ρ, Sp. Gr.	0.89	0.89	1.5 - 2.6	2.0	2.0	2.0	2.0

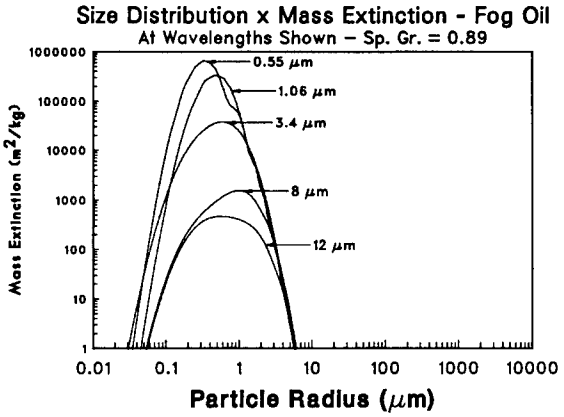

Fig. 6.9 Plot of the product of the logarithmic mass size distribution $m_L(a)$ for fog oil smoke and the mass extinction for fog oil smoke particles computed from Mie theory.

that the dust size distributions from Table 6.2 indicate up to 85% of the total mass is in particles larger than 10 μm in radius. However, Table 6.11 shows that the extinction per unit mass for dust particles from 10- to 100-μm radius is an order of magnitude smaller than that for the 0- to 10-μm particle radius range.

Agreement between measured and computed extinction is good if one considers only particle sizes less than 10 μm in radius. This is consistent with the measured particle size data from the field tests, where cascade impactor mass samplers used to determine α were typically found to have less than 1% mass in sizes larger than about 8-μm radius. It is likely that the samplers used in these field tests had effective aerodynamic cutoffs of about 10 μm that prevented them from collecting any larger particles present in the airborne dust cloud. This example demonstrates that the quantitative value of mass extinction is closely tied to the maximum and minimum radii for which the extinction is defined. For smokes such as fog oil this is generally not a problem because the entire distribution is narrow, confined to small radii with slow particle settling velocities. However, for obscurants with large particles, one faces a significant problem with fallout rates. Fallout can reduce the airborne mass significantly without substantially reducing extinction at some wavelengths.

Fire-Produced Smokes. Table 6.12 shows some mass extinction coefficients used in modeling obscuration by various fire-produced smokes. Data for soot are well documented in a series of laboratory measurements by Roessler and Faxvog,[23] who also report single-scattering albedos of about 0.20 at both the visible and infrared wavelengths. Smokes produced by burning vegetation contain significantly more organic (oil-like) carbon than do soot-type smokes and as a consequence are less absorbing. Vegetative fire smokes are usually white in appearance as opposed to black oil and petroleum fire smokes. The data of Table 6.12 for vegetative fire smokes were obtained from field measurements on large-scale vegetative fires and are thus subject to large variability in detail.

Table 6.12 Best Estimates of Mass Extinction Coefficients for Various Fire-Produced Smokes

Material	Mass Extinction Coefficient (m^2 kg^{-1}) for Wavelength in μm						
	Visible			Mid IR	Far IR		
	0.4-0.7	0.488	1.06	3.39	10.6	35 GHz	94 GHz
Acetylene Soot: (Ref. 23)	9800 ± 800				760 - 940		
Vegetative Fire: (Ref. 48)	2600 - 5100 *						
(Ref. 49)	4500 - 5000						
Petroleum Fire: (Refs. 27, 47)					990 - 1200		
(Ref. 10)	5600 - 6700						
(Ref. 28)		6970 ± 120	3590 ± 160	1260 ± 150	990 ± 120	6.1 ± 0.4	5.16 ± .55

(*) Scattering Component Only.

Petroleum-based fires produce a thick black smoke. The mass extinction coefficient at visible wavelengths is based on field measurements of transmittance and on spectrophone measurements by Bruce and Richardson.[27] The data for extinction coefficients in Table 6.12 reported by Bruce et al.[28] and Bruce and Richardson[30] are based on a series of field and laboratory determinations that yield single-scattering albedos of 0.34 at the visible wavelengths and 0.15 at the infrared wavelengths. Bruce et al.[28] also account for the unburned hydrocarbon fraction through its effect on the indices of refraction rather than as a smaller particle size mode.

6.2.5.4 Effects of Particle Settling on Definition of Coefficients. An argument against using mass extinction as a bulk optical property is that it changes nonlinearly with changes in particle radius. As long as the relative distribution of sizes of particles in an airborne cloud remains fairly constant, there is no problem. However, large particles usually settle out first.

There are two approaches to dealing with this effect. The first is simply to adopt the definition of the mass extinction as the extinction per unit mass concentration of aerosol *currently remaining airborne*. With this definition, the mass extinction is potentially time and space dependent. It can be applied in models by tracking the mass concentration as a distribution of many size bins. A second approach, however, is to separate the sizes into a few broad categories. For HE dust, for example, these might be called *persistent, transitory,* and *ballistic* size ranges. For dust particles the settling rate in calm air is about 0.018 to 0.031 m s^{-1} for 10-μm-radii particles, depending on the specific gravity. Thus, over downwind times of less than 100 s, it is reasonable to consider dust particles smaller than 10-μm radius as persistent in the cloud. Similarly, the settling rate for dust particles larger than 100-μm radius is greater than 1.3 to 2.0 m s^{-1} in calm air. Thus, these particles are nearly ballistic and fall out rapidly. Between these extremes is a transitory size range that is evolving throughout the time period from a few seconds to 100 s after a small HE explosion in soil. In specifying mass extinction values, it is thus important to specify a size range or other conditions for its use.

6.2.5.5 Broadband Wavelength Effects on Transmittance and Extinction. As presented thus far, all equations apply strictly to monochromatic propagation; that is, to propagation of electromagnetic radiation of one specific wavelength, or more realistically to a very narrow wavelength interval over which the obscurant optical properties can be assumed to be sufficiently constant. For those spectral regions where the optical properties of the medium can be assumed slowly varying, the extension to the broadband case can be included rather easily. Values, such as the mass extinction coefficient, are averaged over the band. These averages are then used in the usual (monochromatic) formulations already discussed.

However, if the underlying optical properties are strongly dependent on wavelength, then it is necessary to carry out full calculations for each wavelength (or narrow band), with averaging over the band carried out in the final step. For example, the broadband-averaged transmittance is defined, strictly, as

$$\overline{T} = \frac{1}{\lambda_2 - \lambda_1} \int_{\lambda_1}^{\lambda_2} \exp[-a(\lambda)\mathrm{CL}]\, d\lambda \ , \tag{6.36}$$

where $\alpha(\lambda)$ is the obscurant mass extinction coefficient at wavelength λ; CL is the obscurant path integrated concentration, or CL product; and λ_1 and λ_2 are the lower and upper limits of the bandpass of interest.

For cases where the obscurant mass extinction coefficient is nearly independent of wavelength or for small CL, a simple band-averaged mass extinction can be used along with the usual Beer's law to calculate transmittance. That is,

$$T(\mathrm{CL}) = \exp(-\bar{\alpha}\mathrm{CL}) \ , \tag{6.37}$$

where the band-averaged mass extinction coefficient $\bar{\alpha}$ is simply defined as

$$\bar{\alpha} = \frac{1}{\lambda_2 - \lambda_1} \int_{\lambda_1}^{\lambda_2} \alpha(\lambda)\, d\lambda \ , \tag{6.38}$$

which is referred to as the $\bar{\alpha}$ approximation for obvious reasons.

For large optical depths and a strongly wavelength dependent mass extinction coefficient, the $\bar{\alpha}$ approximation breaks down, and it is more accurate to use the so-called T bar approximation. In this approximation, one defines a CL-dependent mass extinction coefficient to calculate transmittance in a modified Beer's law formulation as

$$\bar{T}(\mathrm{CL}) = \exp[-\bar{\alpha}(\mathrm{CL})\mathrm{CL}] \ , \tag{6.39}$$

where the broadband CL-dependent mass extinction coefficient $\alpha(\mathrm{CL})$ is found by inverting the band-averaged transmittance defined in Eq. (6.36).

For infrared scenarios, it is also convenient to define a band-averaged emissivity as

$$\varepsilon(\lambda,t_k) = \frac{\displaystyle\int_{\lambda_1}^{\lambda_2} \varepsilon(\lambda)B(\lambda,t_k)\, d\lambda}{\displaystyle\int_0^{\infty} B(\lambda,t_k)\, d\lambda} \ , \tag{6.40}$$

where t_k denotes (absolute) temperature and $B(\lambda,t_k)$ is the Planck, or blackbody, function.

6.2.6 Obscurant Properties for Computing Multiple-Scattering Effects

Computing multiple-scattering contributions to the transmitted radiant energy requires knowledge of scattering with angle and the relative fraction of energy scattered and emitted into the LOS.

6.2.6.1 Single-Scattering Albedo and Thermal Emissivity of Aerosols. An important optical parameter is the obscurant single-scattering albedo defined as the ratio of scattering to extinction, that is,

$$\omega_0(\lambda) = \frac{\alpha_{\mathrm{scat}}(\lambda)}{\alpha_{\mathrm{scat}}(\lambda) + \alpha_{\mathrm{abs}}(\lambda)} = \frac{\alpha_{\mathrm{scat}}(\lambda)}{\alpha_{\mathrm{ext}}(\lambda)} \ . \tag{6.41}$$

Note that the single-scattering albedo is a dimensionless quantity and, as the name implies, represents the relative contribution of scattering to the total extinction. Conversely, the quantity $(1 - \omega_0)$ represents the relative contribution of absorption. For infrared scenarios, the quantity $(1 - \omega_0)$ is referred to as the emissivity per unit optical depth, hence the emissivity of a thin slab of optical thickness $d\tau$ is $(1 - \omega_0)\, d\tau$.

6.2.6.2 Single-Scattering Phase Function. Another important optical characteristic needed in obscuration studies is the angular scattering function $P(\mu,\phi;\mu',\phi')$, which is sometimes called the *differential scattering function,* or more often the *phase function.* It represents the portion of an incident beam from direction (μ,ϕ) that is scattered into the particular direction (μ',ϕ'). The angular coordinates are $\mu = |\cos\theta|$ and $\mu' = |\cos\theta'|$, where θ and θ' are zenith angles and ϕ and ϕ' are azimuth angles.

In many applications, $P(\mu,\phi;\mu',\phi')$ is normalized so that the integral of P over all μ' and ϕ' is 1. A common alternative definition normalizes the integral to the single-scattering albedo ω_0: ≡

$$\omega_0 = \frac{1}{4\pi} \int_{-1}^{+1} \int_{0}^{2\pi} P(\mu,\phi;\, \mu',\phi')\, d\phi'\, d\mu' \quad . \tag{6.42}$$

With the phase function so defined, it is clear that the single-scattering albedo simply represents the total contribution to scattering into all angles. Some care is required in applying the phase function to real problems because of the various normalization conventions used.

For spherical, homogeneous aerosols, the phase function can be computed exactly using the previously discussed Mie theory. In Sec. 6.4 we make use of a particularly convenient analytical expression for approximating the form of the phase function for spherical particles.

6.2.6.3 Nonspherical Particle Effects. In many applications, the assumption of spherical aerosols is valid especially for liquid droplets such as fog and certain obscuring smokes. In other situations, however, this assumption requires some assessment such as for snow and other nonspherical particles used as long-wave obscurants and as tracers for weather radar returns. For nonspherical particles, the Mie theory is inadequate. One must return to the fundamental integral equation for wave propagation. For a plane wave, $E_0 \exp(i\mathbf{k}*\mathbf{r})$, incident on an arbitrarily shaped particle of volume V, the appropriate expression for calculating the scattered electric field $E(\mathbf{r})$ at any position $\mathbf{r}$ outside the volume is

$$E(\mathbf{r}) = E_0 \exp(i\mathbf{k}\cdot\mathbf{r}) + [k + \nabla(\nabla\cdot)] \int_V (m^2 - 1) E(\mathbf{r}') G(\mathbf{r},\mathbf{r}')\, dV \quad , \tag{6.43}$$

where

$$G(\mathbf{r},\mathbf{r}') = \frac{\exp(ik|\mathbf{r} - \mathbf{r}'|)}{4\pi|\mathbf{r} - \mathbf{r}'|} \tag{6.44}$$

is the free-space Greens function, **k** is the propagation wavenumber vector ($k = 2\pi/\lambda$), and m is the complex refractive index of the scattering medium. For the scattered field $E_{\text{scat}}(\mathbf{r})$ in the "radiation" zone far from the scattering volume, Eq. (6.43) can be written in the form of a relatively simple scattering amplitude $A(\mathbf{k},\mathbf{r})$ times a spherical wave, that is,

$$E_{\text{scat}}(\mathbf{r}) = E_0 A(\mathbf{k},\mathbf{r}) \frac{\exp(ikr)}{r} , \tag{6.45}$$

where

$$A(\mathbf{k},\mathbf{r}) = k^2[1 - \hat{\mathbf{r}}(\hat{\mathbf{r}}\cdot)] \frac{m^2 - 1}{4\pi} \int_V \frac{E(\mathbf{r}')}{E_0} \exp(-ik\mathbf{r} \cdot \mathbf{r}')\, dV . \tag{6.46}$$

Equations (6.43) through (6.46) have been studied extensively. However, exact solutions in the far field, or "radiation" zone, are available only for a few idealized particle shapes, namely the sphere (Mie theory) and the infinite cylinder (c.f., Ref. 8). Significant progress has been made on numerical models for more arbitrary shapes. Other approaches involve the classical approximations that are usually valid for some restricted range of conditions on particle shape and size. Some results for Q_{ext} using both rigorous solutions and certain classical approximations, such as Rayleigh-Gans (RG), Wentzel-Kramers Brillouin (WKB), and the anomalous diffraction approximation (ADA), are plotted in Fig. 6.10 for both spheres and cylinders. In Fig. 6.10 we have introduced the phase parameter x defined as

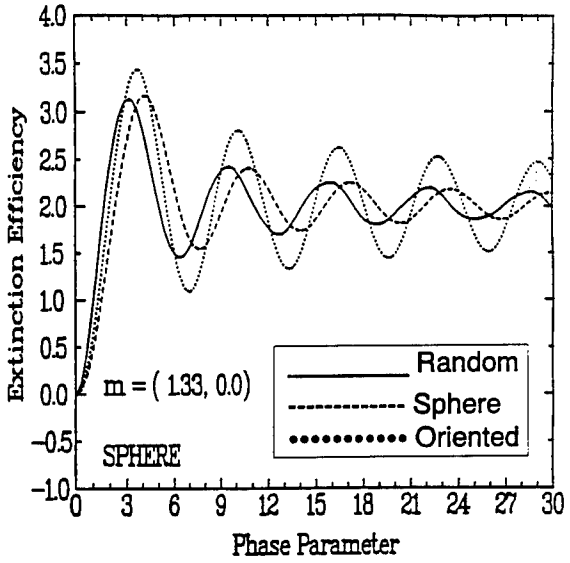

Fig. 6.10 Optical extinction efficiency as a function of phase parameter as calculated for (1) oriented circular cylinder with incident beam perpendicular to long axis, (2) random ensemble of uniform angular distribution of cylinders, and (3) sphere of same radius as cylinder.

$$x = \frac{2\pi a}{\lambda}(m - 1) \ , \tag{6.47}$$

where m is the complex refractive index.[50]

In some applications, it is appropriate to approximate extinction resulting from ensembles of irregular shaped particles by assuming a uniform distribution of orientation angles that results in spherical symmetry. This is reasonable in situations where random tumbling might give rise to a uniformly random orientation of particles. However, in the general case some consideration must be given to effects of (partial) orientation, even in atmospheric turbulence.

6.3 FORWARD SCATTERING

Consider a radiant source that is observed (i.e., its radiant intensity is detected, focused to an image, or otherwise processed) over a LOS under unobscured conditions. An obscuring aerosol is now introduced that alters the observation of this source. By definition, direct transmittance quantifies the fraction of the original radiant intensity that is neither scattered nor absorbed and still arrives undisturbed at the observer. This directly transmitted spectral radiance is available for detection, image formation, etc., in exactly the same manner as that for unobscured conditions. It can be defined as the received *coherent radiant intensity*.[51]

Some of the radiant intensity from the source that is removed by the obscurant via scattering can still reach the observer, however. It can be called the *incoherent radiant intensity*.[51] If an aerosol scatters strongly in the forward direction or if the observer field of view collects energy from the obscurant over a large range of angles surrounding the LOS, then even single-scattering processes in the obscurant can produce a large incoherent radiant intensity from the source. For this reason and because the incoherent radiant intensity has different focusing properties from the coherent radiant intensity, this process of *forward scattering* is particularly important. This section deals with identifying the conditions under which forward scattering can be important to an application and methods for quantifying it.

6.3.1 Magnitude of Forward Scattering Effects on Received Radiance

First we consider conditions for which the magnitude of received incoherent radiant intensity might be significant enough to warrant correcting the total transmission for forward scattering in noncoherent detection. The important parameters are the observer's or sensor's field of view, the area of the collection optics or detector, the obscurant optical depth, the phase function of the aerosol, the wavelength of the radiation, and the geometry of the cloud and its illumination by the source.

Field of view is important because more scattered energy is collected as the observer's angular field of view increases. The area of the collection optics, detector, or equivalent aperture stop is important both because a larger aperture collects more of the scattered power and because it determines the diffraction limit to which the coherent radiance field can be focused. A larger

optical depth implies more scattering. The more highly peaked the phase function in the forward direction, the more the scattered radiant intensity from a specific source concentrates along the LOS. The phase function depends on wavelength relative to the sizes of obscurant particles, on refractive index, and on shape factors. Larger particles generally produce the most forward scatter and are of particular concern. Wavelength also affects the diffraction limit of the collection optics. Finally, the distribution of the aerosol cloud concentration with respect to the source and observer positions is important because the distribution of the aerosol illuminated by the radiant source and available within the field of view of the observer affects the amount of scattered power that is collected.

Table 6.13 gives some examples of computed forward scattering for fog oil smoke, soil-derived dust, fog, rain and snow for optical depths of 1, 5, and 10. The last three adverse weather aerosols are not the main focus of this chapter. However, their large particle sizes produce large forward scattering, providing a useful reference. Calculations were performed using ASCAT, a computer code[52] for forward scattering. A visual wavelength of 0.55 μm was chosen for the examples, at which most of the aerosols of Table 6.13 are highly scattering. The examples use phase functions and extinction coefficients from the PFNDAT data base[53] that applies Mie theory to measured particle size distributions and refractive indices. A 200-m-thick cloud was assumed, with the source and observer each 100 m from the edge of the cloud on opposite sides of the cloud. A small, pointlike source of radiant intensity is assumed, with power spreading uniformly outward into a cone of 52 deg full width, illuminating a large volume of the cloud. The source power is chosen to produce an on-axis irradiance of unity at the receiver under clear conditions. The receiver is assumed to have a narrow but finite field of view of a few tenths of milliradians, corresponding to that typical of individual pixels within an image (3/10 mrad subtends a 1-m object at 3.3 km). With these assumptions, the near-forward multiple-scattering corrections to received on-axis irradiance (W m^{-2}) are shown.

Table 6.13 lists the aerosols in order from smallest particles (fog oil smoke) to largest (snow) particles. For snow, and to some extent for other materials,

Table 6.13 Examples of Forward Multiple-Scattering Corrections to Direct Transmittance for Irradiance at Wavelength λ = 0.55 μm

Optical Depth:	τ = 1.0		τ = 5.0		τ = 10.0	
Direct Transmittance:	T = .3679		T = .006738		T = .000045	
	Direct Transmission Plus Forward Scattering					
Field of View:	0.3 mr	0.7 mr	0.1 mr	0.3 mr	0.1 mr	0.3 mr
Fog Oil Smoke	.3679	.3679	.006738	.006738	.000045	.000045
Dust	.3680	.3683	.006743	.006780	.000048	.000067
Fog	.3681	.3687	.006746	.006814	.000050	.000085
Rain	.3688	.3730	.006791	.007213	.000073	.000295
Snow	.3727	.3939	.007009	.009175	.000188	.001328

the Mie theory assumption of spherical scatterers is not strictly valid. An effective size is assumed so that Mie theory can produce a phase function. The total received on-axis irradiance can be compared to that received by direct transmittance alone. Only when the optical depth is much larger than 5 is the forward-scattering effect significant through dust at these small fields of view. It is insignificant through fog oil smoke, but almost always important for the clouds of fog, rain, and snow particles at optical depths larger than 1.

Table 6.14 shows examples of forward scattering contributions to the total transmitted power on a collector or detector of finite size and for larger receiver fields of view than in Table 6.13. The optical depth is fixed at 5, and only smoke and dust are considered. Values are calculated from ASCAT for various

Table 6.14 Examples of Forward Multiple-Scattering Contributions to Total Received Energy for Wavelength $\lambda = 0.55$ μm

	Forward Scattered Power Plus that from Direct Transmittance for $\tau=5$ (T = 0.00674)			
Receiver Field of View:	3.0 mr	33.0 mr	3.61°	10.5°
Case: 0.5 cm diameter Gaussian laser on 10 cm radius collector				
Fog Oil Smoke	.00674	.00674	.00674	.00674
WP Smoke	.00674	.00674	.00674	.00674
HC Smoke	.00674	.00674	.00674	.00675
HE Dust	.00674	.00687	.00689	.00690
Case: Highly collimated 30.5 cm radii source and 30.5 cm collector				
Fog Oil Smoke	.00674	.00674	.00674	.00674
WP Smoke	.00674	.00674	.00674	.00674
HC Smoke	.00674	.00674	.00674	.00675
HE Dust	.00674	.00685	.00716	.0104
Case: Large 30 m diameter collimated source and 10 cm radius collector				
Fog Oil Smoke	.00674	.00675	.00677	.00685
WP Smoke	.00674	.00678	.00684	.00708
HC Smoke	.00674	.00687	.00707	.00765
HE Dust	.00681	.0120	.0146	.0148
Case: Point Source with 55° divergence and 30.5 cm radius collector				
Fog Oil Smoke	.00674	.00693	.00740	.0122
WP Smoke	.00674	.00730	.00876	.0224
HC Smoke	.00675	.00821	.0120	.0464
HE Dust	.00682	.0211	.0541	.186

source sizes, collector or detector sizes, source beam divergences, and receiver fields of view. The cloud is again uniform and 200 m thick with source and observer 100 m from the cloud edge on opposite sides of the cloud. The direct transmittance is 0.00674 for all cases. Only when the source forms a very large diameter beam or produces a wide-angle-diverging beam are the corrections significant for the screening smokes WP, HC, and fog oil. Dust, however, produces some correction for all fields of view larger than 1 deg in these examples.

Thus, there are many practical situations where forward multiple scattering can be neglected in determining the power available at the detector. However, there can also be situations where the received power is primarily provided by forward scatter and not by the attenuated direct radiation from the source.

6.3.2 Calculation of Forward Scattering

Forward-scattering computations are often simplified by using the *small-angle approximation* to scattering. In this approximation, one assumes that incident electromagnetic waves scatter at small angles when interacting with large aerosol particles. For particles large compared to the wavelength, the phase function is usually highly peaked in the (forward) direction of propagation of the incident electromagnetic wave. However, even particles whose sizes are only on the order of the wavelength of light also usually scatter somewhat preferentially in the forward direction.

For forward scattering, replacing sine θ with θ (the small-angle approximation) leads to a phase function approximating a highly peaked Gaussian function at small angles:

$$P(\Omega) = P(\theta;\phi) = \frac{1}{\pi\theta_0^2}\exp\left[-\left(\frac{\theta}{\theta_0}\right)^2\right] = \frac{\alpha_p}{\pi}\exp(-\alpha_p\theta^2) \ , \tag{6.48}$$

where θ_0 is a small angular half-width of the forward scattering peak[54–56] and α_p, an alternative parameter for defining the width of the forward peak, is used in the following. For θ_0 small, the integral of Eq. (6.48) over all θ and ϕ leads to a phase function normalization value approaching 1.

The ASCAT forward-scattering computer code uses the method of Dolin[57] and Fante[58] to take advantage of small-angle approximations to forward scattering in the radiative transfer equation:

$$\left(\boldsymbol{\phi}\cdot\frac{\partial}{\partial\mathbf{r}} + \frac{\partial}{\partial z} + \sigma_{\text{ext}}\right)I(\boldsymbol{\phi},\mathbf{r},z) = \sigma_{\text{ext}}\omega_0 P(\boldsymbol{\phi}-\boldsymbol{\phi}')I(\boldsymbol{\phi}',\mathbf{r},z)\sin(\theta')\,d\theta'\,d\phi' \ . \tag{6.49}$$

The radiance of the source beam is assumed to have the form

$$I(\boldsymbol{\phi},\mathbf{r},z=0) = \frac{\beta^2\gamma^2}{\pi^2}\exp(-\beta^2\boldsymbol{\phi}^2 - \gamma^2\mathbf{r}^2) \ , \tag{6.50}$$

where

$$\gamma = \frac{\sqrt{2}}{w_0} \quad \text{and} \quad \beta = \frac{2\pi}{\lambda\gamma} \tag{6.51}$$

define the spatial divergence γ and the angular divergence β of the beam. The minimum spot size of the beam is w_0 in these formulas. Note that the ASCAT code as used in these examples assumes a slightly different definition for β based on the Airy diffraction formula for the minimum source spot size w_0:

$$\beta = \frac{w_0}{1.22\lambda} \ . \tag{6.52}$$

With this formalism, the ASCAT computer program calculates the total radiant intensity as the sum of two parts

$$I(\boldsymbol{\phi},\mathbf{r},z) = I^{(u)}(\boldsymbol{\phi},\mathbf{r},z) + I^{(s)}(\boldsymbol{\phi},\mathbf{r},z) \ , \tag{6.53}$$

where the unscattered (coherent) part is

$$I^{(u)}(\boldsymbol{\phi},\mathbf{r},z) = \frac{\beta^2\gamma^2}{\pi^2} \exp(-\sigma_{\text{ext}}z) \exp[-\beta^2\boldsymbol{\phi}^2 - \gamma^2(\mathbf{r} - z\boldsymbol{\phi})^2] \ , \tag{6.54}$$

and the scattered (incoherent) part is

$$I^{(s)}(\boldsymbol{\phi},\mathbf{r},z) = \frac{\sigma_{\text{ext}}\omega_0 \exp(-\sigma_{\text{ext}}z)}{(2\pi)^2} \int dz' \frac{\exp(\sigma_{\text{ext}}z')}{\Delta} \times \left(\exp\left\{-\left[\frac{K(z')\mathbf{r}^2 - L(z')\boldsymbol{\phi}\cdot\mathbf{r} + M(z')\boldsymbol{\phi}^2}{\Delta}\right]\right\}\right) \ , \tag{6.55}$$

$$K(z') = \frac{1}{4\beta^2} + \frac{1 + \sigma_{\text{ext}}\omega_0 z'}{4\alpha_p} \ , \tag{6.56}$$

$$L(z') = \frac{z}{2\beta^2} + \frac{2z' + \sigma_{\text{ext}}\omega_0 z'^2}{4\alpha_p} \ , \tag{6.57}$$

$$M(z') = \frac{z^2}{4\beta^2} + \frac{1}{4\gamma^2} + \frac{z'^2 + (1/3)\sigma_{\text{ext}}\omega_0 z'^3}{4\alpha_p} \ , \tag{6.58}$$

with

$$\Delta = 4KM - L^2 \ . \tag{6.59}$$

The on-axis radiant intensity is found when $\mathbf{r} = 0$.

6.3.3 Modulation Transfer Function

Another potentially important effect at near-forward angles is the effect of aerosols in limiting resolution. Resolution loss through the atmosphere is not usually considered in basic transmittance calculations. However, it can be important to problems of contrast loss, target detection, and target recognition, in which resolution, transmittance, and path radiance each play a role. The total modulation transfer function (MTF) quantifies the image's spatial intensity modulation that survives both the atmosphere and sensor (e.g., the lens system). Intensity modulation quantifies contrast variations spatially across an image; within object detail or between nearby objects in the field of view, for example. Suppose the source is a sinusoidal intensity pattern of a single angular frequency f (cycles rad^{-1}) along one dimension and constant intensity along the other dimension:

$$I_0(\theta) = 1 + \cos(2\pi f\theta) \ , \tag{6.60}$$

where θ is the angle with respect to a line from the center of the lens to the object plane. The resulting distribution of intensity focused on the image plane is then altered by the MTF $M(f)$:

$$I_i(\theta) = 1 + |M(f)| \cos(2\pi\theta) \ . \tag{6.61}$$

The zero frequency component has an MTF of 1, whereas at other frequencies, an MTF of less than 1 reduces the range separating the minimum and maximum intensity at each spatial frequency. The MTF can then be written (see Ref. 51) as the product of two terms:

$$M(f) = K\left(\frac{f}{f_{co}}\right) \exp\left[-\frac{1}{2}D(\lambda f)\right] \ , \tag{6.62}$$

where λ is the radiation wavelength and f_{co} is the cutoff frequency of the lens system relative to the lens diameter D_0:

$$f_{co} = \frac{D_0}{\lambda} \ . \tag{6.63}$$

The function K is the MTF of the optical system alone. The function D, called the *wave structure function,* results from the atmosphere.

Loss of detail (i.e., of high spatial frequencies) in an image is most familiar as an effect of optically turbulent media. For locally homogeneous turbulence with a Kolmogorov spectrum,[51]

$$D(\lambda f) = 2\left(\frac{D_0}{R_c}\right)^{5/3}\left(\frac{f}{f_{co}}\right)^{5/3} \ , \tag{6.64}$$

where D_0 is the lens diameter, and R_c,

$$R_c = (0.547k^2C_n^2L)^{-3/5} \ , \tag{6.65}$$

is called the *correlation distance* for a spherical wave. The wave number is $k = 2\pi/\lambda$, and the strength of turbulence is C_n^2. For frequencies of interest to imaging with this lens, $0 < f < f_{co}$, the atmospheric effects are large only when R_c is smaller than D_0. This occurs when refractive index fluctuations are large (i.e., large C_n^2) or the optical path length L is long.

Similarly, an atmosphere containing large particles of a single radius a distributed with random uniform probability produces a modulation transfer function because of scattering. Suppose the aerosol has a forward-peaked phase function of the form of Eq. (6.48). If the particle is large compared to the wavelength, then its half-angle diffraction spread is

$$\theta_0 = \frac{1.22}{2}\left(\frac{\lambda}{2a}\right) , \tag{6.66}$$

leading to an approximate Gaussian phase function parameter α_p of

$$\alpha_p = 10.7\left(\frac{a}{\lambda}\right)^2 \approx \left(\frac{\pi a}{\lambda}\right)^2 . \tag{6.67}$$

The wave structure function for scattering then becomes[51]

$$D(\lambda f) = 2\tau\left\{1 - \omega_0 \exp\left[-\left(\frac{f}{f_{co}}\right)^2\left(\frac{D_0}{a}\right)^2\right]\right\} . \tag{6.68}$$

Except for very low spatial frequencies $f << f_{co}$ or for particle radii not too much smaller than the lens radius, the MTF approaches the direct transmittance T. This is shown in an example in Fig. 6.11, where typical MTFs for a fine particle smoke, large rain drops, and moderate optical turbulence are compared. Unless the aerosols are large, a random distribution with uniform probability simply reduces the intensity equally at each spatial frequency.

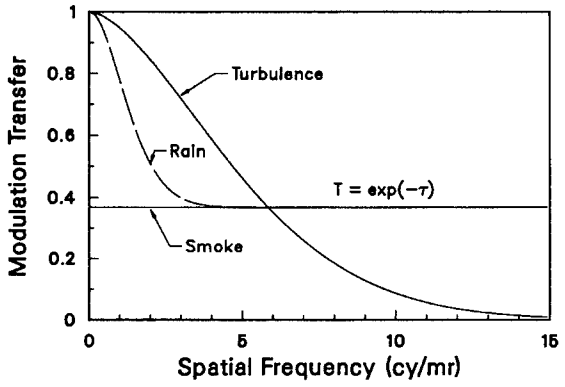

Fig. 6.11 Examples of MTFs of aerosols and optical turbulence.

Often the changes in the point spread function (PSF) produced by the aerosol are of greater interest than the MTF. The PSF is related to the MTF (actually to the complex function of both amplitude and phase, called the *optical transfer function*) by Fourier transforms. When a distant point object is imaged with a circular lens of aperture radius R_0 through a vacuum, the image produces an Airy disk diffraction pattern containing a central bright spot surrounded by concentric bright regions that fall off in intensity with radius r from the center. Now introduce aerosol scatterers with optical depth τ along the LOS, particle radius a, and forward-scattering phase function coefficient α_p. The coherent radiant intensity is then

$$I^{(u)}(r) = I_0 e^{-\tau}\left(\frac{R_0}{r}\right)^2 J_1^2\left(\frac{krR_0}{f_l}\right) , \tag{6.69}$$

where J_1 is a Bessel function of order 1 and f_l is the focal length. The incoherent intensity for $\tau >> 0$ is[51]

$$I^{(s)}(r) = I_0\left(\frac{R_0}{r_i}\right)^2 \exp[-\tau(1 - \omega_0) - (r^2/r_i^2)] , \tag{6.70}$$

where r_i is the radius of the spread in the incoherent intensity. This spread is related to the radius r_a (first minimum) of the Airy pattern,

$$r_a = \frac{3.832 f_l}{kR_0} , \tag{6.71}$$

and the correlation distance R_c of the wave incident on the lens,

$$R_c = \left(\frac{4\alpha_p}{\tau\omega_0 k^2}\right)^{1/2} \approx \frac{1.04a}{(\tau\omega_0)^{1/2}} , \tag{6.72}$$

through the equation

$$r_i = 0.522\left(\frac{R_0}{R_c}\right) r_a = 0.502\left(\frac{R_0}{a}\right)(\tau\omega_0)^{1/2} r_a . \tag{6.73}$$

Thus, for particles that are much smaller than the size of the lens but larger than the wavelength, the scattered incoherent radiant intensity is spread across the image at scales much larger than the coherent Airy disk.

For signal-to-noise considerations, one can also estimate the optical depth at which the incoherent radiant intensity equals the peak intensity of the remaining coherent radiation[51]:

$$\tau\omega_0 \approx 2 \ln\left(\frac{0.963R_0}{a}\right) + \ln\left[2 \ln\left(\frac{0.963R_0}{a}\right)\right] . \tag{6.74}$$

For example, a particle of radius 10 μm, single-scattering albedo ω_0 of 1 at a wavelength of 0.55 μm, and a lens of radius 0.1 m, the estimated optical depth

of 21 should be sufficient to produce an incoherent scattered radiant intensity equal to the remaining focused coherent radiant intensity on the image plane. For optical depths much smaller than this limit, it can be possible to produce a long time exposure to produce a usable final image of the obscured object, although its contrast can be poor.[51]

Large-particle multiple scattering is often dominated by its single-scattering component propagating very close to the LOS into the forward direction. But this is only one source of incoherent radiation that adds to the directly transmitted radiance. Later sections consider the equally important contributions to multiply scattered path radiance from particles of all sizes and from spatially diffuse radiant sources that are off-axis from the LOS.

6.3.4 Fluctuations in Optical Depth

Fluctuations in refractive index (called *optical turbulence* in the last section) are partly responsible for image resolution loss. However, turbulent fluctuations and eddies in aerosol concentration along an LOS and across a target or scene directly affect both the momentary distribution of transmitted radiance and that of scattered diffuse radiance. Random but correlated positions of particles in an obscurant cloud can produce several such types of fluctuation phenomena. These can be described in terms of individual particles or from the statistics underlying atmospheric turbulence.

Consider N identical particles placed with uniform random probability in a column of cross-sectional area A along a LOS. Each particle has an extinction cross section σ_{ext}. The probability that a line of infinitesimal cross section along the LOS will interact with one specific particle is thus (σ_{ext}/A). The maximum probability that the line will interact with at least one of the N particles is $(N\sigma_{ext}/A)$. This maximum probability, up to a value of 1, equals the optical depth τ. Equivalently, at an optical depth of 1, the maximum extinction cross section $N\sigma_{ext}$ just equals the area A of the column. However, this is only the maximum probability because it assumes the unlikely situation that the particles are positioned with no overlap across the column. The probability that no particles interact with the photon or the line of infinitesimal cross section,

$$\lim_{N\to\infty}\left(1-\frac{\sigma_{ext}}{A}\right)^N = \lim_{N\to\infty}\left(1-\frac{\tau}{N}\right)^N = e^{-\tau} = T_{direct}\ , \tag{6.75}$$

is a form of the Beer-Lambert law for direct transmittance.

The average number of interactions is given by the expectation

$$E(m) = \sum_{m=0}^{N} m\binom{N}{m}\left(\frac{\tau}{N}\right)^m\left(1-\frac{\tau}{N}\right)^{(N-m)} = \tau\ . \tag{6.76}$$

This is used in Monte Carlo simulations. A *photon* is launched into an aerosol cloud. The particles are positioned with uniform random probability. Then, on average, the photon is expected to interact (i.e., scatter or be absorbed) once for each unit optical depth traversed along its path through the aerosol.

Next, consider the effect of random placement of particles on fluctuations in optical depth along the LOS. The probability of finding n particles inside a small column of cross section $a << A$ is

$$p(n) = \binom{N}{n}\left(\frac{a}{A}\right)^n\left(1 - \frac{a}{A}\right)^{(N-n)} , \tag{6.77}$$

with average number of particles (Na/A). The average optical depth,

$$\tau = \frac{n_{av}\sigma_{ext}}{a} = \frac{N\sigma_{ext}}{A} , \tag{6.78}$$

is the same as the population aerosol. The variance in n is

$$\langle (n - n_{av})^2 \rangle = N\left(\frac{a}{A}\right)\left(1 - \frac{a}{A}\right) , \tag{6.79}$$

which in terms of optical depth fluctuation $\tau' = (n - n_{av})(\sigma_{ext}/a)$ is

$$\langle \tau'^2 \rangle = \tau\left(\frac{\sigma_{ext}}{a}\right)\left(1 - \frac{a}{A}\right) . \tag{6.80}$$

Thus, unless the field-of-view cross section A is very narrow (such as a distant bright point source in a nearly black sky), the fluctuation in optical depth resulting from particles placed with *uniform probability* within a column surrounding the LOS is very small.

However, macroscopically, particles can exhibit a collective, *nonuniform probability* distribution because of turbulent atmospheric eddies. Concentration fluctuations in homogeneous turbulence follow the well-known Kolmogorov spectrum over the inertial range of scales from about 10^{-4} m to hundreds of meters. The one-dimensional Kolmogorov spectral density is[51]

$$V(K) = \frac{\Gamma(5/3)}{2\pi}\sin\left(\frac{\pi}{3}\right)C_{cf}^2 K^{-5/3} , \tag{6.81}$$

where K is one over the eddy size and C_{cf}^2 is the mean-squared strength of the fluctuation with units of length to the $-2/3$ power. For example, the distribution of eddies produces a spatial structure function for the expected variance in concentration (the mean-squared difference in concentrations at positions $\mathbf{x}$ and $\mathbf{x} + \mathbf{x}'$) of

$$\langle |c(\mathbf{x}) - c(\mathbf{x} + \mathbf{x}')|^2 \rangle = C_{cf}^2 \langle c \rangle^2 |\mathbf{x}'|^{2/3} . \tag{6.82}$$

The fluctuation strength can be estimated in terms of the local mean gradient in concentration and the outer scale of turbulence (largest eddy in the inertial range) L_0 (Ref. 51):

$$C_{cf}^2 = 2.8L_0^{4/3}\left|\frac{\nabla\langle c\rangle}{\langle c\rangle}\right|^2 = 1.91L_0^{-2/3}\sigma_c^2 \ , \tag{6.83}$$

where σ_c is the dimensionless fluctuation standard deviation. Define the fluctuating local concentration $c(\mathbf{x})$:

$$c(\mathbf{x}) = \langle c(\mathbf{x})\rangle[1 + f_c(\mathbf{x})] \ , \tag{6.84}$$

where $\langle c\rangle$ is the local mean concentration. The fluctuations f_c are highly correlated over small separation distances and uncorrelated over distances of the order of the outer scale, with correlation:

$$\langle|f_c(\mathbf{x})f_c(\mathbf{x} + \mathbf{x}')|\rangle = \sigma_c^2\left(1 - 0.955\left|\frac{x'}{L_0}\right|^{2/3}\right) \ . \tag{6.85}$$

Integration of the concentration over a LOS to determine a CL averages out some of the fluctuations in concentration. Using the correlations from Eq. (6.85), the fluctuations in CL over a path of length x through the obscurant has variance

$$\begin{aligned}\langle|\mathrm{CL}(x)|^2\rangle &= \langle\mathrm{CL}\rangle^2\sigma_c^2\left(1 - 0.955L_0^{-2/3}x^{-2}\right.\\ &\qquad\left.\times\int_0^x ds\int_0^x ds'|s - s'|^{2/3}\right)\\ &= \langle\mathrm{CL}\rangle^2\sigma_c^2\left[1 - 0.430\left(\frac{x}{L_0}\right)^{2/3}\right] \ .\end{aligned} \tag{6.86}$$

Thus, CL fluctuations die out over a range of approximately $3.5\,L_0$.

To estimate the effects of concentration fluctuations on direct transmittance T, a fluctuation f_T can be defined in terms of CL as

$$\mathrm{CL}(\rho) = \langle\mathrm{CL}(\rho)\rangle[1 + f_T(\rho)] \ , \tag{6.87}$$

where ρ is a position in the plane perpendicular to the LOS. The fluctuating transmittance T can be written and approximated as

$$\begin{aligned}T(\rho) &= \exp\{-\alpha\langle\mathrm{CL}\rangle[1 + f_T(\rho)]\} = \langle T(\rho)\rangle\exp[-\alpha\langle\mathrm{CL}\rangle f_T(\rho)]\\ &\approx \langle T(\rho)\rangle[1 + f_T(\rho)\ln\langle T(\rho)\rangle] \ .\end{aligned} \tag{6.88}$$

Fluctuations across an image depend on correlations between separated lines of sight and the structure function for the CL fluctuation f_T. Assume two parallel LOS separated by a distance ρ. Each LOS passes through an aerosol cloud over a length x. Using techniques similar to those applied to optical turbulence[59]:

$$\langle |f_T(x,\rho) - f_T(x,0)|^2 \rangle = \left(\frac{C_{cf}}{x}\right)^2 \int_0^x ds \int_0^x ds' \times \{[(s - s')^2 + \rho^2]^{1/3} - (s - s')^{2/3}\}$$

$$= 3.82 \left(\frac{x}{L_0}\right)^{2/3} \sigma_c^2 \int_0^1 dw(1 - w) \times \left\{\left[w^2 + \left(\frac{\rho}{x}\right)^2\right]^{1/3} - w^{2/3}\right\} . \quad (6.89)$$

For optical turbulence an integral such as that in Eq. (6.89) is also performed. However, in that case one confines the LOS path separations to small distances of the order of the sensor lens effective aperture and, applying appropriate approximations, obtains analytic results. Here the LOS separations of interest can be very large, even exceeding the length of the LOS itself. The integral in Eq. (6.89) can be performed numerically without resorting to approximations, however, for various ratios of the LOS separation ρ to the path length through the aerosol x, as shown in Fig. 6.12.

Statistical behavior of transmittance is important to modeling the variations in radiance across an image and to computer visualization of obscurants. Of particular interest is the slope of the log of the integral plotted in Fig. 6.12 with respect to the log of the ratio of path separation to path length. The Hurst parameter H is one half this slope. It is plotted in Fig. 6.13 for the integral plotted in Fig. 6.12. The Hurst parameter is the difference between the Euclidean dimension and the fractal dimension of a self-affine fluctuation process.[60] For time series of self-affine processes, for example, the variance over fixed time separations scale with the Hurst parameter as

$$\langle |V(t) - V(t + \Delta t)|^2 \rangle \propto (\Delta T)^{2H} , \quad (6.90)$$

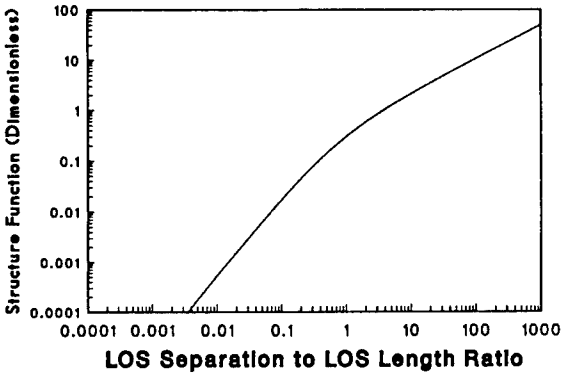

Fig. 6.12 Integral for the structure function of CL and transmittance fluctuations as a function of the ratio of LOS path separation to LOS path length.

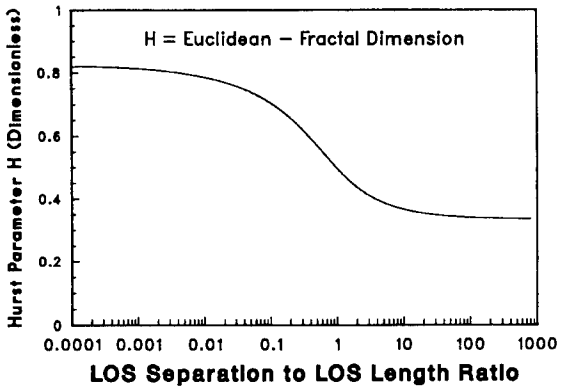

Fig. 6.13 Hurst parameter for the structure function of CL and transmittance fluctuations as a function of the ratio of LOS path separation to LOS path length.

where V is the scalar time process. This variance over time at one spatial point is also related to the spatial structure function for instantaneous fluctuations between two points separated by $\Delta\rho = u\Delta t$, where u is the mean wind velocity. (This is called the *frozen-in hypothesis of turbulence.*) For homogeneous Kolmogorov turbulence, the structure function for point concentrations, Eq. (6.82), thus identifies that H should be 1/3 over all scales up to L_0.

The Hurst parameter for the path-integrated concentration thus determines how smoothly the CL (and thus transmittance) fluctuates between LOS pairs. The Hurst parameter in Fig. 6.13 ranges from 5/6 for very small LOS separations (or small time differences for a cloud blowing across a fixed LOS) to 1/3 for very large separations.

A Hurst parameter of 1/2 is characteristic of Brownian random processes. A Brownian process can be generated by adding an uncorrelated (white noise) random number at each time step to the sum from the previous time step. The random number has mean zero and some Gaussian standard deviation. A Hurst parameter of 1/2 occurs in Fig. 6.13 when the LOS separation is very nearly equal to the path length of the LOS through the obscurant. A Hurst parameter larger than 1/2 is characteristic of persistent fluctuations, smoother than Brownian fluctuations, whereas a Hurst parameter smaller than 1/2 is characteristic of antipersistent fluctuations that vary more rapidly than those of Brownian processes.

This behavior indicates that transmittance fluctuations are relatively smooth over small time scales or LOS separations and have large fluctuations over large time scales or LOS separations. An example of measured transmittance fluctuations with time for a continuous and constant production of carbon smoke is shown[61] in Fig. 6.14. Shown in Fig. 6.15 are the relative structure functions measured for eight such aerosol cloud releases of fog oil, kaolin dust, and carbon. Each data set is of 8- to 10-min duration under somewhat different wind conditions.[61] The clouds were 30 to 50 m wide at the LOS. The mean variance in log transmittance, which is proportional to CL, is shown in Fig. 6.15 as a function of time difference. The variances for all eight trials have been normalized to 1 at a time difference of 1 s to show the slopes more clearly.

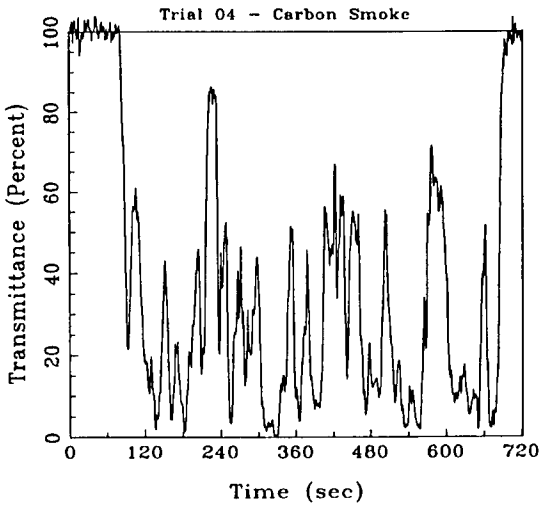

Fig. 6.14 Example of transmittance fluctuations for a crosswind LOS through a carbon smoke cloud released at constant rate.

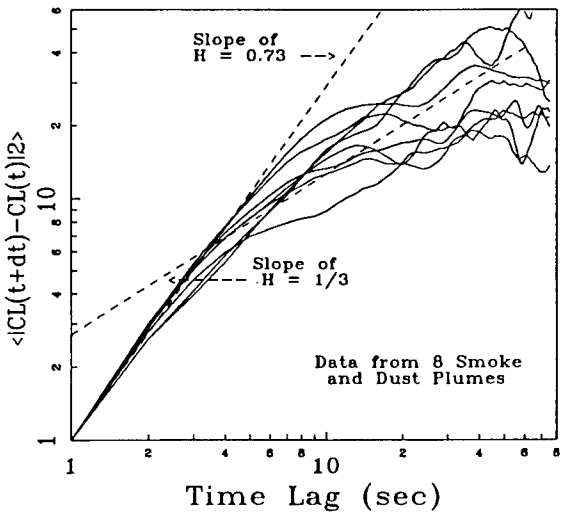

Fig. 6.15 Measured variance in CL difference as a function of time difference for eight continuous, constant releases of fog oil smoke, kaolin dust, and carbon smoke, and the slopes for Hurst parameter behavior of 0.8 and 0.33.

The data roughly agree with the theory that the Hurst parameter should be about 5/6 at small time differences and about 1/3 at large time differences. The transmittance fluctuations are definitely not fractal in the usual sense because the slope in the data is not constant.

Thus, although concentration fluctuations are fractal in homogeneous turbulence, the transmittance and the CL path integral through an aerosol cloud of finite width does not have a constant fractal dimension. The Hurst param-

eter, and thus the fractal dimension, changes with LOS path separations or with time separations for a single LOS. (In recent literature this changing fractal dimension might be characterized as multifractal rather than nonfractal.)

Qualitatively the change in Hurst parameter can be understood as follows. As two closely spaced LOS are separated, they encounter different turbulent eddies for eddy sizes smaller than the separation width. These different small eddies are uncorrelated and relatively numerous over the finite lengths of the LOS through the cloud, so they contribute a large change in variance to the CL. The slope of the mean variance in CL, as in Fig. 6.15, is thus large. However, at greater LOS separations, progressively larger eddies on the two LOS become uncorrelated. There are fewer of the large eddies along the length of the LOS x because of the finite width of the cloud. So they contribute relatively less to the increase in variance. The slope of the mean variance in CL, as in Fig. 6.15, thus gets progressively smaller. It is thus the sampling property of a finite cloud width that causes the Hurst parameter to change. As the outer scale is exceeded, there are almost no additional eddies of these large sizes to contribute to increasing the variance still further. This behavior begins to appear at the larger times in Fig. 6.15.

6.4 RADIATIVE TRANSFER TABLES

6.4.1 Introduction

In a typical obscuration scenario, the basic task is to compute the total radiance, both direct and diffuse, reaching some hypothetical observer and emanating from the direction of some hypothetical target or background. The solution requires repeated application of the radiative transfer equation to account for scattering, absorption, and (thermal) emission by the obscuring medium along the various lines of sight defining the CCD scenario. In this section we present an extensive set of *radiation tables,* similar to those originally published by Van De Hulst,[62] that can be used to compute in-line multiple scattering from external sources (sun, sky, surface, etc.) that give rise to the diffuse radiance. In Section 6.3 we presented tables giving numerical examples showing the magnitude of forward scattering of radiation originating from the actual target that also contributes to the diffuse component. In this section, we consider the large area limit in which the obscuring medium is assumed to be of such horizontal extent that the plane parallel approximation is valid. Furthermore, this section presents methods for computing multiple scattering and (thermal) emission for wavelengths from the ultraviolet through the infrared.

6.4.2 Differential Form of the Radiative Transfer Equation

The rigorous mathematical expression for computing the total radiance incident at some observation point r and emanating from the direction of some target (or background) is the radiative transfer equation, written here in differential form following the notation of Chandrasekhar[63] as

$$-\frac{1}{\alpha C}\hat{\mathbf{r}} \cdot \nabla I(\lambda,\mathbf{r},\hat{s}) = I(\lambda,\mathbf{r},\hat{s}) - \frac{1}{4\pi}\int_{4\pi} P(\lambda;s,s')I(\lambda;\mathbf{r},s')\, d\Omega_s\, d\Omega_{s'}\ , \qquad (6.91)$$

where $I(\lambda,\mathbf{r},\hat{s})$ represents radiance of wavelength λ incident at a point r and propagating along a direction indicated by the unit vector $\hat{s}$. In Eq. (6.91), C is the obscurant mass concentration, α is the obscurant mass extinction coefficient, and $P(\lambda;s,s')$ is the obscurant phase function. Equation (6.91) is valid for any geometry, including inhomogeneous clouds, and for any obscurant that can be defined by a single mass extinction coefficient and phase function.

6.4.3 Integral Form of the Radiative Transfer Equation

It is often convenient to express Eq. (6.91) in integral form, particularly in computing in-line scattering. This is a straightforward task that yields the following expression for the direct and diffuse components of the radiation field:

$$I(\lambda,r;\mu,\phi) = \underbrace{I(\lambda,r_0;\mu,\phi)\exp[-(\tau-\tau_0)]}_{\text{direct}} + \underbrace{\int_0^{\tau} J(\lambda,r';\mu,\phi)\exp[-(\tau-\tau')]\,d\tau'}_{\text{diffuse}}\ , \tag{6.92}$$

where θ and ϕ are, respectively, the zenith and azimuth angles of the path of propagation; τ denotes optical thickness; and $J(\lambda,r;\theta,\phi)$ is the optical source function that accounts for in-line scattering from all directions and from all points along the path of propagation. In this discussion we regard the *target* as an opaque surface at position r_0, reflecting and/or emitting a known radiance $I(\lambda,r_0;\theta,\phi)$ in the direction of the *observer* located at point r. However, in the general case, r_0 could be any point along the path of propagation for which the radiance is known, independent of any physical surface.

The first term on the right side of Eq. (6.92) represents radiance transmitted directly from point r_0 to point r (the direct component), and the second represents contributions resulting from thermal emission and scattering of ambient radiation into the path of propagation at all points r' along the propagation path (the diffuse component).

6.4.4 Optical Source Function

Equation (6.92) is referred to as the formal solution to the radiative transfer equation and has been studied extensively. The term *formal solution* can be somewhat misleading because Eq. (6.92) does not actually represent a final solution to the problem. The major difficulty lies in the determination of the source function, which itself is a function of the entire (unknown) radiation field. That is, the source function, $J(\lambda,r';\mu,\phi)$ accounts both for (thermal) emission from the obscurant and radiation scattered into the line of sight from all directions including sun, sky, and (earth) surface. Formally, the source function is written as a contribution in two parts as:

$$J(\lambda,r';\mu,\phi) = \underbrace{\int_0^{\pi}\int_0^{2\pi} P(\theta,\phi;\theta',\phi')I(\lambda,r';\theta',\phi')\,d\theta'\,d\phi'}_{\text{scattering}} + \underbrace{J'(\lambda,r')}_{\text{emission}}\ , \tag{6.93}$$

where the first term on the right represents effects of multiple scattering and the second represents effects of thermal emission. We have made the assumption that the obscurant single-scattering albedo is implicit in the phase function; that is, the phase function is normalized such that the integration over all angles yields the value of ω_0.

6.4.5 Thermal Emission

In Eq. (6.93) we have included a term $J'(\lambda,r')$ to account for (thermal) emission by the obscurant from all points r' along the path of propagation. Strictly speaking, this term also includes any in-scattering of thermal band radiation originating from thermal emission by the obscurant. Under these circumstances, the most general form of the thermal source function is given by

$$J'(\lambda,r') = \frac{e(\lambda,r')}{\alpha(\lambda,r')} , \tag{6.94}$$

where $e(\lambda,r')$ is the spectral emittance of the medium and $\alpha(\lambda,r')$ is the obscurant mass extinction coefficient. Equation (6.94) is valid for any scenario, but it is difficult to apply because of the difficulty in determining $e(\lambda,r')$. Fortunately, in most cases, the condition of local thermal equilibrium applies, and Eq. (6.94) reduces to

$$\bar{J}'(\lambda,r') = \bar{J}(\lambda,r',t') = \alpha(1 - \bar{\omega}_0)B(\lambda,t') , \tag{6.95}$$

where α is the obscurant mass extinction coefficient, and $B(\lambda,t')$ is the well-known Planck, or blackbody, function. Note that in Eq. (6.95) we have added an overbar to denote the thermal equilibrium value and have added a notation to denote the dependence on the obscurant temperature t' that arises through the Planck function.

For infrared scenarios, one is often interested in a finite bandpass, and in these cases it is customary to define an effective thermal emission term over a finite bandpass $\Delta\lambda$ as

$$F(\Delta\lambda,t) = \frac{\int_{\Delta\lambda} \alpha(\lambda)[1 - \bar{\omega}_0(\lambda)]B(\lambda,t)\, d\lambda}{\int_0^\infty B(\lambda,t)\, d\lambda} , \tag{6.96}$$

in which case the emission term is written as

$$J'(\Delta\lambda,t) = F(\Delta\lambda,t)\frac{\sigma t^4}{\pi} , \tag{6.97}$$

where σ is the Stephan-Boltzmann constant. In the case where α and ω_0 are wavelength independent, the bandpass factor is simply proportional to the fractional blackbody radiance over the bandpass of interest. Some values of the fractional blackbody function appropriate for various window regions are listed in Table 6.15.

Table 6.15 Fractional Blackbody Irradiance as a Function of Absolute Temperature for Several Spectral Bandpasses

	Fraction in Bandpasses (μm)					w/m2
t(oC)	0-5	0-8	0-14	3-5	8-14	Total
-50	0.0011	0.0376	0.3012	0.0010	0.2636	140.6
-45	0.0013	0.0424	0.3168	0.0013	0.2744	153.6
-40	0.0016	0.0474	0.3322	0.0016	0.2848	167.5
-35	0.0024	0.0528	0.3475	0.0020	0.2947	182.4
-30	0.0024	0.0585	0.3626	0.0024	0.3041	198.2
-25	0.0029	0.0645	0.3775	0.0029	0.3130	215.0
-20	0.0024	0.0707	0.3921	0.0034	0.3214	232.8
-15	0.0041	0.0772	0.4065	0.0041	0.3293	251.8
-10	0.0048	0.0839	0.4206	0.0048	0.3366	271.9
-5	0.0056	0.0909	0.4344	0.0056	0.3435	293.1
0	0.0064	0.0982	0.4480	0.0064	0.3498	315.6
+5	0.0074	0.1056	0.4613	0.0074	0.3557	339.4
+10	0.0085	0.1132	0.4743	0.0085	0.3611	364.4
+15	0.0096	0.1211	0.4870	0.0096	0.3660	390.8
+20	0.0109	0.1291	0.4994	0.0108	0.3704	418.7
+25	0.0123	0.1372	0.5116	0.0122	0.3744	448.0
+30	0.0138	0.1455	0.5234	0.0137	0.3779	478.8
+35	0.154	0.1539	0.5350	0.0153	0.3811	511.2
+40	0.0171	0.1625	0.5463	0.0170	0.3838	545.2
+45	0.0190	0.1711	0.5572	0.0188	0.3861	580.9
+50	0.0210	0.1799	0.5680	0.0208	0.3881	618.2

6.4.6 Flux Integrals

Another often required radiative quantity in target acquisition applications is the downward-directed component of the net radiative flux density, or irradiance, obtained from appropriate angular integrations of Eq. (6.93) over the upper (sky) hemisphere. That is,

$$G\downarrow(z) = \int_0^{2\pi}\int_0^{\pi/2} \cos\theta' I(z;\theta',\phi') \sin\theta' \, d\theta' \, d\phi' \ , \tag{6.98}$$

where θ' and ϕ' again represent zenith and azimuth directions and z denotes height above the surface. In target acquisition applications, the surface irradiance serves as an estimate of the ambient radiation level. In other applications, the surface irradiance is sometimes referred to as the *global irradiance* or the total *hemispheric irradiance*. Note in Eq. (6.98) that the integration

includes all sources over the upper hemisphere, including, for example, the direct solar beam and scattered diffuse skylight for daytime scenarios.

6.4.7 Plane Parallel Approximation

To apply the theory of the previous paragraphs to computing obscuration quantities it is necessary to produce a workable solution to the radiative transfer equation for the particular scenario of interest. Rigorous solutions involving all orders of scattering are usually unattainable except for certain idealized geometries. The most widely studied geometry in radiative transfer applications is the plane parallel approximation in which we consider a horizontally uniform, but vertically stratified, obscuring medium of (near) infinite horizontal extent. This scenario represents a very good first approximation to large-area sources and indeed has its origin in the study of planetary atmospheres, including the earth.

6.4.8 Sign Convention for Upward and Downward Propagation

In the plane parallel approximation it is customary to introduce a notation in which the directions specifying propagating radiances are denoted by the arguments $-\mu$ (downward) and $+\mu$ (upward), where μ represents the absolute value of the zenith direction of the path of propagation ($\mu = |\cos\theta|$). This is a standard convention that avoids later confusion in writing the solutions to the radiative transfer equation. As a result, all radiances and irradiances are positive scalar quantities with associated directions indicated by either $\pm\mu$, or in some cases by the up and down arrows ($\uparrow$ $\downarrow$). It is also customary to refer to radiation propagated in the general upward direction as diffuse reflection and radiation propagated in the general downward direction as diffuse transmission. This convention originated in studies of solar scattering in which the solar beam was "transmitted" downward ($-\mu$) through an obscuring atmosphere or was "reflected" upward ($+\mu$).

6.4.9 Vertical Optical Depth

A major simplification afforded by the plane parallel approximation is that the optical thickness along any slant path is related to the vertical optical depth as (Fig. 6.16):

$$\tau(z, \pm\mu) = \frac{B(z)}{\mu} , \tag{6.99}$$

where, as before, μ ($\mu = |\cos\theta|$) represents the zenith direction of the path of propagation. The vertical optical depth B is defined over a vertical distance from some lower level z_0 to an upper level z as

$$B(z) = \alpha(\lambda)\int_{z_0}^{z} C(z')\, dz' , \tag{6.100}$$

where $C(z)$, as before, is the obscurant mass concentration and $\alpha(\lambda)$ is the obscurant mass extinction coefficient. In this section, we assume that the ob-

scurant optical properties, including the phase function, are constant over the extent of the obscuring medium.

6.4.10 Propagation Equations

With the vertical optical depth and sign convention established, it is then customary to substitute Eq. (6.99) into the integral form of the radiative transfer equation, Eq. (6.92). The results can then be rewritten as a set of three expressions for the three cases of generally upward $(+\mu)$ or generally downward $(-\mu)$ propagation through the entire layer, and a horizontal path of finite optical thickness τ at the bottom of the layer. That is,

upward propagation ($\mu > 0$)

$$I(0;+\mu,\phi) = I(B;+\mu,\phi)\exp[-(B/\mu)] + \int_0^B J(b;+\mu,\phi)\exp[-(b/\mu)]\,db/\mu \ , \tag{6.101a}$$

downward propagation ($\mu < 0$)

$$I(B;-\mu,\phi) = I(B;-\mu,\phi)\exp[-(B/\mu)] + \int_0^B J(b;-\mu,\phi) \times \exp\{-[(B-b)/\mu]\}\,db/\mu \ , \tag{6.101b}$$

horizontal propagation ($\mu = 0$)

$$I(r;0,\phi) = I(r_0;0,\phi)e^{-\tau} + J(b;0,\phi)(1-e^{-\tau}) \ , \tag{6.101c}$$

where b denotes vertical optical depth corresponding to some distance z into the layer referenced to zero at the top and B is the total vertical optical depth of the layer (Fig. 6.16). Here and throughout, we use the notation $I(0;\pm\mu,\phi)$ to denote radiance determined at the top of the screen ($b = 0$; $z = Z_0$) and $I(B;\pm\mu,\phi)$ to denote radiance determined at the bottom of the screen ($b = B$; $z = 0$).

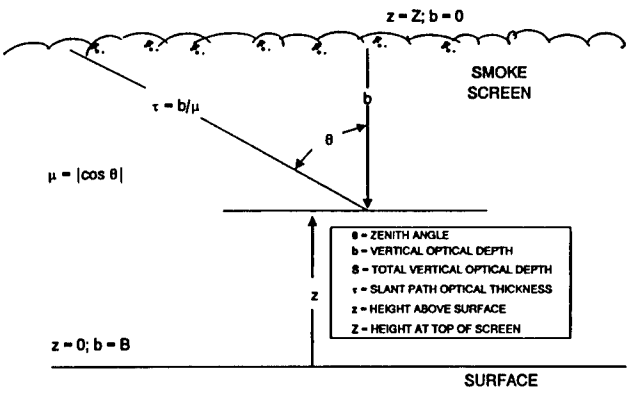

Fig. 6.16 Sketch demonstrating plane parallel geometry and notation.

The first term in each of Eqs. (6.101a) to (6.101c) represents the direct component, and the second term in each represents the diffuse component. It is understood that all terms in these expressions are dependent on the optical properties of the medium, which are generally wavelength dependent, although we have suppressed the notation to avoid cumbersome expressions.

6.4.11 Diffuse Transmission and Reflection Operators

At this point it is convenient to introduce the diffuse transmission and reflection operators, R and T, that are commonly used in the matrix formulation of the radiative transfer equation and that form the basis of the *radiative transfer tables* used later in this section. The full azimuth-dependent operators are defined, assuming an incoming point-parallel beam (e.g., the sun) incident from above, as

reflection:

$$I^*(B;+\mu,\phi) = R(B;\mu,\phi,\mu_0,\phi_0)\frac{\mu_0 F_0}{\pi} , \tag{6.102a}$$

transmission:

$$I^*(B;-\mu,\phi) = T(B;\mu,\phi,\mu_0,\phi_0)\frac{\mu_0 F_0}{\pi} , \tag{6.102b}$$

where F_0 represents the incident beam irradiance, B denotes the total vertical optical depth of the obscuring medium, μ_0 ($\mu_0 = |\cos\theta_0|$) denotes the zenith direction of the incoming beam, and μ ($\mu = |\cos\theta|$) denotes the zenith direction of the scattered beam. The reflection operator $R(B;\mu,\phi,\mu_0,\phi_0)$ represents the fraction of the incident beam that is diffusely reflected (upward) into the direction $(+\mu,\phi)$. Similarly, the transmission operator $T(B;\mu,\phi,\mu_0,\phi_0)$ represents the fraction of the incident beam that is diffusely transmitted (downward) into the direction $(-\mu,\phi)$. Note that in Eqs. (6.102a) and (6.102b) we use the superscript (*) to denote diffuse radiance, which is represented by the second term in Eq. (6.92). The direct term is easily computed using the simple Beer's law and requires no further elaboration.

6.4.12 Henyey-Greenstein Phase Function

In the formulation to follow we make the implicit assumption that the obscurant aerosols are spherical so that the phase function is a function only of the scattering angle. A particularly useful analytical function that approximates the phase function for spherical aerosols is the Henyey-Greenstein form:

$$P(\theta,\phi;\theta',\phi') = P(\Theta) = \frac{\omega_0(1-g)^2}{(1+g^2-2g\cos\Theta)^{3/2}} , \tag{6.103}$$

where ω_0 is the single-scattering albedo and Θ is the angle between the incident and scattered beam [i.e., the angle between the directions denoted by (θ,ϕ) and (θ',ϕ')]. The scattering angle can be computed from simple geometry as

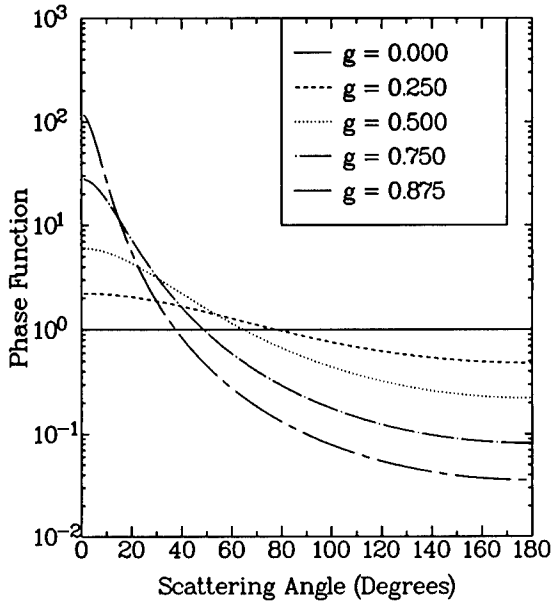

Fig. 6.17 Plots of the Henyey-Greenstein phase function for various values of the asymmetry parameter.

$$\cos\Theta = \cos\theta\cos\theta' + (1 - \cos^2\theta)^{1/2}(1 - \cos^2\theta')^{1/2}\cos(\phi - \phi') \ . \qquad (6.104)$$

The asymmetry parameter g determines the overall shape of the scattering phase function and can vary from near -1 for strong backscattering to near 0 for isotropic scattering and to near $+1$ for strong forward scattering. Typical values of g for visible wavelength obscurants range from 0.750 to 0.875, and for infrared obscurants g ranges from 0.0 to 0.50. Several plots of the Henyey-Greenstein function are given in Fig. 6.17.

6.4.13 Azimuth Averaging

In later applications, we will have occasion to use azimuth-averaged solutions to the radiative transfer equation. This is a standard procedure that is well documented elsewhere and amounts to performing an azimuth average over all quantities of interest. This greatly simplifies matters and helps to keep the sometimes cumbersome notation manageable. For example, the azimuth averaging for the phase function is performed simply as

$$P(\mu,\mu') = \frac{1}{2\pi}\int_0^{2\pi} P(\mu,\phi;\mu',\phi')\, d\phi' \ , \qquad (6.105)$$

which for the Henyey-Greenstein form is expressible in a series of Legendre polynomials as

$$P(\mu,\mu') = \sum_{n=0}^{\infty} \omega_n P_n(\mu) P_n(\mu') \ , \tag{6.106a}$$

$$\omega_n = (2n + 1)g^n \ , \tag{6.106b}$$

where $P_n(\mu)$ represents the Legendre polynomial of order n and g, as before, is the asymmetry parameter.

Similarly, the azimuth-averaged reflection and transmission operators are defined as

$$R(\mu,\mu') = \frac{1}{2\pi} \int_0^{2\pi} R(\mu,\phi;\mu',\phi') \, d\mu' \, d\phi' \ , \tag{6.107a}$$

$$T(\mu,\mu') = \frac{1}{2\pi} \int_0^{2\pi} T(\mu,\phi;\mu',\phi') \, d\mu' \, d\phi' \ . \tag{6.107b}$$

6.4.14 Higher Order Diffuse Transmission and Reflection Moments

The reflection and transmission operators, R and T, are also referred to as the zero-order moments and are applicable only to point-parallel sources, such as the solar beam. The concept can be carried further to define higher order moments applicable to hemispherical sources (sky and surface) and to flux integrals. The first-order moments are defined in terms of the zero-order moments simply as

$$UR(B;\mu) = 2 \int_0^1 \mu' R(B;\mu,\mu') \, d\mu' \ , \tag{6.108a}$$

$$UT(B;\mu) = 2 \int_0^1 \mu' T(B;\mu,\mu') \, d\mu' \ . \tag{6.108b}$$

Likewise the second-order moments are defined in terms of the first-order moments as

$$URU(B) = 2 \int_0^1 \mu' UR(B;\mu') \, d\mu' \ , \tag{6.109a}$$

$$UTU(B) = 2 \int_0^1 \mu' UT(B;\mu') \, d\mu' \ . \tag{6.109b}$$

Note that for the second-order moments, all angular dependence has been integrated out so that these quantities are dependent only on the optical depth B and, of course, the actual phase function used. Note also that for the first-order moments the dependence on μ' has been integrated out so that these quantities are dependent on only one angular coordinate, μ.

6.4.15 Use of the Diffuse Reflection and Transmission Operators

With the radiative transfer equation developed it is convenient to express Eq. (6.101) in terms of the transmission and reflection operators and moments. Furthermore, it is necessary in atmospheric applications to consider sources of ambient radiation from three major areas, namely the direct solar beam, diffuse skylight (assumed uniform), and (Lambertian) reflections/emissions from the underlying earth surface. This consideration then requires three terms for the source function and hence three terms in the propagation equations. Considering all factors, the propagation equations for the diffuse component are recast now in more convenient form as

Upward propagation:

$$I^*(+\mu) = \frac{\mu_0 F_0}{\pi} R(B;\mu,\mu_0) + \frac{D_0}{\pi} UR(B;\mu) + A_0 \frac{G_0}{\pi} UT(B;\mu) \ , \tag{6.110a}$$

Downward propagation:

$$I^*(-\mu) = \frac{\mu_0 F_0}{\pi} T(B;\mu,\mu_0) + \frac{D_0}{\pi} UT(B;\mu) + A_0 \frac{G_0}{\pi} UR(B;\mu) \ , \tag{6.110b}$$

Horizontal propagation:

$$I^*(\mu = 0) = (1 - e^{-\tau}) \left[\frac{\mu_0 F_0}{\pi} T(B;0,\mu_0) + \frac{D_0}{\pi} UT(B;0) + A_0 \frac{G_0}{\pi} UR(B;0) \right] , \tag{6.110c}$$

where μ ($\mu = |\cos\theta|$) denotes the zenith angle of the path of propagation, μ_0 ($\mu_0 = |\cos\theta_0|$) denotes the zenith angle of the solar beam, B is the total vertical optical depth defining the obscuring medium, A_0 is the surface albedo, F_0 is the solar beam normal irradiance, D_0 is the diffuse sky irradiance, and G_0 is the downward-directed hemispherical, or global, irradiance. The first two expressions apply to propagation through an entire plane parallel layer and the third applies to a horizontal path of optical thickness τ at the bottom of the layer. Some confusion may exist when comparing these expressions with other works because some authors include a factor of π into the definition of F_0, but this is not done here. The various transmission reflection operators are complicated functions depending on the form of the scattering phase function and extensive calculations are required to obtain numerical values. However, once the numerical values are determined, the implementation is straightforward using these equations.

6.4.16 Surface Irradiance

The surface irradiance G_0, which appears in Eqs. (6.110a) and (6.110b), is to be computed in the presence of the obscuring medium and is calculated in terms of the diffuse reflection/transmission first moments and second moments (*URU,UTU*) as[64]

$$G_0 = \frac{\mu_0 F_0 \exp(-B/\mu_0) + 2D_0 E_3(B) + \mu_0 F_0 UT(B;\mu_0)/\pi + D_0 UTU(B)/\pi}{1 - A_0 URU(B)/\pi} , \tag{6.111}$$

where $E_3(B)$ is the third-order exponential integral, which is defined and tabulated elsewhere.[65]

6.4.17 Radiative Transfer Tables

The major computational burden in applying the preceding formulation to practical problems lies in the determination of actual numerical values for the various operators and moments. Although several sophisticated mathematical methods have been developed over the years for calculating the various operators, there are no convenient analytical expressions available for computing the moments, even for the case of a Henyey-Greenstein phase function. The most practical solution for engineering estimates is numerical look-up tables similar to those published by Van de Hulst[62] and later extended for obscuration applications by Sutherland and Fowler.[66]

Numerical values of the second-order moments URU and UTU and the third-order exponential integral E_3 are listed in Table 6.16. Similarly, values for the various operators and first moments appropriate to the Henyey-Greenstein phase function are presented for the case of isotropic scattering ($g = 0.0$) in Tables 6.17 and 6.18, and for anisotropic scattering ($g = 0.875$) in Tables 6.19 and 6.20. There are two sets of tables, one accounting for single scattering (Tables 6.21 through 6.24) only and one accounting for all orders of scattering. Each subtable contains two sets of nine matrices, each matrix corresponding to a particular vertical optical depth ranging from 0.03125 to 8.0 and each set corresponding to either reflection or transmission. Each matrix contains 56 elements giving numerical values of the functions R, T, UR, and UT.

The general arrangement of the matrices is as follows. The upper 49 (7×7) matrix elements in each table give the numerical values of either the R or T operators for the seven discrete propagation angles from $\mu = 0.0$ (horizontal) to $\mu = 1.0$ (vertical) identifying the rows and columns. The last column in each matrix gives values of either $UR(\mu)$ or $UT(\mu)$ appropriate for the value of μ listed as the column headings. Note from the tables that the R and T operators are symmetrical, that is,

$$R(\mu_i,\mu_j) = R(\mu_j,\mu_i) , \tag{6.112a}$$

$$T(\mu_i,\mu_j) = T(\mu_j,\mu_i) , \tag{6.112b}$$

where μ_i,μ_j can represent either the direction of the incident beam (e.g., the sun) or the scattered beam (e.g., the target-observer path of propagation).

Table 6.16 Numerical values for the Diffuse Reflection/Transmission Second Moments and the exponential Integral; Subscript *s* Denotes Single-Scattering Component Only and Subscript *m* Denotes all Orders (i.e., Multiple Scattering)

	g = 0.000		g = 0.875		
B	URU_s	UTU_s	URU_s	UTU_s	E3
0.03125	0.02910	0.02910	0.00632	0.05200	0.47100
0.06250	0.05540	0.05510	0.01190	0.09980	0.44500
0.12500	0.10200	0.10000	0.02190	0.18100	0.39900
0.25000	0.18000	0.17100	0.03940	0.31200	0.32500
0.50000	0.29600	0.26100	0.06910	0.48900	0.22200
1.00000	0.44700	0.33400	0.11800	0.66500	0.11000
2.00000	0.61000	0.33000	0.19500	0.75100	0.03010
4.00000	0.74500	0.24000	0.30800	0.69800	0.00276
8.00000	0.85800	0.14100	0.45800	0.56500	$3.11*10^{-5}$
B	URU_s	UTU_s	URU_s	UTU_s	E3
0.03125	0.02710	0.02710	0.00500	0.04950	0.47100
0.06250	0.04901	0.04860	0.00830	0.09060	0.44500
0.12500	0.08290	0.08110	0.01260	0.15500	0.39900
0.25000	0.12700	0.11900	0.01720	0.23800	0.32500
0.50000	0.17000	0.14100	0.02080	0.30100	0.22200
1.00000	0.19700	0.11600	0.02260	0.27400	0.11000
2.00000	0.20400	0.05060	0.02310	0.13800	0.03010
4.00000	0.20500	0.00695	0.02310	0.02320	0.00276
8.00000	0.20500	$1.11*10^{-4}$	0.02310	$4.87*10^{-4}$	$3.11*10^{-5}$

6.4.18 Relative Contributions of Single and Multiple Scattering

The tables can be used to examine the relative contributions of single and multiple scattering. As an example, we consider an incident beam direction $\mu = 0.50$ and a scattered beam direction $\mu = 0.10$. Results using the appropriate look-up values corresponding to the particular row-column elements of interest (0.50, 0.10) are plotted in Fig. 6.18. The values for single scattering were taken directly from the tables. Multiple scattering results were obtained by subtracting the single scattering table value from the multiple scattering table value and are hence labeled "all others."

Results of the exercise are shown for both isotropic and anisotropic scattering for the particular values ($\mu,\mu' = 0.50, 0.10$). The results are qualitatively similar to all cases in that the single-scattering contribution dominates at the lower optical depths, and this fact is indeed the justification for using the much simpler single-scattering solutions for an optically thin medium. At the higher optical depths, however, it is clear that multiple scattering is dominant and cannot be discounted. For transmission, both the single and higher order contributions initially increase with increasing optical depth up to a maximum value. Above this maximum value, both decrease with increasing optical depth down to near zero at the upper limit of the plots. For reflection, both the single and higher order contributions initially increase with increasing optical depth and then level off, or saturate, at higher values, although the saturation point for the higher order contribution is beyond the range of the plots. Results similar to those shown in Fig. 6.18 for other cases can be obtained using the tables.

6.4.19 Effect of Aerosol Absorption

The tables as used here apply only to the case of conservative scattering for which $\omega_0 = 1$, indicative of zero absorption. Strictly, the inclusion of absorption requires either more tables and/or extensive recomputation. However, it turns out that, at least for the higher order moments, the effects can be reasonably approximated by assuming that most of the contribution caused by absorption occurs in first order and that the higher order corrections can be approximated by a monotonically decreasing power series in ω_0 for the various orders. This implies that the scaling to include the effects of absorption can be approximated, for example, as

$$X(\omega_0;\mu,\mu_0) = \omega_0 X_{ss}(1;\mu,\mu_0) + (\omega_0)^d[X_m(1;\mu,\mu_0) - X_s(1;\mu,\mu_0)] \ , \qquad (6.113)$$

where, in this case, X can denote any of the azimuth-independent operators (R, T, UR, UT, URU, and UTU). The first term on the right represents the single-scattering result, which can be obtained directly from the tables or Eq. (6.114) in Sec. 6.4.20 and is scaled by the single-scattering albedo. This in itself represents a rough first-order approximation to account for the albedo. In the second term, the subscripts refer to either multiple m or single s scattering and are obtained directly from the corresponding look-up tables. Defined as such, the second term within the brackets in Eq. (6.113) represents all higher orders of scattering (all except single scatter). The parameter d is an empirical factor that was found to give reasonable results with $d = B + 1$ for the higher order moments.[67]

Table 6.17 Multiple Scattering Reflection Operators for Isotropic Scattering (g = 0.000)

MULTIPLE SCATTERING: g = 0.0000 Reflection Table B = 0.03125

B=.0313	UI= .00	UI= .10	UI= .30	UI= .50	UI= .70	UI= .90	UI=1.00
UJ= .00	1.456E+2	2.625E+0	8.791E-1	5.279E-1	3.771E-1	2.934E-1	2.641E-1
UJ= .10	2.625E+0	6.224E-1	2.284E-1	1.398E-1	1.007E-1	7.868E-2	7.093E-2
UJ= .30	8.791E-1	2.284E-1	8.412E-2	5.150E-2	3.711E-2	2.901E-2	2.615E-2
UJ= .50	5.279E-1	1.398E-1	5.150E-2	3.154E-2	2.273E-2	1.776E-2	1.601E-2
UJ= .70	3.771E-1	1.007E-1	3.711E-2	2.273E-2	1.638E-2	1.280E-2	1.154E-2
UJ= .90	2.934E-1	7.868E-2	2.901E-2	1.776E-2	1.280E-2	1.001E-2	9.020E-3
UJ=1.00	2.641E-1	7.093E-2	2.615E-2	1.601E-2	1.154E-2	9.020E-3	8.132E-3
UR(U)	5.262E-1	1.345E-1	4.951E-2	3.031E-2	2.184E-2	1.707E-2	1.539E-2

Reflection Table B = 0.06250

B=.0625	UI= .00	UI= .10	UI= .30	UI= .50	UI= .70	UI= .90	UI=1.00
UJ= .00	1.456E+2	2.716E+0	9.199E-1	5.538E-1	3.961E-1	3.084E-1	2.776E-1
UJ= .10	2.716E+0	1.005E+0	3.992E-1	2.485E-1	1.803E-1	1.415E-1	1.278E-1
UJ= .30	9.199E-1	3.992E-1	1.605E-1	1.002E-1	7.279E-2	5.716E-2	5.161E-2
UJ= .50	5.538E-1	2.485E-1	1.002E-1	6.255E-2	4.546E-2	3.570E-2	3.224E-2
UJ= .70	3.961E-1	1.803E-1	7.279E-2	4.546E-2	3.304E-2	2.595E-2	2.343E-2
UJ= .90	3.084E-1	1.415E-1	5.716E-2	3.570E-2	2.595E-2	2.038E-2	1.840E-2
UJ=1.00	2.776E-1	1.278E-1	5.161E-2	3.224E-2	2.343E-2	1.840E-2	1.662E-2
UR(U)	5.501E-1	2.347E-1	9.434E-2	5.887E-2	4.277E-2	3.358E-2	3.032E-2

Reflection Table B = 0.12500

B=.1250	UI= .00	UI= .10	UI= .30	UI= .50	UI= .70	UI= .90	UI=1.00
UJ= .00	1.456E+2	2.808E+0	9.733E-1	5.897E-1	4.231E-1	3.299E-1	2.972E-1
UJ= .10	2.808E+0	1.391E+0	6.218E-1	3.981E-1	2.925E-1	2.312E-1	2.092E-1
UJ= .30	9.733E-1	6.218E-1	2.903E-1	1.875E-1	1.384E-1	1.096E-1	9.925E-2
UJ= .50	5.897E-1	3.981E-1	1.875E-1	1.214E-1	8.963E-2	7.102E-2	6.434E-2
UJ= .70	4.231E-1	2.925E-1	1.384E-1	8.963E-2	6.621E-2	5.247E-2	4.754E-2
UJ= .90	3.299E-1	2.312E-1	1.096E-1	7.102E-2	5.247E-2	4.159E-2	3.768E-2
UJ=1.00	2.972E-1	2.092E-1	9.925E-2	6.434E-2	4.754E-2	3.768E-2	3.414E-2
UR(U)	5.822E-1	3.682E-1	1.722E-1	1.113E-1	8.215E-2	6.507E-2	5.894E-2

Reflection Table B = 0.25000

B=.2500	UI= .00	UI= .10	UI= .30	UI= .50	UI= .70	UI= .90	UI=1.00
UJ= .00	1.457E+2	2.886E+0	1.043E+0	6.416E-1	4.639E-1	3.633E-1	3.278E-1
UJ= .10	2.886E+0	1.626E+0	8.284E-1	5.510E-1	4.122E-1	3.292E-1	2.991E-1
UJ= .30	1.043E+0	8.284E-1	4.757E-1	3.256E-1	2.467E-1	1.984E-1	1.807E-1
UJ= .50	6.416E-1	5.510E-1	3.256E-1	2.243E-1	1.705E-1	1.373E-1	1.252E-1
UJ= .70	4.639E-1	4.122E-1	2.467E-1	1.705E-1	1.297E-1	1.046E-1	9.532E-2
UJ= .90	3.633E-1	3.292E-1	1.984E-1	1.373E-1	1.046E-1	8.434E-2	7.689E-2
UJ=1.00	3.278E-1	2.991E-1	1.807E-1	1.252E-1	9.532E-2	7.689E-2	7.009E-2
UR(U)	6.272E-1	5.010E-1	2.921E-1	2.007E-1	1.523E-1	1.226E-1	1.117E-1

Reflection Table B = 0.50000

B=.5000	UI= .00	UI= .10	UI= .30	UI= .50	UI= .70	UI= .90	UI=1.00
UJ= .00	1.457E+2	2.940E+0	1.121E+0	7.106E-1	5.223E-1	4.135E-1	3.745E-1
UJ= .10	2.940E+0	1.722E+0	9.656E-1	6.708E-1	5.135E-1	4.158E-1	3.797E-1
UJ= .30	1.121E+0	9.656E-1	6.746E-1	5.003E-1	3.948E-1	3.254E-1	2.990E-1
UJ= .50	7.106E-1	6.708E-1	5.003E-1	3.784E-1	3.013E-1	2.496E-1	2.297E-1
UJ= .70	5.223E-1	5.135E-1	3.948E-1	3.013E-1	2.409E-1	2.000E-1	1.842E-1
UJ= .90	4.135E-1	4.158E-1	3.254E-1	2.496E-1	2.000E-1	1.663E-1	1.532E-1
UJ=1.00	3.745E-1	3.797E-1	2.990E-1	2.297E-1	1.842E-1	1.532E-1	1.413E-1
UR(U)	6.870E-1	6.049E-1	4.437E-1	3.344E-1	2.659E-1	2.201E-1	2.025E-1

Table 6.17 *(continued)*

MULTIPLE SCATTERING: g = 0.000 Reflection Table B = 1.00000

B=1.000	UI= .00	UI= .10	UI= .30	UI= .50	UI= .70	UI= .90	UI=1.00
UJ= .00	1.457E+2	2.984E+0	1.192E+0	7.877E-1	5.961E-1	4.816E-1	4.397E-1
UJ= .10	2.984E+0	1.779E+0	1.058E+0	7.718E-1	6.100E-1	5.049E-1	4.649E-1
UJ= .30	1.192E+0	1.058E+0	8.253E-1	6.641E-1	5.511E-1	4.694E-1	4.367E-1
UJ= .50	7.877E-1	7.718E-1	6.641E-1	5.569E-1	4.720E-1	4.071E-1	3.805E-1
UJ= .70	5.961E-1	6.100E-1	5.511E-1	4.720E-1	4.044E-1	3.511E-1	3.289E-1
UJ= .90	4.816E-1	5.049E-1	4.694E-1	4.071E-1	3.511E-1	3.060E-1	2.870E-1
UJ=1.00	4.397E-1	4.649E-1	4.367E-1	3.805E-1	3.289E-1	2.870E-1	2.694E-1
UR(U)	7.579E-1	6.977E-1	5.939E-1	4.984E-1	4.229E-1	3.651E-1	3.413E-1

Reflection Table B = 2.00000

B=2.000	UI= .00	UI= .10	UI= .30	UI= .50	UI= .70	UI= .90	UI=1.00
UJ= .00	1.458E+2	3.024E+0	1.249E+0	8.584E-1	6.734E-1	5.604E-1	5.181E-1
UJ= .10	3.024E+0	1.830E+0	1.130E+0	8.605E-1	7.070E-1	6.037E-1	5.632E-1
UJ= .30	1.249E+0	1.130E+0	9.252E-1	7.883E-1	6.867E-1	6.074E-1	5.740E-1
UJ= .50	8.584E-1	8.605E-1	7.883E-1	7.115E-1	6.408E-1	5.791E-1	5.516E-1
UJ= .70	6.734E-1	7.070E-1	6.867E-1	6.408E-1	5.890E-1	5.393E-1	5.162E-1
UJ= .90	5.604E-1	6.037E-1	6.074E-1	5.791E-1	5.393E-1	4.980E-1	4.782E-1
UJ=1.00	5.181E-1	5.632E-1	5.740E-1	5.516E-1	5.162E-1	4.782E-1	4.597E-1
UR(U)	8.306E-1	7.889E-1	7.215E-1	6.572E-1	5.965E-1	5.421E-1	5.175E-1

Reflection Table B = 4.00000

B=4.000	UI= .00	UI= .10	UI= .30	UI= .50	UI= .70	UI= .90	UI=1.00
UJ= .00	1.458E+2	3.058E+0	1.294E+0	9.143E-1	7.389E-1	6.332E-1	5.936E-1
UJ= .10	3.058E+0	1.873E+0	1.186E+0	9.302E-1	7.887E-1	6.945E-1	6.574E-1
UJ= .30	1.294E+0	1.186E+0	9.996E-1	8.806E-1	7.948E-1	7.276E-1	6.986E-1
UJ= .50	9.143E-1	9.302E-1	8.806E-1	8.258E-1	7.748E-1	7.280E-1	7.060E-1
UJ= .70	7.389E-1	7.887E-1	7.948E-1	7.748E-1	7.461E-1	7.138E-1	6.972E-1
UJ= .90	6.332E-1	6.945E-1	7.276E-1	7.280E-1	7.138E-1	6.920E-1	6.794E-1
UJ=1.00	5.936E-1	6.574E-1	6.986E-1	7.060E-1	6.972E-1	6.794E-1	6.685E-1
UR(U)	8.934E-1	8.671E-1	8.250E-1	7.855E-1	7.470E-1	7.093E-1	6.909E-1

Reflection Table B = 8.00000

B=8.000	UI= .00	UI= .10	UI= .30	UI= .50	UI= .70	UI= .90	UI=1.00
UJ= .00	1.458E+2	3.083E+0	1.326E+0	9.538E-1	7.855E-1	6.866E-1	6.504E-1
UJ= .10	3.083E+0	1.903E+0	1.226E+0	9.794E-1	8.468E-1	7.611E-1	7.281E-1
UJ= .30	1.326E+0	1.226E+0	1.052E+0	9.454E-1	8.713E-1	8.153E-1	7.917E-1
UJ= .50	9.538E-1	9.794E-1	9.454E-1	9.053E-1	8.686E-1	8.356E-1	8.201E-1
UJ= .70	7.855E-1	8.468E-1	8.713E-1	8.686E-1	8.568E-1	8.408E-1	8.319E-1
UJ= .90	6.866E-1	7.611E-1	8.153E-1	8.356E-1	8.408E-1	8.377E-1	8.340E-1
UJ=1.00	6.504E-1	7.281E-1	7.917E-1	8.201E-1	8.319E-1	8.340E-1	8.325E-1
UR(U)	9.386E-1	9.235E-1	8.993E-1	8.766E-1	8.545E-1	8.326E-1	8.218E-1

Table 6.18 Multiple Scattering Transmission Operators for Isotropic Scattering (g = 0.000)

MULTIPLE SCATTERING: g = 0.0000 Transmission Table B = 0.03125

B=.0313	UI= .00	UI= .10	UI= .30	UI= .50	UI= .70	UI= .90	UI=1.00
UJ= .00	5.207E-1	1.941E+0	7.945E-1	4.967E-1	3.611E-1	2.836E-1	2.561E-1
UJ= .10	1.941E+0	6.131E-1	2.273E-1	1.393E-1	1.005E-1	7.855E-2	7.082E-2
UJ= .30	7.945E-1	2.273E-1	8.397E-2	5.145E-2	3.708E-2	2.899E-2	2.614E-2
UJ= .50	4.967E-1	1.393E-1	5.145E-2	3.152E-2	2.272E-2	1.776E-2	1.601E-2
UJ= .70	3.611E-1	1.005E-1	3.708E-2	2.272E-2	1.637E-2	1.280E-2	1.154E-2
UJ= .90	2.836E-1	7.855E-2	2.899E-2	1.776E-2	1.280E-2	1.000E-2	9.019E-3
UJ=1.00	2.561E-1	7.082E-2	2.614E-2	1.601E-2	1.154E-2	9.019E-3	8.131E-3
UT(U)	4.645E-1	1.337E-1	4.940E-2	3.027E-2	2.182E-2	1.706E-2	1.538E-2

Transmission Table B = 0.06250

B=.0625	UI= .00	UI= .10	UI= .30	UI= .50	UI= .70	UI= .90	UI=1.00
UJ= .00	3.866E-1	1.541E+0	7.605E-1	4.940E-1	3.651E-1	2.894E-1	2.622E-1
UJ= .10	1.541E+0	9.490E-1	3.916E-1	2.456E-1	1.789E-1	1.406E-1	1.270E-1
UJ= .30	7.605E-1	3.916E-1	1.595E-1	9.980E-2	7.259E-2	5.703E-2	5.151E-2
UJ= .50	4.940E-1	2.456E-1	9.980E-2	6.241E-2	4.538E-2	3.565E-2	3.220E-2
UJ= .70	3.651E-1	1.789E-1	7.259E-2	4.538E-2	3.300E-2	2.592E-2	2.341E-2
UJ= .90	2.894E-1	1.406E-1	5.703E-2	3.565E-2	2.592E-2	2.036E-2	1.839E-2
UJ=1.00	2.622E-1	1.270E-1	5.151E-2	3.220E-2	2.341E-2	1.839E-2	1.661E-2
UT(U)	4.485E-1	2.300E-1	9.370E-2	5.863E-2	4.265E-2	3.351E-2	3.026E-2

Transmission Table B = 0.12500

B=.1250	UI= .00	UI= .10	UI= .30	UI= .50	UI= .70	UI= .90	UI=1.00
UJ= .00	2.603E-1	9.747E-1	6.805E-1	4.756E-1	3.629E-1	2.928E-1	2.669E-1
UJ= .10	9.747E-1	1.128E+0	5.790E-1	3.813E-1	2.837E-1	2.257E-1	2.048E-1
UJ= .30	6.805E-1	5.790E-1	2.833E-1	1.848E-1	1.369E-1	1.087E-1	9.853E-2
UJ= .50	4.756E-1	3.813E-1	1.848E-1	1.203E-1	8.907E-2	7.068E-2	6.406E-2
UJ= .70	3.629E-1	2.837E-1	1.369E-1	8.907E-2	6.591E-2	5.229E-2	4.739E-2
UJ= .90	2.928E-1	2.257E-1	1.087E-1	7.068E-2	5.229E-2	4.148E-2	3.759E-2
UJ=1.00	2.669E-1	2.048E-1	9.853E-2	6.406E-2	4.739E-2	3.759E-2	3.407E-2
UT(U)	4.180E-1	3.455E-1	1.685E-1	1.099E-1	8.139E-2	6.460E-2	5.856E-2

Transmission Table B = 0.25000

B=.2500	UI= .00	UI= .10	UI= .30	UI= .50	UI= .70	UI= .90	UI=1.00
UJ= .00	2.039E-1	4.609E-1	5.423E-1	4.324E-1	3.498E-1	2.917E-1	2.690E-1
UJ= .10	4.609E-1	8.294E-1	6.509E-1	4.764E-1	3.715E-1	3.036E-1	2.780E-1
UJ= .30	5.423E-1	6.509E-1	4.361E-1	3.089E-1	2.376E-1	1.927E-1	1.760E-1
UJ= .50	4.324E-1	4.764E-1	3.089E-1	2.173E-1	1.667E-1	1.349E-1	1.232E-1
UJ= .70	3.498E-1	3.715E-1	2.376E-1	1.667E-1	1.276E-1	1.033E-1	9.424E-2
UJ= .90	2.917E-1	3.036E-1	1.927E-1	1.349E-1	1.033E-1	8.351E-2	7.621E-2
UJ=1.00	2.690E-1	2.780E-1	1.760E-1	1.232E-1	9.424E-2	7.621E-2	6.953E-2
UT(U)	3.728E-1	4.169E-1	2.733E-1	1.928E-1	1.480E-1	1.199E-1	1.095E-1

Transmission Table B = 0.50000

B=.5000	UI= .00	UI= .10	UI= .30	UI= .50	UI= .70	UI= .90	UI=1.00
UJ= .00	1.534E-1	2.164E-1	3.626E-1	3.548E-1	3.170E-1	2.800E-1	2.637E-1
UJ= .10	2.164E-1	3.494E-1	4.942E-1	4.448E-1	3.822E-1	3.303E-1	3.086E-1
UJ= .30	3.626E-1	4.942E-1	5.077E-1	4.201E-1	3.482E-1	2.950E-1	2.737E-1
UJ= .50	3.548E-1	4.448E-1	4.201E-1	3.398E-1	2.788E-1	2.349E-1	2.175E-1
UJ= .70	3.170E-1	3.822E-1	3.482E-1	2.788E-1	2.278E-1	1.915E-1	1.772E-1
UJ= .90	2.800E-1	3.303E-1	2.950E-1	2.349E-1	1.915E-1	1.607E-1	1.486E-1
UJ=1.00	2.637E-1	3.086E-1	2.737E-1	2.175E-1	1.772E-1	1.486E-1	1.374E-1
UT(U)	3.129E-1	3.883E-1	3.675E-1	2.977E-1	2.446E-1	2.062E-1	1.910E-1

Table 6.18 *(continued)*

MULTIPLE SCATTERING: g = 0.0000 Transmission Table B = 1.00000

B=1.000	UI= .00	UI= .10	UI= .30	UI= .50	UI= .70	UI= .90	UI=1.00
UJ= .00	1.101E-1	1.391E-1	2.084E-1	2.502E-1	2.568E-1	2.483E-1	2.417E-1
UJ= .10	1.391E-1	1.775E-1	2.737E-1	3.186E-1	3.190E-1	3.032E-1	2.934E-1
UJ= .30	2.084E-1	2.737E-1	3.818E-1	4.019E-1	3.815E-1	3.515E-1	3.364E-1
UJ= .50	2.502E-1	3.186E-1	4.019E-1	4.014E-1	3.713E-1	3.371E-1	3.209E-1
UJ= .70	2.568E-1	3.190E-1	3.815E-1	3.713E-1	3.392E-1	3.058E-1	2.903E-1
UJ= .90	2.483E-1	3.032E-1	3.515E-1	3.371E-1	3.058E-1	2.744E-1	2.602E-1
UJ=1.00	2.417E-1	2.934E-1	3.364E-1	3.209E-1	2.903E-1	2.602E-1	2.465E-1
UT(U)	2.421E-1	3.023E-1	3.705E-1	3.663E-1	3.375E-1	3.057E-1	2.908E-1

Transmission Table B = 2.00000

B=2.000	UI= .00	UI= .10	UI= .30	UI= .50	UI= .70	UI= .90	UI=1.00
UJ= .00	7.421E-2	9.269E-2	1.239E-1	1.554E-1	1.789E-1	1.920E-1	1.954E-1
UJ= .10	9.269E-2	1.158E-1	1.554E-1	1.953E-1	2.235E-1	2.379E-1	2.413E-1
UJ= .30	1.239E-1	1.554E-1	2.117E-1	2.629E-1	2.937E-1	3.062E-1	3.077E-1
UJ= .50	1.554E-1	1.953E-1	2.629E-1	3.155E-1	3.421E-1	3.492E-1	3.481E-1
UJ= .70	1.789E-1	2.235E-1	2.937E-1	3.421E-1	3.629E-1	3.650E-1	3.619E-1
UJ= .90	1.920E-1	2.379E-1	3.062E-1	3.492E-1	3.650E-1	3.636E-1	3.592E-1
UJ=1.00	1.954E-1	2.413E-1	3.077E-1	3.481E-1	3.619E-1	3.592E-1	3.544E-1
UT(U)	1.694E-1	2.111E-1	2.772E-1	3.245E-1	3.460E-1	3.495E-1	3.471E-1

Transmission Table B = 4.00000

B=4.000	UI= .00	UI= .10	UI= .30	UI= .50	UI= .70	UI= .90	UI=1.00
UJ= .00	4.625E-2	5.764E-2	7.595E-2	9.325E-2	1.101E-1	1.256E-1	1.324E-1
UJ= .10	5.764E-2	7.185E-2	9.467E-2	1.163E-1	1.373E-1	1.564E-1	1.648E-1
UJ= .30	7.595E-2	9.467E-2	1.248E-1	1.535E-1	1.811E-1	2.056E-1	2.160E-1
UJ= .50	9.325E-2	1.163E-1	1.535E-1	1.888E-1	2.221E-1	2.505E-1	2.623E-1
UJ= .70	1.101E-1	1.373E-1	1.811E-1	2.221E-1	2.594E-1	2.900E-1	3.023E-1
UJ= .90	1.256E-1	1.564E-1	2.056E-1	2.505E-1	2.900E-1	3.213E-1	3.335E-1
UJ=1.00	1.324E-1	1.648E-1	2.160E-1	2.623E-1	3.023E-1	3.335E-1	3.456E-1
UT(U)	1.066E-1	1.329E-1	1.750E-1	2.141E-1	2.497E-1	2.789E-1	2.907E-1

Transmission Table B = 8.00000

B=8.000	UI= .00	UI= .10	UI= .30	UI= .50	UI= .70	UI= .90	UI=1.00
UJ= .00	2.658E-2	3.312E-2	4.362E-2	5.345E-2	6.305E-2	7.251E-2	7.719E-2
UJ= .10	3.312E-2	4.128E-2	5.436E-2	6.662E-2	7.857E-2	9.037E-2	9.620E-2
UJ= .30	4.362E-2	5.436E-2	7.158E-2	8.772E-2	1.035E-1	1.190E-1	1.267E-1
UJ= .50	5.345E-2	6.662E-2	8.772E-2	1.075E-1	1.268E-1	1.458E-1	1.552E-1
UJ= .70	6.305E-2	7.857E-2	1.035E-1	1.268E-1	1.496E-1	1.719E-1	1.829E-1
UJ= .90	7.251E-2	9.037E-2	1.190E-1	1.458E-1	1.719E-1	1.975E-1	2.100E-1
UJ=1.00	7.719E-2	9.620E-2	1.267E-1	1.552E-1	1.829E-1	2.100E-1	2.232E-1
UT(U)	6.133E-2	7.643E-2	1.006E-1	1.233E-1	1.455E-1	1.672E-1	1.778E-1

Table 6.19 Multiple Scattering Reflection Operators for Anisotropic Scattering (g = 0.875)

MULTIPLE SCATTERING: g = 0.8750 Reflection Table B = 0.03125

B=.0313	UI= .00	UI= .10	UI= .30	UI= .50	UI= .70	UI= .90	UI=1.00
UJ= .00	6.642E+2	1.002E+1	5.990E-1	2.975E-1	4.905E-2	-9.547E-4	-7.757E-2
UJ= .10	1.002E+1	1.332E+0	1.508E-1	3.465E-2	2.846E-2	1.695E-2	3.012E-2
UJ= .30	5.990E-1	1.508E-1	2.054E-2	1.360E-2	5.314E-4	-9.502E-4	-8.057E-3
UJ= .50	2.975E-1	3.465E-2	1.360E-2	2.782E-4	4.185E-3	3.483E-3	7.866E-3
UJ= .70	4.905E-2	2.846E-2	5.314E-4	4.185E-3	-2.485E-4	-9.162E-4	-3.973E-3
UJ= .90	-9.547E-4	1.695E-2	-9.502E-4	3.483E-3	-9.162E-4	-1.332E-3	-4.819E-3
UJ=1.00	-7.757E-2	3.012E-2	-8.057E-3	7.866E-3	-3.973E-3	-4.819E-3	-1.498E-2
UR(U)	5.546E-1	8.280E-2	1.231E-2	4.217E-3	2.184E-3	1.262E-3	1.195E-3

Reflection Table B = 0.06250

B=.0625	UI= .00	UI= .10	UI= .30	UI= .50	UI= .70	UI= .90	UI=1.00
UJ= .00	6.645E+2	1.049E+1	6.574E-1	3.165E-1	5.757E-2	3.192E-3	-7.334E-2
UJ= .10	1.049E+1	2.376E+0	2.955E-1	7.275E-2	5.337E-2	3.109E-2	5.246E-2
UJ= .30	6.574E-1	2.955E-1	4.485E-2	2.751E-2	1.920E-3	-1.323E-3	-1.483E-2
UJ= .50	3.165E-1	7.275E-2	2.751E-2	1.369E-3	8.290E-3	6.813E-3	1.513E-2
UJ= .70	5.757E-2	5.337E-2	1.920E-3	8.290E-3	-3.458E-4	-1.697E-3	-7.635E-3
UJ= .90	3.192E-3	3.109E-2	-1.323E-3	6.813E-3	-1.697E-3	-2.540E-3	-9.318E-3
UJ=1.00	-7.334E-2	5.246E-2	-1.483E-2	1.513E-2	-7.635E-3	-9.318E-3	-2.907E-2
UR(U)	5.838E-1	1.497E-1	2.474E-2	8.578E-3	4.358E-3	2.506E-3	2.292E-3

Reflection Table B = 0.12500

B=.1250	UI= .00	UI= .10	UI= .30	UI= .50	UI= .70	UI= .90	UI=1.00
UJ= .00	6.646E+2	1.091E+1	7.378E-1	3.410E-1	6.995E-2	9.873E-3	-6.533E-2
UJ= .10	1.091E+1	3.656E+0	5.395E-1	1.427E-1	9.359E-2	5.337E-2	8.401E-2
UJ= .30	7.378E-1	5.395E-1	1.006E-1	5.567E-2	6.755E-3	-6.200E-4	-2.504E-2
UJ= .50	3.410E-1	1.427E-1	5.567E-2	5.404E-3	1.628E-2	1.309E-2	2.818E-2
UJ= .70	6.995E-2	9.359E-2	6.755E-3	1.628E-2	-1.181E-4	-2.878E-3	-1.408E-2
UJ= .90	9.873E-3	5.337E-2	-6.200E-4	1.309E-2	-2.878E-3	-4.606E-3	-1.743E-2
UJ=1.00	-6.533E-2	8.401E-2	-2.504E-2	2.818E-2	-1.408E-2	-1.743E-2	-5.483E-2
UR(U)	6.166E-1	2.480E-1	4.939E-2	1.756E-2	8.728E-3	4.988E-3	4.351E-3

Reflection Table B = 0.25000

B=.2500	UI= .00	UI= .10	UI= .30	UI= .50	UI= .70	UI= .90	UI=1.00
UJ= .00	6.647E+2	1.120E+1	8.396E-1	3.737E-1	8.702E-2	1.952E-2	-5.400E-2
UJ= .10	1.120E+1	4.611E+0	8.571E-1	2.443E-1	1.470E-1	8.278E-2	1.204E-1
UJ= .30	8.396E-1	8.571E-1	2.227E-1	1.117E-1	2.209E-2	4.955E-3	-3.551E-2
UJ= .50	3.737E-1	2.443E-1	1.117E-1	1.888E-2	3.161E-2	2.447E-2	4.961E-2
UJ= .70	8.702E-2	1.470E-1	2.209E-2	3.161E-2	1.830E-3	-3.899E-3	-2.388E-2
UJ= .90	1.952E-2	8.278E-2	4.955E-3	2.447E-2	-3.899E-3	-7.510E-3	-3.053E-2
UJ=1.00	-5.400E-2	1.204E-1	-3.551E-2	4.961E-2	-2.388E-2	-3.053E-2	-9.780E-2
UR(U)	6.522E-1	3.602E-1	9.618E-2	3.601E-2	1.766E-2	1.003E-2	8.315E-3

Reflection Table B = 0.50000

B=.5000	UI= .00	UI= .10	UI= .30	UI= .50	UI= .70	UI= .90	UI=1.00
UJ= .00	6.647E+2	1.134E+1	9.478E-1	4.170E-1	1.093E-1	3.211E-2	-4.137E-2
UJ= .10	1.134E+1	5.000E+0	1.138E+0	3.549E-1	2.035E-1	1.142E-1	1.530E-1
UJ= .30	9.478E-1	1.138E+0	4.406E-1	2.153E-1	6.266E-2	2.433E-2	-3.485E-2
UJ= .50	4.170E-1	3.549E-1	2.153E-1	5.834E-2	6.116E-2	4.457E-2	8.045E-2
UJ= .70	1.093E-1	2.035E-1	6.266E-2	6.116E-2	1.038E-2	-1.783E-3	-3.417E-2
UJ= .90	3.211E-2	1.142E-1	2.433E-2	4.457E-2	-1.783E-3	-9.494E-3	-4.718E-2
UJ=1.00	-4.137E-2	1.530E-1	-3.485E-2	8.045E-2	-3.417E-2	-4.718E-2	-1.574E-1
UR(U)	6.895E-1	4.563E-1	1.755E-1	7.295E-2	3.627E-2	2.061E-2	1.647E-2

Table 6.19 *(continued)*

MULTIPLE SCATTERING: g = 0.8750 Reflection Table B = 1.00000

B=1.000	UI= .00	UI= .10	UI= .30	UI= .50	UI= .70	UI= .90	UI=1.00
UJ= .00	6.648E+2	1.141E+1	1.037E+0	4.693E-1	1.379E-1	4.855E-2	-2.767E-2
UJ= .10	1.141E+1	5.135E+0	1.324E+0	4.613E-1	2.614E-1	1.472E-1	1.807E-1
UJ= .30	1.037E+0	1.324E+0	6.970E-1	3.712E-1	1.427E-1	6.809E-2	-8.438E-3
UJ= .50	4.693E-1	4.613E-1	3.712E-1	1.509E-1	1.193E-1	8.106E-2	1.206E-1
UJ= .70	1.379E-1	2.614E-1	1.427E-1	1.193E-1	3.886E-2	1.273E-2	-3.332E-2
UJ= .90	4.855E-2	1.472E-1	6.809E-2	8.106E-2	1.273E-2	-3.813E-3	-5.753E-2
UJ=1.00	-2.767E-2	1.807E-1	-8.438E-3	1.206E-1	-3.332E-2	-5.753E-2	-2.133E-1
UR(U)	7.270E-1	5.327E-1	2.843E-1	1.414E-1	7.495E-2	4.340E-2	3.431E-2

Reflection Table B = 2.00000

B=2.000	UI= .00	UI= .10	UI= .30	UI= .50	UI= .70	UI= .90	UI=1.00
UJ= .00	6.648E+2	1.144E+1	1.098E+0	5.236E-1	1.749E-1	7.207E-2	-8.776E-3
UJ= .10	1.144E+1	5.201E+0	1.434E+0	5.604E-1	3.286E-1	1.897E-1	2.147E-1
UJ= .30	1.098E+0	1.434E+0	8.804E-1	5.361E-1	2.535E-1	1.377E-1	4.551E-2
UJ= .50	5.236E-1	5.604E-1	5.361E-1	3.014E-1	2.248E-1	1.497E-1	1.795E-1
UJ= .70	1.749E-1	3.286E-1	2.535E-1	2.248E-1	1.119E-1	5.962E-2	1.476E-4
UJ= .90	7.207E-2	1.897E-1	1.377E-1	1.497E-1	5.962E-2	2.592E-2	-4.094E-2
UJ=1.00	-8.776E-3	2.147E-1	4.551E-2	1.795E-1	1.476E-4	-4.094E-2	-2.260E-1
UR(U)	7.652E-1	6.023E-1	3.997E-1	2.484E-1	1.499E-1	9.219E-2	7.371E-2

Reflection Table B = 4.00000

B=4.000	UI= .00	UI= .10	UI= .30	UI= .50	UI= .70	UI= .90	UI=1.00
UJ= .00	6.648E+2	1.147E+1	1.138E+0	5.718E-1	2.191E-1	1.067E-1	2.091E-2
UJ= .10	1.147E+1	5.245E+0	1.504E+0	6.439E-1	4.051E-1	2.495E-1	2.659E-1
UJ= .30	1.138E+0	1.504E+0	9.915E-1	6.683E-1	3.744E-1	2.319E-1	1.260E-1
UJ= .50	5.718E-1	6.439E-1	6.683E-1	4.591E-1	3.698E-1	2.633E-1	2.772E-1
UJ= .70	2.191E-1	4.051E-1	3.744E-1	3.698E-1	2.466E-1	1.662E-1	9.150E-2
UJ= .90	1.067E-1	2.495E-1	2.319E-1	2.633E-1	1.662E-1	1.112E-1	3.178E-2
UJ=1.00	2.091E-2	2.659E-1	1.260E-1	2.772E-1	9.150E-2	3.178E-2	-1.676E-1
UR(U)	8.054E-1	6.719E-1	5.097E-1	3.802E-1	2.722E-1	1.891E-1	1.572E-1

Reflection Table B = 8.00000

B=8.000	UI= .00	UI= .10	UI= .30	UI= .50	UI= .70	UI= .90	UI=1.00
UJ= .00	6.648E+2	1.149E+1	1.171E+0	6.137E-1	2.661E-1	1.535E-1	6.573E-2
UJ= .10	1.149E+1	5.283E+0	1.560E+0	7.149E-1	4.848E-1	3.288E-1	3.419E-1
UJ= .30	1.171E+0	1.560E+0	1.076E+0	7.757E-1	4.950E-1	3.518E-1	2.408E-1
UJ= .50	6.137E-1	7.149E-1	7.757E-1	5.950E-1	5.223E-1	4.149E-1	4.224E-1
UJ= .70	2.661E-1	4.848E-1	4.950E-1	5.223E-1	4.180E-1	3.371E-1	2.554E-1
UJ= .90	1.535E-1	3.288E-1	3.518E-1	4.149E-1	3.371E-1	2.824E-1	1.963E-1
UJ=1.00	6.573E-2	3.419E-1	2.408E-1	4.224E-1	2.554E-1	1.963E-1	-9.217E-3
UR(U)	8.487E-1	7.452E-1	6.206E-1	5.205E-1	4.300E-1	3.466E-1	3.083E-1

Table 6.20 Multiple Scattering Transmission Operators for Anisotropic Scattering (g = 0.875)

MULTIPLE SCATTERING: g = 0.8750 Transmission Table B = 0.03125

B=.0313	UI= .00	UI= .10	UI= .30	UI= .50	UI= .70	UI= .90	UI=1.00
UJ= .00	3.778E+0	8.044E+0	6.629E-1	3.113E-1	4.822E-2	-2.645E-3	-8.762E-2
UJ= .10	8.044E+0	3.025E+0	4.110E-1	9.270E-2	1.451E-2	3.392E-3	-1.918E-2
UJ= .30	6.629E-1	4.110E-1	3.898E-1	8.073E-2	2.376E-2	9.413E-3	1.320E-2
UJ= .50	3.113E-1	9.270E-2	8.073E-2	1.577E-1	3.001E-2	7.309E-3	2.164E-3
UJ= .70	4.822E-2	1.451E-2	2.376E-2	3.001E-2	9.729E-2	1.054E-2	-2.430E-3
UJ= .90	-2.645E-3	3.392E-3	9.413E-3	7.309E-3	1.054E-2	9.969E-2	2.186E-2
UJ=1.00	-8.762E-2	-1.918E-2	1.320E-2	2.164E-3	-2.430E-3	2.186E-2	5.760E-1
UT(U)	4.362E-1	1.853E-1	8.660E-2	5.637E-2	4.148E-2	3.286E-2	2.957E-2

Transmission Table B = 0.06250

B=.0625	UI= .00	UI= .10	UI= .30	UI= .50	UI= .70	UI= .90	UI=1.00
UJ= .00	2.552E+0	6.892E+0	7.623E-1	3.390E-1	5.780E-2	1.392E-3	-8.819E-2
UJ= .10	6.892E+0	4.898E+0	7.510E-1	1.765E-1	3.056E-2	8.013E-3	-3.299E-2
UJ= .30	7.623E-1	7.510E-1	7.300E-1	1.572E-1	4.667E-2	1.854E-2	2.530E-2
UJ= .50	3.390E-1	1.765E-1	1.572E-1	3.028E-1	5.921E-2	1.462E-2	4.451E-3
UJ= .70	5.780E-2	3.056E-2	4.667E-2	5.921E-2	1.888E-1	2.120E-2	-4.225E-3
UJ= .90	1.392E-3	8.013E-3	1.854E-2	1.462E-2	2.120E-2	1.947E-1	4.353E-2
UJ=1.00	-8.819E-2	-3.299E-2	2.530E-2	4.451E-3	-4.225E-3	4.353E-2	1.124E+0
UT(U)	4.148E-1	3.149E-1	1.633E-1	1.089E-1	8.106E-2	6.458E-2	5.830E-2

Transmission Table B = 0.12500

B=.1250	UI= .00	UI= .10	UI= .30	UI= .50	UI= .70	UI= .90	UI=1.00
UJ= .00	1.403E+0	4.831E+0	8.832E-1	3.729E-1	7.519E-2	1.033E-2	-8.174E-2
UJ= .10	4.831E+0	6.266E+0	1.244E+0	3.120E-1	6.358E-2	1.969E-2	-4.644E-2
UJ= .30	8.832E-1	1.244E+0	1.281E+0	2.973E-1	9.007E-2	3.605E-2	4.685E-2
UJ= .50	3.729E-1	3.120E-1	2.973E-1	5.579E-1	1.152E-1	2.924E-2	9.522E-3
UJ= .70	7.519E-2	6.358E-2	9.007E-2	1.152E-1	3.556E-1	4.285E-2	-6.052E-3
UJ= .90	1.033E-2	1.969E-2	3.605E-2	2.924E-2	4.285E-2	3.714E-1	8.626E-2
UJ=1.00	-8.174E-2	-4.644E-2	4.685E-2	9.522E-3	-6.052E-3	8.626E-2	2.138E+0
UT(U)	3.836E-1	4.657E-1	2.913E-1	2.036E-1	1.548E-1	1.247E-1	1.132E-1

Transmission Table B = 0.25000

B=.2500	UI= .00	UI= .10	UI= .30	UI= .50	UI= .70	UI= .90	UI=1.00
UJ= .00	7.816E-1	2.455E+0	9.690E-1	4.101E-1	1.054E-1	2.776E-2	-6.183E-2
UJ= .10	2.455E+0	5.146E+0	1.712E+0	4.852E-1	1.248E-1	4.634E-2	-4.060E-2
UJ= .30	9.690E-1	1.712E+0	1.976E+0	5.298E-1	1.680E-1	6.841E-2	8.168E-2
UJ= .50	4.101E-1	4.852E-1	5.298E-1	9.489E-1	2.179E-1	5.847E-2	2.168E-2
UJ= .70	1.054E-1	1.248E-1	1.680E-1	2.179E-1	6.319E-1	8.687E-2	-3.612E-3
UJ= .90	2.776E-2	4.634E-2	6.841E-2	5.847E-2	8.687E-2	6.764E-1	1.690E-1
UJ=1.00	-6.183E-2	-4.060E-2	8.168E-2	2.168E-2	-3.612E-3	1.690E-1	3.872E+0
UT(U)	3.477E-1	5.577E-1	4.692E-1	3.575E-1	2.827E-1	2.325E-1	2.129E-1

Transmission Table B = 0.50000

B=.5000	UI= .00	UI= .10	UI= .30	UI= .50	UI= .70	UI= .90	UI=1.00
UJ= .00	3.956E-1	9.362E-1	8.947E-1	4.384E-1	1.517E-1	5.722E-2	-2.273E-2
UJ= .10	9.362E-1	2.250E+0	1.740E+0	6.394E-1	2.189E-1	9.479E-2	5.961E-3
UJ= .30	8.947E-1	1.740E+0	2.392E+0	8.377E-1	2.938E-1	1.244E-1	1.297E-1
UJ= .50	4.384E-1	6.394E-1	8.377E-1	1.388E+0	3.886E-1	1.162E-1	5.241E-2
UJ= .70	1.517E-1	2.189E-1	2.938E-1	3.886E-1	1.004E+0	1.748E-1	1.946E-2
UJ= .90	5.722E-2	9.479E-2	1.244E-1	1.162E-1	1.748E-1	1.126E+0	3.228E-1
UJ=1.00	-2.273E-2	5.961E-3	1.297E-1	5.241E-2	1.946E-2	3.228E-1	6.358E+0
UT(U)	3.105E-1	5.369E-1	6.356E-1	5.592E-1	4.742E-1	4.056E-1	3.770E-1

Table 6.20 *(continued)*

MULTIPLE SCATTERING: g = 0.8750 Transmission Table B = 1.00000

B=1.000	UI= .00	UI= .10	UI= .30	UI= .50	UI= .70	UI= .90	UI=1.00
UJ= .00	1.976E-1	3.835E-1	6.072E-1	4.251E-1	2.064E-1	9.937E-2	3.444E-2
UJ= .10	3.835E-1	7.672E-1	1.174E+0	6.972E-1	3.282E-1	1.633E-1	8.493E-2
UJ= .30	6.072E-1	1.174E+0	1.920E+0	1.054E+0	4.573E-1	2.117E-1	1.859E-1
UJ= .50	4.251E-1	6.972E-1	1.054E+0	1.562E+0	6.145E-1	2.235E-1	1.259E-1
UJ= .70	2.064E-1	3.282E-1	4.573E-1	6.145E-1	1.302E+0	3.349E-1	1.048E-1
UJ= .90	9.937E-2	1.633E-1	2.117E-1	2.235E-1	3.349E-1	1.583E+0	5.798E-1
UJ=1.00	3.444E-2	8.493E-2	1.859E-1	1.259E-1	1.048E-1	5.798E-1	8.622E+0
UT(U)	2.730E-1	4.672E-1	6.800E-1	7.232E-1	6.854E-1	6.274E-1	5.978E-1

Transmission Table B = 2.00000

B=2.000	UI= .00	UI= .10	UI= .30	UI= .50	UI= .70	UI= .90	UI=1.00
UJ= .00	1.072E-1	1.908E-1	3.158E-1	3.346E-1	2.401E-1	1.484E-1	1.007E-1
UJ= .10	1.908E-1	3.422E-1	5.719E-1	5.773E-1	3.991E-1	2.432E-1	1.756E-1
UJ= .30	3.158E-1	5.719E-1	9.682E-1	9.189E-1	5.831E-1	3.295E-1	2.610E-1
UJ= .50	3.346E-1	5.773E-1	9.189E-1	1.218E+0	7.758E-1	3.885E-1	2.666E-1
UJ= .70	2.401E-1	3.991E-1	5.831E-1	7.758E-1	1.237E+0	5.575E-1	3.027E-1
UJ= .90	1.484E-1	2.432E-1	3.295E-1	3.885E-1	5.575E-1	1.674E+0	9.069E-1
UJ=1.00	1.007E-1	1.756E-1	2.610E-1	2.666E-1	3.027E-1	9.069E-1	8.154E+0
UT(U)	2.348E-1	3.977E-1	5.990E-1	7.333E-1	7.927E-1	7.994E-1	7.909E-1

Transmission Table B = 4.00000

B=4.000	UI= .00	UI= .10	UI= .30	UI= .50	UI= .70	UI= .90	UI=1.00
UJ= .00	6.459E-2	1.106E-1	1.709E-1	2.141E-1	2.178E-1	1.832E-1	1.577E-1
UJ= .10	1.106E-1	1.896E-1	2.940E-1	3.672E-1	3.679E-1	3.039E-1	2.613E-1
UJ= .30	1.709E-1	2.940E-1	4.592E-1	5.696E-1	5.520E-1	4.355E-1	3.702E-1
UJ= .50	2.141E-1	3.672E-1	5.696E-1	7.245E-1	7.105E-1	5.412E-1	4.455E-1
UJ= .70	2.178E-1	3.679E-1	5.520E-1	7.105E-1	8.822E-1	7.095E-1	5.574E-1
UJ= .90	1.832E-1	3.039E-1	4.355E-1	5.412E-1	7.095E-1	1.250E+0	1.079E+0
UJ=1.00	1.577E-1	2.613E-1	3.702E-1	4.455E-1	5.574E-1	1.079E+0	4.240E+0
UT(U)	1.946E-1	3.281E-1	4.903E-1	6.194E-1	7.244E-1	7.992E-1	8.244E-1

Transmission Table B = 8.00000

B=8.000	UI= .00	UI= .10	UI= .30	UI= .50	UI= .70	UI= .90	UI=1.00
UJ= .00	4.305E-2	7.267E-2	1.089E-1	1.378E-1	1.610E-1	1.731E-1	1.730E-1
UJ= .10	7.267E-2	1.227E-1	1.839E-1	2.329E-1	2.716E-1	2.905E-1	2.894E-1
UJ= .30	1.089E-1	1.839E-1	2.759E-1	3.495E-1	4.061E-1	4.295E-1	4.244E-1
UJ= .50	1.378E-1	2.329E-1	3.495E-1	4.428E-1	5.144E-1	5.414E-1	5.319E-1
UJ= .70	1.610E-1	2.716E-1	4.061E-1	5.144E-1	6.070E-1	6.566E-1	6.501E-1
UJ= .90	1.731E-1	2.905E-1	4.295E-1	5.414E-1	6.566E-1	8.175E-1	8.829E-1
UJ=1.00	1.730E-1	2.894E-1	4.244E-1	5.319E-1	6.501E-1	8.829E-1	1.330E+0
UT(U)	1.513E-1	2.547E-1	3.794E-1	4.795E-1	5.699E-1	6.532E-1	6.913E-1

Table 6.21 Single-Scattering Reflection Operators for Isotropic Scattering ($g = 0.000$)

SINGLE SCATTERING: g = 0.0000 Reflection Table B = 0.03125

μ	.00	.10	.30	.50	.70	.90	1.00
.00	0.00E+00	2.50E+00	8.33E-01	5.00E-01	3.57E-01	2.78E-01	2.50E-01
.10	2.50E+00	5.81E-01	2.13E-01	1.30E-01	9.39E-02	7.33E-02	6.61E-02
.30	8.33E-01	2.13E-01	7.84E-02	4.80E-02	3.46E-02	2.70E-02	2.44E-02
.50	5.00E-01	1.30E-01	4.80E-02	2.94E-02	2.12E-02	1.65E-02	1.49E-02
.70	3.57E-01	9.39E-02	3.46E-02	2.12E-02	1.53E-02	1.19E-02	1.07E-02
.90	2.78E-01	7.33E-02	2.70E-02	1.65E-02	1.19E-02	9.32E-03	8.40E-03
1.00	2.50E-01	6.61E-02	2.44E-02	1.49E-02	1.07E-02	8.40E-03	7.57E-03
UR	0.00E+00	1.25E-01	4.61E-02	2.82E-02	2.03E-02	1.59E-02	1.43E-02

Reflection Table B = 0.06250

μ	.00	.10	.30	.50	.70	.90	1.00
.00	0.00E+00	2.50E+00	8.33E-01	5.00E-01	3.57E-01	2.78E-01	2.50E-01
.10	2.50E+00	8.92E-01	3.53E-01	2.20E-01	1.60E-01	1.25E-01	1.13E-01
.30	8.33E-01	3.53E-01	1.42E-01	8.86E-02	6.44E-02	5.05E-02	4.56E-02
.50	5.00E-01	2.20E-01	8.86E-02	5.53E-02	4.02E-02	3.16E-02	2.85E-02
.70	3.57E-01	1.60E-01	6.44E-02	4.02E-02	2.92E-02	2.29E-02	2.07E-02
.90	2.78E-01	1.25E-01	5.05E-02	3.16E-02	2.29E-02	1.80E-02	1.63E-02
1.00	2.50E-01	1.13E-01	4.56E-02	2.85E-02	2.07E-02	1.63E-02	1.47E-02
UR	0.00E+00	2.08E-01	8.34E-02	5.20E-02	3.78E-02	2.97E-02	2.68E-02

Reflection Table B = 0.12500

μ	.00	.10	.30	.50	.70	.90	1.00
.00	0.00E+00	2.50E+00	8.33E-01	5.00E-01	3.57E-01	2.78E-01	2.50E-01
.10	2.50E+00	1.15E+00	5.07E-01	3.24E-01	2.38E-01	1.88E-01	1.70E-01
.30	8.33E-01	5.07E-01	2.36E-01	1.52E-01	1.12E-01	8.88E-02	8.04E-02
.50	5.00E-01	3.24E-01	1.52E-01	9.84E-02	7.26E-02	5.75E-02	5.21E-02
.70	3.57E-01	2.38E-01	1.12E-01	7.26E-02	5.36E-02	4.25E-02	3.85E-02
.90	2.78E-01	1.88E-01	8.88E-02	5.75E-02	4.25E-02	3.37E-02	3.05E-02
1.00	2.50E-01	1.70E-01	8.04E-02	5.21E-02	3.85E-02	3.05E-02	2.76E-02
UR	0.00E+00	3.00E-01	1.40E-01	9.03E-02	6.66E-02	5.27E-02	4.78E-02

Reflection Table B = 0.25000

μ	.00	.10	.30	.50	.70	.90	1.00
.00	0.00E+00	2.50E+00	8.33E-01	5.00E-01	3.57E-01	2.78E-01	2.50E-01
.10	2.50E+00	1.24E+00	6.03E-01	3.96E-01	2.95E-01	2.34E-01	2.13E-01
.30	8.33E-01	6.03E-01	3.38E-01	2.30E-01	1.74E-01	1.40E-01	1.27E-01
.50	5.00E-01	3.96E-01	2.30E-01	1.58E-01	1.20E-01	9.65E-02	8.79E-02
.70	3.57E-01	2.95E-01	1.74E-01	1.20E-01	9.12E-02	7.34E-02	6.69E-02
.90	2.78E-01	2.34E-01	1.40E-01	9.65E-02	7.34E-02	5.92E-02	5.40E-02
1.00	2.50E-01	2.13E-01	1.27E-01	8.79E-02	6.69E-02	5.40E-02	4.92E-02
UR	0.00E+00	3.62E-01	2.07E-01	1.42E-01	1.07E-01	8.63E-02	7.86E-02

Reflection Table B = 0.50000

μ	.00	.10	.30	.50	.70	.90	1.00
.00	0.00E+00	2.50E+00	8.33E-01	5.00E-01	3.57E-01	2.78E-01	2.50E-01
.10	2.50E+00	1.25E+00	6.24E-01	4.16E-01	3.11E-01	2.49E-01	2.26E-01
.30	8.33E-01	6.24E-01	4.02E-01	2.91E-01	2.27E-01	1.86E-01	1.70E-01
.50	5.00E-01	4.16E-01	2.91E-01	2.16E-01	1.71E-01	1.41E-01	1.29E-01
.70	3.57E-01	3.11E-01	2.27E-01	1.71E-01	1.36E-01	1.12E-01	1.03E-01
.90	2.78E-01	2.49E-01	1.86E-01	1.41E-01	1.12E-01	9.32E-02	8.58E-02
1.00	2.50E-01	2.26E-01	1.70E-01	1.29E-01	1.03E-01	8.58E-02	7.90E-02
UR	0.00E+00	3.79E-01	2.59E-01	1.92E-01	1.51E-01	1.25E-01	1.14E-01

Table 6.21 *(continued)*

SINGLE SCATTERING: g = 0.0000 Reflection Table B = 1.00000

μ	.00	.10	.30	.50	.70	.90	1.00
.00	0.00E+00	2.50E+00	8.33E-01	5.00E-01	3.57E-01	2.78E-01	2.50E-01
.10	2.50E+00	1.25E+00	6.25E-01	4.17E-01	3.12E-01	2.50E-01	2.27E-01
.30	8.33E-01	6.25E-01	4.16E-01	3.11E-01	2.48E-01	2.06E-01	1.90E-01
.50	5.00E-01	4.17E-01	3.11E-01	2.45E-01	2.02E-01	1.71E-01	1.58E-01
.70	3.57E-01	3.12E-01	2.48E-01	2.02E-01	1.68E-01	1.44E-01	1.34E-01
.90	2.78E-01	2.50E-01	2.06E-01	1.71E-01	1.44E-01	1.24E-01	1.16E-01
1.00	2.50E-01	2.27E-01	1.90E-01	1.58E-01	1.34E-01	1.16E-01	1.08E-01
UR	0.00E+00	3.80E-01	2.78E-01	2.19E-01	1.80E-01	1.53E-01	1.42E-01

Reflection Table B = 2.00000

μ	.00	.10	.30	.50	.70	.90	1.00
.00	0.00E+00	2.50E+00	8.33E-01	5.00E-01	3.57E-01	2.78E-01	2.50E-01
.10	2.50E+00	1.25E+00	6.25E-01	4.17E-01	3.13E-01	2.50E-01	2.27E-01
.30	8.33E-01	6.25E-01	4.17E-01	3.12E-01	2.50E-01	2.08E-01	1.92E-01
.50	5.00E-01	4.17E-01	3.12E-01	2.50E-01	2.08E-01	1.78E-01	1.66E-01
.70	3.57E-01	3.13E-01	2.50E-01	2.08E-01	1.78E-01	1.55E-01	1.46E-01
.90	2.78E-01	2.50E-01	2.08E-01	1.78E-01	1.55E-01	1.37E-01	1.30E-01
1.00	2.50E-01	2.27E-01	1.92E-01	1.66E-01	1.46E-01	1.30E-01	1.23E-01
UR	0.00E+00	3.80E-01	2.80E-01	2.25E-01	1.89E-01	1.63E-01	1.52E-01

Reflection Table B = 4.00000

μ	.00	.10	.30	.50	.70	.90	1.00
.00	0.00E+00	2.50E+00	8.33E-01	5.00E-01	3.57E-01	2.78E-01	2.50E-01
.10	2.50E+00	1.25E+00	6.25E-01	4.17E-01	3.13E-01	2.50E-01	2.27E-01
.30	8.33E-01	6.25E-01	4.17E-01	3.13E-01	2.50E-01	2.08E-01	1.92E-01
.50	5.00E-01	4.17E-01	3.13E-01	2.50E-01	2.08E-01	1.79E-01	1.67E-01
.70	3.57E-01	3.13E-01	2.50E-01	2.08E-01	1.79E-01	1.56E-01	1.47E-01
.90	2.78E-01	2.50E-01	2.08E-01	1.79E-01	1.56E-01	1.39E-01	1.32E-01
1.00	2.50E-01	2.27E-01	1.92E-01	1.67E-01	1.47E-01	1.32E-01	1.25E-01
UR	0.00E+00	3.80E-01	2.80E-01	2.25E-01	1.89E-01	1.64E-01	1.53E-01

Reflection Table B = 8.00000

μ	.00	.10	.30	.50	.70	.90	1.00
.00	0.00E+00	2.50E+00	8.33E-01	5.00E-01	3.57E-01	2.78E-01	2.50E-01
.10	2.50E+00	1.25E+00	6.25E-01	4.17E-01	3.13E-01	2.50E-01	2.27E-01
.30	8.33E-01	6.25E-01	4.17E-01	3.13E-01	2.50E-01	2.08E-01	1.92E-01
.50	5.00E-01	4.17E-01	3.13E-01	2.50E-01	2.08E-01	1.79E-01	1.67E-01
.70	3.57E-01	3.13E-01	2.50E-01	2.08E-01	1.79E-01	1.56E-01	1.47E-01
.90	2.78E-01	2.50E-01	2.08E-01	1.79E-01	1.56E-01	1.39E-01	1.32E-01
1.00	2.50E-01	2.27E-01	1.92E-01	1.67E-01	1.47E-01	1.32E-01	1.25E-01
UR	0.00E+00	3.80E-01	2.80E-01	2.25E-01	1.89E-01	1.64E-01	1.53E-01

Table 6.22 Single-Scattering Transmission Operators for Isotropic Scattering ($g = 0.000$)

SINGLE SCATTERING: g = 0.0000 Transmission Table B = 0.03125

μ	.00	.10	.30	.50	.70	.90	1.00
.00	0.00E+00	1.83E+00	7.51E-01	4.70E-01	3.42E-01	2.68E-01	2.42E-01
.10	1.83E+00	5.72E-01	2.12E-01	1.30E-01	9.36E-02	7.32E-02	6.60E-02
.30	7.51E-01	2.12E-01	7.82E-02	4.79E-02	3.45E-02	2.70E-02	2.43E-02
.50	4.70E-01	1.30E-01	4.79E-02	2.94E-02	2.12E-02	1.65E-02	1.49E-02
.70	3.42E-01	9.36E-02	3.45E-02	2.12E-02	1.52E-02	1.19E-02	1.07E-02
.90	2.68E-01	7.32E-02	2.70E-02	1.65E-02	1.19E-02	9.32E-03	8.40E-03
1.00	2.42E-01	6.60E-02	2.43E-02	1.49E-02	1.07E-02	8.40E-03	7.57E-03
UT	0.00E+00	1.25E-01	4.60E-02	2.82E-02	2.03E-02	1.59E-02	1.43E-02

Transmission Table B = 0.06250

μ	.00	.10	.30	.50	.70	.90	1.00
.00	0.00E+00	1.34E+00	6.77E-01	4.41E-01	3.27E-01	2.59E-01	2.35E-01
.10	1.34E+00	8.36E-01	3.46E-01	2.17E-01	1.58E-01	1.24E-01	1.12E-01
.30	6.77E-01	3.46E-01	1.41E-01	8.82E-02	6.42E-02	5.04E-02	4.55E-02
.50	4.41E-01	2.17E-01	8.82E-02	5.52E-02	4.01E-02	3.15E-02	2.85E-02
.70	3.27E-01	1.58E-01	6.42E-02	4.01E-02	2.92E-02	2.29E-02	2.07E-02
.90	2.59E-01	1.24E-01	5.04E-02	3.15E-02	2.29E-02	1.80E-02	1.63E-02
1.00	2.35E-01	1.12E-01	4.55E-02	2.85E-02	2.07E-02	1.63E-02	1.47E-02
UT	0.00E+00	2.03E-01	8.28E-02	5.18E-02	3.77E-02	2.96E-02	2.67E-02

Transmission Table B = 0.12500

μ	.00	.10	.30	.50	.70	.90	1.00
.00	0.00E+00	7.16E-01	5.49E-01	3.89E-01	2.99E-01	2.42E-01	2.21E-01
.10	7.16E-01	8.95E-01	4.66E-01	3.08E-01	2.29E-01	1.82E-01	1.66E-01
.30	5.49E-01	4.66E-01	2.29E-01	1.49E-01	1.11E-01	8.80E-02	7.97E-02
.50	3.89E-01	3.08E-01	1.49E-01	9.74E-02	7.21E-02	5.72E-02	5.18E-02
.70	2.99E-01	2.29E-01	1.11E-01	7.21E-02	5.33E-02	4.23E-02	3.84E-02
.90	2.42E-01	1.82E-01	8.80E-02	5.72E-02	4.23E-02	3.36E-02	3.04E-02
1.00	2.21E-01	1.66E-01	7.97E-02	5.18E-02	3.84E-02	3.04E-02	2.76E-02
UT	0.00E+00	2.78E-01	1.36E-01	8.89E-02	6.59E-02	5.23E-02	4.74E-02

Transmission Table B = 0.25000

μ	.00	.10	.30	.50	.70	.90	1.00
.00	0.00E+00	2.05E-01	3.62E-01	3.03E-01	2.50E-01	2.10E-01	1.95E-01
.10	2.05E-01	5.13E-01	4.41E-01	3.28E-01	2.57E-01	2.11E-01	1.94E-01
.30	3.62E-01	4.41E-01	3.02E-01	2.15E-01	1.66E-01	1.35E-01	1.23E-01
.50	3.03E-01	3.28E-01	2.15E-01	1.52E-01	1.16E-01	9.43E-02	8.61E-02
.70	2.50E-01	2.57E-01	1.66E-01	1.16E-01	8.92E-02	7.22E-02	6.59E-02
.90	2.10E-01	2.11E-01	1.35E-01	9.43E-02	7.22E-02	5.84E-02	5.33E-02
1.00	1.95E-01	1.94E-01	1.23E-01	8.61E-02	6.59E-02	5.33E-02	4.87E-02
UT	0.00E+00	2.85E-01	1.90E-01	1.34E-01	1.03E-01	8.38E-02	7.66E-02

Transmission Table B = 0.50000

μ	.00	.10	.30	.50	.70	.90	1.00
.00	0.00E+00	1.68E-02	1.57E-01	1.84E-01	1.75E-01	1.59E-01	1.52E-01
.10	1.68E-02	8.42E-02	2.28E-01	2.26E-01	2.01E-01	1.77E-01	1.67E-01
.30	1.57E-01	2.28E-01	2.62E-01	2.24E-01	1.88E-01	1.60E-01	1.49E-01
.50	1.84E-01	2.26E-01	2.24E-01	1.84E-01	1.52E-01	1.29E-01	1.19E-01
.70	1.75E-01	2.01E-01	1.88E-01	1.52E-01	1.25E-01	1.05E-01	9.75E-02
.90	1.59E-01	1.77E-01	1.60E-01	1.29E-01	1.05E-01	8.85E-02	8.19E-02
1.00	1.52E-01	1.67E-01	1.49E-01	1.19E-01	9.75E-02	8.19E-02	7.58E-02
UT	0.00E+00	1.97E-01	1.95E-01	1.61E-01	1.33E-01	1.13E-01	1.05E-01

Table 6.22 *(continued)*

SINGLE SCATTERING: g = 0.0000 Transmission Table B = 1.00000

μ	.00	.10	.30	.50	.70	.90	1.00
.00	0.00E+00	1.13E-04	2.97E-02	6.77E-02	8.56E-02	9.14E-02	9.20E-02
.10	1.13E-04	1.13E-03	4.45E-02	8.46E-02	9.98E-02	1.03E-01	1.02E-01
.30	2.97E-02	4.45E-02	9.91E-02	1.25E-01	1.27E-01	1.22E-01	1.19E-01
.50	6.77E-02	8.46E-02	1.25E-01	1.35E-01	1.30E-01	1.21E-01	1.16E-01
.70	8.56E-02	9.98E-02	1.27E-01	1.30E-01	1.22E-01	1.12E-01	1.07E-01
.90	9.14E-02	1.03E-01	1.22E-01	1.21E-01	1.12E-01	1.02E-01	9.67E-02
1.00	9.20E-02	1.02E-01	1.19E-01	1.16E-01	1.07E-01	9.67E-02	9.20E-02
UT	0.00E+00	8.75E-02	1.18E-01	1.26E-01	1.20E-01	1.11E-01	1.06E-01

Transmission Table B = 2.00000

μ	.00	.10	.30	.50	.70	.90	1.00
.00	0.00E+00	5.15E-09	1.06E-03	9.16E-03	2.05E-02	3.01E-02	3.38E-02
.10	5.15E-09	1.03E-07	1.59E-03	1.14E-02	2.39E-02	3.39E-02	3.76E-02
.30	1.06E-03	1.59E-03	7.07E-03	2.13E-02	3.51E-02	4.46E-02	4.79E-02
.50	9.16E-03	1.14E-02	2.13E-02	3.66E-02	4.89E-02	5.63E-02	5.85E-02
.70	2.05E-02	2.39E-02	3.51E-02	4.89E-02	5.86E-02	6.37E-02	6.49E-02
.90	3.01E-02	3.39E-02	4.46E-02	5.63E-02	6.37E-02	6.69E-02	6.74E-02
1.00	3.38E-02	3.76E-02	4.79E-02	5.85E-02	6.49E-02	6.74E-02	6.77E-02
UT	0.00E+00	2.16E-02	3.13E-02	4.45E-02	5.45E-02	6.00E-02	6.15E-02

Transmission Table B = 4.00000

μ	.00	.10	.30	.50	.70	.90	1.00
.00	0.00E+00	1.06E-17	1.35E-06	1.68E-04	1.18E-03	3.26E-03	4.58E-03
.10	1.06E-17	4.25E-16	2.02E-06	2.10E-04	1.37E-03	3.67E-03	5.09E-03
.30	1.35E-06	2.02E-06	1.80E-05	4.17E-04	2.06E-03	4.89E-03	6.54E-03
.50	1.68E-04	2.10E-04	4.17E-04	1.34E-03	3.70E-03	7.13E-03	8.99E-03
.70	1.18E-03	1.37E-03	2.06E-03	3.70E-03	6.73E-03	1.06E-02	1.25E-02
.90	3.26E-03	3.67E-03	4.89E-03	7.13E-03	1.06E-02	1.45E-02	1.64E-02
1.00	4.58E-03	5.09E-03	6.54E-03	8.99E-03	1.25E-02	1.64E-02	1.83E-02
UT	0.00E+00	1.81E-03	2.50E-03	4.02E-03	6.83E-03	1.04E-02	1.23E-02

Transmission Table B = 8.00000

μ	.00	.10	.30	.50	.70	.90	1.00
.00	0.00E+00	4.51E-35	2.19E-12	5.63E-08	3.89E-06	3.83E-05	8.39E-05
.10	4.51E-35	3.61E-33	3.28E-12	7.03E-08	4.53E-06	4.31E-05	9.32E-05
.30	2.19E-12	3.28E-12	5.83E-11	1.41E-07	6.80E-06	5.75E-05	1.20E-04
.50	5.63E-08	7.03E-08	1.41E-07	9.00E-07	1.35E-05	8.61E-05	1.68E-04
.70	3.89E-06	4.53E-06	6.80E-06	1.35E-05	4.44E-05	1.59E-04	2.70E-04
.90	3.83E-05	4.31E-05	5.75E-05	8.61E-05	1.59E-04	3.41E-04	4.94E-04
1.00	8.39E-05	9.32E-05	1.20E-04	1.68E-04	2.70E-04	4.94E-04	6.71E-04
UT	0.00E+00	1.90E-05	2.56E-05	3.88E-05	7.86E-05	2.00E-04	3.14E-04

Table 6.23 Single-Scattering Reflection Operators for Anisotropic Scattering ($g = 0.875$)

SINGLE SCATTERING: g = 0.8750 Reflection Table B = 0.03125

μ	.00	.10	.30	.50	.70	.90	1.00
.00	0.00E+00	8.26E+00	7.24E-01	1.79E-01	6.89E-02	3.37E-02	2.48E-02
.10	8.26E+00	9.33E-01	1.14E-01	3.40E-02	1.45E-02	7.55E-03	5.68E-03
.30	7.24E-01	1.14E-01	2.07E-02	7.63E-03	3.70E-03	2.10E-03	1.65E-03
.50	1.79E-01	3.40E-02	7.63E-03	3.18E-03	1.68E-03	1.01E-03	8.12E-04
.70	6.89E-02	1.45E-02	3.70E-03	1.68E-03	9.45E-04	5.96E-04	4.92E-04
.90	3.37E-02	7.55E-03	2.10E-03	1.01E-03	5.96E-04	3.90E-04	3.30E-04
1.00	2.48E-02	5.68E-03	1.65E-03	8.12E-04	4.92E-04	3.30E-04	3.13E-04
UR	0.00E+00	6.24E-02	1.00E-02	3.62E-03	1.78E-03	1.03E-03	8.21E-04

Reflection Table B = 0.06250

μ	.00	.10	.30	.50	.70	.90	1.00
.00	0.00E+00	8.26E+00	7.24E-01	1.79E-01	6.89E-02	3.37E-02	2.48E-02
.10	8.26E+00	1.43E+00	1.90E-01	5.74E-02	2.47E-02	1.29E-02	9.71E-03
.30	7.24E-01	1.90E-01	3.76E-02	1.41E-02	6.89E-03	3.93E-03	3.10E-03
.50	1.79E-01	5.74E-02	1.41E-02	5.99E-03	3.19E-03	1.93E-03	1.55E-03
.70	6.89E-02	2.47E-02	6.89E-03	3.19E-03	1.81E-03	1.15E-03	9.48E-04
.90	3.37E-02	1.29E-02	3.93E-03	1.93E-03	1.15E-03	7.53E-04	6.38E-04
1.00	2.48E-02	9.71E-03	3.10E-03	1.55E-03	9.48E-04	6.38E-04	6.07E-04
UR	0.00E+00	9.69E-02	1.73E-02	6.48E-03	3.25E-03	1.90E-03	1.51E-03

Reflection Table B = 0.12500

μ	.00	.10	.30	.50	.70	.90	1.00
.00	0.00E+00	8.26E+00	7.24E-01	1.79E-01	6.89E-02	3.37E-02	2.48E-02
.10	8.26E+00	1.84E+00	2.73E-01	8.45E-02	3.67E-02	1.93E-02	1.46E-02
.30	7.24E-01	2.73E-01	6.24E-02	2.42E-02	1.20E-02	6.91E-03	5.46E-03
.50	1.79E-01	8.45E-02	2.42E-02	1.07E-02	5.77E-03	3.53E-03	2.84E-03
.70	6.89E-02	3.67E-02	1.20E-02	5.77E-03	3.32E-03	2.13E-03	1.76E-03
.90	3.37E-02	1.93E-02	6.91E-03	3.53E-03	2.13E-03	1.41E-03	1.20E-03
1.00	2.48E-02	1.46E-02	5.46E-03	2.84E-03	1.76E-03	1.20E-03	1.14E-03
UR	0.00E+00	1.31E-01	2.74E-02	1.08E-02	5.55E-03	3.30E-03	2.64E-03

Reflection Table B = 0.25000

μ	.00	.10	.30	.50	.70	.90	1.00
.00	0.00E+00	8.26E+00	7.24E-01	1.79E-01	6.89E-02	3.37E-02	2.48E-02
.10	8.26E+00	1.99E+00	3.24E-01	1.03E-01	4.55E-02	2.41E-02	1.83E-02
.30	7.24E-01	3.24E-01	8.95E-02	3.66E-02	1.86E-02	1.09E-02	8.63E-03
.50	1.79E-01	1.03E-01	3.66E-02	1.71E-02	9.53E-03	5.92E-03	4.79E-03
.70	6.89E-02	4.55E-02	1.86E-02	9.53E-03	5.65E-03	3.67E-03	3.06E-03
.90	3.37E-02	2.41E-02	1.09E-02	5.92E-03	3.67E-03	2.48E-03	2.12E-03
1.00	2.48E-02	1.83E-02	8.63E-03	4.79E-03	3.06E-03	2.12E-03	2.03E-03
UR	0.00E+00	1.50E-01	3.82E-02	1.62E-02	8.62E-03	5.24E-03	4.24E-03

Reflection Table B = 0.50000

μ	.00	.10	.30	.50	.70	.90	1.00
.00	0.00E+00	8.26E+00	7.24E-01	1.79E-01	6.89E-02	3.37E-02	2.48E-02
.10	8.26E+00	2.01E+00	3.36E-01	1.08E-01	4.81E-02	2.56E-02	1.95E-02
.30	7.24E-01	3.36E-01	1.06E-01	4.62E-02	2.43E-02	1.44E-02	1.16E-02
.50	1.79E-01	1.08E-01	4.62E-02	2.34E-02	1.36E-02	8.63E-03	7.05E-03
.70	6.89E-02	4.81E-02	2.43E-02	1.36E-02	8.41E-03	5.62E-03	4.73E-03
.90	3.37E-02	2.56E-02	1.44E-02	8.63E-03	5.62E-03	3.90E-03	3.37E-03
1.00	2.48E-02	1.95E-02	1.16E-02	7.05E-03	4.73E-03	3.37E-03	3.27E-03
UR	0.00E+00	1.54E-01	4.56E-02	2.09E-02	1.17E-02	7.34E-03	6.01E-03

Table 6.23 *(continued)*

SINGLE SCATTERING: g = 0.8750 Reflection Table B = 1.00000

μ	.00	.10	.30	.50	.70	.90	1.00
.00	0.00E+00	8.26E+00	7.24E-01	1.79E-01	6.89E-02	3.37E-02	2.48E-02
.10	8.26E+00	2.01E+00	3.36E-01	1.09E-01	4.83E-02	2.57E-02	1.95E-02
.30	7.24E-01	3.36E-01	1.10E-01	4.94E-02	2.66E-02	1.60E-02	1.29E-02
.50	1.79E-01	1.09E-01	4.94E-02	2.66E-02	1.60E-02	1.05E-02	8.63E-03
.70	6.89E-02	4.83E-02	2.66E-02	1.60E-02	1.04E-02	7.20E-03	6.14E-03
.90	3.37E-02	2.57E-02	1.60E-02	1.05E-02	7.20E-03	5.18E-03	4.54E-03
1.00	2.48E-02	1.95E-02	1.29E-02	8.63E-03	6.14E-03	4.54E-03	4.47E-03
UR	0.00E+00	1.54E-01	4.79E-02	2.33E-02	1.36E-02	8.80E-03	7.29E-03

Reflection Table B = 2.00000

μ	.00	.10	.30	.50	.70	.90	1.00
.00	0.00E+00	8.26E+00	7.24E-01	1.79E-01	6.89E-02	3.37E-02	2.48E-02
.10	8.26E+00	2.01E+00	3.36E-01	1.09E-01	4.83E-02	2.57E-02	1.95E-02
.30	7.24E-01	3.36E-01	1.10E-01	4.97E-02	2.68E-02	1.62E-02	1.30E-02
.50	1.79E-01	1.09E-01	4.97E-02	2.71E-02	1.65E-02	1.09E-02	9.06E-03
.70	6.89E-02	4.83E-02	2.68E-02	1.65E-02	1.10E-02	7.77E-03	6.68E-03
.90	3.37E-02	2.57E-02	1.62E-02	1.09E-02	7.77E-03	5.74E-03	5.09E-03
1.00	2.48E-02	1.95E-02	1.30E-02	9.06E-03	6.68E-03	5.09E-03	5.07E-03
UR	0.00E+00	1.54E-01	4.81E-02	2.37E-02	1.41E-02	9.28E-03	7.74E-03

Reflection Table B = 4.00000

μ	.00	.10	.30	.50	.70	.90	1.00
.00	0.00E+00	8.26E+00	7.24E-01	1.79E-01	6.89E-02	3.37E-02	2.48E-02
.10	8.26E+00	2.01E+00	3.36E-01	1.09E-01	4.83E-02	2.57E-02	1.95E-02
.30	7.24E-01	3.36E-01	1.10E-01	4.97E-02	2.68E-02	1.62E-02	1.31E-02
.50	1.79E-01	1.09E-01	4.97E-02	2.71E-02	1.66E-02	1.09E-02	9.08E-03
.70	6.89E-02	4.83E-02	2.68E-02	1.66E-02	1.11E-02	7.81E-03	6.73E-03
.90	3.37E-02	2.57E-02	1.62E-02	1.09E-02	7.81E-03	5.81E-03	5.16E-03
1.00	2.48E-02	1.95E-02	1.31E-02	9.08E-03	6.73E-03	5.16E-03	5.17E-03
UR	0.00E+00	1.54E-01	4.81E-02	2.38E-02	1.41E-02	9.32E-03	7.79E-03

Reflection Table B = 8.00000

μ	.00	.10	.30	.50	.70	.90	1.00
.00	0.00E+00	8.26E+00	7.24E-01	1.79E-01	6.89E-02	3.37E-02	2.48E-02
.10	8.26E+00	2.01E+00	3.36E-01	1.09E-01	4.83E-02	2.57E-02	1.95E-02
.30	7.24E-01	3.36E-01	1.10E-01	4.97E-02	2.68E-02	1.62E-02	1.31E-02
.50	1.79E-01	1.09E-01	4.97E-02	2.71E-02	1.66E-02	1.09E-02	9.08E-03
.70	6.89E-02	4.83E-02	2.68E-02	1.66E-02	1.11E-02	7.81E-03	6.73E-03
.90	3.37E-02	2.57E-02	1.62E-02	1.09E-02	7.81E-03	5.81E-03	5.16E-03
1.00	2.48E-02	1.95E-02	1.31E-02	9.08E-03	6.73E-03	5.16E-03	5.17E-03
UR	0.00E+00	1.54E-01	4.81E-02	2.38E-02	1.41E-02	9.32E-03	7.79E-03

Table 6.24 Single-Scattering Transmission Operators for Anisotropic Scattering ($g = 0.875$)

SINGLE SCATTERING: g = 0.8750 Transmission Table B = 0.03125

μ	.00	.10	.30	.50	.70	.90	1.00
.00	0.00E+00	6.04E+00	6.52E-01	1.68E-01	6.59E-02	3.25E-02	2.41E-02
.10	6.04E+00	2.95E+00	3.38E-01	6.78E-02	2.33E-02	1.07E-02	7.72E-03
.30	6.52E-01	3.38E-01	4.21E-01	7.46E-02	1.69E-02	6.17E-03	4.15E-03
.50	1.68E-01	6.78E-02	7.46E-02	1.74E-01	3.11E-02	7.13E-03	4.14E-03
.70	6.59E-02	2.33E-02	1.69E-02	3.11E-02	1.10E-01	1.51E-02	6.32E-03
.90	3.25E-02	1.07E-02	6.17E-03	7.13E-03	1.51E-02	1.11E-01	2.36E-02
1.00	2.41E-02	7.72E-03	4.15E-03	4.14E-03	6.32E-03	2.36E-02	9.08E-01
UT	3.38E-01	1.62E-01	8.12E-02	5.41E-02	4.05E-02	3.22E-02	3.20E-02

Transmission Table B = 0.06250

μ	.00	.10	.30	.50	.70	.90	1.00
.00	0.00E+00	4.42E+00	5.87E-01	1.58E-01	6.30E-02	3.14E-02	2.33E-02
.10	4.42E+00	4.32E+00	5.52E-01	1.13E-01	3.94E-02	1.81E-02	1.31E-02
.30	5.87E-01	5.52E-01	7.59E-01	1.37E-01	3.14E-02	1.15E-02	7.76E-03
.50	1.58E-01	1.13E-01	1.37E-01	3.27E-01	5.89E-02	1.36E-02	7.90E-03
.70	6.30E-02	3.94E-02	3.14E-02	5.89E-02	2.10E-01	2.90E-02	1.22E-02
.90	3.14E-02	1.81E-02	1.15E-02	1.36E-02	2.90E-02	2.15E-01	4.57E-02
1.00	2.33E-02	1.31E-02	7.76E-03	7.90E-03	1.22E-02	4.57E-02	1.76E+00
UT	2.64E-01	2.47E-01	1.45E-01	1.01E-01	7.70E-02	6.21E-02	6.19E-02

Transmission Table B = 0.12500

μ	.00	.10	.30	.50	.70	.90	1.00
.00	0.00E+00	2.37E+00	4.77E-01	1.39E-01	5.76E-02	2.93E-02	2.19E-02
.10	2.37E+00	4.62E+00	7.43E-01	1.61E-01	5.71E-02	2.66E-02	1.94E-02
.30	4.77E-01	7.43E-01	1.23E+00	2.33E-01	5.42E-02	2.01E-02	1.36E-02
.50	1.39E-01	1.61E-01	2.33E-01	5.78E-01	1.06E-01	2.46E-02	1.44E-02
.70	5.76E-02	5.71E-02	5.42E-02	1.06E-01	3.85E-01	5.35E-02	2.26E-02
.90	2.93E-02	2.66E-02	2.01E-02	2.46E-02	5.35E-02	4.01E-01	8.56E-02
1.00	2.19E-02	1.94E-02	1.36E-02	1.44E-02	2.26E-02	8.56E-02	3.31E+00
UT	1.83E-01	2.97E-01	2.33E-01	1.76E-01	1.40E-01	1.15E-01	1.16E-01

Transmission Table B = 0.25000

μ	.00	.10	.30	.50	.70	.90	1.00
.00	0.00E+00	6.78E-01	3.14E-01	1.08E-01	4.82E-02	2.55E-02	1.94E-02
.10	6.78E-01	2.65E+00	7.03E-01	1.71E-01	6.42E-02	3.08E-02	2.26E-02
.30	3.14E-01	7.03E-01	1.62E+00	3.35E-01	8.11E-02	3.07E-02	2.10E-02
.50	1.08E-01	1.71E-01	3.35E-01	9.00E-01	1.71E-01	4.06E-02	2.39E-02
.70	4.82E-02	6.42E-02	8.11E-02	1.71E-01	6.44E-01	9.14E-02	3.88E-02
.90	2.55E-02	3.08E-02	3.07E-02	4.06E-02	9.14E-02	6.98E-01	1.50E-01
1.00	1.94E-02	2.26E-02	2.10E-02	2.39E-02	3.88E-02	1.50E-01	5.84E+00
UT	1.07E-01	2.42E-01	3.07E-01	2.71E-01	2.31E-01	1.98E-01	2.03E-01

Transmission Table B = 0.50000

μ	.00	.10	.30	.50	.70	.90	1.00
.00	0.00E+00	5.57E-02	1.37E-01	6.57E-02	3.37E-02	1.93E-02	1.51E-02
.10	5.57E-02	4.35E-01	3.63E-01	1.18E-01	5.02E-02	2.58E-02	1.95E-02
.30	1.37E-01	3.63E-01	1.41E+00	3.48E-01	9.20E-02	3.66E-02	2.54E-02
.50	6.57E-02	1.18E-01	3.48E-01	1.09E+00	2.23E-01	5.54E-02	3.31E-02
.70	3.37E-02	5.02E-02	9.20E-02	2.23E-01	9.01E-01	1.33E-01	5.73E-02
.90	1.93E-02	2.58E-02	3.66E-02	5.54E-02	1.33E-01	1.06E+00	2.31E-01
1.00	1.51E-02	1.95E-02	2.54E-02	3.31E-02	5.73E-02	2.31E-01	9.09E+00
UT	4.95E-02	1.12E-01	2.79E-01	3.25E-01	3.18E-01	2.96E-01	3.11E-01

Table 6.24 *(continued)*

SINGLE SCATTERING: g = 0.8750 Transmission Table B = 1.00000

μ	.00	.10	.30	.50	.70	.90	1.00
.00	0.00E+00	3.75E-04	2.58E-02	2.42E-02	1.65E-02	1.11E-02	9.14E-03
.10	3.75E-04	5.86E-03	7.10E-02	4.42E-02	2.49E-02	1.50E-02	1.19E-02
.30	2.58E-02	7.10E-02	5.33E-01	1.94E-01	6.24E-02	2.79E-02	2.02E-02
.50	2.42E-02	4.42E-02	1.94E-01	8.03E-01	1.91E-01	5.22E-02	3.23E-02
.70	1.65E-02	2.49E-02	6.24E-02	1.91E-01	8.82E-01	1.42E-01	6.29E-02
.90	1.11E-02	1.50E-02	2.79E-02	5.22E-02	1.42E-01	1.21E+00	2.72E-01
1.00	9.14E-03	1.19E-02	2.02E-02	3.23E-02	6.29E-02	2.72E-01	1.10E+01
UT	1.65E-02	3.01E-02	1.28E-01	2.42E-01	3.06E-01	3.31E-01	3.70E-01

Transmission Table B = 2.00000

μ	.00	.10	.30	.50	.70	.90	1.00
.00	0.00E+00	1.70E-08	9.21E-04	3.27E-03	3.96E-03	3.65E-03	3.36E-03
.10	1.70E-08	5.32E-07	2.54E-03	5.98E-03	5.97E-03	4.93E-03	4.40E-03
.30	9.21E-04	2.54E-03	3.81E-02	3.32E-02	1.72E-02	1.02E-02	8.16E-03
.50	3.27E-03	5.98E-03	3.32E-02	2.17E-01	7.18E-02	2.43E-02	1.63E-02
.70	3.96E-03	5.97E-03	1.72E-02	7.18E-02	4.23E-01	8.05E-02	3.82E-02
.90	3.65E-03	4.93E-03	1.02E-02	2.43E-02	8.05E-02	7.99E-01	1.90E-01
1.00	3.36E-03	4.40E-03	8.16E-03	1.63E-02	3.82E-02	1.90E-01	8.11E+00
UT	4.26E-03	4.94E-03	1.97E-02	7.25E-02	1.45E-01	2.11E-01	2.63E-01

Transmission Table B = 4.00000

μ	.00	.10	.30	.50	.70	.90	1.00
.00	0.00E+00	3.51E-17	1.17E-06	5.99E-05	2.27E-04	3.96E-04	4.55E-04
.10	3.51E-17	2.19E-15	3.23E-06	1.10E-04	3.43E-04	5.35E-04	5.95E-04
.30	1.17E-06	3.23E-06	9.69E-05	6.50E-04	1.01E-03	1.12E-03	1.11E-03
.50	5.99E-05	1.10E-04	6.50E-04	7.97E-03	5.44E-03	3.07E-03	2.50E-03
.70	2.27E-04	3.43E-04	1.01E-03	5.44E-03	4.86E-02	1.34E-02	7.36E-03
.90	3.96E-04	5.35E-04	1.12E-03	3.07E-03	1.34E-02	1.73E-01	4.62E-02
1.00	4.55E-04	5.95E-04	1.11E-03	2.50E-03	7.36E-03	4.62E-02	2.20E+00
UT	1.29E-03	3.14E-04	8.31E-04	4.21E-03	1.76E-02	4.41E-02	6.80E-02

Transmission Table B = 8.00000

μ	.00	.10	.30	.50	.70	.90	1.00
.00	0.00E+00	1.49E-34	1.90E-12	2.01E-08	7.50E-07	4.64E-06	8.34E-06
.10	1.49E-34	1.86E-32	5.23E-12	3.67E-08	1.13E-06	6.28E-06	1.09E-05
.30	1.90E-12	5.23E-12	3.14E-10	2.19E-07	3.33E-06	1.31E-05	2.04E-05
.50	2.01E-08	3.67E-08	2.19E-07	5.34E-06	1.98E-05	3.71E-05	4.66E-05
.70	7.50E-07	1.13E-06	3.33E-06	1.98E-05	3.20E-04	2.01E-04	1.59E-04
.90	4.64E-06	6.28E-06	1.31E-05	3.71E-05	2.01E-04	4.07E-03	1.39E-03
1.00	8.34E-06	1.09E-05	2.04E-05	4.66E-05	1.59E-04	1.39E-03	8.04E-02
UT	2.14E-03	2.80E-06	6.03E-06	2.05E-05	1.57E-04	1.01E-03	2.33E-03

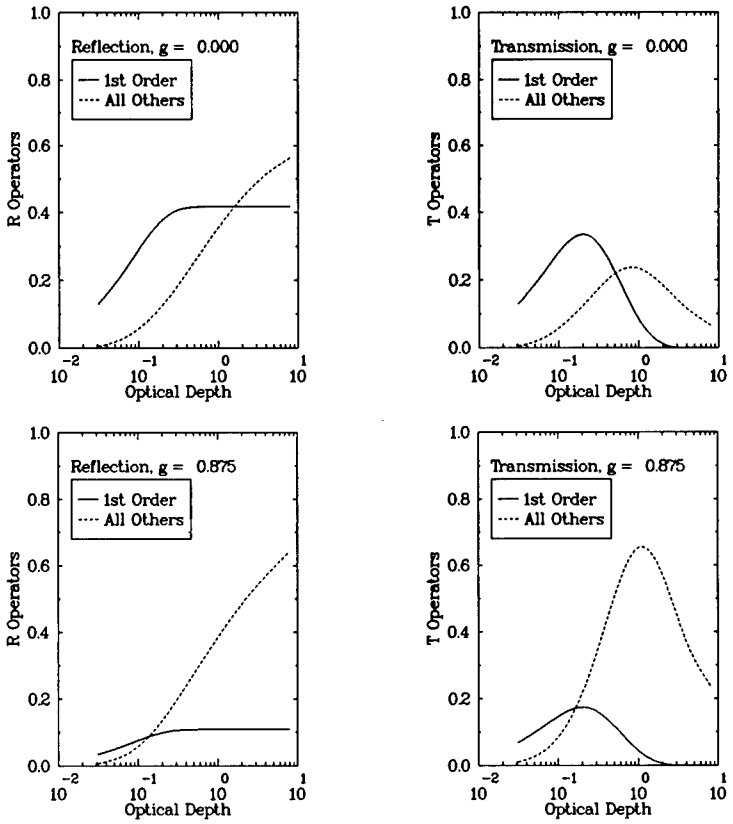

Fig. 6.18 Example from radiative transfer tables showing magnitudes of single and multiple scattering.

Some results using the algorithm for the UTU and URU moments are listed in Table 6.25 along with the rigorous results of Van De Hulst.[62] The reasonably good results shown here are more or less typical of applications involving the higher order moments. The algorithm can also be applied to the R and T operators, however, the accuracy decreases significantly for large departures from the conservative case.

6.4.20 Azimuthal Dependence and Single Scattering

Although the general theory does treat azimuthal dependence, we have elected to list only the azimuth-averaged results in the tables. This is done primarily because of the inordinate number of tables that would be required to cover the full range of angles needed; however, detailed results are available elsewhere.[68]

One can gain a great deal of insight into the azimuthal dependence by applying the single-scattering approximation, in which case the azimuth dependence is explicit and relatively easy to compute. The single-scattering, azimuth-dependent transmission and reflection operators, from previous sections, are written in the plane parallel approximation following the notation of Liou[69] as

$$R_{ss} = \frac{1}{4}\frac{1}{\mu + \mu_0}P(\mu,\phi;\mu',\phi')\left\{1 - \exp\left[-\left(\frac{1}{\mu_0} + \frac{1}{\mu}\right)B\right]\right\} , \tag{6.114a}$$

and

$$T_{ss} = \frac{1}{4}\frac{1}{\mu - \mu_0}\mathrm{P}(\mu,\phi;\mu',\phi')\exp(-B/\mu_0)\left\{1 - \exp\left[-\left(\frac{1}{\mu_0} - \frac{1}{\mu}\right)\right]\right\} , \tag{6.114b}$$

where $P(\mu,\phi;\mu',\phi')$ is the azimuth-dependent obscurant phase function, which for the Henyey-Greenstein case is given by Eq. (6.103).

For completeness, the azimuth-averaged reflection and transmission operators that are represented in the single-scattering tables are written simply as

$$R_0(B;\mu,\mu') = \frac{1}{4}\frac{1}{\mu + \mu'}P(\mu,\mu')\{1 - \exp[-(1/\mu' + 1/\mu)B]\} , \tag{6.115a}$$

$$T_0(B;\mu,\mu') = \frac{1}{4}\frac{1}{\mu - \mu'}P(\mu,\mu')\exp(-B/\mu')\{1 - \exp[-(1/\mu' - 1/\mu)B]\} . \tag{6.115b}$$

Figure 6.19 shows several plots of the azimuth-dependent reflection and transmission operators along with the azimuth-averaged result from the tables. The general trends showing the monotonic increase for reflection and the peaks in transmission at a characteristic optical depth are evident for all azimuths. It is apparent from the plots that the azimuth dependence can be quite significant for most values of optical depth. This is especially true for the reflection operator even at the highest optical depths. For transmission, however, all orders of scattering tend toward zero at the higher optical depths, including the azimuth-dependent single scattering contribution.

It is clear from physical reasoning that the single-scattering approximation tends to underestimate simply because there is certain to be some added azimuth contributions from the higher orders. There is, however, some strong evidence[62] that a good portion of the higher order contributions are nearly isotropic, and this is borne out in some cases from direct comparisons.

6.4.21 Example 1: Surface Global Irradiance

As an example to demonstrate the utility of the radiation tables, we use Eq. (6.111) and the radiation tables to calculate the downward-directed surface irradiance as propagated through a plane parallel layer of total vertical optical depth B. To complete the problem we specify the solar beam irradiance as $F_0 = 500\ \mathrm{W\ m^{-2}}$, the solar zenith direction as $\mu_0 = 0.50$, the sky contribution to the total global irradiance as $D_0 = 50\ \mathrm{W\ m^{-2}}$, the surface albedo as $A_0 = 0.20$, the vertical optical depth of the layer as $B = 0.500$, and consider both

Table 6.25 Effects of Aerosol Absorption as Calculated using the Scaling Algorithm; Numbers in Parentheses Refer to Rigorous Results

REFLECTION (URU, g = 0.0)

ω_0	B=1.00	B=2.00	B=4.00	B=8.00
0.20	0.049 (0.044)	0.044 (0.046)	0.041 (0.046)	0.041 (0.046)
0.40	0.119 (0.100)	0.108 (0.107)	0.088 (0.107)	0.082 (0.107)
0.60	0.208 (0.174)	0.210 (0.192)	0.166 (0.195)	0.129 (0.195)
0.80	0.317 (0.280)	0.371 (0.328)	0.344 (0.341)	0.251 (0.342)
0.90	0.380 (0.353)	0.480 (0.437)	0.509 (0.473)	0.437 (0.478)
0.95	0.412 (0.396)	0.542 (0.512)	0.619 (0.579)	0.606 (0.596)
0.99	0.440 (0.436)	0.596 (0.588)	0.725 (0.710)	0.799 (0.776)
1.00	0.447 (0.447)	0.610 (0.610)	0.754 (0.754)	0.858 (0.858)

TRANSMISSION (UTU, g = 0.0)

ω_0	B=1.00	B=2.00	B=4.00	B=8.00
0.20	0.251 (0.246)	0.073 (0.070)	0.007 (0.007)	0.000 (0.000)
0.40	0.301 (0.283)	0.098 (0.093)	0.011 (0.011)	0.000 (0.000)
0.60	0.367 (0.336)	0.151 (0.126)	0.028 (0.019)	0.002 (0.001)
0.80	0.452 (0.416)	0.243 (0.197)	0.088 (0.047)	0.019 (0.003)
0.90	0.500 (0.475)	0.309 (0.266)	0.149 (0.091)	0.055 (0.011)
0.95	0.526 (0.511)	0.348 (0.317)	0.193 (0.140)	0.089 (0.030)
0.99	0.548 (0.544)	0.381 (0.373)	0.234 (0.217)	0.129 (0.096)
1.00	0.553 (0.553)	0.390 (0.390)	0.246 (0.246)	0.142 (0.142)

Table 6.25 *(continued)*

REFLECTION (URU, g = 0.750)

ω_0	B=1.00	B=2.00	B=4.00	B=8.00
0.20	0.015 (0.011)	0.011 (0.012)	0.010 (0.012)	0.009 (0.012)
0.40	0.042 (0.028)	0.035 (0.030)	0.023 (0.030)	0.019 (0.030)
0.60	0.080 (0.055)	0.084 (0.062)	0.060 (0.064)	0.034 (0.064)
0.80	0.130 (0.101)	0.169 (0.127)	0.169 (0.141)	0.113 (0.143)
0.90	0.160 (0.138)	0.230 (0.191)	0.280 (0.232)	0.261 (0.247)
0.95	0.176 (0.163)	0.265 (0.239)	0.356 (0.313)	0.400 (0.358)
0.99	0.189 (0.186)	0.260 (0.289)	0.430 (0.416)	0.562 (0.537)
1.00	0.192 (0.192)	0.304 (0.304)	0.450 (0.450)	0.611 (0.611)

TRANSMISSION (UTU, g = 0.750)

ω_0	B=1.00	B=2.00	B=4.00	B=8.00
0.20	0.282 (0.276)	0.089 (0.091)	0.010 (0.012)	0.000 (0.000)
0.40	0.373 (0.350)	0.141 (0.141)	0.019 (0.025)	0.000 (0.001)
0.60	0.490 (0.451)	0.244 (0.224)	0.058 (0.059)	0.004 (0.005)
0.80	0.636 (0.594)	0.421 (0.376)	0.193 (0.157)	0.052 (0.028)
0.90	0.718 (0.689)	0.545 (0.502)	0.333 (0.276)	0.151 (0.087)
0.95	0.763 (0.745)	0.616 (0.587)	0.430 (0.381)	0.245 (0.169)
0.99	0.799 (0.795)	0.676 (0.672)	0.524 (0.509)	0.355 (0.322)
1.00	0.808 (0.808)	0.696 (0.696)	0.550 (0.550)	0.390 (0.390)

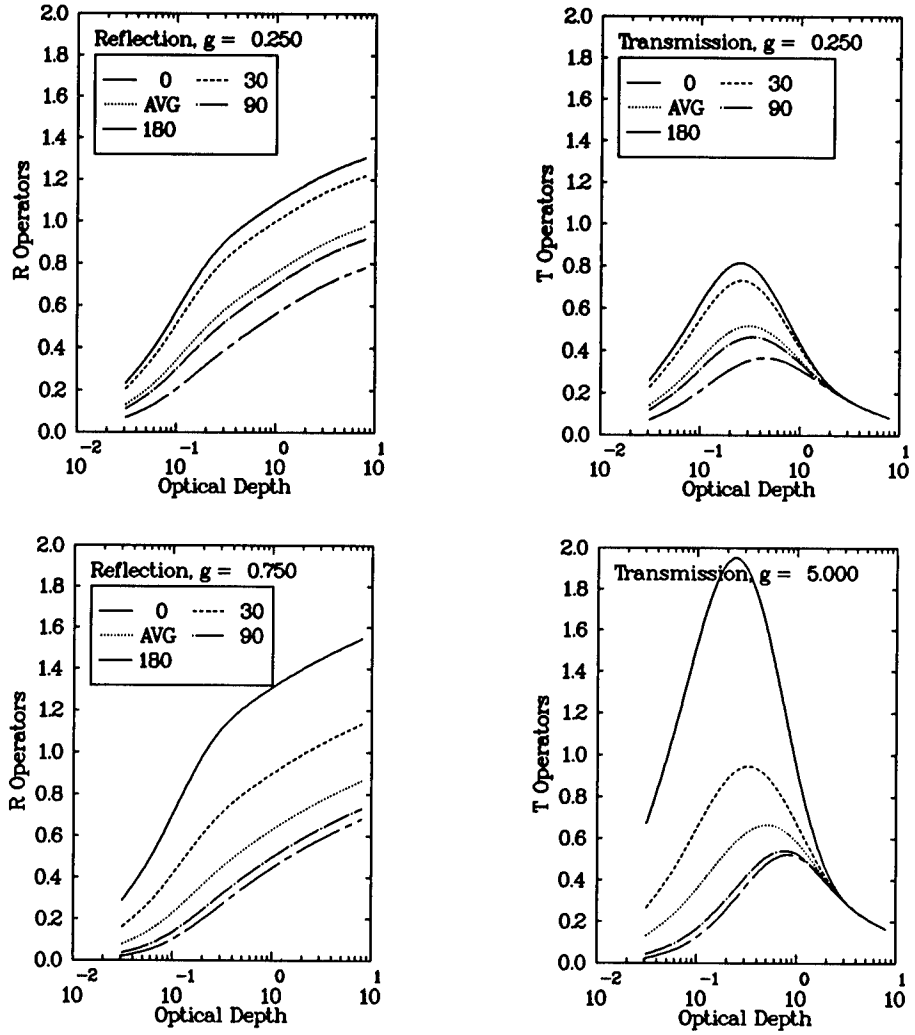

Fig. 6.19 Example of azimuth-dependent reflection and transmission operators.

isotropic ($g = 0.000$) and anisotropic ($g = 0.875$) scattering. The appropriate computational factors are as follows:

Factor	$g = 0.000$	$g = 0.875$
$\exp(-B/\mu_0)$	0.368	0.368
$E_3(B)$	0.222	0.222
$UT(B;\mu_0)$	0.298	0.560
$UTU(B)$	0.261	0.489
$URU(B)$	0.296	0.0691

where the numerical values for the second moments UTU, URU, and the third-order exponential integral $E_3(B)$ are obtained from Table 6.16 and the first

moments UT are obtained from Table 6.18 ($g = 0.000$, $t = 0.500$) or Table 6.20 ($g = 0.875$, $t = 0.500$). Using these listed values for URU and $A_0 = 0.20$, the albedo correction factors in the denominator (DENOM) of Eq. (6.111) become DENOM = 0.981 for $g = 0.000$ and DENOM = 0.996 for $g = 0.875$.

Other factors in Eq. (6.111) are as follows:

Factor	$g = 0.000$	$g = 0.875$
$[\mu_0 F_0 \exp(-B/\mu_0)]$/DENOM	93.78 (W m^{-2})	92.36 (W m^{-2})
$[2D_0E_3(B)]$/DENOM	22.63	22.29
$[(F_0/\pi)UT(B;\mu_0)]$/DENOM	48.35	89.48
$[D_0/\pi)UTU(B)]$/DENOM	4.23	7.81
Total	168.99	211.94

Note that for this particular scenario, anisotropic scattering accounts for a higher diffuse contribution than does isotropic scattering under otherwise identical conditions. This effect is, of course, to be expected and is a manifestation of the stronger forward (in this case generally downward) scattering in the anisotropic case. In both of these cases the first two terms that account for the DIRECT components are nearly identical and differ only by the albedo correction factors DENOM.

6.4.22 Example 2: Upward and Downward Propagation

For this example we use Eqs. (6.110a) and (6.110b) to demonstrate the use of the tables to calculate path radiance (also referred to as diffuse radiance) propagated in either the upward (reflection) or downward (transmission) direction along a particular straight line path. We choose the same general scenario of Sec. 6.4.20, and to complete the problem we choose the path of propagation direction to be $\mu = 0.10$. The following appropriate mathematical factors are obtained directly from Tables 6.17 and 6.18 for $g = 0.000$ and Tables 6.19 and 6.20 for $g = 0.875$ (note $\mu_0 = 0.50$, $\mu = 0.10$):

Factor	$g = 0.000$	$g = 0.875$
$R(B;\mu,\mu_0)$	0.670	0.356
$UR(B;\mu)$	0.605	0.456
$T(B;\mu,\mu_0)$	0.444	0.639
$UT(B;\mu)$	0.388	0.537

The various factors required to evaluate Eqs. (6.110a) and (6.110b) are as follows (note from previous example that $G_0 = 168.99$ for $g = 0.000$ and $G_0 = 211.94$ for $g = 0.875$):

Reflection	$g = 0.000$	$g = 0.875$
$(\mu_0 F_0/\pi)R(B;\mu,\mu_0)$	53.32 (W m^{-2} sr^{-1})	28.32 (W m^{-2} sr^{-1})
$(D_0/\pi)UR(B;\mu)$	9.63	7.26
$(A_0 G_0/\pi)UT(B;\mu)$	4.17	7.24
Total	67.12	45.82
Transmission	$g = 0.000$	$g = 0.875$
$(\mu_0 F_0/\pi)T(B;\mu,\mu_0)$	35.33 (W m^{-2} sr^{-1})	50.85 (W m^{-2} sr^{-1})
$(D_0/\pi)UT(B;\mu)$	6.17	8.54
$(A_0 G_0/\pi)UR(B;\mu)$	6.51	6.15
Total	48.01	65.54

Note that for upward propagation (reflection) the anisotropic value is lower than the isotropic value. However, for the case of downward propagation (transmission) the situation is reversed because the anisotropic value is lower. Note also that in both cases the values for reflection and transmission are not symmetrical; that is, for $g = 0.000$ reflection is higher than transmission and for $g = 0.875$ transmission is higher than reflection. Note that these results pertain only to the diffuse component of the radiation field that treats only effects of single and multiple scattering. To get the total radiation field one must add the direct component in accordance with the Beer's law.

6.5 SIMULATION MODELING AND CONTRAST TRANSMISSION

6.5.1 Introduction

The formalism developed in the previous sections can be used to evaluate the effectiveness of obscuration on various CCD-O operations and countermeasures. The conventional approach used in contemporary target acquisition models is based on the degradation of LOS direct transmission and (diffuse) contrast transmission. Most applications are based on well-established principles first developed for atmospheric applications by the early pioneers Middleton[72] and Duntley.[73] Another approach described in both Middleton[72] and Duntley[73] is to simulate effects using a variety of obscuration models and modern image-processing and display technology to superimpose obscuration effects directly on digitized versions of real scene imagery. The latter approach, when combined with conventional image-processing algorithms holds promise for the future. We focus here on the more standard LOS formulation that can be used more or less directly in contemporary system evaluation models.[74,75]

6.5.2 Definition of Apparent Contrast[a]

The target-background contrast as perceived over some observer-target distance through an obscuring medium is defined in most target acquisition models as[74]

[a]At least two other definitions of contrast are often used; one is the modulation contrast, $C = [I_t(r) - I_b(r)]/[I_t(r) + I_b(r)]$ and another is $C = [I_t(r) - I_b(r)]/I_t(r)$.

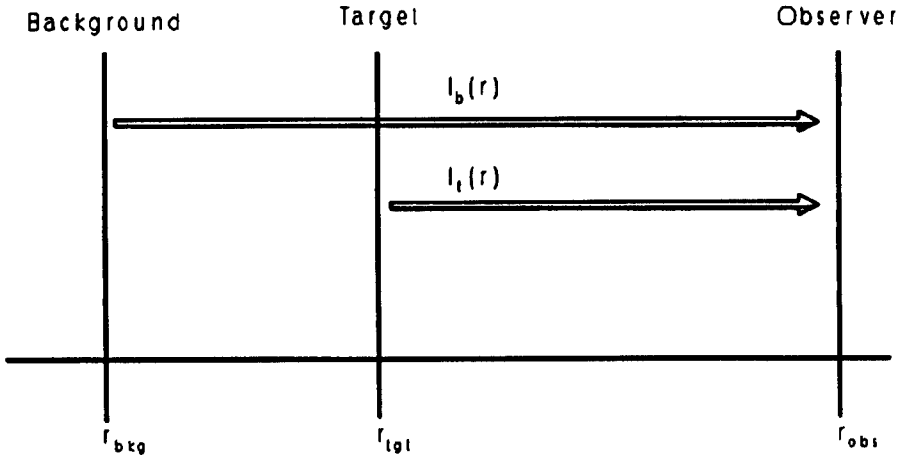

Fig. 6.20 Sketch demonstrating contrast scenario and nomenclature of Eq. (6.116).

$$C(r) = \frac{I_t(r) - I_b(r)}{I_b(r)} , \tag{6.116}$$

where $I_t(r)$ denotes radiance emanating from the direction of some hypothetical target and $I_b(r)$ denotes radiance emanating from the direction of some hypothetical background (see Fig. 6.20). In Eq.(6.116) both terms are evaluated at the observer location denoted by r. Note in Eq. (6.116) that to avoid cumbersome detail we have suppressed much of the notation introduced in the previous section. It is, of course, understood that all quantities are scenario dependent as explained in previous sections.

The target-background contrast, as perceived in the absence of any atmospheric or obscuring effects, is termed the *inherent contrast* and can be represented as the contrast as perceived at the target location, that is,

$$C_0 = C(r_0) = \frac{I_t(r_0) - I_b(r_0)}{I_b(r_0)} , \tag{6.117}$$

where r_0 represents the location of the actual target. In either Eq. (6.116) or Eq. (6.117) the target and background need not be located at the same point, however, the background radiance $I_b(r_0)$ does need to be evaluated at the target location r_0 in the formalism developed here. In applications, the background may be some definite object such as a distant natural or man-made landscape or may simply be the background sky.

In any case, the total radiance can, in general, be separated into the two parts representing the direct and diffuse components as

$$I(r) = I^d(r) + I^*(r) , \tag{6.118}$$

where the superscript d denotes the direct component and superscript * denotes the diffuse component, which are expressed in the notation of the previous sections as

$$\text{direct} = I^d(\tau;\mu,\phi) = I(r_0;\mu,\phi)\exp[-(\tau - \tau_0)] \ , \tag{6.119a}$$

$$\text{diffuse} = I^*(\tau;\mu,\phi) = \int_{\tau_0}^{\tau} J(\tau';\mu,\phi)\exp[-(\tau - \tau')\,d\tau' \ , \tag{6.119b}$$

where τ is the optical thickness at the observer location and τ_0 is the optical thickness at the target (or background) location, both computed along the path of propagation, and $J(r';\mu,\phi)$ is the optical source function, which can include effects of both multiple scattering and thermal emission. All notation is similar to that used in the previous section.

6.5.3 Contrast Transmission

Contrast transmission is defined as the ratio of the contrast as perceived at some arbitrary observer location r to the contrast perceived at some target (or background) location r_0. That is,

$$T_C = \frac{C(r)}{C(r_0)} \ , \tag{6.120}$$

where both the transmitted contrast $C(r)$, as perceived at the observer location r, and the inherent contrast $C(r_0)$, as perceived at the target, or background, location r_0, are found by appropriate substitution into Eq. (6.116).

After some algebraic manipulation, the contrast transmission can be written in terms of the direct and diffuse contributions quite simply and generally as

$$T_C = \frac{1}{1 + (\text{diffuse/direct})} \ , \tag{6.121}$$

where the direct and diffuse components are defined in Eq. (6.118).

6.5.4 Lambertian Reflection and Emissivity

The target radiance, assuming a Lambertian reflector and the target located at (or near) the (earth) surface, is modeled simply as

$$I(r_0;\mu,\phi) = \frac{A_0 G\downarrow(0)}{\pi} \ , \tag{6.122}$$

where A_0 is the target surface reflectivity, or albedo, and $G\downarrow(0)$ is the total downward directed irradiance, which accounts for all ambient radiation from the sun, sky, and surface (appropriately averaged over the particular spectral band of interest). For infrared scenarios, the target radiance can include a term to account for thermal emission as

$$I(r_0;\mu,\phi) = (1 - \varepsilon)\frac{G\downarrow(0)}{\pi} + \varepsilon F(\Delta\lambda,t)\frac{\sigma t_0^4}{\pi} , \tag{6.123}$$

where ε is the emissivity of the target, $F(\Delta\lambda,t)$ is the fractional blackbody irradiance over the bandpass of interest denoted by $\Delta\lambda$, σ is the Stefan-Boltzmann constant, and t_0 is the absolute temperature of the target. The first term in Eq. (6.123) accounts for reflection of the ambient radiation from the target surface and the second accounts for thermal emission from the target surface.

6.5.5 Generalized Sky-to-Ground Ratio

After some minor substitution and rearrangement, Eq. (6.120) can be rewritten in more specific terms as

$$T_C = \frac{1}{1 + [D^*(\tau;\mu,\phi)/A_0 e^{-\tau}]} , \tag{6.124}$$

where we have introduced a new factor $D^*(\tau;\mu,\phi)$ as

$$D^*(\tau;\mu,\phi) = \frac{I^*(\tau;\mu,\phi)}{G\downarrow(0)/\pi} , \tag{6.125}$$

which we refer to as the *generalized sky-to-ground ratio*, or more simply the *Duntley factor.*

For the special case of horizontal propagation, it is usual to refer to the quantity in the numerator of Eq. (6.125) as the sky radiance and to refer to the quantity in the denominator as the ground radiance. Hence, for this special case the Duntley factor is referred to as the sky-to-ground ratio, although this restricted terminology can lead to ambiguities and confusion in obscuration scenarios involving the general case and slant-path propagation in an obscuring medium.

The significance of this approach is that the concepts of inherent contrast and contrast transmission allow for the separation of target effects from atmospheric effects. Specifically, the obscuring medium, either for the clear case or for the obscured atmosphere, can be characterized in terms of an optical thickness and a Duntley factor from which the transmission and contrast required in acquisition models can be computed.

6.6 METEOROLOGICAL FACTORS

6.6.1 Introduction

In this section we review and describe some of the meteorological factors that have a significant effect on obscuration scenarios. Factors will include both standard meteorological observables that affect (obscurant) material concentration levels through transport and diffusion processes, and radiative quantities that directly affect electromagnetic propagation. For bookkeeping purposes we loosely categorize these factors as mechanical and radiative quantities.

Table 6.26 Meteorological Factors in Obscuring Atmospheres

MECHANICAL	RADIATIVE
WIND SPEED/DIRECTION	AMBIENT RADIATION
STABILITY	SOLAR/LUNAR IRRADIANCE
SURFACE HEAT FLUX	SKY CLOUD IRRADIANCE
MIXING HEIGHT	SURFACE IRRADIANCE/ALBEDO
RELATIVE HUMIDITY	VISIBILITY/TRANSMISSION
SURFACE ROUGHNESS	THERMAL EMISSION

In some cases the treatment is only descriptive and in other cases quantitative. For point of reference, Table 6.26 lists some of the major meteorological factors to consider in obscuration modeling.

6.6.2 Effect of Wind

The major effect of the ambient wind is to transport an obscurant at the (approximate) speed and direction of the ambient wind. The diffusion of the obscurant is driven by statistical fluctuations in wind speed and direction (turbulence). Increased turbulence generally leads to increased diffusion and increased spreading of the obscurant. For localized obscurants, at short distances from the point of release, wind fluctuations give rise to concentration fluctuations that can lead to regions of thin optical depth or even holes in smoke plumes. Wind effects on material transport and diffusion are most pronounced near the source of release and are significantly decreased downwind where the obscurant is well mixed and dispersed.

6.6.3 Wind Speed Vertical Profile

Wind speed generally increases with height and turbulence generally decreases with height. An approximate relationship giving the (mean) wind speed vertical profile is the power law model:

$$\frac{u(z)}{u(z_r)} = \left(\frac{z}{z_r}\right)^p , \tag{6.126}$$

where $u(z)$ is the mean wind speed at height z, z_r is a reference height (usually 10 m), and p is an empirical parameter called the *power law exponent,* which is generally a function of the atmospheric stability and the surface roughness parameter. Some typical values of the wind power law exponent obtained from Sutherland and Fowler[76] are listed in Table 6.27. Equation (6.126) applies for heights up to the level of the mixing height and is strictly valid only for neutral stability. For nonneutral conditions, the wind speed profile is often approximated with the logarithmic form as[77,78]

$$u(z) = \left(\frac{u_*}{k}\right)\left[\ln\left(\frac{z}{z_0}\right) + \psi\left(\frac{z}{L}\right)\right] , \tag{6.127}$$

Table 6.27 Representative Values for Various Key Atmospheric Parameters

Roughness Factor z_0 (m)	Parameter	Pasquill Stability Category					
		A(1)	B(2)	C(3)	D(4)	E(5)	F(6)
		Mean Windspeed (m/s)					
		3	4	5	8	5	3
		Mixing Height (m)					
		1000–3000	500–2000	250–1000	100–800	50–200	30–50
0.01	u_*	0.201	0.259	0.279	0.463	0.230	0.094
	p	0.062	0.083	0.100	0.145	0.319	0.536
	R_i	-3.58	-0.87	-0.34	0	0.33	2.66
	L	-7.8	-16.8	-51.5	∞	65.3	14.0
	μ	-157	-94.0	-33.0	0	21.5	40.9
	s	-1.24	-0.96	-0.85	0	0.84	0.69
0.05	u_*	0.275	0.346	0.413	0.604	0.304	0.155
	p	0.086	0.119	0.144	0.189	0.348	0.588
	R_i	-3.26	-0.67	-0.21	0	0.09	0.34
	L	-9.4	-23.6	-94.4	∞	113.7	22.6
	μ	-178	-89.4	-26.7	0	18.3	41.8
	s	-2.17	-1.52	-1.09	0	2.72	1.06
0.10	u_*	0.326	0.404	0.475	0.695	0.354	0.128
	p	0.103	0.143	0.175	0.217	0.363	0.617
	R_i	-3.12	-0.57	-0.16	0	0.14	1.86
	L	-10.4	-29.0	-137	∞	163.9	28.9
	μ	-191	-84.9	-21.1	0	13.2	27.0
	s	-1.98	-1.89	-1.23	0	4.61	6.37
0.50	u_*	0.547	0.649	0.714	1.068	0.554	0.176
	p	0.189	0.262	0.311	0.334	0.447	0.419
	R_i	-2.66	-0.62	-0.05	0	0.07	1.23
	L	-14.1	-70.8	-568	∞	332.0	65.0
	μ	-236	-55.9	-7.7	0	10.2	16.5
	s	-8.55	-3.57	-1.21	0	3.50	1.94

where k is the von Karman constant ($= 0.40$), u_* is the friction velocity, z_0 is the surface roughness parameter, and L is the Monin-Obukhov stability parameter. In Eq. (6.127), $\psi(z/L)$ is a universal scaling function, the form of which is dependent on stability; note that for nonneutral conditions there is no uniform agreement on the exact form. However, the following empirically derived functions are often used in atmospheric applications.[78,79] For stable conditions,

$$\psi\left(\frac{z}{L}\right) = 4.7\left(\frac{z}{L}\right) , \tag{6.128a}$$

and for unstable conditions,

$$\psi\left(\frac{z}{L}\right) = \ln\left(\frac{1 + x^2}{2}\right) + 2\ln\left(\frac{1 - x}{2}\right) - 2\tan^{-1}x + \frac{\pi}{2} , \tag{6.128b}$$

where

$$x = \left(1 - 15\frac{z}{L}\right)^{1/4} , \tag{6.128c}$$

and for neutral conditions,

$$\psi\left(\frac{z}{L}\right) = 0 . \tag{6.128d}$$

Some representative values of the wind speed power law exponent p, the friction velocity u_*, the Monin-Obukhov length L, and other often used stability parameters are listed in Table 6.27. Other parameters in Table 6.27 are the Richardson number R_i, the Kazanski-Monin stability parameter μ, and the static stability S.

6.6.4 Surface Roughness Parameter

Surface conditions have a marked influence on turbulent intensities and the wind speed profile near the ground. The surface roughness parameter z_0 is an empirical factor to account for roughness that enters directly into the equations for wind speed vertical profile. This parameter is also incorporated into empirical transport and diffusion models. The magnitude of z_0 can vary from near zero for smooth surfaces to about 10 cm for tall grass to a few meters for forests and low hills. An often-used empirical equation relating z_0 to the height of the ambient surface elements is the logarithmic relationship[80,81]

$$\ln(z_0) = 1.19\ln(z_e) - 2.85 \quad [\text{m}] , \tag{6.129}$$

where z_e is the mean height of surrounding terrain elements such as trees, grass, hills, etc.

6.6.5 Atmospheric Mixing Height

The atmospheric mixing height can be defined as the height above which dynamic processes are not influenced by the surface conditions. The mixing height is about the same magnitude as the inversion height under stable conditions (approximately 10 to 100 m) but can be as high as a few kilometers for unstable conditions. The significance of the mixing height to obscuration operations is that ground releases seldom penetrate beyond this upper limit. Some typical values of the mixing height for various atmospheric conditions are listed in Table 6.27.

6.6.6 Atmospheric Stability

The term *stability,* as applied to the atmosphere near the earth surface, refers to some measure of the ratio of buoyant to mechanical forces acting on turbulent eddies. The most common quantitative measures of stability are the Richardson number R_i, the Monin-Obukhov length L, the Kazanski-Monin stability μ, and the static stability S (Table 6.27), all of which are defined in various sources throughout the literature. The first three are essentially equivalent measures of the dynamic stability that accounts for both mechanical and thermal mechanisms. The last, the static stability, accounts for thermal mechanisms only. These definitions, although useful in theoretical studies, are difficult to apply in practical situations because the required data are usually unavailable. A more pragmatic approach employs the widely used Pasquill[82] stability category (PSC) method that ranks stability into broad categories labeled A through G (or 1 through 7) in order of increasing stability according to the following scheme:

PSC	Condition
A(1)	Extremely unstable
B(2)	Moderately unstable
C(3)	Slightly unstable
D(4)	Neutral
E(5)	Slightly stable
F(6)	Moderately stable
G(7)	Extremely stable

Unstable conditions (categories A to C) usually occur in daytime and generally imply high levels of turbulence, with air temperature decreasing with height (i.e., a lapse condition). Stable conditions (categories E to G) usually occur at night and generally imply low levels of turbulence, with air temperature increasing with height (i.e., an inversion condition). Neutral conditions can occur either day or night.

An advantage of the PSC scheme is that once the appropriate category is established, other difficult to determine parameters, such as diffusion coefficients, can be inferred from look-up tables.[83] Another advantage is that several practical schemes have been devised to determine the PSC from common meteorological observations.[84] A more quantitative approach relating surface

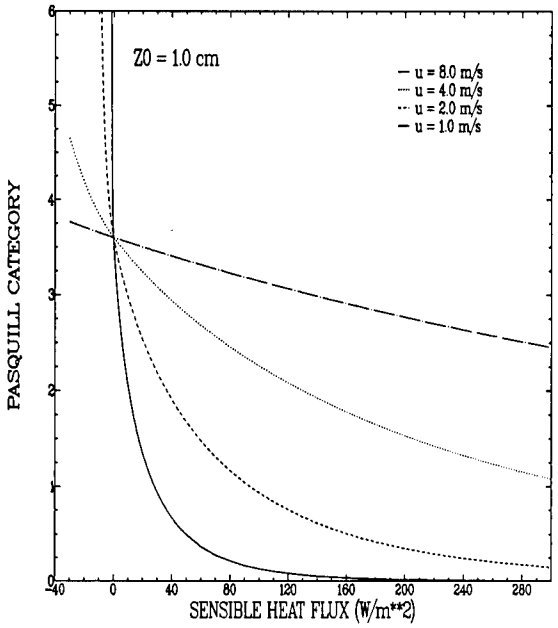

Fig. 6.21 Plot of Pasquill stability class as a function of wind speed and sensible heat flux density.

heat flux H and wind speed U to the PSC is shown in the plot of Fig. 6.21. The plot is based on a scheme originally developed in Smith[85] for unstable conditions and extended to the general case in Sutherland et al.[79]

6.6.7 Relative Humidity

The major direct impact of increased relative humidity on obscuration, for the unperturbed, clear atmosphere (devoid of clouds and fog), is increased electromagnetic absorption resulting from water vapor in the 8- to 14-μm spectral window. Generally, for a given temperature, the result of increased atmospheric moisture is a decrease in thermal band transmission and an increase in thermal emission. As discussed in previous sections, relative humidity also has a significant effect on the growth of hygroscopic aerosols and therefore haze levels.[86,87] Effects of moisture can also influence ambient temperature profiles and stability, especially during phase transitions where large amounts of latent heat are exchanged.

6.6.8 Ambient Radiation

The term *ambient radiation,* as used here, refers to electromagnetic energy of all wavelengths propagated from all directions over the upper (sun plus sky) and lower (surface) hemispheres. The ambient radiation influences obscurant behavior in two major ways: first, as the primary source of electromagnetic radiation that ultimately either propagates through or scatters off the obscurant and, second, as the primary source of heat energy that generates turbulence and subsequently causes obscurant diffusion.

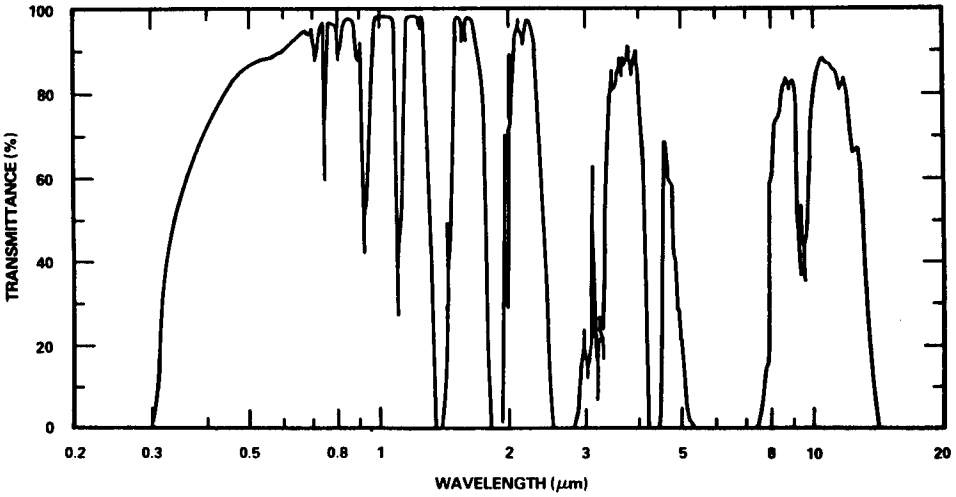

Fig. 6.22 Spectral vertical transmission of a standard atmosphere (0.20 to 10 μm).

The sources and processes that comprise ambient radiation exhibit an involved wavelength dependence and, for strict accuracy, all radiative quantities should be treated on a wavelength-by-wavelength basis. In atmospheric applications, however, several wavelength regions naturally lend themselves to separation into discrete bandpasses because of certain common properties in the bandpass. In meteorological applications, the electromagnetic spectrum is usually separated into a short-wave band that has solar origin and a long-wave band that has thermal origin. Other special wavelength regions are identified as *windows* because of their overall high transparency to electromagnetic radiation (Fig. 6.22).

For reference purposes we define the following wavelength bands that have special significance in meteorological and obscuration applications:

Band	Wavelengths	Window	Wavelengths
Short wave (solar)	0.30–2.00 (μm)	Visible	0.40–0.70 (μm)
Photopic	0.40–0.70	Near IR	0.70–1.20
Long wave (thermal)	2.0–200.0	Mid IR	3.00–5.00
		Far IR	8.00–14.0

Virtually all of the ambient radiation in the short-wave region has true origin in the sun (including lunar reflection). In this spectral region, sky and surface irradiance components arise almost entirely from scattering and reflection of radiation originally emitted by the sun. In the long-wave region, the solar emissions are diminished and the situation is reversed. At these long wavelengths, the ambient radiation originates in thermal emissions from the

surface and sky (including clouds). The ambient radiation is dominated by the solar band in daytime and by the thermal band at night.

6.6.9 Equation for Short-Wave Global Irradiance

A simple semiempirical estimate of the short-wave surface irradiance at the earth surface for cloudless conditions accounting for both the direct and diffuse components is[88]

$$G\downarrow = \mu_0 F_0 \exp(-B/\mu_0)$$

$$+ \frac{(2\mu_0 - 1)2\mu_0(1 - A_0)\exp(\mu B/\mu_0) + (1 - 2A_0\mu_0) \times \exp\{-[\beta(2\mu_0 - 1) + 1]B/\mu_0\}}{2\mu_0(1 - A_0) - (1 - 2A_0\mu_0)\exp[-\beta(2\mu_0 - 1)B/\mu_0]}\mu_0 F_0 \ , \qquad (6.130)$$

where μ_0 ($\mu_0 = |\cos\theta_0|$) is the solar (or lunar) zenith angle; F_0 is the extraterrestrial solar/lunar beam irradiance; B is the vertical optical depth of the atmosphere; A_0 is the reflectivity, or albedo, of the earth surface; and β is an empirical parameter for the planetary backscatter and can vary from about 0.10 for a relatively clear day to about 0.30 for a hazy day.

The vertical optical depth of the atmosphere B can be computed for various meteorological conditions using the atmospheric transmittance model LOWTRAN,[89] such as is used for the plot of Fig. 6.22. For wavelengths where absorption is weak, the optical depth for any wavelength λ (in micrometers) can be estimated from Rayleigh scattering $B = (\lambda/0.3128)e^{-4.09} + \beta\lambda e^{-a}$, where the coefficient a is near unity and the coefficient β has a value between 0 for a perfectly clear Rayleigh atmosphere and 0.30 for a hazy atmosphere.

6.6.10 Equation for Long-Wave Global Irradiance

Equation (6.130) is based on a two stream radiative transfer approximation.[88] It is most accurate at high solar angles and low surface albedos, and applies only to short-wave radiation. In the long-wave regime, the solar output is negligible, and thermal emissions from the sky and surroundings are the dominant source of ambient radiation. A useful empirical relation for estimating the surface irradiance over the long-wave and infrared window regions in terms of common surface observations (again for cloudless conditions) is[90,91]

$$G_l^{\downarrow} = (\sigma t_0^4)[0.66 + 3.56 \times 10^{-5}(e_0)\exp(1500/t_0)] \ , \qquad (6.131a)$$

$$G_w^{\downarrow} = (\sigma t_0^4)[0.24 + 2.98 \times 10^{-8}(e_0)^2\exp(3000/t_0)] \ , \qquad (6.131b)$$

where σ is the Stefan-Boltzmann constant (5.67×10^{-8} W m^{-2} K^{-4}), t_0 and e_0 are the ambient temperature in kelvins and water vapor partial pressure in millibars, both determined at or near the surface (usually 1.5 m).

Table 6.28 Values of $a(i)$ To Be Used in Eq. (6.132)

Value of a(i)	t > 0° C	t < 0° C
a_0	6.107799961E+0	6.109177956E+0
a_1	4.436518521E-1	5.034698970E-1
a_2	1.428945805E-2	1.886013408E-2
a_3	2.650648471E-4	4.176223716E-4
a_4	3.031240396E-6	5.824720280E-6
a_5	2.034080948E-8	4.838803174E-8
a_6	6.136820929E-11	1.838826904E-10

6.6.11 Equations for Partial (Water) Vapor Pressure

In most applications, the ambient dew point temperature or relative humidity is more accessible than the water vapor partial pressure. An empirical relationship connecting the three parameters is[92]

$$e(x) = a_0 + x[a_1 + x(a_2 + x\{a_3 + x[a_4 + x(a_5 + a_6x)]\})] \ , \tag{6.132}$$

where the substitution $x = t_{\text{dew}}$ (the dew point temperature in degrees Celsius) gives the actual water vapor partial pressure in millibars, and substitution of $x = t_0$ (ambient air temperature in degrees Celsius) gives the saturation water vapor partial pressure. The relative humidity is then given as $f = e(x = t_{\text{dew}})/e(x = t_0)$. Values of the constants in Eq. (6.132) are given in Table 6.28.

6.6.12 Cloud Parameterization Schemes

In the presence of significant cloud cover, the equations for clear sky irradiance must be modified to account for increased extinction and scattering in the short-wave region and increased thermal emission in the long-wave region. Rigorous solutions to the problem are, of course, quite involved because of the sheer complexity, and we again resort to semiempirical approximations that, although limited in pure accuracy, are reasonably reliable in indicating sensitivities. Two common empirical schemes that account for cloud cover for short-wave and long-wave regions are given by[93]

$$G_{s,\text{cloud}}^{\downarrow} = G_s^{\downarrow}(1 - 0.80N_l - 0.50N_m - 0.20N_u) \ , \tag{6.133a}$$

$$G_{l,\text{cloud}}^{\downarrow} = G_l^{\downarrow}[1 + 74N_l + 62N_m + 40N_u(1 - N_l)(1 - N_m)] \ , \tag{6.133b}$$

where N_l, N_m, and N_u are, respectively, the fractional cloud cover for lower (0.0 to 1.2 km), middle (1.2 to 3.6 km) and upper (3.6 to 8.0 km) cloud levels.

It is understood that the expressions here represent empirical estimates and that more detailed calculations can be made using more sophisticated models provided that the detailed profiles of temperature, moisture, etc., are known.

6.7 PROPAGATION EFFECTS IN ACQUISITION/PERCEPTION MODELS

6.7.1 Use of Obscurants in Concealment

Obscurants can be used as countermeasures to target acquisition. For concealment, an obscurant can be introduced with a total transmittance sufficiently low to reduce the target radiant intensity below some sensor-dependent threshold. However, diffusely scattered ambient energy from the cloud also plays a role in reducing the contrast of the target against its background and thus also affects the required threshold transmittance. In this section, we consider the amount of obscurant required to produce total obscuration and concealment.

6.7.1.1 Detectable Energy Reduction. Detection of a target requires that the received radiant power from the target (a signal that also depends on transmittance losses) be sufficiently different from the received power not coming from the target (background, atmosphere, and sensor noise) that it exceeds some sensor-dependent (signal-to-noise) threshold. In this interpretation, *noise* can thus include average and fluctuating radiance from the atmosphere and the background surrounding the target as well as that introduced by the sensor.

If the average, or dc, component of the received radiance is important to detection or display, then one can identify apparent contrast of the target against the background as an important quantity. If an average, or dc, component can be removed, such as in scanning IR detection systems, then it is the absolute difference in target and background radiance that is important. (However, the dc component can still be indirectly significant because it determines where the detector must operate within its available dynamic range, thus affecting sensor linearity and sensor noise over that range.)

Contrast is reduced with distance from the target. The *zero-range* or *inherent* contrast $C(0)$ of an object of radiant intensity I_t against a background of radiant intensity I_b is defined as

$$C(0) = \frac{I_t(0) - I_b(0)}{I_b(0)} \ . \tag{6.134}$$

Note that the range here is measured with respect to distance from the target. The background radiance $I_b(0)$ is the background *as seen from the target position,* by definition, at zero range. Thus, a physical background surface, if any, could be some distance behind the target, and the background radiant intensity $I_b(0)$ as seen from the target position can already include some atmospheric propagation effects.

The radiant intensity of the target observed at range s is given by

$$I_t(s) = I_t(0)T(s) + I_p(s) \ , \tag{6.135}$$

where $I_p(s)$ is a combination of scattered radiation from haze and obscurant aerosols and emitted radiation along the path. It is therefore called the *path radiance.* Similarly the radiant intensity of the background at the same distance s is

$$I_b(s) = I_b(0)T(s) + I_p(s) \ . \tag{6.136}$$

Thus, the apparent contrast at range s is

$$C(s) = \frac{I_t(s) - I_b(s)}{I_b(s)}$$

$$= \frac{I_t(0) - I_b(0)}{I_b(0) + I_p(s)[1/T(s)]} = \frac{C(0)}{1 + [I_p(s)/I_b(0)][1/T(s)]} \ . \tag{6.137}$$

Equation (6.137) can be compared to that for the Duntley factor described in Sec. 6.5.5. In fact, the formalism of this section is essentially equivalent to that of Sec. 6.5, but is derived somewhat differently to emphasize more directly the way in which path radiance and transmittance are typically found in existing acquisition models.

The ratio of $C(s)$ to $C(0)$ from Eq. (6.137) is called the *contrast transmittance,* as distinct from the direct transmittance $T(s)$. Contrast transmittance quantifies the fractional loss in contrast with range over a given propagation path.

To understand path radiance contributions one must examine the details of how the original energy from the target or background is lost and how the scattered and emission energy builds up along the propagation path as the range s increases. The change in radiant intensity dI over an increment of range ds along the propagation path in the angular direction $\boldsymbol{\Omega}$ at a distance s from the target is

$$\frac{dI(s;\boldsymbol{\Omega})}{ds} = \alpha c(s)[-I(s;\boldsymbol{\Omega}) + \omega_0 \int_{\boldsymbol{\Omega}'} I_{\text{in}}(s;\boldsymbol{\Omega}')P(\boldsymbol{\Omega};\boldsymbol{\Omega}')\, d\boldsymbol{\Omega}' + (1 - \omega_0)B(\lambda,t)] \ . \tag{6.138}$$

Radiant intensity $I_{\text{in}}(s;\boldsymbol{\Omega}')$ is the incident external illumination at point s from direction $\boldsymbol{\Omega}'$ that is available for scattering into the LOS. It thus includes the diffusely transmitted radiance from sky, terrain, sun and other sources as discussed earlier. The phase function $P(\boldsymbol{\Omega};\boldsymbol{\Omega}')$ defines the scattering directional dependence averaged over single particle scattering of incident unit radiance from direction $\boldsymbol{\Omega}'$ into the propagation path direction $\boldsymbol{\Omega}$. The phase function, as it is written here, is normalized to 1 when integrated over all directions. The integral of I_{in} times P over all incident directions $\boldsymbol{\Omega}'$ thus provides the cumulative contribution to the LOS radiance at point s in direction $\boldsymbol{\Omega}$. Finally, $B(\lambda,t)$ is the Planck emission source term (if any) for a blackbody of temperature t in isotropic radiance per unit solid angle.

Under certain conditions, Eq. (6.138) can be integrated to a simple result. In particular, suppose $I_s(s;\boldsymbol{\Omega})$, defined as the last two terms inside the square brackets, is constant or slowly varying with s:

$$I_s(s;\boldsymbol{\Omega}) = \omega_0 \int_{\boldsymbol{\Omega}'} I_{\text{in}}(s;\boldsymbol{\Omega}')P(\boldsymbol{\Omega};\boldsymbol{\Omega}')\, d\boldsymbol{\Omega}' + (1 - \omega_0)B(\lambda,t) \ . \tag{6.139}$$

Then Eq. (6.138) is easily integrated to give

$$I(s;\Omega) = I(0;\Omega)T(s) + I_s(\Omega)[1 - T(s)] \ , \tag{6.140}$$

where the direct transmittance $T(s)$ is, as usual,

$$T(s) = \exp\left[-\alpha \int_0^s C(s')\, ds' \right] . \tag{6.141}$$

The quantity I_s is called the *path radiance limit.* Because the direction Ω is now implied to point along the propagation path, it can be formally suppressed and, comparing Eq. (6.140) with Eq. (6.136),

$$I_p(s) = I_s[1 - T(s)] \ . \tag{6.142}$$

It follows that if the aerosol concentration is increased along the line of sight, and correspondingly the transmittance decreases to 0, then the path radiance approaches I_s. Apparent contrast under conditions of constant I_s is thus equivalently found from

$$C(s) = \frac{C(0)}{1 + [I_s/I_b(0)]\{[1/T(s)] - 1\}} = \frac{C(0)}{1 + S_g\{[1/T(s)] - 1\}} \ , \tag{6.143}$$

which is often the fundamental equation of propagation effects on contrast that is found in acquisition models.

The ratio $I_s/I_b(0)$ is called the *sky-to-ground ratio* S_g. The origin of this name is based on a specific idealized case of a horizontal propagation path over uniform terrain and illumination conditions. Then, S_g is simply the ratio of the sky brightness just above the horizon to the background radiance just below the horizon.

More generally, however, a value of S_g can be defined for any path and orientation. Note that even though Ω was explicitly suppressed as a variable, contrast transmittance and S_g do depend on the specific orientation of the LOS, in particular with respect to sun angle.

Table 6.29 shows variations that can occur in S_g for examples of slightly depressed downward-looking angles and various sun angles at visual wavelengths. A clear sky with the sun 30 deg above the horizon and a Lambertian terrain surface of reflectance 0.3 are assumed. A phase function for rural haze and 70% relative humidity is also assumed. The integral for I_s and the value of $I_b(0)$ were computed, and their ratio taken to determine S_g. (To simplify the integration, the ambient sky radiance as well as radiance from the terrain were each assumed to be uniform.) Results are shown in Table 6.29 for various observation angles with respect to the sun (180 deg for the sun at the observer's back) and for small down-looking depression angles with respect to the horizon. The value of S_g is particularly large when looking near the direction of the sun, and S_g decreases with larger depression angles because there is less scattered radiance in the forward angles from the terrain than from the sky.

For finite obscurant clouds the scattered ambient illumination also contributes[94] to S_g. Figure 6.23 shows the product of sky-to-ground ratio times terrain albedo A_g for different optical depths of a vertical smoke *slab.* Values

Table 6.29 Examples of Sky-to-Ground Ratios for a Rural Haze, Sun at 30 deg Above the Horizon and Lambertian Terrain of Reflectance 0.3

Solar Angle (deg) with the LOS	Computed Sky-to-Ground Ratios		
	5° Depression	10° Depression	20° Depression
40	9.16	9.03	n/a
60	4.73	4.61	4.41
80	3.13	3.00	2.81
100	2.53	2.40	2.21
120	2.36	2.24	2.04
140	2.43	2.30	2.10
160	2.62	2.49	2.29
180	2.95	2.83	2.63

are computed for a smoke with single-scattering albedo of 1.0 and Henyey-Greenstein phase function with asymmetry factor of 0.875 using multiple-scattering tables.[95] Curves marked 0 are for the sun 30 deg above the horizon on the far side of the cloud. Curves marked 180 are for the sun 30 deg above the horizon at the observer's back. Both the contribution of forward-scattered (direct) sunlight and radiant flux averaged over the face of the cloud are shown. Figure 6.24 shows the results computed for a finite (cubic) cloud with the same optical properties as for the slab. These flux-derived values over the faces of the cloud show that S_g falls off with optical depth for an observer with the sun on the far side of the cloud and increases for the sun at the observer's back. At an optical depth of about 8 to 10, the curves cross and the cloud is thick enough that at higher optical depths the light escaping from the top and sides of the cloud causes shadowing effects.

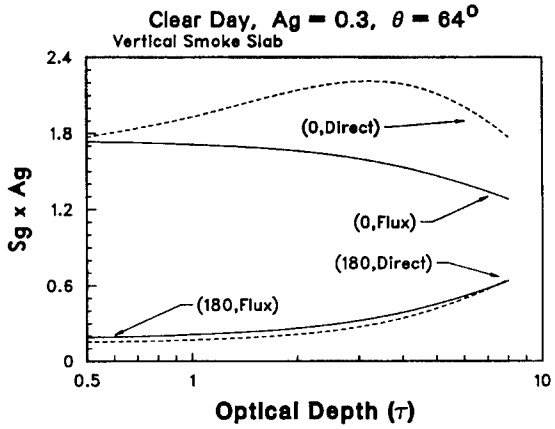

Fig. 6.23 Example of computed white smoke sky-to-ground ratio versus optical depth for a two-dimensional vertical slab using solar flux and direct solar illumination corrections. Sun elevation is 30 deg, clear day, g = 0.875. Solar Azimuths: 0 deg, sun beyond the cloud, and 180 deg, sun at observer's back.

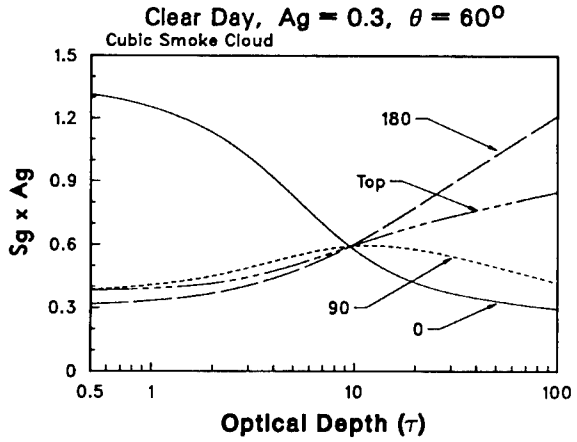

Fig. 6.24 Example of computed white smoke sky-to-ground ratio versus optical depth for a three-dimensional cubic cloud. Sun elevation is 32 deg, clear day, $g = 0.875$. Observation angles with respect to sun are 0 deg, sun beyond the cloud; 180 deg, sun at observer's back; 90 deg, sun off to observer's side; and top, observer above cloud.

Scanning thermal sensors are often used to remove the mean radiance background from the incoming radiance. For a perfect sensor only the difference in radiance between the target and its background is then important. The path radiance from both the target and its background is thus removed by the scan if the path radiance is constant. Fluctuations in path radiance and transmittance, discussed in a previous section, still remain, however, such that

$$\Delta t_c = T(s)(t_{ct} - t_{cb})[1 + f_T \ln(T)] \ , \tag{6.144}$$

where t_{ct} is the target radiant temperature, t_{cb} is the background radiant temperature, T is the mean transmittance, and f_T is a propagation fluctuation between target LOS and background LOS. The sensor applies gain to this detected temperature difference to overcome transmittance losses. This introduces additional sensor noise.

A system can respond differently to different levels of the dc radiance. An obscurant that is much warmer than the background and that has a small single-scattering albedo ω_0 can contribute significant path radiance along the LOS while absorbing energy from the target and background. There are also some solar scattering effects at the shorter infrared wavelengths out to about 5 μm. However, a significant contribution to path radiance can also be present from the ambient atmosphere if the detector is not filtered to confine its response inside the atmospheric windows. Beyond the edges of the atmospheric windows the atmospheric path radiance can be especially large, while suppressing the radiant signatures from the target and background at these wavelengths. The magnitude of this effect must be computed by integrating the wavelength-dependent path radiance times the wavelength-dependent sensor response function.

Staring thermal sensors that detect the absolute radiance across the scene require that thermal contrast be used. An effective S_g can be computed in the

discussed manner using Eqs. (6.139) and (6.143). Scattering of thermal radiance from terrain and cloudy skies can still be an important addition to the thermal emission at thermal wavelengths for dust and other obscurants with nonzero single-scattering albedos. Optically dense obscurant clouds often present a thermal signature comparable to that of the background because of scattering of radiance from the terrain below it. The cloud can appear effectively cooler than the background, however, if a clear cold sky does not provide ambient radiance to the scattering. Detailed calculations of I_s are required for specific geometries.

6.7.1.2 Resolvable Temperature and Resolvable Contrast Thresholds. The minimum resolvable contrast (MRC) and minimum resolvable temperature (MRT), or noise equivalent detectable temperature (NEΔT), are sensor specific characteristics that determine the noise-limited thresholds for detection and recognition of objects. They vary with SNR and with resolution of the displayed target. Define a spatial (angular) frequency f in cycles per milliradian in terms of scene details of scale h in meters observed at range R in kilometers as

$$f = \frac{R}{h} \,. \tag{6.145}$$

Perception models are often employed to determine the level of detail or scale h required to detect, recognize, or identify a target. These range from h equal to the average or maximum target dimension for 50% probability of detection to ⅓ to ¼ of that dimension for 50% probability of recognition to about ⅙ to ⅛ of that dimension for 50% probability of identification. These matters are well documented elsewhere.[96]

Assuming magnification factors are included in the MRC(f) function for the sensor, the required transmittance for total obscuration is

$$T_{\text{thresh}} = \frac{S_g}{(S_g - 1) + [|C_0|/\text{MRC}(f)]} \,, \tag{6.146}$$

where S_g is the sky-to-ground ratio. If S_g happens to be 1 (typically a sky background), then the threshold transmittance is simply the ratio of the MRC(f) of the sensor to the inherent contrast of the target. The MRC curve generally increases with increasing frequency f and can depend on ambient illumination levels. The transmittance threshold for use with temperature differences (excluding fluctuations) is similarly

$$T_{\text{thresh}} = \frac{\text{MRT}(f)}{|t_{ct} - t_{cb}|} \,. \tag{6.147}$$

The transmittance threshold thus determines the required CL of the obscurant to be

$$\text{CL}_{\text{thresh}} = -\frac{\ln(T_{\text{thresh}}/T_{\text{atmos}})}{\alpha} \,, \tag{6.148}$$

where T_{atmos} is the transmittance already provided by the ambient atmosphere. Corrections for variations in S_g with optical depth, forward scattering of the target signature, atmospheric MTF, and fluctuations can also be made to these simple relationships. The threshold CL is then determined by iteratively adjusting parameters.

6.7.1.3 Benefits and Problems with Total Obscuration. Total target obscuration can be effective for concealment if the obscurant cloud provides a hidden area much larger than the target. Large-area smoke can force aircraft to higher altitudes to reduce slant path lengths through the smoke. Thick obscurant clouds can also effectively absorb or scatter laser energy away from targets.

A major drawback to using obscurants is that the cloud itself can act as a cue to the possible presence of targets. Other factors are the amounts of aerosol needed to keep a target obscured for long times, the need to see and operate within the obscured environment, the difficulty in performing target acquisition back through the cloud, and the "holes" generated by atmospheric turbulence if the cloud is not physically thick enough to sample a range of the largest eddies.

6.7.2 Use of Obscurants in Camouflage

It is not always necessary to completely obscure a target to reduce acquisition probability. The sensor noise is not always the limiting factor for target acquisition. Partial obscuration, background clutter, camouflage, optical turbulence, and contrast losses each contribute to reducing target acquisition probability. Even with the dc component removed, any spatial fluctuations in obscurant optical properties and variations (texture, clutter, etc.) in the physical background and camouflaged target remain in addition to the internal sensor noise.

The detection of a camouflaged object thus depends on whether the contrast or radiance difference between some perceivable feature of the object and its surroundings exceeds some (sensor-dependent) thresholds at one or more spatial frequencies. This section considers how the atmosphere affects the contrast and radiance of such features.

6.7.2.1 Connection with Meteorological Visibility. Meteorological visibility or visual range is related to but does not necessarily equal the visual detection range of targets at visible wavelengths. It is worthwhile to review the utility and the meaning of meteorological visibility here as an example of the detection problem.

In 1924, Koschmieder derived expressions for visual contrast of objects in the atmosphere useful for estimating meteorological visibility conditions of the ambient atmosphere.[97] Meteorological visibility itself is actually defined in terms of detecting a target under a very specific set of contrast conditions. A meteorological visual range of 20 km, for example, does not imply that *any* object large enough to be resolved can be seen up to that range.

The Koschmieder relation is used extensively in propagation models to estimate a volume extinction coefficient K_{ext} in inverse kilometers at visible wavelengths when a meteorological visibility or visual range V in kilometers is known. The Koschmieder relation is usually written as

$$K_{\text{ext}} = \frac{3.912}{V} \ . \tag{6.149}$$

Once K_{ext} is known, the direct transmittance $T(s)$, which is dimensionless, over any range s in kilometers at visible wavelengths can be determined from

$$T_{\text{tot}}(s) = T_{\text{obsc}} \exp(-K_{\text{ext}} s) \ , \tag{6.150}$$

where T_{obsc} is the transmittance contribution by any additional local obscuring aerosol and the exponential term accounts for ambient haze.

The Koschmieder relation and meteorological visibility measurements are defined only within a very restricted set of operational conditions. In particular, conditions for measuring the meteorological visual range operationally (as discussed more generally in Ref. 97) are as follows:

1. A black object is used as the target [i.e., $I_t(0) = 0$]. Then, from Eq. (6.1), the inherent contrast is -1, independent of the brightness of the background.
2. The target object is large enough to be easily resolved by the eye. Thus, a minimum contrast threshold can be defined unambiguously. (For smaller objects, a greater contrast threshold is required for visual detection at a corresponding higher spatial resolution.)
3. A contrast threshold of 0.02 is required to barely detect the target visually. The visual range, or visibility, is thus that range at which the black target contrast is reduced (in absolute value) to 0.02. This threshold is arguably more traditional than factual, because extensive perception experiments have indicated that the threshold can range from 0.01 to 0.15, although 0.02 to 0.05 seem to be most favored. Nonetheless, *as a definition* there is nothing wrong with choosing 0.02.
4. The prevailing sky-to-ground ratio S_g is 1.0. This condition can be seen to be required, so that from Eq. (6.143),

$$C(s) = C(0)T(s) = C(0) \exp(-K_{\text{ext}} s) \ . \tag{6.151}$$

Then, at the visual range $s = V$ and threshold contrast 0.02,

$$0.02 = \exp(-K_{\text{ext}} V) \ , \tag{6.152}$$

so that Koschmeider's relation results:

$$K_{\text{ext}} = -\frac{\ln(0.02)}{V} = \frac{3.912}{V} \ . \tag{6.153}$$

From a practical standpoint a sky-to-ground ratio of 1 can be provided if the background $I_b(0)$ is the horizon sky. This follows because typically, $I_b(s) = I_b(0)$ for the horizon sky. Combining Eqs. (6.136) and (6.142), I_s then also equals $I_b(0)$, and S_g is 1.

However, if the inherent contrast of an actual object used to estimate meteorological visibility is not -1, or S_g is not 1, then K_{ext} can still be determined

by solving Eqs. (6.143) and (6.150). Similarly, in computing whether an actual target has enough contrast to be detectable to the eye, one must use a sky-to-ground ratio appropriate to the geometry of the scenario in addition to the appropriate transmittance, even if meteorological visibility is known or can be determined from K_{ext} and the Koschmieder relation.

Thus, visibility and visual range are meteorological terms used to describe the ideal *detection* of a uniform object against a uniform background for low spatial frequencies and under a very specific set of circumstances. Modification of one's ability to detect such an object was discussed in Sec. 6.7.1 with respect to changes in inherent contrast, apparent contrast, and spatial frequency. The changes in contrast were shown to vary with transmittance, sky-to-ground ratio, and range.

Suppose, however, that the target object has no particularly dominant contrast feature associated with any single dominant spatial frequency. Then, as shown in the following sections, one must apply atmospheric and obscuration effects to distributions of radiances.

6.7.2.2 Obscurant Effects on Edges, Moments, and Image Metrics

Gray-Level Histograms. Define an image as an array of pixels of radiant intensities $I(x,y)$. An intensity histogram $N(i)$ totals the number of pixels having intensities between $I(i)$ and $I(i + 1)$ for a series of intervals $i = 1, 2, \ldots$ that span the range of intensities. Although it does not provide information about spatial correlations between the pixels, a histogram does provide information on the average intensity and the spread in intensities. It can have different modes that can be identified with different regions in the image, and target pixels can stand out from the distribution of background pixel intensities if there is sufficient contrast.

A normalized histogram can be used to estimate the probability that any pixel chosen at random will have a given intensity between $I(i)$ and $I(i + 1)$. Obscurant properties are generally uncorrelated with the scene background except, perhaps, for the overall effects of terrain and sky illumination on path radiance. Thus, using the path radiance limit I_s, the received intensity at a specific pixel (x,y) partially obscured by an aerosol cloud is

$$I_c(x,y) = T(x,y)I_b(x,y) + I_s(x,y)[1 - T(x,y)] \ , \tag{6.154}$$

where I_c is the obscured pixel intensity and I_b would be the pixel intensity if obscurant was not present. The path radiance limit I_s, already discussed as part of the sky-to-ground ratio, can vary across an image. Generally, however, I_s varies much more slowly with transmittance changes than does the path radiance I_p. The average values over the image can be found from the histograms as

$$I_c^{\text{av}} = \int I\, P_c(I)\, dI, \quad I_b^{\text{av}} = \int I\, P_b(I)\, dI \ ,$$

$$T^{\text{av}} = \int T\, P_T(T)\, dT \ , \quad I_s^{\text{av}} = \int I\, P_s(I)\, dI \ , \tag{6.155}$$

where probabilities can be estimated from the histograms as

$$P(I) = \frac{N(I)}{\int N(I)\, dI} \ . \tag{6.156}$$

Now assume the transmittance T, path radiance limit I_s, and clear air image I_b are statistically independent. For any pixel chosen at random, the joint probability that it has values I_b, I_s, and T is then

$$P(I_b,I_s,T) = P_b(I_b)P_s(I_s)P_T(T) \ . \tag{6.157}$$

It follows that

$$I_c^{\text{av}} = I_b^{\text{av}} T^{\text{av}} + I_s^{\text{av}}(1 - T^{\text{av}}) \ , \tag{6.158}$$

and if the variances are defined as

$$\begin{aligned} \sigma_c^2 &= \int [I_c(I) - I_c^{\text{av}}]^2 P_c(I)\, dI \ , \quad \sigma_b^2 = \int [I_b(I) - I_b^{\text{av}}]^2 P_b(I)\, dI \ , \\ \sigma_T^2 &= \int [T(T) - T^{\text{av}}]^2 P_T(T)\, dT \ , \quad \sigma_s^2 = \int [I_s(I) - I_s^{\text{av}}]^2 P_s(I)\, dI \ , \end{aligned} \tag{6.159}$$

then one can also derive that

$$\sigma_c^2 = \sigma_b^2[\sigma_T^2 + (T^{\text{av}})^2] + \sigma_T^2(I_s^{\text{av}} - I_b^{\text{av}})^2 + \sigma_s^2[\sigma_T^2 + (1 - T^{\text{av}})^2] \ . \tag{6.160}$$

These equations quantify the effects of partial obscuration on the histogram distribution mean intensity and on its width, as characterized by a standard deviation. The first of the three additive terms on the right-hand side of Eq. (6.160) represents transmittance effects on the histogram. The second additive term is significant when the obscuring cloud has an average radiance that is very different from that of the clear air scene. The third term is often negligible. It quantifies the effects of variance in path radiance limit when the cloud has low transmittance or a wide variation in transmittance. Note that the assumption of independent probability between T and I_s is not strictly valid because I_s has a moderate dependence on optical depth (see Figs. 6.23 and 6.24) for optical depths larger than about 3. Tables 6.30 and 6.31 give values of both T^{av} and σ_T for Gaussian-distributed concentrations in continuous obscurant plumes (aerosols released continuously from a point source) and instantaneous obscurant puffs (a momentary release of aerosol from a point source). These tables are useful if the known quantities are the minimum transmittance through the cloud and the transmittance value chosen to define the edges of the cloud.

The predictions of Eq. (6.160) have been compared to histograms of measured clear air and obscured images and were found to be good estimates within a few percent error. They also give reasonable estimates for non-Gaussian clouds, both measured and modeled.[98]

Table 6.30 Estimates of T^{av} for Gaussian Plumes and Puffs Based on Minimum Cloud Transmittance and Cloud Edge Transmittance Definition

Minimum T in Cloud	Maximum T in Cloud Used as Cloud Boundary Definition for a Gaussian Plume				for a Gaussian Puff			
	0.98	0.90	0.70	0.50	0.98	0.90	0.70	0.50
0.02	.43	.38	.21	.14	.63	.49	.32	.22
0.05	.47	.36	.25	.18	.67	.53	.36	.25
0.10	.52	.41	.30	.22	.70	.57	.40	.29
0.20	.58	.49	.37	.30	.74	.62	.46	.35
0.40	.69	.61	.51	.43	.81	.70	.56	.45
0.60	.79	.72	.63	---	.87	.78	.65	---
0.80	.89	.84	---	---	.92	.86	---	---
0.90	.94	---	---	---	.95	---	---	---
0.95	.96	---	---	---	.97	---	---	---

Table 6.31 Estimates of σ_T for Gaussian Plumes and Puffs Based on Minimum Cloud Transmittance and Cloud Edge Transmittance Definition.

Minimum T in Cloud	Maximum T in Cloud Used as Cloud Boundary Definition for a Gaussian Plume				for a Gaussian Puff			
	0.98	0.90	0.70	0.50	0.98	0.90	0.70	0.50
0.02	.36	.30	.21	.14	.32	.29	.22	.15
0.05	.35	.29	.20	.13	.30	.27	.20	.14
0.10	.32	.27	.19	.12	.27	.25	.18	.12
0.20	.28	.23	.16	.09	.23	.21	.15	.09
0.40	.20	.16	.09	.03	.16	.15	.09	.03
0.60	.13	.10	.03	---	.11	.09	.03	---
0.80	.06	.03	---	---	.05	.03	---	---
0.90	.03	---	---	---	.02	---	---	---
0.95	.01	---	---	---	.01	---	---	---

Moments. Image moments determine centroid positions of objects in images and can be used as features for target classification. The image moment m_{pq} is defined as

$$m_{pq} = \iint x^p y^q I(x,y)\, dx\, dy \ . \tag{6.161}$$

The translation-invariant (central) moment is M_{pq}:

$$M_{pq} = \iint (x - \mu_x)^p (y - \mu_y)^q I(x,y)\, dx\, dy \ , \tag{6.162}$$

where μ_x is m_{10}/m_{00} and μ_y is m_{01}/m_{00}. The central moments are independent of the origin chosen for x and y.

Scaled moments are also used. For example, moments that are invariant with respect to range (i.e., object size in the image) are sometimes defined as

$$N_{pq} = \frac{M_{pq}}{M_{00}^{(p+q+2)/2}} \cdot \tag{6.163}$$

The N_{pq} moments N_{11}, N_{02}, N_{20}, N_{12}, N_{21}, N_{03}, and N_{30} are also sometimes combined into seven Hu moments[99] P_1, P_2, ..., P_7, which are also invariant with respect to rotation of the image.

Partial obscuration affects these moments in somewhat different ways.[100] For example, normalized (noncentral) moments under obscured conditions, which can be defined as m'_{pq}/m'_{00} are related to the clear air moments m_{pq}/m_{00} by

$$\begin{aligned}\frac{m'_{pq}}{m'_{00}} &= \frac{\iint x^p y^q [TI(x,y) + I_p(x,y)]\, dx\, dy}{\iint [TI(x,y) + I_p(x,y)]\, dx\, dy} \\ &= \frac{m_{pq}/m_{00} + 1/T \int x^p y^q [I_p(x,y)/m_{00}]\, dx\, dy}{1 + 1/T \left[\int I_p(x,y)\, dx\, dy\right] \Big/ \left[\int I(x,y)\, dx\, dy\right]},\end{aligned} \tag{6.164}$$

which can be interpreted as follows. The ratio of the moment of the path radiance across the image to m_{00} is divided by transmittance and added to the unobscured moment m_{pq}/m_{00}. This is then multiplied by a term that is effectively an average contrast transmittance (represented by the terms in the denominator) where the background in the path radiance-to-background radiance ratio (the Duntley factor of an earlier section) is the integrated radiance of the unobscured image m_{00}. Thus, not only is the moment reduced by contrast losses, it is also contaminated by the moment of the obscurant path radiance itself, which dominates when the transmittance is low.

Translation-invariant moments M_{pq} are affected by the shift in μ_x and μ_y as well as contrast effects on the image radiance:

$$\mu'_x = \frac{m_{10}T + \iint x I_p(x,y)\, dx\, dy}{m_{00}T + \iint I_p(x,y)\, dx\, dy} \qquad \mu'_y = \frac{m_{01}T + \iint y I_p(x,y)\, dx\, dy}{m_{00}T + \iint I_p(x,y)\, dx\, dy}, \tag{6.165}$$

so that the central moments become

$$M_{pq} = \iint (x - \mu_x')^p (y - \mu_y')^q [T(x,y)I(x,y) + I_p(x,y)]\, dx\, dy \ . \tag{6.166}$$

The range-invariant moments are therefore very sensitive to atmospheric transmittance. Approximately,

$$N_{pq}' = \frac{M_{pq}'}{M_{00}'^{(p+q+2)/2}} \propto T^{-(p+q)/2} \ . \tag{6.167}$$

Rotationally invariant Hu moments are similarly very sensitive to transmittance. In fact, the Hu moments vary with different powers of transmittance so that Hu moments can even cross when they are plotted versus transmittance. Their approximate dependence on transmittance T is:

$$\begin{aligned} &P_1' \propto T^{-1}P_1 \ , \quad P_2' \propto T^{-2}P_2 \ , \quad P_3' \propto T^{-3}P_3 \ , \quad P_4' \propto T^{-3}P_4 \ , \\ &P_5' \propto T^{-6}P_5 \ , \quad P_6' \propto T^{-4}P_6 \ , \quad P_7' \propto T^{-6}P_7 \ . \end{aligned} \tag{6.168}$$

Edge Enhancement. Edge detection and related gradient operations exploit differences in pixel intensity across the image by enhancing edges along the gradients and extending edges perpendicular to the gradients. The Sobel edge operator for an image pixel array is

$$G_{il} = (G_{il}^{v2} + G_{il}^{h2})^{1/2} \ , \quad G_{il}^{v} = \mathbf{A}_{ij} I_{jk} \mathbf{S}_{kl} \ , \quad G_{il}^{h} = \mathbf{S}_{ij} I_{jk} \mathbf{A}_{kl} \ , \tag{6.169}$$

where the v and h represent vertical and horizontal gradient operations. The matrices **A** and **S** are, respectively, an antisymmetric difference operator and a symmetric spread operator. They have the form

$$\mathbf{A} = \begin{bmatrix} 0 & -1 & 0 & 0 & 0 \\ 1 & 0 & -1 & 0 & 0 \\ 0 & 1 & 0 & -1 & 0 \\ 0 & 0 & 1 & 0 & -1 \\ 0 & 0 & 0 & 1 & 0 \end{bmatrix} \quad \text{and} \quad \mathbf{S} = \begin{bmatrix} 2 & 1 & 0 & 0 & 0 \\ 1 & 2 & 1 & 0 & 0 \\ 0 & 1 & 2 & 1 & 0 \\ 0 & 0 & 1 & 2 & 1 \\ 0 & 0 & 0 & 1 & 2 \end{bmatrix} \ . \tag{6.170}$$

The effects of transmittance T and path radiance $I_s(1 - T)$ on the horizontal component are

$$G_{il}'^{h} = \mathbf{S}_{ij}[T_{jk}I_{jk} + I_{s,jk}(1 - T_{jk})]\mathbf{A}_{kl} \ , \tag{6.171}$$

and similarly on the vertical component. For the simple case where the transmittance and path radiance can be assumed constant over the local 3×3 operator regions, the result is

$$G_{il}'^{h} = T_{il}G_{il}^{h} \tag{6.172}$$

and similarly for the vertical component.

Edge and gradient operations are insensitive to uniform path radiance because $\mathbf{AS} = \mathbf{SA} = 0$. However, as a secondary effect, any added path radiance

reduces the dynamic range available to the gradient operation. Multiplicative mean transmittance rescales the amplitude of the resulting edge map so that transmittance reduction applied to the input image is equivalent to transmittance reduction in the final edge map.

More generally, image noise and fluctuations in transmittance and path radiance are also enhanced in an edge-enhanced image. For example, suppose the additive fluctuations, such as nonuniform path radiance or image noise, can be approximated as having a zero mean, a standard deviation in intensity σ, and an intensity correlation ρ over the two-pixel differencing distance. Then the expected effect on the G'^2 components is to introduce an additional variance of $(1 - \rho)\sigma^2$.

For a small multiplicative fluctuation in transmittance f_T, the additional expected contribution to the G'^2 components is on the order of $T \ln(T)$ times the following fluctuation variance:

$$\langle |f_T(j+1)I(j+1) - f_T(j-1)I(j-1)|^2 \rangle = I(j-1)I(j+1)\langle |f_T(j+1) - f_T(j-1)|^2 \rangle + [I(j+1) - I(j-1)]^2 \langle |f_T(j)|^2 \rangle \ , \tag{6.173}$$

where the $f_T(j)^2$ term is the variance in f_T over a single LOS (one pixel) and the $[f_T(j+1) - f_T(j-1)]^2$ term is the structure function between two parallel LOS (two-pixel separation) as detailed in an earlier section. Fortunately the relatively large Hurst parameter for small LOS separations implies that the transmittance variations will be slow over these pixel separations unless the obscurant cloud is physically thin compared to the largest atmospheric eddies.

Image Metrics. Various image metrics found in the literature also have atmospheric sensitivities. Many metrics based on a ratio or comparison of target to background are so designed, however, that they are insensitive to constant transmittance and constant path radiance in images. Consider a rectangle of pixels surrounding a target and a frame of background pixels surrounding the target rectangle, perhaps with a small boundary region (or *guard band*) of unused pixels in between. The mean intensities and variances are

$$\mu_t = \frac{1}{N_t} \sum_{\text{target}} \sum I(i,j) \ , \quad \mu_b = \frac{1}{N_b} \sum_{\text{background}} \sum I(i,j) \ ,$$
$$\sigma_t^2 = \frac{1}{N_t} \sum_{\text{target}} \sum [I(i,j) - \mu_t]^2 \ , \quad \sigma_b^2 = \frac{1}{N_b} \sum_{\text{background}} \sum [I(i,j) - \mu_b]^2 \ , \tag{6.174}$$

where the average over the target sometimes includes the entire rectangle and other times can be over a mask of pixels belonging to the target alone. Often the number of background region pixels N_b is chosen to equal the number of target region pixels N_t.

For a constant transmittance and constant path radiance, the individual means are modified by multiplying by transmittance and then adding the path radiance. The individual variances, however, are affected only by multiplying by the square of the transmittance, because the path radiance terms cancel out in taking the difference from the mean.

Examples of metrics that are measures of target contrast are the *target interference ratio squared* (TIR^2) and *target-background interference ratio squared* ($TBIR^2$) defined as

$$TIR^2 = \frac{(\mu_t - \mu_b)^2}{\sigma_b^2}, \quad TBIR^2 = \frac{(\mu_t - \mu_b)^2}{\sigma_t \sigma_b}. \tag{6.175}$$

Obviously these metrics are also unaffected by a constant transmittance and constant path radiance because the differencing in the numerator removes the path radiance and the ratio with the variance removes the square of the transmittance. This is also true for variants of these metrics that use for a numerator the mean of the absolute value of the difference in each target pixel from the mean background intensity.

Sensor noise induced by obscurant reductions in signatures, camouflage textures applied to targets, changes in background clutter and fluctuations in path radiance and transmittance, however, do affect these metrics. The effect on histogram variance, Eq. (6.160), obviously has direct application here to the denominator variances and can be substituted directly. Even random variations with a zero population mean are generally not completely averaged out in the numerator unless the number of pixels is large.

The edge strength ratio (ESR) averages the edge map over the target rectangle and divides by the background variance:

$$ESR = \frac{1/N_t \sum\sum_{\text{target}} G_{ij}^2}{\sigma_b^2}, \tag{6.176}$$

where the specific algorithms used are usually written

$$G_{ij}^2 = \left\{\frac{1}{3}\sum_{k=1}^{3}\sum_{m=1}^{3} \mathbf{W}_{km} I[(i + k - 1), (j + m - 1)]\right\}^2 + \left\{\frac{1}{3}\sum_{k=1}^{3}\sum_{m=1}^{3} \mathbf{W}'_{km} I[(i + k - 1), (j + m - 1)]\right\}^2 \tag{6.177}$$

and where

$$\mathbf{W} = \begin{bmatrix} 1 & 2 & 1 \\ 0 & 0 & 0 \\ -1 & -2 & -1 \end{bmatrix}, \quad \mathbf{W}' = \begin{bmatrix} 1 & 0 & -1 \\ 2 & 0 & -2 \\ 1 & 0 & -1 \end{bmatrix}. \tag{6.178}$$

A variation on this definition uses the square of the sum of absolute values rather than the sum of squares in Eq. (6.177).

From the analysis of the atmospheric effects on edge enhancement operations given earlier, the following observations can be made. The edge map is multiplied by transmittance and is independent of constant path radiance. Constant transmittance changes have no effect on the metric because the transmittance squared appears in both the numerator and denominator. Ef-

fects of fluctuations can be determined using Eq. (6.160) in the denominator and Eq. (6.173) with the numerator.

The *number of resolvable cells on object* N_0 is a metric that has no obvious transmittance and path radiance effects. However, it is affected by the optical turbulence MTF and, for very large particles, the MTF from forward scattering. The atmosphere thus reduces the sensor resolution by the atmospheric MTF, and fewer resolution elements (which can be larger than single pixel elements) cover the target.

The *normalized entropy* S is defined in terms of the histogram probabilities $P(i)$ discussed earlier as

$$S_t = -\left(\frac{1}{N_i}\right) \sum_{\text{target}} P_t(i) \ln[P_t(i)] \ , \quad S_b = -\left(\frac{1}{N_i}\right) \sum_{\text{background}} P_b(i) \ln[P_b(i)] \ , \tag{6.179}$$

over the target and over the background, where N_i is the number of gray levels. These values are then differenced to provide a measure of texture difference. The atmosphere affects the histograms as discussed earlier. The effect on the entropy measure depends on the methods used. Viewed one way, the atmosphere shifts the intensity boundaries,

$$I_i' = TI_i + I_p \ , \quad i = 1, 2, 3, \ldots \ , \tag{6.180}$$

of the histogram, and the numbers of pixels inside each of these new boundaries remains unchanged. With this transformation, the entropy does not change. However, if the width of the original intensity bins is held fixed, then the atmosphere affects the number of pixels $N(i)$ in each bin, and thus the probabilities scale approximately as

$$(\Delta I)' = T(\Delta I) \ , \quad P'(I) \approx \frac{P(I)}{T} \ , \tag{6.181}$$

so that

$$S' = \frac{S}{T} + \frac{\ln(T)}{TN_i} \ . \tag{6.182}$$

Differences in target and background entropies thus scale as T^{-1}.

Finally, one can consider what happens to the Kolmogorov-Smirnov (KS) statistic used to measure the probability that the target and background metric values are from different distributions. Cumulative statistical distributions $M_t(i)$ and $M_b(i)$ are computed for target and background metrics. For example, the cumulative gray-level histograms of the image or its edge map could be used. The function $D(i)$,

$$D(i) = \left(\frac{N_t N_b}{N_t + N_b}\right)^{1/2} [M_t(i) - M_b(i)] \ , \tag{6.183}$$

is formed, where N_t and N_b are the number of samples (intervals, etc.) in the cumulative distributions. The minimum value $D_{\min}$, maximum value $D_{\max}$, and the maximum absolute value D_{abs} are then used as metrics to determine the distance between the M_t and M_b distributions. If the distance is large, then the target is considered to be different statistically from the background.

If one considers the implications of atmospheric effects on histogram gray levels discussed with respect to Eqs. (6.158) and (6.160), then several possibilities arise in their effects on KS statistics. Assume, for example, that the target and background have the same histogram standard deviations but different means. The cumulative distributions are then fairly parallel near the median points in the cumulative distributions. Constant path radiance simply shifts the cumulative distributions by equal amounts and thus does not affect the statistics. But constant transmittance shifts the distributions to lower intensities by the same fraction but different absolute amounts as well as narrowing the standard deviations by the same multiplicative factor. If there are relatively large fluctuations in transmittance σ_T, however, then the standard deviations can narrow or broaden because then

$$\begin{aligned} \sigma_t' &= [\sigma_t^2(\sigma_T^2 + T^{\text{av}2}) + \sigma_T^2(I_s^{\text{av}} - I_t^{\text{av}})^2]^{1/2} , \\ \sigma_b' &= [\sigma_b^2(\sigma_T^2 + T^{\text{av}2}) + \sigma_T^2(I_s^{\text{av}} - I_b^{\text{av}})^2]^{1/2} . \end{aligned} \tag{6.184}$$

The intensity of the mean path radiance I_s^{av} relative to I_t^{av} of the target and relative to I_b^{av} of the background can produce different positive values in the second term in the brackets.

6.7.2.3 Benefits of Partial Obscuration to Camouflage. A target becomes more difficult to acquire if its contrast, absolute value of temperature difference, or image metric is reduced relative to its background. One method to achieve this end is to give a target a surface that reduces the absolute difference between its average radiance and its background radiance. It can be just as important to alter the target's variance in radiance or texture to more closely match that of the background. This is camouflage. If a target already has a moderately low signature or small metric relative to nontargets in a scene, then it can require only a small amount of obscurant to significantly reduce acquisition probability even if many other objects in the scene can still be discerned.

The last section showed that some operations on images and some image metrics should be unaffected by constant transmittance and constant path radiance changes produced by obscurants. Others were shown to be extremely sensitive to such changes. In all cases, however, introduction of fluctuations or image noise, whether caused directly or indirectly by the atmosphere, target camouflage, background clutter, or sensor noise, can have potentially significant effects.

For example, a constant transmittance reduction by a uniform absorbing obscurant (e.g., a large-area haze of black smoke) was shown not to change the TIR^2 metric. However, the absolute value of the temperature difference of the target relative to its background is reduced. A thermal sensor would thus use gain to attempt to recover that signal. But the effect of gain is to also

increase sensor noise, which can reduce the ability to acquire the target on a display. This apparent paradox is resolved by computing TIR^2 based on the display output rather than based on the direct effect of the atmosphere on the metric alone.

Path radiance from obscurants was also shown to be important. As obscurant is introduced, both the apparent radiance of the target and that of the background approach the obscurant's limiting path radiance I_s. If I_s is close to that of the background terrain or background sky, then the cloud is difficult to see. If the obscurant is very much brighter or very much darker than the range of radiances in the natural scene, then the sensor requires a greater dynamic range and the apparent target and background radiances appear within a smaller radiance range to the detector and on the display.

Fluctuations in obscurant cloud transmittance and path radiance were shown to modify the radiance distributions of targets and backgrounds, and in some cases to modify their variances differently. Such fluctuations thus modify textures and add to confusion.

6.7.3 Use of Obscurants in Deception

Dust and smoke clouds have sometimes been used in deception to mimic the movement or presence of a nonexistent force. For this purpose, it is important to consider how easily the obscurant cloud itself can be seen. In other applications, large-area smoke screens are helpful in enhancing the effectiveness of inexpensive decoys, in breaking tracker lock and, perhaps, luring the tracker away from a low-signature target.

6.7.3.1 EO Detection of Obscurants. In some applications it can be desirable to see an obscurant cloud and in others it can be undesirable. To determine whether an aerosol cloud is detectable one can treat the cloud itself as a target and apply the relevant propagation and target acquisition equations.

The background I_b as seen through the cloud is I_c:

$$I_c = TI_b + (1 - T)I_s \ , \tag{6.185}$$

where T is transmittance and I_s is the path radiance limit. Note that the cloud intensity nearly equals that of its background when the path radiance limit is nearly equal to the background intensity. The maximum absolute contrast of the cloud I_c against its background I_b thus equals the contrast of the path radiance limit I_s against the background (at zero transmittance). If I_s is constant, then cloud contrast linearly decreases in absolute magnitude as transmittance increases:

$$C_c = \frac{I_s - I_b}{I_b}(1 - T) \ . \tag{6.186}$$

As discussed earlier, I_s does in fact change with transmittance, especially for conditions of total obscuration with optical depths greater than about 3 (i.e., below about 5% transmittance). But, for detection of thin clouds or cloud edges against the background, I_s is fairly independent of transmittance.

Sometimes a thin aerosol cloud can still be detected even though its average apparent intensity I_c^{av} equals the average background intensity I_b^{av}. This is caused by the *clutter contrast* produced by the difference between the apparent background clutter seen through the cloud and the unobscured background clutter. The contrast equation for mean values predicts zero contrast in this situation, as seen in Eq. (6.53), and thus predicts that the cloud cannot be detected. However, one can introduce the variance about the mean intensity for both the background clutter and the cloud fluctuations to provide a more general contrast equation.This cannot be done unambiguously, however. One method is to introduce the root-mean-square values of the numerator and denominator in Eq. (6.53):

$$\begin{aligned} C_c &= \frac{\langle |(I_s - I_b)(1 - T)|^2 \rangle^{1/2}}{\langle |I_b|^2 \rangle^{1/2}} \\ &= \left[\frac{(I_s^{av} - I_b^{av})^2 + \sigma_s^2 + \sigma_b^2}{L_b^{av2} + \sigma_b^2} \right]^{1/2} [(1 - T^{av})^2 + \sigma_T^2]^{1/2} . \end{aligned} \tag{6.187}$$

Another possible definition might be

$$\begin{aligned} C_c &= \frac{\langle |(I_s - I_b)(I_s + I_b)| \rangle}{\langle |I_b(I_s + I_b)| \rangle} \langle |(1 - T)|^2 \rangle \\ &= \frac{I_s^{av2} + \sigma_s^2 - I_b^{av2} - \sigma_b^2}{I_b^{av}(I_s^{av} + I_b^{av}) + \sigma_b^2} [(1 - T^{av})^2 + \sigma_b^2]^{1/2} \\ &= \left[\frac{I_s^{av}(I_s^{av} + I_b^{av}) + \sigma_s^2}{I_b^{av}(I_s^{av} + I_b^{av}) + \sigma_b^2} - 1 \right] [(1 - T^{av})^2 + \sigma_b^2]^{1/2} . \end{aligned} \tag{6.188}$$

Both approaches reduce to Eq. (6.186) in magnitude when the variances are zero and both provide a contrast when $L_s^{av} = L_b^{av}$. However, Eq. (6.187) has some deficiencies in that the computed contrast is always positive, so one cannot distinguish when the cloud is lighter or darker than the background. Even worse, when the average intensities are zero and the variances are equal, the contrast from Eq. (6.187) is nonzero. In Eq. (6.188), however, the contrast is negative if the average path radiance and its variance are less than those of the background.

Also, for the case when the cloud and its background have the same mean intensity, Eq. (6.188) becomes:

$$C_c = \frac{\sigma_s^2 - \sigma_b^2}{2I_b^{av2} + \sigma_b^2} [(1 - T^{av})^2 + \sigma_T^2]^{1/2} . \tag{6.189}$$

Thus, the contrast from Eq. (6.188) is negative when the variance in path radiance σ_s^2 is less than that of the background clutter σ_b^2, and the contrast is zero if the cloud and background variances as well as their mean intensities are equal.

A model for detection of an obscurant against its background can be constructed as follows. The scenario is defined, requiring that I_b^{av} and σ_b^2 be known; that I_s be computed from Eq. (6.139) for the illumination, viewing angle, and obscurant optical properties; that σ_s^2 be assigned (usually small or zero); and that σ_T^2 be estimated, perhaps from the fluctuation $f_T \ln(T)$ discussed earlier, or from Table 6.31. One then computes a table of cloud contrast from Eq. (6.188) for different average cloud transmittance values. A scenario-specific model of or estimate for the obscurant plume or puff is then used to determine its apparent size for the different edge transmittances or average transmittances tabulated in the table of cloud contrast. The cloud size is transformed into a spatial frequency f for the observer's distance from the cloud using Eq. (6.145). The cloud will be visible if there is any cloud size in the table of cloud contrasts for which the cloud contrast exceeds the MRC(f) of the sensor, and will not be detectable by that sensor if none of the contrasts exceeds the corresponding MRC(f) contrasts. Although this process seems complicated, it can be implemented with more or less effort depending on how elaborate are the models chosen for the background, the obscurant cloud, and the computation of I_s.

6.7.3.2 Obscurants as Scene Backgrounds. Obscurants are not always applied in front of a target to conceal it. They can also be used to actually enhance target acquisition. By placing the obscurant cloud behind the target, the background clutter can be suppressed and the target contrast enhanced. Obscurants are also excellent for providing range cues and markers. As a target emerges from the obscurant, it is both silhouetted and ranged to by the known location of the cloud.

Acknowledgments

The authors wish to acknowledge Drs. Patti Gillespie, James Gillespie, and Wendell Watkins of the U.S. Army Research Laboratory, Battlefield Environment Directorate, for reviewing the manuscript. Also Mr. Miklos Kiss and Mr. Craig Foster, who were students at New Mexico State University at the time, helped with the numerous figures and tables.

References

1. R. A. Sutherland and R. R. Williams, "The NATO FISSE program: a systematic approach to the evaluation of CCD countermeasures," in *Proceedings of the Smoke/Obscurants Symposium XIII,* Technical Report AMCPM-SMK-T-001-89, pp. 633–644, U.S. Army Aberdeen Proving Ground, MD (1989).
2. R. R. Williams and R. A. Sutherland, "CCD-O: integration for synergism," in *Proceedings of the Smoke/Obscurants Symposium XI,* Technical Report AMCPM-SMK-T-001-87, pp. 595–600, U.S. Army Aberdeen Proving Ground, MD (1987).
3. R. E. Huschke, Ed., *Glossary of Meteorology,* American Meteorological Society, Boston, MA (1970).
4. R. A. Sutherland, D. W. Hoock, and R. B. Gomez, "Objective summary of U.S. Army electro-optical modeling and field testing in an obscuring environment," *Optical Engineering* **22**(1), 2–19 (1983).
5. Robert W. Boyd, *Radiometry and the Detection of Optical Radiation,* Wiley-Interscience, John Wiley & Sons, New York (1983).

6. S. Chandrasekhar, *Radiative Transfer,* Dover, New York (1960).
7. Kuo-Nan Liou, *An Introduction to Atmospheric Radiation,* Academic Press, New York (1980).
8. M. Kerker, *The Scattering of Light and Other Electromagnetic Radiation,* Academic Press, New York (1969).
9. U.S. Department of Agriculture, *Soil Taxonomy,* Soil Conservation Service Handbook 436, U.S. Government Printing Office, Washington, DC (1975).
10. R. A. Sutherland, D. W. Hoock, and R. K. Khanna, "Extinction properties of battlefield fire smokes," in *Proceedings of the Fifth Annual EOSAEL/TWI Conference,* New Mexico State University Physical Sciences Laboratory, Las Cruces (1985).
11. R. G. Pinnick and S. G. Jennings, "Relationships between radiative properties and mass content of phosphoric acid, HC, petroleum oil, and sulfuric acid military smokes," U.S. Army Atmospheric Sciences Laboratory Report ASL-TR-0052, White Sands Missile Range, NM (1980).
12. R. A. Sutherland, "Determination and use of the Hänel growth factor for modeling hygroscopic aerosols," U.S. Army Atmospheric Sciences Laboratory Technical Report, White Sands Missile Range, NM (1983).
13. G. Hänel, "The properties of atmospheric particulates as functions of the relative humidity at thermodynamic equilibrium with the surrounding moist air," in *Advances in Geophysics,* Academic Press, New York (1976).
14. H. R. Carlon, "Infrared extinction spectra of some common liquid aerosols," *Applied Optics* **16,** 1598–1605 (1977).
15. S. G. Jennings, R. G. Pinnick, and H. J. Auvermann, "Effects of particulate complex refractive index and particle size distribution variations on atmospheric extinction and absorption for visible through middle IR wavelengths," *Applied Optics* **17,** 3922–3928 (1978).
16. R. G. Pinnick, G. Fernandez, B. Hinds, C. W. Bruce, R. W. Schaefer, and J. D. Pendleton, "Dust generated by vehicular traffic on unpaved roadways: sizes and infrared extinction coefficients," *Aerosol Science and Technology* **4,** 99–121 (1985).
17. E. M. Patterson and D A. Gillette, "Commonalities in measured size distributions for aerosols having a soil-derived component," *Journal of Geophysical Research* **82,** 2074–2082 (1977).
18. E. M. Patterson, "Atmospheric extinction between 0.55 μm and 10.6 μm due to soil-derived aerosols," *Applied Optics* **16,** 2414–2418 (1977).
19. R. C. Shirkey, R. Sutherland, and M. Seagraves, "EOSAEL 84, volume 3: aerosol phase function data base PFNDAT," U.S. Army Atmospheric Sciences Laboratory Report ASL-TR-0160-3, White Sands Missile Range, NM (1986).
20. R. G. Pinnick, G. Fernandez, and B. D. Hinds, "Explosion dust particle size measurements," *Applied Optics* **22,** 95–102 (1983).
21. R. A. Sutherland and R. H. Khanna, "Optical properties of organic-based aerosols produced by burning vegetation," *Aerosol Science and Technology* **14**(3), 331–342 (1991).
22. D. M. Roessler, F. R. Faxvog, R. Stevenson, and G. W. Smith, "Optical properties and morphology of particulate carbon: variation with air/fuel ratio," General Motors Research Laboratory Report GMR-3467, Warren, MI (1980).
23. D. M. Roessler and F. R. Faxvog, "Optoacoustical measurement of optical absorption in acetylene smoke," *Journal of the Optical Society of America* **69**(12), 1699–1704 (1979).
24. P. Chylek, V. Ramaswamy, R. Cheng, and R. G. Pinnick, "Optical properties and mass concentration of carbonaceous smokes," *Applied Optics* **20**(17), 2980–2985 (1981).
25. C. Helsper, H. J. Fissan, J. Muggli, and A. Scheidweiler, "Particle number distribution of aerosols from test fires," *Journal of Aerosol Science* **11,** 439–446 (1980).
26. G. Mulholland and T. J. Ohlemiller, "Aerosol characterization of a smoldering source," *Aerosol Science and Technology* **1,** 59–71 (1982).
27. C. W. Bruce and N. M. Richardson, "Propagation at 10 μm through smoke produced by atmospheric combustion of diesel fuel," *Applied Optics* **22**(7), 1051–1055 (1983).
28. C. W. Bruce, T. F. Stromberg, K. P. Gurton, and J. B. Mozer, "Trans-spectral absorption and scattering of electromagnetic radiation by diesel soot," *Applied Optics* **30**(12), 1537–1546 (1991).
29. R. G. Pinnick, G. Fernandez, B. D. Hinds, and P. Fishburn, "Fire products and smoke particle size and mass concentration measurements in BIC 3," U.S. Army Atmospheric Sciences Laboratory Internal Report (Sep. 1982).

30. C. W. Bruce and N. M. Richardson, "Millimeter wave gas/aerosol spectrophone and application to diesel smoke," *Applied Optics* **23,** 13–15 (1984).

31. J. D. Klett and R. A. Sutherland, "Effects of moisture in determining obscurant optical properties from field data," in *Proceedings of the 9th Annual EOSAEL/TWI Conference,* New Mexico State University, Las Cruces (Nov. 1988).

32. M. Hale and M. R. Querry, "Optical constants of water in the 200-nm to 200-μm wavelength region," *Applied Optics* **12**(3), 555–562 (1973).

33. M. R. Querry, "Optical constants," U.S. Army Chemical Research, Development and Engineering Center Technical Report CRDC-CR-85034, Aberdeen Proving Ground, MD (1985).

34. M. R. Querry, "Optical constants of minerals and other materials from the millimeter to ultraviolet wavelengths," U.S. Army Chemical Research, Development and Engineering Center Technical Report CRDEC-CR-8809, Aberdeen Proving Ground, MD (1987).

35. W. G. Egan and T. W. Hilgeman, *Properties of Inhomogeneous Materials,* Academic Press, New York (1979).

36. O. B. Toon, J. B. Pollack, and C. Sagan, "Physical properties of the particles composing the Martian dust storm of 1971–1972," *Icarus* **30,** 663–696 (1977).

37. F. E. Volz, "Infrared optical constants of ammonium sulphate, Sahara dust, volcanic pumice, and flyash," *Applied Optics* **12,** 564–568 (1973).

38. J. B. Pollack, O. B. Toon, and B. N. Khare, "Optical properties of some terrestrial rocks and glasses," *Icarus* **19,** 372–389 (1973).

39. M. R. Querry, G. Osborne, K. Lies, R. Jordan, and M. Coveney, Jr., "Complex refractive index of limestone in the visible and infrared," *Applied Optics* **17**(3), 353–356 (1978).

40. J. T. Peterson and J. A. Weinman, "Optical properties of quartz dust particles at infrared wavelengths," *Journal of Geophysical Research* **74**(28), 6947–6952 (1969).

41. American Institute of Physics, *American Institute of Physics Handbook,* McGraw-Hill, New York (1972).

42. G. Mie, *Annalen der Physik* **25,** 377 (1908).

43. C. F. Bohren and D. R. Huffman, *Absorption and Scattering of Light by Small Particles,* John Wiley & Sons, New York (1983).

44. H. C. Van de Hulst, *Light Scattering by Small Particles,* Dover, New York (1981).

45. M. E. Milham and D. H. Anderson, *Obscuration Sciences Smoke Data Compendium: Standard Smokes,* U.S. Army Chemical Research and Development Center Report ARCSL-TR-82024, Aberdeen Proving Ground, MD (1983).

46. D. W. Hoock, "Computational models for battlefield dust clouds," in *Proceedings of the Battlefield Dust Environment Symposium II,* K. S. Long, Ed., U.S. Army Corps of Engineers, Waterways Experiment Station, Vicksburg, MS (Oct. 1985).

47. C. W. Bruce, S. B.Crow, Y. P. Yee, B. D. Hinds, D. Marlin, and A. V. Jelinek, "Infrared optical properties of diesel smoke plumes," *Applied Optics* **28**(19), 4071–4076 (1989).

48. J. A. Weinman, Harshvardhan, and W. S. Olson, "Infrared radiation emerging from smoke produced by brush fires," *Applied Optics* **20**(2), 199–206 (1981).

49. A. J. Eccleston, N. K. King, and D. R. Packham, "The scattering coefficient and mass concentration of smoke from some Australian forest fires," *Journal of the Air Pollution Control Association* **24**(11), 1047–1050 (1974).

50. J. D. Klett and R. A. Sutherland, "Approximate methods for modeling the scattering properties of non-spherical particles: evaluation of the WKB method," *Applied Optics* **31**(3), 373–386 (1992).

51. A. Ishimaru, *Wave Propagation and Scattering in Random Media,* Academic Press, New York (1978).

52. A. Zardecki, S. A. Gerstl, and R. Shirkey, "EOSAEL 84, vol. 20: approximate multiple scattering module ASCAT," U.S. Army Atmospheric Sciences Laboratory Technical Report ASL-TR-0160-20, White Sands Missile Range, NM (1984).

53. R. C. Shirkey, R. A. Sutherland, and M. A. Seagraves, "EOSAEL 84, vol. 3: aerosol phase function data base PFNDAT," U.S. Army Atmospheric Sciences Laboratory, Technical Report ASL-TR-0160-3, White Sands Missile Range, NM (1986).

54. W. G. Tam and A. Zardecki, "Laser beam propagation in particulate media," *Journal of the Optical Society of America* **69,** 68 (1979).

55. W. G. Tam and A. Zardecki, "Multiple scattering corrections to the Beer-Lambert law. 1. Open detector," *Applied Optics* **21,** 2405 (1982).
56. A. Zardecki and W. G. Tam, "Multiple scattering corrections to the Beer-Lambert law. 2. Detector with a variable field of view," *Applied Optics* **21,** 2413 (1982).
57. L. S. Dolin, *Izvestiya Vysshikh Uchebnykh Zavedenni, Radiofizika* **9,** 61 (1966).
58. R. L. Fante, *Journal of the Optical Society of America* **64,** 592 (1974).
59. J. W. Goodman, *Statistical Optics,* John Wiley & Sons, New York (1985).
60. M. F. Barnsley, R. L. Devaney, B. B. Mandelbrot, H.-O. Peitgen, D. Saupe, and R. F. Voss, in *The Science of Fractal Images,* H.-O. Peitgan and D. Saupe, Eds., Springer Verlag, New York (1988).
61. D. W. Hoock, "Modeling time-dependent obscuration for simulated imaging of dust and smoke clouds," in *Characterization, Propagation, and Simulation of Sources and Backgrounds, Proceedings of the SPIE* **1486,** 164–175 (1991).
62. H. C. Van de Hulst, *Multiple Scattering Tables, Formulas, and Applications, Vols. 1 and 2,* Academic Press, New York (1980).
63. S. Chandrasekhar, *Radiative Transfer,* Dover, New York (1960).
64. R. A. Sutherland, "Determination and use of the Chandrasekhar-Van de Hulst "F" and "G" functions extended to anisotropic scattering," Atmospheric Sciences Laboratory Technical Report ASL-TR-0238, White Sands Missile Range, NM (1989).
65. M. Abramowitz and I. Stegun, *Handbook of Mathematical Functions,* Dover, New York (1970).
66. R. A. Sutherland and B. W. Fowler, "Standards for large area screening systems (LASS) modeling," Joint Technical Coordinating Group for Munitions Effectiveness (JTCG/ME) Special Report 61 JTCG/ME 85.4 (1985).
67. R. A. Sutherland, "Methods of radiative transfer for electro-optical obscuration modeling," in *Proceedings of the 1988 Army Science Conference,* Ft. Monroe, VA (Oct. 1988).
68. A. Miller and R. A. Sutherland, "Verification of the multiple scattering model AGSCAT for the Henyey-Greenstein phase function," Atmospheric Sciences Laboratory Technical Report ASL-TR, in preparation (1993).
69. K. N. Liou, *An Introduction to Atmospheric Radiation,* Academic Press, New York (1980).
70. R. R. Williams and R. A. Sutherland, "CCD-O: integration for synergism," in *Proceedings of Smoke/Obscurants Symposium XI,* Technical Report AMCPM-SMK-T-001-87, pp. 595–600 (1987).
71. R. A. Sutherland and R. R. Williams, "The NATO FISSE program: a systematic approach to the evaluation of CCD countermeasures," in *Proceedings of Smoke/Obscurants Symposium XIII,* Technical Report AMCPM-SMK-T-001-89, pp. 633–644 (1989).
72. W. E. K. Middleton, *Vision Through the Atmosphere,* University of Toronto Press, Canada (1963).
73. S. Q. Duntley, "The reduction of apparent contrast by the atmosphere," *Journal of the Optical Society of America* **38,** 179–191 (1948).
74. R. A. Sutherland and B. W. Fowler, "Standards for large area screening systems (LASS) modeling," Joint Technical Coordinating Group for Munitions Effectiveness (JTCG/ME) Special Report 61 JTCG/ME 85.4 (1985).
75. J. M. Lloyd, *Thermal Imaging Systems,* Plenum, New York (1975).
76. R. A. Sutherland and B. W. Fowler, "Standards for large area screening systems modeling," U.S. Joint Technical Coordinating Group for Munitions Effectiveness Special Publication 61 JTCG/ME 85.4 (1985).
77. M. Danard, "Proposed bulk mesoscale models for the atmospheric boundary layer," U.S. Army Atmospheric Sciences Laboratory Contractor Technical Report DAAD07-83-C-0126 (Apr. 1984).
78. F. V. Hansen, "Engineering estimates for calculating atmospheric dispersion coefficients," U.S. Army Atmospheric Sciences Laboratory Internal Report (Nov. 1979).
79. R. A. Sutherland, F. V. Hansen, and W. D. Bach, "A quantitative method for estimating Pasquill stability class from windspeed and sensible heat flux density," *Boundary Layer Meteorology* **37,** 357–369 (1986).
80. A. S. Smedman-Hogstrom and V. Hogstrom, "A practical method for determining wind frequency distributions in the lowest 200 meters from routine meteorological data," *Journal of Applied Meteorology* **17,** 942–954 (1978).

81. C. D. MacArthur and P. A. Haines, "The roughness lengths associated with regions of heterogeneous vegetation and elevation," U.S. Army Atmospheric Sciences Laboratory Contractor Report ASL-CR-82-0206-1 (May 1982).

82. F. Pasquill, *Atmospheric Diffusion,* 2nd ed., John Wiley & Sons, New York (1974).

83. S. G. Hanna, G. Briggs, and R. Hosker, *Handbook on Atmospheric Diffusion,* DOE/TIC-11223, Technical Information Center, U.S. Department of Energy, Washington, DC (1982).

84. B. Turner, "A diffusion model for an urban area," *Journal of Applied Meteorology* **3,** 83–91 (1964).

85. F. B. Smith, "The relation between Pasquill stability and Kazanski-Monin stability (in neutral conditions)," *Atmospheric Environment* **13,** 879–881 (1979).

86. R. A. Sutherland, "Determination and use of the Hänel growth factor for modeling hygroscopic aerosols," U.S. Army Atmospheric Sciences Laboratory Internal Report (1983).

87. G. Hänel, "The properties of atmospheric particulates as functions of relative humidity at thermodynamic equilibrium with the surrounding moist air," in *Advances in Geophysics,* E. H. Lansburg and J. Van Miefhen, Eds., Academic Press, New York (1976).

88. K. Kondratyev, *Radiation in the Atmosphere,* Academic Press, New York (1969).

89. J. E. Selby, F. X. Kneizys, J. H. Chetwood, and R. A. McClatchey, "Atmospheric transmittance/radiance: computer code LOWTRAN4," U.S. Air Force Geophysics Laboratory Technical Report AFGL-TR-0053 (1978).

90. S. B. Idso, "A set of equations for full spectrum 8–14 μm and 10.5–12.5 μm thermal radiation from cloudless skies," *Water Resources Research* **17,** 295–304 (1981).

91. D. B. Hodges, G. J. Higgens, P. F. Hilton, R. E. Hood, R. Shapiro, C. N. Youart, and R. F. Wachtmann, "Final tactical decision aid (FTDA) for infrared (8–12 μm) systems—technical background," U.S. Air Force Geophysics Laboratory Technical Report AFGL-TR-83-0022 (1983).

92. H. R. Pruppacher and J. D. Klett, *Microphysics of Clouds and Precipitation,* D. Reidel, Dordrecht, Holland (1978).

93. R. J. Lind and K. B. Katsaros, "A model of longwave irradiance for use with surface observations," *Journal of Applied Meteorology* **21,** 1015–1023 (1982).

94. D. W. Hoock, "Modeling path radiance effects from aerosol clouds," in *Optical, Infrared and Millimeter Wave Propagation Engineering, Proceedings of the SPIE* **926,** 185–194 (1988).

95. H. C. Van de Hulst, *Multiple Light Scattering, Tables, Formulas and Applications,* Vols. 1 and 2, Academic Press, New York (1980).

96. J. M. Lloyd, *Thermal Imaging Systems,* Plenum Press, New York (1975).

97. W. E. Middleton, *Vision Through the Atmosphere,* University of Toronto Press, Canada (1963).

98. D. W. Hoock, "Detectability and simulation of smoke and dust clouds in images," in *Propagation Engineering: Third in a Series, Proceedings of the SPIE* **1312,** 298–309 (1990).

99. Zu-Han Gu and Sing H. Lee, "Recognition of images of Markov-1 model by least squares linear mapping technique," *Applied Optics* **23,** 822–827 (1984).

100. D. W. Hoock and J. C. Giever, "Accounting for the atmosphere in extrapolating system performance to different environments," in *Propagation Engineering, Proceedings of the SPIE* **1115,** 308–319 (1989).

Index